

# KURRI

# Progress Report

# 2014

*The Research Reactor Institute, Kyoto University*

# **KURRI Progress Report 2014**

APRIL 2014 – MARCH 2015

*Published by  
The Research Reactor Institute, Kyoto University,  
Kumatori-cho, Sennan-gun, Osaka 590-0494, Japan*

## Preface

It is a great pleasure for us to publish the KURRI Progress Report 2014. This report contains all of the accomplishments of research and related activities at the Research Reactor Institute, Kyoto University (KURRI) during the fiscal year 2014 from April 2014 to March 2015

The institute was established in 1963 for the joint use program among Japanese universities to promote experimental research and education in the fields of nuclear energy and radiation application. The main facility, called the Kyoto University research Reactor (KUR), has been widely used for various experiments since its first criticality in 1964. It has been successfully operated, and has served as one of the most useful inter-university research reactors in our country. The Kyoto University Critical Assembly (KUCA), accelerators and other research facilities are also open to researchers and students for their experiments.

In the past fiscal year, KUR was subjected to some facility refurbishments and operated for 360 hours, while KUCA was not operated. In total, we accepted 3,628 man-day researchers and students for using research facilities and for attending scientific meetings held at KURRI. A large number of research subjects has been enrolled, which covers various fields of nuclear science and technology, material science, radiation life science and radiation medical science. It is noted that 30 patients have been treated in the clinical studies of the boron neutron capture therapy (BNCT) using KUR in this period. The results of these activities are given in this report.

Some special research projects are in progress at KURRI. One is the project on the Accelerator Driven System (ADS) by using a Fixed Field Alternating Gradient (FFAG) accelerator combined with KUCA. The world's first ADS experiment has been successfully conducted on March 2009, and the 150 MeV proton beam is being provided for the ADS experiment and for the related studies including development of target materials. In another project, the world's first clinical trial of the BNCT is being promoted using a proton accelerator, based on the successful clinical studies using KUR. Such leading research activities as well as educational activities at the institute are highly rated in a recent external evaluation.

Efficient utilization of nuclear energy and radiation is expected to provide solutions to maintain, sustain and even to develop human society. However, it is now required to again ensure the safety of nuclear energy for its continued use. With the joint use of such research resources as reactors and accelerators, our program is thus to strengthen the scientific basis for improved safety and to promote leading research toward efficient utilization of multidisciplinary nuclear science and technology. Our program also emphasizes the importance of experimental education for fostering young people in the related fields.

The high standing of the institute in research and related activities relies on the enthusiasm and dedication of all the participants. Details of their work and achievements during the year are given in the following pages. I am grateful to all of my colleagues who have taken time to prepare this report, and thank them for their cooperation. Also, I would like to express my sincere thanks for the continued support from the national and local governments, scientific communities and residents in the neighborhood of KURRI.

Kumatori, June 14, 2015

Yuji Kawabata  
Director, KURRI

## CONTENTS

<b>I. ANNUAL SUMMARY OF EXPERIMENTAL RESEARCH ACTIVITIES</b> .....	1
<b>I-1. PROJECT RESEARCHES</b> .....	2
<b>Project 1</b> Analyzing Tumor Microenvironment and Exploiting its Characteristics for Controlling Malignant Solid Tumors and Distant Metastatic Potential S. Masunaga (26P1) .....	3
<b>PR1-1</b> Significance of Fractionated Thalidomide Administration Combined with $\gamma$ -Ray Irradiation from the Viewpoint of Local Tumor Response and Lung Metastasis S. Masunaga <i>et al.</i> (26P1-1) .....	4
<b>PR1-2</b> Development of Nuclear-targeting Boron Carriers Based on the Chemistry of Direct Cell-penetrating Peptides A. Isono <i>et al.</i> (26P1-2) .....	5
<b>PR1-3</b> Genetic Screening of Upstream Activators of Hypoxia-inducible Factor 1 for the Development of Novel Anti-cancer Strategies H. Harada <i>et al.</i> (26P1-3) .....	6
<b>PR1-4</b> Quantitative Detection of Metastasized B16BL6 Cells in Lung by Using TaqMan RT-PCR Assay T. Nagasaki <i>et al.</i> (26P1-6) .....	7
<b>PR1-5</b> Response of Tumor Cells to BNCT S. Imamichi <i>et al.</i> (26P1-9) .....	8
<b>PR1-6</b> Additive effect of Gadolinium to Cell Survival Analysis for Neutron Capture Therapy K. Nakai <i>et al.</i> (26P1-10) .....	9
<b>Project 2</b> Direct Observation of the Proton or Protonation in a Protein Molecule by Neutron and High Resolution X-ray Joint Analysis Y. Morimoto (26P2) .....	10
<b>PR2-1</b> Degradation Control and Structural Motion of the 20S/26S Proteasome Elucidated by Genetic Mutation and Atomic Force Microscope T. Murakami <i>et al.</i> (26P2-1) .....	11
<b>PR2-2</b> Development of Improved Techniques for Neutron Biology T. Chatake <i>et al.</i> (26P2-2) .....	12
<b>PR2-3</b> Identification and Characterization of Proteolytic Enzymes Derived from <i>NephilaClavata</i> Y. Hidaka <i>et al.</i> (26P2-3) .....	13
<b>Project 3</b> Project Research on the New Applicant Development Using the Characteristics of the Particles from the Neutron Capture Reaction K. Kinashi (26P3) .....	14
<b>PR3-1</b> The Effect of Ascorbic Acid on the HPRT Mutation Induction after the Neutron Irradiation Y. Kinashi <i>et al.</i> (26P3-1) .....	15
<b>PR3-2</b> Analysis of DNA Double Strand Breaks in the Mammalian Cells Induced by BNCR S. Takahashi <i>et al.</i> (26P3-2) .....	16
<b>Project 4</b> Project Research on Development of Scattering Spectrometers Utilizing Small and Medium Class Neutron Source M. Sugiyama (26P4) .....	17
<b>PR4-1</b> KUR-SANS Observations and Analyses of Surfactants' Nano-structural Change by Capturing Heavy Metal K. Hara <i>et al.</i> (26P4-5) .....	18
<b>Project 5</b> Behavior of Radioactive Nuclides in Intense Radiation Fields in Accelerator Facilities Y. Oki (26P5) .....	19
<b>PR5-1</b> Radioactivity Size Distribution of Airborne Aerosols Formed in Target Room Estimated from Number Size Distribution S. Yokoyama <i>et al.</i> (26P5-1) .....	20

<b>PR5-2</b>	Production of Airborne Nano-Particles by Proton Irradiation in an FFAG Accelerator Y. Oki <i>et al.</i> (26P5-2) .....	21
<b>PR5-3</b>	Corrosion of Various Metals in Water and Formation of Metal-related Colloidal Particles under Intense Photon-Raiation Field K. Bessho <i>et al.</i> (26P5-3) .....	22
<b>Project 6</b>	Irradiation Effects on Nuclear Advanced Materials Irradiated by Particles with High Energy Q. Xu (26P6) .....	23
<b>PR6-1</b>	Compensation Mechanism of DX-like Center in Neutron Transmutation Doped GaN K. Kuriyama <i>et al.</i> (26P6-1) .....	24
<b>PR6-2</b>	Neutron Irradiation Effects of Superconducting Magnet Materials at Low Temperature T. Nakamoto <i>et al.</i> (26P6-2) .....	25
<b>PR6-3</b>	Study on Fine Structures Formed by High Energy Particle Irradiation A. Kinomura <i>et al.</i> (26P6-3) .....	26
<b>PR6-4</b>	Thermoluminescence of Synthesized Calcite T. Awata <i>et al.</i> (26P6-4) .....	27
<b>PR6-5</b>	Electron irradiation on W around 500°C using KURRI-LINAC M. Akiyoshi <i>et al.</i> (26P6-5) .....	28
<b>PR6-6</b>	The Development of New Positron Beam System Using KUR Y. Nagai <i>et al.</i> (26P6-6) .....	29
<b>PR6-7</b>	Radiation Damage in Bulk Amorphous Alloys by Electron Irradiation F. Hori <i>et al.</i> (26P6-7) .....	30
<b>PR6-8</b>	Positron Annihilation Study of Fe-Cr Alloys After Neutron Irradiation in KUR R. Kasada <i>et al.</i> (26P6-10) .....	31
<b>PR6-9</b>	Positron Annihilation Lifetime Measurements of Austenitic Stainless Steels Irradiated in the SINQ Target Irradiation Program K. Sato <i>et al.</i> (26P6-12) .....	32
<b>PR6-10</b>	Effects of High Energy Particle Irradiation on Hydrogen Retention in Refractory Metals K. Tokunaga <i>et al.</i> (26P6-13) .....	33
<b>PR6-11</b>	Depenedence of Cellular Structure Formation on Ion Species N. Nitta <i>et al.</i> (26P6-14) .....	34
<b>Project 8</b>	Development on Neutron Imaging Application Y. Saito (26P8) .....	35
<b>PR8-1</b>	Dynamic Observation of Two-Phase Flow Using Neutron Radiography Y. Saito <i>et al.</i> (26P8-1) .....	36
<b>PR8-2</b>	Quantitative Measurement of Adsorbed Ethanol Amount in Activated Carbon Adsorber for Adsorption Heat Pump H. Asano <i>et al.</i> (26P8-2) .....	37
<b>PR8-3</b>	Neutron Radiography on Tubular Flow Reactor for Supercritical Hydrothermal Synthesis of Nanoparticles T. Tsukada <i>et al.</i> (26P8-3) .....	38
<b>PR8-4</b>	Neutron Imaging and Optics Development Using Simulation of VCAD Systems Y. Yamagata <i>et al.</i> (26P8-5) .....	39
<b>PR8-5</b>	Evaluation of the Moisture Movement in High-Performance Concrete Subjected to Heating M. Kanematsu <i>et al.</i> (26P8-10) .....	40
<b>PR8-6</b>	Effect of Gravity on Coolant Distribution in FGHP Heat Spreader K. Mizuta <i>et al.</i> (26P8-11) .....	41
<b>PR8-7</b>	Study on Visualization of Organic Materials between Metals for Advance of Industrial Products K. Hirota <i>et al.</i> (26P8-12) .....	42
<b>PR8-8</b>	Visualization of Flow Inside Fine Scale Wick of Heat Pipe Y. Tsuji <i>et al.</i> (26P8-13) .....	43
<b>Project 10</b>	Project Research on the Elucidation of Generating Mechanism of Damaged Protein Induced by Aging and Irradiation N. Fujii (26P10) .....	44

<b>PR10-1</b>	Detection of D-Aspartyl Endopeptidases Activity in Floral Tissues of Broccoli ( <i>Brassica oleracea</i> var. <i>Italica</i> ) T. Kinouchi <i>et al.</i> (26P10-1) .....	45
<b>PR10-2</b>	Damage to Biological Molecules Induced by Ionizing Irradiation and Biological Defense Mechanisms against Ionizing Radiation I T. Saito <i>et al.</i> (26P10-2) .....	46
<b>PR10-3</b>	Analysis of Aspartate Isomerization Using Protein L-Isoaspartyl Methyltransferase (PIMT) Y. Sadakane <i>et al.</i> (26P10-3) .....	47
<b>PR10-4</b>	Analysis of Imbalance in Mice Exposed to Environmental Stress N. Ohgami <i>et al.</i> (26P10-4) .....	48
<b>PR10-5</b>	Identification of Biologically Uncommon $\beta$ -aspartyl Residues in Proteins Using MS N. Fujii <i>et al.</i> (26P10-5) .....	49
<b>PR10-6</b>	Side Chain Conformers of Aspartyl Isomers in Crystallin Mimic Peptide K. Aki <i>et al.</i> (26P10-6) .....	50
<b>PR10-7</b>	Rapid survey of Asp isomers in disease-related proteins by LC-MS/MS combined with Commercial Enzymes H. Maeda <i>et al.</i> (26P10-7) .....	51
<b>Project 11</b>	Studies on Actinides and Fission Products Performed at the KURRI Hot Laboratory T. Fujii (26P11) .....	52
<b>PR11-1</b>	Apparent Formation Constant of Metal Ions with Humic Substances; Modelling T. Sasaki <i>et al.</i> (26P11-1) .....	53
<b>PR11-2</b>	Temperature Effect on the Solubility and Solid Phase of Tetravalent Metal Hydroxide T. Kobayashi <i>et al.</i> (26P11-2) .....	54
<b>PR11-3</b>	Research on The Behavior of Actinides and FPs in Fuel Debris N. Sato <i>et al.</i> (26P11-3) .....	55
<b>PR11-4</b>	Effect on Borosilicate Glass Structure by Neutron Irradiation T. Nagai <i>et al.</i> (26P11-4) .....	56
<b>PR11-5</b>	Ligand Exchange of Uranium (IV) Chloro- and Fluoro- Complexes in High Temperature Molten NaCl-CsCl Eutectic A. Uehara <i>et al.</i> (26P11-5) .....	57
<b>PR11-6</b>	Evaluation of Parameters Governing Anodic Dissolution of U-Zr Alloy in Molten LiCl-KCl M. Iizuka <i>et al.</i> (26P11-6) .....	58
<b>PR11-7</b>	Electrochemistry and Structural Analysis of Cations in Molten Sub-halide Systems: Fluoride Addition Effect on Voltammograms and UV-vis Spectra of Neodymium Cation in Molten Chlorides H. Matsuura <i>et al.</i> (26P11-7) .....	59
<b>PR11-8</b>	Polarization Effect of Chloride Ions on Uranyl Ion in Molten LiCl N. Ohtori <i>et al.</i> (26P11-8) .....	60
<b>PR11-9</b>	Study of Isotope Separation of Strontium and Calcium via Chemical Exchange Reaction R. Hazama <i>et al.</i> (26P11-10) .....	61
<b>PR11-10</b>	Experimental and Calculated Optical Properties of Molten Aluminium Chloride Melts T. Goto <i>et al.</i> (26P11-11) .....	62
<b>PR11-11</b>	Precipitation Behavior of Trivalent Dysprosium Ion by Reaction with Oxide Ion in CaCl <sub>2</sub> -LiCl Molten Salt H. Sekimoto <i>et al.</i> (26P11-12) .....	63
<b>PR11-12</b>	Elucidation of the Uptake Route of Radionuclides in Deciduous and Coniferous Trees Using Radio Cesium and Radio Potassium in Annual Tree Rings T. Ohta <i>et al.</i> (26P11-13) .....	64
<b>PR11-13</b>	Photon activation analysis of alkali earth elements and arsenic with bremsstrahlung at the KURRI-LINAC T. Kubota <i>et al.</i> (26P11-14) .....	65
<b>PR11-14</b>	Study of Applicability of Isotopic Ratio Measurement for Analysis of Radionuclide in Environmental Samples Y. Shibahara <i>et al.</i> (26P11-15) .....	66
<b>PR11-15</b>	Tracing Halogen and Noble Gas Recycling in the Northern Izu Subduction Zone by Neutron Irradiation and Noble Gas Mass Spectrometry H. Sumino <i>et al.</i> (26P11-16) .....	67

<b>PR11-16</b>	Volcanic and Tectonic History of Philippine Sea Plate (South of Japan) Revealed by $^{40}\text{Ar}/^{39}\text{Ar}$ Dating Technique O. Ishizuka <i>et al.</i> (26P11-17) .....	68
<b>PR11-17</b>	Ar–Ar Age Determination of Minamitorishima N. Hirano <i>et al.</i> (26P11-18) .....	69
<b>Project 12</b>	Project Research on Nuclear Spectroscopy and Condensed Matter Physics Using Short-Lived Nuclei Y. Ohkubo (26P12) .....	70
<b>PR12-1</b>	$\beta^-$ Decay of $^{150}\text{Ce}$ to $^{150}\text{Pr}$ Y. Kojima <i>et al.</i> (26P12-3) .....	71
<b>PR12-2</b>	Interaction between He and Elements with $A = 140$ in Fe Y. Ohkubo <i>et al.</i> (26P12-4) .....	72
<b>PR12-3</b>	Atmosphere Dependence of Stability of Local Fields in Al-Doped ZnO S. Komatsuda <i>et al.</i> (26P12-5) .....	73
<b>PR12-4</b>	Extranuclear Dynamic Motion of $^{111}\text{Cd}$ ( $\leftarrow^{111}\text{Ag}$ ) Doped in AgI Nanoparticles W. Sato <i>et al.</i> (26P12-6) .....	74
<b>Project 13</b>	Project Research on the Advanced Utilization of Multi-Element Mössbauer Spectroscopy for the Study of Condensed Matter M. Seto (26P13) .....	75
<b>PR13-1</b>	Magnetism of an iron oxynictide Cr-doped CeFePO T. Okano <i>et al.</i> (26P13-2) .....	76
<b>PR13-2</b>	A study of Formation of Au(III) Surface Complex on Manganese Dioxide by $^{197}\text{Au}$ Mössbauer Spectroscopy T. Yokoyama <i>et al.</i> (26P13-3) .....	77
<b>PR13-3</b>	Mössbauer Spectroscopy of Novel Ferroelectric Materials S. Nakamura <i>et al.</i> (26P13-5) .....	78
<b>PR13-4</b>	Mössbauer Spectra of Oriented Thin Sections and Small Grain of Magnetite Single Crystal T. Kamiryo <i>et al.</i> (26P13-6) .....	79
<b>PR13-5</b>	Electronic States of Negative/Zero Thermal Expansion Materials I. Yamada <i>et al.</i> (26P13-7) .....	80
<b>PR13-6</b>	Mössbauer Study of Fe-Based Superconductors, $\text{Ba}_{1-x}\text{K}_x\text{Fe}_2\text{As}_2$ S. Kitao <i>et al.</i> (26P13-7) .....	81
<b>Project 14</b>	Translational Research on BNCT for Clinical Application M. Suzuki (26P14) .....	82
<b>PR14-1</b>	Boron Neutron Capture Therapy for Radiation-induced Osteosarcoma from the Skull S. Miyatake <i>et al.</i> (26P14-4) .....	83
<b>PR14-2</b>	Clinical Studies on BNCT for 6 Cases of Head and Neck Cancer I. Kato <i>et al.</i> (26P14-5) .....	84
<b>PR14-3</b>	Boron Uptake in Tumour of Local Recurred Breast Cancer by $^{18}\text{F}$ -BPA Positron Emission Tomography for Application to Boron Neutron Capture Therapy H. Yanagie <i>et al.</i> (26P14-8) .....	85
<b>PR14-4</b>	High Boron-Accumulated Liposomes as Efficient Boron Carriers for Neutron Capture Therapy H. Nakamura <i>et al.</i> (26P14-16) .....	86
<b>PR14-5</b>	Boron Carbide Particle as a Boron Compound for BNCT in vivo S Tada <i>et al.</i> (26P14-18) .....	87
<b>PR14-6</b>	Boron Neutron Capture Therapy Selectively Destroys Human Clear Cell Sarcoma (CCS) Metastasis to Lung in CCS-bearing Animal Model T. Fujimoto <i>et al.</i> (26P14-19) .....	88
<b>PR14-7</b>	Nanoparticle-assisted Boron Neutron Capture Therapeutics: Design of Novel Boron-containing Nanoparticle for ROS Scavenging Ability Improving Therapeutic Efficiency with Low Adverse Effect Z. Gaoa <i>et al.</i> (26P14-20) .....	89
<b>PR14-8</b>	Evaluation of Component in WOW Emulsion as Intra-arterial Boron Delivery Carrier for Neutron Capture Therapy to Hepatocellular Carcinoma H. Yanagie <i>et al.</i> (26P14-22) .....	90

<b>PR14-9</b>	Establishment of QA/QC Using Ionization Chamber and Bonner Sphere in BNCT Field H. Ueda <i>et al.</i> (26P14-26) .....	91
<b>PR14-10</b>	Study on the Real-time dose Monitor System Using Prompt Gamma Rays or Boron Neutron Capture Therapy H. Tanaka <i>et al.</i> (26P14-27) .....	92
<b>PR14-11</b>	Quality Assurance of Irradiation Field for BNCT Using Twin Imaging Plate System K. Tanaka <i>et al.</i> (26P14-28) .....	93
<b>PR14-12</b>	Development and Evaluation of 3D Polymer Gel Dosimeter for the Measurement of dose Distribution in BNCT S. Hayashi <i>et al.</i> (26P14-29) .....	94
<b>I-2. COLLABORATION RESEARCHES</b> .....		95
<i>1. Slow Neutron Physics and Neutron Scattering</i>		
<b>CO1-1</b>	Analysis of Heavy Metal Elements in Chinese Medicine and Herbs E. Furuta <i>et al.</i> (26001) .....	96
<b>CO1-2</b>	Status Report 2014 for B-3 Beam Port of KUR K. Mori <i>et al.</i> (26007) .....	97
<b>CO1-3</b>	Synthesis of Metal Nanoparticles under the Gamma-ray Irradiation Field F. Hori <i>et al.</i> (26010) .....	98
<b>CO1-4</b>	The Role of Human Oxidation Resistance 1 (OXR1) in Cellular Response to Radiation A. Matsui <i>et al.</i> (26018) .....	99
<b>CO1-5</b>	Development of an Advanced Optical Fiber Type Neutron Detector K. Watanabe <i>et al.</i> (26021) .....	100
<b>CO1-6</b>	Focusing Test of an Ellipsoidal Neutron Mirror with a Metal Substrate M. Hino <i>et al.</i> (26065) .....	101
<b>CO1-7</b>	Examination of the Usefulness as the New Boron Compound of KA-BSH for Born Neutron Capture Therapy G. Fitamura <i>et al.</i> (26078) .....	102
<i>2. Nuclear Physics and Nuclear Data</i>		
<b>CO2-1</b>	Development of Measurement Method for Epi-Thermal Neutrons Using the $^{10}\text{B}(n,\alpha\gamma)$ Reaction T. Matsumoto <i>et al.</i> (26055) .....	103
<b>CO2-2</b>	Measurement of Gamma Ray and Neutron Spectrum of Curium Isotope (3) Y. Nauchi <i>et al.</i> (26057) .....	104
<b>CO2-3</b>	Development of Hybrid Ce:LiCAF Scintillator for Nuclear Data Measurement T. Fujiwara <i>et al.</i> (26058) .....	105
<b>CO2-4</b>	Investigation of Variable Neutron Field for Accurate Determination of Thermal Neutron Capture Cross Section at KURRI-LINAC J. Hori <i>et al.</i> (26069) .....	106
<b>CO2-5</b>	Experimental Study on Non-destructive Assay with a Pulsed Neutron Source J. Hori <i>et al.</i> (26070) .....	107
<i>3. Reactor Physics and Reactor Engineering</i>		
<b>CO3-1</b>	Development of In-reactor Observation System Using Cherenkov Light (VI) T. Takeuchi <i>et al.</i> (26040) .....	108
<b>CO3-2</b>	Neutron Irradiation Effect of High-density MoO <sub>3</sub> Pellets for Mo-99 Production (2) K. Nishikata <i>et al.</i> (26041) .....	109
<i>4. Material Science and Radiation Effects</i>		
<b>CO4-1</b>	Development of Radiation Tolerant Image Sensor with Field Emitter Array Y. Gotoh <i>et al.</i> (26002) .....	110
<b>CO4-2</b>	Sub-terahertz Absorption of Ionic Liquid T. Awano <i>et al.</i> (26015) .....	111
<b>CO4-3</b>	Generation of Circular Polarization using Linearly Polarized Coherent Transition Radiation T. Takahashi <i>et al.</i> (26016) .....	112



<b>CO4-4</b>	Basic Study on Radiation-induced Luminescence from Natural Mineral H. Fujita <i>et al.</i> (26027) .....	113
<b>CO4-5</b>	Complex Structure of Ions Coordinated with Hydrophilic Polymer. 15. Applied Discussion with Ionic Behavior in Hydrophobic Matrixes A. Kawaguchi <i>et al.</i> (26052) .....	114
<b>CO4-6</b>	Elucidation of Tritium Dynamics in Neutron Irradiated Tungsten Y. Oya <i>et al.</i> (26063) .....	115
<b>5. Geochemistry and Environmental Science</b>		
<b>CO5-1</b>	Central Diameters and Concentrations of Element in the Atmospheric Aerosols at Sakai, Osaka N. Ito <i>et al.</i> (26011) .....	116
<b>CO5-2</b>	Study of Earth and Planetary Matters by Thermoluminescence K. Ninagawa <i>et al.</i> (26024) .....	117
<b>CO5-3</b>	Evaluation of Redox Conditions at Dredged Trenches in Tokyo Bay by the Concentrations of Elements in the Sediments T. Yamagata <i>et al.</i> (26028) .....	118
<b>CO5-4</b>	Characteristics of Synthetic Calcite Thermoluminescence Studied Reconstruction of East Asia N. Hasebe <i>et al.</i> (26029) .....	119
<b>CO5-5</b>	Fission Track Ages of Sedimentary Rocks from Accretionary Belt in the Kii Peninsula H. Ohira <i>et al.</i> (26036) .....	120
<b>CO5-6</b>	Trace Amounts of Halogens (Cl, Br and I) in Manganese Nodule Reference Materials M. Ebihara <i>et al.</i> (26043) .....	121
<b>CO5-7</b>	Application of Neutron Activation Analysis to Micro Gram Scale of Solid Samples S. Sekimoto <i>et al.</i> (26048) .....	122
<b>CO5-8</b>	Probability Distribution of SEL Occurred on on-board Computer (OBC) Mounted on Small-scale Satellite S. Sekimoto <i>et al.</i> (26053) .....	123
<b>CO5-9</b>	Instrumental Photon Activation Analysis of Geological and Cosmochemical Samples N. Shirai <i>et al.</i> (26067) .....	124
<b>CO5-10</b>	Decomposition of Perfluorooctane Sulfonate by Gamma Ray Irradiation A. Hashiguchi <i>et al.</i> (26074) .....	125
<b>6. Life Science and Medical Science</b>		
<b>CO6-1</b>	D-serine Acting as Competitive Inhibitor on Tryptophanase A. Shimada <i>et al.</i> (26012) .....	126
<b>CO6-2</b>	Study of Localization Estimation of Abasic Sites in DNA Irradiated with Ionizing Radiation K. Akamatsu <i>et al.</i> (26017) .....	127
<b>CO6-3</b>	The Effect of Boron Neutron Capture Therapy (BNCT) on Anti-tumor Immune Response T. Suzuki <i>et al.</i> (26049) .....	128
<b>CO6-4</b>	<i>In situ</i> Visualization of Boron in Plants Using Neutron Capture Radiography M. Kobayashi <i>et al.</i> (26056) .....	129
<b>CO6-5</b>	Measurement of Transmittance Spectra of a Cryo-Sectioned Tissue of Brain Tumor C6 Model in the Sub-Terahertz Region-II N. Miyoshi <i>et al.</i> (26072) .....	130
<b>CO6-6</b>	Design and Synthesis of New Drugs for Boron Neutron Capture Therapy and Boron Magnetic Resonance Imaging S. Aoki <i>et al.</i> (26077) .....	131
<b>7. Neutron Capture Therapy</b>		
<b>CO7-1</b>	Evaluation of Boron-containing Rare Earth Oxides Nanoparticles as an Agent for Boron Neutron Capture Therapy T. Nagasaki <i>et al.</i> (26005) .....	132
<b>CO7-2</b>	<i>In vivo</i> Evaluation of Gd-DTPA-incorporated Calcium Phosphate Nanoparticles as Neutron Capture Therapy Agent N. Dewi <i>et al.</i> (26014) .....	133

<b>CO7-3</b>	Development of a Phantom for Estimation of Beam Quality in BNCT Y. Sakurai <i>et al.</i> (26034) .....	134
<b>CO7-4</b>	A Fundamental Experiment for the Measure Against the Activation of the Irradiation-room Concrete at BNCT Facility Y. Sakurai <i>et al.</i> (26035) .....	135
<b>CO7-5</b>	Radiosensitizing Effect of Purinergic Antagonists on the Damage of Melanoma by BNCT M. Tsukimoto <i>et al.</i> (26061) .....	136
<b>CO7-6</b>	Feasibility Study for Establishing QA Method for Hospital- and Reactor-based BNCT S. Nakamura <i>et al.</i> (26068) .....	137
<b>9. TRU and Nuclear Chemistry</b>		
<b>CO9-1</b>	Stability of Caprolactam Resin against $\gamma$ -Ray Irradiation in HNO <sub>3</sub> T. Nishida <i>et al.</i> (26013) .....	138
<b>CO9-2</b>	Search for Ultraviolet Photons from Precipitated <sup>229m</sup> Th Samples Y. Yasuda <i>et al.</i> (26079) .....	139
<b>10. Health Physics and Waste Management</b>		
<b>CO10-1</b>	Study on the Behavior of Cs and Sr in Soil as Waste M. Yoneda <i>et al.</i> (26075) .....	140
<b>11. Accelerator Physics</b>		
<b>CO11-1</b>	Study of Intense Terahertz Light Source Based on Superimposing Backward Coherent Diffraction Radiation N. Sei <i>et al.</i> (26004) .....	141
<b>CO11-2</b>	The XEP-e (eXtremely High Energy Plasma/ Particle Sensor for Electron) of the ERG Satellite N. Higashio <i>et al.</i> (26071) .....	142
<b>12. Others</b>		
<b>CO12-1</b>	Precise Determination of Br in ABS Resin by Instrumental Neutron Activation Analysis T. Miura <i>et al.</i> (26008) .....	143
<b>CO12-2</b>	Thickness and Density of Adsorbed Additive Layer onto Metal Surface T. Hirayama <i>et al.</i> (26020) .....	144
<b>CO12-3</b>	Characteristic Measurement of Neutron Detector for Fukushima Debris M. Kureta <i>et al.</i> (26022) .....	145
<b>CO12-4</b>	Evaluation of Multiwire-type Two-Dimensional Neutron Detector with Individual Line Readout K. Toh <i>et al.</i> (26042) .....	146
<b>CO12-5</b>	Development of Neutron Resonance Densitometry for Nuclear Material Quantification in Melted Fuel F. Kitatani <i>et al.</i> (26044) .....	147
<b>CO12-6</b>	Test of a Microcell Multi-Wire Proportional Chamber for a Muon-Electron Conversion Search Experiment, DeeMe H. Natori <i>et al.</i> (26046) .....	148
<b>CO12-7</b>	Ethnographic Study of Nuclear Reactor M. Takagaki <i>et al.</i> (26051) .....	149
<b>CO12-8</b>	Effective Measures on Safety, Security, Hygiene and Disaster Prevention in Laboratories T. Iimoto <i>et al.</i> (26054) .....	150
<b>CO12-9</b>	Development of New NiMo Neutron Mirror for Fundamental Physics Y. Arimoto <i>et al.</i> (26059) .....	151
<b>II. PUBLICATION LIST (April 2014 – March 2015)</b> .....		152

# **I. ANNUAL SUMMARY OF EXPERIMENTAL RESEARCH ACTIVITIES**

## **I-1. PROJECT RESEARCHES**

S. Masunaga

Research Reactor Institute, Kyoto University

**BACKGROUNDS AND PURPOSES:** Human solid tumors contain moderately large fractions of quiescent (Q) tumor cells that are out of the cell cycle and stop cell division, but are viable compared with established experimental animal tumor cell lines. The presence of Q cells is probably due, in part, to hypoxia and the depletion of nutrition in the tumor core, which is another consequence of poor vascular supply. As a result, Q cells are viable and clonogenic, but stop cell division. In general, radiation and many DNA-damaging chemotherapeutic agents kill proliferating (P) tumor cells more efficiently than Q tumor cells, resulting in many clonogenic Q cells remaining following radiotherapy or chemotherapy. Therefore, it is harder to control Q tumor cells than to control P tumor cells, and many post-radiotherapy recurrent tumors result partly from the regrowth of Q tumor cells that could not be killed by radiotherapy. Similarly, sufficient doses of drugs cannot be distributed into Q tumor cells mainly due to heterogeneous and poor vascularity within solid tumors. Thus, one of the major causes of post-chemotherapy recurrent tumors is an insufficient dose distribution into the Q cell fractions.

With regard to boron neutron capture therapy (BNCT), with  $^{10}\text{B}$ -compounds, boronophenylalanine- $^{10}\text{B}$  (BPA) increased the sensitivity of the total cells to a greater extent than mercaptoundecahydrododecaborate- $^{10}\text{B}$  (BSH). However, the sensitivity of Q cells treated with BPA was lower than that in BSH-treated Q cells. The difference in the sensitivity between the total and Q cells was greater with  $^{10}\text{B}$ -compounds, especially with BPA. These findings concerning the difference in sensitivity, including other recovery and reoxygenation following neutron irradiation after  $^{10}\text{B}$ -compound administration were mainly based on the fact that it is difficult to deliver a therapeutic amount of  $^{10}\text{B}$  from  $^{10}\text{B}$ -carriers throughout the target tumors, especially into intratumor hypoxic cells with low uptake capacities.

Hypoxia is suggested to enhance metastasis by increasing genetic instability. Acute, but not chronic, hypoxia was reported to increase the number of macroscopic metastases in mouse lungs. We recently reported the significance of the injection of an acute hypoxia-releasing agent, nicotinamide, into tumor-bearing mice as a combined treatment with  $\gamma$ -ray irradiation in terms of repressing lung metastasis. As the delivered total dose increased with irradiation, the number of macroscopic lung metastases decreased reflecting the decrease in the number of clonogenically viable tumor cells in the primary tumor. The metastasis-repressing effect achieved through a reduction in the number of clonogenic tumor cells by irradiation is much greater than that achieved by releasing tumor cells from acute hypoxia. On the other hand, more  $^{10}\text{B}$  from BPA than from BSH could be distributed into the acute hypoxia-rich total tumor cell population, resulting in a greater decrease in the number of highly clonogenic P tumor cells with BPA-BNCT than with BSH-BNCT and with neutron beam irradiation only. BPA-BNCT rather than BSH-BNCT has some potential

to decrease the number of lung metastases, and an acute hypoxia-releasing treatment such as the administration of nicotinamide or bevacizumab may be promising for reducing numbers of lung metastases. Consequently, BPA-BNCT in combination with nicotinamide and/or bevacizumab treatment may show a little more potential to reduce the number of metastases. Now, it has been elucidated that control of the chronic hypoxia-rich Q cell population in the primary solid tumor has the potential to impact the control of local tumors as a whole, and that control of the acute hypoxia-rich total tumor cell population in the primary solid tumor has the potential to impact the control of lung metastases.

The aim of this research project is focused on clarifying and analyzing the characteristics of intratumor microenvironment including hypoxia within malignant solid tumors and optimizing cancer therapeutic modalities, especially radiotherapy including BNCT in the use of newly-developed  $^{10}\text{B}$ -carriers based on the revealed findings on intratumor microenvironmental characteristics.

### RESEARCH SUBJECTS:

The collaborators and allotted research subjects (ARS) were organized as follows;

**ARS-1 (26P1-1):** Optimization of Radiation Therapy Including BNCT in terms of the Effect on a Specific Cell Fraction within a Solid Tumor and the Suppressing Effect of Distant Metastasis. (S. Masunaga, *et al.*)

**ARS-2 (26P1-2):** Development of Hypoxic Microenvironment-Oriented  $^{10}\text{B}$ -Carriers. (H. Nagasawa, *et al.*)

**ARS-3 (26P1-3):** Clarification of Mechanism of Radio-Resistance in Cancer Using Optical Imaging at Tissue Level. (H. Harada, *et al.*)

**ARS-4 (26P1-4)\*:** Analysis of Radiation-Induced Cell-Killing Effect in Neutron Capture Reaction. (R. Hirayama, *et al.*)

**ARS-5 (26P1-5):** Transdermal Drug Delivery System using Hyaluronan-Conjugated Liposomes as  $^{10}\text{B}$ -Carrier in Boron Neutron Capture Therapy for Melanoma (S. Kasaoka, *et al.*)

**ARS-6 (26P1-6):** Evaluation of Inclusion Complex of Carborane Modified Kojic Acid and Cyclodextrin as  $^{10}\text{B}$ -Carrier in Boron Neutron Capture Therapy. (T. Nagasaki, *et al.*)

**ARS-7 (26P1-7)\*:** Molecular Design and Synthesis and Functional Evaluation of Anticancer and Molecular Targeting Agents. (Y. Uto, *et al.*)

**ARS-8 (26P1-8)\*:** Analyzing Biological Effect of BNCT from the Viewpoint of the Changes in Oxygenation Level. (H. Yasui, *et al.*)

**ARS-9 (26P1-9):** Analyses on the Responsiveness of Malignant Tumors to BNCT. (M. Masutani, *et al.*)

**ARS-10 (26P1-10):** Assay for Tumor Cell Survival and Tumor Growth Delay through Neutron Capture Reaction according to the Changes in Intracellular Concentrations within Solid Tumors of Newly-Developed  $^{10}\text{B}$ -Carriers. (K. Nakai, *et al.*)

**ARS-11 (26P1-11)\*:** Antitumor and Metastasis-Repressing Effect of BNCT on Human Breast and Pancreatic Cancer Cell Lines. (Y. Matsumoto, *et al.*)

(\* Due to the irregular and short operation period of our reactor in 2014, the data could not be shown here.)

## PR1-1 Significance of Fractionated Thalidomide Administration Combined with $\gamma$ -Ray Irradiation from the Viewpoint of Local Tumor Response and Lung Metastasis

S. Masunaga<sup>1</sup>, Y. Sanada<sup>1</sup>, T. Moriwaki<sup>2</sup>, K. Tano<sup>1</sup>, Y. Sakurai<sup>1</sup>, H. Tanaka<sup>1</sup>, M. Suzuki<sup>1</sup>, N. Kondo<sup>1</sup>, M. Narabayashi<sup>1</sup>, T. Watanabe<sup>1</sup>, Y. Nakagawa<sup>1</sup>, A. Maruhashi<sup>1</sup> and K. Ono<sup>1</sup>

<sup>1</sup>Research Reactor Institute, Kyoto University

<sup>2</sup>Faculty of Medicine, Kyoto University

**INTRODUCTION:** Thalidomide has been reported to induce tumor blood vessel normalization in a mouse model [8, 9]. Today, thalidomide is being mainly applied as a treatment of certain cancers (multiple myeloma) and of a complication of leprosy. Here, using a readily metastasizing murine melanoma cell line, we tried to analyze the significance of combined treatment with thalidomide in radiotherapy with  $\gamma$ -rays in combination with an acute hypoxia-releasing agent nicotinamide or mild temperature hyperthermia (MTH), already shown to have the potential to release tumor cells from diffusion-limited chronic hypoxia [1, 2], in terms of local tumor response and lung metastatic potential. Concerning the local tumor response, the effect not only on the total (= proliferating (P) + quiescent (Q)) tumor cell population but also on the Q cell population was evaluated using our original method for selectively detecting the response of Q cells in solid tumors.

**Materials and Methods:** B16-BL6 melanoma tumor-bearing C57BL/6 mice were continuously given 5-bromo-2'-deoxyuridine (BrdU) to label all P cells. The tumor-bearing mice then received  $\gamma$ -ray irradiation after thalidomide treatment through a single or two consecutive daily intraperitoneal administrations up to a total dose of 400 mg/kg in combination with nicotinamide or mild MTH. Immediately after the irradiation, cells from some tumors were isolated and incubated with a cytokinesis blocker. The responses of the Q and total (= P + Q) cell populations were assessed based on the frequency of micronuclei using immunofluorescence staining for BrdU. In other tumor-bearing mice, 17 days after irradiation, macroscopic lung metastases were enumerated.

**Results:** Thalidomide raised the sensitivity of the total cell population more remarkably than Q cells in both single and daily administrations. Daily fractionated administration of thalidomide elevated the sensitivity of both the total and Q cell populations, but especially the total cell population, compared with single administration. Daily administration, especially combined with MTH, decreased the number of lung metastases.

**Discussion:** Thalidomide was originally introduced as a non-barbiturate hypnotic, but withdrawn from the market due to teratogenic effects. However, it has been reintroduced and used for a number of immunological and inflammatory disorders due to its immunosuppressive and anti-angiogenic activity. It inhibits release of tumor ne-

crosis factor from monocytes, and modulates other cytokine action. Thalidomide is racemic, and contains both left and right handed isomers in equal amounts: one enantiomer is effective against morning sickness, and the other is teratogenic. The enantiomers are converted to each other at physiological conditions (pH = 7.0) *in vivo*. That is, if a human is given D-thalidomide ((+)- or R-) or L-thalidomide ((-)- or S-), both isomers can be found in the serum. Hence, administering only one enantiomer will not prevent the teratogenic effect in humans. It is employed for the acute treatment of the cutaneous manifestations of moderate to severe erythema nodosum leprosum (ENL). Available data from *in vitro* studies and preliminary clinical trials suggest that its immunologic effects can vary substantially under different conditions, but may be related to suppression of excessive tumor necrosis factor production and down-modulation of selected cell surface adhesion molecules involved in leukocyte migration [3].

As a cancer treatment, thalidomide was shown to inhibit basic fibroblast growth factor (bFGF) as well as VEGF, two promoters of angiogenesis. It was reported to measure the modifications in the tumor environment early after an angiogenic treatment of thalidomide, with a special focus on possible normalization of the tumor vasculature that could be beneficial for radiotherapy [4]. Incidentally, angiogenesis also is critical during limb development of the foetus. Thalidomide directly inhibits angiogenesis induced by bFGF or VEGF *in vivo*. In 2009, it was confirmed that loss of newly formed blood vessels is the primary cause of thalidomide teratogenesis, and that developing limbs are particularly susceptible because of their relatively immature, highly angiogenic vessel network. Thus inhibition of angiogenesis is now thought to be a main mechanism of its teratogenicity [3,5].

**Conclusion:** It was elucidated that control of the chronic hypoxia-rich Q cell population in primary solid tumors has the potential to impact the control of local tumors as a whole, while control of the acute hypoxia-rich total tumor cell population has the potential to impact the control of lung metastases. Namely, in conventional radiotherapy, daily fractionated administration of thalidomide combined with MTH is thought to have a great potential to control both local solid tumors and lung metastases from the local tumors [6].

### REFERENCES:

- [1] S. Masunaga, *et al.*, Int J Hyperthermia **13** (1997) 401-411.
- [2] S. Masunaga, *et al.*, Clin Exp Metastasis **26** (2009) 693-700.
- [3] M. E. Franks, *et al.*, Lancet **363** (2004) 1802-1811.
- [4] R. Ansiaux, *et al.*, Clin Cancer Res **11** (2005) 743-750.
- [5] C. Therapontos, *et al.*, Proc Natl Acad Sci U S A **106** (2009) 8573-8578.
- [6] S. Masunaga *et al.*, World J Oncol **5** (2014) 155-165.

## PR1-2 Development of Nuclear-targeting Boron Carriers Based on the Chemistry of Direct Cell-penetrating Peptides

A. Isono<sup>1</sup>, K. Okuda<sup>1</sup>, T. Hirayama<sup>1</sup>, S. Masunaga<sup>2</sup>, and H. Nagasawa<sup>1</sup>

<sup>1</sup> Laboratory of Medicinal & Pharmaceutical Chemistry, Gifu Pharmaceutical University

<sup>2</sup> Research Reactor Institute, Kyoto University

**INTRODUCTION:** For the success of boron neutron capture therapy (BNCT), it is essential to selectively deliver sufficient amount of <sup>10</sup>B atoms to tumor cells. To achieve intracellular molecular targeting of drug delivery, we focused on the direct cell-penetrating lipopeptides, pepducins which were developed as allosteric modulators of GPCRs[1]. By the study of fluorescence resonance energy transfer (FRET)-based imaging of pepducins, we demonstrated that they penetrate directly into cells by trans-membrane lipid translocation [2]. Accordingly, we envisaged that the pepducin moiety may be exploitable for intracellular deliver of membrane impermeable molecules such as anionic boron cluster, sodium borocaptate (BSH).

**MOLECULAR DESIGN:** As shown in Fig. 1, we designed new hybrid molecules comprising pepducin (Pep) as a vehicle, and boron cluster (BS) attached with fluorescent dyes such as 7-hydroxycoumarin (Cou) and Hoechst 33342 dye (Hoe) as a cargo; Pep-SS-BS-Cou and Pep-SS-BS-Hoe. The cargo is supposed to be released into cytosol after reductive cleavage of the disulfide bond by intracellular glutathione when it is carried into the cytosol.

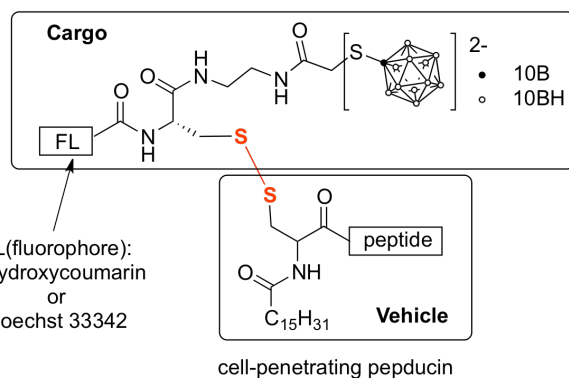


Fig. 1 Design of boron carriers

**RESULTS AND DISCUSSION:** The lipidated peptides were prepared by solid-phase synthesis and then combined with BSH and the corresponding fluorophore through an appropriate linker to afford the boron carriers (Fig. 2 and 3). We performed live cell imaging experiments using MCF-7 cells with the probes and confocal microscopy. By the treatment with Pep-SS-BS-Cou, the fluorescence signal was localized on cell-membrane for more than 30 min, which suggested that the boron carrier

was likely to be anchored on the plasma membrane but could not be translocated into the cytosol. To evaluate the structure activity relationship of the peptide sequence for controlling cellular distribution, we synthesized pepducins containing various peptides to conjugate with the cargo moiety.

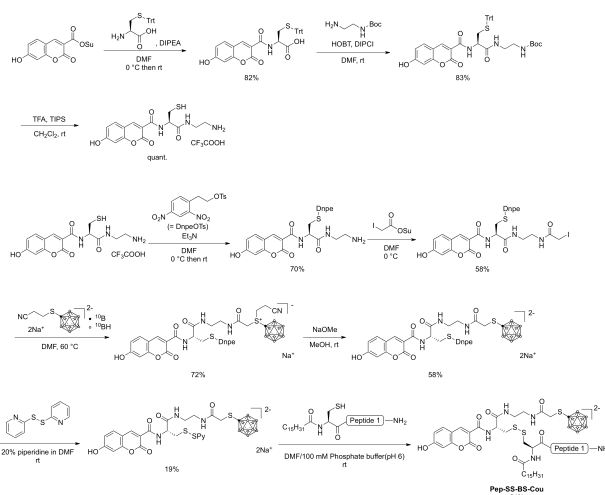


Fig. 2 Synthesis of Pep-SS-BS-Cou

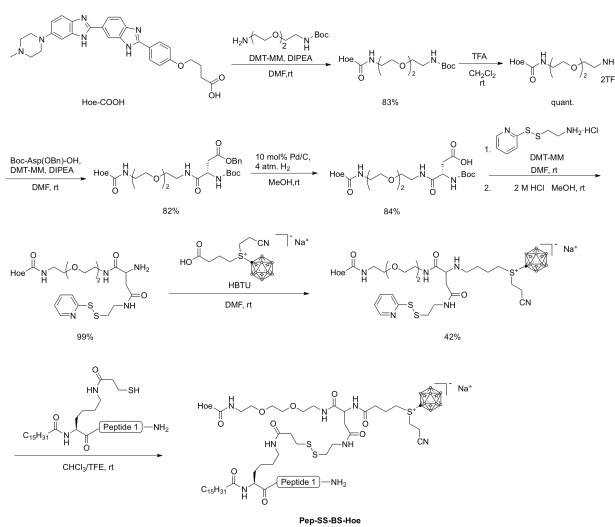


Fig. 3 Synthesis of Pep-SS-BS-Hoe

We also synthesized Pep-SS-BSs by connecting of various pepducins to the boron cluster without any fluorophores. To quantify their intracellular boron concentration, ICP-MS analyses of nuclear and cytoplasmic extracts will be conducted.

### REFERENCES:

- [1] L. Covic *et al.*, Proc. Natl. Acad. Sci. USA., **99** (2002) 643–648.
- [2] M. Tsuji *et al.*, *Org. Biomol. Chem.*, **11**(2013), 3030-3037

## PR1-3 Genetic Screening of Upstream Activators of Hypoxia-inducible Factor 1 for the Development of Novel Anti-cancer Strategies

H. Harada<sup>1</sup>, S. Masunaga<sup>2</sup>, M.

<sup>1</sup>Department of Radiation Oncology and Image-applied Therapy, Graduate School of Medicine, Kyoto University.

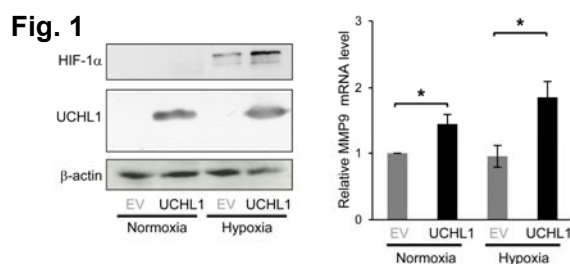
<sup>2</sup>Research Reactor Institute, Kyoto University

**INTRODUCTION:** Accumulating evidence has shown that hypoxia-inducible factor 1 (HIF-1) plays critical roles in distant tumor metastases at multiple steps [1] and eventually causes death among cancer patients. Clinical studies have demonstrated consistent data that HIF-1 could be used as an adverse prognostic factor for not only local tumor recurrence but also distant tumor metastasis in cancer patients. These findings justify targeting HIF-1 for cancer therapies.

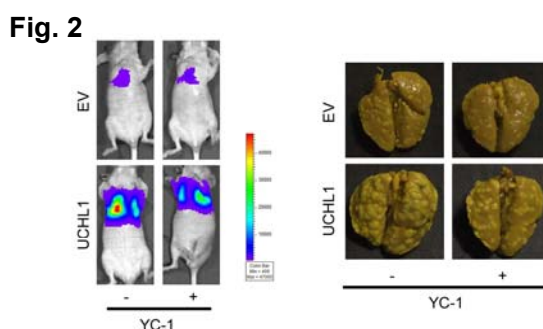
HIF-1, a heterodimeric transcription factor composed of an  $\alpha$ -subunit (HIF-1 $\alpha$ ) and a  $\beta$ -subunit (HIF-1 $\beta$ ), is known to become activate mainly through the stabilization of HIF-1 $\alpha$  protein. Under normoxic conditions, prolyl-4-hydroxylases (PHDs) hydroxylate proline residues, P402 and P564, in the oxygen-dependent degradation domain (ODD domain) of HIF-1 $\alpha$  in an oxygen-dependent manner. The hydroxylations trigger polyubiquitination and subsequent proteasomal degradation of HIF-1 $\alpha$ . On the contrary, HIF-1 $\alpha$  becomes active under hypoxic conditions because of the inactivation of the hydroxylases, and then, interacts with its binding partner, HIF-1 $\beta$ . Resultant heterodimer, HIF-1, binds to its cognate enhancer sequence, the hypoxia-responsive element (HRE), and induces transcriptions of various genes related to the escape from hypoxia (invasion and metastasis of cancer cells) as well as the improvement of oxygen-availability (angiogenesis) and adaptation of cellular metabolism to hypoxia (metabolic reprogramming).

In order to explore novel genes which are responsible for the HIF-1-mediated tumor metastasis, we recently established a new genetic screening method [2] and found that overexpression of ubiquitin C-terminal hydrolase L1 (UCHL1) is responsible for the activation of HIF-1. In the present study, we analyzed both the molecular mechanisms underlying the UCHL1-mediated activation of HIF-1 and the involvement of UCHL1-HIF-1 axis in distant tumor metastases.

**EXPERIMENTS & RESULTS:** We established stable transfectants of HeLa cells with the UCHL1 expression vector (HeLa/UCHL1) or its empty vector (HeLa/EV) [3]. We found that aberrant expression of UCH-L1 in cancer cells abrogated von Hippel-Lindau-mediated ubiquitination of HIF-1 $\alpha$ , leading to the stabilization of HIF-1 $\alpha$  and subsequent activation of HIF-1 (Fig. 1) [3].

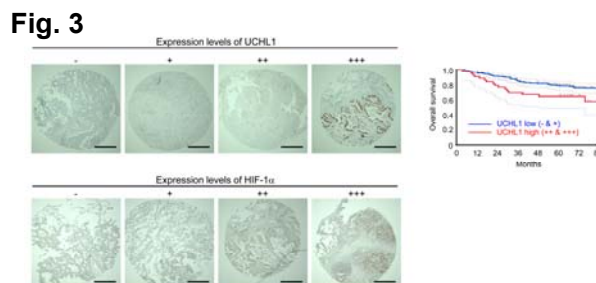


A murine model of pulmonary metastasis demonstrated that the forced expression of UCH-L1 facilitated tumor metastases in a HIF-1-dependent manner (Fig. 2) [3].



On the other hand, silencing of the aberrantly expressed UCH-L1 suppressed the metastatic tumor formation by inactivating HIF-1[3].

Moreover, we revealed that UCH-L1 expression levels were associated with poor prognosis of patients with breast and lung cancers (Fig. 3) [3].



**DISCUSSIONS:** Together, these results demonstrate that UCH-L1 functions in distant tumor metastasis as a deubiquitinating enzyme for HIF-1 $\alpha$ , and thus, justify exploiting it as a prognostic marker and therapeutic target for individualization of cancer therapy.

### REFERENCES (papers published from our lab):

- [1] Zhao T et al. *Sci Rep.* 4:3793. 2014.
- [2] Zeng L et al. *Oncogene.* in press.
- [3] Goto Y et al. *Nature Communications.* 6:6153. 2015.

採択課題番号26 P1-3 低酸素誘導性因子1 (HIF-1) を活性化する新規遺伝子の探索と プロジェクト機能解析、および局所腫瘍制御への展開

(京大・院医) 原田浩 (京大・原子炉) 増永慎一郎



## Quantitative Detection of Metastasized B16BL6 Cells in Lung by Using TaqMan RT-PCR Assay

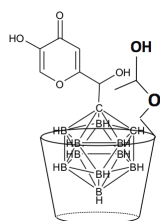
T. Nagasaki, J. Kawaguchi, R. Kawasaki, M. Sakuramoto, M. Kirihata<sup>1</sup>, Y. Hattori<sup>1</sup>, S. Masunaga<sup>2</sup> and Y. Sakurai<sup>2</sup>

Graduate School of Engineering, Osaka City University

<sup>1</sup> BNCT Research Center, Osaka Prefecture University,

<sup>2</sup> Research Reactor Institute, Kyoto University

**INTRODUCTION:** Although melanoma boron neutron capture therapy (BNCT) with L-<sup>10</sup>B-p-boronophenyl alanine has been treated for melanoma patient, the enhancement of <sup>10</sup>B accumulation in melanoma cells would lead to improved efficacy of malignant melanoma BNCT. Recently, we have evaluated the inclusion complex of kojic acid-appended carborane (CKA) with hydroxypropyl-β-cyclodextrin (HP-β-CD) as a novel boron agent for BNCT toward melanoma. CKA/HP-β-CD complex showed melanoma cells selectivity, unique nuclear localization, and high tumor-suppression effect on BNCT toward melanoma-bearing mice. Furthermore, CKA/HP-β-CD complex was found to be the potent inhibitor of hypoxia-induced HIF-1α and to have a strong effect on tumor metastasis [1]. Herein, in order to evaluate quantitatively metastasis-suppression, TaqMan RT-PCR assay of melanoma gene GP100 was carried out toward melanoma B16BL6 cells metastasis from thigh subcutaneous to lung in melanoma-bearing mice [2].



Structure of CKA/HP-β-CD

**EXPERIMENTS:** B16BL6 cells ( $2.5 \times 10^{12}$  cells) were implanted into thigh subcutaneous. Mice were euthanized and lung and spleen were isolated and snap frozen in liquid nitrogen before being stored at  $-80^\circ\text{C}$ . Total RNA was extracted using NucleoSpinRNA Kit (Takara). Total RNA concentration and purity were measured using NanoDrop 2000c Spectrometer (Thermo Scientific). Subsequently, cDNA synthesis was performed by using PrimeScript<sup>TM</sup> RT reagent Kit (Perfect Real Time) (Takara). Quantitative real time polymerase chain reac-

tion (Q-PCR) was performed according to the manufacturer's manual using FastStart Universal Probe Master (Roche) and Q-PCR was run in a STRAGENE Mx3000P using the following program:  $95^\circ\text{C}/10 \text{ min} + 40 \times (95^\circ\text{C}/15 \text{ s} + 60^\circ\text{C}/1 \text{ min} + 72^\circ\text{C}/1 \text{ min})$ . Primers and probe were used: GP100 forward: 5' AGC ACC TGG AAC CAC ATC TA 3', GP100 revers: 59 CCA GAG GGC GTT TGT GTA GT 3', GP100 probe: 5'Hex-CAC TAC AAA AGT TGT GGG TAC TAC ACC TG-BHQ-1-3'.

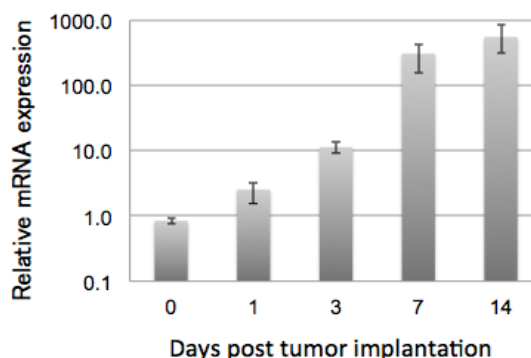


**Fig.1** Relative mRNA expression of melanoma gene GP100 in lungs.

**RESULTS AND DISCUSSION:** GP100 is highly expressed in melanoma B16BL6 cells, but not to any substantial degree in normal tissues. GP100 expression exceeded background levels when at least  $5 \times 10^3$  B16BL6 cells are contained in metastasized tissue. In order to quantify the increase of metastasized B16BL6 cells, lungs were collected 1, 3, 7, or 14 days post tumor implantation. On day 7 increase of GP100 expression reached a level of about 100 times the lowest point (Fig. 1).

TaqMan RT-PCR Assay toward GP100 is potent to estimate quantitatively the metastasis of melanoma cells to lung. The quantitative evaluation of metastasis-suppression effect of CKA/HP-β-CD complex is proceeding in our laboratory.

### REFERENCES:

- [1] K. Shimizu *et al.*, Bioorg. Med. Chem. Lett., **20** (2010) 1453-1456.  
 [2] M. R. Sorensen *et al.*, PLoS One., **9** (2001) e87831.

S. Imamichi<sup>1</sup>, T. Itoh<sup>1,2</sup>, S. Kikuhara<sup>1,2</sup>, H. Fujimori<sup>1</sup>, A. Sato<sup>3</sup>, T. Hirai<sup>1,4</sup>, S. Masunaga<sup>5</sup> and M. Masutani<sup>1,6</sup>

<sup>1</sup>Division of Chemotherapy and Clinical Research, National Cancer Center Research Institute, <sup>2</sup>Faculty of Industrial Science and Technology, Tokyo University of Science, <sup>3</sup>Faculty of Pharmaceutical Sciences, Tokyo University of Science, <sup>4</sup>Department of Radiation Oncology, Juntendo University Faculty of Medicine, <sup>5</sup>Research Reactor Institute, Kyoto University, <sup>6</sup>Department of Frontier Life Sciences, Nagasaki University Graduate School of Biomedical Sciences

**INTRODUCTION:** Tumors are consisted of heterogeneous populations of cells, including hypoxic cells, cancer stem cells and differentiating cells. These populations affect the consequence of the boron neutron capture therapy (BNCT) [1]. Boron neutron capture reaction (BNCR) causes extensive DNA double strand breaks and micronuclei formation has been used to estimate the level of DNA damage induced by BNCR [2]. In rat xenograft model, BNCR caused the up-regulation of  $\gamma$ H2AX and HMGB1, then induction of poly(ADP-ribose) [3]. The cell death process and the factors affecting tumor cell killing, side effects and effectiveness of BNCT are not fully understood. To elucidate the cell death process after BNCR, we have taken approaches of comprehensive analysis of the tumor cells by using transcriptome and proteome analysis.

**EXPERIMENTS:** Human oral squamous cancer SAS cells [1] was used for the comprehensive analysis with transcriptome and proteome analysis. <sup>10</sup>B-boronophenylalanine (<sup>10</sup>B-BPA)-fructose solution was prepared as described previously [4]. SAS cell was suspended and incubated 2 h with or without 25 ppm of <sup>10</sup>B-BPA as previously reported [3]. After neutron-beam irradiation operated at 1 MW, cells were inoculated for colony formation, RNA and protein preparation. To analyze the early response of cancer cells, RNA and protein were prepared 6 and 24 hrs after irradiation at the supposal doses of 4 Gy-eq and 24 Gy-eq conditions.

For mouse xenograft model, male BALB/c-nu/nu mice were used and SAS cells were injected subcutaneously into left legs of the mice. <sup>10</sup>B-BPA at the dose of 250 mg/kg bodyweight was intraperitoneally injected 1 h before irradiation operated at 1 MW. Tumors, tissues, and blood were sampled for the analysis of early responses after irradiation. The animal studies were performed in accordance with the relevant laws and institutional guidelines of KUR and NCC. <sup>10</sup>B concentration was measured by prompt-gamma ray analysis (PGA). Thermal neutron fluence was measured with gold foils activation analysis. Gamma-ray dose was measured with thermal-

minescence dosimeter. These physical radiation doses were measured with the kind help of Drs. Yoshinori Sakurai and Hiroki Tanaka of KUR.

**RESULTS:**

The measured results of total physical dose, neutron and gamma ray dose were shown in Fig. 1 and confirmed that the dose estimation was in the expected range. Twenty-four hrs after 24 Gy-eq irradiation, SAS cells showed the cleavage of

PARP1, caspase-9 and caspase-3, suggesting that apoptosis started to occur. Meanwhile, the low levels of necrotic cleavage pattern of PARP1 were also observed, implying that necrotic cell death is also involved after BNCR. The isolated RNA 6 and 24 hrs after irradiation was evaluated by electrophoresis and RT-PCR. As shown in Fig. 2, the expression levels of *PARP1* and *GUSB* were not different among the irradiation conditions, confirming the quality of RNA. In the microarray analysis, we found that the expression of the genes related to cell death, transcription, and inflammatory and immune responses was augmented after BNCR and the further evaluation is ongoing.

By proteome analysis, proteins involved in the vesicle regulation, mRNA processing, transcription were observed with changes after BNCR and being studied further. The observation suggests that dynamic changes in cellular responses could be induced after BNCR reaction at an early phase. SAS xenograft model in nude mice was also set up, and the boron concentration in the blood and tissues was measured. Using the experimental system, the genes and proteins associated with BNCR response will be further elucidated.

**REFERENCES:**

- [1] Masunaga et al, Jpn. J. Cancer Res., 93(12) (2002) 1366-77.
- [2] Kinashi et al, Radiat. Oncol., 5;6 (2011) 106.
- [3] M. Masutani et al, Appl. Radiat Isot.88 (2014) 104-8.
- [4] Yoshino et al, Strahlen. Onkol., 165: (1998) 127-12

Fig. 1. The physical dose measurement.

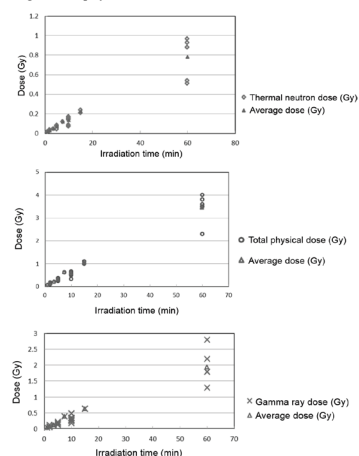
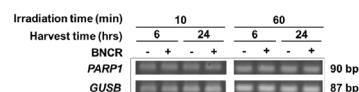


Fig. 2. Gene expression analysis of *PARP1* and *GUSB* by RT-PCR.



K. Nakai<sup>1</sup>, F. Yoshida<sup>1</sup>, T. Kurita<sup>1</sup>, Y. Yamamoto<sup>1</sup>, M. Shirakawa<sup>2</sup>, T. Yamamoto<sup>1</sup>, H. Tanaka<sup>3</sup>, Y. Sakurai<sup>3</sup>, S. Masunaga<sup>3</sup>

<sup>1</sup>Department of Neurosurgery, Faculty of Medicine, University of Tsukuba

<sup>2</sup>Department of Pharmaceutical Sciences, International University of Health and Welfare

<sup>3</sup>Research Reactor Institute, Kyoto University

**INTRODUCTION:** In neutron capture therapy; the therapeutic effect of a boron compound is based on alpha particle production in a  $^{10}\text{B}(n, \alpha) ^7\text{Li}$  reaction, while a gadolinium compound effect is based on producing gamma rays derived from a  $^{157}\text{Gd}(n, \gamma)$  reaction[1,2]. Gadolinium containing agents has been used for contrast enhance of MRI scan, and are commercially available as pharmaceutical products.

If gadolinium is administered simultaneously with boron and irradiated with neutrons, it might become a source of additional local gamma rays, which correspond with recent BNCT clinical trial protocol for glioblastoma. We analyzed the additive effect of gadolinium on boron based neutron capture reaction.

### Materials and Methods:

#### Boron and Gadolinium compounds

p-boronophenylalanine (BPA) was obtained from Interpharma Praha (Praha, Czech Republic). Gd-DTPA (Magnevist) was purchased from Shering (Berlin, Germany). BPA and fructose were dissolved and prepared as previously described. Briefly, BPA was converted to BPA-fructose complex by mixing BPA and fructose in NaOH. The pH was adjusted to 7.4 with HCl. Dissolution solvent for Gd-DTPA was cell culture medium.

Cell lines; C6 rat glioma cell lines and V79 Chinese hamster cell lines were maintained in Eagle's Minimum Essential Medium (MEM; Sigma-Aldrich), supplemented with 10% fetal bovine serum.

Colony Formation Assay ;V79 cells and C6 cells after exposition with the compounds were irradiated with neutron mixed beam for 90 min at the Kyoto University Research Reactor (KUR). We use the combination of BPA (0, 10, 20, 40 Bu  $\mu\mu\text{g}/\text{mL}$ ) and Gd-DTPA (0, 0.5, 5, 10 Gd $\mu\text{g}/\text{mL}$ ) with  $10^4$  of cells of each line. The number of cells was sufficient to produce 20-100 colonies at each boron concentration. After 7days of incubation, the plates were stained with 0.25 % methylene blue in 90 % ethanol. Colonies of more than 50 cells were counted.

**RESULTS:** As shown in Fig. 1, Radiation-related damage significantly increased with the increase of gadolinium concentration. When 5 ppm of Gd-DTPA was added to 40 ppm of BPA in C6 cells, the additive effect was obtained. In radiosensitive V79 cells the survival fraction dramatically decreased after irradiation and was lower than 10% at boron concentration of 40ppm.

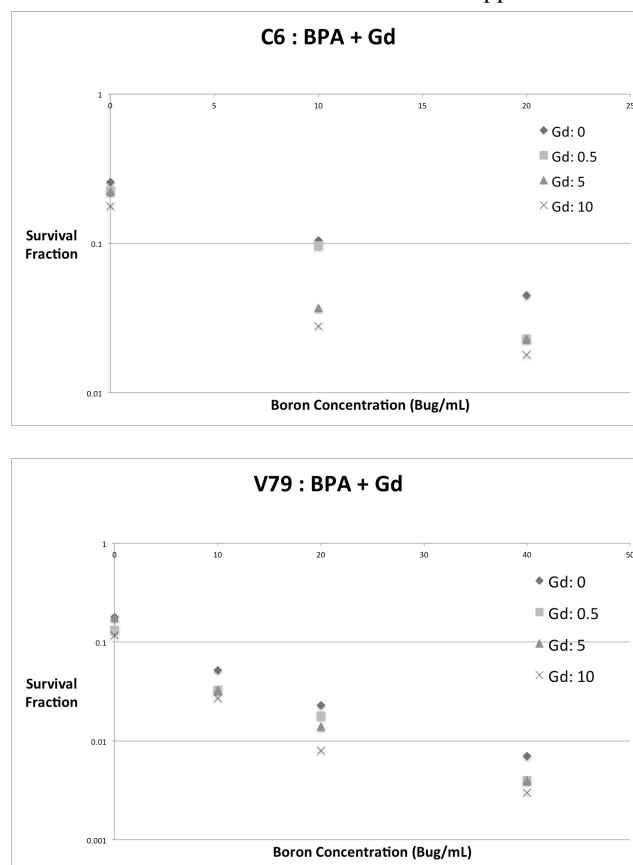


**Fig. 1.** Influence of Gd on BNCT in C6 (upper), V79 (lower) cell lines. The symbols  $\blacklozenge$  show the control (BPA only);  $\blacksquare$  show the result of additional 0.5 ppm of Gd;  $\blacktriangle$  show the result of additional 5 ppm of Gd and  $\times$  show the result of additional 10 ppm of Gd.

### REFERENCES:

- [1] A. Matsumura *et al.*, J Exp Clin Cancer Res. (2005)24.  
[2] Shikata F., *et al.* Eur. J. Pharm. Biopharm(2002)53.

採択課題番号26P1-10 新規ホウ素化合物等を用いた中性子捕捉反応による細胞生存試験および腫瘍増殖抑制効果 プロジェクト (筑波大・医) 中井 啓、吉田文代、山本陽平、高 振宇、栗田 正 (国際医療大・薬) 白川 真 (京大・原子炉) 田中浩基、櫻井良憲、増永慎一郎

## PR2 Direct observation of the proton or protonation in a protein molecule by neutron and high resolution X-ray joint analysis

Y.Morimoto

Research Reactor Institute, Kyoto University

**OBJECTIVES:** Protein sciences are accelerated with use of a neutron and an X-ray beam to clarify the tertiary and quaternary structural information. Proton and/or protonation of the amino acids in the protein molecule affect a chemical reaction in the biological macromolecule, neutron is well useful to isolate findings of such reaction mechanisms and can determine a precise position and roles of hydrogen or protonation in active amino acids. Drugs, as reagents, anti-cancer compounds, play important roles in a host-protein molecule with electrons or protons, hydrogen (deuterium) atoms should be determined clearly to design a compound molecule. X-ray analysis is good method to find a whole molecule and neutron is sensitive and selective to hydrogen (deuterium), the both complementary usage or joint refinement of the protein molecule is very powerful technique to analyze a precise reaction mechanism with atomic resolution.

I have called for members to carry out the examination of this purpose.

- (1) Structural investigation of the 20S/26S Proteasome in the highly structural organization, Y.Morimoto
- (2) Improved Techniques for Neutron Biology. T.Chatke
- (3) Proteolytic enzymes derived from *NephilaClavata*. Y.Hidaka

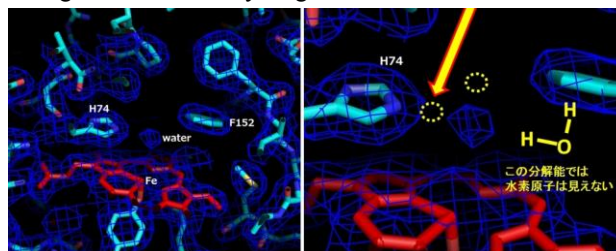
### RESULTS:

#### 26P2-1

T. Murakami, M. Unno, I. Hisatome, K.Hosokawa, H. Yamaguchi and Y. Morimoto reported "Degradation control and structural motion of the 20S/26S proteasome elucidated by genetic mutation and atomic force microscope". A newly inhibitor of the 20S proteasome and its complex is described. Since the wild-type 20S proteasome has gradual decrease against drug concentration, Y170A, Y170L and Y170F has no clear decreasing. Drug A has an aromatic ring in its structure, the aromatic ring interacts the Y( Tyr ) ring but F( Phe ) has also a ring structure. 26S whole structure has been investigated by the AFM. The 26S has two large components (19S) at the both ends of 20S particle. The AFM images show the size of the whole particle of 26S, but a single-capped particles are also observed with self-rotating images. We have tried to detect when a substrate molecule, 6 x His tagged protein generated by expression system of the *E*

*coli*, enter into the 20S particle by the AFM. The *in situ* detection of the degradation will make clear *in vivo* mechanism in the living cell.

Other research of the structure analyses, catalase from bovine liver has been crystallized in deuterium solution. Diffraction data of the Spring-8 showed clear electron densities at an active site, heme, and water passing tunnel (following figure). However, the resolution 2.5 Å is not enough to determine hydrogen atoms.



An ultra-high resolution (~0.9Å) analysis of the lysozyme crystallized under deuterium solution has been investigated by thermal turbulence refinement of carbon and/or nitrogen atoms with use of the Photon Factory data.

#### 26P2-2

T. Chatake, S. Fujiwara, I. Tanaka, Y. Yanagisawa reported "Development of Improved Techniques for Neutron Biology" of the result for the three interesting works. The first is a newly structure determination method of the neutron crystallography by use of a H/D contrast density mapping, like to be a solvent flattening of the X-ray determination. The second describes a fully deuterated protein production method by overexpression system, and modification of a cultivation and purification of the kinase. The last is interesting view point on the neutron scattering or diffraction, by use of dynamic polarization technique for a neutron biology.

#### 26P2-3

Y. Hidaka, M. Fujiwara, T. Nakanishi, S. Shimamoto, and M. Miyazawa reported "Identification and characterization of proteolytic enzymes derived from *NephilaClavata*" focusing to the spider protease digesting amyloid fibers including pathogenic  $\beta$ -amyloid, such as amyloid fibrils, associated with the development of Alzheimer's disease. The N-terminal amino acid sequence of spider protease was determined by Edman degradation. Spider genes were amplified using generating primers, base on the N-terminal amino acid sequence, by RT-PCR and cloned into pBR-SKII(-). The cloning of spider protease genes is in progress.

## Degradation control and structural motion of the 20S/26S proteasome elucidated by genetic mutation and atomic force microscope

T.Murakami<sup>1</sup>, M.Unno<sup>2</sup>, I.Hisatome<sup>3</sup>, K.Hosokawa<sup>1</sup>,  
H.Yamaguchi<sup>1</sup> and Y.Morimoto

Research Reactor Institute, Kyoto University

<sup>1</sup>School of Science and Technology,

Kwansei Gakuin University

<sup>2</sup>Graduate School of Science and Engineering,

Ibaraki University

<sup>3</sup>Institute of Regenerative Medicine and Biofunction,

Tottori University

**INTRODUCTION:** Proteasomes are the multicatalytic protein complexes with huge molecular weight. It is well known that the ubiquitin proteasome system plays an important role in regulated proteolysis. Proteasomes are known to act as antigen-processing enzymes responsible for the generation of peptide ligands presented by major histocompatibility complex (MHC) class I molecules. In the 20S proteasome each of 1, 2 and 5  $\beta$  subunits has different enzyme activities; 1 has caspase-, 2 tryptic- and 5 chymotryptic-like activities. It was found recently that inhibition of 20S proteasome activity resulted in decrease and disappearance of cancer cells. Since weak interaction of compounds to active amino acid residues we found, processing or degradation assay have been clarified by use of genetic mutations of the yeast 20S proteasome. The whole particle, 26S proteasome, including such 20S core is very important in the actual living cell for a degradation or stabilization on the cell circulation. Especially, a motion or behavior of the 26S proteasome when a regulatory particles bound should be clarified at atomic- or nano-scale resolution, we have tried to visualize such behavior as a motion capture of the atomic force microscopy (AFM) technique.

**EXPERIMENTS:** Genetic modification such as Y170A, Y170L and Y170F are succeeded in the  $\beta$ 5 subunit of the yeast. Wild and mutant cells were homogenized by glass beads and the crude extracts were purified by M2 affinity chromatography and Mono-Q anion exchange one. When the 26S particle was isolated, gel-filtration chromatography was continuously applied with a buffer solution including ATP. Isolated 20S proteasome was concentrated by ultrafiltration, and co-crystallized with small ligand and inhibitor molecules. AFM measurements of the 26S particle were carried out in the Research Institute of Biomolecule Metrology in Tsukuba.

**RESULTS:** The electron densities with a resolution of 2.85Å have been observed at the active site in the  $\beta$ -ring.

Binding site of inhibitor is closed to Tyr170 and Thr1 of the  $\beta$ 5 subunit. It is considered that an aromatic ring of the inhibitor interacts with Y170 by ring-stacking force. Genetic mutation for Y170 would have activities because of a lack of aromatic ring in the amino acid residue in the Ala and Leu, binding ability of the inhibitor might be lost. Typical activity assay for wild-type 20S shows reduction (Fig.1), but its concentration is slightly high rather than a clinical usage.

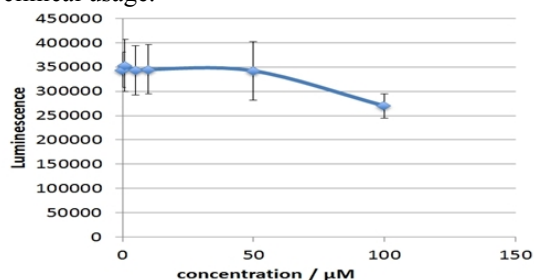


Fig.1 Activities of the 20S proteasome with inhibitor concentration.

The AFM measurement shows whole structure of the 26S particle, and analyses of resultant images describe a shape and size, and also a structural motion (Fig.2).

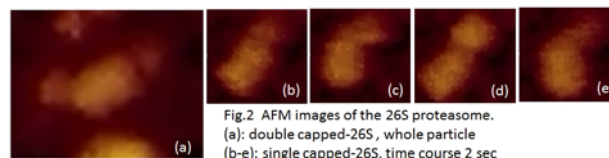


Fig.2 AFM images of the 26S proteasome.  
(a): double capped-26S, whole particle  
(b-e): single capped-26S, time course 2 sec

Fig.2a shows a double-capped whole 26S particle composed of central 20S and the both ends (19S regulatory particles). Those ends, however, are same direction like square brackets. Fig.2b-e shows a single-capped 26S, it means that preparation of the 26S is insufficient or scarce of ATP. Fig.2b to 2e is spent six seconds, in the meantime 19S part seems like to bow twice. In this case, since a preparation buffer includes no ATP reagents, it is interesting in such a motion by random movement or biologically functional changes. On the other hand the images are also considered the single-capped particle to be rotated in a solution, physical fixation of the 20S core to a basal plate should be required and the subject for a future study. This work was supported by a grants-in-aid for the Customer Care Plan Foundation (YM). The synchrotron radiation experiments were conducted under the approvals 2013AB6856, 2014A1855 and 2014AB6956, of SPring-8.

T. Chatake, S. Fujiwara<sup>1</sup>, I. Tanaka<sup>2</sup>, Y. Yanagisawa<sup>3</sup>

Research Reactor Institute, Kyoto University

<sup>1</sup>Japan Atomic Energy Agency

<sup>2</sup>Faculty of Engineering, Ibaraki University

<sup>3</sup>Faculty of Pharmacy, Chiba Institute of Science

**INTRODUCTION:** The neutron diffraction technique is undoubtedly one of important methods for elucidating behavior of hydrogen atoms in biological systems, as well as neutron scattering technique. Nevertheless, neutron diffraction analysis is not a popular method for structural biology yet, in comparison to a large number of X-ray diffraction analyses. The main reason of the limitation of neutron diffraction experiments is, of course, the lower flux of neutron beam against those of X-ray sources. On the other hand, several technical problems, which derive from to the lack of experimental experience, become obstacles for this forefront science. In this project, the following three themes were studied for neutron structural biology.

(1) A new technique for neutron structure determination.

(Fujiwara and Chatake).

A new technique for the deuterium/hydrogen (D/H) contrast map (the neutron scattering length of D and H atoms is largely different.) in neutron macromolecular crystallography is in developing by us. Our results suggested that this type of neutron map had advantages on the neutron structure determinations.

(2) An improved technique for production of deuterated biomolecule in bacteria.

(Yanagisawa and Chatake)

Deuteration of protein has been the important technique for neutron biology, and the most popular method is the overexpression of the target protein using genetically engineered E. coli. Meanwhile, in food industry, a considerable number of materials and supplements are produced in native bacteria. In this project, the protocols of producing deuterated biomacromolecules in *Bacillus subtilis natto* have been developed and improved.

(3) The basic research of the application of dynamic neutron polarization (DNP) for neutron protein crystallography (NPC).

(Tanaka and Chatake)

DNP is the sophisticated technique in neutron science. In DNP, polarized neutron alters its coherent and incoherent scattering depending on the nuclear spin of the polarized hydrogen. DNP is already applied for neutron scattering except biomolecules. In this project, the basic experiments essential for DNP were carried out.

**EXPERIMENTS and RESULTS:**

(1) A new technique for neutron structure determination.

In the previous study, D<sub>2</sub>O- and H<sub>2</sub>O- solvent crystals of bovine pancreatic ribonuclease A were prepared (21P9-6), and their neutron diffraction images were collected at BIX-3 at JRR-3M (JAEA). In this fiscal year, The D/H contrast neutron map was calculated in real space, and discrete peaks could be observed at the positions of D/H exchangeable atoms inside and outside of the protein [1]. The detailed investigation of the hydration of the protein is in progress.

(2) An improved technique for production of deuterated biomolecule in bacteria.

In the previous study, nattokinase (NK) and menaquinone-7 (MK-7) from *Bacillus subtilis natto* were purified, and the non-hydrogen structure of NK was determined by X-ray diffraction technique [2]. In addition, D<sub>2</sub>O-resistant *Bacillus subtilis natto* was obtained by successive cultivation in D<sub>2</sub>O medium [3] (21P9-3, 22P6-2, 23P2-2,3 and 24P5-4). NK and MK-7 are expected for good samples for neutron biology, NK neutron crystallography, MK-7 neutron small angle scattering. In order to perform these neutron experiments, deuterated NK and MK were necessary. In this fiscal year, the improvement of the amount of production was tried. The temperature of the cultivation was estimated to be 42 degree. In addition, hipolyptone was not good for the cultivation, although hipolyptone was superior to polypeptone in the cultivation of native *Bacillus subtilis natto* in H<sub>2</sub>O medium.

(3) The basic research of the application of dynamic neutron polarization (DNP) for neutron protein crystallography (NPC).

2,2,6,6-tetramethyl-1-piperidinyloxy (TEMPO) is a kind of radical, which is widely used for DNP. In the previous study, TEMPO was introduced in crystals of hen egg white lysozyme, and was confirmed in physicochemical method [4]. Recently, death-associated protein kinase (DAPK) was expressed and purified for neutron crystallography, and its X-ray structure was reported [5].

**REFERENCES:**

- [1] T. Chatake, S. Fujiwara, to be published.
- [2] Y. Yanagisawa *et al.*, Acta Crystallogr. F66 (2010) F66 (2010) 1670-1673.
- [3] Yanagisawa, Y. *et al.*, J. Synchrotron Rad. 20 (2013) 875-879.
- [4] Tanaka, I. *et al.*, J. Synchrotron Rad. 20 (2013) 958-61.
- [5] Yamaguchi, A. *et al.*, JPS Conference Proceedings, in press.

## PR2-3 Identification and characterization of proteolytic enzymes derived from *NephilaClavata*

Y. Hidaka<sup>1</sup>, M. Fujiwara<sup>1</sup>, T. Nakanishi<sup>1</sup>, S. Shimamoto<sup>1</sup>,  
and M. Miyazawa<sup>2</sup>

<sup>1</sup>Graduate School of Science and Engineering Kinki  
University

<sup>2</sup>National Institute of Agrobiological Sciences

**INTRODUCTION:** Spiders hunt insects using a web net. The fact that they eat them without chewing, indicate that spiders possesses highly efficient digestive enzymes [1]. Our previous studies suggest that spider's proteolytic enzymes are able to digest synthetic spider dragline amyloid fibers [2,3]. Thus, the spider protease has the potential ability to digest amyloid fibers including pathogenic  $\beta$ -amyloid, such as amyloid fibrils, that are associated with the development of Alzheimer's disease [1]. Therefore, we purified, identified, and characterized the enzymes derived from *Nephila Clavata*. The sequence analyses of the blotted protein on a PVDF membrane showed N-terminal amino acid residues. Based on this sequence information, we tried to clone the protease gene.

**EXPERIMENTS:** The spiders (*Nephila Clavata*) were collected in the field of Kyoto University Research Reactor Institute and the spider saliva including proteolytic enzymes was obtained from *Nephila Clavata* (50 heads) by electrical stimulation. The extracts were stored in a deep freezer until use.

Casein protease assay [4] of the crude spider enzymes was performed, as previously reported [1]. Peptide substrates for the assay of the protease activity of spider enzymes were chemically synthesized by the Boc solid phase method, treated with hydrogen fluoride, and purified by reversed phase HPLC [1, 4].

The N-terminal protein sequence was determined by the Edman degradation. First, the spider saliva was applied to SDS-PAGE, and the proteins bands were electrically transferred to a PVDF membrane. The electro-blotting of spider proteases was performed using the semi-dry blotting method then applied to then-terminal sequence analysis

Based on the N-terminal sequence, we prepared generated primers for the gene cloning and RT-PCR was performed using mRNA's from gut cells of *Nephila Clavata*.

**RESULTS:** Spider's digestive fluid that includes proteolytic enzymes was obtained from *Nephila Clavata* by

electrical stimulation using a micropipet. The extracts were applied to SDS-PAGE and the enzymatic activity of the protein bands was estimated by a casein protease assay [4]. Two protein bands showed protease activities and their molecular weights were estimated to be approximately 21.9 and 19.5 kDa, based on the SDS-PAGE analysis [1]. To characterize the enzymes, FLGLPA-KADA-NH<sub>2</sub> and SIFKTLRTIA-NH<sub>2</sub> were synthesized as model peptide substrates and treated with the crude spider protease. The results indicated that the spider protease can be classified as a Ca<sup>2+</sup>-dependent carboxypeptidase.

To further characterize the spider protease, the N-terminal amino acid sequence was determined by Edman degradation using blotted protein bands on PVDF membrane after SDS-PAGE separation. The results suggested the N-terminal amino acid sequence of the spider protease. Based on the amino acid sequence, generated primers for the gene cloning of the protease were prepared and RT-PCR was performed using mRNA's from gut cells of *Nephila Clavata*. Three clones were isolated and provided second PCR to produce cDNA's of spider proteases. The purified candidate cDNA's were inserted pBluescript SKII(-) and sequence analyses were performed. However, the sequence analysis of the cloned spider protease gene revealed that the cloned genes were non-specifically amplified during RT-PCR.

In conclusion, Spider protease was extracted from its digestive fluid and exhibited strong protease activity. The protease can be classified as a Ca<sup>2+</sup>-dependent carboxypeptidase, based on the results of protease inhibition assays. The N-terminal amino acid sequence of spider protease was determined by Edman degradation. Spider genes were amplified using generating primers, base on the N-terminal amino acid sequence, by RT-PCR and cloned into pBR-SKII(-). However, DNA sequence analysis indicated that the cloned DNA was non-specifically amplified during RT-PCR. The cloning of spider protease genes is in progress.

### REFERENCES:

- [1] M. Fujiwara *et al.*, *Peptide Science*, **2013**, 447-448 (2014).
- [2] S. Zheng, *et al.*, *Appl. Spectrosc.*, **43**, 1269-1272 (1989).
- [3] Y. Hidaka, *et al.*, *Biopolymers*, **96**, 222-227 (2011).
- [4] C. Dicko, *et al.*, *Biochemistry*, **43**, 1269-1272 (2004).

Y. Kinashi

Research Reactor Institute, Kyoto University

### Objectives and Participating Research Subjects

In this project, we are intending to develop the new application using the characteristics of the particles from the neutron capture reaction.

- PRS-1 Analysis of mutation in the mammalian cells induced by BNCR (boron neutron capture reaction)  
( Y. Kinashi *et al.* )
- PRS-2 Analysis of double strand breaks in the mammalian cells induced by BNCR  
( S.Takahashi *et al.* )
- PRS-3 Application of BNCR to plant tissue culture for mutation breeding  
( T.Morikawa *et al.* )
- PRS-4 Development of pharmacokinetic using boron trace drugs  
( H. Hori *et al.* )

### Main Results and Contents

PRS-1 inspected whether ascorbic acid was effective in protection of the mutation induction of neutron radiation beam used for BNCT in Kyoto University Research Reactor (KUR). The mutagenicity measured by the frequency of mutations induced by neutron irradiation with or without boron compound. The HPRT locus was examined in Chinese hamster ovary (CHO) cells irradiated with neutrons of KUR. High dose rate neutron irradiation was 0.2Gy/min with 5MW of KUR, and low dose rate neutron irradiation was 0.04Gy/min with 1MW of KUR. They investigated that dose rate effect is exist neutron irradiation in BNCT. Ascorbic acid treatment reduced mutation induction following neutron radiation. In neutron irradiation at high dose rate with BPA, the mutation induction was controlled most effectively. This result suggests that the ascorbate may protect the mutagenic effects of BNCT on the normal tissue cells that take up the low dose of boron compounds. They confirmed that the ascorbic acid was effective in protection of the mutation induction of neutron radiation beam used for BNCT.

PRS-2 investigated the most important biological effects, i.e., DNA damages, after the irradiation with heavy ion particles from BNCR and neutron beam. They advanced research related to the status of p53

and biological effects (cell killing and induction of DNA double strand breaks (DNA-dsb) using human glioblastoma cells, A172 and T98G. A172 are wild type of p53, and T98G cells are mutant type.

The results showed that difference of radiation sensitivity between A172 and T98G was decreased by BPA addition irradiation of neutron beam. These results indicate that the difference between the radiation sensitivity was observed between the T98G cells and A172 cells boron neutron capture reaction. Interestingly, it was reduced with BPA where the irradiation mainly depends on the particle radiation emitted by BNCR (Boron Neutron Capture Reaction). This result suggests that BNCT is an effective treatment with glioblastoma that can reduce the difference of radio sensitivity by p53 functional status.

PRS-3 compared the different damage effects on plants between BNCR and  $^{60}\text{Co}\gamma$ -ray. To determine the effectiveness of BNCR for plant mutagenesis at irradiation of dry seeds, two-row-barley was easily used because of its compact size of the seeds and higher mutation rate. The dry seeds of *Hordeum-vulgare* cv.Hayadori were immersed in different concentrations of  $^{10}\text{B}$ -enriched *p*-boronophenylalanine (BPA) for 24hours, and all the materials were irradiated with thermal neutron for 120 minutes in the Kyoto University Research Reactor (KUR).  $^{60}\text{Co}\gamma$ -ray irradiations were also carried out on the „Hayadori“ dry seeds in the different doses using the Kyoto University’s  $^{60}\text{Co}\gamma$ -ray irradiation facility. They found out that the semi-lethality dose ( $\text{LD}_{50}$ ) and  $\text{RD}_{50}$  in the reduced rate of 4-week-seedlings was 74.2 $\mu\text{M}$  BPA. The 469 $\mu\text{M}$  value was transformed to the total physical doses as 17.98 Gy, and the 74.2 $\mu\text{M}$  as 11.2Gy by using the transformation equation.

PRS-4 developed boron tracedrugs with their “on demand” traceability and their physical force for neutron dynamic therapy (NDT). The boron tracedrug, UTX-51 was studied that their dynamic, beyond chemical, effects when acquired by weak thermal neutron irradiation of glycated BSA as a model of advanced glycation end-products (AGEs), which is linked to diabetes and aged diseases. They found that all doses of the boron tracedrug UTX-51 caused destructive dynamic damage against Gly-BSA during thermal neutron irradiation, suggesting boron tracedrugs could be used as dynamic drugs for NDT targeted glycated proteins, such as Gly-BSA, for serum protein-quality-control treatment of AGEs-related diseases.



## PR3-1 The effect of ascorbic acid on the HPRT mutation induction after the neutron irradiation

Y. Kinashi<sup>1</sup>, K. Ono<sup>1</sup>, S. Takahashi<sup>1</sup>

<sup>1</sup>Research Reactor Institute, Kyoto University

**INTRODUCTION:** We have previously reported the increased mutagenicity of thermal neutrons and the dose rate effect of the neutron radiation beam [1]. Clinically, the mutagenic effects of BNCT on the normal tissue cells that do not take up the boron compounds may cause the genetic instability and second cancer decades years after BNCT. In this study, we inspected whether ascorbic acid was effective in protection of the mutation induction of neutron radiation beam used for BNCT in Kyoto University Research Reactor (KUR).

**MATERIALS & METHODS:** The mutagenicity measured by the frequency of mutations induced by neutron irradiation with or without boron compound. The hypoxanthine-guanin-phosphoribosyl-transferase (HPRT) locus was examined in Chinese hamster ovary (CHO) cells irradiated with neutrons of KUR. A stock solution of 10B-para-boronophenylalanine (BPA) was used for this experiment. Cell suspensions were incubated with BPA at 10 ppm concentration 1 hour before neutron irradiation. High dose rate neutron irradiation was 0.2Gy/min with 5MW of KUR, and low dose rate neutron irradiation was 0.04Gy/min with 1MW of KUR. Neutron fluencies were measured by radioactivation of gold foil and gamma-ray dose by TLD. After neutron exposure, L-ascorbic acid was added to cells at a final concentration of 5mmol/L and removed after 150 min of neutron irradiation. To determine mutation frequencies, each treated culture was incubated with non-selective medium for 7-9 days to allow phenotype expression. Then,  $2 \times 10^5$  cells were added to each dish containing 6-thioguanine and incubated for 10-14 days, after which time the mutant colonies were counted. The mutation frequency is expressed as the number of resistant colonies divided by the total number of viable cells as determined by cloning efficiency at the time of selection.

**RESULTS and DISCUSSION:** Figure 1 shows the mutation frequency in the HPRT locus in CHO cells after neutron irradiation at 0.2Gy/min or at 0.04Gy/min with or without BPA. The frequency of mutations after neutron irradiation with 10ppm BPA at

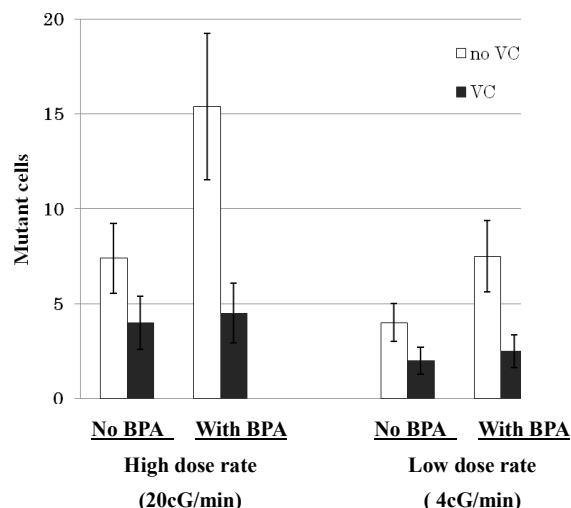


Fig.1 Induction of mutations in the HPRT locus in CHO cells with or without BPA under the ascorbic acid treatment. VC means Vitamin C which is an ascorbate popular name.

0.2Gy/min in was 1.5-1.9 times and more increased than at 0.04Gy/min in the function dose over the 1.8Gy.

These results suggested that dose rate effect is exist neutron irradiation in BNCT. Ascorbic acid treatment reduced mutation induction following neutron radiation. This protective effect of mutation induction was more effective with BPA than without BPA. This result shows that an ascorbate scavenged long-lived radicals due to the nuclear capture reaction that of alpha particles or  $^7\text{Li}$  nuclei produced by  $^{10}\text{B}(n,\alpha)^7\text{Li}$  reaction, not due to the reaction with normal tissue hydrogen and nitrogen. In neutron irradiation at high dose rate (0.2Gy/min) with BPA, the mutation induction was controlled most effectively. This result suggests that the ascorbate may protect the mutagenic effects of BNCT on the normal tissue cells that take up the low dose of boron compounds, for example the peri-tumoral stroma cells after BNCT.

In this study, we found that the ascorbic acid was effective in protection of the mutation induction of neutron radiation beam used for BNCT dose rate effect of the neutron radiation beam used for BNCT.

### REFERENCES:

- [1] K. Kinashi *et al.*, Appl. Radiat. Isot., **88** (2014) 153-156.

## PR3-2 Analysis of DNA Double Strand Breaks in the Mammalian Cells Induced by BNCR

S. Takahashi, Y. Kinashi, K. Seki, N. Yokomizo<sup>1</sup>, T. Ikawa<sup>1</sup>, K. Ono, Y. Kubota<sup>2</sup>, and R. Okayasu<sup>2</sup>

Research Reactor Institute of Kyoto University,

<sup>1</sup>Graduate School of Agriculture, Kyoto University,

<sup>2</sup>National Institute of Radiological Sciences

**INTRODUCTION:** Boron neutron capture therapy (BNCT) is a unique and effective treatment for cancer, and now becoming a clinical application stage. However, little is known about the biological effects of particle radiation induced by BNC reaction (BNCR) nor thermal-epithermal neutron beams for BNCT. In the present study, we have investigated the most important biological effects, i.e., DNA damages, after the irradiation with heavy ion particles from BNCR and neutron beam. In the FY 2014, the relationship between the status of p53 and biological effects (cell killing and induction of DNA double strand breaks (DNA-dsb) was investigated.

**EXPERIMENTS:** Two types of human glioblastoma cells, A172 and T98G were cultured. Both cells were purchased from Riken BRC Cell Bank. A172 are wild type of p53, and T98G cells are mutant type. The cells were cultured in MEM $\alpha$  medium (Invitrogen) supplemented with 10% heat-inactivated FBS (Biowest) and maintained at 37°C in a humidified atmosphere with 5.0% CO<sub>2</sub>. The cells were irradiated at the KUR irradiation field for BNCT, with/without BPA. As a reference radiation, Co-60 gamma-ray was used at the same dose rate as the mixed irradiation. The cells were assayed for conventional colony formation, and DNA double strand breaks (DSBs) were detected by immune-staining using 53BP1 antibodies.

**RESULTS & DISCUSSION:** The data on the cell survival are shown in Fig. 1 for the cell lines of A172 and T98G. In the case of not BPA added cells, A172 got the steep slope graph of survival fraction. This shows T98G cells have lower sensitivity to neutron mixed beam irradiation than A172. On the other hand, in the case of BPA added cells, survival fraction curves of both cells were similar. This shows difference of radiation sensitivity which confirmed the case of not added BPA cells declined by addition of BPA. When compared at 10% survival, in the case of not added BPA cells, A172 cells were required 1.663Gy radiation dose to cause 90% cell death, but T98G required 5.245Gy. This shows T98G were required the dose of 3 times more than the A172 to cause 90% cell death in the case of not added BPA, neutron mixed beam irradiation alone cases. On the other hand, in the case of added BPA cells, D10 of A172 indicated 0.821 Gy, and T98G indicated 1.076 Gy. This data indicated

that difference of radiation sensitivity between A172 and T98G was decreased by BPA addition irradiation of neutron mixed beam.

These results indicate that the difference between the radiation sensitivity was observed between the T98G cells and A172 cells boron neutron capture reaction. Interestingly, it was reduced with BPA where the irradiation mainly depends on the particle radiation emitted by BNCR (Boron Neutron Capture Reaction). This result suggests that BNCT is an effective treatment with glioblastoma that can reduce the difference of radiosensitivity by p53 functional status.

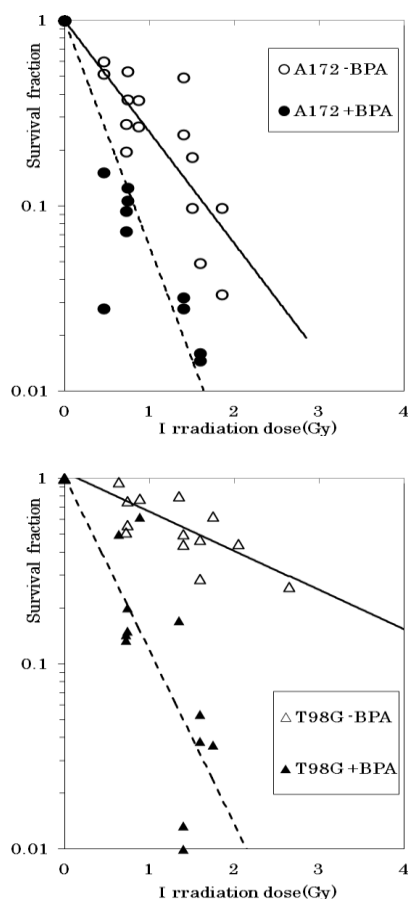


Fig. 1. Survival of glioblastoma cells (A172 and T98G) irradiated with thermal- to epithermal neutron beam of KUR with/without BPA.

### PUBLICATION:

[1] K. Seki, Y. Kinashi, S. Takahashi:

The influence of p53 status in glioblastoma on the effects of boron neutron capture therapy. *Anticancer Research*, 35: 169~174, 2015.

## PR4 Project Research on Development of Scattering Spectrometers Utilizing Small and Medium Class Neutron Source

Masaaki Sugiyama

*Research Reactor Institute, Kyoto University*

**Objectives and Allotted Research Subjects:** It is no doubt that Small-angle neutron scattering is one of the most powerful tools to investigate nanoscale structures in variety of materials. However, the less opportunity to do SANS is a bottleneck that SANS becomes general method to observe nanoscale structure. Utilizing small and medium size reactor as a neutron source for SANS spectrometer gives one answer for this difficulty. Under this line, this project proves it through showing the feasibility and upgrade of KUR-SANS.

**ARS-1:** Challenge for Development of Analyzer for Particle-Size distribution with Small-Angle Scattering. (M. Sugiyama, R.Inoue, N.Sato and Y. Oba)

**ARS-2:** Are Size Upgrading of Compact Monochromator for SANS. (M. Hino, Y. Oba, M.Sugiyama, T. Oda and S.Tasaki)

**ARS-3:** Structural Analysis of PVA gel by adding Inorganic Salt (R.Inoue, Y. Oba, N. Sato, T.Kanaya and M. Sugiyama)

**ARS-4:** Estimation of Fine Structure in Metallic Materials by SANS (Y. Oba, S.Morooka, M. Ohnuma, N. Sato, M. Sugiyama)

**ARS-5:** KUR-SANS Observations and Analysis Surfactants' Nano-structural Change by Capturing Heavy Metal. (K. Hara, T. Miyazaki, Y. Oba, N. Sato, M. Sugiyama, Y. Hidaka and H. Okabe,)

**ARS-6:** Small-Angle Neutron Scattering Analysis of the Nanostructure of Wheat Proteins. (R. Urade, Y. Higashino, S.Funaki, Y.Kitao, N. Sato and M. Sugiyama)

**ARS-7:** Structural Investigation on Radiation-Fabricated Functional Gel. (N. Sato, Y. Oba and M. Sugiyama)

**ARS-7:** Quantitative Analysis for TiN particle by Effect of Thermal Weld in Steel (S. Morooka, Y. Oba, and M. Sugiyama)

**ARS-8:** Nano structure of metal hydride by neutron small angle scattering. (K. Iwase, K. Mori, Y.Oba and M. Sugiyama)

### **Main Results and Contents of This Project:**

ARS-1: Not performed by no operation of KUR.

ARS-2: Not performed by no operation of KUR.

ARS-3: Not performed by no operation of KUR.

ARS-4: Not performed by no operation of KUR.

ARS-5: Hara et.al. continued to analyze nano-structural change of a surfactant (Sodium Oleate, NaOl) with KUR-SANS. (The data was obtained in 2013). They analyzed the surfacta system with pair distance distribution function and revealed spherical scatterers in the solution.

ARS-6: Not performed by no operation of KUR.

ARS-7: Not performed by no operation of KUR.

ARS-8: Not performed by no operation of KUR.

K. Hara, T. Miyazaki, Y. Oba<sup>1</sup>, N. Sato<sup>1</sup>, M. Sugiyama<sup>1</sup>,  
Y. Hidaka, H. Okabe

*Department of Applied Quantum Physics and Nuclear Engineering, Kyushu University*

<sup>1</sup>*Division of Quantum Beam Material Science, Research Reactor Institute, Kyoto University*

### INTRODUCTION:

Ion flotation is well-known as a simple and useful method to remove hazardous ions or to recover valuable ions [1,2]. Besides, because the surfactants are known to exhibit various nano-scale structural changes in the flotation process as scavengers or collectors, such a nano-structural change will be useful for examining the performance of KUR-SANS system installed at Research Reactor Institute, Kyoto University. Therefore, in the present study, the nano-structural changes of a surfactant (Sodium Oleate, NaOl) in the flotation process have been investigated.

### EXPERIMENTS:

CuCl<sub>2</sub> (5 mM) was added to respective NaOl (30 mM)-D<sub>2</sub>O solutions after adjusting their pH's at 7, 8, 10 and 12 with HCl and NaOH. Then the solutions were bubbled for 10 min and were poured into quartz cells for the SANS measurements. The SANS profiles were measured at room temperature with the KUR-SANS system (CN-2) with a 2.8 Å neutron beam.

### RESULTS:

Figures 1 and 2 show SANS profiles of the CuCl<sub>2</sub>-added Sodium Oleate in D<sub>2</sub>O at several pH's before and after the flotation, respectively. Except for the pH=12 specimen, the lower-*q* region intensity decreased greatly indicating the larger substances are effectively recovered by flotation. In the present study, the SANS profiles have been further analyzed with pair distance distribution functions (PDDF) for deriving semi-quantitative scatterer-shape information [3]. As an example, the PDDF of Cu-added pH=10 specimen is shown in Fig. 3, of which the well-defined symmetric bell-shape indicates the existence of spherical scatterers in the solution. Such features demonstrates a high quality of the SANS profiles measured by the KUR-SANS system.

### REFERENCE:

- [1] F. Sebba, *Ion flotation* (Elsevier, Amsterdam, 1962)
- [2] E. J. Mahne and T. A. Pinfeld, *J. Appl. Chem.*, **18** (1968) 52-54
- [3] O. Glatter, *J. Appl. Cryst.*, **10** (1977) 415-421

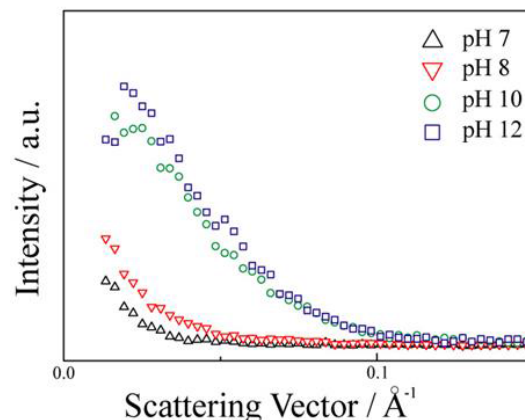


Fig.1 SANS profiles of Sodium Oleate in D<sub>2</sub>O containing CuCl<sub>2</sub> before flotation.

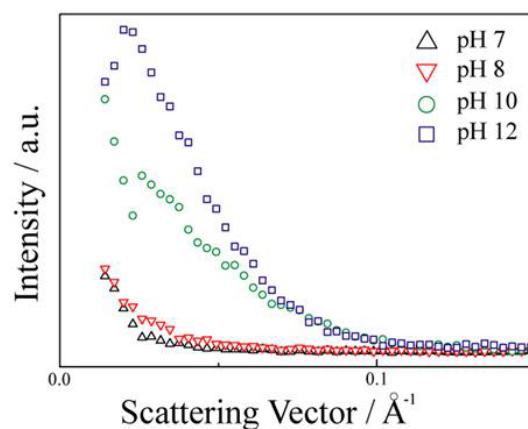


Fig.2 SANS profiles of Sodium Oleate in D<sub>2</sub>O containing CuCl<sub>2</sub> after flotation.

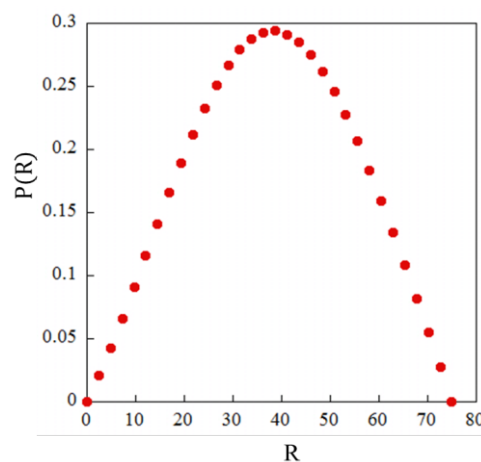


Fig.3 Pair distance distribution function of Sodium Oleate in D<sub>2</sub>O containing CuCl<sub>2</sub>.

## PR5 Behavior of Radioactive Nuclides in Intense Radiation Fields in Accelerator Facilities

Y. Oki

*Research Reactor Institute, Kyoto University*

### OBJECTIVES AND RESEARCH SUBJECTS:

High-energy and high-intensity accelerators are widely used for many fields such as physics, chemistry and cancer therapy. The high-energy proton accelerators produce a variety of radionuclides through nuclear reactions including spallation reactions in high-energy accelerator facilities. The activation takes place in accelerator hardware, air, cooling water and other materials such as soil outside of shielding concrete walls. From the viewpoints of radiation safety and safe accelerator operation, the management of the radionuclides is very important. The behavior and property of the radionuclides are the most important information to estimate radiation exposure and to ensure the accelerator safety.

In this work, the behavior and property were investigated in the air of the accelerator rooms and the cooling water.

The following problems are studied in this work.

1. The property of radioactive airborne species (radioactive aerosols and radioactive gases) in the air.
2. The behavior of dissolved metals from cooling water tubes and radioactive nuclides formed in the water.
3. Problems related to activation in accelerator facilities such as development of new radiation detectors for high energy accelerators and measurement of formation cross section of the principal radionuclides for dose estimation.

The participating research subjects (PRS) in the final year of this project research (Fiscal 2014) and co-workers in each subject are listed below.

PRS-1 (26P5-1) Radioactivity Size Distribution of Airborne Aerosols Formed in Target Room Estimated from Number Size Distribution  
(S. Yokoyama, Y. Oki and S. Sekimoto)

PRS-2 (26P5-2) Production of Airborne Nano-Particles by Proton Irradiation in an FFAG Accelerator  
(Y. Oki, N. Osada, S. Yokoyama, Y. Ishi, T. Uesugi, Y. Kuriyama and M. Sakamoto)

PRS-3 (26P5-3) Corrosion of Various Metals in Water and Formation of Metal-related Colloidal Particles under Intense Photon-Radiation Field  
(K. Bessho, H. Matsumura, Y. Oki, S. Sekimoto, K. Masumoto and N. Abe)

### MAIN RESULTS:

PRS-1

The present study analyzed a distribution of radioac-

tive aerosols in the target room of the KUR-LINAC. The size and radioactivity of the aerosol sampled from two sampling positions (40 cm and 230 cm apart from the Ta target) were compared. The target was irradiated with the 30-MeV electron beams of 10, 50, and 100- $\mu$ A currents for  $\sim$ 2 h per experiment. Radioactive aerosols were collected with a low-pressure cascade impactor to obtain the particle size distribution. Under 10  $\mu$ A and 50  $\mu$ m, the particle size distribution for radioactive aerosols showed no significant difference between the two sampling positions. Total radioactivity at both positions increased with beam current.

PRS-2

An air irradiation experiment was performed in the 150-MeV FFAG proton accelerator using an air-irradiation chamber under various beam conditions. The size and concentration of the aerosol particles produced in the irradiation were studied for applications to the instrument calibration and other experiments using standard aerosol particles. The size was increased as the air supplying flow rate to the chamber was decreased. In other words, the particles grew as the irradiation time was increased. The size was possible to be varied by changing the flow rate to the chamber. In the case of 1 nA, beam current, the size was able to be changed from approximately 10 to 20 nm in geometric mean diameter. The size and concentration were also dependent on the beam current. An increase in size and concentration was observed above the proton current of approximately 300 pA and they were almost saturated above 1 nA at the flow rate of 18 L/min

PRS-3

In this work, experimental metal vessels filled with pure water were irradiated by  $\gamma$ -rays or bremsstrahlung / neutrons generated at electron linear accelerator (LINAC) facility as model environments for cooling water used inside accelerator facilities. Radiation effects on corrosion of various metals in water and colloid/particle formation of metal elements were systematically studied. After the irradiation of  $\gamma$ -rays or bremsstrahlung, soluble (<3 nm), colloidal (3-200 nm), and particulate (>200 nm) metal elements were detected in water. The size profiles for each element in water and characteristics in radiation effects were dependent on vessel materials. In the experiments using Al and Fe vessels, total Al/Fe concentrations became higher dependent on photon irradiation intensity. In the water supernatant obtained after the irradiations, Al and Fe were found to be mainly present as relatively-large particles (>200 nm). Concentrations of soluble species and fine colloidal species are quite small compared to those of the large particle species. Their chemical states were also discussed in this work.

採択課題番号 26P5

加速器施設の高線量場における放射性核種の挙動に関する研究

プロジェクト

(京大・原子炉) 沖 雄一

S. Yokoyama,<sup>1</sup> Y. Oki,<sup>2</sup> and S. Sekimoto<sup>2</sup>

<sup>1</sup> School of Health Science, Fujita Health University

<sup>2</sup> Graduate School of Engineering, Kyoto University

**INTRODUCTION:** To assess internal exposure of accelerator facility workers due to inhaling radioactive aerosols and gases, the radioactivity size distribution and the amount of radioactive aerosols formed in the facilities must be estimated [1–4]. In previous studies, aerosol radioactivity and number size distributions were measured in the target room of KUR-LINAC and the radioactivity size distributions were estimated from the number-size distributions [3, 4]. In addition, the relationship between radioactivity size distribution of aerosols and beam currents was investigated. The present study analyzes a distribution of radioactive aerosols in a target room.

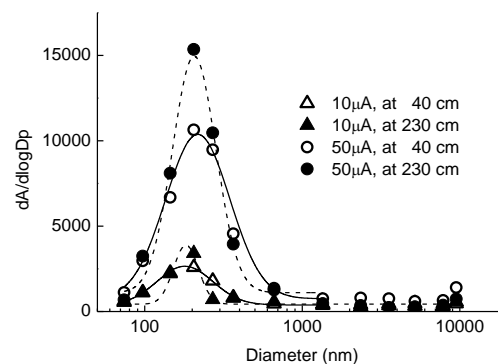
**EXPERIMENTS:** Two sampling ports were prepared 40 cm (port 1) and 230 cm (port 2, near the wall surface) from the target of KUR-LINAC. Electron beams were generated under a 30-MeV voltage and 10-, 50-, and 100- $\mu$ A currents for  $\sim$ 2 h per experiment. A water-cooled Ta target was placed at the end of the beam line as a neutron generator. Radioactive aerosols were collected by a 13-stage low-pressure cascade impactor (Tokyo Dylec Corp.). Stainless steel plates coated with grease were set in each stage, except for the lowest stage, in which a filter was set. The collection started at 60 min after irradiation began and continued for 30 min. After collection, the plate and filter radioactivities were measured by a GM survey meter (TGS123-C, Aloka). Radionuclides formed in the target room confirmed that  $^{13}\text{N}$  contributed significantly to total activity, when compared with the lower radioactivity measured in the previous study [4].

**RESULTS:** Figure 1 shows the radioactivity size distribution of aerosols under 10- and 50- $\mu$ A beam currents at ports 1 and 2. Under 10  $\mu$ A, the median diameters of radioactive aerosols were 270 and 189 nm ( $\sigma$ : 1.5 and 1.2) at ports 1 and 2, respectively. Under 50  $\mu$ A, median diameters of radioactive aerosols were 270 and 229 nm ( $\sigma$ : 1.6 and 1.4) at ports 1 and 2, respectively. In the previous study, the median diameter of radioactive aerosols collected near the target was  $261 \pm 3.9$  nm under 20-100  $\mu$ A [3, 4]. Figure 2 illustrates the total radioactivity of aerosols under 10, 50 and 100  $\mu$ A. Total radioactivity at ports 1 and 2 increased with beam current.

Radionuclides are mainly generated by interaction between neutrons and the atmospheric nitrogen and oxygen proximal to the target just after the electron beam hits the target. Non-radioactive aerosols were formed by irradiation by electrons leaked from the beam line and gamma

rays induced by electrons.

Under 50  $\mu$ A, the peak radioactivity count collected at port 2 was 1.3 times higher than that at port 1, as shown in Fig. 1. The number size distributions of aerosols simultaneously measured by a Scanning Mobility Particle Sizer (TSI, Model 3080) showed a similar result. Radioactive aerosols are formed by deposition of radionuclides on non-radioactive aerosols. Thus, the number of radioactive aerosols at port 2 under 50  $\mu$ A should increase. No clear difference existed between median diameters of radioactive size distributions at ports 1 and 2. This means that the non-radioactive aerosols were generated not only around the target, but also throughout the target room.



F

fig. 1. Activity size distribution of radioactive aerosols collected at ports 1 and 2.

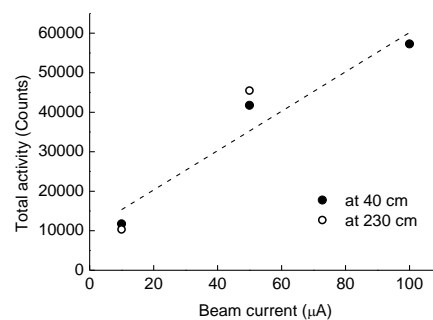


Fig. 2. Total activity of radioactive aerosols at ports 1 and 2.

### REFERENCES:

- [1] S. YOKOYAMA *et al.*, Jpn. J. Health. Phys., **43** (2008) 333–340.
- [2] S. YOKOYAMA *et al.*, Rad. Prot. Dosi., **127** (2007) 392–397.
- [3] S. YOKOYAMA *et al.*, KURRI progress report 2012, PR11-1 (2013), <http://www.rri.kyoto-u.ac.jp/JRS/>.
- [4] S. YOKOYAMA *et al.*, KURRI progress report 2013, <http://www.rri.kyoto-u.ac.jp/PUB/report/PR/ProgRep2013/Project8.pdf>

## PR5-2 Production of Airborne Nano-Particles by Proton Irradiation in an FFAG Accelerator

Y. Oki, N. Osada<sup>1</sup>, S. Yokoyama<sup>2</sup>, Y. Ishi, T. Uesugi, Y. Kuriyama and M. Sakamoto

Research Reactor Institute, Kyoto University

<sup>1</sup>Advanced Science Research Center, Okayama University

<sup>2</sup>School of Health Science, Fujita Health University

**INTRODUCTION:** In accelerator facilities, very fine radiation-induced aerosol particles were often produced in air of accelerator rooms during machine operation. The size and concentration of the particles are generally very stable under a given beam condition. This particle generation may be applicable to calibration of size-measuring instrument for the fine particles in the diameter range of nm to 0.1  $\mu\text{m}$ .

In this work, an air irradiation experiment was performed in an FFAG (Fixed Field Alternating Gradient) proton accelerator under various beam conditions. The size and concentration of the aerosol particles produced in the irradiation were studied for applications to the instrument calibration and other experiments using standard aerosol particles.

**EXPERIMENTS:** The irradiation experiment was performed in the 150-MeV FFAG proton accelerator of Research Reactor Institute, Kyoto University (KURRI). The FFAG accelerator system consists of the 11-MeV  $\text{H}^-$  linear accelerator (Injector) and the FFAG main ring. The injected protons are accelerated in the main ring to 150 MeV after conversion of  $\text{H}^-$  ions to protons. The nominal 150-MeV proton beams were extracted to an air irradiation chamber in the specimen irradiation beam line. Figure 1 shows the irradiation chamber together with the specimen irradiation beam line and the main ring.

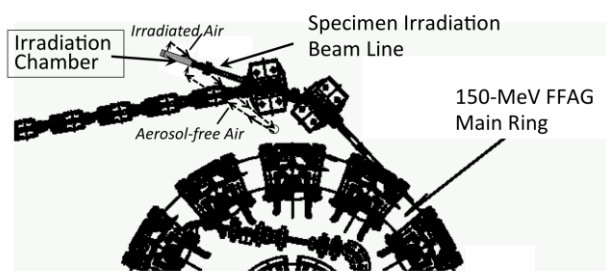


Fig.1 Irradiation Chamber

The air-irradiation chamber was a 1-m long stainless steel cylinder (i.d. 15 cm). It was installed upstream of

the beam dump of the specimen irradiation beam line. The 1-mm thick aluminum plates were used as both ends of the chamber. The aerosol-free air was prepared by filtration and was introduced to the chamber at the constant flow rate, and the irradiated air was sampled from the chamber at the same flow rate.

The size distribution and the total concentration of the aerosol particles were measured with SMPS (Scanning Mobility Particle Sizer).

**RESULTS AND DISCUSSION:** The size of formed aerosol particles showed very steady mono-modal log-normal distributions. The size was increased as the air supplying flow rate was decreased. In other words, the particles grew as the irradiation time was increased. The size was possible to be varied by changing the flow rate to the chamber. In the case of 1 nA, beam current, the size was able to be changed from approximately 10 nm (the flow rate: 18 L/min) to 20 nm (8 L/min) in geometric mean diameter. The size and concentration were also dependent on the beam current. An increase in size and concentration was observed above the proton current of approximately 300 pA and they were almost saturated above 1 nA at the flow rate of 18 L/min [1].

During the air irradiation, principal radionuclides formed in the accelerator air,  $^{15}\text{O}$  (half life: 2 min),  $^{13}\text{N}$  (10 min),  $^{11}\text{C}$  (20 min) [2] and  $^7\text{Be}$  (53 d), are formed together with the radiation-induced aerosol particles. The aerosol particles form radioactive aerosols by incorporating the radioactive atoms into the radiation-induced particles. The size distribution of  $^7\text{Be}$ -bearing aerosol particles were successfully measured with a graded screen array system in the same air-irradiation chamber [1]. The  $^7\text{Be}$  aerosol particles can be also used in various research including calibration of aerosol instruments for radioactive fine particles.

In conclusion, the air-irradiation chamber was capable of producing aerosol particles in the diameter range of 10 to 20 nm by the 1-nA proton irradiation carried out in the FFAG accelerator.

### REFERENCES:

- [1] Y. Oki, N. Osada, Y. Ishi, T. Uesugi, Y. Kuriyama and M. Sakamoto, KEK Proceedings **2014-7**, 52-57.
- [2] A. Endo, Y. Oki, Y. Kanda, T. Oishi, and K. Kondo, Radiat. Prot. Dosim., **93** (2001) 223-230.

## PR5-3 Corrosion of Various Metals in Water and Formation of Metal-related Colloidal Particles under Intense Photon-Radiation Field

K. Bessho, H. Matsumura, Y. Oki<sup>1</sup>, S. Sekimoto<sup>1</sup>,  
K. Masumoto, N. Abe<sup>1</sup>

Radiation Science Center, KEK

<sup>1</sup>Research Reactor Institute, Kyoto University

**INTRODUCTION:** At high-energy accelerator facilities, intense radiations affect chemical states of elements including radionuclides inside the facilities. In the cooling-waters for various accelerator components, corrosion of metal components and formation of metal related colloids/particles in water are important subjects in the radiation safety managements at accelerator facilities, because some radionuclides are incorporated in colloidal species and it complicate the behavior of nuclides [1,2].

In this work, experimental metal vessels filled with pure water were irradiated by  $\gamma$ -rays or bremsstrahlung / neutrons generated at electron linear accelerator (LINAC) facility as model environments for cooling water used inside accelerator facilities. Radiation effects on corrosion of various metals in water and colloid/particle formation of metal elements were systematically studied.

**EXPERIMENTS:** Metal vessels (*I. D.* 19 x 75 mm) filled with pure water were irradiated by  $\gamma$ -rays generated at the <sup>60</sup>Co  $\gamma$ -ray irradiation facility, or bremsstrahlung / neutrons generated by 30 MeV electron beam hitting on a Ta target ( $\Phi$ 50 x 62 mm) at the LINAC facility. Samples at the LINAC experiments were placed at the downstream position (40 or 80 mm from Ta target) and perpendicular position (40 or 80 mm from Ta target). Monte Carlo calculations and activation experiments using metal foils (Au, Al) demonstrated that radiation effects observed in the present LINAC experiments could be ascribed to the effects of photon irradiations (maximum fluxes; 3 MeV for 0-deg and 0.7 MeV for 90-deg). Contribution of neutrons was found to be much smaller than those of photons in these experiments.

After the irradiations, water in metal vessels were poured out and treated with four kinds of ultrafiltration (UF) membrane units for particle size separation contained in water supernatant. Estimated pore sizes of the UF units were 200, 16, 7 and 3 nm. Concentrations of metal elements in the filtrates and unfiltered samples were determined by ICP-AES analyses.

**RESULTS:** After the irradiation of  $\gamma$ -rays or bremsstrahlung, soluble (<3 nm), colloidal (3-200nm), and particulate (>200nm) metal elements were detected in water. The size profiles for each elements in water and characteristics in radiation effects were dependent on vessel materials (pure Fe, Al, Cu, and SUS-304, A6061

alloys). In this report, some characteristics observed for pure Al, Fe and Cu are described.

In the experiments using Al and Fe vessels, irradiations were carried out at LINAC with two kinds of beam currents (20, 100  $\mu$ A) and the irradiation times of 2 h. Total Al/Fe concentrations became higher dependent on photon irradiation intensity. In the water supernatant obtained after the irradiations, Al and Fe were found to be mainly present as relatively-large particles (>200 nm). Concentrations of soluble species and fine colloidal species are quite small compared to those of the large particle species. Al and Fe in non-degassed water are considered to be in the oxidation states of III (Al<sup>3+</sup>, Fe<sup>3+</sup>), which tend to form hydroxide precipitations in neutral pH conditions. It can be supposed that photon irradiation facilitates the corrosion (oxidation) of pure Al and Fe metals in water, consequently Al and Fe are released as Al<sup>3+</sup>, Fe<sup>3+</sup> ions from the metal surface to water, finally form Al(OH)<sub>3</sub> and Fe(OH)<sub>3</sub> particles in water phase.

In case of the experiments using Cu metal vessels, effects of radiation were mainly observed as increase in soluble Cu species (<3 nm) and production of large particle Cu species (>200 nm). Under irradiation conditions, soluble Cu concentration increased with time depend on photon doses and finally reached to plateau, which may be originated from hydrolysis of Cu(II) ions. On the other hand, production of particle Cu species was observed remarkably after long irradiation times (> 20-30 h). These characteristic time-dependence imply that particle Cu species were initially generated at the Cu/water interface as particle-like corrosion products. These products grew up at the interface in a time scale of several tens hours, and were finally released into water phase as particles (> 200 nm). The particle production processes at the interface were also promoted by photon irradiations [3].

Radiation effects on corrosions of metals in water are explained by production of oxidative reactive species, such as OH radicals and H<sub>2</sub>O<sub>2</sub>, induced by radiolysis of water molecules. By using water quality testing kits, it was demonstrated that several mg/L of H<sub>2</sub>O<sub>2</sub> and O<sub>3</sub> were produced by irradiation of water by  $\gamma$ -rays or bremsstrahlung, and these oxidative species should induce various radiation effects clarified by this work.

### REFERENCES:

- [1] K. Bessho *et al.*, J. Radioanal. Nucl. Chem., **303** (2015) 1719-1725.
- [2] H. Matsumura *et al.*, Progress in Nucl. Sci. Technol., **4** (2014) 372-375.
- [3] K. Bessho *et al.*, J. Radioanal. Nucl. Chem., **303** (2015) 1117-1121.

採択課題番号 26P5-3 高線量放射線場における水中金属材料の腐食および

プロジェクト

コロイド生成挙動の解析 2

(KEK・放射線) 別所光太郎、松村宏、榎本和義

(京大・原子炉) 沖雄一、関本俊



Q. Xu

*Research Reactor Institute, Kyoto University*

**OBJECTIVES:** Neutron irradiation is usually used to investigate radiation effects in solid materials and develop new materials. Unfortunately, because the operation time of KUR was limited, and the laboratory for neutron-irradiated samples could not be used in 2014, the research activities were severely restricted. In the present report, instead of neutron irradiation, ion, electron and  $\gamma$  ray irradiations were used to estimate degradation mechanical properties of materials, such as material for optoelectronic and high-power devices.

**RESULTS:** The allotted research subject (ARS) and the name of co-researchers in each ARS are listed below.

## ARS-1

Compensation mechanism of DX-like center in neutron transmutation doped GaN

(K. Kuriyama, T. Nakamura, A. Shikawa, K. Kushida, and Q. Xu)

## ARS-2

Neutron irradiation effects of superconducting magnet materials at low temperature

(T. Nakamoto, M. Yoshida, T. Ogitsu, Y. Makida, K. Sasaki, S. Mihara, K. Yoshimura, H. Nishiguchi, M. Sugano, M. Iio, Y. Yang, Y. Kuno, M. Aoki, A. Sato, Q. Xu, K. Sato, Y. Kuriyama and Y. Mori)

Candidate materials, such as Al and Cu alloys, for superconducting magnets of upgraded LHC at CERN and the muon source for the COMET experiment at J-PARC were irradiated by LTL at  $\sim 10$  K. In Al alloys, almost 100% of the defects produced by the irradiation was recovered after warming up to room temperature, however, several percent of the defects was remained in Cu alloy even at room temperature.

## ARS-3

Study on fine structures formed by high energy particle irradiation

(A. Kinomura, K. Sato, Q. Xu and T. Yoshiie)

## ARS-4

Thermoluminescence of Synthesized Calcite

(T. Awata, K. Nakashima and Q. Xu)

## ARS-5

Electron irradiation on W at around 500 °C using KURRI-LINAC

(M. Akiyoshi, T. Yoshiie, Q. Xu and K. Sato)

## ARS-6

The development of new positron beam system using KUR

(Y. Nagai, K. Inoue, T. Toyama, Y. Shimizu, K. Nagumo, M. Shimodaira, T. Hirota, K. Sato, T. Yoshiie and Q. Xu)

## ARS-7

Radiation damage in bulk amorphous alloys by electron irradiation

(F. Hori, K. Ishii, T. Ishiyama, K. Kobayashi, A. Iwase, Y. Yokoyama, Q. Xu and K. Sato)

## ARS-10

Positron annihilation study of Fe-Cr alloys after neutron irradiation in KUR

(R. Kasada, K. Sato and Q. Xu)

## ARS-12

Positron annihilation lifetime measurements austenitic stainless steels irradiated in the SINQ target irradiation program

(K. Sato, Q. Xu, T. Yoshiie, Y. Dai and K. Kikuchi)

## ARS-13

Effects of high energy particle irradiation on hydrogen retention in refractory metals

(K. Tokunaga, M. Matsuyama, S. Abe, H. Osaki, K. Araki, T. Fujiwara, M. Hasegawa, K. Nakamura, Q. Xu and K. Sato)

## ARS-14

Dependence of cellular structure formation on ion species

(N. Nitta, C. Watanabe, M. Taniwaki, Q. Xu and T. Yoshiie)

**CONCLUSIONS:** The defects induced by irradiation degrade the physical mechanical properties of solid materials. Part of the physical and mechanical properties can be recovered at high temperatures where defects are mobile. Some experimental results are important for development of large equipment. For example, the results of ARS-2 indicate that Al alloys can be used in high energy, high-power accelerator as the material of superconducting magnets since the defects produced by the irradiation recover when the magnets are warmed up to room temperature.

## PR6-1 Compensation Mechanism of DX-like Center in Neutron Transmutation Doped GaN

K. Kuriyama, T. Nakamura, A. Shinkawa, K. Kushida<sup>1</sup>, and Q. Xu<sup>2</sup>

College of Engineering and Research Center of Ion Beam Technology, Hosei University

<sup>1</sup>Osaka Kyoiku University

<sup>2</sup>Research Reactor Institute, Kyoto University

**INTRODUCTION:** The 1000 °C annealed neutron transmutation doped (NTD)-GaN keeps having high resistivity of  $10^8 \Omega\text{cm}$  at room temperature. In the present study, we report the compensation mechanism of DX-like center of the neutron transmuted Ge in NTD-GaN.

**EXPERIMENTS:** GaN epitaxial films on sapphire substrates were irradiated with fast and thermal neutrons at fluences of  $6.7 \times 10^{18} \text{ cm}^{-2}$  and  $1.4 \times 10^{19} \text{ cm}^{-2}$ , respectively. We carried out an alternating current (ac)-Hall effect measurement and clarified the existence of deep energy level from the temperature dependence of carrier concentration in high temperature region.

**RESULTS:** The resistivity and carrier concentration of the 1000 °C annealed samples were  $2.47 \times 10^6 \Omega\text{cm}$ ,  $4.13 \times 10^{10} \text{ cm}^{-3}$  at 150 °C and  $2.37 \times 10^3 \Omega\text{cm}$ ,  $1.60 \times 10^{14} \text{ cm}^{-3}$  at 400 °C, respectively. All annealed samples showed the n-type conduction. The carrier concentration at both 150 °C and 400 °C were much lower than the calculated transmuted-Ge concentration ( $1.24 \times 10^{18} \text{ cm}^{-3}$ ). Fig. 1 (a) and (b) show the schematic diagram of impurity levels of NTD-GaN. Ge atoms transmuted in GaN by the two (n, $\gamma$ ) reactions of  $^{69}\text{Ga}$  and  $^{71}\text{Ga}$  form the DX-like center as donor [1]. Ge is localized at 500 meV below the bottom of the conduction band from results of photoluminescence (PL) measurements [1], supporting the results of the theoretical calculation [2]. N interstitial ( $\text{N}_i$ ) atoms generated by NTD-process form the deep acceptor level at 960 meV below the bottom of the conduction band from present study.  $^{14}\text{C}$  atoms generated by the (n,p) reaction are substituted to N sites and forms the acceptor level at 230 meV above the top of the valence band [3], consistent with the result from the PL measurements[4]. Since the carrier concentration of NTD-GaN cannot be measured at room temperature, DX-like center of Ge is compensated by both  $^{14}\text{C}$  and  $\text{N}_i$  acceptors. The Fermi level estimated from the following equation [5] for a temperature range of 150 - 400 °C was  $650 \pm 25 \text{ meV}$ .

$$n = 2(m_e k_B T / 2\pi \hbar^2)^{3/2} \exp[(E_F - E_g) / k_B T],$$

where  $m_e$  is the effective mass of GaN,  $k_B$  the Boltzmann's constant. Therefore, the increase of the carrier concentration with increasing the temperature would be attributed to the thermal excitation to the conduction band of electrons trapped in  $\text{N}_i$  acceptors, as shown in Fig. 1 (b).

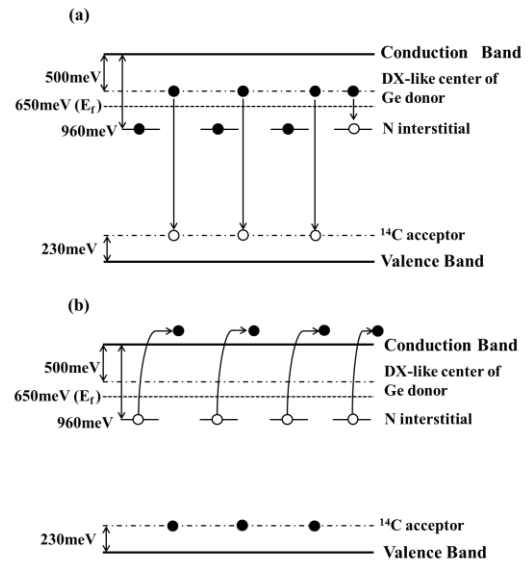


Fig 1. The schematic diagram of impurity levels in NTD-GaN. (a) the compensation of DX-like center of Ge donors by  $^{14}\text{C}$  and  $\text{N}_i$  acceptors. (b) the thermal excitation from the energy level of N interstitial.

A part of KURRI Progress Report has been published in Solid State Communications, 205, 1 (2015).

### REFERENCES:

- [1] K. Kuriyama, T. Tokumasu, Jun Takahashi, H. Kondo, and M. Okada, Appl. Phys. Lett. 80, 3328 (2002); Proceedings of 26th Int. Conf. Physics of Semiconductors (Edinburgh, UK) D46 (2002).
- [2] P. Boguslawski, J. Bernholc, Phys. Rev. B 56, 9496 (1997).
- [3] J. Neugebauer, C. G. Van de Walle, Phys. Rev. B 50, 8067 (1994).
- [4] T. Ida, T. Oga, K. Kuriyama, K. Kushida, Q. Xu, and S. Fukutani, AIP Conference Proceedings, 1566, 67 (2013) (31st Int. Conf. Physics of Semiconductors, Zurich, Switzerland, 2012).
- [5] G. Burns, in Solid State Physics, (Academic Press, Inc, 1985) Chap.2.

T. Nakamoto, M. Yoshida, T. Ogitsu, Y. Makida, K. Sasaki, S. Mihara, K. Yoshimura, H. Nishiguchi, M. Sugano, M. Iio, Y. Yang<sup>1</sup>, Y. Kuno<sup>2</sup>, M. Aoki<sup>2</sup>, A. Sato<sup>2</sup>, Q. Xu<sup>3</sup>, K. Sato<sup>3</sup>, Y. Kuriyama<sup>3</sup>, and Y. Mori<sup>3</sup>

*J-PARC Center, KEK*

<sup>1</sup>*Department of Applied Quantum Physics & Nuclear Engineering, Kyushu University*

<sup>2</sup>*Department of Physics, Osaka University*

<sup>3</sup>*Research Reactor Institute, Kyoto University*

**INTRODUCTION:** Superconducting magnets will be subjected to a high neutron fluence of  $10^{21}$  n/m<sup>2</sup> or higher in the operation lifetime in the high energy particle physics experiments, such as a high luminosity upgrade of the LHC at CERN and the muon source for the COMET experiment at J-PARC. Since electrical resistivity of a stabilizer at low temperature, which is very sensitive to neutron irradiation, is one of the important parameters for the quench protection of the magnet system. A series of electrical resistivity measurement at neutron irradiation for the aluminum stabilizer with additives of yttrium taken from the prototype superconducting cable as well as copper stabilizer was started in 2011. In 2014, the fourth irradiation test with the same samples which were irradiated so far was performed to observe the effect of the multiple irradiations and the thermal cycles to room temperature on the electrical resistivity.

**EXPERIMENTS:** The irradiation tests have been carried out at a low temperature irradiation facility (LTL) at E-4 line of KUR. Detailed experimental procedure was reported in [1]. The aluminum stabilizer samples with dimensions of 1 mm x 1 mm x 70 mm were cut from the superconducting cable manufactured by Hitachi Cable. The copper stabilizer sample has the dimensions of  $\phi$ 1mm x 50mm. The electric resistance was measured by a 4-wire method employing a Keithley 6221 current source and a Keithley 2182A voltmeter. The temperature was determined by using a thermocouple of Au(Fe) and Chromel, since the Cernox sensor (CX-1050-SD for

2011 - 2013, CX-1070-SD for 2013 - 2014) showed a temperature drift during neutron exposure due to the irradiation damage. The thermocouple and the Cernox sensor were placed just behind the samples to measure the temperature of the helium gas coolant.

**RESULTS:** The fourth irradiation test for the aluminum sample (Al-Y2) and the copper sample was carried out in April 2014. Another type of aluminum sample with Ni additive (Al-Ni) was also irradiated at second time. The irradiation condition is basically same as the previous irradiations. After cooling down to 12 K, the reactor was turned on to a power of 1 MW. The estimated fast neutron fluence in 53.5 hours operation is  $2.7 \times 10^{20}$  n/m<sup>2</sup>. Behavior of the induced resistance by the neutron irradiation is very similar to the previous results. Degradation rates of the electrical resistivity for both aluminum samples are quite similar:  $2.2 \times 10^{-31} \Omega m^3$  and  $2.3 \times 10^{-31} \Omega m^3$  for Al-Y2 and Al-Ni, respectively. For copper sample, the degradation rate is  $7.3 \times 10^{-31} \Omega m$ . After the irradiation, all samples were warmed up to room temperature. Anneal effects of the samples were measured at the subsequent cooling test to 12 K in December 2014 without irradiation. Table 1 lists the summary of irradiation tests so far. For the aluminum samples, the induced resistance was fully recovered to be the original resistance for all cases while the degradation rate is much higher than copper. This means that the degraded electrical resistivity of aluminum stabilizer in the superconducting magnet due to the irradiation can be completely recovered by the adequate intervention of warming up to room temperature. For the copper sample, however, the recovery of the resistance by the thermal cycle was imperfect for all cases: the recovery rates were 82 % to 96 %. This will concern the safe operation of the superconducting magnet at severe radiation environment.

### REFERENCES:

[1] M. Yoshida *et al.*, Proc. of ICEC 24-ICMC 2012, 685-688, 2013.

Table 1. Summary of irradiation effects on electrical resistivity of stabilizers with multiple neutron irradiations.

Sample, irradiation year	Initial RRR	T <sub>irr</sub> (K)	$\Phi_{tot}$ (>0.1 MeV) (n/m <sup>2</sup> )	$\Delta\rho_{irr}/\Phi_{tot} \times 10^{-31}$ ( $\Omega m^3$ )	Recovery Rate (%)	
Al-Y2	2011	360	12	$2.6 \times 10^{20}$	2.8	100
	2012	360	15	$2.6 \times 10^{20}$	2.9	100
	2013	368	15	$2.6 \times 10^{20}$	2.5	100
	2014	367	14	$2.7 \times 10^{20}$	2.2	100
Al-Ni	2013	561	15	$2.6 \times 10^{20}$	2.6	100
	2014	566	14	$2.7 \times 10^{20}$	2.7	100
Copper	2011	308	12	$2.6 \times 10^{20}$	0.93	82
	2012	291	15	$2.6 \times 10^{20}$	1.02	92
	2013	285	15	$2.6 \times 10^{20}$	0.77	95
	2014	277	14	$2.7 \times 10^{20}$	0.73	96

## PR6-3 Study on Fine Structures Formed by High Energy Particle Irradiation

A. Kinomura\*, K. Sato<sup>1</sup>, Q. Xu<sup>1</sup> and T. Yoshiie<sup>1</sup>

National Institute of Advanced Industrial Science and Technology (AIST)

<sup>1</sup>Research Reactor Institute, Kyoto University

\*Present address: Research Reactor Institute, Kyoto University

**INTRODUCTION:** The effects of ion irradiation have been extensively studied for various crystalline materials. It is known that irradiation causes the damage of crystallinity, leading to the degradation of original material properties. However, under particular irradiation conditions, the irradiation effects can induce interesting phenomena such as ion beam annealing in Si, where crystallinity of implantation-induced damage layers are recovered by other ion irradiation. Thus, it is important to investigate the irradiation effects of energetic particles (ions and neutrons) and the influence on crystallinity of materials.

**EXPERIMENTS:** Neutron enhanced annealing (crystalline recovery) of ion-implantation induced damage in single-crystalline Si has been investigated to compare the difference in annealing effects between ion and neutron irradiations. Si ion implantation to (100)-oriented Si was performed at 200 keV to a dose of  $5 \times 10^{14} \text{ cm}^{-2}$  to introduce irradiation damage in the sample. The Si-implanted sample was encapsulated in an Al capsule with He ambient gas and neutron irradiated for 12 weeks in the core irradiation facility of the Kyoto University Reactor (KUR) operating at 5 MW. Control samples were thermally annealed at 90 °C in a quartz tube furnace with flowing Ar gas for the same annealing time as the neutron irradiation. The damage levels of samples were measured by Rutherford backscattering with channeling (RBS/C) using a 2 MeV He ion beam.

**RESULTS:** Sample temperatures cannot be directly measured during reactor operation in the case of the KUR core irradiation facility. In this study, the sample temperature during the neutron irradiation was estimated to be below 90 °C by solving a partial differential equation describing the heat flow inside the sample capsule made of Al. Since the thermal annealing rate for heavily damaged Si was nearly constant around 90 °C, the error of estimated temperature rise does not affect the result of this irradiation experiment.

The samples before and after irradiation were measured and damage levels were calculated by taking account of dechanneling fractions in RBS/C spectra. Annealing efficiencies obtained in this and previous studies [1, 2] were plotted (closed circles), under the assumption that the irradiation temperature in this study was 90 °C. For comparison, efficiencies of ion beam annealing of disorder were also calculated from the data by other groups and plotted in Fig. 4 (closed square and

triangle), where the room temperature was assumed to be 27 °C.

Types of major annealed defects are different depending on the irradiation temperature in the current temperature range (from room temperature to 400 °C). Damage peak after thermal annealing at 400 °C was close to the undamaged level in the RBS/C spectrum, whereas the damage peak after thermal annealing at 90 °C (in this study) was close to the random level. In spite of the difference in annealed defects, the Arrhenius plot provides some insights in terms of the comparison between neutron-enhanced and ion-beam annealing. The difference in efficiency between neutron-enhanced and ion-beam annealing was within one order of magnitude, implying that a similar mechanism may be at work for both of annealing methods.

In summary, the effect of neutron irradiation on ion-implantation induced damage in Si was investigated using the neutron irradiation in KUR. Similar annealing efficiencies were obtained for neutron-enhanced and ion-beam annealing experiments.

**ACKNOWLEDGMENT:** We would like to thank K. Yasuda and R. Ishigami of the Wakasa Wan Energy Research Center and colleagues of AIST for their assistance on this study.

### REFERENCES:

- [1] A. Kinomura, T. Yoshiie, A. Chayahara, Y. Mokuno, N. Tsubouchi, Y. Horino, Q. Xu, K. Sato, K. Yasuda, and R. Ishigami, Nucl. Instrum. Methods Phys. Res. B 334 (2014) 48.
- [2] A. Kinomura, A. Chayahara, Y. Mokuno, N. Tsubouchi, Y. Horino, T. Yoshiie, Y. Hayashi, Q. Xu, Y. Ito, R. Ishigami and K. Yasuda, Appl. Phys. Lett. 88 (2006) 241921.

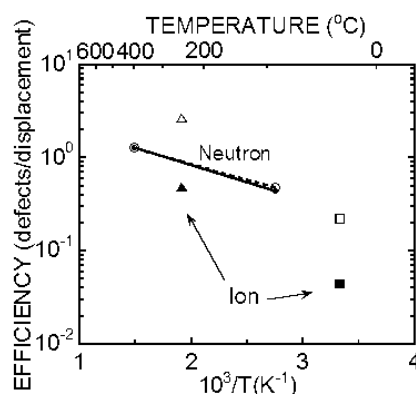


Fig. 1 Annealing efficiencies of neutron and ion-beam irradiations. Closed circles (neutron), triangle and square (ion) correspond to the original efficiencies. Open circles (neutron), triangle and squares (ion) correspond to the efficiencies corrected based on displacement-rate dependence.

T. Awata, K. Iwasaki, S. Tanaka, Q. Xu<sup>1</sup>

Department of Physics, Naruto University of Education  
<sup>1</sup>Research Reactor Institute, Kyoto University

**INTRODUCTION:** We reported that thermoluminescence (TL) of natural calcite ( $\text{CaCO}_3$ ) irradiated by gamma rays [1-2]. In that result, it was shown that the almost spectra of TL had only one orange emission peak at 620nm, and that may be originated from a small amount of impurity of  $\text{Mn}^{2+}$  in Calcite [3]. In this study, we have artificially synthesized calcite with different kinds of impurity using chemical reaction in water solution, and compared TL spectra of these with natural calcite, and to clear the relationship with emission and kinds of impurity.

**EXPERIMENTS:** Calcites were synthesized by a chemical reaction method in water solution [4]. 1.5% of  $(\text{NH}_4)_2\text{CO}_3 \cdot \text{H}_2\text{O}$  (1.5g in 100mL pure water) and 1.8% of  $\text{CaCl}_2 \cdot 6\text{H}_2\text{O}$  (2g in 100mL pure water) with 0.01g element impurity were mixed at room temperature. After mixed, these solutions were precipitated by holding for two weeks, and filtering. After filtering, samples were shaped by a tablet machine. We have made three samples with different element impurities (Mn, Mn+Ce, Mn+Pb). These samples were irradiated  $^{60}\text{Co}$  gamma rays for 1h (about 20kGy) at 77K using KUR gamma-ray facility. The thermoluminescence spectra were measured by a photo-spectrometer (Princeton Instrument Spectra Pro 300i) with a temperature controlled system (77K to 413K).

**RESULTS and DISCUSSION:** Figure 1 shows the thermoluminescence picture of synthesized calcite with an impurity Mn and Mn+Ce by gamma rays irradiation. This picture was taken by stereo microscope after pick-

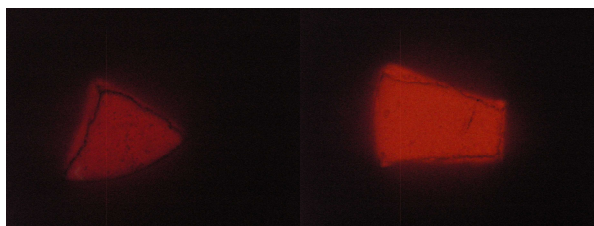


Fig. 1 Thermoluminescence of synthesized calcite with an impurity of Mn (left) and Mn+Ce (right).

ing out from liquid nitrogen. Both pictures show orange emission almost same as natural calcite with Mn element [2]. Figure 2 shows a 3D thermoluminescence spectrum of calcite with Mn impurity irradiated by  $\gamma$  rays at 77K from 93K to 413K with heating speed at 0.32K/second.

X-, Y- and Z- axes indicate emission wavelength (nm) of emission, temperature and intensity, respectively. There is one peak at 620nm starting from 285K same result as

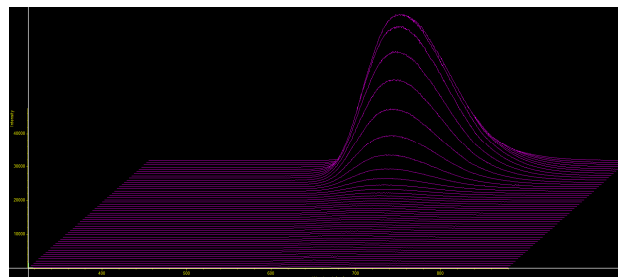


Fig. 2 TL 3D spectrum of synthesized calcite with Mn irradiated by gamma rays.

former our experiment of natural calcite [2]. It is clear that 620nm emission peak at calcite is originating from existence of small amount of Mn. This result is supported by study of Medlin [3]. Figure 3 shows those TL spectra of synthesized calcite with Mn, Mn+Ce and Mn+Pb at maximum intensity temperature. Mn and Mn+Pb spectra looks alike, and have one peak at 620nm same as former our experiment. As Mn+Ce spectra, it has one peak at 640nm which is different from other two samples. Comparing this result with photoluminescence one makes it possible to be clear that reason.

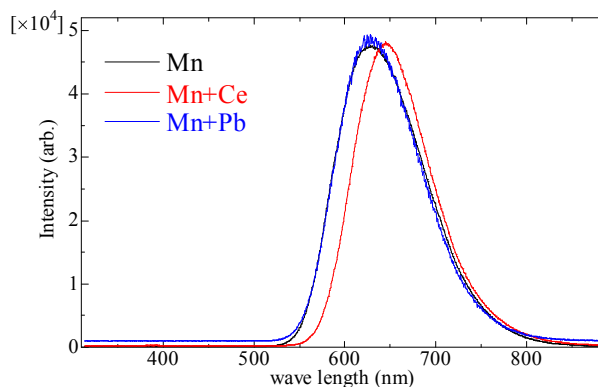


Fig.3 TL spectra of synthesized calcite with Mn, Mn+Ce and Mn+Pb.

#### REFERENCES:

- [1] T. Awata, T. Kishino, F. Maki and Q. Xu, KURRI Progress Report **2011**, p.143.
- [2] T. Awata, K. Nakashima and Q. Xu, KURRI Progress Report **2013** p.169.
- [3] W. L. Medlin, *J. Opt. Soc. Am.* **53**(1963)1276.
- [4] G. R. Fonda, *J. Phys. Chem.* **44**(1940)435.

M. Akiyoshi<sup>1</sup>, T. Yoshiie<sup>2</sup>, Q. Xu<sup>2</sup>, K. Sato<sup>2</sup>

<sup>1</sup>Faculty of Engineering, Kyoto University  
(from 2015.04: Radiation Research Center, Osaka Prefecture University)

<sup>2</sup>Research Reactor Institute, Kyoto University

### INTRODUCTION:

It is well known that irradiation induced damages in ceramics showed significant degradation in thermal diffusivity unlike metals. In addition, the dependence of thermal diffusivity on measurement temperature is affected with irradiation induced damages. Therefore, thermal diffusivity during the irradiation is still not estimated. To resolve this problem, kinetic analysis is required where most important information is the behavior of point defects. Electron irradiation is the best choice to induce simple Frenkel pairs.

In these days, W (tungsten) material is considered as a candidate for divertor material in future fusion reactor. W is metal, of course, but showed a similar behavior of thermal diffusivity. It shows relatively small thermal diffusivity arisen from low electron conductivity, but shows dependence on measurement temperature like ceramics caused by phonon-phonon scattering.

In this study, we irradiated W specimen using KURRI-LINAC and check the specimen temperature during the irradiation, and also radio-activity of specimens.

### EXPERIMENTS:

In the previous work, 30MeV electron accelerator KURRI-Linac is used to induce point-defects in bulk specimens of typical structural ceramics to  $1.5 \times 10^{24} \text{e/m}^2$  which correspond to 0.01dpa in typical ceramics. The irradiation was performed in a new irradiation system constructed to achieve an irradiation at around 400°C where interstitial atoms have enough mobility to migrate.

In the previous work, ceramic specimens were irradiated using this irradiation system. In the system, a specimen is settled in a Cu specimen-holder, and holders are piled between Cu heat spread plates and graphite heat spread seats. Usually, a graphite seat spreads heat well horizontally, but the graphite seat in this system is 'Vertical-Graphite' (produced by Hitachi Chemical) of which thermal conductivity vertical to the seat is  $90 \text{W/m} \cdot \text{K}$ . This vertical-graphite sheet was 0.15mm in thickness and was cut into  $\phi 10$  that cover the specimen to have good thermal contact on the surface. In conventional system, heat contact is achieved by thermal grease that contains Ag powders. But in this system, neutrons from photo-

nuclear reaction will activate Ag atoms very strongly, so it cannot be used. In addition, conventional (horizontal) graphite sheet (Panasonic PGS graphite sheet, EYGS-182310  $t=0.10\text{mm}$ ,  $\text{TC}=700\text{W/m} \cdot \text{K}$ ) is used to spread heat horizontally.

The piled graphite sheets and specimen holders are tighten with screws and nuts made by Ti to avoid radio activation. This pile is put between Al square tubes with the vertical-graphite seats. All specimens and Cu plates are coated by BN spray to avoid surficial oxidation. In addition, a Cu aperture was put in front of the specimen pile to trim down the beam irradiated on out side of the specimen that heats the pile wastefully.

Pure W specimens (Nilaco) was cut into  $\phi 10$  and the thickness was 0.5mm (2 pieces) and 1.0mm (1 piece).  $\alpha$ - $\text{Al}_2\text{O}_3$ ,  $\beta$ -SiC specimens ( $\phi 10 \times 0.5\text{mm}$ ) are also irradiated.

### RESULTS:

The beam condition was Acc. Energy: 32MeV, Pulse length  $4\mu\text{s}$ , Peak current: 550mA. The frequency was once increased to 110Hz, but specimens showed a trend of over heating, so the frequency was settled down to 100Hz. Even at that frequency, the total beam energy was 7.0kW in several  $\text{cm}^2$  that can compare with the heat flux on divertor in the fusion reactor ITER which is planed as  $10\text{MW/m}^2$ . This irradiation system got over this high heat flux and achieved reliable irradiation at around 550°C.

The irradiation damage induced by the electron irradiation is calculated. For the most ceramics,  $2.82 \times 10^{20}$  electrons in  $2\text{cm}^2$  accelerated to 32MeV induces defects up to  $1.00 \times 10^{-2} \text{dpa}$  (target mass  $M=16\text{amu}$ , atomic number  $Z=8$ , knock on energy  $E_d=30\text{eV}$ ). W is far heavier ( $M=183.8\text{amu}$ ) and knock on energy is larger ( $E_d=100\text{eV}$ ), but the collision cross section is 48.4barn while ceramics shows only 18.7barn. It is said that the  $E_d$  of W is a little smaller, and if it is 80eV, the cross section is 60.1barn. Therefore, induced damage in W is larger than typical ceramics,  $1.48 \times 10^{-2} \text{dpa}$  ( $E_d: 100\text{eV}$ )  $\sim 1.95 \times 10^{-2} \text{dpa}$  ( $E_d: 80\text{eV}$ ).

After the irradiation, radio-activity of the specimen holder and specimens was investigated. The whole irradiation holder showed over 100mSv/h in the surface at 17h after the beam stop, 55mSv/h at 33h and 38mSv/h at 40h that corresponds  $t_{1/2} = 13.7\text{h}$ . The half-time of W-185 is 75.1day and W-187 is 23.7h while Cu-64 is 12.7h, so the most of the activity was assumed to be arisen from Cu-64.

Y. Nagai, K. Inoue, T. Toyama, Y. Shimizu, K. Nagumo, M. Shimodaira, T. Hirota, K. Sato<sup>1</sup>, T. Yoshiie<sup>1</sup>, Q. Xu<sup>1</sup>  
*Institute for Materials Research, Tohoku University,*  
<sup>1</sup>*Research Reactor Institute, Kyoto University*

**INTRODUCTION:** Positron annihilation spectroscopy is well-known to be a powerful tool to detect vacancy-type defects. In 2000 years, it is found that the positron is also sensitive to (sub)nano embedded particles (SNEPs) with higher positron affinities than that of the host, even if the SNEPs are free from open-volume defects. The representative case is ultrafine Cu precipitates in Fe.

We are developing a new positron annihilation apparatus, positron age-momentum correlation (AMOC), to study the correlation between the Cu precipitates and the vacancy-type defect induced by neutron irradiation in the light water reactor pressure vessel (RPV) steels, which is important to understand the irradiation induced embrittlement of the RPV steels due to long-term in-service exposure to neutron irradiation. For this study, an intense positron source is required to achieve higher count rates because typically it takes more than one week for one spectrum by the conventional AMOC system using <sup>22</sup>Na positron source.

In this work, a new positron beam facility with high positron intensity is constructed at the Kyoto University Research Reactor (KUR), which is the first reactor based positron beam in Japan[1].

**EXPERIMENTS and RESULTS:** An in-pile positron source was installed at the B-1 hole (20 cm in diameter) in KUR. The positron beam line consists of two parts: one is located inside the reactor, and the other is located outside the reactor as shown in Fig. 1 [1,2]. Positrons are generated by pair production from high-energy  $\gamma$ -rays. The  $\gamma$ -ray flux and the thermal neutron flux at the positron source position are about  $1.5 \times 10^{12}$  n/cm<sup>2</sup> and  $10^5$  Gy/h, respectively, at 5 MW. A W converter of 1 mm thick and 3 cm diameter and W moderators with a Cd shroud are used to obtain slow positrons as shown in Fig. 2. In order to enhance the positron generation, a 1 mm thick Cd shroud covered with an Al plate was mounted on the top of the magnetic field to cap the converter and moderator, because high energy  $\gamma$ -ray are generated by the  $^{113}\text{Cd}(n, \gamma)^{114}\text{Cd}$  reaction. The moderators were annealed after the W strips were set in lattices. When annealing, they were encased in covered boxes of 50  $\mu\text{m}$ -thick W foil and the boxes were irradiated on the covering lids with electron beam welder at KEK in Tsukuba [3]. The annealing temperature was elevated to approximately 2400°C. The vacuum of the welder chamber was about  $10^{-5}$  torr. The slow positrons emitted from the moderator were subsequently accelerated up to 30 eV and confined magnetic fields of several mT. In order to eliminate the background of fast neutrons and  $\gamma$ -rays from the reactor core, the slow positron beam passes two bends in shields consisting of polyethylene, concrete and lead

blocks. After passing the bends, the slow positrons are transported to sample chamber at an energy up to 20 keV.

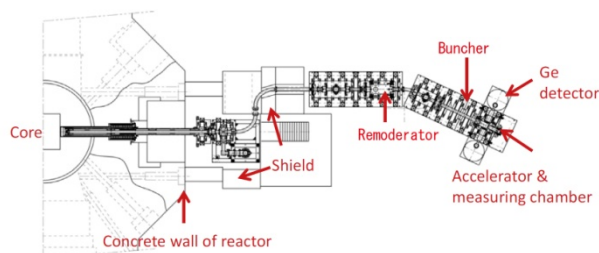


Figure 1: A schematic diagram of KUR positron beam system [1,2].

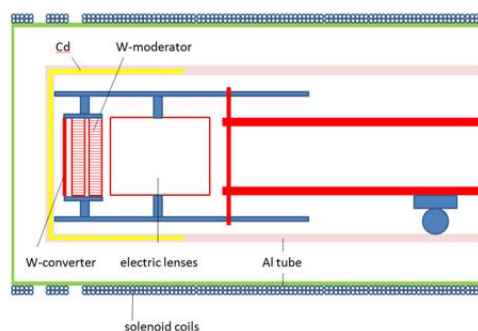


Figure 2: A schematic diagram of the in-pile positron source at KUR [1,2].

Figure 3 shows the positron beam spot recorded using a microchannel plate (MCP). The beam has a slightly elliptical shape and the major and minor axes have length about 2.0 and 1.5cm, respectively. The lattice structure of W moderator is clearly visible. The positron beam intensity is determined about  $10^6$  e<sup>+</sup>/s at 1 MW by Ge detector.

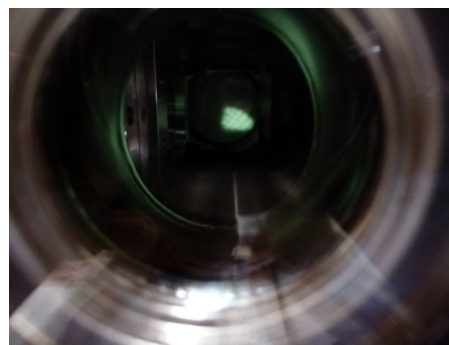


Figure 3: The observation of positron beam from KUR using microchannel plate.

#### REFERENCES:

- [1] Q Xu *et al*, J. Phys. Conf. Ser. **505** (2014) 012030.
- [2] K Sato *et al*, Nucl. Inst. Meth. Phys. Resear. B **342** (2015) 104.
- [3] K Wada *et al*, Eur. Phys. J. D **66** (2012) 37.

採択課題番号 26P6-6 KUR を用いた新しい陽電子源の開発と材料研究への応用 プロジェクト  
 (東北大・金研) 永井康介、井上耕治、外山健、清水康雄、南雲一章、下平昌樹、廣田太一  
 (京大・原子炉) 義家敏正、徐虬、佐藤紘一

## PR6-7 Radiation Damage in Bulk Amorphous Alloys by Electron Irradiation

F.Hori, K.Ishii, T.Ishiyama, K.Kobayashi, A.Iwase,  
Y.Yokoyama<sup>1</sup>, Q.Xu<sup>2</sup> and K.Sato<sup>2</sup>

*Dept. of Mater. Sci., Osaka Prefecture University*

<sup>2</sup>*Institute of Materials Research, Tohoku University*

<sup>1</sup>*Research Reactor Institute, Kyoto University*

**INTRODUCTION:** Bulk amorphous alloys are expected to be useful for various applications because they have superior mechanical properties such as strength, hardness and corrosion resistance. We have been suggested that the properties of bulk glassy alloys can be improved by high energetic particles irradiation. So far, we have reported that effects of free volume and mechanical properties on the bulk amorphous alloys depend upon the irradiation species [1,2]. Also change in free volume by the irradiation strongly reflects various properties such as hardness and ductility of bulk amorphous alloys. Recent years, eutectic ZrCuAl bulk glassy alloy shows the degradation of ductility and toughness by annealing but that for hypoeutectic remains unchanged after annealing. In order to estimate irradiation effects for various compositional bulk amorphous alloys, we performed electron irradiation for various kinds of ZrCuAl bulk amorphous alloys. Before and after irradiation, we have examined X-ray diffraction, differential scanning calorimetry (DSC) and positron annihilation.

**EXPERIMENTS:**  $Zr_xCu_{90-x}Al_{10}$  ( $x=50, 55, 60, 65$ ) bulk amorphous alloys with 8 mm in diameter and 60 mm in length were prepared by a tilt casting technique. For positron annihilation measurements, alloy samples were cut into the size of about 0.5 mm thickness disk. 8 MeV electron irradiations with total dose of  $2 \times 10^{18}$  e/cm<sup>2</sup> was performed for these alloys at 320 K by LINAC at Research Reactor Institute, Kyoto University. During irradiation, samples were cooled in water flow path. Irradiated samples were examined by X-ray diffraction, positron annihilation lifetime and coincidence Doppler broadening measurements at room temperature. The positron annihilation lifetime spectra consist of more than  $1.0 \times 10^6$  counts. The positron lifetime spectra were analyzed by using POSITRONFIT program.

**RESULTS:** The mean positron lifetime  $\tau$  of all as-quenched sample was about  $165 \pm 2$  psec. Before irradiation, no difference of positron lifetime for different amorphous alloy systems was observed. This shows that open volume existing in amorphous is apparently same. However, the CDB spectra of these alloys before irradiation are not necessarily same. Take into account for these facts, it can be deduced that total electron density of open volume in any amorphous alloy is almost same but the real size of open space and chemical ratio around it depending on alloy composition is not same for various compositional alloys. Figure 1 shows the change in positron annihilation lifetime by electron irradiation as a function of Zr composition ratio in bulk amorphous alloys. It found that the increasing trend of positron lifetime becomes smaller with increasing of Zr contents. Especially, we found that radiation induced open volume change is suppressed in glassy alloys including more than 60% Zr atoms.

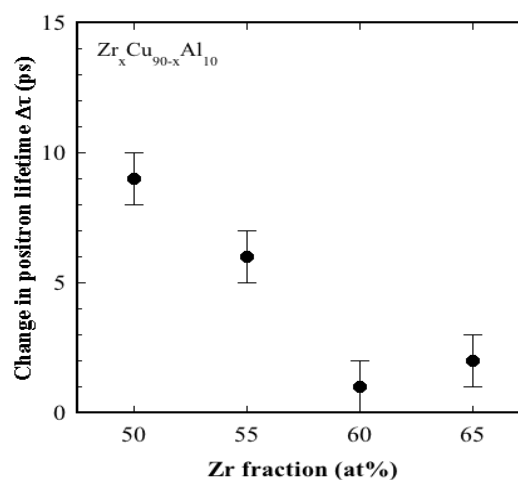


Fig. 1 Change of positron lifetime for various compositions of ZrCuAl bulk amorphous alloys by 8 MeV electron irradiation.

### REFERENCES

- [1] N.Onodera, A.Ishii, Y.Fukumoto, A.Iwase, Y.Yokoyama, and F.Hori, Nucl. Inst. & Meth. B. 282 (2012) 1
- [2] F.Hori, N.Onodera, A.Ishii, Y.Fukumoto, A.Iwase, A.Kawasuso, A.Yabuuchi, M.Maekawa and Y.Yokoyama, J. Phys.: Conf. 262 (2011) 012025



## PR6-8 Positron Annihilation Study of Fe-Cr Alloys after Neutron Irradiation in KUR

R. Kasada<sup>1</sup>, K. Sato<sup>2</sup>, Q. Xu<sup>3</sup>

<sup>1</sup>Institute of Advanced Energy, Kyoto University

<sup>2</sup>Department of Mechanical Engineering, Kagoshima University

<sup>3</sup>Research Reactor Institute, Kyoto University

**INTRODUCTION:** Ferritic steels containing Cr are expected to be used for the first-wall component of the fusion reactors as well as for the fuel pin cladding of the Generation IV nuclear fission systems [1]. However, high-Cr steels may suffer from thermal aging embrittlement, which is well-known 475 °C embrittlement. This is mainly due to hardening phenomenon through the phase separation of Fe and Cr as shown in the phase diagram. In the previous study [2], we applied a positron annihilation spectrometry to detect the phase separation in the Fe-Cr alloys after thermal aging at 475 °C.

The present collaborative research has investigate the neutron irradiation effect on the positron annihilation lifetime of Fe-Cr alloys.

**Experimental Procedure:** Materials used in the present study are Fe<sub>x</sub>Cr binary alloys. Neutron irradiation on these materials was carried out at 300 °C up to 199 h in KUR. The displacement damage is  $2.1 \times 10^{-3}$  dpa ( $5.1 \times$

$10^{18}$  n/cm<sup>2</sup>). Positron annihilation lifetime spectrometry was carried out for investigating open-volume type defects produced by irradiation.

**Results and Discussions:** Results of positron annihilation lifetime spectrometry is shown in Table 1. There is no meaningful difference in the mean lifetime of unirradiated Fe-Cr binary alloys. After the neutron irradiation in KUR, the mean lifetime of pure Fe and Fe-*x*Cr alloys for  $x \leq 85$  slightly increased but not decomposed into multi-components. On the other hand, that of Fe-91Cr and pure Cr showed two- and three components, respectively. This results indicate that Fe atom suppress vacancy cluster formation in the Fe-Cr binary alloys from a view of the Cr-rich side. Further investigation is needed for understanding the effect of Cr (or Fe) atom on the formation of vacancy type cluster in Fe-Cr alloys.

### REFERENCES:

- [1] A. Kimura, et al., Journal of Nuclear Science and Technology, 44 (2007) 323-328.  
 [2] R. Kasada and K. Sato, submitted to J. Alloys and Compounds.

Table 1 Results of positron annihilation lifetime spectrometry of Fe-Cr alloys before and after neutron irradiation in KUR.

Materials	Unirr.		Irr.				
	$\tau_m$ (ps)	$\tau_1$ (ps)	I1 (%)	$\tau_2$ (ps)	I2 (%)	$\tau_3$ (ps)	I3 (%)
Fe	104 ± 1	109 ± 1					
Fe-9Cr	107 ± 1	109 ± 1					
Fe-15Cr	105 ± 1	109 ± 1					
Fe-30Cr	105 ± 1	109 ± 1					
Fe-45Cr	105 ± 1	109 ± 1					
Fe-50Cr	105 ± 1	108 ± 1					
Fe-70Cr	105 ± 1	107 ± 1					
Fe-85Cr	104 ± 1	110 ± 1					
Fe-91Cr	105 ± 1	113 ± 1	93 ± 1	383 ± 9	7 ± 1		
Cr	103 ± 1	24 ± 4	9 ± 1	156 ± 2	48 ± 1	502 ± 3	43 ± 1

## PR6-9 Positron Annihilation Lifetime Measurements of Austenitic Stainless Steels Irradiated in the SINQ Target Irradiation Program

K. Sato, Q. Xu<sup>1</sup>, T. Yoshiie<sup>1</sup>, Y. Dai<sup>2</sup> and K. Kikuchi<sup>3</sup>

Graduate School of Science and Engineering, Kagoshima University

<sup>1</sup> Research Reactor Institute, Kyoto University

<sup>2</sup> Spallation Neutron Source Division, Paul Scherrer Institut

<sup>3</sup> Frontier Research Center for Applied Atomic Sciences, Ibaraki University

**INTRODUCTION:** Austenitic stainless steels have been known as highly corrosion resistant materials and important nuclear materials. There have been a number of studies on the void swelling behavior of them [1,2]. Recent theoretical and experimental analyses have revealed the importance of incubation period, a transient stage before the steady growth of voids. However, experimental results of void swelling in austenitic stainless steels have been limited to high dose. Because most of experimental studies have been performed by transmission electron microscopy after observable void formation, and point defects and their clusters under the resolution limits are impossible to detect. Therefore, point defect processes during the incubation period are not clear. In this study, the effect of alloying elements on defect structures in austenitic stainless steels and their model metals during the incubation period was studied after neutron irradiation by using positron annihilation lifetime measurement.

**EXPERIMENTS:** Titanium-doped 316-type austenitic stainless steel, called Japanese Primary Candidate Alloy (JPCA), and the reduced activated ferritic/martensitic steel F82H were used in this study. The JPCA was irradiated in the first SINQ (Swiss Spallation Neutron Source) target irradiation program (STIP-I). More details of the STIP-I experiments have been previously reported [3]. Irradiation position was F21. Irradiation temperature was 413K, and irradiation dose was 6.3dpa. After implementing a fatigue test on JPCA at room temperature, the positron annihilation lifetimes of the undeformed area of the sample were measured at the Research Reactor Institute, Kyoto University. A three-detector system using a fast digital oscilloscope and BaF<sub>2</sub> scintillators [4] was adopted for the positron annihilation lifetime measurements, thereby reducing the background counts and making it possible to measure highly radioactive samples. The time resolution of the system was 150 ps (full width at half maximum). Each spectrum was accumulated to a total of  $1.5 \times 10^6$  counts. The resulting spectra were analyzed using the PALSfit program [5]. The isochronal annealing of the positron annihilation lifetime was examined every

100 K from 423 to 1323 K. After annealing, samples were cooled down by air cooling. Cool time to room temperature was about 20 minutes.

**RESULTS:** Short and long lifetime component in the two component analysis was 150 (6) ps and 237 (7) ps, respectively. Intensity of short and long lifetime component was 49 (7) % and 51 (7) %, respectively. Errors are shown in parentheses. The long lifetimes result from the formation of vacancy-cluster-He-atom ( $V_m\text{-He}_n$ ) complexes (large open space defects), while the short lifetimes denote the formation of stacking fault tetrahedra (SFTs), dislocation loop, and single-vacancy-He-atom ( $V\text{-He}_n$ ) complexes (small open space defects). The experimental value of 230 ps is slightly smaller than the calculated positron lifetime of 249 ps for 4-vacancy clusters ( $V_4$ ) in Ni. Yet the vacancy cluster size is not likely to be less than 4, because many He atoms formed in the samples during irradiation. The positron lifetime of the He bubbles decreases as the number of He atoms in a vacancy cluster increases. Thus the exact vacancy cluster size cannot be determined, because they are too small to be directly observed by TEM.

The positron lifetime does not change after isochronal annealing up to 623 K. The spectra only show one component for annealing between 723 and 923 K, but they resolve into two components when annealed above 1023 K. It is expected that  $V_m\text{-He}_n$  complexes absorb He atoms by annealing at temperatures up to 623 K. Because the complexes incorporate many He atoms after irradiation, the lifetime decrease caused by absorption of helium may become saturated. In this stage, the He bubble concentration does not change because the long lifetime intensity is almost constant. SFTs and  $V\text{-He}_n$  complexes are expected to dissociate after annealing at 623 K. These defects, which have a short lifetime for annealing at up to 523 K, tend to aggregate and  $V_m\text{-He}_n$  complexes are formed. It is impossible to resolve them into two components. A small increase in the mean lifetime arises because of both the growth of  $V_m\text{-He}_n$  complexes and their release of H atoms. The  $V_m\text{-He}_n$  complexes dissociate after annealing at 1023 K. In this stage, the absorption of vacancies is larger than that of He atoms, and therefore, the long lifetime increases.

### REFERENCES:

- [1] F.A. Garner, Materials Science and Technology, Vol. 10 (VCH Weinheim, 1994), p. 419.
- [2] T. Okita *et al.*, J. Nucl. Mater. **307–311** (2002) 322.
- [3] Y. Dai and G.S. Bauer, J. Nucl. Mater. **296** (2001) 43.
- [4] H. Saito *et al.*, Nucl. Instr. Meth. Phys. Res. A **487** (2002) 612.
- [5] J.V. Olsen *et al.*, Phys. Stat. Sol. C **4** (2007) 4004.

採択課題番号 26P6-12 電子照射と中性子照射によって形成した金属中の格子欠陥と プロジェクト  
ガス原子の相互作用の解明

(鹿児島大院・理工) 佐藤紘一 (京大・原子炉) 徐虬、義家敏正 (九大・応力研) 大澤一人  
(産総研) 大島永康

# PR6-10 Effects of High Energy Particle Irradiation on Hydrogen Retention in Refractory Metals

K. Tokunaga, M. Matsuyama<sup>1</sup>, S. Abe<sup>1</sup>, H. Osaki<sup>2</sup>, K. Araki, T. Fujiwara, M. Hasegawa, K. Nakamura, Q. Xu<sup>3</sup> and K. Sato<sup>3</sup>

Research Institute for Applied Mechanics, Kyushu University

<sup>1</sup>Hydrogen Isotope Research Center, University of Toyama

<sup>2</sup>Interdisciplinary Graduate School of Engineering Sciences, Kyushu University

<sup>3</sup>Research Reactor Institute, Kyoto University

**INTRODUCTION:** It is of importance to clarify phenomena of implantation, retention, diffusion and permeation of tritium on surface of the armor materials of the first wall/blanket and the divertor on fusion device from a viewpoint of precise control of fuel particles, reduction of tritium inventory and safe waste management of materials contaminated with tritium (T). Refractory metals such as tungsten (W) is potential candidate for an armor of the first wall and the divertor plate of the fusion reactor because of its low erosion yield and good thermal properties. The armor material will be subjected to heavy thermal loads in the steady state or transient mode combined with high energy neutron irradiation that will cause serious material degradation. In addition, high energy runaway electrons would bombard the armor materials along the equatorial plane in fusion device. It is considered that these cause radiation damage and enhance tritium retention. In the present works, T exposure experiments have been carried out on W samples which were irradiated by high energy electrons using LINAC in KURRI of Research Reactor Institute, Kyoto University to investigate effects of high energy electrons irradiation and microstructure on tritium retention of W.

**EXPERIMENTS:** W samples used in the present experiments were two oriented ITER grade W. One was W sample (ITER grade W(1)) which the surface were manufactured to be oriented parallel to the rolling surface and rolling direction. The other was W sample (ITER grade W(3)) which the surface were manufactured to be oriented perpendicular to the rolling surface and rolling direction. The sizes of W samples were 10mm x 10mm x 1mm. The surface of the both samples were polished to be mirrored. High energy electrons irradiation has been carried out using LINAC in KURRI of Research Reactor Institute, Kyoto University. An energy of electron irradiated was 10 MeV and DPA was  $3.26 \times 10^{-3}$ . Temperature during the irradiation was measured by thermocouples which was contacted with a backside of the W samples. After the electron beam irradiation, T exposure experiments have been carried out using a T exposure device in University of Toyama. Pressure of the T gas was 1.3 kPa and T exposure was kept for 4 h. T concentration in the

gas was about 5 %. Temperatures of pre-heating and T exposures were 100 °C. After the exposure to T gas, T amount retained in surface layers of the sample was evaluated by  $\beta$ -ray-induced X-ray spectrometry (BIXS) and imaging plate (IP) measurements.

**RESULTS:** Temperature of the W samples during the electron irradiation was 85 °C. Figure 1 shows the result of the IP measurement of ITER grade W(1) (IG W(1)) and ITER grade W(3)(IG W(3)). The IP images indicate that amount of T on the surface of IG W(3) is larger than that of the surface of IG W(1). Comparison with the standard samples shows that amount of T of the surface of IG W(1) and IG W(2) are 0.0604 kBq/mm<sup>2</sup> and 0.166 kBq/mm<sup>2</sup>, respectively. Figure 2 show line analyses of PLS value of the surface of IG W(3) (a) and IG W(1) (b) after the T exposure. It can be seen that line profiles are almost constant. These result indicates that T is easy to diffuse parallel direction for rolling direction. Electron beam irradiation effect will be discussed by comparing with the result of un-irradiated W samples.

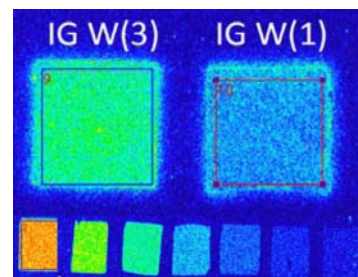


Fig. 1. Tritium image of ITER grade W(3) (IG W(3)) and ITER grade W(1)(IG W(1)). Bottom parts are standard samples.

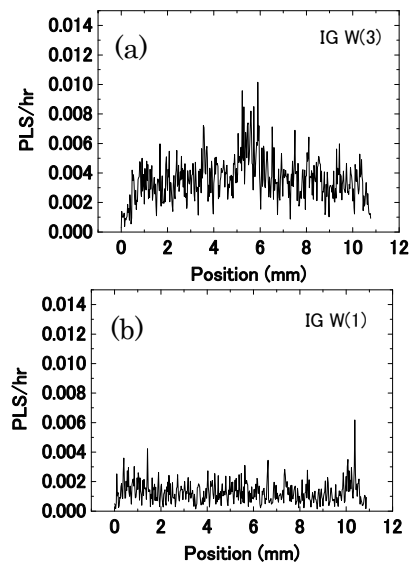


Fig. 2. Line analyses of IG W(3) (a) and IG W(1) (b) after tritium exposure.

N. Nitta<sup>1</sup>, C. Watanabe<sup>1</sup>, M. Taniwaki<sup>1</sup>, Q. Xu<sup>2</sup>, T. Yoshiie<sup>2</sup>

<sup>1</sup>*School of Environmental Science and Engineering,  
Kochi University of Technology*

<sup>2</sup>*Research Reactor Institute, Kyoto University*

**INTRODUCTION:** Fine cellular structure is formed on GaSb, InSb and Ge semiconductors by ion irradiation as shown by Fig. 1[1]-[6]. The authors proposed an idea that this structure is formed by the behavior of point defects induced by ion irradiation, that is, first the voids form from the oversaturated vacancies and they develop by absorbing point defects induced continuously during ion irradiation. This idea has been proved by intense studies on the ion dose dependence and temperature dependence of the cellular structure. However, the authors do not have detailed understanding over all the cell formation process. Especially, the details of the formation mechanism of voids are not yet clear. Though the authors have surely observed the voids prior to the development of the cellular structure, the diameter of these voids are so large (30-50 nm) and the smaller voids are not yet found, then large voids appear suddenly during ion irradiation, not developing from small voids. Therefore another effect on voids formation, for example, the thermal spike, is suspected. Thermal spike effect depends on the mass of ions, then, the authors aim to investigate the ion mass dependence of the voids formation and development in this work. In addition, the chemical effect of implanted ions is studied.

**EXPERIMENTS:** The GaSb (001) wafers were implanted by C, Si, Ge, Pb (IV elements as Sn), Al and P ions by accelerated by 60 kV voltage to the dose of  $10^{15}$  ions/cm<sup>2</sup>. The wafers were kept at 100-110 K during ion irradiation. The surface morphology of the implanted wafers was observed by a FE-SEM.

**RESULTS:** Voids removed their top surfaces were observed on the relatively large mass ions (Ge and Pb) irradiated wafer surfaces, and they were scarcely formed the small mass ions (Si and Al) irradiated surfaces.

In the case of Pb with the largest atom mass (207.2), the diameter of voids was widely distributed from 10 nm - 300 nm. The density of voids with a diameter of 100 nm and over are  $4.4/1 \mu\text{m}^2$ , and they are formed by coalesce of neighboring voids (these void diameters are less than about 100 nm), consequently, the maximum diameter of individual voids is 100 nm at most.

Most of the voids observed in Ge (atomic mass =72.64)

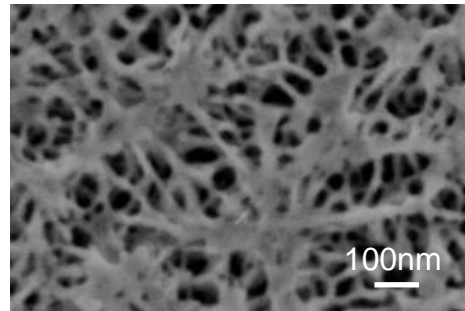


Fig. 1. FE-SEM image of GaSb surface by 60 keV Sn<sup>+</sup> implanted GaSb to a dose of  $1.2 \times 10^{15}$  ions/cm<sup>2</sup> at 150 K.

irradiated sample have small diameters less than 30 nm, but some of the voids (the density is about  $2/1 \mu\text{m}^2$ ) have about 100 nm diameter. These relatively large voids are removed their top surfaces but seem to consist of single void.

In Si irradiated wafer, some small contrasts which might show the voids were observed, and their density was about  $2/1 \mu\text{m}^2$ . However, in Al ion irradiated samples, the void contrast was not observed. These atom masses are so small (26.98 and 28.09) that the ion range is large and distribution is wide, therefore it is considered that the point defects density is too small for voids formation and development.

By SEM study which has been performed until now, it was assured that the atomic mass of irradiated ion affects the voids formation and development. However, from SEM study we cannot know much under the surface, then, the details are not yet clarified. The authors will study under the surface by cross-sectional TEM in order to understand the void formation mechanism.

#### REFERENCES:

- [1] 新田紀子, 谷脇雅文, 鈴木朝夫, 林 禎彦, 佐藤裕樹, 義家敏正, 日本金属学会誌, **64** (2000), 1141-1147.
- [2] N. Nitta, M. Taniwaki, T. Suzuki, Y. Hayashi, Y. Satoh and T. Yoshiie, Materials Transactions, **43** (2002), 674-680.
- [3] N. Nitta, M. Taniwaki, Y. Hayashi and T. Yoshiie, J. Appl. Phys., **92** (2002), 1799-1802.
- [4] N. Nitta, M. Taniwaki, Y. Hayashi and T. Yoshiie, Physica B, **376-377** (2006), 881-885.
- [6] N. Nitta, T. Hasegawa, H. Yasuda, Y. Hayashi, T. Yoshiie, and M. Taniwaki, Materials Transactions **52**, (2011) 127-129.

Y. Saito

Research Reactor Institute, Kyoto University

### 1. Objectives and Allotted Research Subjects

Neutron imaging provides valuable information which cannot be obtained from an optical or X-ray imaging. The purpose of this project is to develop the imaging method itself and also the experimental environment for expanding the application area of the neutron imaging. The allotted research subjects are as follows:

- ARS-1 Measurements of Multiphase Dynamics by Neutron Radiography (Y. Saito *et al.*)
- ARS-2 Quantitative Measurement of Adsorbed Ethanol Amount in Activated Carbon Adsorber for Adsorption Heat Pump (N. Takenaka *et al.*)
- ARS-3 Neutron Radiography on Tubular Flow Reactor for Supercritical Hydrothermal Synthesis of Nanoparticles (T. Tsukada *et al.*)
- ARS-4 Characteristics of the Void Fraction under Transient Condition (H. Umekawa *et al.*)
- ARS-5 Neutron imaging and optics development using simulation of VCAD Systems (Y. Yamagata *et al.*)
- ARS-6 Water and Salt Distribution in a Rice Hull Medium under Sodium Chloride Solution Culture (U. Matsushima *et al.*)
- ARS-7 Measurement of Water Content in Hardened Cement Paste by Neutron Imaging (T. Numao *et al.*)
- ARS-8 Hydrazine Thickness Measurement by Neutron Radiography at a Catalyst Bed during Operation (H. Kagawa *et al.*)
- ARS-9 Development of Neutron Imaging Devices (H. Iikura *et al.*)
- ARS-10 Evaluation of the Moisture Movement in High-Performance Concrete Subjected to Heating (M. Kanematsu *et al.*)
- ARS-11 Effect of gravity on coolant distribution in FGHP heat spreader (K. Mizuta *et al.*)
- ARS-12 Study on Visualization of Organic Materials between Metals for Advance of Industrial Products (A. Uritani *et al.*)
- ARS-12 Study on Visualization of Organic Materials between Metals for Advance of Industrial Products (A. Uritani *et al.*)
- ARS-13 Visualization of Flow inside Fine Scale of Heat Pipe (Y. Tsuji *et al.*)

### 2. Main results and the contents of this report

In ARS-1, simultaneous measurements of water film distribution in an air-water two-phase flow were performed by using a Liquid Film Sensor (LFS) and a high

frame rate neutron radiography to measure the film thickness distribution.

ARS-2 applied neutron radiography to heat transfer study on an adsorption refrigerator. In this ARS, visualization of adsorption amount distributions of ethanol in an activated carbon powder bed, using Umbra method in neutron radiography.

ARS-3 visualized the flow in a tubular flow reactor for supercritical hydrothermal synthesis of nanoparticle using neutron radiography. Measured mixing behaviors in the tubular flow reactor were compared with the size distributions of the synthesized nanoparticles.

ARS-4 was not performed this year.

ARS-5 was trying to develop a visualization technique for molding process by using neutron radiography and also a neutron focusing mirror. A 100mm rotational ellipsoid mirror was fabricated and its focusing performance was investigated at the CN-3 port

ARS-6 was not performed this year.

ARS-7 was not performed this year.

ARS-8 was not performed this year.

ARS-9 was not performed this year.

ARS-10 evaluated the water distribution in the hardened cement paste (HPC) using neutron radiography. In this study, experiments were carried out to investigate two-dimensional moisture movement in HPC.

ARS-11 applied neutron radiography to observe coolant distributions in a flat heat spreader (FGHP). The effect of gravity on coolant distribution in the FGHP was investigated by varying the heat load to the FGHP. At present experimental conditions, at least 0.1 mm thick liquid layer in the wick area exists in the middle plates of the FGHP.

ARS-12 applied neutron radiography to observe organic materials between metals for advance of industrial products. Experiments were conducted at the E-2 port and the test samples were bearing with and without grease. From the CT reconstruction of the neutron images, the grease distributions could be clearly observed.

ARS-13 applied neutron radiography to observe working fluid distributions in a house-made heat pipe, to understand the heat transfer process on a solid surface. Experiments were conducted at the E-2 port, and the heat pipe was visualized by changing the heat load from 6W to 30W. Cross sectional distributions of the working fluid could be measured by the neutron radiography.

# PR8-1 Dynamic Observation of Two-Phase Flow using Neutron Radiography

Y. Saito and D. Ito

Research Reactor Institute, Kyoto University

**INTRODUCTION:** Neutron radiography (NRG) is a powerful tool for fluid flow visualization as well as two-phase flow research. Gas-liquid two-phase flows in a metallic pipe have been visualized clearly by using NRG. However, it would be still difficult to obtain dynamic information on such flows by NRG, because of insufficient neutron flux from neutron sources and poor efficiency of imaging devices. In this work, our imaging system was improved and a denoising method for acquired image sequence was developed for high frame rate NRG. Then, they were applied to air-water two-phase flow measurements in a narrow rectangular channel. In addition, a simultaneous measurement with an electrical conductance method was performed to investigate the detailed structure of the two-phase flow.

**EXPERIMENTS:** Experiments were performed at the B-4 supermirror neutron guide facility [1] of the Research Reactor Institute, Kyoto University. The neutron flux of the B-4 port is  $5 \times 10^7$  n/cm<sup>2</sup>s and the beam width and height at the beam exit are 10 mm and 75 mm, respectively. An imaging system for high frame rate NRG consists of a neutron converter, a dark box with a single mirror, a megapixel lens, an image intensifier and a high speed camera, as shown in Fig.1. NRG images acquired by this system were used to estimate the void fraction in the channel gap. Since the measured data include severe signal noises due to the statistical error in counting neutrons, a spatio-temporal filter was applied to enhance the quality of the void fraction distributions [2]. The test section has a rectangular cross section with 12 mm width and 2 mm gap. The vertical channel was placed at 1 m away from the neutron beam exit. The test fluids are air and tap water at room temperature. A liquid film sensor (LFS) [3] based on an electrical conductance measurement was applied to visualize the water film flowing in the narrow channel, which was installed on one side of the channel walls. LFS has 7×32 measurement points and the distance between the points was 1.5 mm. The temporal resolutions of both measurements were 200 Hz for NRG and 10,000 Hz for LFS.

**RESULTS:** The typical void fraction distributions measured by NRG are shown in Fig.2 (a) and (b). High void fraction values indicate where the bubble exists, and the size of bubbles could be roughly estimated from the distribution. However, several signal noises were found not only in the liquid phase region but also in the gas phase. Thus, the 3-D non-local mean filter was applied to the original images. The distributions filtered from Fig.2 (a) and (b) are shown in (c) and (d), respectively. The remarkable noises were reduced by the filtering process.

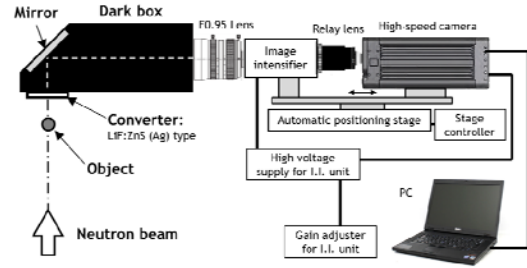


Fig. 1. High frame-rate neutron radiography system

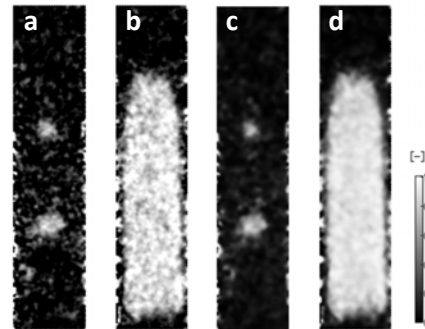


Fig. 2. Measured and filtered results of void fraction distribution

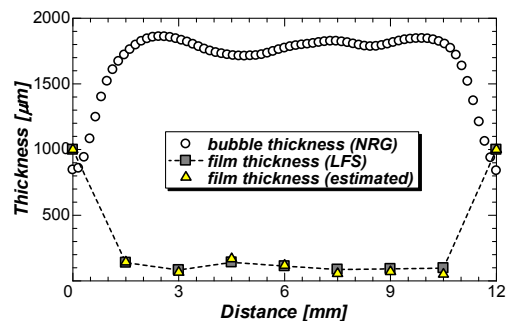


Fig. 3. Bubble and liquid film thickness profiles

The typical results obtained by a simultaneous measurement with NRG and LFS were shown in Fig.3. The horizontal profiles of the bubble and film thicknesses are represented. It is seen that the bubble occupies most of the gap in the channel. Thin film on the LFS could be measured by LFS. The film thickness on the opposing wall, which was estimated from the measured data of NRG and LFS, is also plotted in Fig. 3. This thickness profile agreed well with LFS result. Thus, the possibility of liquid film measurement on another wall was shown by the hybrid measurement with NRG and LFS.

**REFERENCES:**

- [1] Y. Saito, *et al.*, Nucl. Instr. Meth. Phys. Res., A, **651** (2011) 36-41.
- [2] Y. Saito and D. Ito, Proc. WCNR-10, (2014).
- [3] D. Ito, *et al.*, Exp. Fluids., **51-3** (2011) 821-833.

H. Asano, K. Murata, N. Takenaka, H. Murakawa, K. Sugimoto, Y. Saito<sup>1</sup>, D. Ito<sup>1</sup>, Y. Kawabata<sup>1</sup>

*Department of Mechanical Engineering, Kobe University*  
*<sup>1</sup>Research Reactor Institute, Kyoto University*

**INTRODUCTION:** Adsorption refrigerator is one of the efficient tools to recover waste heat at a low temperature. A design of the adsorber, in which refrigerant is adsorbed in adsorbent particle bed, is a key part for the improvement in the performance. To design the configuration of adsorber, it is required to clarify the adsorbed refrigerant distribution in the adsorbent particle bed during adsorption/desorption process. Neutron radiography was applied to visualize the adsorption amount distribution of ethanol in an activated carbon particle bed. The umbra method was applied to compensate the neutron scattering effect for quantitative measurement.

**EXPERIMENTS:** Activated carbon and ethanol was used as the adsorbent and refrigerant, respectively. The activated carbon MAXSORB® III produced by Kansai Coke and Chemical co., Ltd. was used as the adsorbent. At first, the mass attenuation coefficient of liquid ethanol was measured using an ethanol step. Then, quantifiability in the measurement of adsorbed ethanol amount in activated carbon particle bed was evaluated by the measurement of an adsorbent step in dry and adsorption equilibrium condition. The adsorbent temperature was 21.5 °C and the pressure was 4.09 kPa. The umbra method using neutron absorber was applied to the quantitative measurement. A checked neutron absorber grid shown in Fig.1 was newly made for two-dimensional measurements. The offset value for an observed area can be measured by interpolating the brightness at the position covered by the neutron absorber surrounding the observed area. The width of the grid was 3 mm.

**RESULTS:** The measured results of the liquid methanol step are plotted with the symbol of ▲ in Fig. 2. The vertical axis shows the product of density,  $\rho$ , mass attenuation coefficient,  $\mu_m$ , and thickness along the neutron beam,  $\delta$ . The subscript r means ethanol as the refrigerant. A liner relationship between ethanol thicknesses and  $\rho_r \mu_{m,r} \delta_r$  could be successfully obtained. The mass attenuation coefficient calculated from the gradient was 3.86 cm<sup>2</sup>/g. For the measured results of adsorbed ethanol without the compensation plotted with the symbol of ○, the values seemed to become saturated due to the effect of neutron scattering and stray light in the camera system. It could be seen that the linear

relationship could be obtained for the adsorbed ethanol by the umbra method as plotted with the symbol of ●. The measured values by neutron radiography was compared with those reported by El-sharkawy et al. [2] in Figure 7. They proposed the Dubinin–Astakhov equation for adsorbed ethanol amount on the same activated carbon based on the experimental results. It was confirmed that the adsorbed refrigerant amount could be measured quantitatively by the neutron radiography.

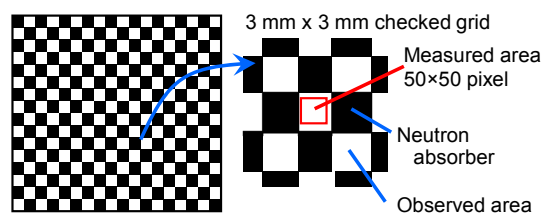


Fig. 1 Neutron absorber grid for umbra method.

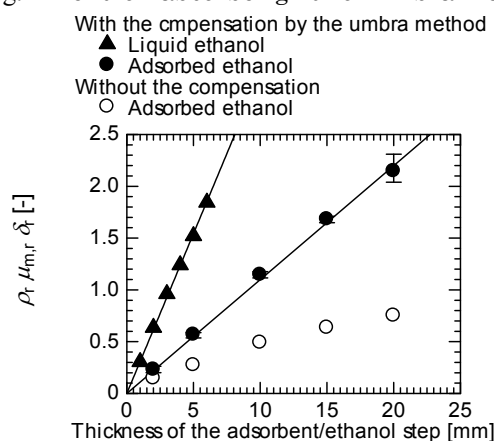


Fig. 2 Attenuation of neutron beam for various thickness of the adsorbent or ethanol step.

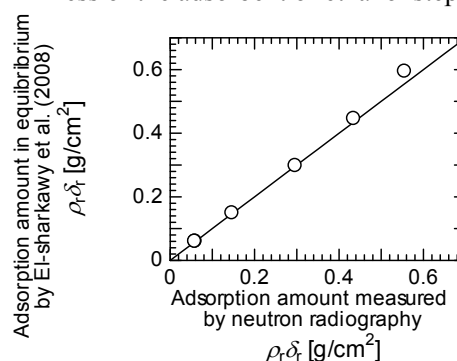


Fig. 3 Comparison of adsorption amount in equilibrium with the calculation by El-sharkawy et al.[2].

### REFERENCES:

- [1] N. Takenaka, et al., Nondestructive Testing and Evaluation, **16**-693 (2001), 345-354.
- [2] I.I. El-Sharkawy, et al., Int. J. of Refrigeration, **31**-8 (2008), 1407-1413.

## PR8-3 Neutron Radiography on Tubular Flow Reactor for Supercritical Hydrothermal Synthesis of Nanoparticles

T. Tsukada, K. Sugioka, M. Kubo, K. Ozawa, S. Takami<sup>1</sup>, T. Adschiri<sup>2</sup>, K. Sugimoto<sup>3</sup>, N. Takenaka<sup>3</sup>, Y. Saito<sup>4</sup> and Y. Kawabata<sup>4</sup>

Dept. of Chemical Engineering, Tohoku University

<sup>1</sup>IMRAM, Tohoku University

<sup>2</sup>WPI-AIMR, Tohoku University

<sup>3</sup>Dept. of Mechanical Engineering, Kobe University

<sup>4</sup>RRI, Kyoto University

**INTRODUCTION:** Recently, a variety of metal-oxide nanoparticles have been synthesized by supercritical hydrothermal synthesis [1]. For the design and optimization of the process, it is important to acquire the correct knowledge about the mixing behavior of cold aqueous feed solution and supercritical water in a hydrothermal reactor. Therefore, we used neutron radiography to visualize the flow in a tubular flow reactor for supercritical hydrothermal synthesis, and investigated the effects of the flow rates of two fluids and reactor configurations on the mixing behavior in the reactor [2-4]. In this work, CeO<sub>2</sub> nanoparticles were actually synthesized by supercritical hydrothermal synthesis under the same conditions as those in neutron radiography, and then the size distributions of synthesized nanoparticles were discussed comparing with the flow and thermal fields observed by neutron radiography.

**EXPERIMENTS:** The tubular flow reactor, which was comprised of a Swagelok union tee and SUS316 tubes whose outer diameter and wall thickness were 1/8 inch and 0.71 mm, respectively, was used for synthesizing CeO<sub>2</sub> nanoparticles. Two streams of 10 mM Ce(NO<sub>3</sub>)<sub>3</sub> aqueous solution and supercritical water were mixed and reacted at the T-junction in the reactor under approximately 25 MPa. The size distributions and average diameters of synthesized nanoparticles were evaluated using SEM (S-4800, Hitachi High-Technologies Co., Japan).

Neutron radiography of the tubular flow reactor was the same as that in our previous works [2-4], where a thermal neutron beam emitted from the B4 port in KUR was used. The imaging method of neutron radiography and subsequent analysis of the images were also similar to those in our previous work [3].

**RESULTS:** Figures 1 (a) and (b) shows SEM images and size distributions of nanoparticles synthesized using tubular flow reactors with two different configurations, when the flow rates of supercritical water and Ce(NO<sub>3</sub>)<sub>3</sub> aqueous solutions were 8.0 and 1.0 g/min, respectively. In the figures, the temperature distributions obtained by neutron radiography are also shown. Octahedral CeO<sub>2</sub> nanoparticles are found to be synthesized hydrothermally

in supercritical water. The size distribution of nanoparticles in (b) is much broader than those in (a), and the average sizes and the CV values of synthesized nanoparticles in (a) is smaller than those in (b). Here, the average size of an octahedral particle was defined by  $(ls)^{1/2}$  with the lengths of major and minor axes,  $l$  and  $s$ , of particle. Such size distribution dependence of nanoparticles on reactor configuration is due to the difference in flow and thermal fields in the reactors. As the results of neutron radiography show, the stream of supercritical water flowing down through the vertical tube penetrates into the horizontal tube, and a thermally, density-stratified layer is generated in the horizontal tube of (a), while it seems from the temperature distributions in (b) that thermal buoyancy convection occupies the vertical tube just above the T-junction.

**CONCLUSIONS:** The relationship between the size distributions of synthesized nanoparticles and the mixing behaviors of the metal salt aqueous solution and supercritical water in the reactor was clarified by comparing between the results of supercritical hydrothermal synthesis and neutron radiography in the reactor.

### REFERENCES:

- [1] T. Adschiri *et al.*, *Green Chemistry*, **13** (2011) 1380.
- [2] S. Takami *et al.*, *J. Supercrit. Fluids*, **63** (2012) 46.
- [3] N. Takenaka *et al.*, *Phys. Procedia*, **43** (2013) 264.
- [4] K. Sugioka *et al.*, *AIChE J.*, **60**, (2014) 1168.

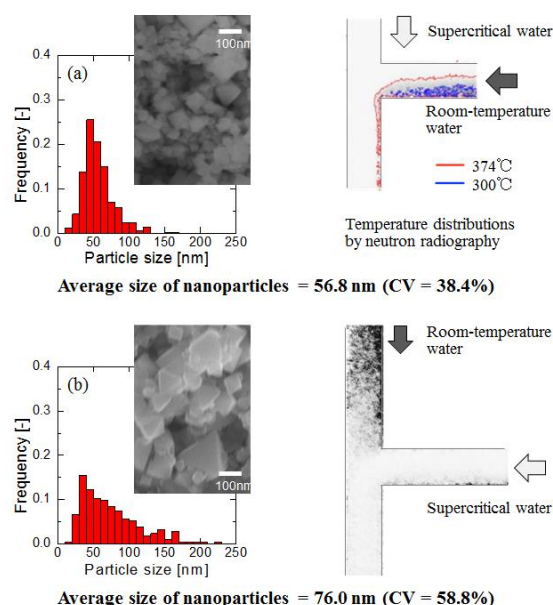


Figure 1 SEM images and size distributions of synthesized nanoparticles, and temperature distributions observed by neutron radiography.

採択課題番号 26P8-3 中性子ラジオグラフィを利用した超臨界水反応場の in-situ 観察 プロジェクト (東北大院・工) 塚田隆夫、杉岡健一、久保正樹、小澤恭兵、(東北大・多元研) 高見誠一、(東北大・WPI) 阿尻雅文、(神戸大院・工) 杉本勝美、竹中信幸、(京大・原子炉) 齊藤泰司、川端祐司



## PR8-4 Neutron imaging and optics development using simulation of VCAD Systems

Y.Yamagata<sup>\*1</sup>, S.Morita<sup>\*1</sup>, J.Guo<sup>\*1</sup>, J.Kato<sup>\*1</sup>, H.Yokota<sup>\*1</sup>,  
T.Sera<sup>\*1\*2</sup>, Y.Kawabata<sup>\*3</sup>, Y. Saitoh<sup>\*3</sup>, M.Hino<sup>\*3</sup>,  
M.Sugiyama<sup>\*3</sup>, D.Ito<sup>\*3</sup>

RIKEN Center for Advanced Photonics, RIKEN<sup>\*1</sup>,  
Osaka University<sup>\*2</sup>, Kyoto University Research Reactor  
Institute<sup>\*3</sup>

### INTRODUCTION:

VCAD System is a cluster of software codes, which can generate "real" object model in a computer and perform various numerical simulation. Those software codes include geometry conversion and input tools, 3D visualization, segmentation and mesh-generation tools, and various FEM-based simulation tools. The authors have been applied the neutron radiography data to VCAD systems to generate 3D geometry data and FEM analysis. Those software also include a simulation code for "real" optical components. We did a consideration about possible application of neutron radiography for the production process visualization for glass press mold lens and also conducted focusing experiments of small rotational ellipsoid mirror.

### EXPERIMENTS:

#### (1) Consideration of visualization of molding process

It was not possible to carry out a neutron radiography, but we have considered the possibility of neutron radiography to visualization of glass molding process of aspherical lens. Many lenses for digital cameras today include at least a few aspherical lenses. Those aspherical lenses are manufactured by glass press molding using tungsten-carbide molding die at very high temperature of 500 to 900 degree. Since the process is done with high temperature inside tungsten carbide die, it was not possible to visualize the process. Total cross section of tungsten (W) is 23.1 for thermal neutron and considering that most glass material contain boron which has very high cross section, it may be possible to visualize the molding process through tungsten carbide die.

#### (2) Neutron beam focusing experiment

To manufacture a neutron focusing mirror with relatively lower cost and manufacturing time, the authors have started the development of neutron focusing mirror using metallic substrate.[1] The advantage of metallic substrate are easier mechanical handling and shorter manufacturing time. A 100mm rotational ellipsoid mirror was fabricated and focusing performance was tested at CN-3 port.[2]

### RESULTS:

Fig. 1 shows the photo of the ellipsoid mirror through the manufacturing process. Fig.2 shows the beamline setup for ellipsoid mirror testing. The beam came through pinhole (1mm) and U-shaped slit to eliminate the neutron beams that will not reflect on the mirror surface. The focused beam is detected by RPMT detector. It was possible to detect neutron beam focusing using this small mirror as shown in Fig.3. Focusing performance using VCAD software will be conducted in the near future.

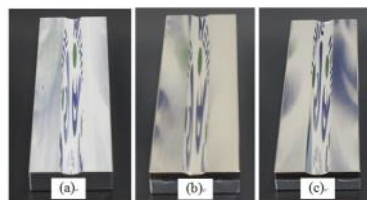


Fig.1 Manufactured ellipsoid mirror (a)aluminum substrate (b)NiP plated (c)polish finished

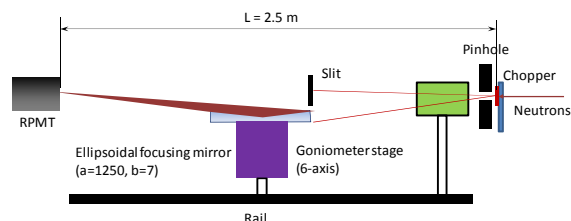


Fig.2 Experimental setup for neutron focusing experiment

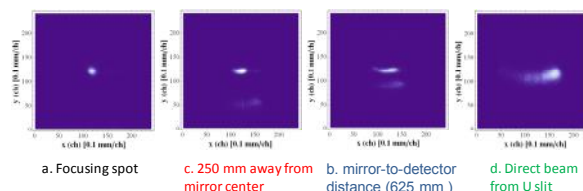


Fig.3 Focusing experiment result

### REFERENCES:

- [1] S.Takeda, H.Ohno, H.Sato, M.Furusaka, S.Morita, Y.Yamagata, M.Hino, "Development of an ellipsoidal neutron supermirror with metal substrate", International Workshop on Neutron Optics and Detectors, July (2013)
- [2] J.Guo, S.Takeda, S.Morita, M.Hino, T.Oda, J.Kato, Y.Yamagata, and M.Furusaka, "New Fabrication Method for an ellipsoidal neutron focusing mirror with a metal substrate", Optics Express, Vol.22 No.20 DOI: 10.1364/OE.22.024666 (2014)

M. Kanematsu<sup>1</sup>, S. Bae<sup>1</sup>, T. Koyama<sup>1</sup>, R. Inose<sup>1</sup>,  
N. Tuchiya<sup>2</sup>, M. Tamura<sup>3</sup>, Y. Nishio<sup>3</sup>, T. Noguchi<sup>3</sup>  
D. Ito<sup>4</sup> and Y. Saitou<sup>4</sup>

<sup>1</sup>Department of Architecture, Tokyo University of Science

<sup>2</sup>Building Research Institute, Material Study Group

<sup>3</sup>Department of Architecture, The University of Tokyo

<sup>4</sup> Research Reactor Institute Kyoto University

**INTRODUCTION:** High-performance concrete (HPC) has low water-to-binder ratio and it is vulnerable to the fire exposure, resulting in the explosive spalling of HPC surface at the early stage of fire. The spalling phenomena has been explained to occur due to the moisture pressure accumulated inside the pore of HPC [1]. However, the actual mechanism of the spalling has not been fully understood. To understand the detailed mechanism of spalling in HPC, 2-dimensional moisture movement in HPC subjected to heating was quantitatively assessed in this study.

**EXPERIMENTS:** The concrete specimen (100×100×20 mm<sup>3</sup>) with water-to-binder ratio of 18 % was prepared. The initial moisture contents of the specimen was 14.1 % and the heating condition referred to the previous work [2]. The TNRF in the B-4 beam-line of neutron flux  $1 \times 10^7 \text{ n/cm}^2$  was utilized for neutron radiography and the noise pixel in the images deviating more than 10 grayscale values were replaced by the median value of the pixels around the circle with 2-pixels radius.

**RESULTS:** Fig.1 presents 2-dimensional distribution of differential moisture contents of paste in the specimen per unit volume. The correlation between the change of water content and the intensity of transmitted neutron was examined using specimens with predetermined specific water contents. As shown in Fig.1, the moisture condensed areas were observed at the boundary of dried areas, moving up to the top with the temperature elevation. This phenomenon was also confirmed in our previous work, in the case of high strength mortar [2]. Furthermore, the presence of moisture condensed areas was observed around the coarse aggregates and the holes created for the internal temperature measurement, which is in good agreement with the previous numerical model [4]. The interfacial transition zone around the coarse aggregates is assumed to provide the space that the condensed moisture can pass through. The explosive spalling occurred for two times, at 1m26s and 1m27s, respectively. In the area of 0 to 5 mm from heating surface, moisture content increase was monitored with the value of  $5.0 \times 10^2 \text{ g/cm}^3$   $6.0 \times 10^2 \text{ g/cm}^3$  at each spalling. The influence of vapor pressure induced by moisture movement on the spalling phenomena of HPC will be further investigated in the future.

#### REFERENCES:

[1] T.Z.Harmathy, ASTM, Philadelphia, No.385, 75-95

[2] M.kanematsu et al, PJCI, vol36, No.1, 2014

[3] J. Zhao, Cem. Concr. Res., 65, 64-75, 2014

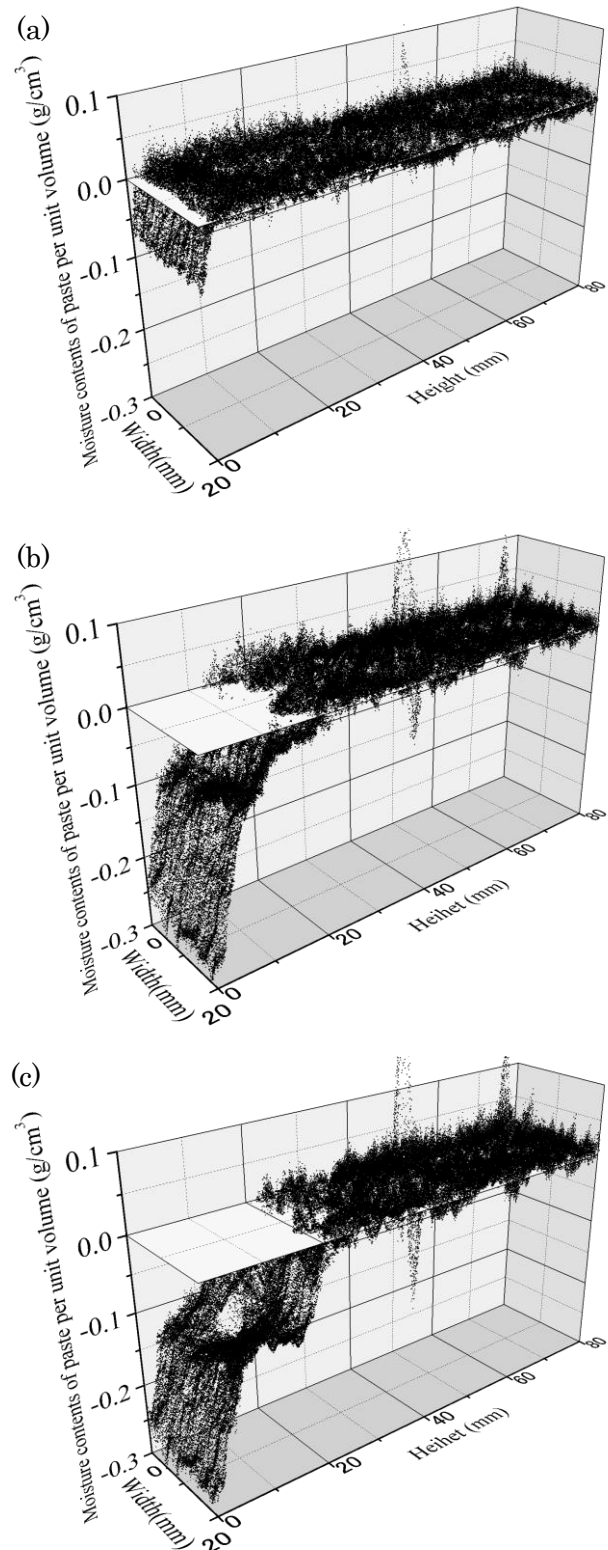


**Fig.1** Two-dimensional distribution of differential moisture contents of paste of HPC per unit volume at (a) 1 min, (b) 4 min, and (c) 8 min after heating

採択課題番号26P8-10 高温加熱環境下における高強度コンクリートの水分移動の研究 プロジェクト

(東理大・理工) 兼松学、Sungchul Bae、小山拓、猪瀬亮 (建研・材料) 土屋直子

(東大・工) 田村政道、西尾悠平、野口貴文 (京大炉) 伊藤大介、齊藤泰司

## PR8-6 Effect of Gravity on Coolant Distribution in FGHP Heat Spreader

K. Mizuta, Y. Saito<sup>1</sup>, D. Ito<sup>1</sup>

Faculty of Engineering, Kagoshima University

<sup>1</sup> Research Reactor Institute, Kyoto University

**INTRODUCTION:** Recently, the importance of thermal management in electronic devices has become much higher than ever, because the lack in cooling ability in such devices leads to various reliability problems and low working efficiency. Particularly, in a light-emitting diode (LED) array, non-uniform temperature distributions caused by poor heat spreading ability of its substrate ruins the quality of lightning, because the light emitting efficiency of LED gets lowered with higher working temperature. To tackle with such problems in thermal management, vapor chambers would be one of the hopeful candidates as the substrate for its higher effective thermal conductivity compared with metal heat spreaders [1]. In an ordinary vapor chamber, however, it has been reported that the heat transfer characteristics are strongly affected by its installation posture, because the coolant circulation inside the vapor chamber is strongly affected by the gravity, which spoils the adoption of vapor chambers for the LED substrate. The authors have been trying to solve such problems by utilizing a newly developed vapor chamber called FGHP which is manufactured by precise etching technique by Molex Kiire Co., Ltd. located in Kagoshima, Japan. In this study, we investigated the gravitational effects on the coolant distribution in the FGHP by using neutron radiography at the Kyoto University Research Reactor (KUR).

**EXPERIMENTS:** Experiment was conducted at the E-2 port of the KUR, where the thermal neutron flux at the sample position was about  $3 \times 10^5 \text{ cm}^{-2}\text{s}$  at 5 MW operation. The size of the test sample of FGHP heat spreader was 65 mm square and 2 mm thick. The test sample was set vertically, which means that its bottom and top plate was placed parallel to the gravitational direction. A ceramic heater of  $25 \times 25 \times 1.75 \text{ mm}^3$  was attached to the central part of the bottom plate as a heat source, and the top plate was cooled by three pin-fin type aluminum heat sinks of  $35 \times 35 \text{ mm}^2$  under natural convection conditions. K-type thermocouples were utilized to measure both the surface temperature of the heat spreader and the atmospheric temperature to estimate the thermal resistance of the FGHP. A CCD camera (BU-53LN, BITRAN Co. Ltd.) was utilized, which has  $4008 \times 2672$  pixels and  $^6\text{LiFZnS}$  (50  $\mu\text{m}$  thickness) was used as a scintillator screen. The spatial resolution was 9.0  $\mu\text{m}/\text{pixel}$  at the present system setup, however, the effective spatial resolution was about 50  $\mu\text{m}/\text{pixel}$  due to the scintillator screen characteristics.

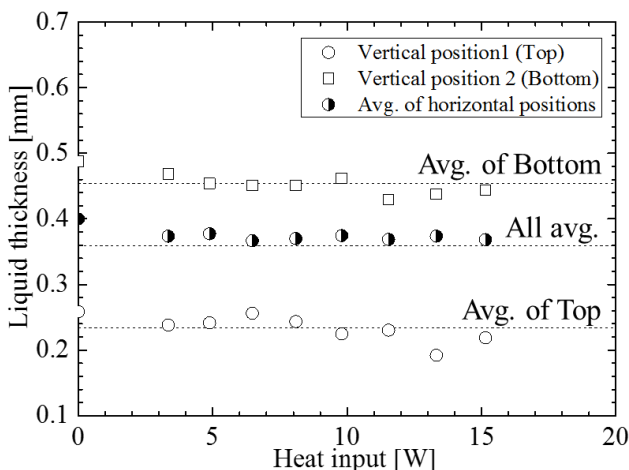


Fig. 1. Variation of the liquid thickness in the wick area with input power.

Neutron imaging of the sample was performed at the 1 MW operation mode of the KUR and the exposure time was 300 s. Neutron images of the sample were utilized to calculate liquid thickness in the FGHP. The effect of gravity on the coolant distribution was evaluated by the calculated liquid thickness in the wick area at different positions as follows:

1. Vertical position 1 (Top),
2. Vertical position 2 (Bottom),
3. Horizontal position 1 (Left),
4. Horizontal position 2 (Right).

Interrogation window size was  $0.4 \times 1.5 \text{ mm}^2$  at each position.

**RESULTS:** Figure 1 shows the variation of liquid thickness with heat input. As shown in Fig. 1, the measured values of the liquid thickness in the wick area take the smallest at the top and the largest at the bottom positions. The measured values range from 200 to 480  $\mu\text{m}$  and increases along with the gravitational direction. However the liquid thickness remains nearly constant regardless of the heat input. From the design of the inner structure of the FGHP heat spreader, the maximum liquid thickness in the wick area can be estimated as 0.6 mm (about 0.1 mm in the middle plates and 0.5 mm in the top and the bottom plates), therefore, at least 0.1 mm thick liquid layer would be considered to cover the surface of the middle plates as the wick structure, which may suggest the surface of the whole wick area does not dry out even when the FGHP is installed in the vertical posture.

### REFERENCES:

- [1] J. C. Wang, Int. J Heat and Mass Trans., **53** (2010) 3990-4001.

K. Hirota<sup>1</sup>, A. Uritani, K. Watanabe, A. Yamazaki,  
D. Sugimoto, Y. Kiyonagi, Y. Shiota, H. M. Shimizu<sup>1</sup>,  
G. Ichikawa<sup>1</sup>, M. Kitaguchi<sup>2</sup>, Y. Saito<sup>3</sup>

*Graduate School of Engineering, Nagoya University*

<sup>1</sup> *Graduate School of Science, Nagoya University*

<sup>2</sup> *Kobayashi-Maskawa Institute, Nagoya University*

<sup>3</sup> *Research Reactor Institute, Kyoto University*

**INTRODUCTION:** The machinery industry products including automobile and aircraft are progressing to high performance and high precision. One of the desired technique in these development fields of state-of-art technology products is visualization of organic film (oil film grease, etc.) exist between metals. In the present work we explore the possibility of observation of the characteristics(shape, nature and the distribution of thickness) of the organic skin and its dynamic changes.

**EXPERIMENTS:** The measurement was done at E2 beam port in the reactor room. Bearings and an oil pump are using for the sample materials. The CCD system is Bitran BU-53LN and the scintillator is <sup>6</sup>Li/Zns(Ag) of thickness 200 μm, which is prepared RIKEN group and normally equipped at E2. The neutron (static) radiography image and CT reconstruction images were taken for both bearings and oil pump. The CT reconstruction system is also equipped at E2. The typical exposure time is one minute for static image in 1 MW mode. This exposure time is decrease to 1/5 at 5MW mode. In the case of CT measurement, 30 seconds exposure time and 300 images, which are corresponding to 0.6-degree sample rotation step, are taken.

**RESULTS:** Figure 1 shows the neutron radiography image of bearings. These bearings are all commercial products. Half of these bearings are removed grease. White color area means that the neutron beam is easily transmitted, and black area means absorption. Neutron beam is expected to be well aborted by grease because of including of hydrogen. Clear grease image were available to find by comparing the picture between with and without grease. Figure 2 shows the CT reconstruction image of bearing include grease. Black-and-white shade is inverted to fig. 1. White area indicated the grease in the case of fig. 2. The grease skin is available to see between the boll and the frame of the bearing.

We want to observe how to move the grease with bearing rotation as next plan.

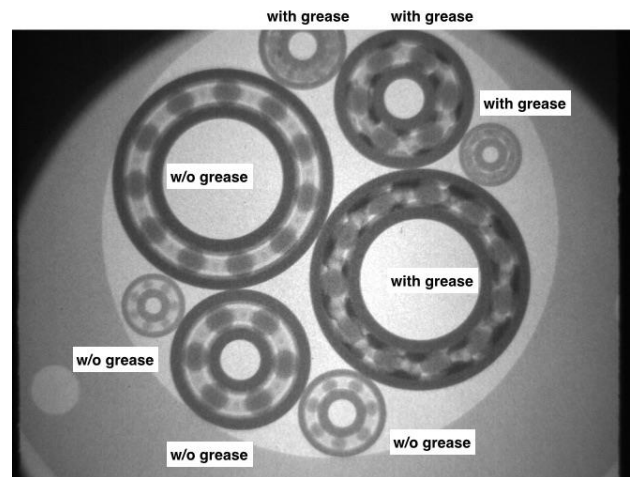


Fig. 1. Neutron radiography image of the bearings. Half of these bearings are removed the grease.

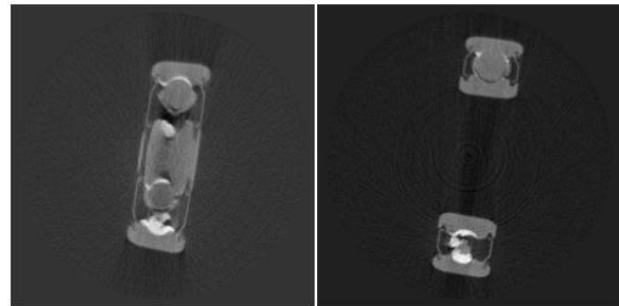


Fig. 2. CT reconstruction image. Black-and-white shade is inverted to fig. 1.

Y. Tsuji, T. Ito, M. Ogasawara, S. Yanagisawa,  
M. Tamaki<sup>1</sup>, D. Ito<sup>2</sup> and Y. Saito<sup>2</sup>

Graduate School of Engineering, Nagoya University

<sup>1</sup>Department of Energy Engineering and Science

Graduate School of Science, Kyoto University

<sup>2</sup>Research Reactor Institute, Kyoto University

**INTRODUCTION:** We study the heat transfer process on the solid surface covered with liquid water. It is not clearly understand how the heat transfer is enhanced by changing the condition of solid surface, characteristics of liquid and flow conditions. We study the heat pipe (Fig.1) as the simple equipment to study the heat transfer process, and the following points are focused. (1) Character of solid surface is changed, such as a water-repellent coat, a hydrophilic coat, and/or a monomolecular film are added over the solid surface. (2) To change the solid surface condition as a complicated shape (wick). Such as porous media is attached on the surface and visualize the boiling process inside it. The boiling process is significantly affected by a porous shape and surface condition. (3) Heat transfer is measured independently, and it is compared with boiling process inside the porous media is visualized by NRG.

The purpose of this study is to enhance the heat transfer and understand its physical process by analyzing the visualized images by NRG.

**EXPERIMENTS:** House-made heat pipe is operated with supplying the heat by the Peltier module. We change the conditions of heat transfer with monitoring the NRG image. The heat pipe is made of aluminum, whose dimension is  $20 \times 110 \times 110$ mm. Heater power is varied from 6 W to 30W, and the temperature of heater section changes from  $40^\circ\text{C}$  to  $70^\circ\text{C}$ . The maximum inside pressure is 36 kPa.

In this measurement, we have to check the basic performance of NRG technique for observing the air, vapor and water states and their motions. Working fluid is water (20ml), and three different amounts of air (0, 5, 10ml) are supplied inside the heat pipe. The E2 beam port was used for NRG experiments.

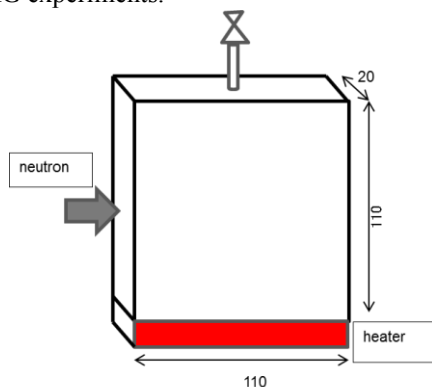


Fig.1 Schematic view of experimental setup

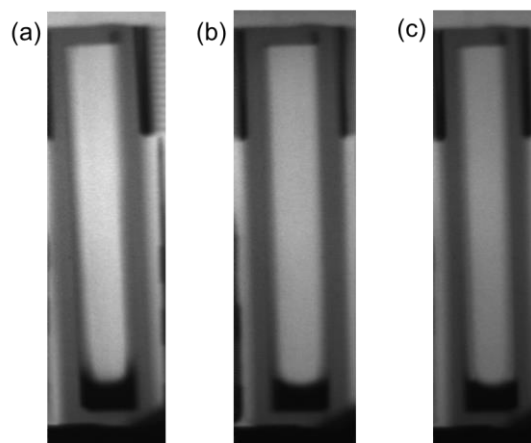


Fig.2 Neutron radiography image. (a) air=0ml, (b)air=5ml, (c)air=10ml.

**RESULTS:** The neutron radiography images are shown in Fig.2. We hope to observe the air, vapor and water phases inside the heat pipe, however it was difficult to distinguish them clearly. The water phase (black) is suppressed in (c) compared with (a) condition. This may be due to the increase of vapor pressure by adding the air. As the heat pipe is slightly tilted along the side wall, we can observe the thin liquid film flowing from top to down. This is caused by the liquid (water) condensed at the upper region and return to the bottom. On the left-side wall, the liquid film is thicker than that of right wall.

For the qualitative analysis from the digitized image intensity, the effect of aluminum wall is removed. We visualized the heat pipe, which does not contain the working fluid. By using this calibration image, background image is subtracted, that is usually adopted as NRG procedure. Figure 3 shows the averaged intensity profiles along the vertical direction of heat pipe. The intensity corresponds to the ratio of water averaged over the cross direction. The different colors show the conditions (a), (b), and (c), respectively. At the bottom region close to heater, the intensity of (a) shows the smaller value than other conditions. This indicates the water region remains much more in (a) condition. However, we can not distinguish the vapor and air regions. For the final purpose of our research, the vapor region should be distinguished from other states (water and air phases). The present techniques are revised in the next stage.

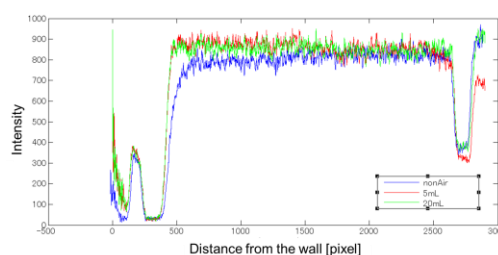


Fig.3 NRG intensity profiles along the heat pipe.

N. Fujii

*Research Reactor Institute, Kyoto University*

### Objectives and Allotted Research Subjects:

The aim of this project research is to elucidate the correlation between the change of the protein structure induced by various post-translational modifications with UV irradiation, gamma-irradiation, aging and protein function. We also investigate the repair mechanism for the damaged protein by irradiation. This research program has started in 2013. In this year, the 6 research subjects were carried out. The allotted research subjects (ARS) are as follows;

**ARS-1:** Detection of D-aspartyl endopeptidases activity in floral tissues of broccoli (*Brassica oleracea* var. *Italica*). (T. Kinouchi and N. Fujii)

**ARS-2:** Damage to biological molecules induced by ionizing irradiation and biological defense mechanisms against ionizing radiation I. (T. Saito and N. Fujii)

**ARS-3:** Analysis of aspartate isomerization using protein L-isoaspartyl methyltransferase (PIMT) (Y. Sadakane and N. Fujii)

**ARS-4:** Analysis of imbalance in mice exposed to environmental stress. (N. Ohgami and N. Fujii)

**ARS-5:** Identification of biologically uncommon  $\beta$ -aspartyl residues in proteins using LC-MS/MS (N. Fujii, S. Kishimoto and N. Fujii)

**ARS-6:** Sidechain conformers of aspartyl isomers in crystallin mimic peptide (K. Aki, E. Okamura)

**ARS-7:** Rapid survey of Asp isomers in disease-related proteins by LC-MS/MS combined with Commercial Enzymes (H. Maeda, T. Takata, N. Fujii, H. Sakaue, H. Sasaki and N. Fujii)

### Main Results and Contents of This Project

ARS-1: Kinouchi et al. detected high D-aspartyl endopeptidase (DAEP) activity in the floret of fresh broccoli (*Brassica oleracea* var. *Italica*). DAEP is commonly distributed in animals, and their testes and ovaries are especially shown to have the high DAEP activity. Broccoli floret is a cluster of numerous small flowers and also encloses the reproductive organs. Since DAEP activity in other parts of plants, such as stems, leaves and roots, was not detectable or quite low, it was suggested that the physiological function of DAEP would contribute to the early development.

ARS-2: Saito *et al.* revealed that carotenoids have no effect on the initial rapid peroxidation during the process of damage to lipid induced by gamma irradiation, but an optimum concentration of carotenoids inhibits the subsequent oxidative degradation involving radical reactions during this process.

ARS-3: Sadakane et al prepared a repair enzyme for aged proteins, protein L-isoaspartyl methyltransferase (PIMT) by E. coli expression system, and analyzed the effect of substrate size on the activity of PIMT. PIMT activity is affected by length of peptides and the activity is weaker in the shorter peptide. However, the peptides which consist of 5 to 9 amino acids are good substrates for PIMT regardless the position of L-isoAsp. The feature is useful to analyze various types of peptide because the shorter peptides are easily prepared.

ARS-4: Ohgami et al. showed that exposure of mice to low frequency noise (LFN) at moderate levels causes imbalance and tried to detect protein aggregation in vestibule of inner ears. Our results suggest that incidence of protein aggregation was undetectably low at least in the exposure condition to moderate LFN.

ARS-5: Fujii et al. established a new method to identify the  $\beta$ -Asp containing peptides by the analysis of the 2nd generation product ion spectrum of liquid chromatography - tandem mass spectrometry (LC-MS/MS).

ARS-6: Aki et al. investigated populations of side chain conformers of Asp isomers (L- $\alpha$ -, D- $\alpha$ -, D- $\beta$ -Asp) in  $\alpha$ A-crystallin mimic peptides by using solution NMR. As a result, trans conformer was preferred in D- $\beta$ -Asp, whereas gauche conformer was abundant in L- $\alpha$ - and D- $\alpha$ -Asp. Trans is thought to be disadvantageous to Asp isomerization. Therefore, the D- $\beta$ -Asp is thought to be the most stable in the 3 isomers.

ARS-7: Fujii et al. demonstrated a new method for rap-

## PR10-1 Detection of D-Aspartyl Endopeptidases Activity in Floral Tissues of Broccoli (*Brassica oleracea* var. *Italica*)

T. Kinouchi and N. Fujii

Research Reactor Institute, Kyoto University

**INTRODUCTION:** D-isomer of aspartate (D-Asp) residue is detected in abnormally folded and aggregated proteins: i.e., crystalline, prion protein and  $\beta$ -amyloid protein. Accordingly, it is suggested that the formation of D-Asp in those proteins is responsible for the related diseases: cataract, prion disease and Alzheimer's disease, respectively. The D-aspartyl endopeptidase (DAEP), which we identified from mammalian liver, stereoselectively degrades its substrate at the internal D-Asp residue, and seems to physiologically serve as a scavenger against the noxious D-Asp containing-protein and to maintain the normal protein turnover [1]-[3]. However, the distribution of DAEP in other living-things was not as clear as in animals. As a result of searching the distribution of DAEP in various animals, reproductive organs were shown to have the high DAEP activity as a common feature. Especially this tendency was evident among aquatic animals, for example, in African clawed frogs (*Xenopus laevis*) and Japanese green sea urchins (*Hemiacentrotus pulcherrimus*). The high DAEP activity was practically detectable in their testes, ovaries and unfertilized eggs.

On the other hand, the existence of DAEP in plants is ambiguous. Considering the distribution of DAEP in animals, we searched the DAEP activity in the reproductive organ such as a floral tissue of plants.

**EXPERIMENTS:** Plant Material> Fresh broccoli (*Brassica oleracea* var. *Italica*) was purchased from a local supermarket and the floret was separated. After any damaged parts were removed from the floret, the remainder was cut into fine pieces and then homogenized by Polytron® PT2100 agitator in ice-cold sodium phosphate buffer (pH 7.0). The suspension was filtered through a double layer of cheesecloth and centrifuged at 600 xg for 10 min at 4°C. Since the supernatant was crude enzyme mixtures that might include not only DAEP but also other proteases, the appropriate dose of protease inhibitor cocktail for plant cell extracts (purchased from Sigma-Aldrich, Inc) was added into it.

Measurement of DAEP activity> We developed an assay system for DAEP activity using the synthetic D-Asp containing substrate, Succinyl-D-Aspartic acid  $\alpha$ -(4-methyl-coumaryl-7-amide) (Suc-D-Asp-MCA) [1]. Supernatant of the above biological materials was mixed and incubated with 0.1 mM Suc-D-Asp-MCA and the assay buffer (10 mM Tris-HCl (pH 8.5), 200 mM NaCl, 3 mM MgCl<sub>2</sub>) at 25°C. The fluorescence of aminomethylcoumarin liberated from Suc-D-Asp-MCA by

DAEP was measured at  $\lambda_{ex} = 380$  nm and  $\lambda_{em} = 460$  nm.

**RESULTS & DISCUSSION:** As described in this last report, radish taproots were shown to have the DAEP activity but in quite low amounts [4]. And in tomato fruits, the DAEP activity was not detectable because endogenous pigments in the extract of tomato fruits would disturb the measurement. Although the supernatant extracted from broccoli floret also had a high amount of the green pigment, the DAEP activity showed 15 times higher than in radish taproots.

In this report, four broccoli florets were used for the DAEP assay, and each measured value of the specific activity was not stable ( $\sim\pm 20\%$ ). Since each broccoli was purchased on different day, the different storage periods of those broccoli florets may have affected the postharvest senescence. Therefore we would like to make the next issue to observe chronological changes of the DAEP activity in plant embryo.

Table. Specific activities of DAEP in various samples.

Samples (tissue)	Specific activity (% of max in frog)
African clawed frog (Ovary)	100
Radish (taproot)	$\sim 1.5$
Broccoli (floret)	$\sim 30$

### REFERENCES:

- [1] T. Kinouchi *et al.*, Biochem. Biophys. Res. Commun., **314** (2004) 730-736.
- [2] T. Kinouchi *et al.*, Chem. Biodivers., **7** (2010) 1403-1407.
- [3] T. Kinouchi *et al.*, J. Chromat. B., **879** (2011) 3349-3352.
- [4] T. Kinouchi and N. Fujii, KURRI Prog. Rep. **2013** (2014) 110.

## PR10-2      **Damage to Biological Molecules Induced by Ionizing Irradiation and Biological Defense Mechanisms against Ionizing Radiation I**

Takeshi Saito and Noriko Fujii

*Research Reactor Institute, Kyoto University*

**INTRODUCTION:** Some bacteria exhibit extreme resistance to ionizing radiation [1]. A common feature of these bacteria is that they contain red carotenoid pigments [1]. Colorless mutants of these radioresistant bacteria are more sensitive to gamma irradiation than wild types [1]. Therefore, carotenoids are thought to be involved in the bacterial defense mechanisms against ionizing radiation [1]. Biological effects induced by low-linear energy transfer ionizing radiation are mainly attributed to radicals generated by radiolysis. Carotenoids have high radical scavenging activity, and they are localized in cell surface lipids in prokaryotes. These facts indicate that carotenoids are likely to defend the cell surface lipids of radioresistant bacteria against ionizing radiation.

When considering the biological defense mechanism of these radioresistant bacteria against ionizing radiation, it is important to elucidate the effects of carotenoids on damage to biological molecules, especially biological lipids. In this study, we analyzed the effect of two typical carotenoids,  $\beta$ -carotene and astaxanthin, on the oxidative degradation as well as peroxidation of biological lipids,  $\alpha$ -linolenic acid, induced by gamma irradiation.

**EXPERIMENTS:** Sample Preparation:  $\alpha$ -Linolenic acid was dissolved in benzene at a final concentration of  $5.0 \times 10^{-1}$  M, and  $\beta$ -carotene and astaxanthin were added at a final concentration of  $5.0 \times 10^{-6}$  to  $5.8 \times 10^{-3}$  M and  $5.0 \times 10^{-8}$  to  $5.0 \times 10^{-4}$  M, respectively. Gamma Irradiation: The prepared solutions were irradiated with  $^{60}\text{Co}$  gamma rays at a dose of 30 kGy and a dose rate of 400 Gy/min. Analysis of Oxidative Degradation of  $\alpha$ -Linolenic Acid: The method described by Buege and Aust was used with some modifications [2]. TCA-TBA-BHT-HCl reagent (15% trichloroacetic acid, 0.375% thiobarbituric acid, 0.04% butylated hydroxytoluene, and 0.25N hydrochloric acid) was prepared. The gamma irradiated sample was diluted 50-fold with benzene. The diluted solution (3.0 mL) was evaporated under reduced pressure. The resulting residue was dispersed in 9.0 mL of PBS(-) with a sonicator. The dispersed solution (1.0 mL) was combined with 2.0 mL of TCA-TBA-BHT-HCl reagent and thoroughly mixed. The mixed solution was heated in a boiling water bath for 15

min, and absorption at 535 nm was measured. The amount of malondialdehyde (MDA) formed was calculated using the molar absorption coefficient ( $\epsilon$ ) of the color substance formed by the reaction (i.e.,  $1.56 \times 10^5$  at 535 nm). Thus, the level of oxidative degradation of  $\alpha$ -linolenic acid was evaluated by measuring the amount of MDA. Analysis of Peroxidation of  $\alpha$ -Linolenic Acid: The method described by Kennedy and Liebler was used with some modifications [3]. The gamma-irradiated samples were diluted 600-fold with *n*-hexane, and then 5.0 mL of this solution was evaporated under reduced pressure. The resulting residue was dissolved in 5.0 mL of *n*-hexane, and the average absorbance of this solution in the 230–236 nm range, which was derived from the conjugated diene formed, was measured. In this study, the level of peroxidation of  $\alpha$ -linolenic acid was evaluated by determining the relative amount of conjugated diene formed.

**RESULTS:** The analyses revealed that  $8.5 \times 10^{-3}$  M  $\beta$ -carotene and  $5.0 \times 10^{-4}$  M astaxanthin inhibited gamma radiation-induced oxidative degradation of  $\alpha$ -linolenic acid; in contrast,  $5.0 \times 10^{-5}$  and  $5.0 \times 10^{-6}$  M  $\beta$ -carotene, and  $5.0 \times 10^{-7}$  and  $5.0 \times 10^{-8}$  M astaxanthin promoted its degradation. On the other hand,  $\beta$ -carotene and astaxanthin did not affect gamma radiation-induced peroxidation of  $\alpha$ -linolenic acid. These facts indicated that carotenoids have no effect on the rapid initial peroxidation during the process of damage to lipid induced by gamma irradiation, but an optimum concentration of carotenoids inhibits the subsequent oxidative degradation during this process. The present study suggests that radioresistant bacteria possess the biological defense mechanism involving the scavenging of ionizing radiation-induced radicals in lipid regions, such as cell membranes, by red carotenoid pigments, thereby protecting biological lipids and other biomolecules in the vicinity of the carotenoid against damage induced by radical reactions.

### REFERENCES:

- [1] T. Saito, *Viva Origino*, **30** (2007) 85–92.
- [2] J. A. Buege and S. D. Aust, *Meth. Enzymol.*, **52**, (1978) 302–310.
- [3] T.A. Kennedy and D.C. Liebler, *J. Biol. Chem.* **267**, (1992) 4658–4663.

採択課題番号26P10-2 放射線照射による生体分子損傷と放射線に対する生体防御機構 プロジェクト  
(京大・原子炉) 齊藤 毅、藤井 紀子



Y. Sadakane<sup>1</sup>, N. Fujii<sup>2</sup>

<sup>1</sup>Department of Pharmaceutical Sciences, Suzuka University of Medical Science

<sup>2</sup>Research Reactor Institute, Kyoto University

**INTRODUCTION:** The stereoconversion of aspartyl (Asp) residue arise through intramolecular rearrangement, such as *via* a succinimide intermediate. L-isoaspartyl methyltransferase (PIMT) catalyzes repair of L-isoAsp peptide bonds in aged proteins by transferring a methyl group from S-adenosylmethionine to a  $\alpha$ -carboxyl group of L-isoAsp residue (Fig.1).

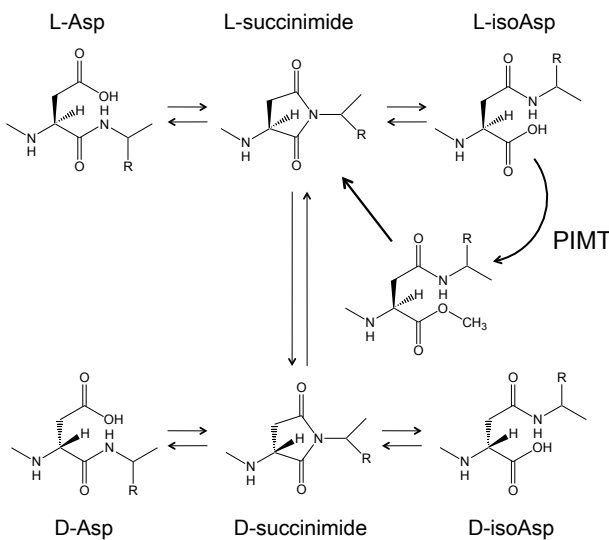


**Fig. 1** The  $\beta$ -linkage isomerization and stereoinversion to D-form of aspartyl residue and PIMT repair system.

In this study, we prepared PIMT by *E. coli* expression system, and analyzed the effect of various length of substrate on the activity of PIMT.

**EXPERIMENTS:** The recombinant PIMT protein was prepared by His-tag conjugated *E. coli* expression system, and the various lengths of peptide fragments were synthesized by using Fmoc amino acids. To be the substrate for PIMT, L-isoAsp was substituted for the aspartate residues in these peptides. The PIMT activity was measured by HPLC analysis of S-adenosyl homocysteine (SAH), which was demethylated product of co-substrate S-adenosyl methionine for PIMT.

**RESULTS:** The various lengths of peptide bearing

L-isoAsp were incubated in recombinant PIMT with co-substrate S-adenosyl methionine and the production of SAH was analyzed by reversed-phased HPLC with 4 % acetonitrile solving in pH 4.6 acetate buffer (Fig. 2).

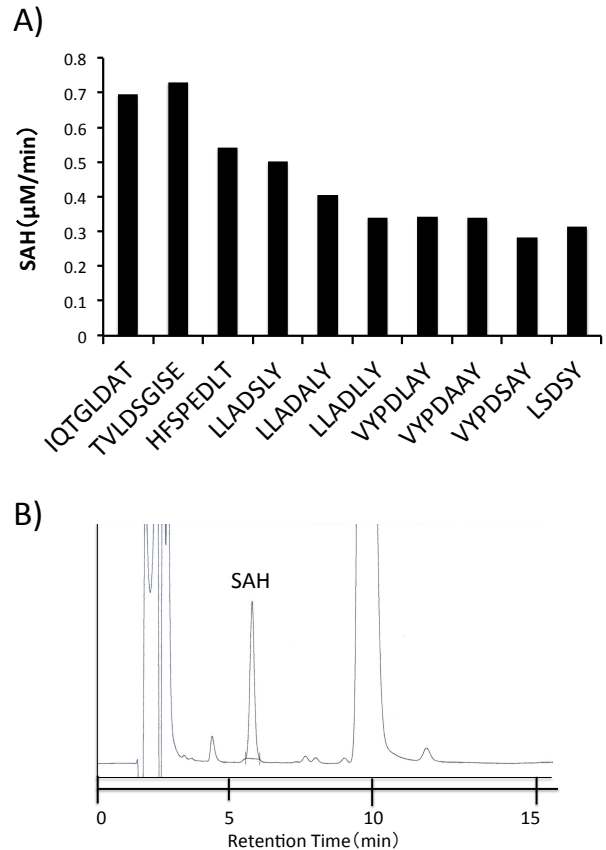


**Fig 2** Effect of substrate length on the PIMT activity (A) and the determination of PIMT activity by HPLC (B). Various lengths of peptide were incubated with PIMT and the generation rates of S-adenosyl homocysteine (SAH) were determined by HPLC analysis.

The HPLC profile (Fig 2B) ensures quantitative analysis of SAH. Fig 2A shows that PIMT activity is affected by length of peptides and the activity is weaker in the shorter substrate. However, the peptides which consist of 9 to 5 amino acids are good substrates for PIMT regardless the position of L-isoAsp. Our recombinant PIMT is able to repair the L-isoAsp residue in the short peptide that consists of five amino acids. The feature is useful to analyze various types of peptide because the shorter peptides are easily prepared.

## PR10-4 Analysis of Imbalance in Mice Exposed to Environmental Stress

Nobutaka Ohgami<sup>1,2</sup> and Noriko Fujii<sup>3</sup>

<sup>1</sup>*Department of Occupational and Environmental Health, Nagoya University Graduate School of Medicine and* <sup>2</sup>*Nutritional Health Science Research Center, Chubu University*

<sup>3</sup>*Research Reactor Institute, Kyoto University*

**INTRODUCTION:** Exposure to noise generated in occupational and daily environments is one of the risk factors threatening our health [1,2]. Although noise contains sound with broad frequencies, there is very limited information about the frequency-dependent influence of noise on health. Low frequency noise (LFN) is generated from industrial devices and home electrical appliances at all times. Thus, we are exposed to LFN generated from various devices on a daily basis. LFN is defined as noise having the frequency range below 100 Hz [3]. On the other hand, inner ears contain the vestibule as well as the organ of Corti. Vestibular hair cells covered with otoconia to sense gravity stimulus. Impairments of vestibular hair cells have been shown to cause imbalance [4]. Meanwhile, excessive exposure to noise at 1-20 kHz which is audible sound for mice and humans has been shown to induce damage of hair cells with enhanced oxidative stress in the organ of Corti in the inner ear in mice. Also, increased oxidative stress has been shown to cause aggregation of proteins in central nervous system. At present, however, most of the previous studies used broadband noise with no consideration of specific frequencies. Our previous study has shown that chronic exposure to LFN at moderate levels causes imbalance involving morphological impairments of the vestibule with enhanced levels of oxidative stress and positive signals stained by anti-D-beta-Asp antibody. However, there is limited information about whether exposure to LFN can cause protein aggregation in vestibular hair cells. In this study, therefore, we exposed mice to LFN (100 Hz) for exposure of mice to noise in order to detect the protein aggregation in vestibules caused by LFN stress.

**EXPERIMENTS:** Randomly bred wild-type mice

(ICR) at 6 weeks of age were used for exposure experiments. All experiments were authorized by the Institutional Animal Care and Use Committee in Nagoya University (approval number: 27241) and Chubu University (approval number: 2610016) and followed the Japanese Government Regulations for Animal Experiments. Mice were continuously exposed for 1 month to LFN as previously reported [5]. In order to morphologically detect protein aggregation, thioflavin-S staining was performed as previously reported [6].

**RESULTS:** After exposure for one month to LFN, behavior analyses including rotarod, beam-crossing and footprint analysis showed impaired balance in LFN-exposed mice but not in non-exposed mice. In contrast, thioflavin-S staining of vestibule in inner ears did not show positive signals in exposed mice at least in this exposure condition. Immunohistochemistry with anti-alpha-synuclein also did not show typical pattern of the aggregation. Our results suggest that incidence of protein aggregation was undetectably low at least in this exposure condition to moderate LFN. At present, output level of LFN is limited in our LFN generator system. Therefore, we will renew the generator system to output LFN at larger level. Also, we will set up an organ culture system of inner ears to directly expose to LFN. Sensitivity of thioflavin-S staining is affected by fixation conditions once in a while. Further study is needed to improve the detection system of protein aggregation in inner ears.

### REFERENCES:

- [1] J.D. Dougherty, O.L. Welsh *N Engl J Med* (1966) **275**, 759-765.
- [2] M. Wallenius *J Environ Psych* (2004) **24**, 167-177.
- [3] G. Leventhall (2003) *A Review of Published Research on Low Frequency Noise and its Effects*, Department of Environment, Food, and Rural Affairs (DEFRA), United Kingdom.
- [4] X. Zhao *et al.*, *Neuroscience* (2008) **153**, 289-299.
- [5] H. Tamura, N. Ohgami *et al.*, *PLoS ONE*, (2012) **7**(6), e39807
- [6] A. Sun *et al.*, *J. Histochem. Cytochem.*, (2002) **50**, 463-472.

## PR10-5 Identification of Biologically Uncommon $\beta$ -aspartyl Residues in Proteins Using MS

N. Fujii, S. Kishimoto<sup>1</sup> and N. Fujii<sup>2</sup>

Radioisotope Research Center, Teikyo University

<sup>1</sup>Faculty of Pharma Sciences, Teikyo University

<sup>2</sup>Research Reactor Institute, Kyoto University

**INTRODUCTION:** We recently developed a new method for determining peptides containing Asp isomers at individual sites and for detecting inverted Asp residues in any protein by using a liquid chromatography - tandem mass spectrometry system [1]. In order to determine which types of Asp isomer are present, however, standard peptides containing L $\alpha$ , L $\beta$ , D $\alpha$ , D $\beta$  isomers must be synthesized and their retention times on LC-MS must be compared with those of the sample peptides. The synthesis of the standard peptide contain 4 different Asp isomers per one peptide is time-consuming. Hence, we developed an advanced method for rapidly identifying the Asp isomers by detecting the specific 2nd generation product ions for the  $\beta$ -Asp containing peptides using an ion trap mass spectrometer (ion trap MS).

**EXPERIMENTS:** The peptides containing four different Asp isomers were made using a Fmoc solid-phase chemistry. The synthetic peptides were human  $\alpha$ A-crystallin sequence from residues 146 to 157 peptides ( $\alpha$ AT18 peptide) containing four different Asp isomers; IQTGLD(L $\alpha$ -Asp)ATHAER ( $\alpha$ AT18 L $\alpha$ -Asp), IQTGLD(L $\beta$ -Asp)ATHAER ( $\alpha$ AT18 L $\beta$ -Asp), IQTGLD(D $\alpha$ -Asp)ATHAER ( $\alpha$ AT18 D $\alpha$ -Asp), IQTGLD(D $\beta$ -Asp)ATHAER ( $\alpha$ AT18 D $\beta$ -Asp) and human  $\alpha$ B-crystallin sequence from residues 57 to 69 peptides ( $\alpha$ BT4 peptide) containing four different Asp isomers; APSWFD(L $\alpha$ -Asp)TGLSEMR ( $\alpha$ BT4 L $\alpha$ -Asp), APSWFD(L $\beta$ -Asp)TGLSEMR ( $\alpha$ BT4 L $\beta$ -Asp), APSWFD(D $\alpha$ -Asp)TGLSEMR ( $\alpha$ BT4 D $\alpha$ -Asp), APSWFD(D $\beta$ -Asp)TGLSEMR ( $\alpha$ B T4 D $\beta$ -Asp).

A mass spectrometry (MS) was performed on an ion trap system (LCQ Fleet, Thermo). The 1st and 2nd generation precursor ion of  $\alpha$ AT18 peptides were selected the  $[M+2H]^{2+}$  ion at 656.3 m/z and the  $y_7$  fragment ion at 799.3 m/z. The 1st and 2nd generation precursor ion of  $\alpha$ BT4 peptides was selected the  $[M+2H]^{2+}$  ion at 748.8 m/z and the  $y_8$  fragment ion at 908.4 m/z.

**RESULTS:** Fig. 1 shows the 2nd generation product ion spectrum of  $\alpha$ AT18 peptide containing four different Asp isomers. The specific fragment ions of 726 m/z ( $y_7$ -73) and 708 m/z ( $y_7$ -91) were observed in the spectrum of  $\alpha$ AT18 D $\beta$ -Asp and  $\alpha$ AT18 L $\beta$ -Asp. Fig. 2 shows the 2nd generation product ion spectrum of  $\alpha$ BT4 peptide containing four different Asp isomers. The specific fragment ions of 835 m/z ( $y_8$ -73) and 817 m/z ( $y_8$ -91) were observed in the spectrum of  $\alpha$ BT4 D $\beta$ -Asp and  $\alpha$ BT4 L $\beta$ -Asp. The  $y_7$ -91 and  $y_7$ -73 were observed in the 2nd generation product ion spectrum of  $\beta$ -Asp containing

$\alpha$ AT18 peptide (Fig 1a, c), while these product ions were not observed for  $\alpha$ -Asp containing  $\alpha$ AT18 peptide (Fig 1b, d). In addition, the  $y_8$ -91 and  $y_8$ -73 were also observed in the 2nd generation product ion spectrum of  $\beta$ -Asp containing  $\alpha$ BT4 peptide (Fig 2a, c) but not for  $\alpha$ -Asp containing  $\alpha$ BT4 peptide (Fig 2b, d). These results clearly indicated that the  $y_{(l-n+1)}-91$  and  $y_{(l-n+1)}-73$  ions (“l” and “n” represent the length of the peptide and the position of the Asp residue) of the 2nd generation product ion of the peptides distinguish the  $\beta$ -Asp containing peptide from the  $\alpha$ -Asp containing peptide.

**CONCLUSION:** Identification of biologically uncommon  $\beta$ -Asp containing peptide has been established by the analysis of the 2nd generation product ion spectrum of ion trap MS.

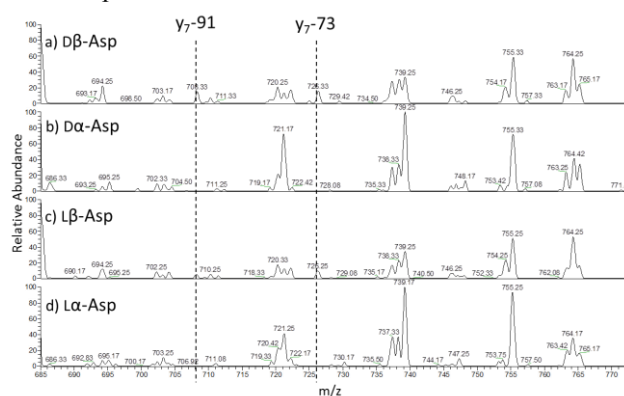


Fig. 1. Second generation product ion spectra of four isomeric Asp in  $\alpha$ AT18 peptide. a)  $\alpha$ AT18 D $\beta$ -Asp, b)  $\alpha$ AT18 D $\alpha$ -Asp, c)  $\alpha$ AT18 L $\beta$ -Asp, d)  $\alpha$ AT18 L $\alpha$ -Asp

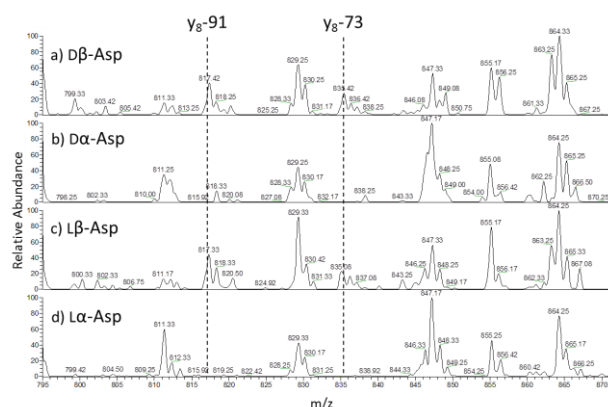


Fig. 2. Second generation product ion spectra of four isomeric Asp in  $\alpha$ BT4 peptide. a)  $\alpha$ BT4 D $\beta$ -Asp, b)  $\alpha$ BT4 D $\alpha$ -Asp, c)  $\alpha$ BT4 L $\beta$ -Asp, d)  $\alpha$ BT4 L $\alpha$ -Asp

### REFERENCES:

[1] N. Fujii *et al.*, J. Biol. Chem. 287 (2012) 39992 - 40002.

## PR10-6 Side Chain Conformers of Aspartyl Isomers in Crystallin Mimic Peptide

K. Aki., E. Okamura

Faculty of Pharmaceutical Sciences Himeji Dokkyo University

**INTRODUCTION:** D-β-aspartyl (Asp) residues are accumulated in aged human-lens αA-crystallin [1] [2]. Natural L-α-Asp isomerize to the uncommon D-β-Asp form via a succinimide intermediate. D-β-Asp is responsible for the structural change of proteins or peptides, because D-isomers with different side-chain orientation and β-isomers which prolong main peptide bond can induce uncommon main chain structures, to trigger the abnormal unfolding or aggregation leading to a disease. Previous studies have suggested that D-β-Asp is more stable than L-α-Asp in human-lens αA-crystallin peptides [3]. However, it remains unsolved why the β-Asp is stable as compared to α-Asp in such peptides.

In this study, the stability between α- and β-Asp forms in the peptide is discussed in relation to the population of side-chain conformers (trans (T), gauche<sup>+</sup> (G<sup>+</sup>) and gauche<sup>-</sup> (G<sup>-</sup>)) of Asp isomers. By using human-lens αA-crystallin fragment, (T6f: T<sup>55</sup>V CF<sub>3</sub>-Phe D<sup>58</sup>SGISEVR<sup>65</sup>) composed of L-α-, D-α-, and D-β-Asp 58 residues, the vicinal spin-spin coupling constants (*J*) of Asp 58 H<sub>α</sub>-H<sub>β1</sub> (*J*<sub>αβ1</sub>) and Asp 58 H<sub>α</sub>-H<sub>β2</sub> (*J*<sub>αβ2</sub>) are quantified and compared by high-resolution solution NMR to calculate the population of side-chain conformers. Here, the difference in the population of side chain conformers between L-α-, D-α-, and D-β-Asp is interpreted by how easily the succinimide is formed.

**EXPERIMENTS:** The isomers of T6f in which L-α-Asp was replaced with D-α- and D-β-Asp at position 58 were synthesized by using an automated solid-phase peptide synthesizer (Shimadzu PSSM-8)[4]. Proton-NMR measurements were carried out on 400 MHz spectrometer (JEOL ECA400) equipped with a super conducting magnet of 9.4 T. A high sensitivity probe (JEOL, NM40T10A/AT) for 10 mm o.d. sample tube was used. About 2 mg of T6f peptides was dissolved in 4 ml PBS/D<sub>2</sub>O (pD 7.6) and subject to NMR measurement at 10-60 °C. Free-induction decays were accumulated 2048 times. The digital resolution was as high as 0.02 Hz to obtain the coupling constants with high accuracy[4]. The coupling constants of Asp H<sub>α</sub>-H<sub>β1</sub> (*J*<sub>αβ1</sub>) and H<sub>α</sub>-H<sub>β2</sub> (*J*<sub>αβ2</sub>) were evaluated by using Asp 58 H<sub>β</sub> at 2.5–2.9 ppm. Using *J*<sub>αβ1</sub> and *J*<sub>αβ2</sub> obtained by the high-resolution 1H NMR measurement, the population of side-chain conformers of Asp in T6f isomers is calculated by the following equations [5].

$$J_{\alpha\beta1} = P(T)J_t + P(G^+)J_g + P(G^-)J_g$$

$$J_{\alpha\beta2} = P(T)J_g + P(G^+)J_t + P(G^-)J_g$$

$$P(T) + P(G^+) + P(G^-) = 1$$

Here *P*(*T*), *P*(*G*<sup>+</sup>), and *P*(*G*<sup>-</sup>) are the probabilities for conformers T, G<sup>+</sup>, and G<sup>-</sup>, and *J*<sub>t</sub> and *J*<sub>g</sub> are the vicinal spin-spin coupling constants between the α- and β-protons in the trans and the gauche conformers, respectively[6].

**RESULTS:** In T6fLα at 37° C, the population of G<sup>+</sup> is 39%, the highest in the side-chain conformers of Asp. In T6fDα at 37° C, the population of G<sup>-</sup> is the highest (45%), whereas the T conformer is the least (24%). In contrast, the population of T conformer is most preferable in T6fDβ at 37° C; more than 50% of the Asp side-chain is in the T state[4]. Such preferences are the case at all the temperatures examined. The result shows that the population of the gauche conformers, G<sup>+</sup> and G<sup>-</sup> is relatively high in α-Asp containing T6fLα and T6fDα, as compared to the T conformer.

The racemization and isomerization of Asp proceed as: (i) when the carboxylate carbon (C<sub>COO-</sub>) of the Asp 58 side chain is attacked by the nitrogen (N) of Ser 59, L(or D)-succinimide is formed by the intramolecular cyclization; (ii) L(or D)-succinimide is converted to D (or L)-succinimide through an intermediate that has the prochiral α-carbon in the plane of the ring; and (iii) the D- and L-succinimide are hydrolyzed at either side of their two carbonyl groups, yielding both α- and β-Asp residues, respectively [7]. The close distance between Asp 58 C<sub>COO-</sub> and Ser 59 N should be advantageous to this cyclization. For G<sup>+</sup> and G<sup>-</sup> conformers, the distance between Asp C<sub>COO-</sub> and Ser N is, actually, 3.5 ± 0.7 Å, smaller than the distance 4.5 ± 0.5 Å for the T conformer. Therefore, Asp C<sub>COO-</sub> in G<sup>+</sup> and G<sup>-</sup> conformers are easily attacked by Ser N for the isomerization of Asp 58. In contrast, T6fDβ has the highest population of the T conformer of Asp 58 side-chain. In such case, Ser 59 N in T6fDβ is hard to attack Asp 58 C<sub>COO-</sub> to form succinimide due to rather long distance between Asp C<sub>COO-</sub> and Ser N. Thus, the Dβ form is thought to be the most stable in the 3 isomers of Asp 58.

### REFERENCES:

- [1] N. Fujii *et al.*, J. Biochem. **116** (1994) 663–669.
- [2] N. Fujii *et al.*, J. Biol Chem. **287**(NO.47) (2012) 39992–40002,
- [3] K. Aki *et al.*, PLoS One **8** (2013) e58515
- [4] K. Aki and E. Okamura Biophys Chem **196** (2015) 10-15.
- [5] T. Kimura *et al.*, J. Phys Chem B **106** (2002) 12336-12343.
- [6] Pachler, K GR Spectrochim Acta **20** (1964) 581-587
- [7] T. Geiger *et al.*, J. Biol. Chem. **262** (1987) 785–794.

## PR10-7 Rapid Survey of Asp Isomers in Disease-related Proteins by LC-MS/MS Combined with Commercial Enzymes

Hiroki Maeda<sup>1</sup>, Takumi Takata<sup>2</sup>, Norihiko Fujii<sup>3</sup>, Hiroaki Sakaue<sup>4</sup>, Hiroshi Sasaki<sup>5</sup> and Noriko Fujii<sup>1,2</sup>

<sup>1</sup>Graduate School of Science, Kyoto University

<sup>2</sup>Research Reactor Institute, Kyoto University

<sup>3</sup>Teikyo University

<sup>4</sup>International University of Health and Welfare

<sup>5</sup>Kanazawa Medical University

**INTRODUCTION:** Until relatively recently, it was considered that D-amino acids were excluded from living systems except for the cell wall of microorganisms. However, D -aspartate residues have now been detected in long-lived proteins from various tissues of elderly humans. Formation of D -aspartate in proteins induces aggregation and loss of function, leading to age-related disorders such as cataracts and Alzheimer disease. A recent study used a liquid chromatography - tandem mass spectrometry (LC-MS/MS) to analyze isomers of Asp residues in proteins precisely without complex purification of the proteins. However, to identify the four Asp isomers (L $\alpha$ , L $\beta$ , D $\beta$  and D $\alpha$ ) on the chromatogram, it was necessary to synthesize reference peptides containing the 4 different Asp isomers as standards. Here, we describe a method for rapidly and comprehensively identifying Asp isomers in proteins using a combination of LC-MS/MS and commercial enzymes without synthesizing reference peptides.

### EXPERIMENTS:

**Synthesis of peptides containing four different Asp isomers.** The following peptides and their diastereoisomers corresponding to the human  $\alpha$ A-crystallin sequence from residues 55 to 65 ( $\alpha$ AT6 peptide) were synthesized by a Shimadzu PSSM-8 peptide synthesizer. The purity of each peptide was confirmed to be >95% by analytical RP-HPLC and mass spectrometry.

**Preparation of lens proteins.** Lens samples (one sample each) from elderly individuals (aged 80 years) were homogenized under physiological conditions and fractionated into water-soluble (WS) and water-insoluble (WI) fractions by centrifugation. The WS protein was dissolved in 50 mM Tris/HCl (pH 7.8), 1 mM CaCl<sub>2</sub> buffer before enzymatic digestion.

**Identification of the tryptic peptides and the quantification of the Asp isomers.** The protein sample is treated with trypsin, trypsin plus endoprotease Asp-N (Asp-N), trypsin plus L-isoaspartyl methyltransferase (PIMT) or trypsin plus paenidase, and the resulting peptides are applied to LC-MS/MS. Because Asp-N hydrolyzes peptide bonds on the N-terminus of only L $\alpha$ -Asp residues, it differentiates between peptides containing L $\alpha$ -Asp and those containing the other three iso-

mers. Similarly, PIMT recognizes only peptides containing L $\beta$ -Asp residues, and paenidase internally cleaves the C-terminus of D $\alpha$ -Asp residues.

**RESULTS:** Figure 1 shows a typical example of the identification of the Asp 58 isomers in the  $\alpha$ A 55-65 peptide (TVLD<sup>58</sup>SGISEVR, [M+2H]<sup>2+</sup> = 588.3) from  $\alpha$ A-crystallin in lens from elderly people. This simplified approach has been successfully applied to the analysis of all tryptic peptides in aged lens.

**CONCLUSION:** This new method is able to search comprehensively for the Asp isomers in damaged or aged proteins from all living tissues and cells.

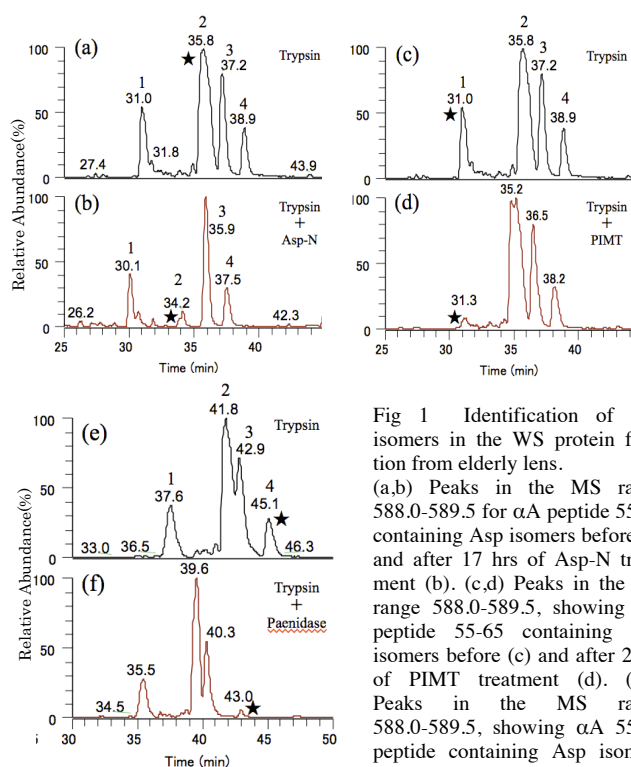


Fig 1 Identification of Asp isomers in the WS protein fraction from elderly lens. (a,b) Peaks in the MS range 588.0-589.5 for  $\alpha$ A peptide 55-65 containing Asp isomers before (a) and after 17 hrs of Asp-N treatment (b). (c,d) Peaks in the MS range 588.0-589.5, showing  $\alpha$ A peptide 55-65 containing Asp isomers before (c) and after 2 hrs of PIMT treatment (d). (e,f) Peaks in the MS range 588.0-589.5, showing  $\alpha$ A 55-65 peptide containing Asp isomers before (e) and after 20 hrs of paenidase treatment (f). The asterisked peaks indicate peptide disappearance.

### REFERENCES:

- [1] N. Fujii, H. Sakaue, H. Sasaki H. and N. Fujii. *J. Biol. Chem.* **287**, (2012) 39992-40002.
- [2] H. Maeda, T. Takata, N. Fujii, H. Sakaue, S. Nirasawa, S. Takahashi, H. Sasaki, Rapid survey of four Asp isomers in disease-related proteins by LC-MS combined with commercial enzymes, *Anal Chem*, **87** (2015) 561-568.

## PR11 Studies on Actinides and Fission Products Performed at the KURRI Hot Laboratory

T. Fujii

Research Reactor Institute, Kyoto University

### 1. Objectives and Allotted Research Subjects

Studies on actinide and fission product nuclides with careful management are being more important for reprocessing, disposal, partitioning, and transmutation processes in the nuclear fuel cycle. Hot laboratory of KURRI is one of core facilities in Japan, in which various nuclides can be handled. This project enhances utilization of the KURRI hot laboratory by opening for fundamental and application studies related to radiochemistry, nuclear chemistry, environmental chemistry, geochemistry, and so on. Allotted research subjects are;

- ARS-1 Complexation of actinides with organic substances (T. Sasaki *et al.*).
- ARS-2 Solubility of actinide compounds in aqueous media (T. Kobayashi *et al.*).
- ARS-3 Leaching of actinides and FPs from fuel debris (N. Sato *et al.*).
- ARS-4 Neutron irradiation damage of vitrified waste matrices (T. Nagai *et al.*).
- ARS-5 Ligand exchange reaction of actinides in molten salts (A. Uehara *et al.*).
- ARS-6 Electrochemical behavior of uranium in pyroprocessing system (Y. Sakamura *et al.*).
- ARS-7 Structural study of f-elements in molten halides (H. Matsuura *et al.*).
- ARS-8 Molecular dynamics simulation of uranyl ion in molten salts (N. Ohtori *et al.*).
- ARS-9 Fundamental study of fission products for trans-actinide chemistry (Y. Kasamatsu *et al.*).
- ARS-10 Isotope separation by using microreactor (R. Hazama *et al.*).
- ARS-11 Optical properties of molten aluminum halides (T. Goto *et al.*).
- ARS-12 Precipitation of f-element oxides in molten halides (H. Sekimoto *et al.*).
- ARS-13 Uptake of radiocesium and radiopotassium in plants (T. Ohta *et al.*).
- ARS-14 Quantitative analysis of radionuclides in seawater (T. Kubota *et al.*).
- ARS-15 Isotopic composition of radionuclides in environmental samples (Y. Shibahara *et al.*).
- ARS-16 Noble gas mass spectrometry of neutron irradiated geological samples (H. Sumino *et al.*).

ARS-17  $^{40}\text{Ar}/^{39}\text{Ar}$  dating of neutron irradiated minerals and glasses (O. Ishizuka *et al.*).

ARS-18 Radiometric Ar-Ar dating of neutron irradiated lavas (N. Hirano *et al.*).

### 2. Main Results and Contents

ARS-1, 2, 3, and 4 were performed in order to deepen the knowledge of nuclear waste management issues. In ARS-1 and 2, stability constants and solubility products of actinides were obtained. In ARS-3, leaching kinetics of actinides and FPs from irradiated Zr alloy was clarified. In ARS-4, a structural change of borosilicate by neutron irradiation was found. ARS-5, 6, 7, and 8 were performed with the viewpoint of pyroprocessing. In ARS-5 and 7, ligand exchange of  $\text{F}^-$  and  $\text{Cl}^-$  for  $\text{U}^{4+}$  and  $\text{Nd}^{3+}$  in molten halides was clarified. In ARS-6, effective diffusion coefficient of  $\text{U}^{3+}$  in porous Zr was determined. In ARS-8, atomic distances of  $\text{UO}_2^{2+}$  in LiCl melt were computed. Polarization of  $\text{Cl}^-$  around  $\text{UO}_2^{2+}$  was found. ARS-11 and 12 seek applications of molten salt systems for industrial use, for example, refining. ARS-11 studied optical properties of molten alkaline chlorides containing Al. Raman spectra obtained were interpreted by using *ab initio* method. ARS-12 focuses on recycling of rare earths. Solubility of Dy(III) under the coexistence of Dy oxide and oxychloride in chloride melts was discussed. ARS-10 studied isotope fractionation of Ca. A possible fractionation of  $^{48}\text{Ca}/^{40}\text{Ca}$  was found. ARS-13, 14, and 15 studied on radionuclides in soils, plants, seawater, and so on. In ARS-13, distribution of radiocesium in plants was clarified. ARS-14 presented an effective preparation method of radiotracers which are useful for environmental science. ARS-15 suggested that precise isotopic analysis of Cs and Sr is helpful for a rapid source analysis of nuclear accident. ARS-16, 17, and 18 demonstrated that neutron irradiation at KUR is usable for the Ar-Ar and I-Xe dating of geological samples.

### 3. Summaries of the achievements

In this research, by using various unique facilities of KURRI for actinides and fission products, new and characteristic chemical, kinetic, structural, and thermodynamic data were obtained. These new information encompass solid chemistry, molten salt and solution chemistry, as well as nuclear reactions of f-elements and FPs. The results are useful either for scientific purpose or for technological purpose for nuclear science, environmental science, geoscience, and general industry.

## PR11-1 Apparent Formation Constant of Metal Ions with Humic Substances; Modelling

T. Sasaki, T. Kobayashi, T. Koukami, A. Uehara<sup>1</sup>, T. Fujii<sup>1</sup>, H. Yamana<sup>1</sup>, H. Moriyama<sup>1</sup>

Graduate School of Engineering, Kyoto University  
<sup>1</sup>Research Reactor Institute, Kyoto University

### INTRODUCTION:

A semi-empirical thermodynamic model was developed to estimate the apparent formation constants of metal ions with humic substances (HSs), humic and fulvic acids, over a wide range of solution conditions, i.e., pH, ionic strength, and HS and metal concentrations.

To understand the fundamental rules of metal complexation with HSs, many researchers have attempted to characterize the physical and chemical properties of HSs in soils, sediments, and natural waters. It has been determined that randomly cross-linked heterogeneous organic substances generally have similar distributions of a number of specific functional groups, including carboxyl, phenolic, and alcoholic groups. Towards the ultimate goal of characterizing natural HSs, researchers have proposed hypothetical HS chemical structures based on results obtained using several analytical methods.

The discrete fragment model has been proposed by our group; it decomposes the organic ligands into discrete fragments of functional groups and chelating bridges that connect the functional groups. The ligand fragments called as basic ligands were clipped from a “pragmatic” chemical structure of a humic acid (HA) proposed [1], which were distributed statistically in the HA framework. The fixed formation constant values of the metal ion with each ligand was taken from the literature; benzoic acid, phthalic acid, isophthalic acid, 1,2,3-benzenetricarboxylic acid, 1,2,4-benzenetricarboxylic acid, 2-hydroxybenzoic acid, phenol, butanedioic acid, and acetic acid. The steric effect of bidentate binding sites due to the additional stabilization by chelate formation was considered, while the electrostatic surface potential of the HA molecule in solution was not considered for simplification. The model has yielded satisfactory results for the apparent complex formation constant of trivalent europium with Aldrich HA under varied solution conditions, including pH, ionic strength, and the concentrations of metal ions and HA [2].

### THEORETICAL:

The model was modified and applied to several kinds of metal ions including actinides, i.e., Th(IV), Pu(IV), and Np(V), according to following steps; 1) a number of datasets for acid dissociation of various HSs were analyzed to obtain the representative values for the abundance ratios of the basic ligands and the heterogeneity parameter of HSs, 2) the datasets for complexation of various multivalent metal ions with HSs were analyzed to obtain the

representative values for the intramolecular chelating effect of the bidentate site fraction. In the case of tetravalent metal ions, the hydrolysis reactions are taken into account for the analysis of the experimental datasets [3].

### RESULTS:

The present model fairly well reproduced the literature apparent formation constants of tetravalent Pu/Th (Fig. 1), pentavalent Np, divalent Ca/Co, and trivalent Al/Eu with the hypothetical humic acid and of tetravalent Th, pentavalent Np, divalent Mg/Ca/Co/Mn/Ni/Cu/Zn/Pb, and trivalent Eu with the hypothetical fulvic acid under a wide range of pH,  $I$ , and initial HSs and metal concentration [3]. Some discrepancies between the calculated and experimental values were recognized and discussed; one is the  $I$  dependence of the values of some metal ions such as neptunium, and the other is the discrepancy observed for the system of ultra-trace amount of neptunium, suggesting further effects of not yet identified but much stronger binding sites in HS. Although the present hypothetical structure is only one example of HS, it provides a basis for further studies of the thermodynamic and kinetic parameters for complexation reactions.

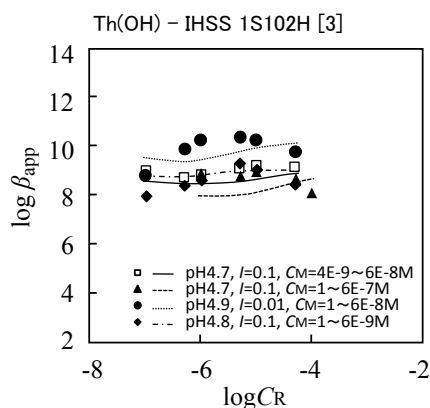


Fig. 1. Example of comparison between the experimental apparent formation constants  $\beta_{app}$  of Th(IV) with humic acid (purchased from IHSS) and the simulated curves;  $C_R$ , molar concentration of HS,  $C_M$ , initial concentration of metal ion.

### REFERENCES:

- [1] Schulten, H. R., Schnitzer, M. *Naturwissenschaften*, **80** (1993) 29–30.
- [2] Sasaki, T., Kobayashi, T., Takagi I., Moriyama, H. J. *Nucl. Sci. Technol.*, **45** (2008) 718–724.
- [3] Sasaki, T., Yoshida, H., Aoyama, S., Kobayashi, T., Takagi I., Moriyama, H. *Radiochimica Acta*. (2015) *in press*.

## PR11-2 Temperature Effect on the Solubility and Solid Phase of Tetravalent Metal Hydroxide

T. Kobayashi, T. Sasaki, A. Uehara<sup>1</sup>, T. Fujii<sup>1</sup>,  
H. Yamana<sup>1</sup>, H. Moriyama<sup>1</sup>

Graduate School of Engineering, Kyoto University  
<sup>1</sup>Research Reactor Institute, Kyoto University

### INTRODUCTION:

The decay heat emission from vitrified high level radioactive waste in the repository will be transferred to groundwater aquifers through surrounding engineered and geological barrier systems. In the early failure scenario of the waste package, long-lived radionuclides including tetravalent actinides (An(IV)) leached in the groundwater are considered to be exposed to an elevated temperature environment up to 100°C [1]. For the safety assessment of geological disposal, it is required to evaluate a possible impact of elevated temperature on the solubility of An(IV). At 25°C, the steady-state solubility is generally controlled by amorphous hydroxide as solubility-limiting solid phase, and described using relevant thermodynamic constants [1]. However, the amorphous hydroxide was dehydrated and crystallized at elevated temperature [2]. Therefore, the thermodynamic estimation of An(IV) solubility needs to clarify the both of hydrolysis constants and solubility product ( $K_{sp}$ ) at a given elevated temperature [3].

In the present study, the apparent solubility of zirconium hydroxide as chemical analogue for An(IV) and the crystallinity of the solid phase were investigated under several conditions of temperature (5 to 60°C). The temperature dependence of solubility product and the enthalpy change were discussed.

### EXPERIMENTS:

Sample solutions by oversaturation method were prepared by adding NaOH or HClO<sub>4</sub> to the acidic Zr perchlorate solutions ([Zr] = 0.01 mol/dm<sup>3</sup> (M)). The ionic strength ( $I$ ) was adjusted to be  $I = 0.5$  by adding appropriate amount of NaClO<sub>4</sub>. After aging the sample solutions in temperature chambers controlled at 5°C, 40°C and 60°C, the samples were transferred to the thermostat dry-bath followed by the ultrafiltration and pH measurement at different temperature conditions. After filtration of supernatants through the ultrafiltration membranes (3 kDa – 100 kDa NMWL, Millipore), the apparent solubility of zirconium was determined by ICP-MS. XRD was used to characterize the crystallinity and the particle size of the solid phase.

### RESULTS:

The apparent solubility after aging at 40 and 60°C and measured at 25°C were lower than those kept at 25°C,

indicating the progress of crystallization of initial amorphous hydroxide. The  $K_{sp}$  values after aging at different temperatures were determined from the analysis of the solubility dataset in Fig.1. After aging at 60°C, the solubility was measured at 5, 25, 40 and 60°C (Fig. 2) and the  $K_{sp}$  at different temperatures. Assuming no temperature dependence of enthalpy change ( $\Delta_r H^\circ$ ), the  $\Delta_r H^\circ$  was calculated for  $Zr^{4+} + 4OH^- \rightleftharpoons Zr(OH)_4(s, 60^\circ C)$ , where  $Zr(OH)_4(s, 60^\circ C)$  represents the solid phase formed at 60°C. The obtained  $\Delta_r H^\circ$  was slightly higher than the  $\Delta_r H^\circ$  (-133.6 kJ/mol) for  $Zr(OH)_4(am)$  calculated from the standard enthalpy of formation [3]. Similar analysis was performed for the solubility after aging at 5 and 40°C, and a trend of  $\Delta_r H^\circ$  for the solid phases formed at different temperatures suggested that the solid phase transformation is endothermic reaction within the investigated temperature range.

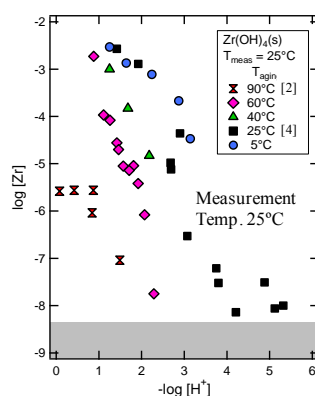


Fig. 1. Solubility of  $Zr(OH)_4(s)$  after aging at different temperatures.

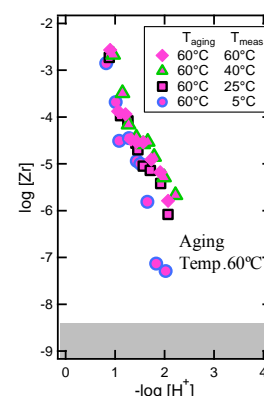


Fig. 2. Solubility of  $Zr(OH)_4(s)$  measured at different temperatures after aging at 60°C.

### REFERENCES:

- [1] 2nd progress report on research and development for the geological disposal of HLW in Japan, JNC Report TN1410 2000-001, JNC, Tokai, Japan.
- [2] Kobayashi T. et al., Radiochim. Acta, 101, (2013) 645.
- [3] Brown P. et al., Chemical Thermodynamics of Zirconium, Elsevier, North-Holland, Amsterdam (2005).
- [4] Sasaki, T. et al., Radiochim. Acta 94, 489 (2006).



N. Sato<sup>1</sup>, A. Kirishima<sup>1</sup>, M. Hirano, T. Sasaki<sup>2</sup>, T. Kobayashi<sup>2</sup>, Y. Takeno<sup>2</sup>, A. Uehira<sup>3</sup>, T. Fujii<sup>3</sup>, K. Takamiya<sup>3</sup> and H. Yamana<sup>3</sup>

<sup>1</sup> Institute of Multidisciplinary Research for Advanced Materials, Tohoku University

<sup>2</sup> Graduate School of Engineering, Kyoto University

<sup>3</sup> Research Reactor Institute, Kyoto University

### INTRODUCTION:

After the LOCA of Fukushima Daiichi NPS, the melted core reacted with coolant at high temperature forming fuel debris containing fuel and structural materials such as zirconium. Under high temperature condition in the pressure vessel, several kinds of FPs and TRU were possibly released into the cooling water mixed with seawater and the air from the melted core and its fine debris. Information on the radionuclide behavior in fuel debris and surface seawater will be helpful to analyze the forthcoming analysis data about the contents of minor FPs and TRU in contaminated water, and to manage associated secondary wastes. First, the simulated fuel debris composed of uranium and zirconium oxides as main constituents was prepared by heat treatment in reductive or oxidative conditions. Then the dissolution behavior of typical gamma-ray fission products and neutron activated nuclides as well as uranium in solid solutions was investigated by neutron irradiation and following leaching in the non-filtrated seawater. Dissolution behavior of MA was also studied by the used of MA doped simulated fuel debris.

### EXPERIMENTAL:

Three types of  $\text{UO}_2\text{-ZrO}_2$  solid solution samples with Zr concentration of 10, 50 and 90 mol% were prepared by mechanochemical and heat treatments under reductive and oxidative atmosphere. The sample was vacuum-sealed in quartz tube and irradiated for 20 min using the pneumatic transferring system (Pn-2) at KUR. For reducing the high radioactivity of short-lived nuclides, the sample was left in glove box, and then suspended in 30 ml of fresh seawater from Minamisoma city, Fukushima. After the aging time in the atmospheric condition at R.T., a 10 mL of supernatant was transferred to new sample tube after filtration with 0.45  $\mu\text{m}$  (Advantec) or 3 kDa (Microcon, Millipore) membranes, followed by evaporation of the seawater at 363 K in order to repare a solidified point-like source. For MA doped sample, similar preparation techniques were applied by using  $\text{U}_3\text{O}_8$  powder with  $^{237}\text{Np}$ ,  $^{243}\text{Am}$  and  $^{236}\text{Pu}$ . Gamma- and alpha- ray

spectrometry were performed using a Ge detector and Si detector to determine the nuclides leached.

### RESULTS:

Figure 1 shows the leaching ratios ( $R(\%)$ ) of actinides to seawater. There, the clear time dependence cannot be seen in the leaching of Np, Am and Pu during 31 days leaching test. Also, their leaching ratios were suppressed in the very low extent (0.02 % or less). The leaching of these actinides are expected to be suppressed to very low extent regardless of the oxidation state in the solid phase since the solubilities of both M(III) and M(IV) for Am and Pu, and  $\text{Np(IV)}$  are very low at the pH of seawater. On the other hand, the  $R_{\text{U}}$  value was about 0.1 % during the leaching test. From this result, it is considered that the uranium dissolution from the simulated fuel debris was governed by the solubility limitation of  $\text{UO}_3 \cdot 2\text{H}_2\text{O}(\text{cr})$ ,  $\text{UO}_3 \cdot 2\text{H}_2\text{O}(\text{am})$  or maybe their intermediate phase as discussed in our previous study [1]. These results suggest that both dissolution and structure data are essential for fuel debris behaviour. In further study, behavior of actinides and FP's from different types of fuel debris will be discussed.

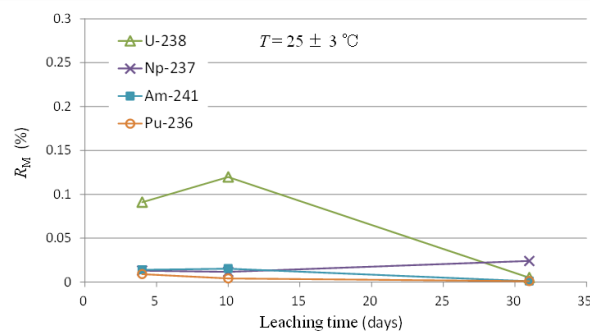


Figure 1 Time dependence of actinides leaching from the simulated fuel debris to the Fukushima seawater [2].

### REFERENCES:

- [1] T. Sasaki, Y. Takeno, A. Kirishima, N. Sato, J. Nucl. Sci. Technol., 52 (2015) 146-150.
- [2] A. Kirishima, M. Hirano, T. Sasaki, N. Sato, J. Nucl. Sci. Technol., in press, doi: 10.1080/00223131.2015.1017545.

採択課題番号 26P11-3 燃料デブリ中のアクチノイドおよびFP元素の挙動に関する研究プロジェクト (東北大多元研) 佐藤修彰、桐島 陽、平野正彦 (京大院工) 佐々木隆之、小林大志、竹野 佑 (京大・原子炉) 上原章寛、藤井俊行、高宮幸一、山名 元

T. Nagai, A. Miyauchi, Y. Morikawa, A. Uehara<sup>1</sup>, and T. Fujii<sup>1</sup>

Japan Atomic Energy Agency (JAEA)

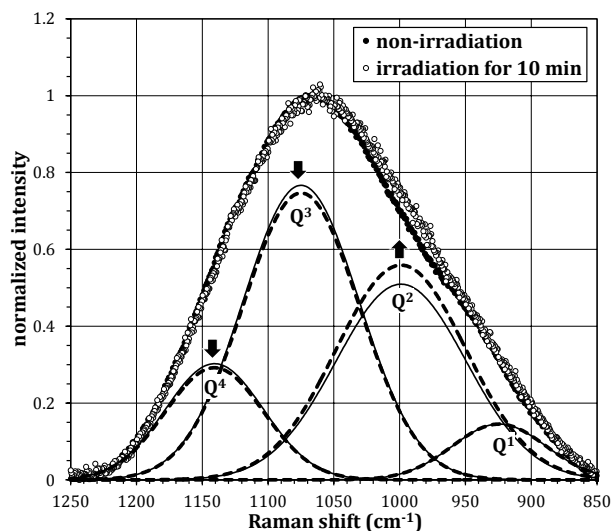
<sup>1</sup>Research Reactor Institute, Kyoto University

**INTRODUCTION:** A high-level radioactive liquid waste including fission products, FPs, from a reprocessing process for spent nuclear fuels is processed into a solidified waste glass made by using a borosilicate glass as media. Many studies of the effect on borosilicate glass structure by irradiation have been carried out by irradiation of  $\alpha$  ray,  $\beta$  ray, and  $\gamma$  ray which would be generated from FPs of the waste glass. However, that effect by a neutron irradiation has not been much evaluated. In this study, the borosilicate glass samples were irradiated by neutrons, and the glass structure change after the irradiation was measured by Raman spectrometry.

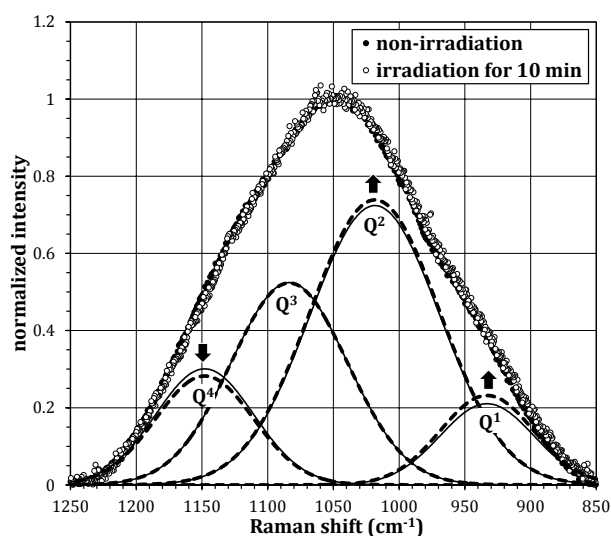
**EXPERIMENTS:** The borosilicate glass samples were prepared 2 compositions. The raw material reagents of  $\text{SiO}_2$ ,  $\text{H}_3\text{BO}_3$ ,  $\text{Na}_2\text{CO}_3$ ,  $\text{Li}_2\text{CO}_3$ , and rare earth oxides as simulated FPs were placed in an alumina crucible and were melted at  $1150^\circ\text{C}$  in an electric furnace. After the molten samples were solidified by cooling to room temperature, they were cut into thin plates. In the irradiation, the glass samples of thin plate were set in a polyethylene tube and were irradiated under the condition of 1000 kW for 10 min in the Pn-2 of KUR. After the radioactivity of the samples was sufficiently attenuated, the Raman spectra of the glass sample were measured by using a laser Raman spectrometer, NRS-3100 of JASCO. For the effect on borosilicate glass by the nuclear reaction of  $^{10}\text{B}(n,\alpha)^7\text{Li}$ , Peugeot, *et al* have evaluated the B-O structure by using NMR measurement and Raman spectrometry<sup>[1]</sup>, our study was examined the Si-O structure.

**RESULTS:** As a structural change of the sample by the irradiation, an amount of Li would be increased by the  $^{10}\text{B}(n,\alpha)^7\text{Li}$  reaction, and Li was expected to disconnect to the Si-O bridging structure. By evaluating the Raman shift of the Si-O structure, it was confirmed to be the effect on the borosilicate glass structure by the irradiation. The Raman shifts of Si-O structure of a silicate glass were in the wavenumber of  $850\text{--}1200\text{ cm}^{-1}$ , and the peak positions of Raman shifts were different from the number of non-bridging oxygen, NBO, of the Si-O structure.<sup>[2]</sup> In this measurement of borosilicate glass, those Raman shifts were observed in  $850\text{--}1250\text{ cm}^{-1}$  and the measured spectra could be separated into Gaussian waves as shown in Fig. 1. The Raman peak of  $Q^4$  structure without NBO appeared in  $1140\text{--}1150\text{ cm}^{-1}$ , and those of  $Q^3$ ,  $Q^2$ , and  $Q^1$  structures with the NBO number = 1, 2, and 3 were in  $1070\text{--}1090$ ,  $1000\text{--}1020$ , and  $920\text{--}930\text{ cm}^{-1}$  respectively. Comparing with the Raman shifts before and after irradiation,

it could be observed that the peak heights of  $Q^4$  and  $Q^3$  decreased and those of  $Q^2$  and  $Q^1$  increased after the irradiation, as shown in Fig. 1. These height changes of  $Q^n$ ,  $n=1\text{--}4$ , suggested the feasibility that a generated Li by the neutron irradiation disconnects the Si-O bridging structure in a borosilicate glass. However, this Si-O bridging structure is direct disconnected by  $\gamma$  ray included in the neutron irradiation and the additional experiments needs for understanding of the irradiation effect.



(1)  $63\text{SiO}_2\text{-}16.6\text{B}_2\text{O}_3\text{-}19\text{Na}_2\text{O}\text{-}1.4\text{RE}_2\text{O}_3$ .



(2)  $63\text{SiO}_2\text{-}16.6\text{B}_2\text{O}_3\text{-}8.1\text{Li}_2\text{O}\text{-}10.9\text{Na}_2\text{O}\text{-}1.4\text{RE}_2\text{O}_3$ .

Fig. 1. Raman spectra of glass samples and their separated Gaussian waves. Open circles and fine lines are a non-irradiation sample, and closed circles and dotted lines are after irradiation.

#### REFERENCES:

- [1] S. Peugeot, *et al*, Nucl. Inst. Methods in Phys. Res. B, **327** (2014) 22-28.  
 [2] P. McMillan, Am. Mineralogist, **69** (1984) 622-644.

A. Uehara<sup>1</sup>, T. Nagai<sup>2</sup>, T. Fujii<sup>1</sup>, H. Moriyama<sup>1</sup>, and H. Yamana<sup>1</sup>

<sup>1</sup> Research Reactor Institute, Kyoto University

<sup>2</sup> Nuclear Fuel Cycle Engineering Lab., Japan Atomic Energy Agency

### INTRODUCTION:

In the non-aqueous reprocessing process of spent nuclear fuels by the pyrometallurgical and the electrowinning methods, a spent fuel is dissolved into molten LiCl-KCl or NaCl-CsCl eutectic melt and dissolved uranium and plutonium ions are recovered as metal or oxide. In the present study, the chemical property and coordination circumstance of the complexes of U<sup>4+</sup> under the coexistence of fluoride ions in molten NaCl-CsCl eutectic were investigated by absorption spectrum measurements.

### EXPERIMENTAL:

All experiments were carried out under an argon atmosphere, in which humidity and oxygen impurity were continuously kept less than 1 ppm. The electronic absorption spectra of uranium ions in the melts were measured by using an UV/Vis/NIR spectrometer (V-570, JASCO Co.). The analytical light from a light source (a tungsten halogen lamp and D<sub>2</sub>O lamp) was guided to the electric furnace with quartz windows by using optical fibers, and the light passed through the sample in a quartz tube with a 10 mm light path inside the furnace. The light which traveled through the furnace was again guided to the spectrophotometer, and a monochromator was set in front of the detectors to decrease the background noise. The light intensity for the molten alkali chloride ( $I_0$ ) and that including uranium ( $I$ ) was measured in the wavelength range of 300 – 2000 nm at 1 nm intervals. Wavelength was converted to wavenumber in this work. The molar absorptivity was calculated by using  $-\log(I/I_0)$  and total volume of the solution. All the experiments were performed at 923K  $\pm$  3K.

### RESULTS:

Molar absorptivity of absorption spectra of U<sup>4+</sup> in the presence of F<sup>-</sup> was plotted as a function of wavenumber in Fig. 1. When an absorption spectrum of 0.106 M U<sup>4+</sup> in the absence of F<sup>-</sup> was measured, molar absorptivities of each peak wavenumber at 14903, 16501 and 22123 cm<sup>-1</sup> agreed with the reported values [1]. By comparing these values with the crystal field

analysis data of U<sup>4+</sup> in CsCdBr<sub>3</sub> [2] and LiYF<sub>4</sub> [3], absorption bands of the 5f<sup>2</sup>-5f<sup>2</sup> transition of U<sup>4+</sup> were assigned as follows; the <sup>1</sup>I<sub>6</sub>  $\leftarrow$  <sup>3</sup>H<sub>4</sub> transition at 22500-19000 cm<sup>-1</sup>, the <sup>3</sup>P<sub>1</sub>  $\leftarrow$  <sup>3</sup>H<sub>4</sub> transition at 17800 cm<sup>-1</sup>, the <sup>1</sup>G<sub>4</sub>, <sup>1</sup>D<sub>2</sub>, <sup>3</sup>P<sub>0</sub>  $\leftarrow$  <sup>3</sup>H<sub>4</sub> transition at 17000-14000 cm<sup>-1</sup>, the <sup>3</sup>H<sub>6</sub>  $\leftarrow$  <sup>3</sup>H<sub>4</sub> transition at 13100-12000 cm<sup>-1</sup>, the <sup>3</sup>F<sub>3</sub>, <sup>3</sup>F<sub>4</sub>  $\leftarrow$  <sup>3</sup>H<sub>4</sub> transition at 11100-7500 cm<sup>-1</sup>, and the <sup>3</sup>H<sub>5</sub>  $\leftarrow$  <sup>3</sup>H<sub>4</sub> transition at 6500-5000 cm<sup>-1</sup>.

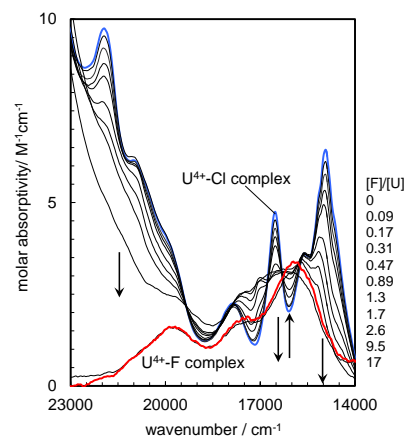


Fig. 1. Molar absorptivity of U<sup>4+</sup> depended on the concentration of NaF in molten NaCl-CsCl eutectic at 923K. Concentration ratios of F<sup>-</sup> by U<sup>4+</sup> ( $r_F$ ) are 0, 0.09, 0.17, 0.31, 0.47, 0.89, 1.3, 1.7, 2.6, 9.5, and 17.

When  $9.36 \times 10^{-3}$  M NaF was added in the melt, absorption peaks decreased. Molar ratio of fluorine by uranium ( $r_F$ ) added in the melt was changed from 0.09 to 17 by adding NaF pellet as shown in Fig. 1. Absorption peaks corresponding to 14903, 16501, and 22123 cm<sup>-1</sup> decreased with the increase of  $r_F$  from 0.09 to 1.7 and isosbestic points at 13774, 15772, 16181, 17793, and 19305 cm<sup>-1</sup> were observed. This result means that two species of complexes composed of U<sup>4+</sup>, Cl<sup>-</sup> and F<sup>-</sup> are equilibrated. However, when  $r_F$  was over 9.5, another peaks at 15847, 17331, and 19646 cm<sup>-1</sup> were observed. This indicates that another complex composed of U<sup>4+</sup>, Cl<sup>-</sup>, and F<sup>-</sup> is formed. After 10 hours aging, red color precipitates were found on the bottom of the cell.

### REFERENCES:

- [1] Nagai, et al., *J. Nucl. Sci. Technol.*, **42**, 1025-1031 (2005).
- [2] Karbowskiak, et al., *Chem. Phys.*, **308**, 135-145 (2005)
- [3] Hubert, et al, *J. Luminescence*, **60&61**, 245-249 (1994)

M. Iizuka<sup>1</sup>, Y. Sakamura<sup>1</sup>,  
T. Fujii<sup>2</sup>, A. Uehara<sup>2</sup> and H. Yamana<sup>2</sup>

<sup>1</sup>Central Research Institute of Electric Power Industry

<sup>2</sup>Research Reactor Institute, Kyoto University

**INTRODUCTION:** Analyses of the electrorefining process for the pyrometallurgical reprocessing of metallic fast reactor fuel using the multi diffusion layer anode model [1] have shown that (a) solubility of  $UCl_3$  in LiCl-KCl melt, and (b) the diffusion coefficient of actinide ions in the porous Zr layer formed at the surface of the spent metallic fuel by selective dissolution of the actinides, have great influence on major performance, such as processing rate and separation between the actinides and Zr. In this study, chronopotentiometry (CP) was applied to evaluation of these important parameters at U-9wt%Zr alloy anode.

**EXPERIMENTS:** Modification of CP theory to be adapted to a situation, where the concentration reaches saturation by a constant current producing the species electrochemically, has been reported before [2]. Since diffusion coefficient of U(III) in LiCl-KCl is known [3], solubility of  $UCl_3$  in LiCl-KCl was evaluated using this data and  $\tau$  obtained by CP in this study. After formation of a porous Zr layer by selective anodic dissolution of U from the U-Zr alloy, CP was performed again. In this step, theoretically, the effective diffusion coefficient of  $UCl_3$  in the porous Zr layer can be estimated using its solubility data which has been just evaluated in the previous step. The experimental setup and procedure have been also reported before [4]. All the experiments were carried out at 773 K, in a high-purity Ar atmosphere glove box in KURR hot cell laboratory.

**RESULTS:** The CPs obtained using U-Zr alloy before the formation of the porous Zr layer are shown in Fig. 1. The solubility of  $UCl_3$  was evaluated to be  $0.00449 \text{ mol-U/cm}^3$  so that its averaged diffusion coefficient determined from these CPs agrees with the value in literature ( $1.45 \times 10^{-5} \text{ cm}^2/\text{s}$ ) [3]. Subsequently, CPs were measured after the formation of the porous Zr layer. In this case, the diffusion coefficient could not be evaluated directly from  $\tau$  value, since the period until diffusion limit of U(III) varied in every measurement even with the same current density, as shown in Fig. 2. The reason for this behavior was considered that the decay of  $UCl_3$  concentration gradient in the porous Zr layer caused by the CP measurement requires a long duration due to the expected lower diffusion coefficient and the large thickness of the layer. Such complicated condition and resulting behavior in the actual CP measurement cannot be explained using either the basic electrochemical theory [2]

or simple multi-diffusion layer model [1]. Then, the series of the electrochemical operations, including the CP measurement at constant current density and the rest period in open circuit situation between the measurements, were digitally simulated by discretization of the diffusion layers around the U-Zr alloy into elements of 10 to 20  $\mu\text{m}$  thickness using finite element method. The calculation result indicated that the transition time evaluated from CPs shown in Fig. 2 can be properly reproduced by assuming the effective diffusion coefficient of U(III) in the porous Zr layer to be  $0.6 \sim 0.8 \times 10^{-5} \text{ cm}^2/\text{s}$ , which is consistent with the value  $0.7 \times 10^{-5} \text{ cm}^2/\text{s}$  evaluated from the analysis of the longer-term electrorefining experiments [1].

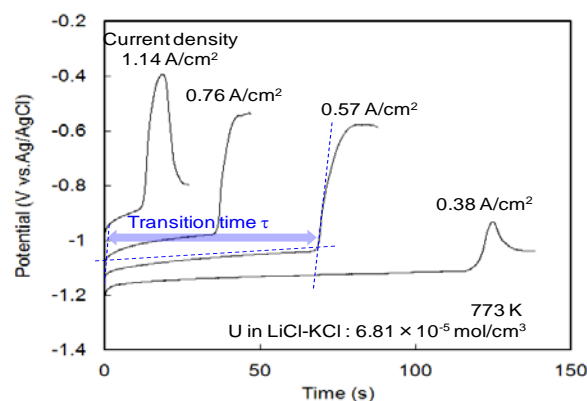


Fig. 1. Chronopotentiograms obtained with U-Zr alloy before formation of porous Zr layer.

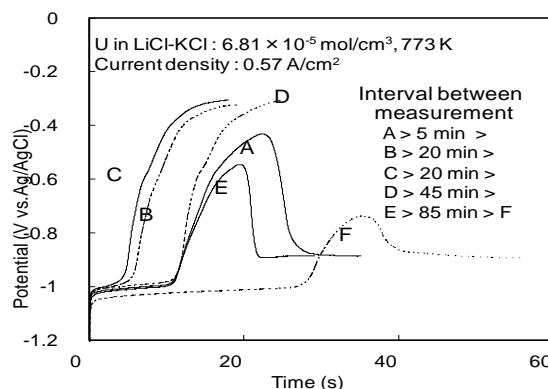


Fig. 2. Chronopotentiograms obtained with U-Zr alloy after formation of porous Zr layer.

#### REFERENCES:

- [1] M. Iizuka *et al.*, J. Nucl.Sci.Technol., **47** (2010) 1140.
- [2] M. Iizuka *et al.*, KURR annual report 2010.
- [3] S. A. Kuznetsov, *et al.*, Electrochim. Acta, **51** (2006) 2463.
- [4] M. Iizuka *et al.*, KURR annual report 2005.

## PR11-7 Electrochemistry and Structural Analysis of Cations in Molten Subhalide Systems: Fluoride Addition Effect on Voltammograms and UV-vis Spectra of Neodymium cation in Molten Chlorides

H. Matsuura, A. Nezu, H. Akatsuka, A. Uehara<sup>1</sup>,  
H. Yamana<sup>1</sup>, T. Fujii<sup>1</sup>

Research Laboratory for Nuclear Reactors,  
Tokyo Institute of Technology

<sup>1</sup>Research Reactor Institute, Kyoto University

**INTRODUCTION:** Neodymium is one of the rare earth fission products and was used as the prototype of some trans uranium elements due to its similarity of electrochemical behavior. Also, neodymium is one of important materials since it has been widely utilized at magnets in the motors, and effective recycling technology from the end products has been waiting for a long time. Although molten salt should be relatively constructed by a simple structural model due to the predominant ionic species in liquid phase, electrochemical behavior has not been well understood by the microscopic point of view. For a recent few years, the electrochemical behavior of rare earths including neodymium in the molten chlorides with small amount of fluorides has been focused, and structural elucidation by extended absorption fine structure and UV-vis spectroscopy of neodymium in molten salts has been performed [1,2]. In this year, fluoride concentration dependence on the voltammograms of neodymium in molten LiCl-KCl and spectra of neodymium in molten NaCl-2CsCl was remeasured and the structural variation is discussed newly by some parameters derived from the Judd-Ofelt analysis.

**EXPERIMENTS:** All the electrochemical experiments using molten salts have been performed in an electric furnace which is built inside a glove box filled with an argon atmosphere in high purity using an electrochemical analyzer. Cyclic voltammetry, differential pulsed voltammetry and linear sweep voltammetry have been performed by using the electrodes as follows: working electrode: tungsten, counter electrode: pyrocarbon and reference electrode: silver wire dipped in molten LiCl-KCl eutectic + AgCl (1 mol%) inside the borosilicate tube, respectively. Silica glass tube was used as a crucible. To observe the fluoride addition effect, 0 to 20 times amount of LiF to the concentration of neodymium was added to the molten salt. All measurements have been performed at 773 K. UV-vis spectroscopy of neodymium in molten NaCl-CsCl-NaF at 953 K has been carried out by using the spectrophotometer. A quartz cell with 10 mm of light path was used for the molten salt container, and experimental procedure was exactly the same as that described in the report of the last year. For the calculation of oscillator strength of the hypersensitive transition and derivation of  $\Omega_{2,4,6}$  parameters by the Judd-Ofelt analysis, den-

sity was assumed to be the additivity of molar volume of each component, and refractive index was temporary used from the value of KCl due to the non-availability of the data of CsCl.

**RESULTS and DISCUSSION:** Figure 1 shows the differential pulsed voltammograms of cathodic sweeps which exhibit mainly neodymium reduction peaks. On the contrary to previous measurements[1,2], the potential of neodymium reduction to metal was not shifted positively, however, drastic negative shift depending on fluoride addition did not occur as well. More strikingly, with increasing fluoride amount, the potential gap between  $\text{Nd}^{3+}/\text{Nd}^{2+}$  and  $\text{Nd}^{2+}/\text{Nd}$  decreased, thus disproportionation reaction may be restricted by addition of fluoride. The variation of oscillator strength of hypersensitive transition absorption of neodymium at ca. 589 nm depending on fluoride addition has been evaluated. This absorption peak has been considered to the indication of coordination symmetry around neodymium cation, i.e. 6 coordinated octahedral species, and the smaller value relates to more perfectly symmetric. One striking feature is that with increasing fluoride amount until ca.  $\text{F}/\text{Nd} = 2$  in molten NaCl-CsCl-NaF, the value of oscillator strength once increases until  $\text{F}/\text{Nd} = 2$ , and decreases rapidly. While in molten LiCl-KCl-LiF, the value of oscillator strength decreases almost linearly.

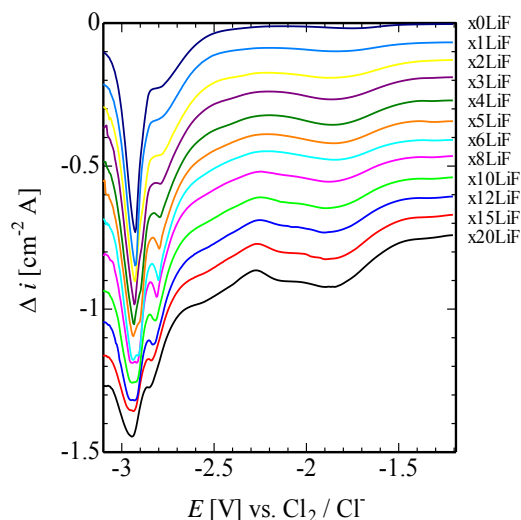


Fig. 1 Differential pulsed voltammograms of cathodic sweeps of neodymium in molten LiCl-KCl-LiF.

### REFERENCES:

- [1] Y. Shimohara *et al*, Molten salt chemistry and technology, John Wiley & Sons (2014) 577.
- [2] K. Fujita *et al*, Proc. AMS4, (2012) 264.

N. Ohtori, Y. Ishii, A. Uehara<sup>1</sup>, T. Fujii<sup>1</sup>, H. Yamana<sup>1</sup>

Department of Chemistry, Niigata University  
<sup>1</sup>Research Reactor Institute, Kyoto University

**INTRODUCTION:** Molten salts are promising solvents for actinides in reprocessing of nuclear fuel. However, knowledge of chemical stability of ionic species in melts is still inadequate to maximize their potential abilities. Information on local structure around ionic species in melts may provide useful measures for their stability in melts. Molecular dynamics (MD) simulation is a powerful tool to elucidate such structures microscopically. In particular, recent MD simulations with polarizable ionic model (PIM)[1,2] have brought much progress in understanding of structure in ionic melts: they have successfully revealed more reliable picture of local structure in  $\text{UCl}_3$ [2] which is comparable with those from XRD study. In this work, we have performed MD calculations of molten LiCl containing uranyl ion using PIM for chloride ions, and investigated the effect of polarization of  $\text{Cl}^-$  ions on local structures around uranyl ion.

**CALCULATION:** MD calculations have been carried out using PIM for molten LiCl containing  $\text{UO}_2^{2+}$  ion. The system included 500, 502, and 1 ions for  $\text{Li}^+$ ,  $\text{Cl}^-$ , and  $\text{UO}_2^{2+}$ , respectively. MD calculation without polarization of  $\text{Cl}^-$  ions has also performed, which is referred here to as RIM: rigid ion model. Furthermore, first principle MD simulation has been performed using the CPMD code[3] for the system with similar composition but smaller size. The temperature was set at 1073 K in all the calculations.

**RESULTS:** Figures 1 and 2 show radial distribution functions for U and Cl pair and U and Li pair, respectively, obtained from the present calculations. Table 1 summarizes intraionic distance between U and O in uranyl ion and interionic distance between U and Cl which are near neighbors with each other. These results clearly show effects of polarization of  $\text{Cl}^-$  ions on the coordination structures around uranyl ion. That is, we have found that PIM can reproduce the results by first-principle MD simulation better than RIM.

Table 1 Intraionic distance between U and O in uranyl ion and interionic distance between U and Cl in molten LiCl containing uranyl ion

	Expt.	CPMD	PIM	RIM
U=O	1.77 Å	1.80 Å	1.78 Å	1.77 Å
U-Cl	2.73 Å	2.64-2.71 Å	2.78 Å	2.94 Å

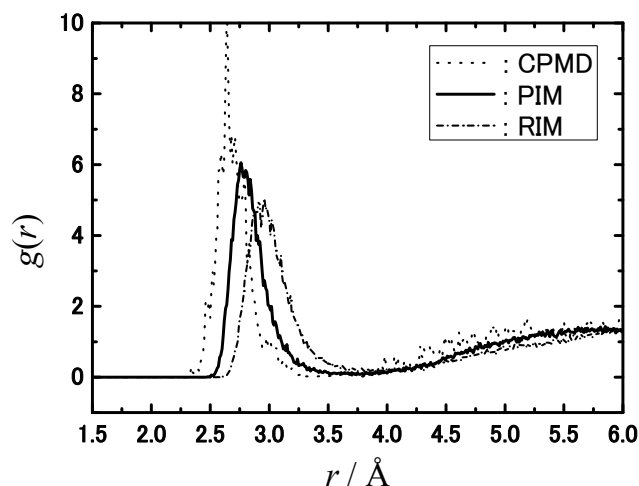


Fig.1 Radial distribution functions for U and Cl pair obtained from the present calculations.

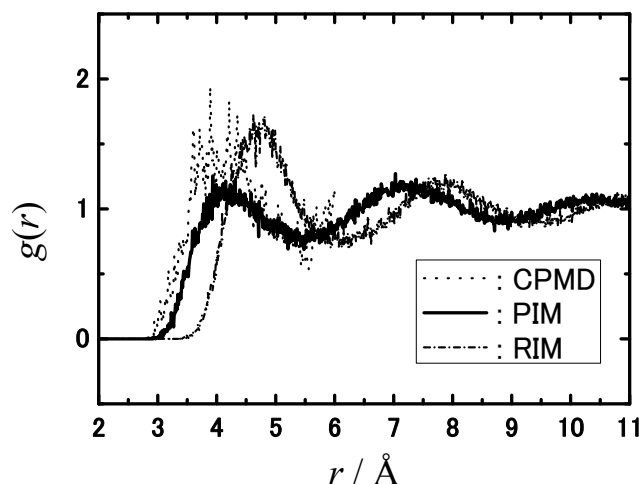


Fig.2 Radial distribution functions for U and Li pair obtained from the present calculations.

#### REFERENCES:

- [1] P. A. Madden, R. Heaton, A. Aguado and S. Jahn, *J. Mol. Struct.:THEOCHEM*, **771** (2006) 9-18.
- [2] Y. Okamoto, P. A. Madden and K. Minato, *J. Nucl. Mater.* **344** (2005) 109-114.
- [3] <http://www.cpmd.org/>

R. Hazama, Y. Sakuma<sup>1</sup>, A. Ito, T. Fujii<sup>2</sup>, S. Fukutani<sup>2</sup>, Y. Shibahara<sup>2</sup>

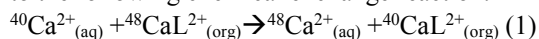
Graduate School of Human Environment, Osaka Sangyo University

<sup>1</sup>Research Laboratory for Nuclear Reactors, Tokyo Institute of Technology,

<sup>2</sup>Research Reactor Institute, Kyoto University

**INTRODUCTION:** Anomalous mass dependence was experimentally observed in uranium isotope fractionation by Fujii et al., in the late 80's[1] and Nishizawa et al., suggested that odd-even staggering may be due to the nuclear charge density difference in the middle of 90's[2] for the case of strontium. Calcium is congener of strontium and easy to handle to check the isotope effects[3,4].

**EXPERIMENTS:** Isotopic enrichment occurs according to the following chemical exchange reaction:



where L represents macrocyclic polyether(18-crown-6). As a result, <sup>40</sup>Ca is enriched in the organic-phase (org) crown solution and the heavy isotopes of <sup>48</sup>Ca tend to concentrate in the aqueous (aq) phase. The mass effect is observed by the thermal ionization mass spectrometer (TIMS) measurement of calcium isotope ratios for the mass range from 40-48 atomic mass unit (amu).

**RESULTS:** Unit mass enrichment factors of Sr and Ca isotope separation are summarized in Table 1. In general, a crown ether gives a large separation factor with more than ten times, compared with an ion exchange method and has an applicable ability of separation in reality.

$\epsilon / \Delta M$ [ $\times 10^{-5}$ ]	Method and system	Temp. (°C)	Ref.
51-17 (Sr)	Liquid-liquid extraction (LLE) with dicyclohexano-18-crown-6 (DC18C6). 2.3M-0.5M Sr in aqueous phase.	20±0.5	[2]
14 (Sr)	Crown-ether resin chromatography (CRC). 1.3m 0.1-0.01M Sr + 2M HCl	35±2	[5]
5.6 (Sr)	CRC. 1.3m 0.1M Sr + 3M HNO <sub>3</sub>	35±2	
2.3 (Sr)	$\alpha$ -hydroxyisobutyrate	Not specified	[6]

0.31 (Sr)	Cation-exchange chromatography with Sr lactate.	25±0.2	[7]
100 (Ca)	LLE with DC18C6. 0.07M CHCl <sub>3</sub>	25	[8]
36-15 (Ca)	LLE with HDEHP(di(2-ethylhexyl) orthophosphoric acid)	10-50	[9]
130 (Ca)	LLE with amalgam. 0.27-0.68M Ca/liter Hg	25	[10]
2.3 (Ca)	Ion exchange chromatography with Dowex50	room temp.	[11]
98 (Ca)	CRC(cryptand2B.2.2). 0.01M CaCl <sub>2</sub> +CH <sub>3</sub> OH/CHCl <sub>3</sub>	20	[12]
63 (Ca)	CRC (18C6) 0.01M CaCl <sub>2</sub> +CH <sub>3</sub> OH/CHCl <sub>3</sub>	20	
2.8 (Ca)	Iminodiacetate resin 0.95M NaCl+0.05M CaCl <sub>2</sub>	25	
56-130 (Ca)	CRC (cryptand2B.2.2) CH <sub>3</sub> OH/CHCl <sub>3</sub> /H <sub>2</sub> O	-21-21	[13]
24 (Ca)	CRC (benzo-18C6). 0.02M Ca + 9M HCl	30	[14]
76 (Ca)	CRC (benzo-18C6). 9M HCl (0.8mm $\phi$ , 1m)	40	[15]
8.9 (Ca)	CRC (benzo-15C5). 12M HCl (0.8mm $\phi$ , 1m)	50	
150 * (Ca)	LLE with DC18C6 0.07M CHCl <sub>3</sub>	20	This work

Table 1. Unit mass enrichment factors of Sr and Ca isotope separation. \*: Preliminary

**REFERENCES:**

- [1] Y. Fujii *et al.*, Z. Naturforsch., **44a** (1989) 395.  
 [2] K. Nishizawa *et al.*, J. Nucl. Sci. Technol., **32** (1995) 1230.  
 [3] R. Hazama *et al.*, Proc. of 6th Rencontres du Vietnam, Gioi Publishers (2007) 383: arXiv0710.3840.[nucl-ex].  
 [4] Y. Fujii *et al.*, Isotopes in Environmental and Health Studies, Vol. **46**, No.2, (2010) 233.  
 [5] Y. Ban *et al.*, Sep. Sci. Technol. **36**(2001)2165.  
 [6] J. Aaltonen, Suom. Kem., **B45** (1972) 141.  
 [7] T. Oi *et al.*, Sep. Sci. Technol., **27** (1992) 631.  
 [8] B.E. Jepson *et al.*, J. Inorg. Nucl. Chem. **38**(1976)1175.  
 [9] E.P. Horwitz *et al.*, J. Chromatography **125**(1976)203.  
 [10] D. Zucker *et al.*, J. Chem. Phys. **41**(1964)1678.  
 [11] B.E. Jepson *et al.*, Sep. Sci. Technol. **19**(1984)173.  
 [12] B.E. Jepson *et al.*, Sep. Sci. Technol. **25**(1990)1893.  
 [13] K.G. Heumann *et al.*, Angew. Chem. Int. Ed. Engl. **19**(1980)406.  
 [14] K. Hayasaka *et al.*, Prog. Nucl. Energ. **50**(2008)510.  
 [15] S. Nemoto *et al.*, J. Nucl. Sci. Tech. Vol. **49**, No. 4, (2012) 425.

## PR11-10 Experimental and Calculated Optical Properties of Molten Aluminium Chloride Melts

T. Goto, K. Hachiya<sup>1</sup>, A. Uehara<sup>2</sup>, T. Fujii<sup>2</sup>, H. Yamana<sup>2</sup>

Graduate School of Science and Engineering, Doshisha University

<sup>1</sup>Graduate School of Energy Science, Kyoto University

<sup>2</sup>Research Reactor Institute, Kyoto University

**INTRODUCTION:** Molten  $\text{AlCl}_3$  and  $\text{ACl-AlCl}_3$  ( $A$ : alkaline metals) have been attractive targets of studies from both fundamental and application viewpoints, because of their relatively low melting points which lead to their effectiveness. The structure of the melts contains a variety of coordinations which have long been investigated and mainly consists of covalent bonding between Al-Cl. In this study, Raman scattering measurements are performed to investigate into their bonding structures, and the spectra are analyzed with *ab initio* simulations. We focus our study on  $\text{CsCl-AlCl}_3$  binary and  $\text{LiCl-KCl-CsCl-AlCl}_3$  ternary systems

**EXPERIMENTS:** Raman scattering spectra obtained in KURRI were simulated by calculations with GAUSSIAN09 simulation package. Up to 2 ps trajectories of ions in the melts were calculated with a variant of first-principle molecular dynamics simulations, ADMP (Atom-centered Density Matrix Propagation). The computations of the ionic trajectories were performed for  $\text{CsCl-AlCl}_3$  at 700 K.

**RESULTS:** As comprehensively reviewed in Ref. [1], up to 1 : 1 mixture of  $\text{CsCl/AlCl}_3$  is expected to exclusively contain  $\text{AlCl}_4^-$  cluster as an anion. On the other hand,  $\text{Al}_2\text{Cl}_7^-$  clusters were contained 9.6% of the total anions in the whole snapshots, while  $\text{AlCl}_4^-$  clusters were 73.4%. These numbers of anion rates show that  $\text{AlCl}_4^-$  clusters are not always rigid, and  $\text{Cl}^-$  ions are exchanged among clusters.

Using Einstein relation for the mean square displacements versus time presented in FIG.1, self-diffusion constants were computed to be  $D_{\text{Cs}} = 1.216 \times 10^{-4} \text{ cm}^2 \text{ s}^{-1}$ ,  $D_{\text{Al}} = 1.530 \times 10^{-4} \text{ cm}^2 \text{ s}^{-1}$  and  $D_{\text{Cl}} = 2.671 \times 10^{-4} \text{ cm}^2 \text{ s}^{-1}$ , respectively. As far as we know, there is no direct reference experimental data for this system, while interdiffusion constant for  $\text{NaCl-AlCl}_3$  mixture were reported to be  $4.5 \times 10^{-6} \text{ cm}^2 \text{ s}^{-1}$  at 413 K [2]. The square displacements for each individual atom are presented in FIG. 2. Al atoms, center of each anion clusters, exhibit both diffusing and static dynamics. A part of Cl atoms corresponds to Al atoms, both for two diffusing Al's and remaining non-diffusing two. Nevertheless, the rest of Cl's cannot be categorized to either of them. This result also supports that  $\text{Cl}^-$  ions are exchanged among clusters.

**DISCUSSIONS:** For  $\text{CsCl-AlCl}_3$  mixture system, anion structure of isolate  $\text{AlCl}_4^-$  tetrahedra shift to corner-sharing two-tetrahedron structure,  $\text{Al}_2\text{Cl}_7^-$ , dramati-

cally at 1 : 1-ratio with increasing  $\text{CsCl}$  content. Our calculation seems to reproduce fluctuations in the structural rearrangement at that mixing ratio.

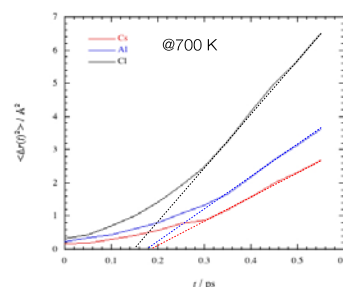


FIG. 1 Mean square displacements versus time for ADMP dynamics of constituent atoms at 700 K.

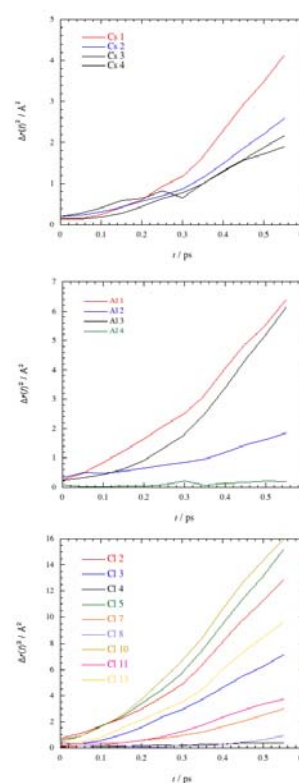


FIG. 2 Square displacements versus time for ADMP dynamics of Cs, Al and Cl atoms at 700 K.

### REFERENCE:

- [1] M. P. Tosi, D. L. Price, M.-L. Saboungi, *Annu. Rev. Phys. Chem.* **44** 173 (1993).  
 [2] B. Gilbert, D. L. Brotherton and G. Mamantov *J. Electrochem. Soc.* **121** 773 (1974).



# PR11-11 Precipitation Behavior of Trivalent Dysprosium Ion by Reaction with Oxide Ion in $\text{CaCl}_2\text{-LiCl}$ Molten Salt

H. Sekimoto, A. Uehara<sup>1</sup>, T. Fujii<sup>1</sup>, H. Yamana<sup>2</sup>

<sup>1</sup>Faculty of Engineering, Iwate University  
Department of Materials Science and Engineering

<sup>2</sup>Graduate School of Science, Kyoto University<sup>4</sup>Research Reactor Institute, Kyoto University

**INTRODUCTION:** Development of recycling technique for neodymium magnet is essentially important to achieve sustainable society. Consequently, we propose and are investigating a new recycling process of neodymium magnet using  $\text{B}_2\text{O}_3$  flux [1]. In the process, the neodymium magnet is melted together with sufficient amount of  $\text{B}_2\text{O}_3$  in graphite crucible to form molten iron based alloy,  $\text{B}_2\text{O}_3$  slag and  $\text{Nd}_2\text{O}_3\text{-B}_2\text{O}_3$  slag, which is recovered and dissolved in molten salt. And then, Fe-Nd-B alloy is produced by electrolysis. For the process, thermodynamic properties such as solubility of rare earth oxide in molten salt is important information. In this study, precipitation behavior of dysprosium with adding oxide ion in  $\text{CaCl}_2\text{-LiCl}$  eutectic molten salt was investigated by spectrophotometry.

**EXPERIMENTS:** Solidified samples of  $\text{CaCl}_2\text{-LiCl}$  eutectic molten salt and 5 mol%  $\text{Li}_2\text{O}\text{-(CaCl}_2\text{-LiCl)}_{\text{eu}}$  molten salt were prepared through the following procedure.  $\text{Li}_2\text{O}$ ,  $\text{CaCl}_2$  and  $\text{LiCl}$  was weighted, mixed, co-melted at 700 °C in cylindrical quartz tube and quenched in Ar atmosphere. 3.01 g of  $\text{CaCl}_2\text{-LiCl}$  eutectic molten salt was inserted in a quartz optical cell and melted at 700 °C. The intensity of the transmitted light through  $\text{CaCl}_2\text{-LiCl}$  eutectic molten salt using a tungsten lamp and a spectrophotometer. Then, adding small amount of  $\text{DyCl}_3$  in the  $\text{CaCl}_2\text{-LiCl}$  molten salt and measuring the intensity of the transmitted light through  $\text{DyCl}_3\text{-(CaCl}_2\text{-LiCl)}_{\text{eu}}$  molten salt was carried out repeatedly to obtain absorption spectra of  $\text{Dy}^{3+}$  at 700 °C. After that, adding small amount of adding  $\text{Li}_2\text{O}\text{-CaCl}_2\text{-LiCl}$  molten salt and measuring the intensity of the transmitted light through  $\text{Li}_2\text{O}\text{-DyCl}_3\text{-CaCl}_2\text{-LiCl}$  molten salt was also carried out repeatedly to obtain absorption spectra of  $\text{Dy}^{3+}$  at 700 °C. Using the data on the intensity of the transmitted light, absorbance was evaluated.

**RESULTS:** Figure 1 shows the absorption spectra of  $\text{Dy}^{3+}$  in  $\text{DyCl}_3\text{-(CaCl}_2\text{-LiCl)}_{\text{eu}}$  molten salt at 700 °C. There are three absorption peak depending on the concentration of  $\text{Dy}^{3+}$  in the range of wavelength,  $\lambda$ , from 800 nm and 1600 nm; a strong absorption peak at 1296

nm and 2 weak absorption peaks at 918 and at 1121. Figure 2 shows the absorption spectra of  $\text{Dy}^{3+}$  in  $\text{Li}_2\text{O}\text{-DyCl}_3\text{-CaCl}_2\text{-LiCl}$  molten salt. The spectra were shifted upward and the difference between the top of the absorption peak and the absorbance on the tangential line between the feet of the peak at around 1296 nm became smaller with introducing  $\text{O}^{2-}$ . These indicates that the formation of  $\text{DyOCl}$  or  $\text{Dy}_2\text{O}_3(\text{s})$  proceeded and the amount of  $\text{Dy}^{3+}$  in molten salt decreased.

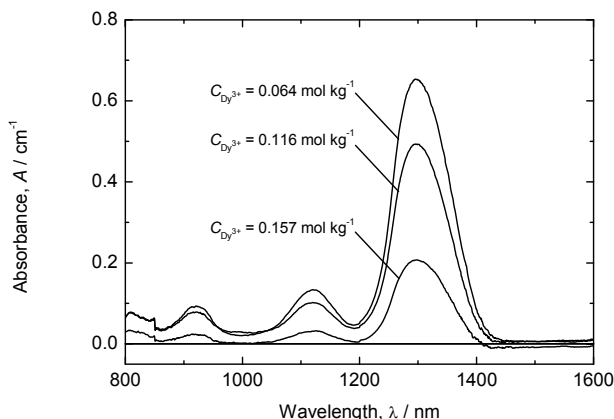


Fig. 1. Flowchart of the recycling process for neodymium magnet proposed in this study.

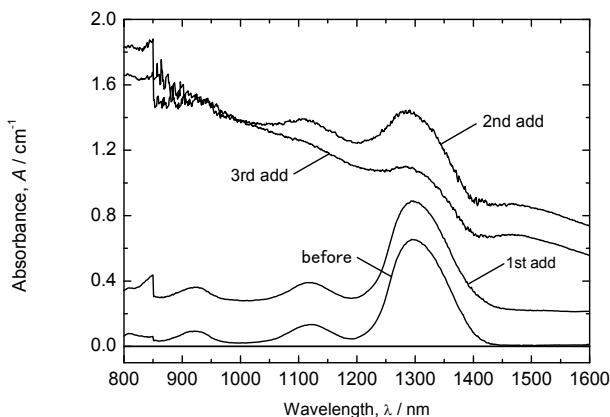


Fig. 2. Cyclic voltammogram of  $\text{CaCl}_2$  molten salt and  $\text{CaCl}_2\text{-Nd}_2\text{O}_3\text{-B}_2\text{O}_3$ .

## REFERENCES

H. Sekimoto, A. Uehara, T. Fujii, H. Yamana, KURRI Progress report, (2012) 102

採択課題番号 26P11-12 吸光分光測定を用いた高温融体中の金属イオンの プロジェクト  
溶存形態に関する研究 (f-元素の有効利用に関わる基礎及び応用研究)

(岩手大・工) 関本 英弘

(京大・原子炉) 上原 章寛、藤井 俊行、山名 元

T. Ohta, T. Kubota<sup>1</sup>, Y. Shibahara<sup>1</sup>, S. Fukutani<sup>1</sup>, T. Fujii<sup>1</sup>,  
T. Igarashi, Y. Mahara<sup>2</sup>

*Faculty of Engineering, Hokkaido University*

<sup>1</sup>*Research Reactor Institute, Kyoto University*

<sup>2</sup>*Professor Emeritus, Kyoto University*

### INTRODUCTION:

Although previous studies have measured the distribution of radionuclides in tree rings, the uptake route of <sup>137</sup>Cs originating from the fallouts of nuclear weapon tests and the Chernobyl accident has undoubtedly argued the roots<sup>1)-4)</sup>. A number of researchers have also reported that <sup>137</sup>Cs and Pu are absorbed by trees through their bark and leaves; although ambiguously, conclusive evidence has been presented<sup>5)</sup>.

Understanding the uptake route of radiocesium (radio-Cs) in the annual tree rings is important for a forest decontaminating in Fukushima. Thus, we investigated the fate of radio-Cs in the Fukushima forestry environment to understand its uptake route using following method: the behavior of radiocesium in the soil and the measurements of radiocesium in the annual tree rings of the deciduous tree konara and the coniferous tree sugi by gamma-ray spectrometry.

### EXPERIMENTS

Our experiment is composed three objectives: 1) depth profile of <sup>137</sup>Cs, <sup>134</sup>Cs, and <sup>40</sup>K in the observed sites, 2) speciation of radio-Cs in soil, 3) measurement of <sup>137</sup>Cs and <sup>40</sup>K in tree rings

### RESULTS:

The behavior of <sup>137</sup>Cs in the soil samples collected in Fukushima showed the following: (1) radio-Cs in the soil was primarily absorbed by soil minerals within the top 1-cm-depth from the surface; and (2) <sup>137</sup>Cs in soil was water insoluble and >95% of <sup>137</sup>Cs was bound to organic and residual matters. These observations suggest that the <sup>137</sup>Cs released from the Fukushima NPP was trapped in

the surface soil and did not penetrate deeper into the soil. The results clearly show that radio-Cs in soil has not moved from the tree roots to the annual tree rings because the active root system rarely was found in the surrounding surface soil. The high <sup>137</sup>Cs concentration in the sapwood zone of konara coincided with the direction of the arriving radioactive plume in the sampling sites. Conversely, the concentrations of <sup>137</sup>Cs and <sup>134</sup>Cs in the annual tree rings of sugi showed non-directionality. As the radioactive Cs moved from the leaves to the tree trunk, the directionality of radio-Cs in the annual tree rings was eventually disappeared. The results of the present study indicate that <sup>134</sup>Cs and <sup>137</sup>Cs, detected in the tree rings, from the Fukushima NPP were directly absorbed from the atmosphere by the bark and leaves rather than the roots. Furthermore, the results suggest that the concentrations of radio-Cs in the trees in Fukushima would not further increase in the future.

On the basis of the distribution of radio-Cs in the annual tree rings of the both trees of konara and sugi, we propose the following guidelines for using contaminated wood from Fukushima when high concentrations <sup>137</sup>Cs have been detected in the trunk: (1) use the parts of wood where the <sup>137</sup>Cs concentrations are low, and (2) use the highest parts of the trees as sources of bio-ethanol and/or biomass, which correspond to the energy sources for the next generation.

### REFERENCES:

- [1] Fesenko et al., *Radiat. Environ. Biophys.*, **40**, 105 (2001).
- [2] Goor and Thirty, *Sci. Total Environ.*, **325**, 163 (2004).
- [3] Momoshima et al., *J. Environ. Radioact.*, **22**, 93 (1994).
- [4] Kagawa et al., *J. Environ. Qual.*, **31**, 2001 (2002).
- [5] Kudo et al., *J. Environ. Radioactivity*, **21**, 55 (1993).

T. Kubota, T. Fujii, S. Fukutani, Y. Shibahara and T. Ohta<sup>1</sup>

Kyoto University Research Reactor Institute

<sup>1</sup>Graduate School of Engineering, Hokkaido University

**INTRODUCTION:** Photonuclear reaction induced by high energy photons can produce nuclides that are hardly produced in a nuclear reactor, for example, neutron deficient nuclides and carrier free isotopes through  $(\gamma, n)$  and  $(\gamma, p)$  reaction, respectively. High energy photon is generated in the bombardment of electrons of 30 MeV to platinum sheets at the KURRI-LINAC. We attempted to conduct activation analysis for silicate salt in the previous report [1]. However, Al-29 expected in  $(\gamma, p)$  reaction was not observed. The results showed the investigation of effective reaction cross-sections was required for various kinds of target samples. In this report alkali earth elements are used as target sample in order to obtain carrier free alkali metal elements, and in addition the concentration of arsenic in seaweed is evaluated as a preliminary test instead of neutron activation [2].

**EXPERIMENTS:** The target samples were once heated to dehydration and disintegrate organic compounds; alkali earth salts were dried at 100°C; and seaweed (*Hizikia fusiformis*) was incinerated at 450°C. Each sample was encapsulated in a quartz tube [3]. The tube in an aluminum vessel was irradiated with photon generated by electron energy of 30 MeV at average current of 200  $\mu\text{A}$  for 4 to 48 hours. Radioactivity,  $A$ , induced by photonuclear reaction was measured by  $\gamma$ -spectrometry and provided the apparent cross-section,  $\theta$ , which is determined by the following equation:

$$A = M_0 \theta (\mu\text{A}) (1 - e^{-\lambda t})$$

where  $M_0$ , ( $\mu\text{A}$ ),  $\lambda$  and  $t$  were mole number of target nuclide, average electron beam current (micro-ampere), decay constant, and irradiation time, respectively.

**RESULTS:** Fig 1 shows the apparent cross-sections as a function of mass number. The cross-section of  $(\gamma, n)$  reaction was larger than that of  $(\gamma, p)$  reaction by one order of magnitude. While the former was the largest at heavy element, seems to be constant between mass number of 40 to 100. The latter was almost constant independent of mass number. For a light element  $(\gamma, np)$  reaction was also observed; however, its cross-section was small. The measurement of activated seaweed shows the peaks of As-74 in Fig. 2. The cross-sections of some photonuclear reactions were obtained for isotope production and activate analysis, even though these values are

empirical.

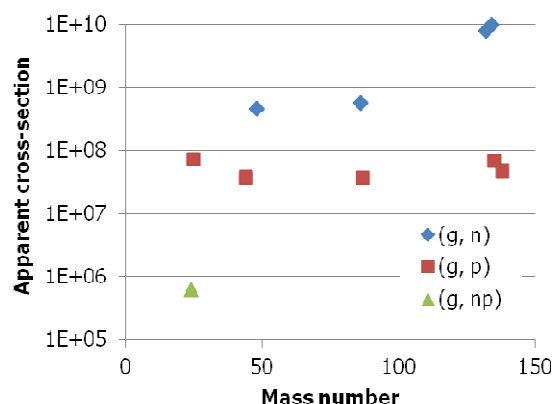


Fig. 1. Apparent cross-section for photonuclear reactions;  $(\gamma, n)$ ,  $(\gamma, p)$  and  $(\gamma, np)$  reaction

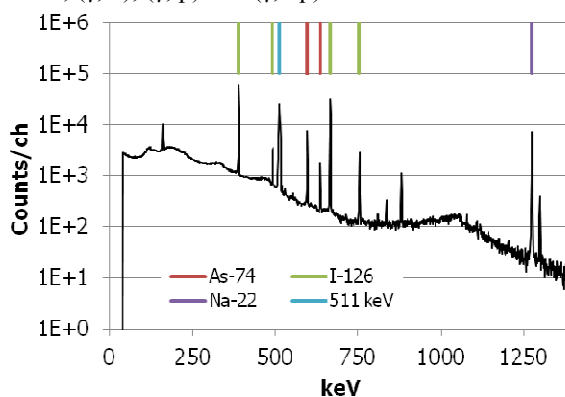


Fig. 2. Gamma spectrometry of seaweed (*Hizikia fusiformis*) irradiated for four hours at the KURRI-LINAC.

**REFERENCES:**

- [1] T. Kubota et al., KURRI PROGRESS REPORT 2013 (2014) CO12-5.
- [2] R. Ogawa et al., Bulletin of the Faculty of Education, Ehime University 53 (2006) 131-136.
- [3] T. Kubota et al., Recent Advances in Actinide Science, RSC Publishing (2006) 68-70

Y. Shibahara, T. Kubota, S. Fukutani, T. Fujii,  
T. Shibata<sup>1</sup>, M. Yoshikawa<sup>1</sup>

Kyoto University Research Reactor Institute  
<sup>1</sup> Kyoto University Institute for Geothermal Sciences

**INTRODUCTION:** For the analysis of radionuclide, the radiation measurement such as  $\gamma$ -spectrometry,  $\beta$ -spectrometry, and  $\alpha$ -spectrometry were mainly performed. Although these methods have been used for the measurement of radioactive nuclide such as nuclear fuel materials and fission products released on the accident of Fukushima Dai-ichi Nuclear Power Plant, they may have disadvantage in the case of the analysis of radionuclide having the long half-life and/or that of isotopic composition including naturally occurring isotopes. Because the mass spectrometry has advantage for the analysis of the isotopic composition of the elements with high accuracy, this method may have the applicability for the analysis of radionuclide released on the accident of Fukushima Dai-ichi Nuclear Power Plant.

Although the amounts of radionuclide such as radioactive Cs and Sr released on this accident were very huge, the contaminated environmental samples show the small radioactivity per unit weight of the contaminated environmental samples, since the contaminated area is very wide. For the study of the recovery/analysis method of cesium and strontium, thus, the radioactive Cs and Sr were generated by the irradiation of natural uranium at KUR.

**EXPERIMENTS:** Radioactive Cs and Sr were generated by the irradiation of 10 mg of  $\text{UO}_2$  of natural uranium at the Kyoto University Research Reactor with the neutron flux for  $5.5 \times 10^{12}$  n/s  $\text{cm}^2$ . The amounts of the major radionuclide of Cs and Sr generated by the irradiation for 3 hours were estimated as  $7.4 \times 10^{-11}$  g ( $^{137}\text{Cs}$ ) and  $4.5 \times 10^{-11}$  g ( $^{90}\text{Sr}$ ). About 2 days later, the irradiated sample was dissolved with 8M  $\text{HNO}_3$  and heated to dryness. The residues were immersed in 8 M  $\text{HNO}_3$  and the insoluble residues were removed by centrifugation. TRU elements in sample solution were removed by the extraction-chromatography with UTEVA-resin [1], and the sample solution was evaporated to dryness. The residues was dissolved with 3 M  $\text{HNO}_3$  solution. After the recovery of Sr by the extraction-chromatography with Sr-resin [2], Cs was recovered by using with ammonium phosphomolybdate (AMP) [3]. The sample solutions for the analysis of isotopic composition of Sr and Cs were obtained with the dissolving 1 M  $\text{HNO}_3$  (10 $\mu\text{L}$  for Sr, 20  $\mu\text{L}$  for Cs, respectively).

Isotopic compositions of Cs and Sr were measured with a TIMS (Triton-T1, Thermo Fisher Scientific). A 1  $\mu\text{L}$  aliquot of each solution was loaded onto a rhenium single filament with a TaO activator [4]. Loading amount of  $^{90}\text{Sr}$  and  $^{137}\text{Cs}$  were  $4.5 \times 10^{-12}$  g and  $3.7 \times 10^{-12}$  g, re-

spectively. Because of the loading amount of Sr and Cs, the mass spectra of radioactive Cs and Sr were obtained with a secondary electron multiplier detector (SEM).

**RESULTS:** In the measurement of radioactive Cs,  $^{135}\text{Cs}$ ,  $^{136}\text{Cs}$  and  $^{137}\text{Cs}$  were detected (Fig.1 (a)):  $^{134}\text{Cs}$  was not detected, because of the amount generated by the irradiation at KUR. In this measurement, it was observed that the isotopic ratios of  $^{135}\text{Cs}/^{137}\text{Cs}$  and  $^{136}\text{Cs}/^{137}\text{Cs}$  were  $0.9103 \pm 0.0008$  and  $0.00022 \pm 0.00001$ , respectively. These mean that the several ten femto-gram of Cs would be detectable with the four orders of the significant figures.

In the measurement of radioactive Sr,  $^{89}\text{Sr}$ ,  $^{90}\text{Sr}$  and  $^{91}\text{Sr}$  were detected at the measurement 2.6 days later. The mass spectra of  $^{91}\text{Sr}$  and  $^{89}\text{Sr}$  were disappeared at the measurement of 31 days later and 574 days later, because of the half-life of  $^{91}\text{Sr}$  ( $T_{1/2} = 9.5$  h) and  $^{89}\text{Sr}$  ( $T_{1/2} = 50.5$  d). The obtained isotopic ratios were agreed with results of the estimation by using ORIGEN-II code [5]. This means that the several ten femto-gram of Sr would also be detectable.

It was confirmed that the recovery/analysis method of Cs and Sr have the applicability for the analysis of radioactive Cs and Sr released on the accident of Fukushima Dai-ichi Nuclear Power Plant. The loading amount of several pico-grams of radioactive Cs and Sr would bring the information of the isotopic ratio with the four orders of significant figure until the ten periods of half-live.

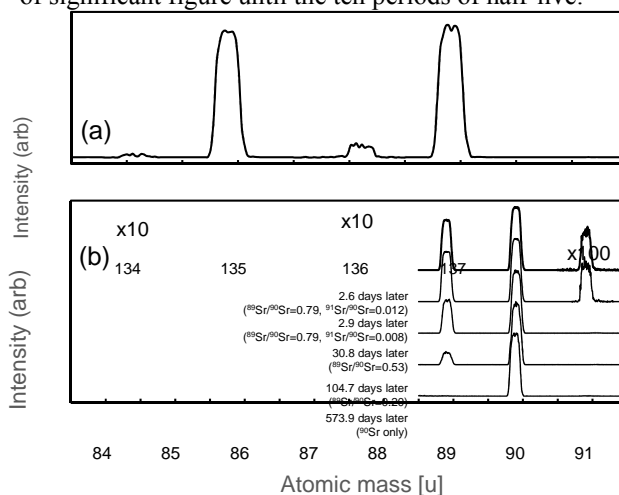


Fig.1 Mass spectra of radioactive Cs and Sr. (a) Cs, (b) Sr.

#### REFERENCES:

- [1] Y. Shibahara et al., J. Radioanal. Nucl. Chem., 303: 1421-1424 (2015).
- [2] T. Kubota et al., J. Radioanal. Nucl. Chem. 303: 39-46 (2015).
- [3] Y. Shibahara et al., J. Nucl. Sci. Technol. 51: 575-579 (2014).
- [4] J. L. Birck, Chem. Geol. 56: 73-83 (1986).

## PR11-15 Tracing Halogen and Noble Gas Recycling in the Northern Izu Subduction Zone by Neutron Irradiation and Noble Gas Mass Spectrometry

H. Sumino, M. Kobayashi, K. Nagao, R. Okumura<sup>1</sup>,  
S. Sekimoto<sup>1</sup> and T. Fujii<sup>1</sup>

*Geochemical Research Center, Graduate School of Science, University of Tokyo*

<sup>1</sup> *Research Reactor Institute, Kyoto University*

**INTRODUCTION:** Recent findings of subducted halogens and noble gases with seawater and sedimentary pore-fluid signatures in exhumed mantle wedge peridotites [1], as well as seawater-derived heavy noble gases (Ar, Kr, and Xe) in the convecting mantle [2], provide observations that allow us to investigate the processes that control the return of volatile and highly incompatible elements into the mantle. To verify whether and how such subduction fluids modify the composition of the mantle beneath subduction zones, we are investigating noble gas and halogen compositions of olivines in arc lavas from northern Izu subduction zone and those of seafloor sediments and basalts from NW margin of the Pacific plate. A combination of neutron irradiation and noble gas mass spectrometry (NI-NGMS), an extension of Ar-Ar and I-Xe dating methods, allows us to simultaneously determine trace amounts of halogens with naturally occurring noble gases by use of ultrahigh-sensitive noble gas mass spectrometry on neutron-irradiated samples [3,4].

**EXPERIMENTS:** The samples and standard samples for NI-NGMS, Hb3gr hornblende and the Shallowater meteorite were neutron-irradiated for six hours during a 5 MW operation of KUR by using the hydraulic conveyor to convert halogens (Cl, Br, and I) to corresponding noble gas isotopes. Noble gases in the unirradiated and irradiated samples were extracted selectively from fluid/melt inclusions using *in vacuo* crushing. The evolved noble gases were analyzed using mass spectrometry at The University of Tokyo [5,6].

**RESULTS:** MORB-like  $^3\text{He}/^4\text{He}$  and halogen ratios of the olivines indicate insignificant contributions to the Izu arc magmas of radiogenic  $^4\text{He}$  and sedimentary-pore-fluid-like halogens, both of which are observed in the subduction fluids released from a slab at a depth of 100 km [1]. On the other hand, a clear difference in  $^{40}\text{Ar}/^{36}\text{Ar}$  ratios between the Izu volcanic front and rear arc, and a comparison with those of the seafloor sediments and altered oceanic crusts suggest that Ar of sedimentary pore-water origin in the subducting slab or hydrated layer of the mantle wedge is liberated continuously with depth and that it affects the noble gas composition of the magma generation region significantly. A small addition of the sediment-derived noble gases to the

rear-arc magma is consistent with the slab melt contribution inferred from trace element and Pb-Sr-Nd-Hf) isotope compositions [7].

The high I/Cl ratios of the seafloor sediments can account for the enrichment of I in subduction fluids relative to sedimentary pore-fluids [1], whereas contributions of halogens and noble gases from altered oceanic basalts are limited.

A simple mass balance calculation of Ar isotopes for the melt generation region beneath the Izu arc revealed that higher subduction flux of pore water other than direct incorporation with its host sediment/crust is necessary, and that serpentinized lithosphere in the subducting slab is regarded as the best candidate if the hydration of the lithosphere by pore fluids is operating in a closed system.

The significantly smaller contributions of subducted noble gases and halogens in the Izu arc magmas relative to those in the mantle wedge peridotites may result from a difference in the P-T condition of the slab in each subduction zone, or from dilution by mantle-derived halogens and He when the subduction fluid induced partial melting. The former implies a relatively small amount of the pore-water-derived subduction fluids would be released from a cold slab at a sub-arc depth resulting in further subduction of halogens, heavy noble gases and potentially water, to great depths in the mantle, which account for the seawater-like heavy noble gases observed in the convecting mantle [2].

### REFERENCES:

- [1] H. Sumino *et al.*, *Earth Planet. Sci. Lett.*, **294** (2010) 163-172.
- [2] G. Holland and C.J. Ballentine, *Nature*, **441** (2006) 186-191.
- [3] G. Turner, *J. Geophys. Res.*, **70** (1965) 5433-5445.
- [4] J.K. Böhlke and J.J. Irwin, *Geochim. Cosmochim. Acta*, **56** (1992) 187-201.
- [5] N. Ebisawa *et al.*, *J. Mass Spectrom. Soc. Jpn.*, **52** (2004) 219-229.
- [6] H. Sumino *et al.*, *J. Mass Spectrom. Soc. Jpn.*, **49** (2001), 61-68.
- [7] J.-I. Kimura *et al.*, *Geochem. Geophys. Geosys.*, **11** (2010) Q10011.

採択課題番号 26P11-16 希ガス化法を用いた極微量ハロゲン測定による  
地球深部の水の起源の解明

プロジェクト

(東大院・理・地殻化学実験施設) 角野浩史、長尾敬介、小林真大  
(京大・原子炉) 藤井俊行、関本 俊、奥村 良

## PR11-16 Volcanic and Tectonic History of Philippine Sea Plate (South of Japan) Revealed by $^{40}\text{Ar}/^{39}\text{Ar}$ Dating Technique

O. Ishizuka, T. Fujii<sup>1</sup>, R. Okumura<sup>1</sup>, S. Sekimoto<sup>1</sup>

Geological Survey of Japan, AIST

<sup>1</sup>Research Reactor Institute, Kyoto University

**INTRODUCTION:** Submarine volcanic rocks are known to give ages different from their true eruption ages in some cases. This is due to the existence of excess  $^{40}\text{Ar}$  in the rapidly quenched glass or Ar loss and K remobilization caused by reaction with seawater or hydrothermal fluids. Stepwise-heating analysis in  $^{40}\text{Ar}/^{39}\text{Ar}$  dating is particularly useful for dating submarine volcanics.

Since this is the first time to use KUR for our laboratory, we investigated neutron flux gradient and production of interfering isotopes for  $^{40}\text{Ar}/^{39}\text{Ar}$  method by irradiating standard minerals and synthetic glasses as preparation for dating of unknown samples.

**EXPERIMENTS:** Samples were wrapped in an aluminum foil packet and the packets were piled up in a pure aluminum (99.5% Al) irradiation capsule (9 mm diameter and 30 mm long). The irradiation capsule was partitioned into 3 compartments to minimize the uncertainty of the sample positions at irradiation. The irradiation capsule was wrapped with 0.5 mm-thick Cd-foil before irradiation. The capsule was irradiated 2 hours at 5MW in Hyd facility of KUR. Analyses were conducted using  $^{40}\text{Ar}/^{39}\text{Ar}$  geochronology facility at the Geological Survey of Japan/AIST following the analytical procedure described in [1].

For the experiments described here, around 15 mg of sample was analyzed in each analysis. Due to alteration of poorly-crystallized part groundmass, basaltic samples were treated at 100°C on hot plate with stirrer in 6N HCl for 60 minutes and then 6N HNO<sub>3</sub> for 60 minutes to remove possible alteration products (clays and carbonates) prior to irradiation. This procedure effectively separated and concentrated fresh plagioclase in groundmass and of microphenocryst. After this acid treatment, these separates were examined under binocular microscope before packed for irradiation.

**RESULTS:** Two basaltic samples recovered from the northern margin of the Palau Basin, southernmost part of the Philippine Sea plate, were studied. The West Philippine Basin and Palau Basin are supposed to have been the oldest oceanic basins in the Philippine Sea Plate. Accordingly, their origin and growth history can be a critical constraint on the tectonic reconstruction of the Philippine Sea Plate. These basins could have existed prior to the Izu-Bonin (Ogasawara)-Mariana arc (IBM arc), or formed as a consequence of subduction initiation along the IBM arc (e.g., backarc basins of the

IBM arc). However, due to the paucity of geological and geophysical data from these basins, their origin and history are yet unclear.

YK10-14 and YK13-08 cruises by R/V Yokosuka (investigated Palau Basin) and southern part of West Philippine Basin obtained crucial geological and geophysical data [2] for reconstruction of the Philippine Sea Plate. 12 dredge hauls and 4 Shinkai submersible dives were made during these cruises.  $^{40}\text{Ar}/^{39}\text{Ar}$  dating of dolerite sample from the Palau Basin crust exposed at the Mindanao Fracture Zone at c. 130°E gave a plateau age of 40.4 Ma. This result implies that the spreading of the Palau Basin was still going on at 40.4 Ma. This age is within an age range of active spreading of the West Philippine Basin.

This year we conducted  $^{40}\text{Ar}/^{39}\text{Ar}$  dating of basaltic samples from 2 locations in the eastern part of the basin along the Mindanao Fracture zone. Fig. 1 shows age spectra for the 2 analyses. Sample 6K1358R11, which was collected by Shinkai 6500 at 4564 m deep gave a plateau age comprising of 63.8% of released gas. YK10-14 D3R14, which was collected further east along the Mindanao Fracture Zone by dredging also gave a well-defined plateau comprising of 96.3% of released gas. The plateau ages shown here are still temporary age because flux monitor measurement has not been completed yet. However, these data strongly imply that the age of formation of the Palau Basin closely matches with that of West Philippine Basin, and this result is crucial for tectonic reconstruction of this area. Final ages will also allow us to determine the direction and rate of seafloor spreading when the Palau Basin formed.

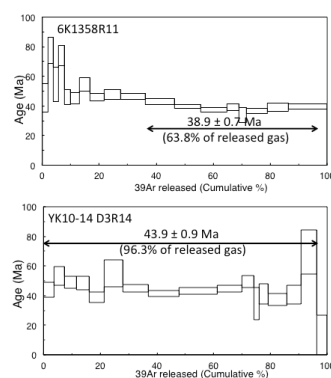


Fig. 1 Age spectra for the basalts from the Palau Basin.

### REFERENCE:

- [1] O. Ishizuka *et al.*, Chem. Geol., **266** (2009), 274-296.
- [2] Sasaki, T., Yamazaki, T., Ishizuka, O., (2014) Earth Planet. Space, 66:83, doi:10.1186/1880-5981-66-83.

採択課題番号 26P11-17  $^{40}\text{Ar}/^{39}\text{Ar}$  年代測定による日本周辺海域の火山活動史及び プロジェクト  
地殻構造発達史の解明

(産総研) 石塚 治 (京大・原子炉) 藤井 俊行、奥村 良、関本 俊

N. Hirano, H. Sumino<sup>1</sup>, T. Fujii<sup>2</sup>, R. Okumura<sup>2</sup>, S. Sekimoto<sup>2</sup>

Center for Northeast Asian Studies, Tohoku University

<sup>1</sup> Geochemical Research Center, Tokyo University

<sup>2</sup> Research Reactor Institute, Kyoto University

**INTRODUCTION:** Most of seamounts on the western Pacific Plate formed before 70 Ma in the so-called West Pacific Seamount Province (WPSP) which is characterized by relatively short seamount chains maybe indicating a significant short-lived hotspot system [1]. The geochronological studies of each Cretaceous seamount, on the other hand, show the long-lived main shield stage of volcanism, because a seamount remained above a hotspot for a long time (approximately 10 m.y. [2]). This may be attributed to either of the following two possibilities: 1) An abundant heat supply as in the superplume episode in the Early Cretaceous [3][4][5]. 2) Slow absolute motion of the Early Cretaceous Pacific Plate (3–6 cm/yr.) [6][7].

The research cruise using R/V *Yokosuka* equipped with the submersible *SHINKAI 6500*, was conducted around the Minamitorishima Island on May 2010 in order to know the detail history during the formation of the island, where volcanic rock samples have never been obtained before (Fig. 1). The shipboard multibeam acoustic surveys showing the detail bathymetry discovered the volcanic cones on seamount slope and the clusters of small conical volcanoes on surrounding abyssal plain (Oikawa and Morishita, 2009). Most of cones are several hundred meters in height and 1–10 km in diameter. We observed the stratigraphy of Minamitorishima using the submersible *SHINKAI 6500*. Highly vesicular lavas were sampled at the volcanic cone on the seamount slope. The olivine-bearing dense lavas, on the other hand, were obtained at the steep slope beneath the lava platform in bathymetry, implying main-shield stage lavas in contrast to volcanic cones probably erupted at the rejuvenated stage during the Minamitorishima's formation.

**EXPERIMENTS:** Radiometric Ar–Ar dating is commonly used to determine the ages of submarine lavas, because the traditional K–Ar dating is impossible to remove the alteration part in such rocks [8]. The rock-samples prepared for dating were crushed to 100–500 μm grains, and leached by the 1N HNO<sub>3</sub> at 70–60 °C for one hour. The leached samples were irradiated by neutrons in a reactor to produce <sup>39</sup>Ar from <sup>39</sup>K during a few hours. During the irradiation, samples were packed with EB-1 biotite flux monitors [9], K<sub>2</sub>SO<sub>4</sub> and CaF<sub>2</sub> as correcting factors in an aluminum capsule. They are shielded by Cd foil in order to reduce neutron-induced <sup>40</sup>Ar from <sup>40</sup>K [10]. Then, radiogenic <sup>40</sup>Ar, daughter nuclide of radioactive <sup>40</sup>K and parent, <sup>39</sup>Ar in-

stead of <sup>40</sup>K, were simultaneously analyzed using a mass-spectrometer with an extraction technique of multi-step heating of approximately every 50 to 100 °C between 500 to 1500 °C.

**RESULTS:** The irradiations of sample in KUR were done in May, 2014. We are going to analyze the irradiated samples after cooling. We note that the Minamitorishima is just only “island” in WPSP in spite of many of larger volcanic edifices of seamount and guyot than Minamitorishima. We have a hypothesis of different process and age to make the island in WPSP, awaiting future analytical results

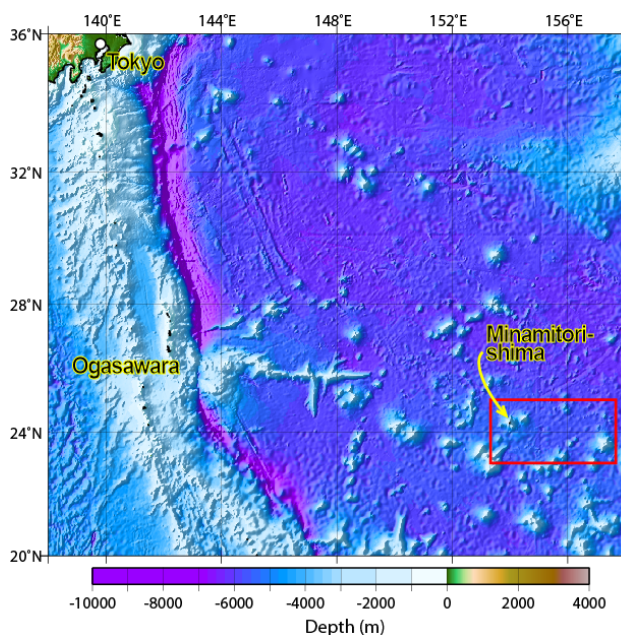


Fig. 1. Bathymetric map of Western Pacific.

#### REFERENCES:

- [1] A. A. P. Koppers *et al.*, *Geochem. Geophys. Geosyst.*, **4** (2003) DOI | 10.1029/2003GC000533
- [2] N. Hirano *et al.*, *Marine Geol.*, **189** (2002) 371-379.
- [3] K. G. Cox, *Nature*, **352** (1991) 564-565.
- [4] R. L. Larson, *Geology*, **19** (1991) 547-550.
- [5] R. L. Larson and C. Kincaid, *Geology*, **24** (1996) 551-554.
- [6] R. A. Duncan and D. A. Clague, in *The ocean basins and margins*, 89-121 (New York, Plenum, 1985)
- [7] J. W. Henderson *et al.*, *Tectonics*, **3** (1984) 121-132.
- [8] I. McDougall and T. M. Harrison, in *Geochronology and Thermochronology by the <sup>40</sup>Ar/<sup>39</sup>Ar Method*, (Oxford, New York, 1988).
- [9] N. Iwata, Ph.D. Thesis, Tokyo Univ. (1998).
- [10] K. Saito, *Sci. Rep. Res. Inst. Tohoku Univ. (RITU), Japan* **A40** (1994) 185-189.

採択課題番号 26P11-18 新種の火山のメカニズムを解明するための <sup>40</sup>Ar/<sup>39</sup>Ar 年代測定 プロジェクト  
(京大・原子炉) 藤井俊行、関本俊、奥村良 (東大院・理・地殻化学実験施設) 角野浩史、(東北大・東北アジア研究センター) 平野直人

Y. Ohkubo

*Research Reactor Institute, Kyoto University*

### Objective and Participating Research Subjects

The main objectives of this project research are the investigation of the nuclear structure of unstable neutron-rich nuclei and also the local properties of materials using short-lived nuclei.

This period is the first year of the project. Unfortunately, no experiments in all six research subjects of the project (26P12) were executed owing to the suspension of the reactor operation. Here, we report some results which were obtained in previous periods and have already been published in journals.

The research subjects (PRS) reported here are as follows:

PRS-1  $\beta^-$  Decay of  $^{150}\text{Ce}$  to  $^{150}\text{Pr}$

PRS-2 Interaction between He and Elements with  $A = 140$  in Fe

PRS-3 Atmosphere Dependence of Stability of Local Fields in Al-Doped ZnO

PRS-4 Extranuclear Dynamic Motion of  $^{111}\text{Cd}(\leftarrow ^{111}\text{Ag})$  Doped in AgI Nanoparticles

### Main Results and Contents of This Report

At KUR-ISOL (the on-line isotope separator installed at the Kyoto University Research Reactor), Y. Kojima *et al.* (PRS-1) studied the  $\beta^-$  decay of  $^{150}\text{Ce}$  having a half-life of 6.05(7) s produced by the thermal-neutron-induced fission of  $^{235}\text{U}$ . From  $\gamma$ -ray singles and  $\gamma$ - $\gamma$  coincidence measurements, they newly found 9 excited states and 37  $\gamma$ -rays and constructed a decay scheme containing 18 excited states and 55  $\gamma$ -rays which include the newly found excited states and  $\gamma$ -rays. They concluded that the dominant  $\beta$ -feeding at the 110-keV excited state of  $^{150}\text{Pr}$  arising from the  $\beta^-$  decay of  $^{150}\text{Ce}$  to be an allowed unhindered spin-flip transition. They furthermore proposed the Nilsson configurations of the ground state and the 110-keV excited state of  $^{150}\text{Pr}$ . A part of the results are described in the next page.

In order to examine whether Ce (or rather, La and Ba) and He form complexes having a definite geometrical structure in Fe as suggested in first-principles density functional theory calculations, Y. Ohkubo *et al.* (PRS-2) projected 100-keV  $^{140}\text{Cs}^+$  at KUR-ISOL and then 4-keV  $\text{He}^+$  using an ion beam gun into an Fe foil and took time-differential perturbed-angular-correlation (TDPAC) spectra at room-temperature of  $^{140}\text{Ce}$  arising through  $^{140}\text{Ba}$ - $^{140}\text{La}$  from  $^{140}\text{Cs}$  in He-doped Fe, unannealed and

annealed in vacuum at various temperatures. They observed no clear signal of such complexes in the TDPAC spectra. However, the TDPAC spectra indicate that Ce and He form complexes having a variety of geometrical structures. Comparison with TDPAC results reported by another research group on  $^{111}\text{Cd}$  arising from  $^{111}\text{In}$  in He-doped stainless steel shows that the parent atoms (La and Ba) of  $^{140}\text{Ce}$  trap He atoms more efficiently than In atoms do, indicating stronger bonding of He to the former atoms, while different from the present case,  $^{111}\text{Cd}$  (In)-He complexes form a unique geometrical structure. A part of the results are described in the following second page.

S. Komatsuda *et al.* (PRS-3) investigated thermal behavior and interacting nature of 100-ppm Al and ~100-ppt In impurities doped in a semiconductor ZnO by means of the TDPAC technique with the  $^{111}\text{In}(\rightarrow ^{111}\text{Cd})$  probe. They observed the following contrasting interactions between Al and In impurities depending on different atmospheric conditions: (1) in air, Al and In impurities irreversibly associate with each other in the process of thermal diffusion of these two species, but (2) in vacuum, these bound states formed in air dissociate by heat treatment at temperature higher than 873 K, and the dissociation reaction is enhanced with increasing temperature. Considering that the dissociation is triggered by the oxygen vacancy formation near the locally associated In-Al structure and using the TDPAC data obtained, they estimated the activation energy of the oxygen-vacancy formation to be 0.72(6) eV. A part of the results are described in the following third page.

Superionic conductivity observed for AgI emerges only at the high-temperature ( $\geq 420$  K)  $\alpha$  phase because of temperature-dependent crystal structures, which is a barrier to the practical applications of this compound. Recently, this problem was attacked by a novel technique: powder AgI coated with poly-N-vinyl-2-pyrrolidone (PVP) can drastically enhance the ionic transport property at room temperature. W. Sato *et al.* (PRS-4) studied dynamic behavior of the extranuclear field relative to the  $^{111}\text{Cd}(\leftarrow ^{111}\text{Ag})$  probe nucleus incorporated in AgI, using the TDPAC method. For PVP-coated AgI nanoparticles, they observed nuclear spin relaxation of the probe at room temperature, which indicates that  $\text{Ag}^+$  ions in the PVP-coated sample make hopping motion from site to site at this low temperature. From the TDPAC data obtained, they estimated the activation energy for the dynamic motion to be 46(10) meV. A part of the results are described in the following fourth page.



Y. Kojima, K. Kosuga<sup>1</sup>, Y. Shima<sup>2</sup>, A. Taniguchi<sup>3</sup>,  
H. Hayashi<sup>4</sup> and M. Shibata

Radioisotope Research Center, Nagoya University

<sup>1</sup>School of Engineering, Nagoya University

<sup>2</sup>Graduate School of Engineering, Nagoya University

<sup>3</sup>Research Reactor Institute, Kyoto University

<sup>4</sup>Institute of Biomedical Science, The University of Tokushima Graduate School

**INTRODUCTION:** Decay data provide valuable information about unstable nuclides. In particular, the  $\beta$ -branching ratio  $I_\beta$  is one of the most important properties from the nuclear structure viewpoint. For even-even  $^{150}\text{Ce}$ , Fogelberg *et al.* briefly reported an intense  $\beta$ -transition to the 110-keV level in  $^{150}\text{Pr}$  [1]. If this  $\beta$ -feeding is an allowed unhindered transition, it will lead to the assignment of the Nilsson orbital for  $^{150}\text{Pr}$ . However, it is uncertain whether this transition is firmly an allowed unhindered transition because of the following reasons. First, ref. [1] did not provide detailed experimental data on  $^{150}\text{Ce}$ . Second, the other published data for  $^{150}\text{Ce}$  are very scarce and partly inconsistent with each other [2,3]. In the present work, decay studies on  $^{150}\text{Ce}$  have been performed using the on-line isotope separator at KUR (KUR-ISOL) [4] to investigate low-energy level structures in  $^{150}\text{Pr}$ . Note that this work was recently published [5]. This report is an outline of the paper.

**EXPERIMENTS:** The  $^{150}\text{Ce}$  nuclides were produced by the thermal neutron induced fission of  $^{235}\text{U}$ . The mass-separated source was periodically moved to a detector port with time intervals of 12.2 s.

Time-dependent  $\gamma$ -ray singles and  $\gamma$ - $\gamma$  coincidence measurements were performed with two Ge detectors in a measurement period of 46 h. The energy and efficiency calibrations were made using standard  $\gamma$ -ray sources.

**RESULTS:** The half-life and coincidence relationships with the Pr KX-ray were analyzed to assign the parent nuclide of each  $\gamma$ -ray observed in this work. From these analyses, 57  $\gamma$ -rays including 39 new  $\gamma$ -transitions were found to be due to the decay of  $^{150}\text{Ce}$ .

Energy spectra gated on the  $\gamma$ -rays from  $^{150}\text{Ce}$  were analyzed to establish  $\gamma$ -ray cascade relations. For example, Fig. 1 is a spectrum gated on the 110-keV  $\gamma$ -ray. This spectrum shows that the 110-keV  $\gamma$ -ray is coincident with 13  $\gamma$ -rays. From these cascade relations and also from energy sum rules, the excited levels in  $^{150}\text{Pr}$  and the  $\gamma$ -ray placements were unambiguously proposed. The decay scheme includes 18 excited levels. Nine levels of them were newly proposed. The 717-keV level seen in ref. [3] was not observed in this work.

The  $\gamma$ -ray intensities relative to that of the 110-keV tran-

sition were deduced from peak counts observed in the singles spectrum or in coincident spectrum. Multipolarities of three  $\gamma$ -rays were also estimated from the intensity ratio between KX and  $\gamma$ -ray peaks observed in the coincident spectrum:  $M1/E2$  for the 103- and 154-keV  $\gamma$ -rays, and  $E1$  for the 110-keV  $\gamma$ -ray.

Finally, the  $I_\beta$  and  $\log-ft$  values were calculated from the transition intensity ( $\gamma$  and conversion electron) imbalance for each excited level. A small  $\log-ft$  value of 4.9 was observed for the 110-keV level. It leads to spin-parity  $J^\pi = 1^+$  for this level.

**DISCUSSION:** The very intense  $\beta$ -feeding to the 110-keV level is an allowed transition, and should be explained by selection rules for  $\beta$ -decays of deformed nuclei [6]. Near the Nilsson orbitals observed in the neighboring nuclides, only the spin-flip transition between  $\nu 3/2^- [532]$  and  $\pi 5/2^- [532]$  satisfies the selection rules. Thus, this  $\beta$ -transition is interpreted as one of the coupled neutron in  $3/2^- [532]$  orbital in  $^{150}\text{Ce}$  changing to a proton in the vacant  $5/2^- [532]$  orbital in  $^{150}\text{Pr}$ . This configuration yields  $J^\pi = 1^+$ , and agrees with our spin-parity assignment. The configuration of  $\pi 5/2^+ [413]-\nu 3/2^- [521]$  was also proposed for the ground state of  $^{150}\text{Pr}$  from the systematics of the neighboring nuclides and from coupling rules.

**CONCLUSIONS:** A detailed decay scheme of  $^{150}\text{Ce}$ , which includes 37 new  $\gamma$ -rays and 9 new excited levels, was proposed from  $\gamma$ -ray measurements. On the basis of the systematics and observation of the allowed spin-flip transition, the Nilsson configurations were newly proposed for the ground and 110-keV level in  $^{150}\text{Pr}$ .

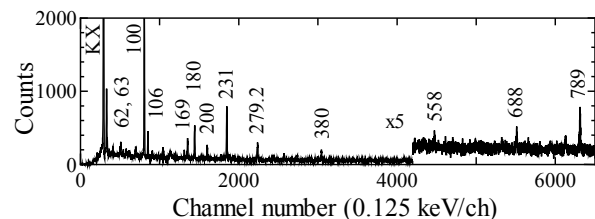


Fig. 1. A  $\gamma$ -ray spectrum gated on the 110-keV  $\gamma$ -transition. Coincident  $\gamma$ -rays are indicated with their energies in units of keV.

#### REFERENCES:

- [1] B. Fogelberg *et al.*, Nucl. Phys. A **453** (1986) 15-25.
- [2] K. Yamauchi *et al.*, KURRI-KR-3 (1996), pp.51-53 (in Japanese).
- [3] K. S. Basu *et al.*, Nucl. Data Sheets **114** (2013) 435.
- [4] A. Taniguchi *et al.*, Nucl. Instr. and Meth. A **351** (1994) 378-382.
- [5] Y. Kojima *et al.*, J. Phys. Soc. Jpn. **84** (2015) 054201/1-8.
- [6] G. Alaga, Phys. Rev. **100** (1955) 432-433.

採択課題番号 26P12-3 核分裂生成物に対する $\gamma$ 線直線偏光度測定を中心とした プロジェクト  
核分光実験

(名大・RI) 小島康明、柴田理尋 (名大院・工) 嶋 洋佑、常少亮太 (名大・工) 小菅数人  
(徳島大・医) 林 裕晃 (京大・原子炉) 谷口秋洋

Y. Ohkubo, A. Taniguchi, Q. Xu, M. Tanigaki and K. Sato

Research Reactor Institute, Kyoto University

**INTRODUCTION:** As far as we know, the state of impurities He and Ce in Fe has not been studied experimentally until our recent work [1]. This knowledge is important in materials science related to nuclear fusion reactor materials. With a nuclear spectroscopic technique, the time-differential perturbed angular correlation (TDPAC) technique, we obtained the result that the parent atoms (La and Ba) of  $^{140}\text{Ce}$  very efficiently trap He and they form complexes in Fe, which do not have a definite geometrical structure. The present report describes the latter result. See [1] for the full description.

**EXPERIMENTS:** 100-keV  $^{140}\text{Cs}^+$  ( $\sim 1.4 \times 10^{12}/0.2 \text{ cm}^2$ ) were projected into an Fe foil at KUR-ISOL.  $^{140}\text{Cs}$  decays through  $^{140}\text{Ba}$  and then  $^{140}\text{La}$  to  $^{140}\text{Ce}$ . We name this sample  $^{140}\text{CeFe}$ . Three additional samples were prepared using the  $^{140}\text{CeFe}$ . The first, second and third were prepared by projecting 4-keV  $\text{He}^+$  of  $\sim 4 \times 10^{13}$ ,  $\sim 5 \times 10^{14}$  and  $\sim 2 \times 10^{16}/\text{cm}^2$  in this sequence into the  $^{140}\text{CeFe}$ . We name them He-doped(1) $^{140}\text{CeFe}$ , He-doped(2) $^{140}\text{CeFe}$  and He-doped(3) $^{140}\text{CeFe}$ , respectively. The profile of the He concentration in Fe overlaps that for  $^{140}\text{Cs}$ . Room-temperature TDPAC spectra of  $^{140}\text{Ce}$  were taken for these four samples.

**RESULTS:** Fig. 1 (from top to bottom) shows the TDPAC spectra obtained at room temperature for  $^{140}\text{CeFe}$ , He-doped(1) $^{140}\text{CeFe}$ , He-doped(2) $^{140}\text{CeFe}$  and He-doped(3) $^{140}\text{CeFe}$ , all four with no annealing. The top spectrum is the one appearing in [2]. As explained there, the oscillation pattern seen in the spectrum is due to a unique static magnetic hyperfine interaction at  $^{140}\text{Ce}$  occupying the Fe substitutional site with no lattice defects nearby (the Larmor frequency equals 1.927(7) Grad/s). Hereafter, we call these  $^{140}\text{Ce}$  "good"  $^{140}\text{Ce}$ . From the value of the amplitude of the oscillation, "good"  $^{140}\text{Ce}$  are only about 30% of the  $^{140}\text{Ce}$  implanted in Fe. In Fig. 1 are also shown the characteristic values for each oscillation component seen in the TDPAC spectra. As the dose of He increases to  $\sim 5 \times 10^{14}/\text{cm}^2$ , the oscillation amplitude gets reduced more and more (note that the amplitude is not damped with time), and at the dose of  $\sim 2 \times 10^{16}/\text{cm}^2$  (He-doped(3) $^{140}\text{CeFe}$ ) no clear oscillation is observed. The dose of  $2 \times 10^{16}/\text{cm}^2$  corresponds to 0.15 dpa (displacement per atom) at the maximum. This large number may imply that He ions directly displace the parent atoms of "good"  $^{140}\text{Ce}$  from the substitutional sites. However, based on the fact that the oscillation amplitude is reduced by as much as  $\sim 50\%$  even for the

He-doped(1) $^{140}\text{CeFe}$  ( $\sim 4 \times 10^{13}/\text{cm}^2$  He corresponding to only 0.0003 dpa), it is unlikely for He ions to directly displace them. We think that He atoms diffused and bonded to the parent atoms of "good"  $^{140}\text{Ce}$  (interstitial He atoms diffuse much more easily than vacancies: the corresponding calculated activation energies are 0.06 and 0.68 eV, respectively). As the dose of He increases, the number of the parent atoms of "good"  $^{140}\text{Ce}$  decreases. If  $^{140}\text{Ce}$ -He complexes take one or a few definite geometrical structures, these would be reflected in the TDPAC spectra and it may be possible to determine whether He atoms are at substitutional or interstitial sites. The observation that the oscillation amplitude is only reduced but not damped with time under the He implantation indicates that  $^{140}\text{Ce}$ -He complexes take a variety of geometrical structures, accordingly these  $^{140}\text{Ce}$  bonded by He feeling various electric field gradients due to He. It is natural to think that many He atoms surround the parent atom and that there is a distribution of the number of He atoms attached to it.

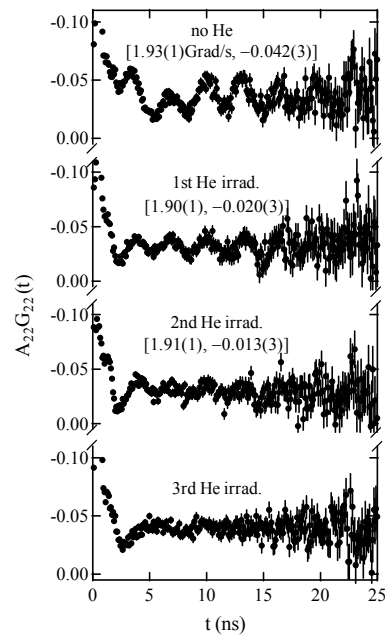


Fig. 1. Room-temperature TDPAC spectra for  $^{140}\text{CeFe}$  before He irradiation, He-doped(1) $^{140}\text{CeFe}$ , He-doped(2) $^{140}\text{CeFe}$ , and He-doped(3) $^{140}\text{CeFe}$ , all with no annealing. The two values in the square brackets in each panel are the Larmor frequency (Grad/s) and the amplitude of the oscillation component.

#### REFERENCES:

- [1] Y. Ohkubo, A. Taniguchi, Q. Xu, M. Tanigaki and K. Sato, *Phil. Mag. Lett.* **94**, 470-477 (2014).
- [2] Y. Ohkubo, A. Taniguchi, Q. Xu, M. Tanigaki, N. Shimizu and T. Otsuka, *Phys. Rev. C* **87**, 044324 (2013).

## PR12-3 Atmosphere Dependence of Stability of Local Fields in Al-Doped ZnO

S. Komatsuda, W. Sato<sup>1</sup> and Y. Ohkubo<sup>2</sup>

Department of General Education, National Institute of Technology, Ichinoseki College

<sup>1</sup>Institute of Science and Engineering, Kanazawa University

<sup>2</sup>Research Reactor Institute, Kyoto University

**INTRODUCTION:** Impurity-induced properties emerging in ZnO has been attracting increasing attention toward its application to functional materials in a wide field of industry. For a practical use of ZnO as a conduction-controlling device, it is of great importance to study the physical and chemical states of doped impurities and/or oxygen vacancies. From this point of view, we have investigated the factors determining the local structures and their stability of Al-doped ZnO samples synthesized on different conditions by means of the time-differential perturbed angular correlation (TDPAC) method. In a series of our TDPAC studies, drastic change of the local structure was observed for Al-doped ZnO sample heat-treated in vacuum [1,2]. In order to provide further insight into the above atmosphere dependence, in the present work, we performed an additional TDPAC measurement for 100 ppm Al-doped ZnO annealed under argon gas flow.

**EXPERIMENTS:** For the synthesis of 100 ppm Al-doped ZnO, stoichiometric amounts of  $\text{Al}(\text{NO}_3)_3 \cdot 9\text{H}_2\text{O}$  and ZnO powder were mixed in ethanol. The suspension was heated to evaporate the ethanol until dryness. The powder was pressed into two disks and sintered in air at 1273 K for 3 h. For TDPAC measurements, commercially available  $^{111}\text{In}$  solution was added in droplets onto the sintered disks at the concentration of 100 ppt. The disks again underwent heat treatment in air at 1373 K for 2 h. After that, a TDPAC measurement was performed for one of these samples prepared in air. The other sample was ground into powder and annealed under argon gas flow at 1373 K for 24 h. A TDPAC measurement was carried out for the  $^{111}\text{In}(\rightarrow^{111}\text{Cd})$  probe on the 171-245 keV cascade  $\gamma$  rays with the intermediate state of  $I = 5/2$  having a half-life of 85.0 ns.

**RESULTS:** Fig. 1 shows the TDPAC spectra of  $^{111}\text{In}(\rightarrow^{111}\text{Cd})$  probe in 100 ppm Al-doped ZnO annealed (a) in air and (b) in argon gas. The directional anisotropy on the ordinate,  $A_{22}G_{22}(t)$ , was deduced by the following relation for delayed coincidence events of the cascade:

$$A_{22}G_{22}(t) = \frac{2[N(\pi, t) - N(\pi/2, t)]}{N(\pi, t) + 2N(\pi/2, t)}$$

Here,  $A_{22}$  denotes the angular correlation coefficient,

$G_{22}(t)$  the time-differential perturbation factor as a function of the time interval,  $t$ , between the relevant cascade  $\gamma$ -ray emissions, and  $N(\theta, t)$  the number of the coincidence events observed at angle,  $\theta$ . The spectrum in Fig. 1(a) shows that 100 ppm Al and 100 ppt  $^{111}\text{In}$  are locally-associated in ZnO matrix, suggesting that there is a strong attractive force between Al and In in ZnO [1,2]. For the spectrum in Fig. 1(b), two different components were observed: one is that appearing in the spectrum in Fig. 1(a) and the other is that observed for undoped ZnO[3]. This observation implies that the probe gradually resides solely at the substitutional Zn site after annealing under argon gas in the same way as the case for the sample heat-treated in vacuum. These observations suggest that the drastic change of local structure formed by Al and In ions is closely related to the presence of  $\text{O}_2$  gas. In oxide compounds, in general, oxygen vacancies are likely to be formed during annealing process at a lower partial pressure of atmospheric oxygen. Therefore, it is suggested that the local association of Al and  $^{111}\text{In}$  becomes unstable in anaerobic atmosphere due to the formation of oxygen vacancies in the sample. For further information on the stability of the local structure, dependence of partial pressure of oxygen for the dissociation process needs to be investigated.

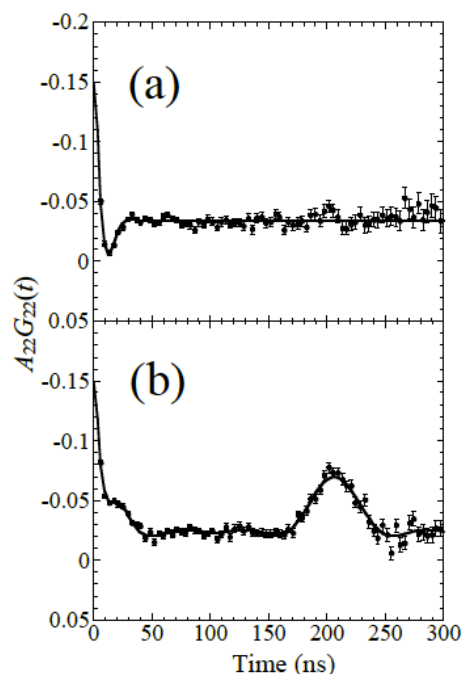


Fig. 1. TDPAC spectra of  $^{111}\text{In}(\rightarrow^{111}\text{Cd})$  in 100 ppm Al-doped ZnO annealed (a) in air and (b) in argon gas. The TDPAC measurements were performed at room temperature.

### REFERENCES:

- [1] S. Komatsuda *et al.*, J. Appl. Phys., **116** (2014) 183502/1-5.
- [2] S. Komatsuda *et al.*, J. Radioanal. Nucl. Chem., **303** (2015) 1249-1252.
- [3] W. Sato *et al.*, Phys. Rev. B, **78** (2008) 045319/1-5.

## PR12-4 Extranuclear Dynamic Motion of $^{111}\text{Cd}(\leftarrow^{111}\text{Ag})$ Doped in AgI Nanoparticles

W. Sato, R. Mizuuchi<sup>1</sup>, N. Irioka<sup>2</sup>, S. Komatsuda<sup>3</sup>, S. Kawata<sup>4</sup>, A. Taoka and Y. Ohkubo<sup>5</sup>

*Institute of Science and Engineering, Kanazawa University*

<sup>1</sup>*Graduate School of Natural Science and Technology, Kanazawa University*

<sup>2</sup>*School of Chemistry, Kanazawa University*

<sup>3</sup>*Department of General Education, National Institute of Technology, Ichinoseki College*

<sup>4</sup>*Department of Chemistry, Faculty of Science, Fukuoka University*

<sup>5</sup>*Research Reactor Institute, Kyoto University*

**INTRODUCTION:** Silver iodide, AgI, is a promising metal halide showing superionic conductivity as in its  $\alpha$  phase, and its application to functional materials such as solid electrolytes is thus highly expected. The conducting phenomenon, however, only emerges at elevated temperature ( $> 420$  K) because the crystal structure depends on temperature; this has indeed been a barrier to the practical applications of this compound.

Recently, an epoch-making technique has broken through this situation: powder AgI coated with poly-N-vinyl-2-pyrrolidone (PVP) can drastically enhance the ionic transport property at room temperature, recording the conductivity of  $1.5 \times 10^2 \Omega^{-1} \text{cm}^{-1}$  [1]. According to the report, this achievement is due to successful control of the particle size as small as nanoscale. In addition to the property in the bulk, it is of great importance to obtain complementary information on the site-to-site hopping motion of  $\text{Ag}^+$  ions on an atomic scale for a detailed understanding of ionic conductivity of this binary solid. For that purpose, in the present work, we have applied the time-differential perturbed angular correlation (TDPAC) technique with the  $^{111}\text{Cd}(\leftarrow^{111}\text{Ag})$  probe nuclei to observe dynamic behavior of  $\text{Ag}^+$  ions. We here report successful evaluation of the activation energy of the dynamic motion of  $\text{Ag}^+$  ions [2,3].

**EXPERIMENTS:** Pd foil was irradiated with thermal neutrons in Kyoto University Reactor to produce the TDPAC probe. After radioequilibrium was achieved between  $^{111}\text{Pd}$  and  $^{111}\text{Ag}$ , the Pd foil was dissolved in  $\text{HNO}_3$  aq. solution, and carrier-free  $^{111}\text{Ag}$  was isolated by an anion-exchange chromatography. The separated  $^{111}\text{Ag}$  was incorporated together in PVP-coated AgI sample when the powder sample was synthesized by precipitation of their raw materials. We confirmed by transmission electron microscopy that microscopic particles with sizes of 10-100 nm were expectedly synthesized for  $^{111}\text{Ag}$ -free PVP-coated AgI.

TDPAC measurements of the  $^{111}\text{Cd}(\leftarrow^{111}\text{Ag})$  probe

were performed for the synthesized sample at various temperatures. The directional anisotropy,  $A_{22}G_{22}(t)$ , was deduced with the following relation:

$$A_{22}G_{22}(t) = \frac{2[N(\pi, t) - N(\pi/2, t)]}{N(\pi, t) + 2N(\pi/2, t)}. \quad (1)$$

Here,  $A_{22}$  denotes the angular correlation coefficient,  $G_{22}(t)$  the time-differential perturbation factor as a function of the time interval,  $t$ , between the relevant cascade  $\gamma$ -ray emissions, and  $N(\theta, t)$  the number of the delayed coincidence events observed at an angle,  $\theta$ .

**RESULTS:** It was found that TDPAC spectra of the  $^{111}\text{Cd}(\leftarrow^{111}\text{Ag})$  probe introduced in PVP-coated AgI measured at different temperatures show exponential relaxation of the directional anisotropy, which signifies that the probe is dynamically perturbed by the extranuclear field. This phenomenon is understandable for the spectra of the sample as in the  $\alpha$  phase ( $> 420$  K). What is to be noted here is that the spectral relaxation was also observed even at room temperature. It was found from this observation that  $\text{Ag}^+$  ions surrounding the probe nuclei exhibit site-to-site hopping motion in the PVP-coated AgI nanoparticle even at this low temperature. Fig. 1 shows the temperature dependence of the relaxation constants. From a least-squares fit to the data with an Arrhenius-type equation, the activation energy,  $E_a$ , of the hopping motion was successfully estimated to be  $E_a = 46$  (10) meV. This value shows fair agreement with that obtained for the superionic conductivity:  $E_a = 60$  meV [1]. The present result is significant in that superionic conduction can be probed with local dynamics observed through nuclear spin relaxation.

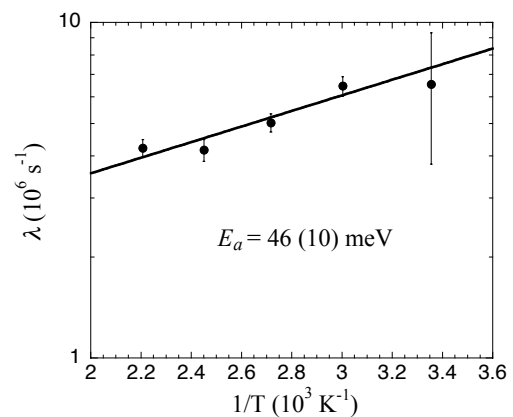


Fig. 1. Temperature dependence of the relaxation constant. The line is the result of a least-squares fit with an Arrhenius-type equation.

### REFERENCE:

- [1] R. Makiura *et al.* *Nature Mater.* **8** (2009) 476-480.
- [2] W. Sato *et al.* *Chem. Phys. Lett.* **609** (2014) 104-107.
- [3] W. Sato *et al.* *Hyperfine Interact.* **231** (2015) 107-113.

## PR13 Project Research on the Advanced Utilization of Multi-Element Mössbauer spectroscopy for the Study of Condensed Matter

M. Seto

Research Reactor Institute, Kyoto University

### OBJECTIVES AND PERFORMED RESEARCH

**SUBJECTS:** Mössbauer spectroscopy is a powerful and well established method in a wide variety of research areas, such as physical-, chemical-, biological-, and earth-sciences. As the Mössbauer resonance line is extremely narrow, hyperfine interactions are well resolved and give us the information on the surrounding electronic states and magnetism. The element specific information, which is one of the most superior features of the Mössbauer spectroscopy, is important and required for modern precise materials science and complex systems such as biological substances. Moreover, Mössbauer spectroscopy is useful and valuable because it usually does not demand the doping of radioactive sources for the measured samples; the decay of the unstable nucleus sometimes induces the unwanted change of local electronic states.

The main objectives of this project research are the investigation of the fundamental properties of new materials and the development of the advanced experimental methods by using multi-element Mössbauer spectroscopy under high-magnetic fields.

However, owing to the unexpected shutdown of the research reactor and the tracer laboratory for the long term, some of the planned researches have not been performed.

The research subjects performed are as follows:

- P13-2 Magnetism of an iron oxypnictide Cr-doped CeFePO (T. Okano *et al.*).
- P13-3 A study of formation of Au(III) surface complex on manganese dioxide by  $^{197}\text{Au}$  Mössbauer spectroscopy (T. Yokoyama *et al.*).
- P13-5 Mössbauer Spectroscopy of Novel Ferroelectric Materials (S. Nakamura, *et al.*).
- P13-6 Mössbauer spectra of oriented thin sections and small grain of magnetite single crystal (T. Kamiryo, *et al.*).
- P13-7 Electronic States of Negative/Zero Thermal Expansion Materials (I. Yamada *et al.*).
- P13-9 Mössbauer Study of Fe-Based Superconductors,  $\text{Ba}_{1-x}\text{K}_x\text{Fe}_2\text{As}_2$  (S. Kitao, *et al.*).

**MAIN RESULTS AND CONTENTS OF THIS REPORT:** The following reports were contributed by research groups in this project research.

T. Okano *et al.* (P13-2) have measured  $^{57}\text{Fe}$  Mössbauer spectra of Cr-doped CeFePO, for which they demonstrated a novel ferromagnetic QCP. From the obtained spectra, they showed that transition metal Cr substitution for Fe in CeFePO gradually generates a FM ordering of Ce sublattice and suppresses the ferromagnetic ordering by further doping, whereas Fe sublattice does not show magnetic ordering.

T. Yokoyama *et al.* (P13-3) performed  $^{197}\text{Au}$  Mössbauer spectroscopic study of manganese dioxides, and the information obtained from the analysis of the measured spectra indicated a formation of Au(III) surface complex on manganese dioxide.

To investigate the origin of the multiferroics and identify phase relation in the ferroelectric catalysis, S. Nakamura *et al.* (P13-5) studied spinel type  $\text{FeCr}_2\text{O}_4$  and  $\text{Sn}/\text{BaTiO}_3$  as multiferroics and ferroelectric catalysis, respectively. From the  $^{57}\text{Fe}$  Mössbauer spectrum of  $\text{FeCr}_2\text{O}_4$  at 4.2 K in applied magnetic field of 2T and the  $^{119}\text{Sn}$  Mössbauer spectrum of  $\text{Sn}/\text{BaTiO}_3$  specimen at room temperature, the electronic states relevant to multiferroics were discussed.

T. Kamiryo, *et al.* (P13-6) measured Mössbauer spectra of oriented thin sections of natural magnetite to observe the dependence of absorption peak intensities on the crystallographic orientation, and the proposed model were discussed to explain the result.

To develop zero thermal expansion (ZTE) materials, I. Yamada *et al.* (P13-7) studied the chemical substitution effect of cubic perovskite oxide  $\text{LaCu}_3\text{Fe}_4\text{O}_{12}$  on thermal expansion property by X-ray diffraction, thermal analysis, and Mössbauer spectroscopy, and the obtained results indicate that the unusual thermal expansion properties of  $\text{LaCu}_3\text{Fe}_{4-x}\text{Mn}_x\text{O}_{12}$  are associated with valence transitions of Fe ions.

To understand the nature of the Fe-oxypnictide superconductors, S. Kitao *et al.* (P13-9) studied the magnetic properties of the optimally-doped superconductor  $\text{Ba}_{0.6}\text{K}_{0.4}\text{Fe}_2\text{As}_2$ , and under-doped superconductor  $\text{Ba}_{0.8}\text{K}_{0.2}\text{Fe}_2\text{As}_2$  using Mössbauer spectroscopy. From the obtained spectra, the co-existence of magnetism and superconductivity was not observed in the optimally-doped  $\text{Ba}_{0.6}\text{K}_{0.4}\text{Fe}_2\text{As}_2$ . On the other hand, Mössbauer spectra of under-doped  $\text{Ba}_{0.8}\text{K}_{0.2}\text{Fe}_2\text{As}_2$  showed magnetic order below around 100 K, implying that the superconductivity and magnetic order co-exist.

T. Okano, M. Matoba, Y. Sakai, A. Sakurai, H. Fujioka, A. Wakatuki, K. Takeuchi, K. Nagamine, S. Kitao<sup>1</sup>, M. Seto<sup>1</sup>, and Y. Kamihara

Department Applied Physics and Physico-Informatics,  
Keio University

<sup>1</sup>Research Reactor Institute, Kyoto University

**INTRODUCTION:** A continuous phase transition, which is stimulated by an external pressure, magnetic field, and/or chemical doping at zero temperature, is called a quantum phase transition (QPT). The critical point of QPT is called a quantum critical point (QCP), where second-order phase transitions have been suppressed to zero from finite temperatures. QCPs have attracted much attention since some materials exhibit superconductivity in chemical compositions proximity to a QCP. [1–5] An iron oxypnictide CeFePO is a related compound of an iron-based superconductor LaFePO [6] CeFePO is also one of heavy-fermion materials with Ce 4f-electron's sublattice inducing Kondo screening. [7,8] In the case of Ruderman-Kittel-Kasuya-Yosida (RKKY) exchange interaction exceeding Kondo screening, long range magnetic order appears. While many Ce-based Kondo lattices show antiferromagnetic (AFM) ground states, only few systems are known with ferromagnetic (FM) order competing Kondo screening. In CeFePO, magnetic ordering is almost quenched and/or suppressed. [8] For Cr-doped CeFePO, we demonstrate a novel ferromagnetic QCP. [1] These ferromagnetic metals are of interest in view point of hyperfine interactions and important for their use in the determinations of nuclear magnetic dipole moments by a variety of methods including those based on low-temperature nuclear orientation.

**EXPERIMENTS:** Polycrystalline CeFe<sub>1-x</sub>Cr<sub>x</sub>PO ( $x = 0.000\text{--}0.692$ ) were prepared by a solid state reaction. Samples were characterized by X-ray diffraction (XRD), magnetization measurements, and <sup>57</sup>Fe Mössbauer spectroscopy (MS) at various temperatures. Magnetization measurements were performed on a superconducting quantum interference device (SQUID).

### RESULTS:

Almost all XRD diffraction peaks are assigned to calculated Bragg positions of the CeFePO phase with space group  $P4/mmm$  (No. 129), although there are several weak peaks which can be attributed to Cr<sub>2</sub>P, Ce<sub>2</sub>O<sub>3</sub>, and CeO<sub>2</sub>. These impurities provide no significant influence on magnetic measurements of CeFe<sub>1-x</sub>Cr<sub>x</sub>PO because it has been confirmed that they do not show ferromagnetic phase down to 2 K. Samples contained less than 1 at.% of Cr<sub>2</sub>P and 2 at.% of Ce<sub>2</sub>O<sub>3</sub> for  $x = 0.500$ . However, for  $x > 0.500$ , a ratio of Ce<sub>2</sub>O<sub>3</sub> phase increases rapidly and CeO<sub>2</sub> phase emerges. Figure 1 shows <sup>57</sup>Fe MS of  $x = 0.10$

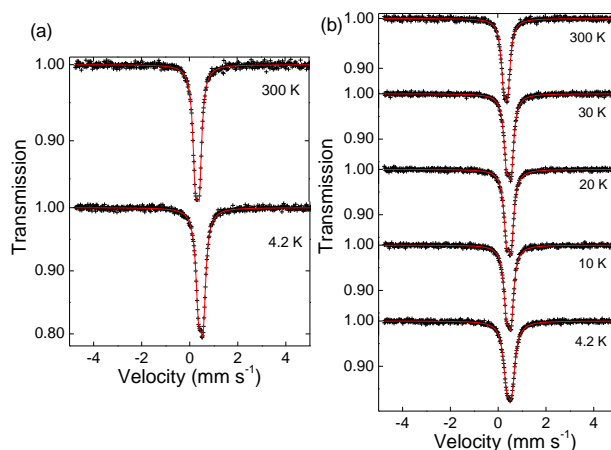


Fig. 1 Observed <sup>57</sup>Fe MS of  $x = 0.100$  (a),  $0.200$  (b) for CeFe<sub>1-x</sub>Cr<sub>x</sub>PO at several temperatures. Each solid line is a theoretical spectrum that includes a finite quadrupole splitting. All MS can be fitted with no magnetic splitting indicating paramagnetic phase of Fe sublattice.

and  $0.20$  for CeFe<sub>1-x</sub>Cr<sub>x</sub>PO from  $4.2$  K to  $300$  K. Our results show that transition metal Cr substitution for Fe in CeFePO gradually generates a FM ordering of Ce sublattice and suppresses the FM ordering by further doping, whereas Fe sublattice does not show magnetic ordering. The ground state of Ce 4f orbital in CeFePO is dependent on interlayer distances.[9] Arrott plot of the  $M$ - $H$  curves determines a ferromagnetic transition temperature ( $T_c$ ) for Cr-doped CeFePO. [1]

### REFERENCES:

- [1] T. Okano, S. Kitao, M. Seto, T. Atou, M. Itoh, M. Matoba, and Y. Kamihara, *J. Appl. Phys.*, 117 (2015) 17E123/1-4.
- [2] C. Krellner, K. S. Kini, E. M. Brüning, K. Koch, H. Rosner, M. Nicklas, M. Baenitz, and C. Geibel, *Phys. Rev. B*, 76 (2007) 104418.
- [3] E. M. Brüning, C. Krellner, M. Baenitz, A. Jesche, F. Steglich, and C. Geibel, *Phys. Rev. Lett.*, 101 (2008) 117206/1-4.
- [4] S. Doniach, *Physica B+C*, 91 (1977) 231-234.
- [5] K. Yoshida, A. Okiji, *Prog. Theor. Phys.*, 34 (1965) 505-522.
- [6] Y. Kamihara, H. Hiramatsu, M. Hirano, R. Kawamura, H. Yanagi, T. Kamiya, and H. Hosono, *J. Am. Chem. Soc.*, 128 (2006) 10012-10013.
- [7] T. Nakamura, T. Yamamoto, M. Matoba, Y. Einaga, and Y. Kamihara, *J. Phys. Soc. Jpn.*, 81 (2012) 064714/1-4.
- [8] S. Kitagawa, H. Ikeda, Y. Nakai, T. Hattori, K. Ishida, Y. Kamihara, M. Hirano, and H. Hosono, *Phys. Rev. Lett.*, 107 (2011) 277002/1-5.
- [9] S. Kitagawa, K. Ishida, T. Nakamura, M. Matoba, and Y. Kamihara, *J. Phys. Soc. Jpn.*, 82 (2013) 033704/1-4.

## A study of formation of Au(III) surface complex on manganese dioxide by $^{197}\text{Au}$ Mössbauer spectroscopy

T. Yokoyama<sup>1</sup>, Y. Okaue<sup>1</sup>, D. Kawamoto<sup>1</sup>, H. Ando<sup>1</sup>, H. Ohashi<sup>2</sup>, S. Kitao<sup>3</sup> and Y. Kobayashi<sup>3</sup>

<sup>1</sup>Faculty of Sciences, Kyushu University

<sup>2</sup>Faculty of Arts and Science, Kyushu University

<sup>3</sup>Research Reactor Institute, Kyoto University

**INTRODUCTION:** It is known that gold nanoparticles supported on metal oxide have been used as various oxidation-reduction catalysts. Gold catalyst made by deposition-precipitation (DP) method has been often used for catalytic study. However, it has been still poorly understood how Au(III) ions are precipitated on the surface of metal oxide. We have studied for Au(III) ions adsorption on the surface of metal oxide. In our study, we concluded that adsorbed Au(III) ions were not physically adsorption but chemical adsorption with surface complex (M—O—Au, M:metal). We did not prove straightforwardly the formation of Au(III) surface complex on metal oxide, which the aim of this study is to prove by means of  $^{197}\text{Au}$  Mössbauer spectroscopy.

**EXPERIMENTS:** Au(III) ion adsorbed on manganese oxide was prepared by batch method. Manganese dioxide (Chuo Denki Kogyo Co., Ltd.) was added into an aqueous solution of  $\text{HAuCl}_4$  under stirring and maintaining pH 6. The suspended solution was filtered with 0.45  $\mu\text{m}$  membrane filter.

The chemical state of gold in the solid samples obtained was determined by  $^{197}\text{Au}$  Mössbauer spectroscopy (home-made equipment). The  $^{197}\text{Pt}$  isotope ( $T_{1/2} = 18.3$  h),  $\gamma$ -ray source feeding the 77.3 keV Mössbauer transition of  $^{197}\text{Au}$ , was prepared by neutron irradiation of isotopically enriched  $^{196}\text{Pt}$  metal at the Kyoto University Reactor. The absorbers were particle specimens. The source and specimens were cooled with a helium refrigerator. The temperature of the specimens was in the range 8 – 15 K. The zero velocity point of the spectra was the peak point of pure bulk gold. The spectra for all the solid samples were fitted to a single Lorentzian function.

**RESULTS:** Figure 1 shows  $^{197}\text{Au}$  Mössbauer spectra of standard materials and Au(III) adsorbed on manganese dioxides. Figure 2 shows relative absorption area estimated from spectra in Fig.1 based on area of gold plate. The area is a measure of the recoilless fraction which is a function of the degree of fluctuation of Au nuclei (structural hardness). In Fig. 2, area of  $\text{KAuBr}_4$  is considerably smaller than that of  $\text{Au}_{\text{ad}}/\text{MnO}_2$ . The result suggests that Au nuclei in  $\text{KAuBr}_4$  can fluctuate more easily than that in  $\text{Au}_{\text{ad}}/\text{MnO}_2$ , deducing that the latter Au(III) ion

may be fixed tightly on the surface of  $\text{MnO}_2$  due to the formation of Au-O-Mn bond (surface complex).

In conclusion, information arising from the analysis of  $^{197}\text{Au}$  Mössbauer spectroscopy indicated Au(III) ion adsorbed chemically to form surface complexes before spontaneous reduction of the Au(III) to Au(0).

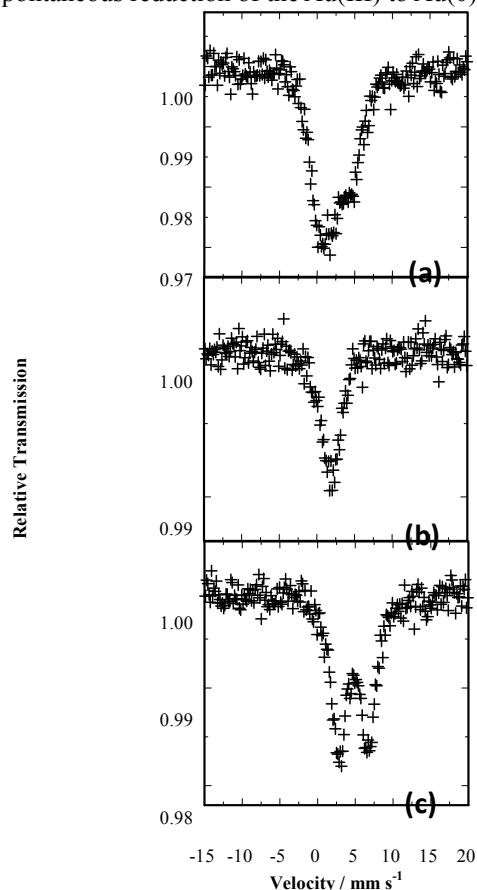


Fig. 1.  $^{197}\text{Au}$  Mössbauer spectra for  $\text{Au}_{\text{ad}}/\text{MnO}_2$ (a),  $\text{KAuBr}_4$ (b) and  $\text{AuMe}_2\text{acac}$ (c).

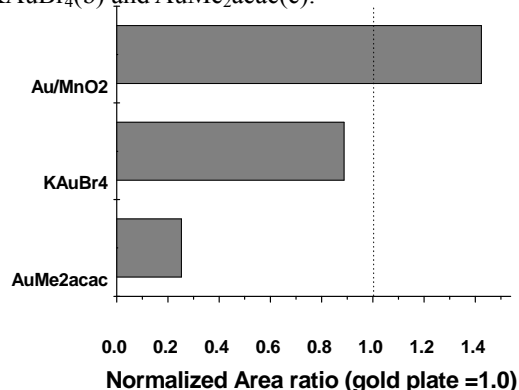


Fig. 2. Normalized area ratio of  $^{197}\text{Au}$  Mössbauer spectra for  $\text{AuMe}_2\text{acac}$ ,  $\text{KAuBr}_4$  and  $\text{Au}_{\text{ad}}/\text{MnO}_2$ .

S. Nakamura, J. Kano<sup>1</sup>, N. Oshime<sup>1</sup>, N. Ikeda<sup>1</sup>, Y. Kobayashi<sup>2</sup>, S. Kitao<sup>2</sup> and M. Seto<sup>2</sup>

Department of Science and Engineering, Teikyo University

<sup>1</sup>Graduate School of Natural Science and Technology, Okayama University

<sup>2</sup>Research Reactor Institute, Kyoto University

**INTRODUCTION:** Recently, novel materials related to ferroelectrics have attracted much interest. One example is multiferroics that has at the same time ferromagnetic (or antiferromagnetic) order and ferroelectric order. The other example is ferroelectric catalysis that is composed of metal nanoparticles supported on ferroelectric particles. In order to investigate the origin of the multiferroics, or identify phase relation in the ferroelectric catalysis, Mössbauer spectroscopy is a useful probe [1-6]. In this research, we deal with a spinel type  $\text{FeCr}_2\text{O}_4$  and  $\text{Sn/BaTiO}_3$  as multiferroics and ferroelectric catalysis, respectively.  $\text{FeCr}_2\text{O}_4$  reveals a ferrimagnetic order below around 70 K (tetragonal phase), followed by a spiral magnetic order below 35 K (orthorhombic phase). In the spiral magnetic state, a multiferroic state is expected. On the other hand,  $\text{Sn/BaTiO}_3$  is expected as a new catalyst for the exhaust emission. The phase relation of the supported Sn compound was not clear, because its amount is too little to be identified by usual X ray diffraction.

**EXPERIMENTS:** For  $\text{FeCr}_2\text{O}_4$ , a single crystal specimen of (100) platelet was used as an absorber. In order to obtain a single domain state in the low temperature phases, a slight compression along [001] axis was added by attaching epoxy resin on its both edges.  $^{57}\text{Fe}$  Mössbauer spectroscopy was conducted in conventional transmission geometry by using  $^{57}\text{Co}$ -in-Rh (50 mCi) as  $\gamma$  ray source. The spectrum was measured at 4.2 K with application of a magnetic field of 2 T. The direction of the  $\gamma$  ray and the magnetic field were parallel to the [100] axis. While for  $\text{Sn/BaTiO}_3$ , a powder specimen was used as an absorber.  $^{119}\text{Sn}$  Mössbauer spectroscopy was conducted by using  $^{119}\text{Sn}$ -in- $\text{CaSnO}_3$  (20 mCi) as  $\gamma$  ray source. The spectrum was measured at room temperature.

**RESULTS:** In Fig. 1,  $^{57}\text{Fe}$  Mössbauer spectrum of  $\text{FeCr}_2\text{O}_4$  at 4.2 K in applied magnetic field of 2 T is shown. The spectrum is composed of two subspectra, which indicates that the magnetic structure is not a simple cone spiral type. Although both magnetic moments lie approximately in the orthorhombic  $c$ -plain, one is directed along the  $a$ -axis (corresponding to the cubic [100]), whereas the other inclines about  $60^\circ$  from the  $a$ -axis. The observed fields ( $H_{\text{obs}}$ ) decrease by 2 and 1 T, respectively, due to the applied magnetic field. This is well consistent

with the estimated direction of the magnetic moments. Note that the quadrupole splitting  $e^2qQ/2$  changes from -3.11 ( $H_{\text{ex}} = 0$ ) to -3.23 mm/s ( $H_{\text{ex}} = 2$  T), which may be indicative of the multiferroicity of this material.

In Fig. 2,  $^{119}\text{Sn}$  Mössbauer spectrum of  $\text{Sn/BaTiO}_3$  specimen at room temperature is shown. The spectrum is composed of a quadrupole doublet with isomer shift of -0.015 mm/s and quadrupole splitting of 0.519 mm/s. Thus we can identify that the supported Sn is in the form of  $\text{SnO}_2$ . The absorption line width is rather large (0.879 mm/s), which is a result of a distribution in quadrupole splitting due to the particle size of nanometers.

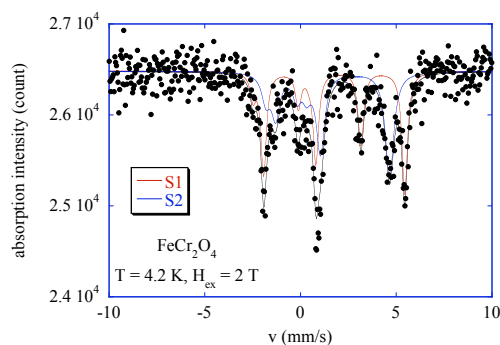


Fig.1  $^{57}\text{Fe}$  Mössbauer spectrum of  $\text{FeCr}_2\text{O}_4$  at 4.2 K

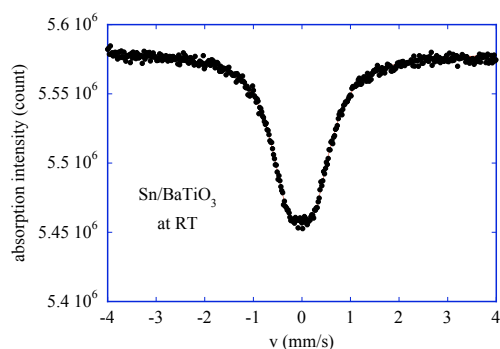


Fig. 2  $^{119}\text{Sn}$  Mössbauer spectrum of  $\text{Sn/BaTiO}_3$  specimen at room temperature

#### REFERENCES:

- [1] S. Nakamura *et al.*, J. Phys. Conf. Ser. **200**, 012140 (2010).
- [2] S. Nakamura *et al.*, J. Phys. Soc. Jpn. **83**, 044701 (2014).
- [3] S. Nakamura *et al.*, J. Phys. Soc. Jpn. **84**, 024719 (2015).
- [4] S. Nakamura *et al.*, J. Phys. Conf. Ser. **592**, 012122 (2015).
- [5] T. Okamoto *et al.*, Hyperfine Interactions **219**, 147-152 (2013).
- [6] J. Kano *et al.*, Jpn. J. Appl. Phys. **53**, 05FB24 (2014).



T. Kamiryo, K. Shinoda, Y. Kobayashi<sup>1</sup>

*Department of Geosciences,  
Graduate School of Science, Osaka City University  
<sup>1</sup>Research Reactor Institute, Kyoto University*

**INTRODUCTION:** We have made Mössbauer micro-spectrometer using a multi-capillary X-ray lens (MCX) and estimated beam size of  $\gamma$ -ray at the focus in order to measure Mössbauer spectra of a single crystal in petrographic thin sections (KURRI Progress Report 2013). As powdered crystals are generally used for conventional Mössbauer spectroscopy, anisotropy of crystal against incident  $\gamma$ -ray can be cancelled by random orientation of powders, and sextet peaks due to internal magnetic field are averaged into intensity ratio of 3:2:1:1:2:3. On the other hand, intensity ratio of sextet of single crystal depends on the crystal orientation. In this study, to observe crystallographic orientational dependence of sextet, Mössbauer spectra of oriented thin sections of natural magnetite were measured.

**EXPERIMENTS and RESULTS:** Two natural magnetite single crystals were prepared. Using X-ray precession camera, (100), (110) and (111) oriented thin sections were made for Mössbauer spectra measurements. Vacancy  $x$  ( $\text{Fe}_{3-x}\text{O}_4$ ,  $0 < x < 0.33$ ) of Brazil and Russia magnetites was estimated to approximately 0 and 0.2, respectively, from Mössbauer spectra. Peak fittings as two sets of sextet were done for 6 thin sections. Sextet of 49T and 46T magnetic fields are shown in table as  $\text{Fe}^{3+}$  and  $\text{Fe}^{2.5+}$ , respectively. Relative intensity in the table is that of the second peak (peak 2) against the third peak (peak 3) among separated 6 peaks. For powdered magnetites, the relative intensity of peak 2 is always 2. But they were deviated from 2 due to crystal anisotropy.

occurrence	index	$\text{Fe}^{2.5+}$	$\text{Fe}^{3+}$
Brazil	(100)	1.96	1.72
	(110)	2.70	2.31
Russia	(111)	2.86	2.56
	(100)	1.98	1.83
	(110)	2.73	2.64
	(111)	2.75	2.63

Table. Relative intensity of peak 2 against peak 3 among sextet of magnetite.

The following two models were discussed to explain this result. In the first model, supposing that magnetic domains with the easiest magnetization axis of crystallographically equivalent  $\langle 100 \rangle$  or  $\langle 110 \rangle$  or  $\langle 111 \rangle$  are present equally in oriented thin sections, the peak 2 ration were always 2 in all cases. This model is not consistent with this result. In the second model, supposing shape magnetic anisotropy, which means possibly high magnetic domains with the magnetized orientation parallel to the thin sections and low magnetic domains normal to the thin sections, this result can be explained only by the  $\langle 111 \rangle$  easiest magnetization axis. This is consistent with the general easiest magnetization axis of spinel ferrite.

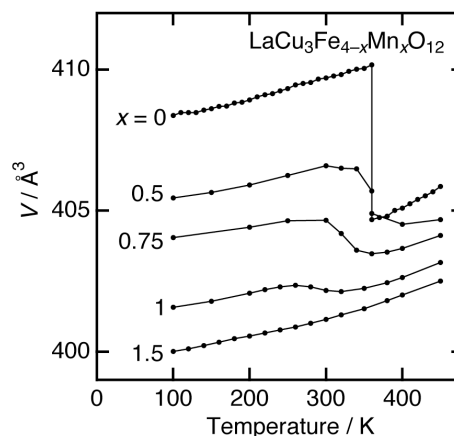
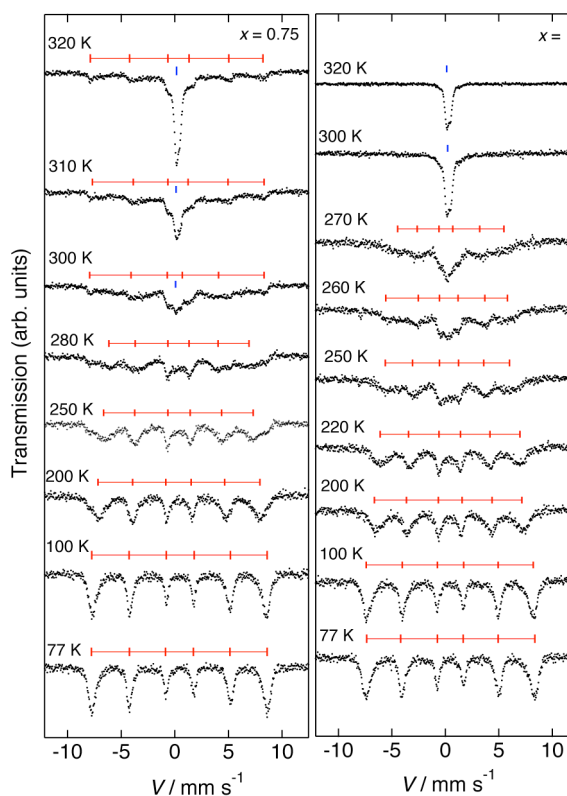
Mössbauer spectra measurements of small single grains of magnetite with MCX were not done, because the Tracer Laboratory was not opened for Mössbauer spectroscopy.

I. Yamada,<sup>1</sup> S. Marukawa,<sup>2</sup> S. Kitao<sup>3</sup>, and M. Seto<sup>3</sup><sup>1</sup>Research Institutes for the Twenty-First Century  
Osaka Prefecture University<sup>2</sup>Department of Chemistry, Osaka Prefecture University<sup>3</sup>Research Reactor Institute, Kyoto University

**INTRODUCTION:** Positive thermal expansion (PTE) is an essential property of materials. A limited number of materials shrink with heating, which is described as negative thermal expansion (NTE). NTE property contributes to development of zero thermal expansion (ZTE) materials, in which the thermal expansion coefficient is almost zero. ZTE materials are desired in a wide range of applications such as precise mechanics, optics, and electronics. We investigated the chemical substitution effect of cubic perovskite oxide  $\text{LaCu}_3\text{Fe}_4\text{O}_{12}$  on thermal expansion property by X-ray diffraction, thermal analysis, and Mössbauer spectroscopy. Eventually, we obtained almost ZTE in Mn-doped sample,  $\text{LaCu}_3\text{Fe}_{4-x}\text{Mn}_x\text{O}_{12}$  [1].

**EXPERIMENTS:**  $\text{LaCu}_3\text{Fe}_{4-x}\text{Mn}_x\text{O}_{12}$  samples were synthesized under high-pressure and high-temperature conditions of 15 GPa and 1473 K, respectively. Synchrotron X-ray powder diffraction (SXRD) data were collected at temperatures between 100 and 450 K at the BL02B2 beamline of SPring-8.  $^{57}\text{Fe}$  Mössbauer spectroscopy measurements were conducted at temperatures in transmission geometry using  $^{57}\text{Co}/\text{Rh}$  as a radiation source.

**RESULTS:** Fig. 1 shows temperature dependence of the unit cell volume for  $\text{LaCu}_3\text{Fe}_{4-x}\text{Mn}_x\text{O}_{12}$ . A systematic trend from abrupt volume expansion/shrinkage ( $x = 0-0.5$ ), NTE ( $x = 0.75$ ), ZTE ( $x = 1$ ), and PTE ( $x = 1.5$ ) was confirmed [1]. This indicates that the thermal expansion properties of this system are adjustable by chemical doping. Fig. 2 shows Mössbauer spectra of the  $x = 0.75$  and 1 samples collected at temperatures between 77 and 320 K. Nonmagnetic component are predominant above room temperature whereas magnetically split sextets are predominant at 77 K. The isomer shift values increased by  $\sim 0.05$  mm/s at magnetic transition temperatures, which is attributed to the Fe valence reduction by inter-site charge transfer ( $\text{Cu}^{2+} + \text{Fe}^{4+} \rightleftharpoons \text{Cu}^{3+} + \text{Fe}^{3+}$ ). These results indicate that the unusual thermal expansion properties of  $\text{LaCu}_3\text{Fe}_{4-x}\text{Mn}_x\text{O}_{12}$  are associated with valence transitions of Fe ions.

**REFERENCES:**[1] I. Yamada *et al.*, Appl. Phys. Lett., **105** (2014) 231906.Fig. 1. Temperature dependence of the unit cell volume for  $\text{LaCu}_3\text{Fe}_{4-x}\text{Mn}_x\text{O}_{12}$ .Fig. 2. Mössbauer spectra of  $\text{LaCu}_3\text{Fe}_{4-x}\text{Mn}_x\text{O}_{12}$  ( $x = 0.75, 1$ ).

S. Kitao, M. Kurokuzu, Y. Kobayashi, M. Saito, and M. Seto

Research Reactor Institute, Kyoto University

**INTRODUCTION:** After the discoveries of the so-called “1111” series of Fe-oxipnictide superconductors,  $\text{LaFePO}$ [1] and  $\text{LaFeAsO}_{1-x}\text{F}_x$ [2], several series of Fe-based superconductors have been successively discovered and extensively investigated to elucidate the mechanism of their superconductivity. Among the related Fe-based superconductors, the so-called “122” series has been found by K-doping (*i.e.* hole-doping) of  $\text{BaFe}_2\text{As}_2$ [3]. This series has become one of the main groups of Fe-based superconductors, since the various superconductors have been found not only by hole-doping but by electron-doping and even by isovalent doping. Such variety of superconductors provides complexity in the understanding of the mechanism of superconductivity, since the character of each Fe-based superconductor shows various different properties.

To promote the understanding of the superconducting mechanism, studies of their Fe magnetism is one of the main approaches, since it is supposed that the Fe acts as a key element and that the magnetism must relate to the superconductivity. To investigate the nature of its magnetism,  $^{57}\text{Fe}$ -Mössbauer spectroscopy is an essential method. Until today, a number of Mössbauer studies on these Fe-based superconductors have been carried out and revealed many important facts, for example, that the superconductivity and magnetic order do not co-exist in  $\text{LaFeAsO}_{1-x}\text{F}_x$ [4]. However, in  $\text{Ba}_{1-x}\text{K}_x\text{Fe}_2\text{As}_2$ , unlike  $\text{LaFeAsO}_{1-x}\text{F}_x$ , it is known that the superconductivity and magnetic order co-exist in some doping region of the under-doped  $\text{Ba}_{1-x}\text{K}_x\text{Fe}_2\text{As}_2$ [5].

In this study, a detailed temperature dependence of Mössbauer spectra was measured to investigate the magnetic properties of the parent compound,  $\text{BaFe}_2\text{As}_2$ , optimally-doped superconductor,  $\text{Ba}_{0.6}\text{K}_{0.4}\text{Fe}_2\text{As}_2$ , and under-doped superconductor,  $\text{Ba}_{0.8}\text{K}_{0.2}\text{Fe}_2\text{As}_2$ .

**EXPERIMENTS:**  $\text{BaFe}_2\text{As}_2$  was synthesized by heating of a stoichiometric mixture of ground Ba and FeAs in a crucible of aluminum oxide sealed in a quartz tube, as in the reported method[3]. K-doped  $\text{Ba}_{1-x}\text{K}_x\text{Fe}_2\text{As}_2$  was synthesized similarly, except that excess amount of K was added and heated in lower temperature. The obtained polycrystalline powder was characterized by x-ray diffraction and magnetic susceptibility measurements. The superconducting transition was observed in  $\text{Ba}_{0.6}\text{K}_{0.4}\text{Fe}_2\text{As}_2$  and  $\text{Ba}_{0.8}\text{K}_{0.2}\text{Fe}_2\text{As}_2$  at around 30 to 40 K.  $^{57}\text{Fe}$ -Mössbauer spectra were measured using a pellet of powder sample using a  $^{57}\text{Co}$  source in Rh matrix with a nominal activity of 1.85 GBq. The velocity scales are referenced to  $\alpha\text{-Fe}$ .

**RESULTS AND DISCUSSION:** Typical Mössbauer spectra for  $\text{BaFe}_2\text{As}_2$  are shown in Fig. 1. The magnetic transition was clearly observed by the temperature dependence of the Mössbauer spectra. The observed internal magnetic field reached around 5.4 T at 2.5 K. The magnetic transition was clearly observed at around 150 K. These values well agreed with the former report[5].

On the other hand,  $\text{Ba}_{0.6}\text{K}_{0.4}\text{Fe}_2\text{As}_2$  showed only a single peak spectrum down to 4 K, implying no magnetic transition occurs in optimally-doped superconductor. Thus, the co-existence of magnetism and superconductivity was not observed in the optimally-doped  $\text{Ba}_{0.6}\text{K}_{0.4}\text{Fe}_2\text{As}_2$ . This fact was similar to the “1111” compound,  $\text{LaFeAsO}_{1-x}\text{F}_x$ [4]. However, Mössbauer spectra in under-doped  $\text{Ba}_{0.8}\text{K}_{0.2}\text{Fe}_2\text{As}_2$  showed magnetic order below around 100 K, implying that the superconductivity and magnetic order co-exist in the under-doped  $\text{Ba}_{0.8}\text{K}_{0.2}\text{Fe}_2\text{As}_2$ . This co-existence in some of Fe-based superconductors is still one of the main controversial issues. Further Mössbauer study will be performed to investigate this issue.

#### REFERENCES:

- [1] Y. Kamihara, H. Hiramatsu, M. Hirano, R. Kawamura, H. Yanagi, T. Kamiya and H. Hosono, *J. Am. Chem. Soc.* **128** (2006)10012.
- [2] Y. Kamihara, T. Watanabe, M. Hirano and H. Hosono, *J. Am. Chem. Soc.* **130** (2008) 3296.
- [3] M. Rotter, M. Tegel, and D. Johrendt, *Phys. Rev. Lett.* **101** (2008) 107006.
- [4] S. Kitao, Y. Kobayashi, S. Higashitaniguchi, M. Saito, Y. Kamihara, M. Hirano, T. Mitsui, H. Hosono and M. Seto, *J. Phys. Soc. Jpn.* **77** (2008) 103706.
- [5] M. Rotter, M. Tegel, I. Schellenberg, F. M. Schappacher, R. Pöttgen, J. Deisenhofer, A. Günther, F. Schrettle, A. Loidl and D. Johrendt, *New J. Phys.* **11** (2009) 025014.

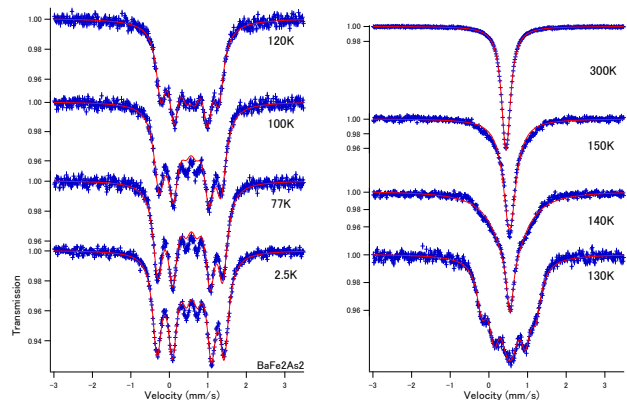


Fig. 1. Typical Mössbauer spectra of  $\text{BaFe}_2\text{As}_2$ .

M. Suzuki

*Research Reactor Institute, Kyoto University*

### Background and Objective

Using Kyoto University Research Reactor (KUR), patients with malignant tumors greater than 500 have been treated with boron neutron capture therapy (BNCT). Malignant brain tumors and head and neck cancers have been main malignancies treated with BNCT. Our laboratory (Division of Particle Radiation Oncology) has investigated the possibilities for new applications for BNCT. According to promising results in pre-clinical study, we have already treated some patients with liver cancers with BNCT and carried out clinical study on phase I study on BNCT for malignant pleural mesothelioma (MPM).

Promising clinical results of BNCT using the research reactor encouraged us to go to further stage of BNCT using an accelerator-based (AB) BNCT system. Co-operation of Kyoto University Research Reactor Institute and Sumitomo Heavy Industry have developed AB BNCT system with compact cyclotron as an accelerator. In 2012 and 2014, clinical studies on BNCT for recurrent malignant brain tumors and head and neck tumors to get an approval as a medical device from the Pharmaceuticals and Medical Devices Agency (PMDA), a Japanese regulatory agency. In a transition period from reactor-based (RB) BNCT into AB-based BNCT, many research issues should be dissolved from impending and long-term viewpoints.

Main objectives of our project is to dissolve many impending clinical issues to perform BNCT safely in AB-BNCT system and to investigate many research projects for many patients with cancer to be treated with AB-BNCT system.

### Research Subjects

To advance RB-BNCT into AB-BNCT, a lot of researchers in various research fields such as clinical radiation oncology, medical physics, pharmacology, boron chemistry, and accelerator engineering are needed to be involved in our research projects. In this viewpoint, this research project consists of three research subjects (RS) as follows,

RS1. Clinical studies on BNCT

RS2. Pre-clinical studies on physiological and pharmacological aspects of BNCT

RS3. Medical physics studies on BNCT.

### Main Results

Unfortunately, KUR has been unavailable since May in 2014. Many research subjects could not be performed.

#### RS1. Clinical studies on BNCT

Two research groups reported case reports treated with BNCT using KUR. Miyatake et al. reported a very important case report from a clinical viewpoint of new application of BNCT. In this report, radiation-induced osteosarcoma in the skull was successfully treated with BNCT. Kat et al, reported case reports of six patients with head and neck cancer.

Yanagie et al. reported the result of <sup>18</sup>F-boronophenylalanine (BPA) – positron emission tomography (PET) study which was taken by breast cancer patient with right supraclavicular lymph node metastasis and treatment planning study.

#### RS2. Pre-clinical studies on physiological and pharmacological aspects of BNCT

Nakamura et al. studied the effects of the counteractions of boron clusters on liposome formation to develop high boron content liposomes for BNCT by overcoming osmotic pressure limitations.

Gao et al. studied the therapeutic efficiency and suppression of the adverse effects of a novel boron-containing nanoparticles which were prepared by mixing a newly synthesized boron-cluster-containing anionic block copolymer and a redox cationic block copolymer.

Fujimoto et al. studied the efficiency and potential of BNCT for lung metastasis using the human clear cell sarcoma lung metastasis mouse model.

Tada et al. studied the feasibility of a boron-rich boron carbide (B<sub>4</sub>C) as a boron-including drug in BNCT for oral cancer using xenograft nude cancer-bearing mice.

Yanagie et al. performed preclinical BNCT study for VX-2 rabbit liver tumor model using borocaptate sodium (BSH) entrapped water-in-oil-in-water (WOW).

#### RS3. Medical physics studies on BNCT

Hayashi et al. studied the NMR response of the standard methacrylic-acid-based polymer gel (MAGAT) with and without boron and examined its availability to measure the depth-dose responses in the irradiation of neutron beams with different energy spectra from nuclear reactor.

Tanaka K et al. reported a calculational approach for measurement of the beam components such as thermal, epithermal, fast neutrons and gamma rays separately using twin imaging plate system.

Sakurai et al. studied the QA/QC in BNCT using ionization chamber and Bonner sphere in BNCT irradiation field.

Tanaka H et al. studied the prototype system of real-time boron concentration monitor.

## PR14-1 Boron Neutron Capture Therapy for Radiation-induced Osteosarcoma from the Skull

S. Miyatake, S. Kawabata, R. Hiramatsu, G. Futamura  
T. Kuroiwa, Y. Sakurai<sup>1</sup>, H. Tanaka<sup>1</sup>, A. Maruhashi<sup>1</sup>,  
M. Suzuki<sup>1</sup>, N. Kondo<sup>1</sup>, S. Masunaga<sup>1</sup>, Y. Kinashi<sup>1</sup> and  
K. Ono<sup>1</sup>

*Department of Neurosurgery, Osaka Medical College*  
*<sup>1</sup>Research Reactor Institute, Kyoto University*

**INTRODUCTION:** From March 2014 to May 2014, we applied boron neutron capture therapy (BNCT) for 11 lesions in KUR. The lesions were composed of 3 recurrent glioblastomas, 2 recurrent anaplastic astrocytomas, 4 high-grade meningiomas, 1 head and neck cancer and 1 recurrent osteosarcoma from the skull. We have already reported the effectiveness of BNCT for malignant gliomas, high-grade meningiomas and head and neck cancers, however, that for osteosarcoma is extremely rare and no report of BNCT was found for radiation-induced osteosarcoma. Therefore we introduce here the successful treatment of BNCT for radiation-induced osteosarcoma from the skull.

### Clinical Presentation:

A 54-year-old female was referred to our institute for treatment by BNCT of a recurrent radiation-induced osteosarcoma involving the left occipital bone. Ten years earlier, she was diagnosed with cancer of the uterine body and underwent resection surgery. Two years after that surgery, she underwent chemotherapy and whole-brain radiation therapy (WBRT, total 30 Gy with 10 fractions) including the cerebellum for brain metastasis. Six years after the WBRT, she was diagnosed with a radiation-induced osteosarcoma involving the left occipital bone, and she underwent resection surgery and successive chemotherapy using methotrexate. One year after that surgery and chemotherapy, the subcutaneous tumor appeared again in the left occipital region and rapidly enlarged over a period of only 3 months (Figure 1 A). Magnetic resonance images (MRI) showed the epidural tumor invasion (Figure 2 A and A'). Eventually, the patient could not walk because of acutely developing cerebellar ataxia. This tumor was diagnosed as a recurrence of the radiation-induced osteosarcoma. We performed BNCT for this radiation-induced osteosarcoma.

At one day after the BNCT, the patient's gait disturbance was aggravated. Computed tomography at that time showed aggravation of peri-lesional edema (data not shown). Remarkably, the MRI taken 4 days after the BNCT demonstrated the definitive shrinkage of the mass, but the left cerebellar edema was still there (Figure 2 B and B'). We then treated the edema with dehydrators and steroids. The symptoms gradually

improved.

At only 3 weeks after the BNCT, the patient was able to walk again stably without aid. The subcutaneous tumor was reduced dramatically without radiation injury of the scalp, with time after BNCT, as shown in Figure 1 B and C. The only adverse effect was hair loss in neutron-irradiation field, as shown in Figure 1 C. MRI showed the further reduction of tumor and the disappearance of the cerebellar edema (Figure 2 C and C'), 3 months after BNCT.

We experienced only a case of successful treatment of BNCT for radiation-induced osteosarcoma. Hopefully these potential therapeutic effects will be applicable for non-radiation-induced osteosarcomas which are generally refractory for other treatment modalities.

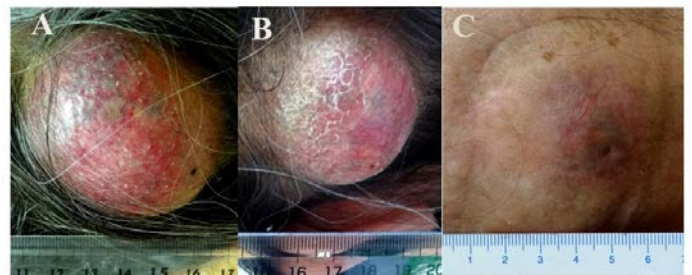


Figure 1. Marked improvement of the subcutaneous tumor at 3 weeks after the application of BNCT.

A: Just prior to the BNCT; B: Seven days after the BNCT; C: At 2 months after the BNCT,

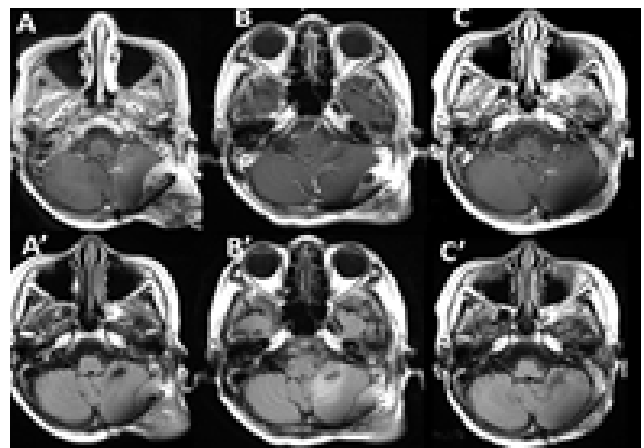


Figure 2. MRI of the patient's brain before and after the BNCT.

A,A': Just prior to BNCT

B,B': 4 days after BNCT

C,C': 3 months after BNCT

I. Kato, T. Iwagami<sup>1</sup>, N. Yamamoto<sup>2</sup>, Y. Fujita<sup>3</sup>, M. Ohmae<sup>4</sup>, M. Suzuki<sup>5</sup>, S. Masunaga<sup>5</sup>, H. Tanaka<sup>5</sup>, M. Nakazawa, T. Sumi, A. S. Iwai, Maruhashi<sup>5</sup>, K. Ono<sup>5</sup>, Y. Yura

Dept. of Oral &Max.fac. Surg. II, Grad. Sch. of Dent., Osaka Univ.

<sup>1</sup>Dept. of Oral &Max.fac. Surg., Han-nan Hosp.

<sup>2</sup>Dept. of Oral &Max.fac. Surg., Saiseikai-Senri Hosp.

<sup>3</sup>Dept. of Oral &Max.fac.Surg., Higashiosaka General Hosp.

<sup>4</sup>Oral &Max. fac. Surg., Rinku,General Med. Center

<sup>5</sup>Research Reactor Institute, Kyoto University

**INTRODUCTION:** We had first reported that six patients with head and neck cancer (HNC) had been treated with BNCT [1]. We also report long term (more than 5-year) clinical outcomes of our 26 patients with recurrent HNC treated with BNCT [2]. We summarized here the latest 6 patients with HNC who had treated with BNCT at KUR in last year in Table 1.

**PURPOSES:** The purpose of this study was to estimate safety and effectiveness of BNCT for patients with advanced/ recurrent HNC for which there were no other treatment options.

**RESULTS:** We also report here the latest clinical outcomes of 37 patients with recurrent HNC

All cases are advanced such as 18 (49%) out of 37 patients had developed regional lymph node metastases. Distant metastases were developed in 10 cases (27%) during treatment. (1) Regression rates were CR:19cases (51%), PR: 14 cases (38%), PD: 3cases (8%), NE (not evaluated):1case (3%). Response rate was 89%. (2) Mean Survival time was 26.3months. 4-year overall survival

rate (OS) and 9-year OS were 42% and 31%, respectively. (3)BNCT improved QOL, PS and survival periods. (4)Survival periods after BNCT were 1-105 months. (5) Adverse events were brain necrosis, osteomyelitis and transient mucositis and alopecia and so on.

**Case 4:** A 56-year old man with SCC at the left margin of tongue (T2N0M0) had got interstitial radiation therapy (60Gy) at the Osaka University Hospital in July 2013, with rejection against his doctor's recommendation of the surgery (tongue hemi-section). About 6 months after the interstitial radiotherapy, he had developed the left lymph node metastasis at upper neck region (level II). However, he had again rejected to the surgery of radical neck dissection against his doctor. During his rejection of the surgery, the lymph node had rapidly grown more than 7cm in diameter, involving carotid vein and artery. He had referred to our department in March 2014. FBPA-PET study resulted that T/B ratio=4.2. The left upper neck lymph node had treated with BNCT in May, 2014. About 3 month later, the huge lymph node had completely disappeared under the CT scan. Then 6-month after BNCT, he had complaint of dyspnea. He had seen his general practitioner and his doctor advised him to see specialist. He had found the left lung lesions which were seemed to be distant metastasis under the CT scan. He had got chemotherapy for treatment of lung lesions at a hospital in his home town.

#### REFERENCES:

- [1] I. Kato, *et al.*, Appl. Radiat. Isot., **61** (2004) 1069-1073.  
[2] R. Barth, *et al.*, Radiat. Oncol., **7** (2012) 146-166

Table 1. Treatment Summary of 6 Cases

(Dec, 2014)

Case No.	Pt's Initial (Age)	Clinical Diag. (Histopathol. Diag.)	10B-conc. Blood(ppm)	T/B ratio	T-max of thermal neutron (D)		Total-RBE-Dose Eq (Gy-Eq)			Irradiation time(min.)	% Reduction (Period) Prognosis (Survival)
					Fluence (E+11n/cm <sup>2</sup> )	History of RT: (Gy)	T-Peak Gy-Eq	T-deepest Gy-E	Skin/Mu cosa		
1	K·M(28)	Rec.of Lt-ZK (SCC)	1st 16.7 2nd 15.0	2.9	1.5(Left-P) 1.4(Left-A)	48	23 20	12 15	5.7/11	1st 66 min. 2nd 46 min.	PR·Alive(6M)
2	K·M(63)	Rt-op.OKK, RND, Lt-LN meta	33.3	3.9	2.8	50	45(2.1 cm)	21(5.8 cm)	4.4/13	52	PD(2M)Alive(9M)
3	A·H(51)	Rt-op.ZK,RND,BNCT, lung meta	23	2.8	1.8	63	26(1.6 cm)	8.8(6 cm)	2.6spine	80	PR(2M),DOC(8M)
4	I·T(56)	Post RT of Lt-ZK, Lt-LN meta	22	4.2	2.52	60(interstitial)	50	18	7.9/12	70	CR(7M),Lung meta
5	S·K(69)	Rt-OGK(SCC)after Proton T.	26.5	2.1	3.79	70(Proton T.)	30	12	8.3/12	44	PD, DOC(3M)
6	S·M(69)	Rec.of Rt-op.UGK, RND,	20.0	2.0	3.36	60	34	13	12/14	63	CR, Lung meta,DOC(6M)

採択課題番号26 P14-5 頭頸部悪性腫瘍におけるホウ素中性子捕捉療法の臨床的研究 プロジェクト  
(阪大2口外) 加藤 逸郎、岩井 聡一、墨 哲郎、中澤 光博、由良 義明 (阪大工) 村田 勲  
(慶大) 岡本 正人 (長崎大) 梅田 博昭、柳本 惣市 (りんくう医療セ) 大前 政利 (東大阪総合)  
千足 浩久 (市立池田) 大西 徹郎 (田中クリニック) 田中 善 (山口大) 上山 吉哉、内田 堅一郎  
(京大炉) 田中 浩基、鈴木 実、櫻井 良憲、増永 慎一郎、丸橋 晃、小野 公二

## PR14-3 Boron Uptake in Tumour of Local Recurrent Breast Cancer by $^{18}\text{F}$ -BPA Positron Emission Tomography for Application to Boron Neutron Capture Therapy

Yanagie H<sup>1,2,3</sup>, Furuya Y<sup>1,4</sup>, Taniike K<sup>5</sup>, Kumada H<sup>6</sup>, Nakamura T<sup>7</sup>, Horiguchi H<sup>7</sup>, Maruyama S<sup>8</sup>, Hatae R<sup>8</sup>, Suzuki M<sup>9</sup>, Ono K<sup>9</sup>, Ono M<sup>3,10</sup>, Nakajima J<sup>3,11</sup>, Eriguchi M<sup>1,8</sup>, and Takahashi H<sup>2,3</sup>

<sup>1</sup>Department of Innovative Cancer Therapeutics: Alpha particle & Immunotherapeutics, Meiji Pharmaceutical University, <sup>2</sup>Department of Nuclear Engineering & Management, Graduate School of Engineering, The University of Tokyo, <sup>3</sup>Cooperative Unit of Medicine & Engineering, The University of Tokyo Hospital, <sup>4</sup>Department of Surgery, Satukidai Hospital, <sup>5</sup>Department of Radiology, Nishijin Hospital, <sup>6</sup>Department of Physics, Tsukuba University, <sup>7</sup>Japan Atomic Research Institute, <sup>8</sup>Department of Surgery, Shin-Yamate Hospital, <sup>9</sup>Research Reactor Institute, Kyoto University, <sup>10</sup>Department of Cardiac Surgery, The University of Tokyo Hospital, <sup>11</sup>Department of Thoracic Surgery, The University of Tokyo Hospital

**INTRODUCTION:** Boron neutron capture therapy (BNCT) is a targeted radiation approach, because tumour cells can be selectively irradiated according to the accumulation of boron compounds. The cytotoxic effect of BNCT is due to the nuclear reaction between  $^{10}\text{B}$  and thermal neutrons. The resulting lithium ions and  $\alpha$ -particles have high linear energy transfer and produce significant biological effects. Their short range in tissue (5 – 9  $\mu\text{m}$ ) restricts radiation damage to cells containing boron atoms at the time of neutron irradiation. If sufficient boron compound can be targeted accurately to the tumour, BNCT can be applied to locally recurrent gastrointestinal cancers, and breast cancers.

Recently, positron emission tomography (PET) is developed for primary detection and metastasis of cancers.  $^{18}\text{F}$  labeled borono-phenylalanine (BPA)-PET are applied to evaluate the accumulation of boron atoms to tumours and the activity of cancer cells in the fields of BNCT.

**CASE REPORT:** We had experienced the  $^{18}\text{F}$ -BPA PET for the case of breast cancer patient who had metastasized to right supraclavicular lymph node. The patient who had been performed modified radical mastectomy with lymph node dissection (Patey's method) and adjuvant chemotherapies, had been occurred right cervical LN metastasis after 3 years. The high accumulating images of metastasized to right supraclavicular lymph node was acquired by  $^{18}\text{F}$ -BPA PET. The tumour / blood ratio was 2.26 (Figure 1). There was no other active images in the body.

**EXPERIMENTS:** In this case of advanced breast cancer, we performed the feasibility estimation of 3D construction of tumour according to the PET-CT imaging of a patient with epithermal neutron mode at Japan

Atomic Research Reactor 4. This simulation was performed optimizing modification to detect the minimum thermal neutron fluence.

**RESULTS:** The blood boron concentration (ppm) and tumour/normal tissue ratio are estimated to 24, 2.26, respectively. Skin RBE dose is restricted to 10 Gy-Eq, the maximum tumour RBE dose, minimum tumour RBE dose, and mean tumour RBE dose are 38.5, 19.9, and 30.6 Gy-Eq, respectively, in 40 minutes irradiation (Figure 2). In this study, we showed the possibility to apply BNCT to local recurrent advanced breast cancer with the estimation of boron accumulation using  $^{18}\text{F}$ -BPA Positron Emission Tomography.

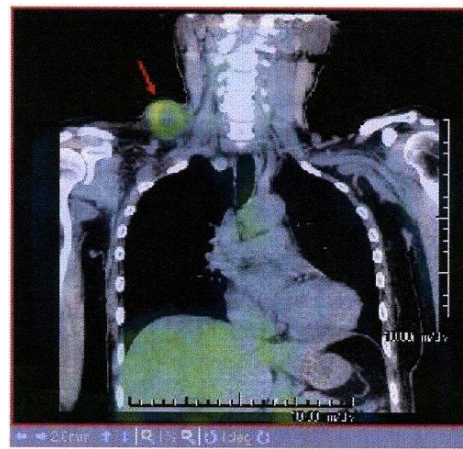


Figure 1.  $^{18}\text{F}$ -BPA PET image of rt cervical LN metastasis.

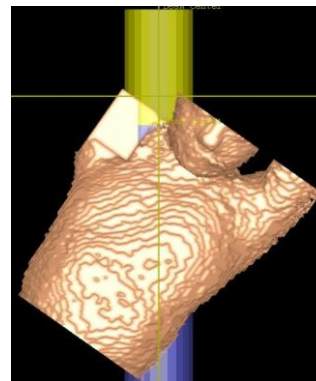


Figure 2. Image of Patient View from frontal side

### REFERENCES:

- [1] Y Imahori *et al.*, Clin Cancer Res. 4(1998)1833-41.
- [2] Y Imahori *et al.*, Clin Cancer Res. 4(1998)1825-32.
- [3] H Yanagie *et al.*, Applied Radiation & Isotopes, 67(2009) S63-66.

採択課題番号26P14-8 中性子捕捉療法的一般外科領域難治性癌への展開に向けた臨床的研究 プロジェクト (明薬大) 柳衛宏宣、野中泰政 (結核予防会新山手病院) 江里口正純、小山和行、大野烈士、丸山正二、波多江 亮 (宏仁会メディカルシティ東部病院) 東 秀史、瀬口浩司 (京大・原子炉) 小野公二、増永慎一郎、鈴木 実、櫻井良憲

## PR14-4 High Boron-Accumulated Liposomes as Efficient Boron Carriers for Neutron Capture Therapy

H. Nakamura<sup>1</sup>, S. Tachikawa<sup>2</sup>, S. Kikuchi<sup>1</sup>, K. Ono<sup>3</sup> and M. Suzuki<sup>3</sup>

<sup>1</sup> Chemical Resources Laboratory, Tokyo Institute of Technology

<sup>2</sup> Faculty of Science, Gakushuin University

<sup>3</sup> Research Reactor Institute, Kyoto University

**INTRODUCTION:** Boron neutron capture therapy (BNCT) has been attracting growing interest as one of the minimally invasive cancer therapies. The accelerator-based BNCT is now undergoing phase I clinical study for the treatment of brain tumor and head and neck cancer patients using L-BPA in Japan. We previously developed Na<sub>2</sub>BSH-encapsulating 10% distearoyl boron lipid (DSBL) liposomes that have high boron content with excellent boron delivery efficacy to tumors.[1] In this report, we studied the effects of the counter cations of boron clusters on liposome formation to develop high boron content liposomes for BNCT by overcoming osmotic pressure limitations.

**EXPERIMENTS:** An aqueous solution of various ammonium chloride salts (1,4-diaminobutane, spermidine, and spermine) of *closo*-dodecaborates Na<sub>2</sub>[B<sub>12</sub>H<sub>12</sub>], Na<sub>2</sub>[B<sub>12</sub>H<sub>11</sub>OH] and Na[B<sub>12</sub>H<sub>11</sub>NH<sub>3</sub>] in addition to Na<sub>2</sub>BSH (Fig. 1), were prepared by adding sodium *closo*-dodecaborates to a mixture of each amine and aqueous 1N HCl solution. Liposomes encapsulated with these ammonium *closo*-dodecaborates were prepared from DSPC, cholesterol and DSPE-PEG (1:1:0.11, molar ratio) by the reverse-phase evaporation method. B/P (boron concentration / phosphorus concentration) ratio was calculated from data obtained by the simultaneous measurement of boron and phosphorus concentrations by inductively coupled plasma atomic emission spectroscopy (ICP-AES, HORIBA, Japan).

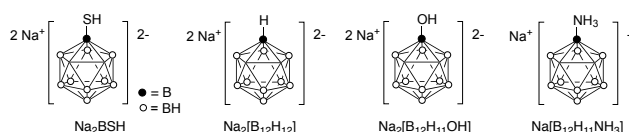


Fig. 1. Structures of *closo*-dodecaborates used for encapsulation in liposomes.

**RESULTS:** Various ammonium salts of *closo*-dodecaborates were prepared and examined their encapsulation into liposomes. Interestingly, the B/P ratio dramatically increased to 3.4 when spermidinium (spd) cation was employed. In addition, liposome yield was markedly increased to 98% and final boron concentration of the liposome solution reached 13,867 ppm. Transmis-

sion electron microscopy analysis of spd-BSH-encapsulating liposomes and Na<sub>2</sub>BSH-encapsulating liposomes was also carried out with Cryo-TEM (Fig. 2). It is notable that the liposomes interacted with each other in the case of Na<sub>2</sub>BSH-encapsulating liposomes, whereas the liposomes dispersed in solution without interacting with each other in the case of spd-BSH-encapsulating liposomes.

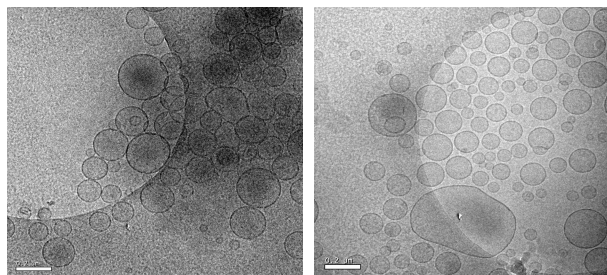


Fig. 2. TEM images of Na<sub>2</sub>BSH-encapsulating liposomes (left) and spd-BSH-encapsulating liposomes (right). Scale bar represents 200 nm.

Fig. 3 shows the survival curve of tumor-bearing mice after thermal neutron irradiation. Thermal neutron irradiation enhanced mouse survival and all mice exposed to thermal neutron irradiation died within 78 days. Remarkable antitumor effect was observed in the mice treated with spd-[<sup>10</sup>BSH]-encapsulating liposomes at the dose of 30 mg [<sup>10</sup>B]/kg; 100% of the mice survived up to 100 days after the thermal neutron irradiation.[2]

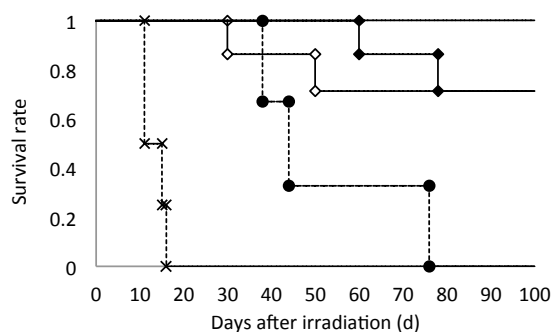


Fig. 3. Survival curve of tumor-bearing mice after thermal neutron irradiation. The irradiation was performed 36 h after injection of *closo*-dodecaborates (–, spd-BSH: 30 mg [<sup>10</sup>B]/kg; ◆, spd-BSH: 15 mg [<sup>10</sup>B]/kg; ◇, spd-<sup>10</sup>B<sub>12</sub>H<sub>11</sub>NH<sub>3</sub>: 15 mg [<sup>10</sup>B]/kg) for 50 min (1.3–2.2 × 10<sup>12</sup> neutrons/cm<sup>2</sup>). ×, Cold control; ●, Hot control.

### REFERENCES:

- [1] H. Koganei, *et al.*, *Bioconjugate Chem.* **24** (2013) 124-132.
- [2] S. Tachikawa, *et al.*, *Chem. Commun.* **50**, (2014) 12325-12328.



S Tada<sup>1</sup>, T Iwagami<sup>2</sup>, Y Ishikawa<sup>3</sup>, N Koshizaki<sup>4</sup>, H Tanaka<sup>5</sup>, S Masunaga<sup>5</sup>, Y Sakurai<sup>5</sup>, I Kato<sup>1</sup>, K Ono<sup>5</sup>, M Suzuki<sup>5</sup>, Y Yura<sup>1</sup>

<sup>1</sup>Osaka University Graduate School of Dentistry

<sup>2</sup>Hannan Municipal Hospital

<sup>3</sup>National Institute of Advanced Industrial Science and Technology

<sup>4</sup>Graduate School of Engineering, Hokkaido University

<sup>5</sup>Research Reactor Institute, Kyoto University

**INTRODUCTION:** We determined whether a boron-rich boron carbide (B4C) nanoparticle could be used for BNCT for oral squamous cell carcinoma (SCC) xenografts in nude mice.

**EXPERIMENTS:** B4C nanoparticles were obtained by the laser fragmentation of boron particles in ethyl acetate and dissolved in PBS. To generate tumors, SAS cells derived from oral SCC were inoculated subcutaneously into the back of the leg of female Balb/c nude mice. Fifty microliters of B4C solution containing 12.5 $\mu$ g B4C particles was infiltrated into tumors. 10B concentrations in these tissues were measured by prompt gamma-ray spectrometry at the Kyoto University Research Reactor (KUR). After injection of B4C solution, tumors were exposed to thermal neutrons. Control tumors were left untreated. Experimental groups included untreated control, neutron only, and B4C-mediated BNCT groups. Neutron irradiation was delivered via a neutron beam at the KUR.

**RESULTS:** Injecting B4C particles into the oral SCC xenografts of nude mice increased the concentration of 10B in the tumors, but not in the kidney, liver, or spleen. Ten minutes after injection of B4C particles the 10B concentration was 18.57 ppm in the tumor. SAS tumor-bearing animals received an intratumoral injection of B4C solution followed by neutron irradiation. No significant differences were observed in body weight among these groups during the experimental period (Figure 1). In control animals, tumors continued to grow and were 5867 mm<sup>3</sup> 42 days after the start of the experiment. When tumors were subjected to B4C-mediated BNCT, tumor volume decreased from 7 days after neutron irradiation. A significant difference was observed between the B4C-mediated BNCT and neutron only groups 42 days after BNCT ( $P < 0.01$ ) (Figure 2).

**CONCLUSION:** These results indicate that B4C particles can be used locally as a boron compound in BNCT for oral SCC in vivo.

Figure 1

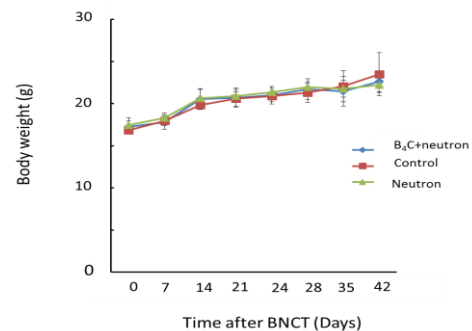


Figure 1: Nude mice carrying SAS tumors received 50  $\mu$ l of 250 ppm B4C solution intratumorally. Ten minutes later, tumors were exposed to thermal neutrons. The experimental groups were as follows: untreated control, neutron only, and B4C-mediated BNCT. n=5

Figure 2

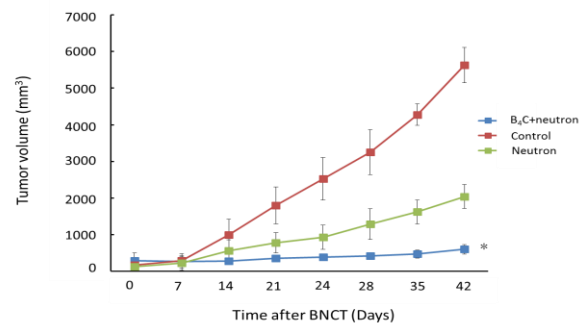


Figure 2: Nude mice carrying SAS tumors were treated as described in Figure 1. After BNCT, tumor size was measured and tumor volume was determined. \* $P < 0.01$  significantly different from neutrons only. n=5

#### References

- [1] Ishikawa Y, Shimizu Y, Sasaki T, Koshizaki N (2007) Boron carbide spherical particles encapsulated in graphite prepared by pulsed laser irradiation of boron in liquid medium. *Applied Physics Letters* 91:161110.
- [2] Ishikawa Y, Sasaki T, Koshizaki N (2010) Submicron-sized boron carbide particles encapsulated in turbostratic graphite prepared by laser fragmentation in liquid medium. *J Nanosci Nanotechnol* 10:5467-5470.
- [3] Yamamoto N, Iwagami T, Kato I, Masunaga S, Sakurai Y, et al. (2013) Sonoporation as an enhancing method for boron neutron capture therapy for squamous cell carcinomas. *Radiat Oncol* 8:280.

## PR14-6 Boron Neutron Capture Therapy Selectively Destroys Human Clear Cell Sarcoma (CCS) Metastasis to Lung in CCS-bearing Animal Model

T. Fujimoto<sup>1</sup>, T. Andoh<sup>2</sup>, Y. Sakurai<sup>3</sup>, K. Ono<sup>3</sup>,  
H. Ichikawa<sup>2</sup> and M. Suzuki<sup>3</sup>

<sup>1</sup>Hyogo Cancer Center,

Department of Orthopaedic Surgery

<sup>2</sup>Faculty of Pharmaceutical Sciences and Cooperative  
Research Center of Life Sciences,

Kobe Gakuin University

<sup>3</sup>Research Reactor Institute, Kyoto University

**INTRODUCTION:** Sarcoma metastasis to the lung is almost the final status for the treatment of sarcoma, and palliative therapy is recommended for reducing severe patient symptoms. Since neither chemotherapy nor radiation therapy is effective for most sarcomas, new therapeutic strategies are required. Clear cell sarcoma (CCS) of tendons and aponeuroses is one such with poor prognosis [1]. We have, however, demonstrated the effectiveness of boron neutron capture therapy (BNCT) for tumors in the limbs of the human CCS-bearing nude mouse model with the use of p-boronophenylalanine (BPA) [2, 3]. Here, therefore, we first created a new model of sarcoma metastasizing to the lung in the human CCS-bearing animal model, and then evaluated the efficacy and potential of BNCT after measuring the distribution of BPA in the lung.

**EXPERIMENTS:** (1) *Creating the lung metastasis model of human CCS-bearing animal model:* All animal experiments were carried out according to the regulations of the Animal Care and Use Committee. Lung metastasis in the human CCS-bearing animal model was created by transplanting cells of CCS cell line (MP-CCS-SY [4]) suspended in Matrigel® into the parenchyma of the left lung of nude mice. After 8 weeks, tumor formation in the lung was confirmed by micro CT scans, and the tumor mass was measured through CT image analysis.

(2) In BNCT trials, the animals were divided into four groups of 4 each, and, under anesthesia, BPA-Fr (24 mg <sup>10</sup>B/kg) was intravenously administered to the BNCT group (A) and to the Cold control group (C), and saline to the Hot control group (B) on day 0. Groups A and B were then irradiated two times with a thermal neutron beam (1MW) to the whole lung at KURRI, once anteriorly between 60 and 80 minutes and once posteriorly between 100 minutes and 120 minutes. The  $\gamma$ -ray group (D) was irradiated with cobalt-60  $\gamma$ -ray at a dose of 0.3 Gy/min. On day 21, the tumor mass was resected from each mouse under anesthesia, routinely formalin-fixed,

paraffin-embedded, and HE stained according to standard protocols for histological examination.

**RESULTS:** The irradiation doses (Gy) absorbed by the CCS-bearing mice were 5.2 (Group A, BNCT), 0.7 (Group B, Hot control) and 0.9 (Group D,  $\gamma$ -ray). In the three control groups, no significant anti-tumor effect was observed; the tumor mass simply increased time-dependently. By contrast, the volume of the tumor mass in the BNCT groups decreased with time [Fig. 1].

**CONCLUSION:** BNCT selectively destroyed CCS cells in the lung of the human CCS-bearing animal model by irradiating the whole lung, without significant complications.

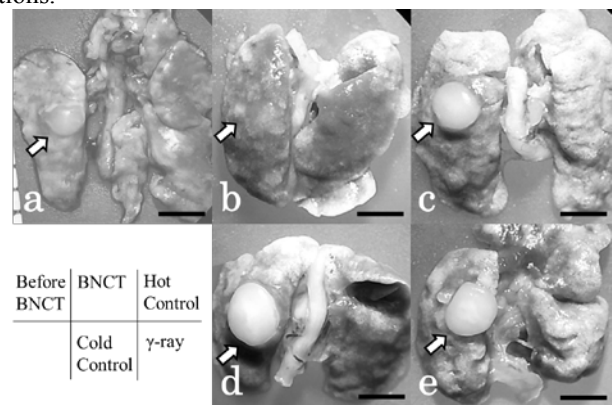


**[Fig.1]** BNCT for the lung metastasis model of CCS-bearing animal model. a: Before neutron irradiation. A well-defined solid tumor mass about 2 mm in diameter was detected in the left lung. b, c and d: three weeks after the neutron irradiation. b: Group A. BNCT. Tumor mass shrank and was hardly discernible. c: Group B. Hot control. Neutron irradiation without administration of BPA. Tumor mass was almost 3 mm in diameter. d: Group C. Cold control. Without neutron irradiation. Tumor mass was almost 4 mm in diameter. e: Group D. Three weeks after the  $\gamma$ -ray irradiation. Tumor mass was almost 4 mm in diameter. Bar = 2.5 mm.

### REFERENCES:

- [1]F.M. Enzinger, *Cancer*, **18**(1965) 1163-1174.
- [2]T. Fujimoto et al., *Appl. Radiat. Isot.* **73**(2013) 96-100.
- [3]T. Andoh et al., *Appl. Radiat. Isot.* **69**(2011)1721-1724.
- [4]H. Moritake et al., *Cancer Genet. Cytogenet.*, **135**(2002) 48-56

採択課題番号 26P14-19

悪性末梢性神経鞘腫および明細胞肉腫

プロジェクト

に対するホウ素中性子捕捉療法 of 検討

(京大・原子炉) 鈴木実、櫻井良憲、小野公二  
(兵庫県立がんセンター・整形外科) 藤本卓也

(神戸学院大・薬) 安藤 徹、市川 秀喜



## PR14-8 Evaluation of Component in WOW Emulsion as Intra-arterial Boron Delivery Carrier for Neutron Capture Therapy to Hepatocellular Carcinoma

Hironobu Yanagie<sup>1,2,3</sup>, Mitsuteru Fujihara<sup>4</sup>, Ryuji Mizumachi<sup>5</sup>, Yuji Murata<sup>5</sup>, Yuriko Sakurai<sup>1,3</sup>, Kikue Mouri<sup>1,3</sup>, Atsuko Shinohara<sup>6,7</sup>, Takehisa Matsukawa<sup>7</sup>, Yasuyuki Morishita<sup>8</sup>, Masashi Yanagawa<sup>9</sup>, Syushi Higashi<sup>10</sup>, Ichiro Ikushima<sup>11</sup>, Kouji Seguchi<sup>10</sup>, Sho Yui<sup>1,3</sup>, Yoshinori Sakurai<sup>12</sup>, Hiroki Tanaka<sup>12</sup>, Minoru Suzuki<sup>12</sup>, Shinichiro Masunaga<sup>12</sup>, Kazuyuki Oyama<sup>13</sup>, Takayuki Nakagawa<sup>14</sup>, Ryohei Nishimura<sup>14</sup>, Koji Ono<sup>12</sup>, Minoru Ono<sup>3,15</sup>, Jun Nakajima<sup>3,16</sup>, Masazumi Eriguchi<sup>13</sup>, and Hiroyuki Takahashi<sup>2,3</sup>

<sup>1</sup>Department of Innovative Cancer Therapeutics: Alpha particle & Immunotherapeutics, Meiji Pharmaceutical University, <sup>2</sup>Department of Nuclear Engineering & Management, Graduate School of Engineering, The University of Tokyo, <sup>3</sup>Cooperative Unit of Medicine & Engineering, The University of Tokyo Hospital, <sup>4</sup>SPG Techno Ltd. Co., <sup>5</sup>Department of Pharmacology, Kumamoto Institute Branch, LSI Medience Ltd Co, <sup>6</sup>Department of Humanities, The Graduate School of Seisen University, <sup>7</sup>Department of Hygines, Faculty of Medicine, Jyuntendo University, <sup>8</sup>Department of Human & Molecular Pathology, Graduate School of Medicine, The University of Tokyo, <sup>9</sup>Department of Small Animal Surgery, Veterinary Medical Center, Obihiro University of Agriculture & Veterinary Medicine, <sup>10</sup>Department of Surgery, Ko-jin Kai Medical City East Hospital, <sup>11</sup>Department of Radiology, Miyakonojyo Metropolitan Hospital, <sup>12</sup>Department of Veterinary Surgery, The University of Tokyo Veterinary Hospital, <sup>13</sup>Research Reactor Institute, Kyoto University, <sup>14</sup>Department of Surgery, Shin-Yamanote Hospital, <sup>15</sup>Department of Cardiac Surgery, The University of Tokyo Hospital, <sup>16</sup>Department of Thoracic Surgery, The University of Tokyo Hospital.

**INTRODUCTION:** We has been used water-in-oil-in-water emulsion (WOW) as the carrier of anti-cancer agents by modifying of IPSO on intra-arterial injections in clinical. Higashi et al prepared a long term inseparable, WOW for use in arterial injection therapy to treat patients with HCC [1]. We performed preclinical BNCT study for VX-2 rabbit tumour model using <sup>10</sup>BSH entrapped WOW [2, 3]. In order to improve the WOW for application to BNCT, we prepared <sup>10</sup>BSH entrapped WOW in verifying the component of surfactant, and evaluated the boron delivery activity to measure the <sup>10</sup>B concentrations of organs in VX-2 hepatic tumour model on time course after intra-arterial injection.

**EXPERIMENTS:** <sup>10</sup>BSH entrapped WOW were administered with intra-arterial injections via proper he-

patic artery (<sup>10</sup>BSH : 75 mg/kg rabbit) on VX-2 rabbit hepatic tumour models. One and three days after arterial injections, the boron concentrations of the tumor nodules and normal liver tissues were determined by ICP- Mass Spectroscopy of Jyuntendo University.

**RESULTS:** VX-2-bearing rabbits (n = 3) were given intra-arterial injection with 2 ml of <sup>10</sup>BSH WOW emulsion consist with surfactant HCO40, or PGCR. We prepared <sup>10</sup>BSH entrapped WOW. The mean <sup>10</sup>B concentration prepared in <sup>10</sup>BSH-WOW was 10000 ppm in this experiment. The size of WOW was controlled to 70 μm. The <sup>10</sup>B concentration in VX-2 tumour was 170.8 ppm, 58.3 ppm by WOW with HCO40 after day1, day3 intra-arterial injection, respectively. The <sup>10</sup>B concentration of tumour was 186.0ppm, 40.4ppm by WOW with PGCR after day1, day3 same injection, respectively. <sup>10</sup>B concentration in normal liver tissue / blood were 8.0 / 0.3 ppm in HCO40 group, and 15.1 / 0.1 ppm in PGCR group at day 3, respectively in the same procedures of WOW. We also perform Oil-O Red staining to detect the lipid components in WOW. We had showed the staining of cytoplasm in the tumours 3 day after intra-arterial injections (Figure 1). These means that the WOW accumulated selectively to the tumours by intra-arterial injections.

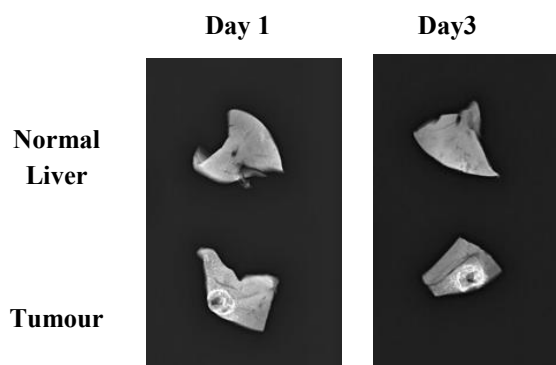


Figure1: IPSO component in WOW was accumulated in the VX-2 tumour by intra-arterial injection of <sup>10</sup>BSH entrapped WOW with HCO40 surfactant by Soft X ray radiography.

### REFERENCES:

- [1] S Higashi S *et al.*, Cancer, **75**(1995):1245–1254.
- [2] S Mikado *et al.*, Nucl. Instr. and Meth. A, **605** (2009) 171-174.
- [3] H Yanagie *et al.*, Biomedicine & Pharmacotherapy, submitted.

H. Ueda, Y. Sakurai, T. Takata, H. Tanaka, R. Uchida, T. Kawamura, N. Fujimoto, M. Suzuki

Research Reactor Institute, Kyoto University

**INTRODUCTION:** After the restart of the operation of Kyoto University Reactor (KUR) in May 2010, 235 clinical studies of boron neutron capture therapy (BNCT) have already been carried out as of May 2015 [1]. Also, the BNCT clinical trial using Cyclotron-based BNCT Epi-thermal Neutron Source (C-BENS) started in November 2012 [2]. In the while, the research and development into several types of accelerator-based irradiation systems are underway by several research groups in the world at present time. With this situation in mind, it is important that the physical and biological estimations for dose quantity and quality are performed consistently among several irradiation fields, and that the equivalency of BNCT is guaranteed, even across BNCT systems. The aim of this research is the establishment of quality assurance and quality control (QA/QC) using ionization chamber and Bonner sphere in BNCT irradiation field. In 2014, the improvement of the energy resolution in epi-thermal neutron region was studied for the Bonner sphere using boric acid solution moderator.

**METHODS:** The Bonner sphere in this research consists of a spherical neutron moderator shell and activation foils placed in the sphere center as thermal neutron detector. The boric acid solution of  $^{10}\text{B}$  0.14wt% was used as the moderator material. Manganin ( $^{55}\text{Mn}$ ) and gold ( $^{197}\text{Au}$ ) were used as activation foil material. The specific saturated activities per neutron flux for each energy group were calculated as the response function of Bonner spheres. The calculations were performed for the sphere diameter of 10, 15 and 20 cm, using the MCNP-5 radiation transport code [3]. The calculated activities were unfolded into the estimated spectrum by UMG unfolding package [4]. The influence of the uncertainty for the moderator concentration and the detector placement to the spectrum estimation, were investigated. The spectrum estimation was performed for the epi-thermal neutron irradiation mode in Heavy Water Neutron Irradiation Facility (HWNIF) of KUR was studied.

**RESULTS:** Figure 1 shows the results in the case that the activation detector displacement of 3 mm occurs on the 10-cm diameter of Bonner sphere. The error was not considered in the unfolding procedure. Figure 2 shows the unfolding results in the same condition as Fig. 1, except the error was considered. In Fig. 1, the neutron energy spectrum is estimated wrongly. In Fig. 2, the neutron energy spectrum is estimated more adequately, but the errors of the estimated spectrum become larger.

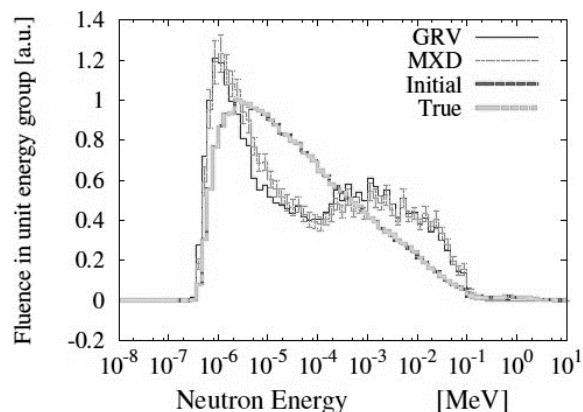


Fig. 1. Unfolding results in the case that the activation detector displacement of 3 mm occurs on the 10-cm diameter Bonner sphere and the error is not considered in the unfolding procedure.

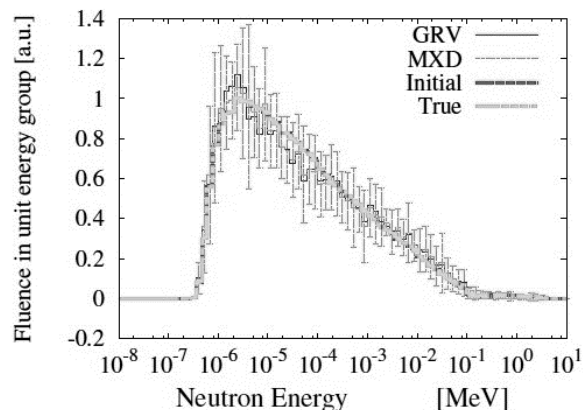


Fig. 2. Unfolding results in the same case as Fig. 1 except the error is considered.

#### REFERENCES:

- [1] Y. Sakurai *et al.*, Nucl. Instr. Meth. A **453** (2000) 569-596.
- [2] H. Tanaka *et al.*, Nucl. Instr. Meth. B **267** (2009) 1970-1977.
- [3] X-5 Monte Carlo Team, LA-UR-03-1987 (2003).
- [4] M. Reginatto, The 'Few-Channel' Unfolding Programs in the UMG Package (Physikalisch-Technische Bundesanstalt) (2004).

## PR14-10 Study on the Real-time dose Monitor System Using Prompt Gamma Rays for Boron Neutron Capture Therapy

H. Tanaka, Y. Sakurai, N. Fujimoto, T. Takata, S. Masunaga, K. Ono, A. Maruhashi, and M. Suzuki

Research Reactor Institute, Kyoto University

**INTRODUCTION:** Over 500 clinical studies of boron neutron capture therapy (BNCT) have been performed using Kyoto University Research Reactor (KUR). The information of neutron flux and boron concentration during the irradiation is needed for the determination of irradiation time. The boron concentration is determined by the prompt gamma rays from the blood sample using thermal neutron guide tube at KUR. On the other hand, neutron flux is measured by the activation material, which is irradiated by the treatment beam and picked up after 10 minutes from the irradiation start. However, the information of boron concentration and neutron flux is not able to be obtained during the irradiation. In order to determine precise dose information, it is important to detect real-time boron concentration and neutron flux. Recently, the real-time neutron flux monitor have been developed using the combination of tiny scintillator and optical fiber. The real-time boron concentration monitor have been studied using SPECT system for BNCT[1]. However, the actual level system have not realized, because the background of gamma rays at the BNCT irradiation field is quite high. The aims of this study are to clarify the gamma rays dose level at the BNCT irradiation field and the development of the prototype system of real-time boron concentration monitor. The measured gamma rays dose during BNCT clinical studies is shown in this report.

**EXPERIMENTS:** The BeO thermoluminescence dosimeters (TLDs) were used for the measurement of gamma rays dose. BeO powder was enclosed in quartz tube to reduce the neutron sensitivity. The TLDs were set at the position that was assumed to set the real-time boron concentration monitor. Figure 1 shows the schematic layout of irradiation field and the TLDs setting positions. The TLDs were set from the center of collimator for the lateral and beam direction with the 20 cm interval. The height of TLDs setting position was the 60 cm, corresponding to beam center height. The irradiation was performed for head and neck tumor. The irradiation time was 63 minutes. After the irradiation, TLDs were processed by the TLD reader and the gamma rays dose were derived with the correction.

**RESULTS:** Figure 2 shows the gamma rays dose rate distribution for lateral and beam direction. For the beam

direction, the patient was set between 0 cm and 60cm. The background of gamma rays were produced by the  $^1\text{H}(n,\gamma)^2\text{D}$  reactions with the energy of 2.22MeV, the annihilation gamma rays of 0.511 MeV, and the decay gamma rays of  $^{41}\text{Ar}$ . The gamma rays at the near the collimator center are almost of 2.22 MeV produced in the human body. For the lateral direction, the level of gamma rays were rapidly reduced. On the other hand, at the distance from the center of 60 cm, the dose rate of beam direction was two times higher than that of lateral direction. This was caused by the  $^{41}\text{Ar}$  or annihilation gamma rays produced by the reaction between thermal neutron and the component of irradiation bed. Therefore, for the beam direction, the level of gamma rays was slowly decreased. If the real-time boron concentration monitor is set at the BNCT field, it is recommended to set at the behind of collimator for the lateral direction.

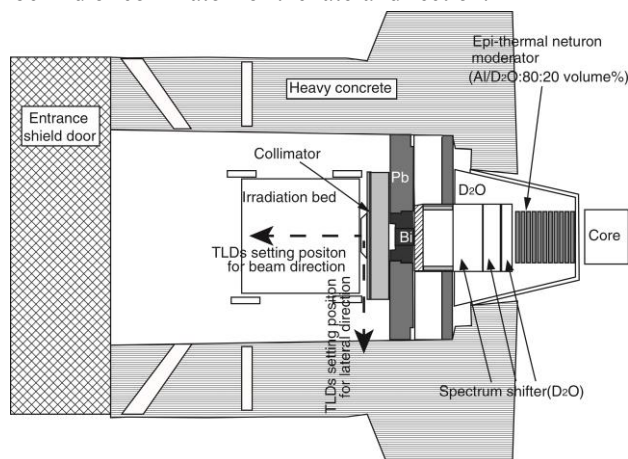


Fig. 1. Schematic layout of BNCT irradiation field of KUR and the setting position of TLDs.

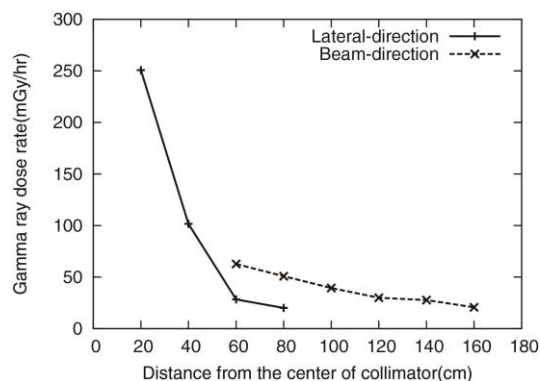


Fig. 2. The relationship between gamma rays dose rate and the distance from the center of collimator.

### REFERENCES:

[1] T. Kobayashi *et al.*, Medical Physics, 27, 2124(2000)

採択課題番号 26P14-27 BNCT のための即発ガンマ線によるリアルタイム  
線量評価システムに関する研究

プロジェクト

(京大・原子炉) 田中浩基、櫻井良憲、藤本望、高田卓志、増永慎一郎、小野公二、丸橋晃、鈴木実

## PR14-11 Quality Assurance of Irradiation Field for BNCT Using Twin Imaging Plate System

Kenichi Tanaka, Yoshinori Sakurai<sup>1</sup>, Tsuyoshi Kajimoto, Hiroki Tanaka<sup>1</sup>, Takushi Takata<sup>1</sup>, Jun Takada<sup>2</sup>, Minoru Suzuki<sup>1</sup>, Satoru Endo

Graduate School of Engineering, Hiroshima University

<sup>1</sup>Research Reactor Institute, Kyoto University

<sup>2</sup>Center of Medical Education, Sapporo Medical University

**INTRODUCTION:** Measurement of the spatial distributions of neutrons and gamma rays is one of the potential and essential options for the quality assurance and quality control for boron neutron capture therapy (BNCT). It is desirable to measure the beam components such as thermal, epithermal, fast neutrons ( $n_{th}$ ,  $n_{epi}$ ,  $n_f$ ) and gamma rays ( $\gamma$ ), separately. This study investigates using the twin imaging plate (IP) system for this purpose. A calculational approach is reported here.

**CALCULATIONS:** The twin IP system consists of the converters to enhance the components, and IPs. The principle is: thermal and epithermal neutrons will be enhanced with the secondary particles of the  $^{10}\text{B}(n,\alpha)^7\text{Li}$  reaction in the epoxy resin doped with boron, fast neutrons with the recoiled protons from the epoxy resin, gamma rays with Graphite, then enhanced components will be detected with the IPs. By comparing two IPs, intensity of a beam component is to be estimated<sup>[1,2]</sup>.

The configuration of the converters was surveyed using Monte Carlo calculations with PHITS 2.52<sup>[3]</sup>. The irradiation field assumed was that by the  $^7\text{Li}(p,n)$  reaction by 2.5 MeV protons moderated with 20 cm thick  $\text{D}_2\text{O}$ . The calculation geometry consisted of an IP (Fujifilm corporation, BAS-TR) and a converter. The IP in dimension of 20 X 20 mm was assumed to be covered with 1 mm thick converter<sup>[1]</sup> in every direction of the IP. Each beam component was separately impinged on the converter as a parallel beam perpendicular to the IP. The epoxy resin assumed was its compound with  $\text{B}_4\text{C}$ , where boron was enriched  $^{10}\text{B}$  with abundance of 100 %. The  $^{10}\text{B}$  concentration in epoxy resin (wt%) was varied in calculations.

**RESULTS:** The energy deposition in IP is shown in Fig. 1. Those for Graphite converter is 425, 546, 1570, and 13300 MeV/sec/mA for  $n_{th}$ ,  $n_{epi}$ ,  $n_f$ , and  $\gamma$ , respectively. The contribution of each beam component to total of the energy deposition is shown in Fig. 2. Again, those for Graphite is 0.3, 0.4, 1.2, 98.1 % for  $n_{th}$ ,  $n_{epi}$ ,  $n_f$ , and  $\gamma$ . In usage in twin IP system, it is desirable that only one beam component has different energy deposition among two IPs while other components have identical values, respectively. In this viewpoint, Epoxy converters with 1 to 50 wt% of  $^{10}\text{B}$  will be potential options for detecting  $n_{th}$ ,  $n_{epi}$ .

Consequently, potential combinations of twin IPs are listed in table 1. The values shown are the contribution of

the beam component to the total of the energy deposition. Here, the configuration “A-B” means that the energy deposition for the converter ‘B’ is subtracted from that for ‘A’. “50% B – 10% B” or “Epoxy – Graphite” is not suitable to use since some of the components have negative value in contribution.

In using two IPs, “50% B – Epoxy or Graphite” is potential for  $n_{epi}$ , while 20 % of the energy deposition is by unintended component,  $n_{th}$ . On the other hand, combining “10% B – Epoxy or Graphite” and “10% B – 1% B”, *i.e.* using triple IP in Epoxy converters at 0, 1, 10 wt % of  $^{10}\text{B}$ , will work in estimating  $n_{th}$  and  $n_{epi}$ .

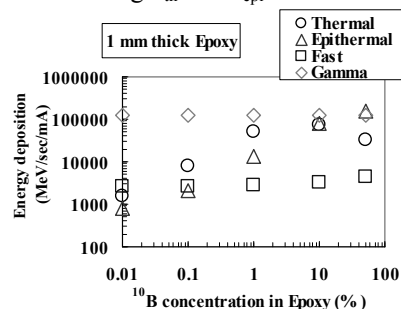


Fig. 1. Energy deposition for Epoxy at varied  $^{10}\text{B}$  concentration.

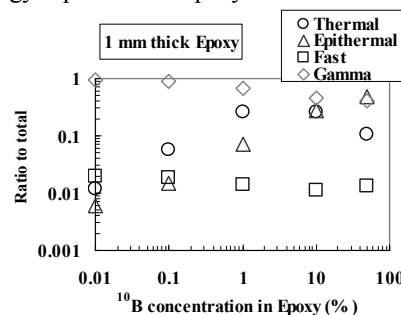


Fig. 2. Beam component contribution to energy deposition.

Table 1 Energy deposition ratio (%) to total for subtraction among two IPs in converters.

Configuration	Contribution (%)			
	$n_{th}$	$n_{epi}$	$n_f$	$\gamma$
10% B – Epoxy or Graphite	50	50	0	0
50% B – Epoxy or Graphite	20	80	0	0
10% B – 1% B	28	72	0	0
50% B – 10% B	-100	200	0	0
Epoxy – Graphite	-14	-5	-43	162

“x %B” specifies the epoxy resin with  $\text{B}_4\text{C}$  at x wt% of  $^{10}\text{B}$  to total weight of the converter.

### REFERENCES:

- [1] K. Tanaka *et al.*, Appl. Rad. Isot. **88** (2014) 143-146.
- [2] K. Tanaka *et al.*, Appl. Rad. Isot. **69** (2011) 1885-1887.
- [3] H. Iwase *et al.*, Jour. Nucl. Sci. Technol. **39** (2002) 1142-1151.

S. Hayashi, Y. Sakurai<sup>1</sup>, M. Suzuki<sup>1</sup>, M. Narabayashi<sup>1</sup> and N. Fujimoto<sup>1</sup>

Department of Clinical Radiology, Hiroshima International University

<sup>1</sup>Research Reactor Institute, Kyoto University

**INTRODUCTION:** Polymer gel dosimeters have been investigated for the three-dimensional (3D) dose measurement of the complex conformal dose distributions in the clinical applications [1]. These devices utilize radiation-induced polymerization reactions of vinyl monomer in the gel to preserve information about the radiation dose. The 3D absorbed dose distribution is deduced from the polymer distribution measured by imaging modalities, such as MRI. The applications to neutron irradiation have been investigated, and the potential as a 3D dosimeter has been suggested [1].

In this work, the NMR response of the standard methacrylic-acid-based polymer gel (MAGAT) with and without boron was examined its availability to measure the depth-dose responses in the irradiation of neutron beams with different energy spectra from nuclear reactor.

**EXPERIMENTS:** Boric acid,  $B(OH)_3$ , containing  $^{10}B$  of 20% naturally was added into the standard gel. The concentration in the gel is the same order (approximately 50 ppm) as the clinical use. The resulting solution was subdivided by pouring into quartz tall beakers (65 mm diameter and 135 mm length, 400 mL).

The neutron irradiations were performed using Heavy Water Neutron Irradiation Facility (HWNIF) of Kyoto University Research Reactor (KUR, power of 1 MW). The samples were irradiated from the bottom direction through the axis with the field size of almost 50 cm diameter in air at room temperature. The three different modes (thermal neutron rich, epi-thermal and fast neutron rich, and the mixed modes) of neutron beams made by heavy water spectrum shifter and cadmium thermal-neutron filters were applied to each sample.

MRI measurements were performed using a 1.5 T scanner (Siemens). A multiple spin-echo sequence was applied and the transverse relaxation rate ( $R_2 = 1/T_2$ ) was estimated.

**RESULTS:** Figure 1 shows the depth- $R_2$  profiles obtained from our polymer gel dosimeters exposed to neu-

tron beams of the different energy spectrum modes. In the thermal neutron mode, both profiles of the gels with and without boron show monotonically decreasing with depth after the peak near the surface. It seems that the decrease for the gels with boron corresponds to decreasing of thermal neutron in tissue and the peak shifts to near the surface significantly due to the reaction with boron. In the epi-thermal and fast neutron mode, broad peaks are observed at deeper position, around from 20 to 25 mm of depth. It is suggested that the  $R_2$  profile for the gel with boron corresponds to the distribution of the thermal neutron due to the moderation of epi-thermal neutron. But for the gels without boron, it seems that the decreases correspond to decreasing of gamma ray. As same as the profiles in thermal mode, the peak shift due to boron was also observed. The depth profiles of the mixed mode (not shown) were similar to that of thermal neutron. It is suggested that the contributions of epi-thermal and fast neutrons are small compared to that of thermal neutron. These results indicate both MAGAT gel dosimeters with and without boron have the effective sensitivity on the thermal neutron rather than on fast neutron.

(These results were presented at 8<sup>th</sup> International Conference on 3D Radiation Dosimetry : IC3DDose 2014 in Ystad, Sweden. [2])

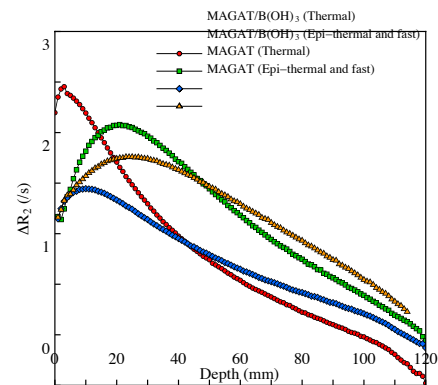


**Figure 1** The depth from phantom surface vs.  $\Delta R_2$  [ $=R_2 - R_{2,bg}$ ] responses in different energy spectra.

#### REFERENCES:

- [1] C. Baldock et al., *Phys. Med. Biol.* **55** (2010) R1-63
- [2] S. Hayashi et al., *J. Phys.: Conf. Ser.* **573** (2015) 012074(4pp)



## **I-2. Collaboration Researches**

- 1. Slow Neutron Physics and Neutron Scattering**
- 2. Nuclear Physics and Nuclear Data**
- 3. Reactor Physics and Reactor Engineering**
- 4. Material Science and Radiation Effects**
- 5. Geochemistry and Environmental Science**
- 6. Life Science and Medical Science**
- 7. Neutron Capture Therapy**
- 9. TRU and Nuclear Chemistry**
- 10. Health Physics and Waste Management**
- 11. Accelerator Physics**
- 12. Others**

E. Furuta, N. Iwasaki, R. Okumura<sup>1</sup> and Y. Inuma<sup>1</sup>

*Ochanomizu University*

<sup>1</sup>*Research Reactor Institute, Kyoto University*

**INTRODUCTION:** Chinese medicines and herbs were analyzed in a previous experiment at KUR. At that results, toxic elements of As and Hg were contained with high concentrations in 2 Chinese medicine; *Niu Huang Jiedu Pian* and *Liushen Wan*. However, when they are sulphide, they were not absorbed into the body. So, the chemical structures are very important. Furthermore, low concentrations of Hg were contained in many Chinese medicines and herbs. However, Chinese medicines and herbs produced in Japan contained these toxic elements rarely. The previous experiment raised mainly 3 queries; 1. Do the same named medicines contain same toxic elements with same level concentrations? 2. What chemical structures were the As and Hg? 3. Do not Chinese medicines and herbs produced in Japan contain toxic elements? The purpose of this study was to clear these issues.

**EXPERIMENTS:** Additional samples used in this study were 30. (The total sample number was 149.) They were grinded into powders with an agate mortar and enclosed each in a double polyethylene bag by measuring their weight. The standard samples used were JA-2 and JR-2 of rock standard, and 50 ppm of As, Hg, Sb, Co and Cr of atomic absorption reagents (Wako) were used applying to 5 filter papers (Advantec 5A). The samples and the standards were irradiated  $1\text{MW} \times 30$  min at KUR. After cooling among 5 to 10 days, the gamma-rays of medium and long half life radionuclides were measured. Also, a XRD was used to study chemical

structure of the 2 Chinese medicines of total 7 samples, which were produced in China and Japan.

**RESULTS and DISCUSSION:** All of *Niu Huang Jiedu Pian*, 3 samples produced in China, were contained from 2.2 to 8.6% of As and from 1.2 to 74 ppm of Hg. The main mineral was realgar by XRD, and the chemical structure of As was sulphide;  $\text{As}_4\text{S}_4$ . We could not find the products except for Chinese one. On the other hand, among 4 samples, 2 of *Liushen Wan* were produced in China, and contained approx. 7% of As and 7.5% of Hg. Also, among 2 Japanese *Liushen Wan*, one for child was contained approx. 1% of As and 30ppm of Hg, and one for adult was contained approx. 550 ppm of As and 1.2 ppm of Hg. The main minerals of these 2 Chinese *Liushen Wan* were realgar and cinnabar by XRD;  $\text{As}_4\text{S}_4$  and HgS. On the other hand, the main minerals of these 2 Japanese *Liushen Wan* were gold and calcite by XRD; Au and  $\text{CaCO}_3$ . So, the same named medicines never contained same toxic elements with same level concentrations. Because the chemical structures were sulphide, they are not absorbed into a body, but just given a shock for the body. So, toxicity of the elements was no problems. Additionally, some minerals in Chinese medicines tended to contain other toxic elements like Co, Cr and Sb by INAA. Furthermore, almost all herbs contained low level concentration of Hg. It was considered the sources of Hg of low concentrations were not minerals but ground contamination or dust contamination in the air.

**Conclusion:** It was clarified that some Chinese medicine contained high concentration of toxic elements and many herbs contained low concentration of Hg; however, it was considered their chemical structures were not dangerous. At the same time, the safety images of Chinese medicines and herbs were not correct.

K. Mori, H. Yoshino, Y. Iinuma, T. Fukunaga, Y. Kawabata, S. Sato<sup>1</sup>, H. Hiraka<sup>1</sup>, K. Iwase<sup>2</sup>, Y. Yamaguchi<sup>3</sup>, K. Enjuji<sup>4</sup>, K. Furuta<sup>4</sup>, and T. Kasai<sup>4</sup>

Research Reactor Institute, Kyoto University (KURRI)

<sup>1</sup>High Energy Accelerator Research Organization (KEK)

<sup>2</sup>Department of Materials and Engineering, Ibaraki University

<sup>3</sup>Institute for Materials Research, Tohoku University

<sup>4</sup>Graduate School of Engineering, Kyoto University

**INTRODUCTION:** The B-3 beam port of Kyoto University Research Reactor (KUR) had long been used as a four-circle single-crystal neutron diffractometer (4CND). For the last decade, however, the 4CND was so old that its research activity on neutron science was quite low. Therefore, the 4CND needed to be replaced and a new neutron diffractometer has been required at the B-3 beam port. Also, the new neutron diffractometer (Compact multipurpose neutron diffractometer) is critical for the structural investigations of energy storage materials such as hydrogen absorbing alloys and rechargeable lithium-ion batteries. The neutron (powder) diffraction is a powerful tool to determine the positions of light elements (e.g., hydrogen and lithium) in solids. Here, we report the current status of the B-3 beam port of KUR and the preliminary neutron diffraction experiments using a hydrogen absorbing alloy.

**INSTRUMENT:** The compact multipurpose neutron diffractometer is now being installed on the B-3 beam port. The neutron wavelength ( $\lambda$ ), which is monochromatized by the (220) plane of a Cu single crystal, is 1 Å. To cover the detector area ( $6^\circ \leq 2\theta \leq 150^\circ$ ), 24 <sup>3</sup>He tube detectors (1/2 inch in diameter) have been prepared. The distances from the monochromator to the sample and from the sample to the detector will be 1.9 m and 1.2 m, respectively. Fig. 1(a) shows the goniometer for the compact multipurpose neutron diffractometer; we performed an operation check. A detector bank including the 24 <sup>3</sup>He tube detectors will be placed on an arm of the goniometer. In addition, the new beam shutter was installed at the B-3 beam port, as shown in Fig. 1(b).

**PRELIMINARY EXPERIMENTS:** The preliminary neutron diffraction experiments were performed using the hydrogen absorbing alloy, (Ti<sub>0.31</sub>Cr<sub>0.33</sub>V<sub>0.36</sub>)D<sub>1.7</sub>, where D is the deuterium. It is worth noting that Ti<sub>0.31</sub>Cr<sub>0.33</sub>V<sub>0.36</sub> is a null alloy for neutron scattering due to its atomic compositions (i.e.,  $b_c[\text{Ti}_{0.31}\text{Cr}_{0.33}\text{V}_{0.36}] = 0$ ;  $b_c[\text{Ti}] = -3.370$  fm,  $b_c[\text{Cr}] = 3.635$  fm, and  $b_c[\text{V}] = -0.443$  fm), where  $b_c$  is the coherent scattering length. The crystal structure has

been refined on the basis of a cubic CaF<sub>2</sub>-type structure with  $a = 4.288(1)$  Å, using X-ray diffraction with Cu  $K\alpha$  radiation (see Fig. 2(b)). As shown in Fig. 2(a), we succeeded to observe several Bragg reflections for the (Ti<sub>0.31</sub>Cr<sub>0.33</sub>V<sub>0.36</sub>)D<sub>1.7</sub> on the B-3 beam port; which could be indexed on the basis of  $\lambda = 1$  Å. Note that the Bragg reflections correspond to the D-D correlations because of the null alloy.

Furthermore, the data acquisition group of the neutron science division of KEK (KEK-KENS DAQ group) has used the B-3 beam port to assess their new <sup>6</sup>Li-glass neutron detector system, LiTA12. The LiTA12 system consists of a <sup>6</sup>Li-glass neutron detector with a multianode photo multiplier tube (MA-PMT), an amplifier, and an analog-to-digital converter (ADC) board. The B-3 beam port has a wide space around the sample position; therefore we can easily install any other system like the LiTA12 system.

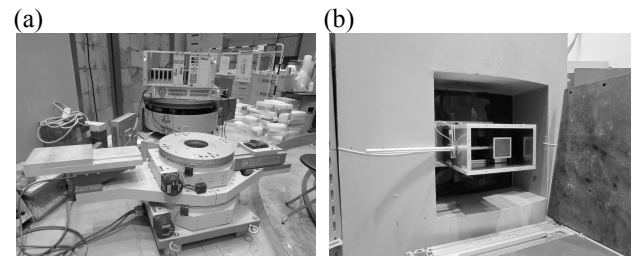


Fig. 1. Current status of the B-3 beam port of KUR: (a) new goniometer for the CMND and (b) new beam shutter installed at the B-3 beam port.

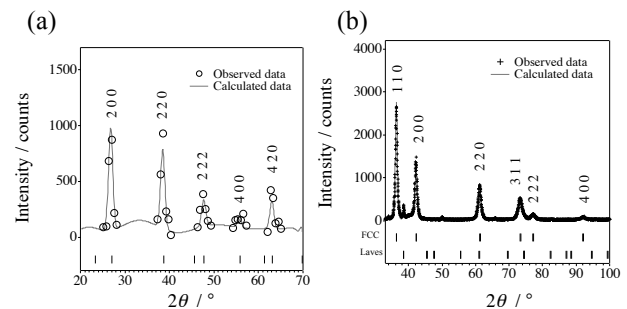


Fig. 2. Neutron and X-ray diffraction data for a hydrogen storage alloy, (Ti<sub>0.31</sub>Cr<sub>0.33</sub>V<sub>0.36</sub>)D<sub>1.7</sub>, collected at (a) the B-3 beam port of KUR and (b) a X-ray diffractometer with Cu  $K\alpha$  radiation.

採択課題番号 26007 材料研究および中性子検出器開発を目的とした  
小型多目的中性子回折装置の建設

通常採択

(京大・原子炉) 森一広、吉野泰史、飯沼勇人、福永俊晴、川端祐司 (高エネ研) 佐藤節夫、平賀晴弘 (茨城大・工) 岩瀬謙二 (東北大・金研) 山口泰男 (京大院・工) 延壽寺啓吾、古田幸三、笠井拓矢

## CO1-3 Synthesis of Metal Nanoparticles under the Gamma-ray Irradiation Field

F.Hori, T.Hori, A.Tohkai, H.Nakanishi, A.Iwase,  
M.Sakamoto<sup>2</sup>

Dept. of Mater. Sci., Osaka Prefecture University  
<sup>1</sup>Research Reactor Institute, Kyoto University

**INTRODUCTION:** It is known that metallic nanoparticles have some specific properties, which are not appear in bulk materials such as catalytic activities, magnetic properties and so on. Also the character of them depends on its size, shape, structure, chemical composition and so on. For instance, it is known that Au nanoparticles exhibit the surface plasmon resonances (SPRs) in specific wavelength at about 520 nm. They have many possibilities to applied for various industrial fields. Generally, many kinds of metal nanoparticles commercially are synthesized by using chemical reaction method. On the other hands, it has been reported that specific feature of metallic nanoparticles can be synthesized under energetic irradiation fields, such as ultrasonic, electron, gamma-ray, plasma and so on. Using these irradiation reduction methods, it is possible to fabricate the unexpected structured nanoparticles. So far, we have successfully synthesized Cu nanoparticles, which is not easy to reduce in aqueous solution by chemical reaction, by using gamma-ray irradiation reduction method [1]. However, many of them are not only pure Cu but also copper oxides. In this study, we have tried to fabricate pure Cu nanoparticles by adding of ethylene glycol instead of diethylene glycol.

**EXPERIMENTS:** Aqueous solutions with a given concentration of copper complex  $((\text{CH}_3\text{COO})_2\text{Cu}\cdot\text{H}_2\text{O})$  with an additive of sodium dodecyl sulfate (SDS) and ethylene glycol (EG). The solution was argon gas purged and sealed into polystyrene vessels. They were irradiated at about 300 K with 1.17 and 1.33 MeV gamma-rays from  $^{60}\text{Co}$  radio active source at gamma irradiation facility in KURRI, Kyoto University. The total dose was fixed to 23.4 kGy with dose rate of 15.6 kGy/h. UV-vis absorption spectra were measured by using Shimadzu UV-2550 spectrophotometer in the wavelength range in 300-800 nm and the shapes and the structures for all colloidal products were observed by conventional TEM

(JEOL JEM-2000FX). Samples for TEM observations were made by putting a drop of colloidal solutions on a carbon film with a Mo mesh and dried them in a vacuum.

### RESULTS:

Figure 1 shows the UV/vis absorption spectra for aqueous solutions before and after gamma-ray irradiation. It appears only one absorption peak around 570 nm, which shows pure Cu nanoparticles production, after gamma-ray irradiation. This is quite different from the result that of adding of DEG [1]. This result clearly shows that only pure Cu nanoparticles were generated and no oxidation takes place during gamma-ray irradiation. This is because ethylene glycol act as the scavenger of oxidation radicals from  $\text{H}_2\text{O}$  by gamma-ray irradiation radiolysis. TEM observation shows that generated particles are monodisperse spherical shape and its average diameter is about 17 nm (fig. 2).

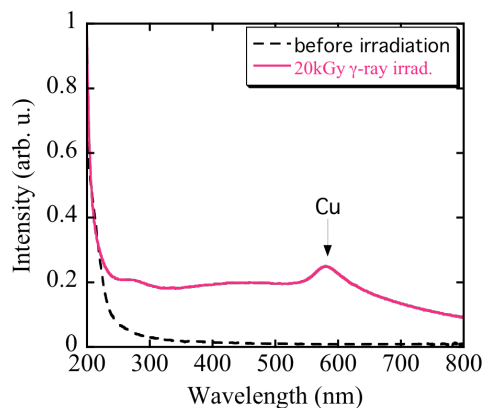


Fig. 1 UV/vis absorption spectra of aqueous solutions including Cu-ions before and after gamma-ray irradiation.

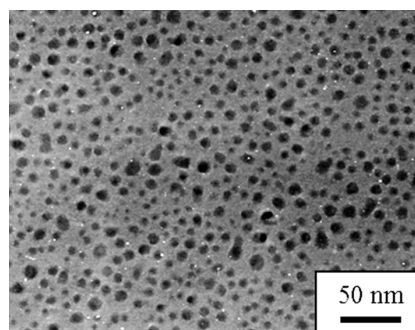


Fig. 2 TEM image of synthesized Cu nanoparticles by gamma-ray irradiation reduction.

### References

- [1] T.Hori, K.Nagata, A.Iwase and F.Hori, Jpn. J. Appl. Phys. 53(5), 2014

## CO1-4 The Role of Human Oxidation Resistance 1 (OXR1) in Cellular Response to Radiation

A. Matsui, Y. Yoshikawa, A. Yamasaki, T. Saito<sup>1</sup>, N. Fujii<sup>1</sup>, K. Tano<sup>1</sup>, Q. Zhang-Akiyama

Graduate School of Science, Kyoto University  
<sup>1</sup>Research Reactor Institute, Kyoto University

**INTRODUCTION:** OXR1 (oxidation resistance 1) is a gene highly conserved in eukaryotes. Previous studies showed that human OXR1 suppressed spontaneous mutation in *E. coli mutH nth* [1]. OXR1 is induced by oxidative stresses such as H<sub>2</sub>O<sub>2</sub> and is localized to mitochondria [2]. However, the function of OXR1 remains to be elucidated. Reactive oxygen species (ROS) act as a mediator of ionizing radiation -induced cellular damage. To clarify the protective functions of OXR1 against oxidative damage, we studied the effects of OXR1 on radiation -generated damage. In this study, we used gamma -ray and high LET heavy -ion beams, which are known of stronger cell killing effect than X -rays (3). Our studies showed that OXR1 proteins in HeLa cells were induced by carbon -ion beam, and that OXR1-knockdown HeLa cells were highly sensitive to heavy -ion beams. This year, we found higher micronucleus formation rate in the cells after irradiation. Then, the cells were released from cell cycle check point earlier than control cells. To study the function of OXR1 further, we are now under constructing OXR1-knockout DT40 cells.

### EXPERIMENTS:

#### Irradiation

HeLa cells stably expressing shRNA targeting OXR1 or luciferase were synchronized at G1/S phase, and irradiated with gamma -ray (0.77 Gy/min), carbon -ion (290MeV/nucleon, 87.0keV/um) or iron -ion (500MeV/nucleon, 64.83 mmH<sub>2</sub>O) beams generated by the Heavy Ion Medical Accelerator in Chiba (HIMAC). The irradiated cells were incubated for about 24 or 34 h, and fixed. The cells were used in the following experiments.

#### Micronucleus formation

The nuclei were counter -stained with DAPI. The micronuclei were detected with fluorescence microscopy.

#### Cell cycle analysis

Nuclei were stained with 50 ug/mL PI. The samples were analyzed with FACS.

#### Targeted disruption of OXR1 in DT40 cells

We prepared chicken OXR1 disruption constructs using puromycin, blasticidin or histidinol resistance gene. The chicken B lymphoma cells DT40 are cultured and transfected with the three gene disruption constructs.

**RESULTS:** The chicken OXR1 targeting constructs, OXR1-pur, OXR1-bsr and OXR1-his were generated. DT40 cells are now transfected with electroplation method. OXR1 -knockout DT40 cells are not gained.

**FUTURE PERSPECTIVE:** We will try constructing OXR1 -knockout TD40 cells. After finishing the step, we will study radation -induced ROS, DNA damages and cell death of the constructed cells.

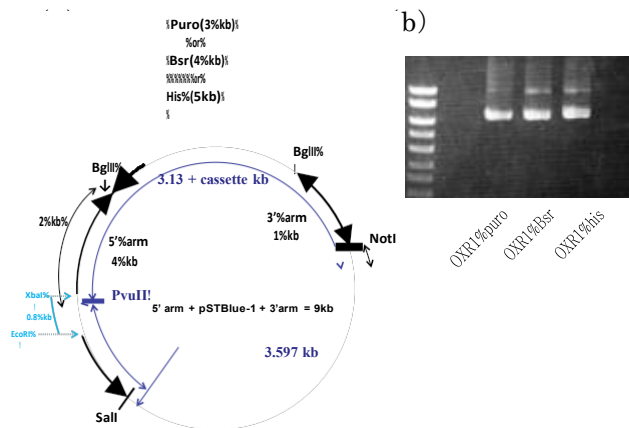


Fig. 1. (a) Schematic representation of the OXR1 disruption constructs. (b) Electrophoresis of three constructs.

### REFERENCES:

- [1] M.R. Volkert *et al.*, Proc. Natl. Acad. Sci., (2000) **97**, 14530-14535.
- [2] N.A. Elliott, M.R. Volkert, Mol. Cell Biol., (2004) **24**, 3180-318.
- [3] M. Suzuki *et al.*, Int. J. Radiat. Oncol. Biol. Phys., (2000) **48**, 241-250

## CO1-5 Development of an Advanced Optical Fiber Type Neutron Detector

K. Watanabe, Y. Kumagai, A. Uritani, A. Yamazaki, Y. Sakurai<sup>1</sup> and H. Tanaka<sup>1</sup>

Graduate School of Engineering, Nagoya University  
<sup>1</sup>Research Reactor Institute, Kyoto University

**INTRODUCTION:** The Boron Neutron Capture Therapy (BNCT) has been developed as one of the promising radiotherapies. In this radiotherapy, the neutron dose evaluation is quite important. Therefore, we are developing a novel small neutron flux monitor using an optical fiber. A small size optical fiber type neutron detector is one of the promising candidates of the on-line small neutron flux monitors in BNCT. The conventional optical fiber neutron detectors, however, show no peak shape corresponding to the neutron absorption reactions, in a pulse height spectrum due to the non-uniform and/or poor light collection [1-3]. These conventional detectors used ZnS-LiF, Li glass or plastic scintillators. On the other hand, we apply a new neutron scintillator Eu:LiCaAlF<sub>6</sub>. This scintillator has some excellent properties, such as high light yield, high lithium content, transparency and chemical stability. The light yield of this scintillator is approximately 5 times higher than that of the Li glass.

Figure 1 shows the conceptual drawing of the small size optical fiber type neutron detector. Features of our detector are use of a bright scintillator and a quite small scintillator size. The scintillator size is controlled larger than ranges of <sup>6</sup>Li(n,t) reaction products and smaller than ranges of fast electrons induced by gamma rays to suppress the signal pulse height only for gamma-ray induced events.

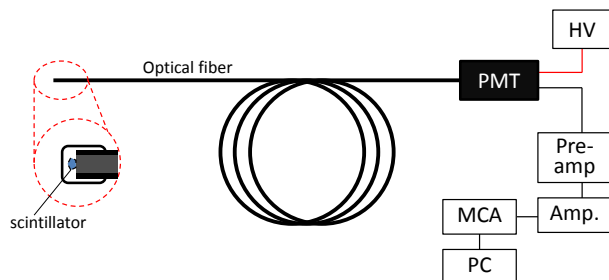


Fig. 1 Conceptual drawing of the optical fiber type neutron detector.

So far, we evaluated dynamic range and long term stability of our detector. Our detector was confirmed to show good linearity up to 10<sup>9</sup> n/cm<sup>2</sup>/s. However, peak pulse height decreases due to neutron irradiation. In this report, we experimentally evaluate neutron radiation hardness of the developed detector.

**RADIATION HARDNESS TEST:** We fabricated the optical fiber type neutron detector using a small Eu:LiCaAlF<sub>6</sub> scintillator and experimentally evaluated its radiation hardness at the Heavy Water Neutron Irradiation Facility (HWNIF) of Kyoto University Research

Reactor (KUR). One of the reasons of decrease of the peak pulse height is expected to be reduction of the transmittance of the optical fiber. We, therefore, irradiated neutrons to the optical fiber used in our detector. The neutron flux was 10<sup>9</sup> n/cm<sup>2</sup>/s. We continuously measured the transmittance of the optical fiber by using a spectrometer during the neutron irradiation. The transmittance of the fiber  $T(t)$  decreases as;

$$T(t) = T_0 \exp(-t/\tau)$$

where  $T_0$ ; initial transmittance,  $\tau$ , life time of the optical fiber. We can determine the lifetime by fitting this equation to the experimental data of decrease of the optical fiber transmittance. Figure 2 shows the wavelength dependence of the lifetime of the optical fiber under neutron irradiation with 10<sup>9</sup> n/cm<sup>2</sup>/s. The lifetime in infrared region is confirmed to be longer than that in ultraviolet and visible region. The emission wavelength of the Eu:LiCaAlF<sub>6</sub> scintillator is 380 nm, where the lifetime of the transmittance is not so long. From these results, one of the reasons of decrease of the peak pulse height is confirmed to be reduction of the transmittance of the optical fiber.

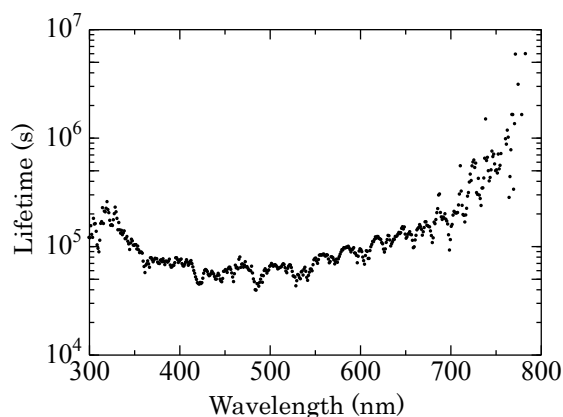


Fig. 2 Wavelength dependence of the lifetime under neutron irradiation.

In infrared region, the neutron radiation hardness is quite high. If we can use a neutron scintillator with infrared emission, the radiation hardness of the optical fiber type neutron detector can be improved.

### REFERENCES:

- [1] M. Ishikawa *et al.*, Appl. Rad. Isotopes, **61** (2004) 775-779.
- [2] M. Ishikawa *et al.*, Nucl. Instr. Meth. A, **551** (2005) 448-457.
- [3] Y. Ito *et al.*, Radiat. Prot. Dosim., **110** (2004) 619-622.

## CO1-6 Focusing Test of an Ellipsoidal Neutron Mirror with a Metal Substrate

M. Hino<sup>1</sup>, J. Guo<sup>2</sup>, S. Takeda<sup>3</sup>, T. Oda<sup>1</sup>, S. Morita<sup>2\*</sup>,  
J. Kato<sup>2</sup>, Y. Yamagata<sup>2</sup>, M. Furusaka<sup>3</sup>, Y. Kawabata<sup>1</sup>

<sup>1</sup>Research Reactor Institute, Kyoto Univ., Japan

<sup>2</sup>RAP, RIKEN, Japan,

<sup>3</sup>Grad. Sch. of Eng., Hokkaido Univ., Japan

\*Present address: Tokyo Denki Univ. Japan

**INTRODUCTION:** Progress of neutron optical devices is significant, however, it is still very difficult for neutron aspherical focusing mirror. Because the required surface roughness is smaller than 0.5 nm even for  $m=3$  supermirror coating and the mirror size is large. In order to realize large ellipsoid neutron focusing mirror, we are doing several trials. In this study, we show the neutron focusing experimental result of ellipsoid mirror with a metal substrate. In general it is very difficult to make a smooth surface on metal due to the grain structure. By using electroless nickel-phosphorus (NiP) plated material, we can overcome this problem. Electroless NiP has great advantages for realizing neutron mirror because of its amorphous structure, good machinability and relatively large critical angle of total reflection for

neutrons without supermirror coating.

**EXPERIMENTS:** The design, manufacturing and polishing of the mirror were carried out by RIKEN [1]. The form accuracy of the mirror was estimated to be 5.3  $\mu\text{m}$  Peak-to-Valley (P-V) and 0.8  $\mu\text{m}$  P-V for the minor-axis and major-axis direction respectively, while the surface roughness was reduced to 0.2 nm rms. The neutron focusing performance of the mirror was evaluated using CN3 beam line at Kyoto University Research Reactor (KUR-CN3).

**RESULTS:** As shown in Fig.1, the two-dimensional (2D) image of neutron beam reflected by an ellipsoid focusing mirror was clearly changed as a function of distance between the mirror center and detector. Cadmium (Cd) pinhole with an aperture size of 1 mm in diameter to choose incident beams from the CN3 guide a Cd U-shape slit to remove unnecessary neutron beams affecting the focusing. The circular focusing spot at the focal point was almost equivalent to that of the pinhole.

**REFERENCES:**

[1] J.Guo, et al., Optics Express, 22(2014)24666-24677.

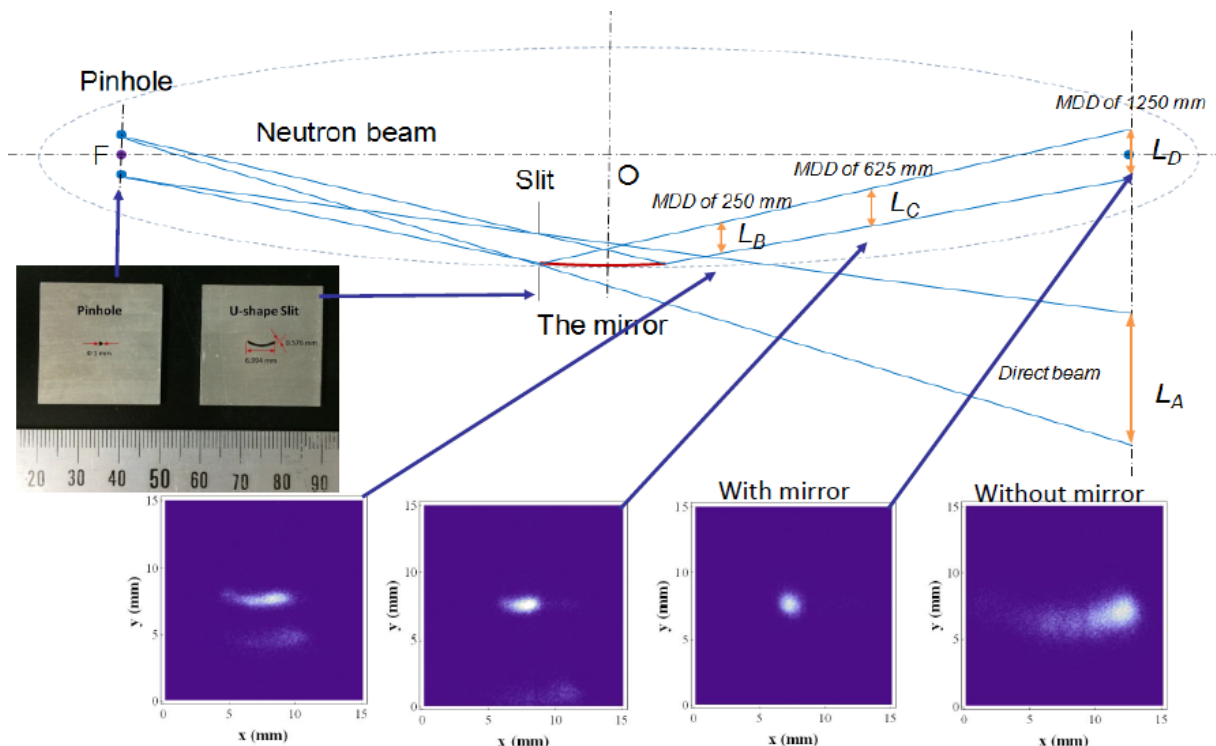


Fig.1 Schematic layout of neutron focusing experiment at KUR-CN3 and the 2D images of beam shapes as a function of the mirror center to detector distance (MDD), and the direct beam shape without the focusing mirror at the focal point.

採択課題番号 26065 次期中性子ビーム科学施設のための中性子光学デバイス開発 通常採択  
(京大・原子炉) 日野正裕、小田達郎、川端祐司 (KEK・IMSS) 山田悟史、遠藤仁、瀬戸秀紀  
(理研) 郭江、森田晋也、加藤純一、山形豊 (北大) 武田晋

## CO1-7 Examination of the Usefulness as the New Boron Compound of KA-BSH for Born Neutron Capture Therapy

Gen Futamura<sup>1</sup>, Shinji Kawabata<sup>1</sup>,  
Shin-Ichi Miyatake<sup>2</sup>, Toshihiko Kuroiwa<sup>1</sup>,  
Yoshihide Hattori<sup>4</sup>, Mitsunori Kirihata<sup>4</sup>, Hiroki Tanaka<sup>3</sup>,  
Yoshinori Sakurai<sup>3</sup>, Shin-Ichiro Masunaga<sup>3</sup>, Koji Ono<sup>3</sup>

<sup>1</sup>Department of Neurosurgery, Osaka Medical College

<sup>2</sup>Division for Advanced Medical Development, Cancer Center, Osaka Medical College

<sup>3</sup>Research Reactor Institute, Kyoto University

<sup>4</sup>Osaka Prefecture University

### INTRODUCTION:

Boron neutron capture therapy (BNCT) is an attractive technique for malignant brain tumor treatment. [1] It is important to have a significant differential uptake of <sup>10</sup>B between tumor cells and normal cells to achieve potent tumor-selective antitumor effects. Today, clinically used dodecaboranethiol (BSH) is transferred to brain tumors only through the disrupted blood-brain barrier (BBB), so it is difficult for BSH to reach regions that tumor cells invade microscopically where the BBB seems to be normal. On the other hand, boronophenylalanine (BPA), which transfers boron via L-type amino acid transporter, can deliver <sup>10</sup>B even in the infiltrating tumor cell population where the BBB is normal. However, some amounts of <sup>10</sup>B are inevitably taken into the normal cells by BPA systemic administration. A wide variety of boron delivery agents have been synthesized to solve these problems. [1] Kojic acid (KA) was reported as the agent which showed intense uptake in malignant tumor. Therefore, we designed and synthesized KA-BSH and evaluated therapeutic effect of KA-BSH as boron delivery agents for BNCT in F98 glioma cell bearing rat brain tumor model.

### MATERIALS AND METHODS:

BNCT was performed 14 days following stereotactic implantation of 10<sup>3</sup> F98 glioma cells implanted rat brain tumor model. Rats were transported to the Nuclear Reactor Laboratory at Kyoto University Research Reactor Institute.

Based on the results of the biodistribution study, we prepared 4 groups. The rats were then randomized on the basis of weight into experimental groups of 6-8 animals each as follows: Group 1, KA-BSH administered by in-

travenous administration (iv) and neutron irradiated; Group 2, KA-BSH administered by convection enhanced delivery (CED) by using Alzet pump, which can deliver solutions directly into the solid tissue with continuous pressure gradient distribution [2, 3], and neutron irradiated; Group 3, neutron irradiation; Group 4, untreated controls. BNCT was initiated 1 h after termination of Alzet pump infusion or i.v. administration. All irradiated rats were anesthetized with a pentobarbital sodium. The rats were irradiated for 60 min with 1MW. The antitumor effects of BNCT were evaluated in the mean survival times (MSTs) of the rat.

### RESULTS:

The estimated physical radiation doses delivered to tumor, brain and blood were calculated according to boron concentrations. The physical radiation doses delivered to the tumor were 1.1Gy for KA-BSH administered by iv. The corresponding normal brain doses were 1.0Gy. The survival data of Group 1, 2, 3 and 4 following BNCT showed that the MSTs were 35.4±8.0 days, 29.8±3.3 days, 30.2±2.2 days and 28.5±3.1 days, respectively. We accepted significantly extend the duration of survival time of the rats group using KA-BSH administered by iv (Group 1), compared with the neutron irradiation only (Group 3) (p<0.005).

### CONCLUSION:

Survival times of group1 were significantly prolonged even compared with irradiation group. The therapeutic effect of KA-BSH administered by iv was higher than that we expected from these tissue boron concentrations and physical radiation doses. This study suggested that KA-BSH might have extremely high compound biological effectiveness (CBE), and KA-BSH might be the drug to add therapeutic effect of clinical BNCT using BPA or in combination with BPA / BSH to.

### REFERENCES:

- [1] Barth RF *et al*: Radiat Oncol 7: 146, 2012.
- [2] Hiramatsu R *et al*: J Pharm Sci 104: 962-70, 2015
- [3] Kawabata S *et al*: J Neurooncol 103: 175-85, 2011



## CO2-1 Development of Measurement Method for Epi-Thermal Neutrons Using the $^{10}\text{B}(n,\alpha\gamma)$ Reaction

T. Matsumoto, A. Masuda, H. Harano, H. Tomita<sup>1</sup>, K. Ito<sup>1</sup>, Y. Ichinose<sup>1</sup>, J. Kawarabayashi<sup>1</sup>, T. Iguchi<sup>1</sup>, K. Watanabe<sup>1</sup>, A. Uritani<sup>1</sup>, J. Hori<sup>2</sup>, Y. Sakurai<sup>2</sup>

National Metrology Institute of Japan, National Institute of Advanced Industrial Science and Technology

<sup>1</sup>Department of Engineering, Nagoya University

<sup>2</sup>Research Reactor Institute, Kyoto University

**INTRODUCTION:** Evaluation of neutron dose equivalent for the epi-thermal neutron region is very important in work places with neutron sources or nuclear fuels as well as irradiation fields in a boron neutron capture therapy. A new calibration method for the response of neutron dosimeters has been developed using a pulse white neutron beam[1]. On the other hand, it is not easy to measure precisely the neutron fluence for epi-thermal neutrons in an irradiation field, although a gold activation method is usually used in a thermal neutron region, and an elastic neutron scattering reaction with hydrogen atoms is adopted in a fast neutron region to measure precise neutron fluence. In the present study, we have developed a measurement method for epi-thermal neutrons using a  $^6\text{Li}^{nat}\text{Gd}^{10}\text{B}_3\text{O}_9:\text{Ce}^+$  (LGB) and an NaI(Tl) scintillators. We also developed an epi-thermal neutron camera consisting of GEMs and resonance filters for neutrons up to 10 keV.

**EXPERIMENTS:** A collimated neutron beam through collimators was obtained by the photo neutron reaction using a water-cooled tantalum target at the KURRI Linac [2]. The 50 mm-diameter and 5-mm thick LGB scintillator was set at the center of the neutron beam. The 76.2 mm-diameter and 76.2 mm thick NaI(Tl) was located out of neutron beam at an angle of 135 degrees with respect to the neutron beam direction. When the LGB scintillator detects neutrons by the  $^{10}\text{B}(n,\alpha\gamma)$  reaction, 478 keV monoenergetic gamma rays are produced and subsequently detected with the NaI(Tl) scintillator. In the coincidence measurements, the neutron capture reaction rate in the LGB scintillator is obtained without detection efficiencies of the LGB and the NaI(Tl) scintillators. Moreover, the absolute neutron fluence is determined by measuring gamma rays from the  $^{10}\text{B}(n,\alpha\gamma)$  reaction with the NaI(Tl) scintillator in setting a 5-cm thick  $^{nat}\text{B}$  total absorption sample in front of the LGB scintillator.

The detection system were experimentally tested using the neutron beam from a neutron source with the photo neutron reaction by means of the TOF method. Fig.1 shows the pulse height spectra of the NaI(Tl) scintillator with and without the coincidence measurements. In the NaI(Tl) scintillator, 478 keV gamma rays due to the  $^{10}\text{B}(n,\alpha\gamma)$  reaction is detected around 600 channel. The counts due to other gamma rays by the coincidence measurements. In the experimental room, many boron is used in shielding materials and collimators. Background measurements with only NaI(Tl) detector were also performed.

Characteristics of a prototype of epithermal neutron imaging camera were also measured using the TOF method. The prototype detector consists of a silver plate as a resonance filter, a  $\text{B}_4\text{C}$  thermal neutron absorber, and a GEM with a neutron converter of  $^{10}\text{B}$ .

**RESULTS:** From the coincidence measurement, count rates for the LGB detector ( $N_\alpha$ ) and the NaI(Tl) detector ( $N_\gamma$ ) and coincidence count rate ( $N_{\alpha\gamma}$ ) are derived. Neutron capture reaction rate due to the  $^{10}\text{B}(n,\alpha\gamma)$  reaction is derived from  $N_\alpha N_\gamma / N_{\alpha\gamma}$ . Neutron fluence was finally determined using ratio of count rates in measurements with and without the thick  $^{nat}\text{B}$  total absorption sample. The experimental results are checked by Monte Carlo simulations in future.

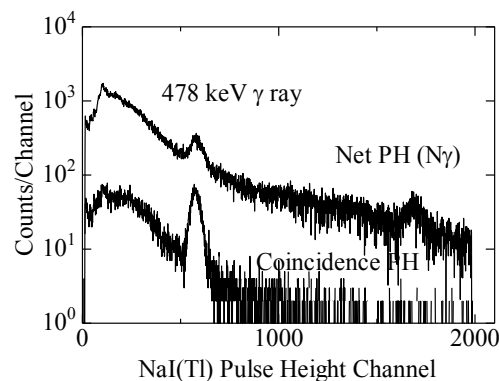


Fig.1. Pulse height spectra measured with the NaI(Tl) detector.

### REFERENCES:

- [1] T. Masumoto et al., KEK proc. 2011 (8), 218-225 (2012).
- [2] K. Kobayashi et al., Annu. Rep. Res. Reactorinst. Kyoto Univ. 22, 142 (1989).

採択課題番号 26055 熱中性子フルエンス率の測定の高度化とその国際標準化に関する研究 通常採択 (産総研) 原野英樹、松本哲郎、増田明彦、(名大) 井口哲夫、瓜谷章、河原林順、渡辺賢一、富田英生、伊藤海、一之瀬裕一郎、杉本大 (京大・原子炉) 堀順一、櫻井良憲

## CO2-2 Measurement of Gamma Ray and Neutron Spectrum of Curium Isotope (3)

Y. Nauchi, J. Hori<sup>1</sup>, T. Sano<sup>1</sup>

Central Research Institute of Electric Power Industry  
<sup>1</sup>Research Reactor Institute, Kyoto University

**INTRODUCTION:** Yields and spectra data of neutrons and higher energy (>3MeV)  $\gamma$  rays from the spontaneous fission of <sup>244</sup>Cm has been focused on since they are major source in spent nuclear fuel. The radiations would be significant indicators of existence of nuclear materials. However those measured data are scarce. KURRI have possessed Cm samples (Table 1 [1]) in which Cm<sub>2</sub>O<sub>3</sub> are diluted in aluminum (Al) powder encapsulated in Al cladding. In this work, preliminary characterizations of CM244 and CM246 are done.

**GAMMA RAY MEASUREMENTS:**  $\gamma$  rays from samples were measured with a Ge detector of 20% efficiency.  $\gamma$  rays radiated subsequent to  $\alpha$  decays were measured. For CM244 and CM246 samples, multiple  $\gamma$  rays of different energies from <sup>243</sup>, <sup>244</sup>, <sup>245</sup>Cm were well measured. The activity ratio of CM244/CM246 are  $0.935 \pm 0.0191$  and  $0.714 \pm 0.004$  for <sup>244</sup>, <sup>245</sup>Cm, respectively. The ratios agree with the data in Table 1.

Then, higher energy  $\gamma$  rays from 2 to 5MeV are focused on to clarify whether noise spectra exist or not for measurements of 2.223MeV and fission  $\gamma$  rays. As shown in Fig. 1 and broader peaks from 2.5 to 5MeV are found for CM244. The bump spectra exist only slightly for CM246 so it is considered the fission  $\gamma$  ray spectrum dominates the energy region above 2.3MeV in CM246. The resolutions of the peaks are poorer than 2.6145MeV  $\gamma$  ray from <sup>208</sup>Tl. That indicates the  $\gamma$  rays are radiated from compound nucleus moving with a certain kinetic energy more than keV. Based on literatures, the 2.235MeV  $\gamma$  rays might be attributed to <sup>27</sup>Al( $\alpha$ , $\gamma$ ) reactions [2]. The origin of the other higher energy  $\gamma$  rays are unknown although neutron direct interactions with Ge detector materials are not the candidates since such bump spectra were not found for a case when <sup>252</sup>Cf was put alternatively to CM samples.

The higher energy bumps should be eliminated to quantify fission  $\gamma$  ray spectrum. For the purpose with the samples, coincidence measurements with multiple detectors would be required as well as studies on nuclear physics to explore the reactions radiating such  $\gamma$  rays.

**NEUTRON MEASUREMENTS:** By putting CM samples and Californium (<sup>252</sup>Cf) neutron source behind polyethylene block of 10cm thickness, the H(n, $\gamma$ ) 2.223MeV  $\gamma$  rays were measured with the Ge detector. As shown in Fig. 2, 2.235MeV  $\gamma$  ray spectrum overlaps the 2.223MeV one for CM samples. The former was subtracted from the latter by normalizing the count rate of the former over a region from 2.235 to 2.250MeV to that of latter. Then the count rate of the 2.223MeV  $\gamma$  rays was estimated. On the other hand, fast neutrons from the CM samples were measured with a NE213 scintillator. The measured count

rates are compared in Table 2. Considering the difference of neutron spectra shown in Fig 3, the count rates in the two detectors agree fairly well (18% difference in CM244). Accordingly, absolute measurement of neutrons from the sample would be capable for CM samples taking the neutron spectrum into account.

### REFERENCES:

[1] T. Fujii et al., Conf. Record 2010 Annual Meeting of AESJ pp58-66 (on CD-ROM).

[2] A. G. Seamster *et al.*, Phys. Rev. C **29** (1984) 394

Table 1: Isotopic composition of Cm samples [1]

Sample	<sup>244</sup> Cm	<sup>245</sup> Cm	<sup>246</sup> Cm	<sup>247</sup> Cm	<sup>248</sup> Cm
CM244	88.53	3.13	8.34		
CM246	24.18	1.11	62.18	3.00	9.53

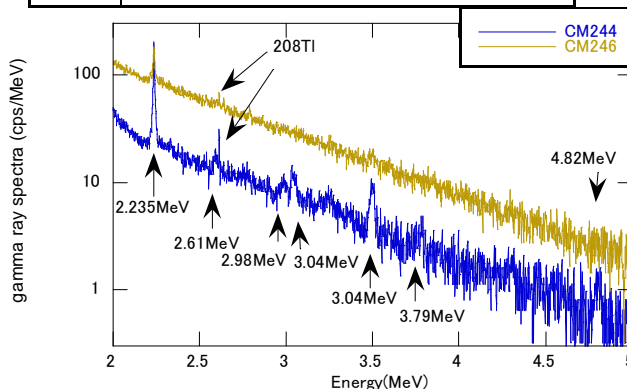


Fig. 1  $\gamma$  ray spectrum measured for CM244 and CM246.

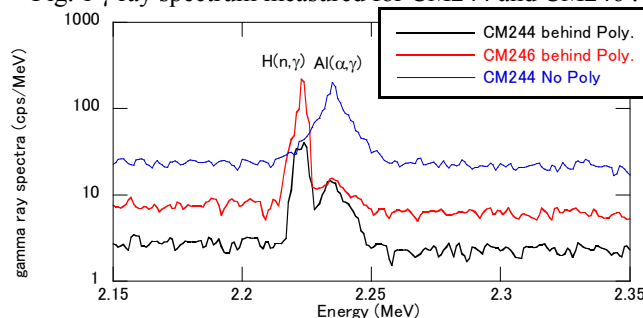


Fig. 2 H(n, $\gamma$ ) spectrum overlapped by Al( $\alpha$ , $\gamma$ ) spectrum

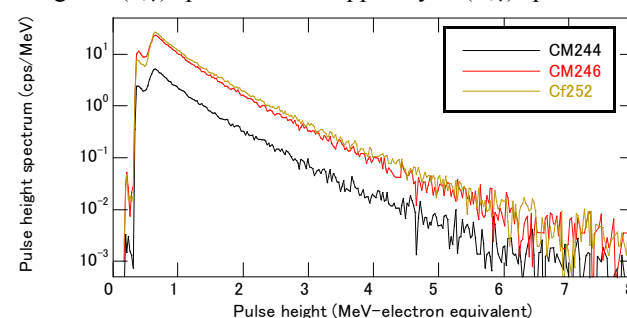


Fig. 3 Neutron spectrum measured with NE213.

Table 2: Count rate ratio of neutrons for CM / <sup>252</sup>Cf

Method	CM244/ <sup>252</sup> Cf	rel.err	CM246/ <sup>252</sup> Cf	rel.err
H(n, $\gamma$ )	0.212	0.030	0.860	0.019
NE213	0.180	0.063	0.843	0.012

## CO2-3 Development of Hybrid Ce:LiCAF Scintillator for Nuclear Data Measurement

T. Fujiwara<sup>1,4</sup>, D. Matsuyama<sup>2</sup>, K. Tagi<sup>2</sup>, Y. Kusumawati<sup>2</sup>, J. Hori<sup>3</sup>, T. Sano<sup>3</sup>, and M. Uesaka<sup>1</sup>

<sup>1</sup>Nuclear Professional School, The University of Tokyo

<sup>2</sup>Department of Nuclear Engineering and Management, The University of Tokyo

<sup>3</sup>Research Reactor Institute, Kyoto University

<sup>4</sup>National Metrology Institute of Japan, National Institute of Advanced Industrial Science and Technology

**INTRODUCTION:** Precise nuclear data measurement is needed for new generation reactor design and development. In this field, neutron Time-of-Flight (TOF) measurement with pulsed neutron source is playing important role.

In this work, we report on the first nuclear data measurement at KURRI-Linac neutron source with hybrid Ce:LiCAF scintillator which has high neutron detection efficiency and better gamma-ray discrimination<sup>[1][2]</sup>. Ce:LiCAF covered with plastic scintillator<sup>[3]</sup> showed excellent characteristics in the detection efficiency and gamma-ray discrimination compared with other conventional scintillators, such as Li-Glass and Li:ZnS scintillators. Especially, excellent pulse height discrimination of neutrons from gamma rays and very short decay time are very promising for a new field of fast neutron detection and great recovery from the gamma-flash.

**EXPERIMENTS:** Neutron transmission experiments (NRTA: Neutron Resonance Transmission) were carried out at 8m TOF line at KURRI-Linac. <sup>237</sup>Np sample was placed at the neutron beam line, and the detector were place in 50 cm behind the sample.

Accelerator was operated in 50Hz and 100ns pulse width. We have fabricated hybrid scintillator based on 10 × 10 × 2mm size Ce:LiCAF scintillator crystal. The crystal were covered with plastic scintillator (PPO and POPOP) and coupled to photo multiplier tube (Hamamtsu R329-05). 5mm thick Pb filter was placed to reduce gamma-rays. *Fast Comtec MPA3* were used for DAQ system.

**RESULTS:** Fig. 1 shows pulse height spectrum of neutron detector. The line in green shows energy spectrum of neutron and gamma-ray mixed field, and the line in pink represents a energy spectrum when neutron were shielded with Boron. As shown in Fig. 1, clear neutron peak and very low sensitivity to gamma-ray were observed, which stands for great gamma-ray discrimination. This is due to coupling Ce:LiCAF scintillator with plastic scintillator which enables to improve alpha/beta ratio. With our detector, we successfully measured high energy neutrons up to 2.4 keV. Fig. 2 shows the absorption neutron cross-section of <sup>237</sup>Np.

We conclude that TOF spectrum of Ce:LiCAF showed

excellent performance for high energy neutron measurement. 8 m TOF line at KURRI.

In addition, low gamma-ray sensitivity great gamma/neutron discrimination with pulse height and showed very quick recovery from gamma-burst which enables high energy neutron measurement.

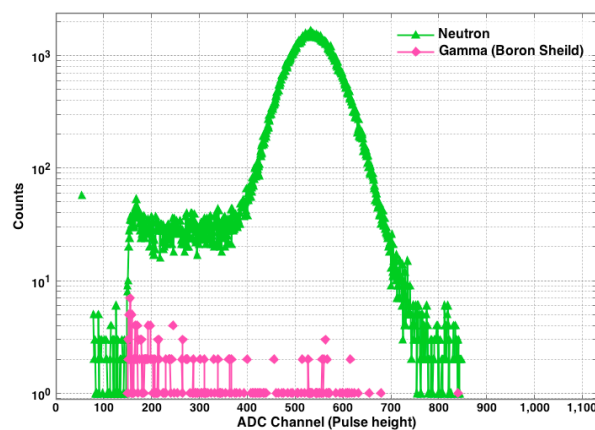


**Fig. 1.** Pulsed height spectrum of Ce:LiCAF based hybrid scintillation neutron detector. Showed clear neutron peak and low sensitivity to gamma-ray.

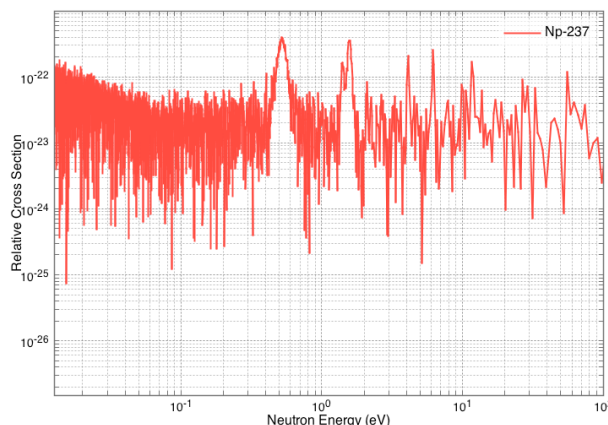


**Fig. 2.** First result of neutron transmission experiment (NRTA: Neutron Resonance Transmission) of <sup>237</sup>Np. The measurement were carried out at 8m TOF line at KURRI-Linac

### REFERENCES:

- [1] A. Yamazaki *et al.*, Nucl. Instr. and Meth. A (2011), doi:10.1016/j.nima.2011.02.064
- [2] K. Watanabe *et al.*, Conference record of NSS IEEE, 201
- [3] T. Fujiwara *et al.*, Neutron News, vol. 23, no. 4, pp. 31–34, Nov. 2012.

採択課題番号 26058 高速シンチレータアレイを用いた二次元核データイメージング装置の開発 通常採択 (東大・工、産総研) 藤原 健 (東大・工) 松山 大樹、田儀 和浩、Yudhitya Kusumawati、上坂 充 (京大・京大炉) 堀 順一、佐野 忠弘

J. Hori, T. Yagi, T. Sano, Y. Takahashi, H. Yashima

Research Reactor Institute, Kyoto University

**INTRODUCTION:** In order to reduce radioactive toxicity, feasibility for nuclear transmutation of minor actinides (MAs) and long-lived fission products (LLFPs) by utilizing innovative nuclear system has been investigated. The report on OECD/NEA No.6410 [1] indicates that there are large gaps on capture cross sections of minor actinides (MAs) between current uncertainty and required accuracy.

Since high-intensity-pulsed neutron sources with spallation reaction such as CERN, LANL and J-PARC become available, statistical error of relative neutron capture cross sections of MAs with time-of-flight (TOF) method was decreasing drastically. However, accurate normalization of TOF data is still an important issue, and unrecognized bias effect needs to be eliminated as much as possible. In this study, we proposed the thermal capture cross section measurement methods using variable neutron fields and developed variable neutron fields in the KURRI-LINAC.

**EXPERIMENTS:** In order to cross checked the neutron capture cross sections by integral measurements using variable neutron flux field, KURRI-LINAC based neutron source was utilized. Neutrons produced by photonuclear reactions were moderated by light water. Four kinds of variable neutron flux fields were constructed by merging boric-acid solution into the light water moderator, as listed in Table. 1. Neutron spectra of these fields were obtained by TOF measurement of the capture gamma-rays from the  $^{10}\text{B}(n,\alpha\gamma)$  reaction with twelve  $\text{Bi}_4\text{Ge}_3\text{O}_{12}$  (BGO) scintillators, which located at  $12.7 \pm 0.02$  m from the photoneutron source. The linac was operated with a repetition rate of 50 Hz, a pulse width of 100 ns, an averaged current was 18  $\mu\text{A}$  and an electron energy of about 30 MeV. Gold foils with and without Cd cover were also irradiated for each moderator. Reaction rates were obtained with an activation foil method.

**RESULTS:** Figure 1 shows the neutron spectra for moderators with different boric-acid concentration measured by the TOF method. The thermal bumps were fitted with the Maxwell distribution and the neutron temperatures were determined from 319.5 to 430.8 K. On the other hands, the reaction rates of  $^{197}\text{Au}(n,\gamma)^{198}\text{Au}$  derived from the activation method experimentally were compared with the calculated reaction rates using the meas-

ured TOF spectra and the evaluated neutron capture cross sections of JENDL-4.0 [2] as listed in Table 2. The calculated reaction rates were in agreement with the experimental ones within 2 % accuracy. As a result, it was confirmed that the neutron spectrum information obtained by the TOF method can be used for activation analysis.

In nearly future, we will apply the spectrum determination method to the activation experiments for MA.

Table 1 Boric-acid concentration of the light water moderator

Case	Concentration [ppm]
Case 1	0
Case 2	318
Case 3	1404
Case 4	2946

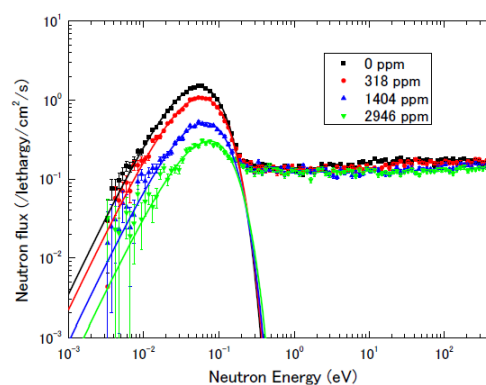


Fig. 1 Neutron spectra for moderators with different boric-acid concentration measured by TOF method

Table 2 Comparison of normalized reaction rates of  $^{197}\text{Au}(n,\gamma)^{198}\text{Au}$

Case	Experiment	Calculation
Case 1	$1.858 \pm 0.040$	1.874
Case 2	$1.535 \pm 0.032$	1.577
Case 3	$1.152 \pm 0.022$	1.141
Case 4(normalized)	1.000	1.000

Present study includes the results of “Research and Development for accuracy improvement of neutron nuclear data on minor actinides” entrusted to the Japan Atomic Energy Agency by the Ministry of Education, Culture, Sports, Science and Technology of Japan (MEXT).

#### REFERENCES:

- [1] M. Salvatores *et al.*, WPEC-26, OECD NEA (2008).  
 [2] K. Shibata *et al.*, *J. Nucl. Sci. Technol.* **48**(1) (2011) 1-30.

## CO2-5 Experimental Study on Non-destructive Assay with a Pulsed Neutron Source

J. Hori, T. Sano, Y. Takahashi, H. Unesaki  
and K. Nakajima

Research Reactor Institute, Kyoto University

**INTRODUCTION:** Non-destructive assay of nuclear fuel materials in spent nuclear fuel is a key technology for nuclear material accountancy and critical safety. Neutron Resonance Densitometry (NRD) with a pulsed neutron source has been developed for a non-destructive assay of material [1]. In this method, we can identify and quantify the target nuclide by measuring the neutron resonance absorption with the Time-of-Flight (TOF) technique. There are two ways to measure the neutron resonance absorption. One is Neutron Resonance Transmission Analysis (NRTA) [2] and another is Neutron Resonance Capture Analysis (NRCA) [3, 4].

In this work, we have proposed a new concept of “self-indication method” combined with NRTA and NRCA. In the self-indication method, we set an indicator consisted of target nuclide with a high purity at the beam-downstream from a sample. By detecting the reaction products such as neutron capture  $\gamma$  rays or fission products from the indicator with the TOF method, the transmission neutron can be measured indirectly. The self-indicator is a transmission neutron detector which has a high efficiency around the objective neutron resonance energies of target nuclide, so that it enables us to quantify effectively the amount of resonance absorption of the target nuclide. Moreover, it is hard to be affected by the decayed  $\gamma$ -rays from the fuel.

**EXPERIMENTS:** We demonstrated a nondestructive assay for nuclear material using a 46-MeV electron linear accelerator at the Kyoto University Research Reactor Institute. A mixture sample of a natural uranium plate and sealed minor actinides such as  $^{237}\text{Np}$  and  $^{243}\text{Am}$  was used as a sample. The natural uranium plate was  $10 \times 20 \text{ mm}^2$  and weighted 5.8 g. The samples of  $^{237}\text{Np}$  and  $^{243}\text{Am}$  were oxide powder, which was pressed into a pellet 20 mm in diameter and encapsulated in an aluminum disk-shaped container 30 mm in diameter with 0.5-mm-thick walls. The activities of  $^{237}\text{Np}$  and  $^{243}\text{Am}$  were 26 and 868 MBq, respectively. The  $^{10}\text{B}$  plug 8 mm thick or a natural uranium plate of  $10 \times 20 \text{ mm}^2$  and weighted 5.8 g was used as an indicator. Prompt-capture  $\gamma$ -rays from the indicator were measured with a pair of  $\text{Bi}_4\text{Ge}_3\text{O}_{12}$ (BGO) detectors in the TOF experiment. Since the  $^{10}\text{B}$  indicator can absorb most neutrons with energies below the epithermal-region, it was equivalent to the conventional NRTA. In the latter case, it was the self-indication measurement.

**RESULTS:** The TOF spectra for the mixture composed of  $^{\text{nat}}\text{U}$ ,  $^{237}\text{Np}$  and  $^{243}\text{Am}$  are shown in Figs. 1 and 2. Although many resonance dips from the impurities of  $^{237}\text{Np}$  and  $^{243}\text{Am}$  were observed (Fig. 1), there are no differences between TOF spectra with only  $^{\text{nat}}\text{U}$  (blue line) and the mixture (red line) (Fig. 2). This result indicates that the self-indication TOF spectrum was not greatly influenced by nuclide impurity. It was experimentally shown that the contribution from the other nuclide can be remarkably suppressed by applying the self-indication method.

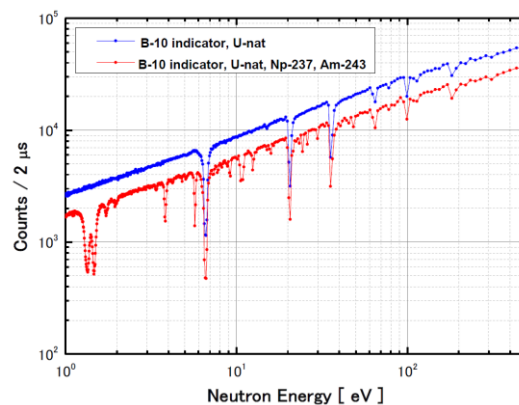


Fig. 1 TOF spectra obtained with NRTA for  $^{\text{nat}}\text{U}$  and mixture of  $^{\text{nat}}\text{U}$ ,  $^{237}\text{Np}$  and  $^{243}\text{Am}$

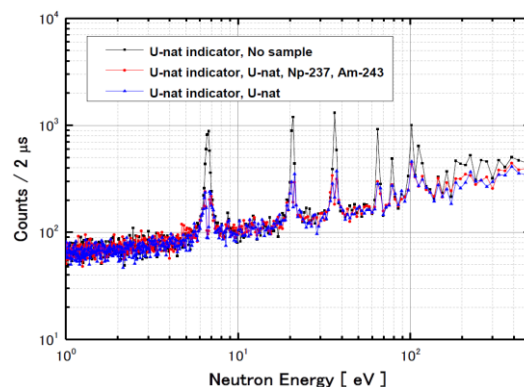


Fig. 2 TOF spectra obtained with the self-indication method for  $^{\text{nat}}\text{U}$  and mixture of  $^{\text{nat}}\text{U}$ ,  $^{237}\text{Np}$  and  $^{243}\text{Am}$

This work was supported by JSPS KAKENHI Grant Number 24760714.

### REFERENCES:

- [1] H. Postma *et al.*, Radioanalytical and Nucl. Chemistry, **248**, (2001) 115-120.
- [2] J. W. Behrens *et al.*, Nucl. Technol., **67**, (1984) 162-168.
- [3] Y. Kiyonagi *et al.*, J. Nucl. Sci. Technol., **42**, (2005) 263-266.
- [4] A. Pietropaolo *et al.*, Applied Spectroscopy, **64**, (2010) 1068-1071.

## CO3-1 Development of In-reactor Observation System Using Cherenkov Light (VI)

T. Takeuchi, K. Yamamoto, N. Otsuka, H. Shibata, A. Shibata, N. Takemoto, K. Tsuchiya, T. Sano<sup>1</sup>, H. Unesaki<sup>1</sup>, Y. Fujihara<sup>1</sup>, Y. Takahashi<sup>1</sup> and K. Nakajima<sup>1</sup>

Neutron Irradiation and Testing Reactor Center, JAEA  
<sup>1</sup>Research Reactor Institute, Kyoto University

**INTRODUCTION:** The surveillance system which can visualize and quantitatively evaluate reactor statuses will contribute to reactor operation management. We started the development of the on-line reactor core imaging system using Cherenkov light<sup>[1]</sup> in 2009. Previously, the total reactor power of the KUR can be estimated using the CCD camera by the method of dissolving the total image brightness to the RGB brightness components<sup>[2]</sup>. In this study, the correlation between the reactor power and the image brightness of the Cherenkov light from a specific fuel element was evaluated in an effort to evaluate the output power of each fuel element.

**EXPERIMENTS:** The CCD camera (AEC-100ZL, Q-I Inc.) was inserted into core-observation pipe of KUR during increasing the reactor power from 1 to 5 MW. The output of the CCD camera was collected by an image recorder. The Cherenkov light from the target fuel element shown in fig. 1 was analyzed. The brightness signal of the output image from the CCD was dissolved to RGB color signals (R:700nm, G:546.1nm, B:435.8nm)<sup>[3]</sup>. The R component without halation was used to correct the total image brightness.

**RESULTS:** Figure 2 shows the results of the analyses of the Cherenkov light from the TC and D2O sides of the target fuel element. Although the averaged brightness changes at an almost same rate as that of the total output power, at the TC and D2O sides of the fuel element,

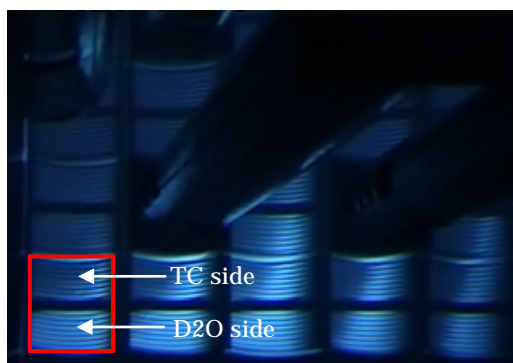


Fig. 1. The array of the fuel elements at the core of KUR. The red boxed fuel is the target one. The black band at the middle of the fuel element is the handle.

the change rates of the brightness are larger and smaller than that of the total output power, respectively. The difference in the change rate between the TC and D2O sides is thought to be due to an inhomogeneous distribution of output power, resulting in the difference in the amount of the Cherenkov light. On the other hand, the absolute value of the brightness of the TC side was smaller than that of the D2O side at from 1 to 2 MW. A possible explanation is that the shadow of the control-rod guide tubes and the other irradiation equipment were included in image of the CCD camera. To suppress the effect of the shadow on the analyses of the brightness, the observations of the Cherenkov light from various positions using a number of cameras might be required.

**CONCLUSION:** As part of the development of the visible on-line core surveillance system, the Cherenkov light at the core of KUR observed by a CCD camera was analyzed on the correlation between the image brightness of the Cherenkov light and the output power about a specific fuel element. The results indicate that the inhomogeneous distribution of output power and the shadow of the control-rod guide tubes and the other irradiation equipment have significant effects on the brightness of the Cherenkov light. These effects could be suppressed by using a number of cameras located at various positions.

### REFERENCES:

- [1] J.V. Jellry, Cherenkov Radiation and its Applications (Pergamon, New York, 1958).
- [2] N. Otsuka, *et al.*, KURRI Progress Report, (2013) P. 215.
- [3] Commission internationale de l'Eclairage proceedings, 1931, Cambridge.

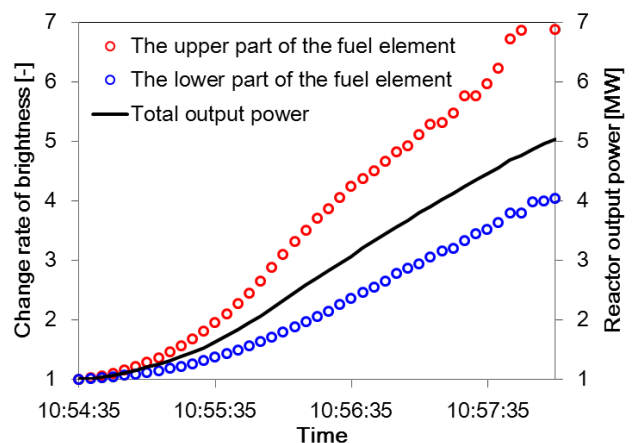


Fig. 2. The change rate of the brightness of the Cherenkov light from the target fuel element with the reactor power.

## CO3-2 Neutron Irradiation Effect of High-density MoO<sub>3</sub> Pellets for Mo-99 Production (2)

K. Nishikata, T. Ishida, M. Yonekawa, Y. Kato,  
M. Kurosawa, A. Kimura, Y. Matsui, K. Tsuchiya,  
T. Sano<sup>1</sup>, Y. Fujihara<sup>1</sup>, Y. Takahashi<sup>1</sup> and J. Zhang<sup>1</sup>

Neutron Irradiation and Testing Reactor Center, JAEA  
<sup>1</sup>Research Reactor Institute, Kyoto University

**INTRODUCTION:** As one of effective applications of the Japan Materials Testing Reactor (JMTR), JAEA has a plan to produce <sup>99</sup>Mo by (n, γ) method ((n, γ)<sup>99</sup>Mo production), a parent nuclide of <sup>99m</sup>Tc [1]. In this study, preliminary irradiation test was carried out with the high-density molybdenum trioxide (MoO<sub>3</sub>) pellets in the hydraulic conveyer (HYD) of the Kyoto University Research Reactor (KUR) and the <sup>99m</sup>Tc solution extracted from <sup>99</sup>Mo was evaluated.

**EXPERIMENTS:** The high-density MoO<sub>3</sub> pellets were fabricated by the Plasma Sintering Method [2]. Dimension and density of MoO<sub>3</sub> pellets were φ18×10 mm and about 92.5%T.D., respectively. The MoO<sub>3</sub> pellets were irradiated in the HYD of the KUR. Before the irradiation test, neutron flux in the HYD was measured with the dosimeters (In foil and In-Ni foil with Cd canning). Table 1 shows the irradiation conditions of MoO<sub>3</sub> pellets in the HYD. After the irradiation tests, the irradiated MoO<sub>3</sub> pellets were transported from KUR to JMTR-HL. The irradiated pellets were dissolved with 6M-NaOH solution in the Lead Cell and the <sup>99m</sup>Tc was extracted from the Mo solution by the solvent extraction method using methyl ethyl ketone (MEK).

Table 1 Irradiation conditions of MoO<sub>3</sub> pellets

Items	Values
Thermal power	1 MW
Thermal neutron flux	$1.82 \times 10^{17} \pm 4.18 \times 10^{15} \text{ m}^{-2}\text{s}^{-1}$
Epithermal neutron flux	$7.08 \times 10^{16} \pm 2.29 \times 10^{15} \text{ m}^{-2}\text{s}^{-1}$
Fast neutron flux	$7.13 \times 10^{16} \pm 1.85 \times 10^{15} \text{ m}^{-2}\text{s}^{-1}$
Irradiation time	3.2 h
Irradiation temperature	below 90°C

**RESULTS:** After the irradiation test, all of the diffraction peaks corresponding to the orthorhombic crystal structure (α-MoO<sub>3</sub>) were assigned to MoO<sub>3</sub> appeared in the irradiated MoO<sub>3</sub> pellet. The Grain sizes of MoO<sub>3</sub> pellet before/after neutron irradiation were almost identical (approx. 1μm). The results suggest that No change of crystal structure and grain size was observed in the MoO<sub>3</sub> pellets irradiated at low temperature and low fluence.

After the dissolution of irradiated MoO<sub>3</sub> pellets and extraction of <sup>99m</sup>Tc solution, <sup>99</sup>Mo and <sup>99m</sup>Tc activities were measured in the Mo solution and <sup>99m</sup>Tc solution by the germanium detector. From the result of the γ-ray spectrum of Mo solution and <sup>99m</sup>Tc solution, the ratio of measured value and calculated value (M/C) was 1.05 and it was confirmed that the calculated <sup>99</sup>Mo marched the measured one within an error of ±5% by the previous method [3]. On the other hand, <sup>92m</sup>Nb observed in the Mo solution as impurities. <sup>92m</sup>Nb was not measured in the <sup>99m</sup>Tc solutions. Table 2 shows the result of <sup>99m</sup>Tc recovery rates from the Mo solution. The recovery rate of the 1<sup>st</sup> and 2<sup>nd</sup> runs achieved the target values (>80%). The 3<sup>rd</sup> and 4<sup>th</sup> runs were less than 60%. In this experimental, different MEKs were used for the extraction tests and it seems that the <sup>99m</sup>Tc recovery rate affected purity of MEK.

Impurities such as Al, Mo and MEK, radiochemical purity and radionuclidic impurity were measured with the <sup>99m</sup>Tc solution in the 1<sup>st</sup> run and the high purity <sup>99m</sup>Tc solution was obtained by this method.

Table 2 Result of <sup>99m</sup>Tc recovery rates from the Mo solution

No.	Activity of <sup>99m</sup> Tc (Bq)	Recovery rate (%)
1 <sup>st</sup> run	$1.09 \times 10^9$	82.3
2 <sup>nd</sup> run	$8.53 \times 10^8$	95.7
3 <sup>rd</sup> run	$3.09 \times 10^8$	56.5
4 <sup>th</sup> run	$2.41 \times 10^8$	55.1

**CONCLUSION:** After the irradiation test of the high-density MoO<sub>3</sub> pellets in the KUR, <sup>99m</sup>Tc was extracted from the Mo solution and the recovery rate of <sup>99m</sup>Tc achieved the target values. The <sup>99m</sup>Tc solution also got the value that satisfied the standard value for <sup>99m</sup>Tc radiopharmaceutical products by the solvent extraction method.

### REFERENCES:

- [1] K. Nishikata, et al., Fabrication and Characterization of High-Density MoO<sub>3</sub> Pellets, Proceedings of 2012 Powder Metallurgy World Congress & Exhibition (2012) CD-ROM.
- [2] K. Tsuchiya, et al., Status of <sup>99</sup>Mo-<sup>99m</sup>Tc Production Development by (n, γ) Reaction, JAEA-Conf 2011-003 (2011).
- [3] K. Nishikata, et al., Neutron Irradiation Effect of High-density MoO<sub>3</sub> pellets for Mo-99 Production, KURR Progress Report 2013, p242.

採択課題番号 26041      高密度 MoO<sub>3</sub>ペレットの照射効果に関する研究      通常採択  
(JAEA) 西方 香緒里、石田 卓也、米川 実、加藤 佳明、黒澤 誠、木村 明博、松井 義典、  
土谷 邦彦  
(京大・原子炉) 佐野 忠史、藤原 靖幸、高橋 佳之、張 俊

## Development of Radiation Tolerant Image Sensor with Field Emitter Array

Y. Gotoh, M. Nagao<sup>1</sup>, T. Okamoto<sup>2</sup>, T. Masuzawa<sup>3</sup>,  
Y. Neo<sup>3</sup>, H. Mimura<sup>3</sup>, H. Tsuji, M. Akiyoshi, I. Takagi,  
N. Sato<sup>4</sup>

Graduate School of Engineering, Kyoto University

<sup>1</sup>National Institute of Advanced Industrial Science and  
Technology

<sup>2</sup>National Institute of Technology, Kisarazu College

<sup>3</sup>Research Institute of Electronics, Shizuoka University

<sup>4</sup>Research Reactor Institute, Kyoto University

**INTRODUCTION:** One of the most serious problems for the observation of interior of the nuclear reactor at the Electric Power Plant, Fukushima the 1<sup>st</sup>, is such that there are no good cameras that can stand for the irradiation from radioactive material can be seen as a commercial product. Therefore, it is necessary to develop a reliable camera that can be used under hard radiation. The purpose of the present study is to develop a compact image sensor for visual light with a field emitter array (FEA). To ensure the radiation tolerance, it is necessary to show the resistance of each element against  $\gamma$ -ray irradiation. Change in the operational characteristics of the key components of the image sensor, FEA [1] and photoconducting diode [2] was investigated.

**EXPERIMENTS:** The FEAs were fabricated at National Institute of Advanced Industrial Science and Technology. Photoconducting CdTe/CdS diodes were fabricated at National Institute of Technology, Kisarazu College. The irradiation of  $\gamma$ -rays to these devices was performed at Kyoto University Research Reactor Institute, Co-60 Gamma-ray Irradiation Facility. Irradiation of  $\gamma$ -ray to the FEAs was performed in a vacuum vessel made of glass. Current-voltage ( $I$ - $V$ ) characteristics of the FEA and CdTe/CdS photodiode were investigated before and after  $\gamma$ -ray irradiation. The dose of irradiation was between 60 and 200 kGy, depending upon the sample position during the irradiation.

**RESULTS:** Fig. 1 shows the  $I$ - $V$  characteristics of the FEA in a triode configuration. No significant change of the  $I$ - $V$  characteristics was observed even after the  $\gamma$ -ray irradiation with the dose of 125 kGy. Fig. 2 shows the  $I$ - $V$  characteristics of the CdTe/CdS photodiode prepared on a graphite substrate (Substrate-type configuration). Also for this case, no significant change of the  $I$ - $V$  characteristics was observed after the  $\gamma$ -ray irradiation with the dose of 75 kGy. Taking the fact that semiconductor image sensors have the life of 100 kGy, the FEA and the photoconducting CdTe/CdS diode have sufficient toler-

ance against  $\gamma$ -ray irradiation.

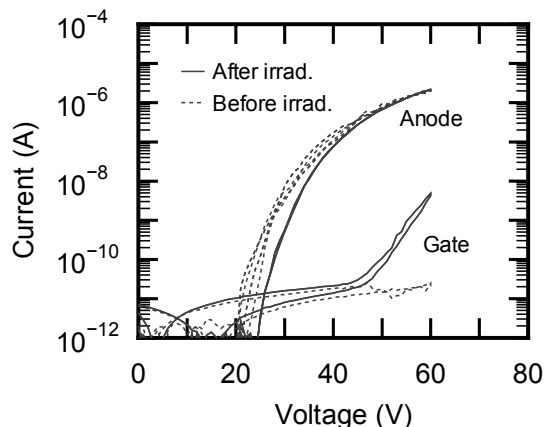


Fig. 1.  $I$ - $V$  characteristics of FEA in triode configuration before and after  $\gamma$ -ray irradiation.

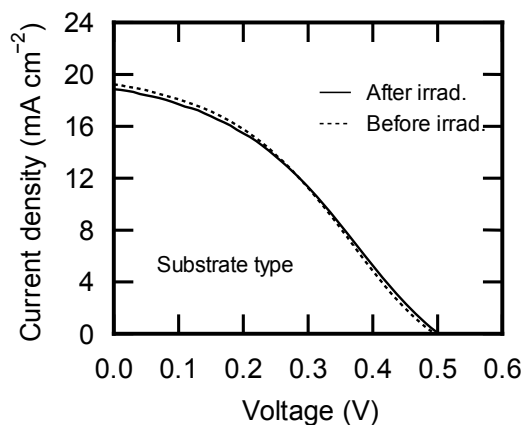


Fig. 2.  $I$ - $V$  characteristics of CdTe/CdS diode in substrate-type configuration before and after  $\gamma$ -ray irradiation.

**ACKNOWLEDGMENT:** A part of this study is the result of “Development of radiation tolerant compact image sensor with a field emitter array”, carried out under the Initiatives for Atomic Energy Basic and Generic Strategic Research by the Ministry of Education, Culture, Sports, Science and Technology of Japan.

**REFERENCES:**

- [1] M. Nagao, Proc. of the 21<sup>st</sup> International Display Workshops, Dec. 3-5, 2015, Niigata (2015) 588-590.
- [2] T. Okamoto, R. Hayashi, S. Hara, Y. Ogawa, Jpn. J. Appl. Phys., **52** (2013) 102301/1-3.



T. Awano and T. Takahashi<sup>1</sup>

Faculty of Engineering, Tohoku Gakuin University

<sup>1</sup>Research Reactor Institute, Kyoto University

**INTRODUCTION:** We have observed millimeter wave absorption bands around 6 and 8  $\text{cm}^{-1}$  in AgI-superionic conductive glasses. These bands were also observed in CuI-superionic ones[1-3]. These bands seem to be due to collective motion of conductive ions, although how conduction ions move in correlation is not clear.

Ionic liquid (IL) is molten salt at room temperature. It is interesting to compare ionic motion in ionic liquids with those in superionic conductor.

Recently, we have measured sub-terahertz absorption spectra of N,N-Diethyl-N-methyl-N-(2-methoxyethyl) ammonium tetrafluoroborate ([DEME][BF<sub>4</sub>]) and N,N-Diethyl-N-methyl-N-(2-methoxyethyl) ammonium bis(trifluoromethanesulfonyl)imide ([DEME][TFSI]) [4]. Two absorption bands were observed around 6 and 8  $\text{cm}^{-1}$ , which are almost coincident with those in AgI-superionic conductive glasses. These bands have almost equal peak positions and intensities in both ILs. This means that these absorption bands are due to cation motion. However, thermal change of these bands are different. This difference seems to be due to the difference of their phase transition temperatures and solid states. The former becomes glassy solid under 182 K. The latter becomes crystal.

To investigate these difference among ILs, measurements of absorption spectra of several ILs have been executed.

**EXPERIMENTS:** Ionic liquids (Tokyo Kasei. co., inc.) were spread into filter paper. Transmission spectra of single and double papers with ionic liquids were measured at room temperature and low temperatures. Absorption spectra were obtained by subtraction of them.

**RESULTS:** Fig. 1 shows absorption spectra of 1-Ethyl-3-methylimidazolium tetrafluoroborate ([Emim][BF<sub>4</sub>]). This ionic liquid becomes solid under 210 K. Fig. 2 shows absorption spectra of 1-Ethyl-3-methylimidazolium bis(trifluoromethanesulfonyl)imide ([Emim][TFSI]). Temperature dependence was different in these ionic liquids. The intensity of the absorption band of the former IL decreased gradually at temperatures above 227 K. On the other hand, that of the latter IL decreased rapidly at temperatures below 213 K. This difference seems to be due to the difference of their phase transition temperatures and glass or crystal structure of solid states of these ILs due to the anion difference.

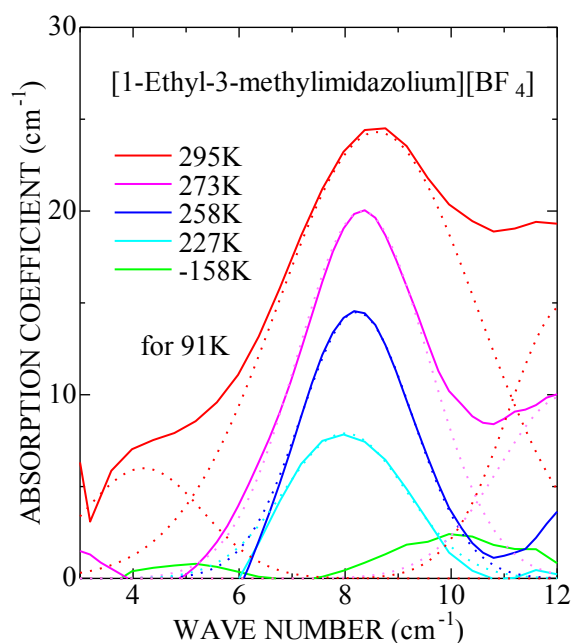


Fig. 1. Absorption increment spectra of [Emim][BF<sub>4</sub>]. The baseline is the absorption spectrum at 91K.

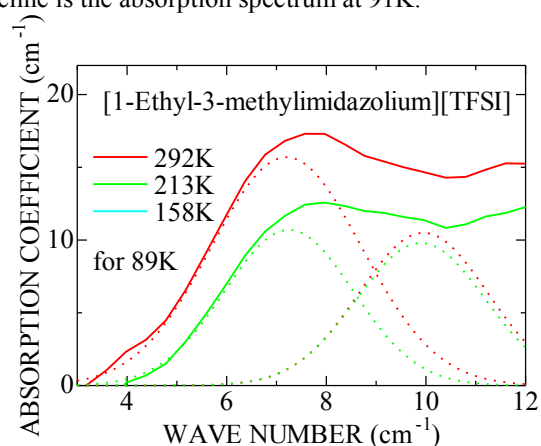


Fig. 2. Absorption increment spectra of [Emim][TFSI]. The baseline is the absorption spectrum at 89 K. The spectrum of 158 K was almost coincident with the baseline.

#### REFERENCES:

- [1] T. Awano and T. Takahashi, J. Phys. Conf., **148** (2009) 012040/1-4.
- [2] T. Awano and T. Takahashi, J. Phys. Soc. Jpn. **79** Suppl. A (2010) 118-121.
- [3] T. Awano and T. Takahashi, Proceedings of the 13<sup>th</sup> Asian Conference on Solid State Ionics, (2012) 569-576.
- [4] T. Awano and T. Takahashi, KURRI Progress Report 2013, CO4-5.

T. Takahashi

*Research Reactor Institute, Kyoto University*

**INTRODUCTION:** In recent years various types of coherent radiation emitted from a short bunch of relativistic electrons have attracted a considerable attention as a bright light source in the THz-wave and millimeter wave regions for the spectroscopic purpose. Coherent transition radiation (CTR), which is emitted from a boundary between two media, is one of such a coherent light source. CTR is usually utilized as a non-polarized light source, because the electric vector of transition radiation (TR) emitted from a metallic screen is axially symmetric with respect to the trajectory of an electron beam. In my previous reports [1, 2] the property of CTR emitted from a pair of wire-grid radiators with the different polarization was experimentally investigated in order to develop a new technique of generation of circular polarized THz radiation. Circularly polarized light has been useful in the circular dichroism spectroscopy. Shibata *et al.* has developed a technique of generation of circularly polarized millimeter-wave radiation with the phase difference between the forward TR and the backward one [3]. However, it was difficult to control the polarization degree in that technique. In this report circularly polarized CTR has been generated with a new technique. With this technique the polarization degree is able to be controlled precisely.

**EXPERIMENTAL PROCEDURES:** The experiment was performed at the coherent radiation beamline [4] at the L-band linac of the Research Reactor Institute, Kyoto University. The energy, the width of the macro pulse, and the repetition rate of the electron beam were 42 MeV, 33 ns, and 20 Hz, respectively. The average current of the electron beam was 0.5  $\mu$ A. Two wire-grid polarizers (WG1 and WG2) 10  $\mu$ m thick with 25  $\mu$ m spacing were used in order to generate the CTR with horizontal and vertical components, respectively. Each CTR was superposed with phase difference through the optical delay system. Although a Martin-Puplett-type interferometer is usually used as a spectrometer, a grating-type monochromator was used in this experiment. The monochromator was set for the wavelength of 2.3 mm. The CTR was detected by a liquid-helium-cooled Si bolometer. In order to analyze the polarization degree a wire-grid polarizer with a rotary holder was used in front

of the detector.

**RESULTS:** The observed polarization diagrams of CTRs from WG1 (horizontal component) and WG2 (vertical component) are shown in Fig.1 and 2, respectively. In these figures the degrees 0 and 180 represent the vertical plane, and 90 and 270 represent the horizontal plane. These results demonstrate that CTR from the wire grid has perfect linear polarizations. The observed polarization diagram of the superposition of these two CTRs is shown in Fig.3. This figure represents that the circular polarized CTR was generated.

### REFERENCES:

- [1] T. Takahashi, *et al.*, KURRI-PR 2012 CO4-15.
- [2] T. Takahashi, *et al.*, KURRI-PR 2013 CO4-12.
- [3] Y. Shibata *et al.*, *Rev. Sci. Instrum.* **72** (2001) 3221.
- [4] T. Takahashi *et al.*, *Rev. Sci. Instrum.* **69** (1998) 3770.

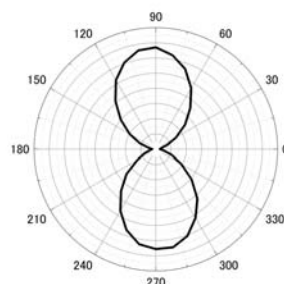


Fig.1. Polarization diagram of CTR from WG1.

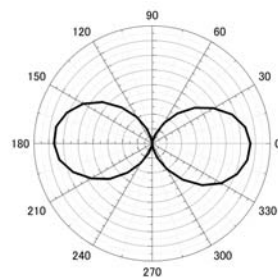


Fig.2. Polarization diagram of CTR from WG2.

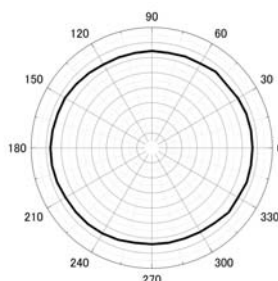


Fig.2. Polarization diagram of superposed CTR from WG1 and WG2.

## CO4-4 Basic Study on Radiation-induced Luminescence from Natural Mineral

H. Fujita, M. Sakamoto<sup>1</sup>, T. Saito<sup>1</sup>

Nuclear Fuel Cycle Engineering Laboratories, JAEA

<sup>1</sup>Research Reactor Institute, Kyoto University

**INTRODUCTION:** Dielectric materials such as natural minerals emit radiation induced luminescence such as thermoluminescence (TL) and optically stimulated luminescence (OSL). OSL is a well-established tool for measuring radiation doses in unfired sediments [1]. It has features in common with TL which has long been used in measuring radiation doses [2]. Both TL and OSL dosimetry with white mineral do not need to be specially installed in advance, prior to dose estimation. Quartz is an excellent material for use in dosimetry, because of its almost ubiquitous availability including an accidental place. Feldspar is an extensive ternary family of minerals appropriate for OSL and TL dosimetry as they display a strong luminescence and are quite common in the Earth's formation. However, the detailed emission mechanisms of TL and OSL from natural minerals such as natural quartz and feldspar are not yet clear. In this study, the emission mechanisms of TL and OSL were investigated in conjunction with various radiation-induced phenomena after annealing treatments of quartz samples, involving TL, OSL and electron spin resonance (ESR) measurements.

**EXPERIMENTS:** Two surface soil samples to 5 cm depth were collected at different places in Ibaraki. Natural quartz samples were extracted from the soils by a usual treatment of 6M hydrochloric acid (HCl), 6M sodium hydroxide (NaOH) followed by 60 min of concentrated hydrofluoric acid (HF). The etching treatment with HF solution was at room temperature. Further purification of the quartz grains was performed by hand selection for the sake of elimination of feldspar grains as low as possible. The purified quartz samples were sieved to adjust the grain sizes ranging from 150  $\mu\text{m}$  to 250  $\mu\text{m}$  in a diameter for ESR spectrometry, TL and OSL measurements. The quartz samples were annealed at 800  $^{\circ}\text{C}$  for 24 hours in an electric furnace. The annealed quartz samples were irradiated a dose of 1 kGy with <sup>60</sup>Co source (0.73 kGy/h at D-30 cm) at room temperature at Kyoto University Research Reactor Institute (KURRI). The irradiated samples were stored at room temperature for one day to eliminate afterglow emission in dark room. The ESR measurement was carried out using an ESR spectrometer (Jeol Ltd., JES-TE 200) at  $-196^{\circ}\text{C}$ . Prior to the ESR measurements, the quartz samples were annealed for

1 min at 50  $^{\circ}\text{C}$  intervals ranging from 150 to 300  $^{\circ}\text{C}$  as preheat treatment. Each remnant of the samples was kept in dark room without preheating treatment. After the ESR measurements, all luminescence measurements were performed using a JREC automated TL/OSL-reader system installed with a small X-ray irradiator (Varian, VF-50J tube). All preparations were carried out under dim red light.

**RESULTS:** In this research, the ESR signals of Al centers and Ti centers ( $[\text{TiO}_4/\text{H}^+]^0$ ,  $[\text{TiO}_4/\text{Li}^+]^0$  and  $[\text{TiO}_4/\text{Na}^+]^0$ ) were detected in the annealed quartz samples. Al centers are hole-trapped centers and Ti centers are electron-trapped centers. Fig. 1 shows the intensity changes of the Al centers and the Ti centers. ESR signal intensity of Al centers decreased with preheating temperatures, gradually. On the other hand, ESR signal intensity of Ti centers showed different tendency from the ESR intensity of Al centers. The intensity of Ti centers increased or was constant up to 150  $^{\circ}\text{C}$  of preheating temperature. After heating over 150  $^{\circ}\text{C}$ , the intensity of Ti center decreased with preheating temperatures. The results agreed to our previous results. However, the intensity tendency of Ti centers was different between two quartz samples.

TL and OSL signals were measured using all kinds of quartz samples. However, their data was not evaluated, completely. Therefore, the data analysis will be conducted in 2015.

In this research, the luminescence emission mechanism could not be identified. Therefore, further work is necessary to identify luminescence mechanism using ESR measurement and annealing experiment.

### REFERENCES:

- [1] Huntley, D. J., et al., Nature 313, 105-107 (1985).
- [2] McKeever, S. W. S., Cambridge University Press, Cambridge, 103-105 (1985).

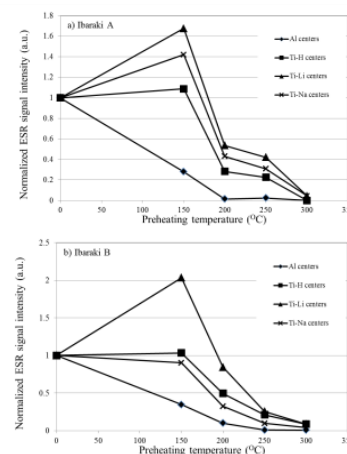


Fig.1 Tendency of ESR signal intensity with preheating temperature.

## CO4-5 Complex Structure of Ions Coordinated with Hydrophilic Polymer. 15. Applied Discussion with Ionic Behavior in Hydrophobic Matrixes.

A. Kawaguchi, Y. Morimoto

Research Reactor Institute, Kyoto University

**INTRODUCTION:** We have reported composite structure brought by *in situ* preparation through "secondary doping" by diffusion of metallic ions into iodine-doped hydrophilic polymers. Polyiodide ions,  $I_n^{m-}$  ( $m, n$ : integer,  $n \neq 1$ ), which have been as solutes in aqueous solution, can be diffused into the polymers through immersing operation at room temperature. Or, the polymer matrix previously iodine-doped enhances following diffusion of other molecules or ions into matrix polymer; if the additional ion makes precipitates of inorganic salt with iodide, hybrid composite can be achieved without melting, nor casting, nor synthesizing.[1-3]

Such singularity suggests microscopic behavior of polymer chains as "pseudo solvents", where ionic diffusion in nano-scale can be achieved or enhanced under affinity with polymer matrix keeping its structure: chain orientation, crystalline structure, self-organization, etc. However, even if matrix is composed by "hydrophilic" polymers, their polarization or ionic affinity are not matched for ordinary hydrophilic solvents, such as water, ethanol, etc.; hydrophilicity of polymeric matrixes should be much lower than that of hydrophilic low molecules, and that is a reason for general difficulty for charged ions to diffuse into the matrixes.

If so, observed rapid diffusion of polyiodides ("1st iodine doping") or additional diffusion of metallic ions ("2nd doping") should consistent with hydrophobicity of matrixes not only their hydrophilicity.[4,5] Then, similar procedures for "1st iodine doping" or "2nd Ag<sup>+</sup> ion doping" in hydrophobic matrixes were investigated as comparison with the previous results in hydrophilic matrixes.

**EXPERIMENTS:** Commercial "SEBS"-elastomer, AR-770C and AR-830C (Aron Kasei) were used as hydrophobic matrixes, which are composed of both polystyrene (hard segment) and polyethylene-polybutylene co-polymer (soft segment).

Iodine doping was achieved with I<sub>2</sub>-KI(aq)/3.0N (for 22 hrs., at R.T.) and secondary doping was done with AgNO<sub>3</sub>(aq)/0.25M (for 30min., at R.T.).

**RESULTS:** Present matrixes are just "hydrophobic" depending on their chemical components; generally, their activity to aqueous solution is so low that ionic diffusion or interaction should be negligible. However, ionic diffusion from aqueous solution into the hydrophobic matrixes was explicitly observed in coexistence of polyiodide ions. As shown in Fig. 1 and 2, "1st iodine doping" and "2nd Ag-doping" easily advanced into both *hydrophobic* matrixes in time of less than an hour at R.T.

even with aqueous solvents. On the other hand, increase in mass ( $\Delta m$ , relative mass at each stage to non-doped sample) was much less than one for the previous hydrophilic matrixes:  $\Delta m$  less than 2%.

Furthermore, not only deep diffusion of polyiodide in "1st iodine doping" but "elution out" of polyiodide or Ag<sup>+</sup> ion in "2nd Ag-doping".(Fig.1&2, right) Such behavior is analogous to "Stage III" which is observed in excessive "Ag-doping" to iodine-doped hydrophilic polymers.[6]

These results indicate that existence of polyiodide in polymeric materials can let ionic diffusion overcome general activation barrier.

**ACKNOWLEDGEMENT:** SEBS elastomers as hydrophobic samples, AR-770C and AR-830C, were presented by Aron Kasei Co.Ltd. The authors express great gratitude for them to inspire unexpected viewpoints.

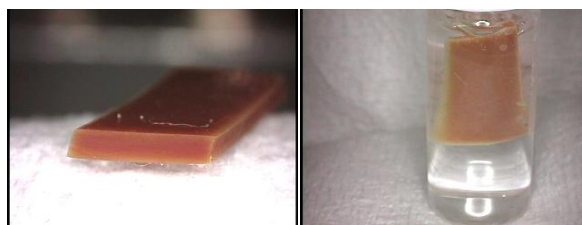


Fig. 1. AR-770C iodine-doped with I<sub>2</sub>-KI(aq) (left) and following "2nd Ag-doping" with AgNO<sub>3</sub>(aq) (right).

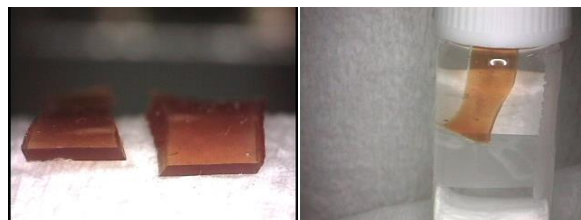


Fig. 2. AR-830C iodine-doped with I<sub>2</sub>-KI(aq) (left) and following "2nd Ag-doping" with AgNO<sub>3</sub>(aq) (right).

### REFERENCES:

- [1] A. Kawaguchi, Sens. Actuators B, **73** (2001) 174-178.
- [2] Y. Gotoh, *et.al.*, Polym. Prep. Jpn., **51** (2002), 2259-2259.
- [3] patent. JPN-5444559 (2014).
- [4] KAWAGUCHI Akio, *et.al.*, SPring-8 User Exp. Rep. **5** (2000A), 354-354. (2000)
- [5] A. Kawaguchi, *et.al.*, Macromol. Sym., **202**, 77-83. (2003)
- [6] A. Kawaguchi, Polym. Prep. Jpn., **62**, 5116-5117. (2013)

## CO4-6 Elucidation of Tritium Dynamics in Neutron Irradiated Tungsten

Y. Oya, M. Sato<sup>1</sup>, K. Yuyama<sup>1</sup>, T. Miyazawa<sup>2</sup>, R. Okumura<sup>3</sup>, Y. Iinuma<sup>3</sup>, T. Fujii<sup>3</sup> and H. Yamana<sup>3</sup>

College of Science, Academic Institute, Shizuoka University

<sup>1</sup>Graduate School of Science, Shizuoka University

<sup>2</sup>Faculty of Science, Shizuoka University

<sup>3</sup>Research Reactor Institute, Kyoto University

**INTRODUCTION:** Tungsten (W) is a candidate material for the plasma facing components in the fusion future reactors due to the lower hydrogen isotopes retention. In a fusion reactor, W will be exposed to 14 MeV neutrons produced by the D-T fusion reaction during the plasma operation. Irradiation defects will be introduced by neutrons where hydrogen isotopes would be stably trapped, leading to the enhancement of fuel retention. Therefore, it is important to evaluate the hydrogen isotopes retention in neutron irradiated W. In this study, the deuterium retention behavior in neutron irradiated W was compared with that in heavy ion implanted W which has typical defects such as dislocation loops, vacancies and voids.

**EXPERIMENTS:** Disk type W (6 mm<sup>φ</sup>×0.5 mm<sup>l</sup>) purchased from A.L.M.T. Corp. Ltd was used as the sample. The samples were heat-treated at 1173 K under ultrahigh vacuum to remove the impurity and damages introduced by the polishing process. The neutron irradiation for the sample was performed at Pn-2 port in Kyoto University Research Reactor Institute (KUR) with the damage up to  $4.3 \times 10^{-4}$  dpa (displacement per atom). For the heavy ion irradiation, 6 MeV Fe<sup>2+</sup> was irradiated into the samples at room temperature with the damage concentrations of 0.01 and 0.1 dpa by Takasaki Ion Accelerators for Advanced Radiation Application (TIARA) at Japan Atomic Energy Agency (JAEA). Thereafter, the samples were transferred to Shizuoka University for D<sub>2</sub><sup>+</sup> implantation. The samples were irradiated at R.T. with 1 keV D<sub>2</sub><sup>+</sup> with a flux of  $8.75 \times 10^{17}$  D m<sup>-2</sup> s<sup>-1</sup> to a fluence of  $1.0 \times 10^{22}$  D m<sup>-2</sup>. The D desorption behavior was evaluated by thermal desorption spectroscopy (TDS) from room temperature up to 1173 K and 1273 K for Fe<sup>2+</sup> irradiated samples and neutron-irradiated sample, respectively, with the heating rate of 0.5 K s<sup>-1</sup>.

**RESULTS:** D<sub>2</sub> TDS spectra for various damaged W were shown in Fig. 1. The D desorption peaks consisted of four peaks at 400 K, 550 K, 650 K, 850 K corresponded to the adsorbed on the sample surface or trapped by dislocation loops, trapped by vacancies, vacancy clusters

and voids [1-3]. No large difference for Peak 1 was found among 0.01 and 0.1 dpa Fe<sup>2+</sup> irradiated samples, indicating that the retention of D adsorbed on the sample surface or trapped by dislocation loops would be almost saturated. However, for 0.1 dpa sample, major D desorption stage was shifted toward higher temperature side at 850 K, showing that voids would be more stable D trapping sites. In the case of fission neutron irradiation, only D retention as Peak 1 was increased, but its retention was almost the same as Fe<sup>2+</sup> irradiated W, indicating that the dislocation loops for D trapping would be almost the saturation and no vacancy for D trapping was produced into the sample due to its lower damage concentration, or rhenium (Re) which produced by the transmutation caused by the thermal neutron irradiation, would contribute on the enhancement of D re-emission, although vacancies were produced. According to Ref. [4], due to the smaller size of Re atom than that of W atom, substitutional Re atom tends to bound to self-interstitial atoms (SIA) because their lattice strain field is opposite. Once the Re-SIA complex is formed, the mobility of the SIA decreases, leading to the enhancement of vacancy-interstitial recombination.

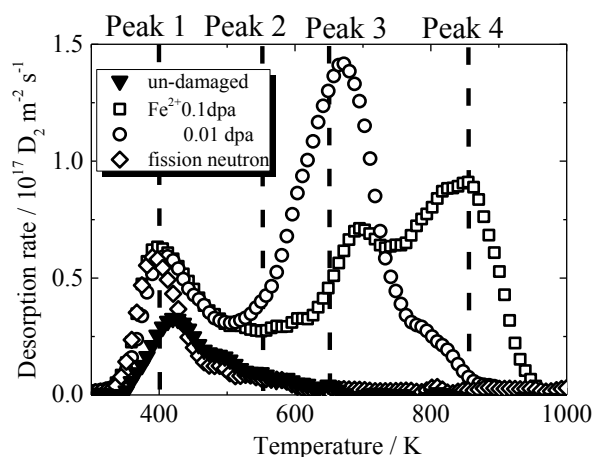


Fig. 1. D<sub>2</sub> TDS spectra for various damaged W.

### REFERENCES:

- [1] Eleveld H and Van Veen A *J. Nucl. Mater.* **191** (1992) 433-438.
- [2] Iwakiri H et al., *J. Nucl. Mater.* **307-311** (2002) 135-138.
- [3] Luo G N et al., *Fusion Eng. Des.* **81** (2006) 957-962.
- [4] Hasegawa A et al., *Fusion Eng. Des.* **89** (2014) 1568-1572.

採択課題番号 26063 中性子照射タングステンにおけるトリチウムダイナミクスの解明 通常採択  
(静大院・理) 大矢恭久、佐藤美咲、湯山健太 (静大・技術) 宮澤俊義 (京大・原子炉) 奥村良、  
飯沼勇人、藤井俊行、山名元

N.Ito, A.Mizohata · R Okumura<sup>1</sup> and Y Iinuma<sup>1</sup>

Radiation Research Center, Osaka Prefecture University,  
<sup>1</sup>Research Reactor Institute, Kyoto University

Central diameters and concentrations of elements (Na, Al, Cl, K, Ca, Ti, V, Cr, Mn, Fe, Co, Ni, Zn, As, Br, Rb, Mo, Sb, Cs, Ba, La, Ce, Sm, Eu, Hf, W and Th) in the atmospheric aerosols collected at Sakai, Osaka in 2012 have been obtained. We have collected aerosols separated by the 9 diameter ranges (<0.43, 0.43~0.65, 0.65~1.1, 1.1~2.1, 2.1~3.3, 3.3~4.7, 4.7~7.0, 7.0~11, >11 μm) using Andersen sampler on one week periods (P1:Feb.14-21, P2:Apr.03-10, P3:Jun05-12, P4:Aug.07-14, P5:Oct.09-16, P6Dec.11-18: in 2012). To collect the samples completely and reduce an affect of contamination we have put polyethylene sheet (80mmΦ, ~1 mg/cm<sup>2</sup>) on the each stage of the sampler.

The element concentrations were analyzed by neutron activation analysis using Kyoto University Nuclear Reactor on following irradiation conditions ( In Pn1 120sec for Al, Cl, Ca, V, Mn, In Pn2 30min for Co, Ni, Zn, As, Br, Rb, Mo, Sb, Cs, Ba, La, Ce, Sm, Eu, Hf, W, Th). Gamma ray spectrum from each irradiated samples were measured by Ge-Solid state detector and 4096channel multiple pulse height analyzer. The measuring time (2000~20000sec) and starts of measurements are determined by the gamma ray intensity of each sample.

From the concentration results in each particle diameter range we have determined the central diameter (d50) which is a diameter of 50% accumulation concentration summing by the each particle diameter range concentration (Fig.1). From the concentrations in each diameter range we get a scatter graph of d50 and total concentrations of each element on 6 sampling periods (Fig.2).

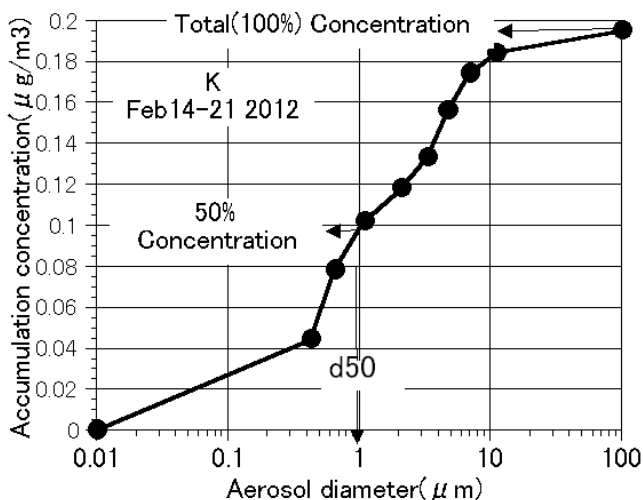


Fig.1 Example of accumulation curve and central diameter (d50) on concentrations of K (Feb14-21 2012) by aerosol diameter in 9 size ranges.

From relations between the d50 and elemental concentrations we have found that Zn, V, Br, Mo, Sb, As have fine d50 (<=2.5 μm) those are Zn (0.9~1.8 μm), V (0.28~0.48 μm), Br (0.34~0.59 μm), Mo (0.24~1.1 μm), Sb (0.957~0.94 μm), As (0.53~1.5 μm).

Al, Na, Fe, Ca, Ti, Ba, Cr, Ce, Co, Th, Hf, Eu have coarse d50 (>=2.5 μm) those are Al (4.6~6.0 μm), Na (3.7~4.3 μm), Fe (3.5~5.1 μm), Ca (4.7~6.2 μm), Ti (4.0~5.9 μm), Ba (2.2~4.1 μm), Cr (2.6~4.9 μm), Ce (3.0~4.7 μm), Co (2.4~4.6 μm), Th (4.0~6.2 μm), Hf (4.5~5.4 μm), Eu (4.4~5.6 μm). Cl, K, Mo, Ni, W, La, Cs have coarse and fine d50 depending on the sampling period. The variation cause changes of the main constituents in fine d50 depending on the sampling period like that, K, Zn, Mn on P1, Zn on P2, K, Zn on P3, Zn on P4, K, Zn on P5, Cl, K, Zn on P6.

In the fine d50 elements ordered by high to low concentration are Cl, K, Zn, Mn, V, Br, Ni, Mo, Sb, As, W, La of which order changes on the sampling period.

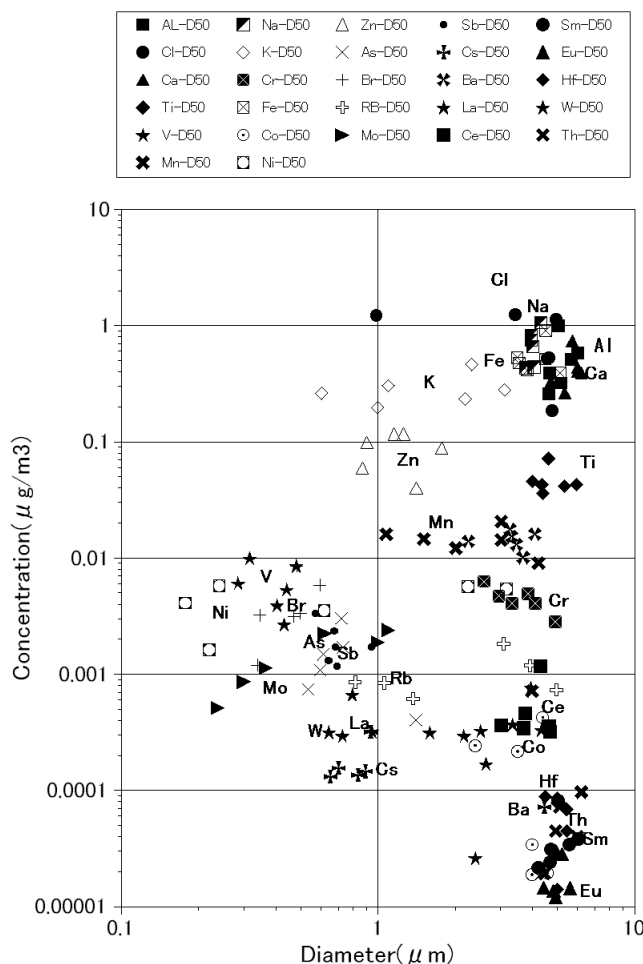


Fig.2 Scatter graph of d50 and total concentrations for each elements in the aerosols collected 2012 at Sakai.

K. Ninagawa, H. Nishido and S. Hamada

Okayama University of Science

### LOW TEMPERATURE TL OF ORDINARY

**CHONDRITES:** Induced TL (thermoluminescence), the response of a luminescent phosphor to a laboratory dose of radiation, reflects the mineralogy and structure of the phosphor, and provides valuable information on the metamorphic and thermal history of meteorites. Thermal metamorphism causes the production of feldspar, the major TL phosphor in ordinary chondrites, by the devitrification of feldspathic mesostasis. Primitive chondrites of petrologic subtype  $\leq 3.4$  with coefficient of variations ( $\sigma$  as a percentage of the mean) over 50%, of fayalite in the olivine have low TL sensitivities under 0.1. The sensitivity of the induced TL is usually used to determine petrologic subtype of unequilibrated ordinary chondrites [1]. On the other hand, TL sensitivity decreases 10-fold after shock-loading to 25-32 GPa [2], and terrestrial weathering makes TL sensitivity decrease 16-fold at maximum in Antarctic chondrites [3]. Then some secondary altered chondrites were reported to have low TL sensitivities, equivalent to primitive chondrites [4].

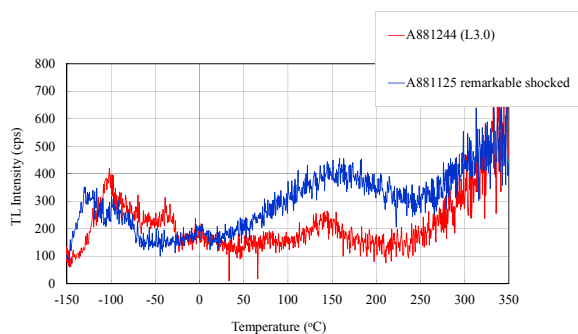


Fig.1. TL glow curves of a primitive ordinary chondrite of A881244 (L3.0) and remarkable shocked chondrite of A8811255.

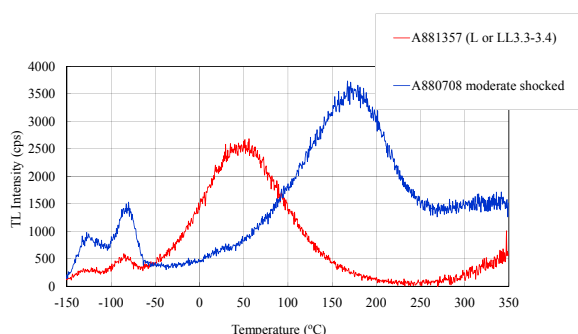


Fig.2. TL glow curves of A881357 and moderate shocked chondrite of A880708. The different peaks at 50 and 150 °C reflected to disordering of feldspar.

The induced TL of unequilibrated ordinary chondrites has been usually measured above room temperature. Then this time low temperature TL (-150~ 0 °C) were investigated to distinguish TL properties between primitive chondrites and secondary altered chondrites. TL glow curves of a primitive ordinary chondrite of A881244 (L3.0) and remarkable shocked chondrite of A8811255 is shown in Fig.1. TL glow curves of a primitive ordinary chondrite of A881357 (L or LL 3.3-3.4) and a moderate shocked chondrite of A880708. There are two peaks near -120 and -80°C lower than room temperature. However we could not find clear difference in TL properties between primitive chondrites and secondary altered chondrites.

**LOW TEMPERATURE TL OF UREILITE:** The ureilites are a major group of primitive achondrites. They are high fractionated rocks from an achondrite parent body. Ureilites are olivine-pyroxene rocks with interstitial C (graphite and microdiamonds) mixed with metal, sulfides, and minor silicate. Most ureilites are essentially devoid of feldspar [6]. This time we measured induced TL of five ureilites to check TL properties of ureilites. Fig.3 shows TL glow curve of Dar al Gani 319 and NWA3223. There were two large peaks at -100 and 0°C.

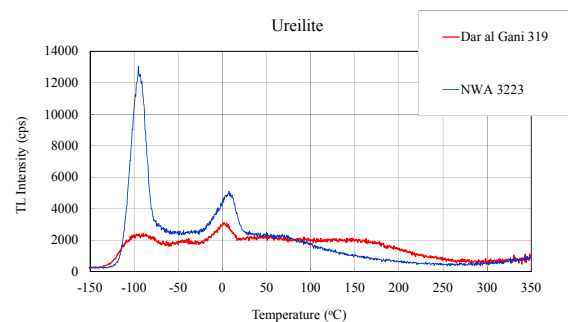


Fig.3. TL glow curve of ureilites, Dar al Gani 319 and NWA3223.

### REFERENCES:

- [1] Sears *et al.*, Proceedings of Lunar and Planetary Science **21** (1991) 493-512.
- [2] Hartmetz *et al.*, Proc. 17th Lunar Planet. Sci. Conf. (J. Geophysical Research), **91**, (1986) E263-E274.
- [3] Benoit and Sears, J. Geophys. Res., **104**, (1999) 14159-14168.
- [4] K. Ninagawa *et al.*, Antarctic Meteorite Research, **15** (2002) 114-121.
- [5] K. Ninagawa *et al.*, Antarctic Meteorite Research **18** (2005) 1-16.
- [6] Weisberg *et al.* Meteorites and the early solar System II, The University of Arizona Press, (2006) 19-52.

T. Yamagata, K. Shozugawa, R. Okumura<sup>1</sup>, K. Takamiya<sup>1</sup> and M. Matsuo

*Graduate School of Arts and Sciences, The Univ. of Tokyo*  
<sup>1</sup>*Research Reactor Institute, Kyoto University*

**INTRODUCTION:** Hypoxia is water mass with little dissolved oxygen (DO) [1]. In Tokyo Bay there are many large and deep dredged trenches, especially off the coast of Makuhari, Chiba. In dredged trenches severe hypoxia has been observed in summer, but the influence of dredged trenches on hypoxia is not revealed yet. Therefore, it is important to estimate the positional and seasonal variations of hypoxia by analyzing sediments.

To estimate the sedimentary environment related to redox conditions, various elements have been used. For example, Fe and Mn are used because their various chemical states on Eh-pH diagrams have become clear [2]. And U is used for the evaluation of weak reductive conditions because the redox potential of U(VI)/U(IV) is between Mn(IV)/Mn(II) and S(VI)/S(-II) [3]. We have applied the elements to evaluate the sedimentary environment in dredged trenches, which are under specific condition. In this study, sediment cores were collected from the Makuhari dredged trenches and concentrations of Fe, Mn, U, Th, and Ce in sediments were analyzed by instrumental neutron activation analysis (INAA).

**EXPERIMENTS:** The sediment samples were collected at a dredged trench (water depth 17.2 m) and reference site (non-dredged seabed, water depth 9.5 m) off the coast of Makuhari in Tokyo Bay in August 2013. Sediments were collected by a core sampler and water quality data were also obtained.

All cores were cut in the vertical direction at 0.6-3.0 cm intervals in the laboratory, and the samples were desalted and freeze-dried within a week.

Approximately 30 mg of sediments were packed in double polyethylene film bags to perform INAA. All samples were irradiated with neutrons at the pneumatic tube, Kyoto University Research Reactor. Three types of gamma-ray measurement were carried out corresponding to half-lives of elements. For analysis of Mn, samples were irradiated for 10 seconds at 1 MW, and then gamma-ray was measured for 600 seconds by Ge detector after 600 seconds cooling. Regarding U, samples were irradiated for 20 minutes at 1 MW or 4 minutes at 5 MW, and then gamma-ray was measured for 1200 seconds by Ge detector after 3-5 days cooling. Regarding Th and Ce, samples were irradiated for 20 minutes at 1 MW or 4 minutes at 5 MW, and the measuring time of gamma-ray was for 9000 seconds after 2-4 weeks cooling.

**RESULTS:** At the dredged trench surface water (< 9 m water depth) had DO about 6 mg/L, and bottom water (> 12 m water depth) had no DO. At both sites, concen-

trations of Fe and Mn in sediments were almost constant from the surface to the lower layers. It is well-known fact that the concentrations of Fe and Mn in sediments decrease due to eluviations of Fe<sup>2+</sup> and Mn<sup>2+</sup> when condition of seawater is reductive like hypoxia. The results indicate that the redox conditions of the surface of sediments were not so reductive as those in August 2011 [4].

On the other hand, we calculated Th/U and Ce/U ratios likewise Honda et al [5], and the depth profiles of the ratios in sediment are shown in Figure. The Th/U and Ce/U ratios in the upper layers (7-8 cm from the surface) were comparatively high, and the ratios settled down to almost constant lower values below 8 cm in depth at most sites. It is known that the concentrations of Th and Ce in sediments increase when condition of seawater is oxidative, and the concentration of U increases when condition of seawater is reductive. It is considered that the sedimentary environment of the upper layers is more oxidative than that of the lower layers. And focusing on the redox potential around U(VI)/U(IV), the method using Th/U and Ce/U ratios is well reflecting the redox states, because those of U, Th, Ce are thought to be preserved from the time of sedimentation.

As mentioned above, the method measuring the concentrations of various elements by INAA and focusing on different redox potentials of the elements is very useful to evaluate the sedimentary environment related to redox conditions.

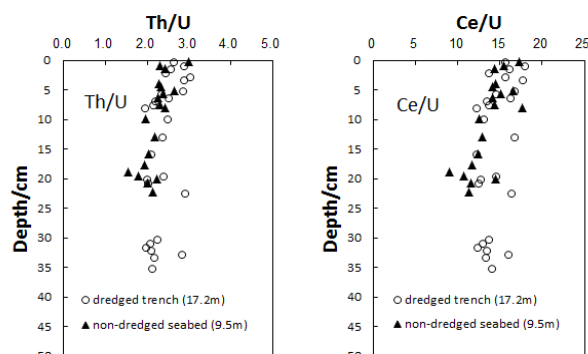


Figure. Depth profiles of Th/U (left) and Ce/U (right) ratios in the sediments collected from Tokyo Bay in August 2013.

### REFERENCES:

- [1] R.J. Diaz *et al.*, *Science*, **321** (2008), 926-929.
- [2] D.G. Brookins, in *Eh-ph diagrams for geochemistry* (Springer-Verlag, 1988).
- [3] D.R. Turner *et al.*, *Geochim. Cosmochim. Acta*, **45** (1981), 855-881.
- [4] T. Yamagata *et al.*, *J. Radioanal. Nucl. Chem.*, **303** (2015), 1179.
- [5] T. Honda *et al.*, *Bull. Soc. Sea Water Sci., Japan*, **57** (2003), 166-180 (in Japanese).



## CO5-4 Characteristics of Synthetic Calcite Thermoluminescence Studied for Paleoenvironmental Reconstruction of East Asia

N. Hasebe, K. Ito, K., K. Miura<sup>1</sup> and M. Ogata<sup>1</sup>

*Institute of Nature and Environmental Technology, Kanazawa University*

<sup>1</sup>*Graduate School of Natural Science and Technology, Kanazawa University*

**INTRODUCTION:** Luminescence dating observes the natural accumulated radiation damage caused by radioisotopes such as U and Th as the form of glow after stimulation by heating or lightening. Thermally stimulated luminescence from calcite shows strong red emission [1]. However, thermoluminescence dating of calcite is less popular because of some unknown problems; e.g., sensitivity change of calcite occurred through repeated heating of samples, possible anomalous fading, difference in characteristics of luminescence response against different kinds of radiation (e.g., gamma-ray, beta-ray, alpha-ray, and X-ray). When thermoluminescence characteristics of calcites are examined using natural occurring calcite, their response to the various radiations depends on minor chemistry (Fe, Mg, Mn and Sr). In this study, calcites with controlled impurity concentrations were synthesized and analyzed to evaluate relationship between multiple impurity concentration and thermoluminescence properties quantitatively.

**EXPERIMENTS:** Calcite were synthesized from sodium carbonate (>99.8wt%) and calcium chloride (>95 wt%). Iron (II) chloride (>99.0-102.0 wt%), magnesium chloride (>98.0wt%), and manganese chloride (>99.0-wt%) were added at different levels to produce calcites with different amount of impurity. Chemical composition of resultant calcite were measured by LA-ICP-MS. Gamma irradiation was carried out at the <sup>60</sup>Co gamma irradiation facility at Kyoto University Research Reactor. Then luminescence images were captured by the digital camera (Inagaki et al., 2010) and luminescence color and intensity were analyzed (Ogata et al., 2014).

**RESULTS:** Except for added elements, all of synthetic calcite contain ~30 ppm of strontium and ~6 ppm of barium. These elements must be contained in original reagent calcium chloride. Mn-added calcites include molybdenum which amount is proportional to the amount of added Mn. Mo must be contaminated to the reagent manganese chloride. As shown in Fig. 1, measured amount of impurity is proportional to the amount of added impurity. When thermoluminescence color image (TLCI) was captured, Mn added samples emitted strong red luminescence (Table 1). A sample with high impurity emit no luminescence. There may be some criteria in Mn concen-

tration to emit luminescence. The TLCI with small amount of Fe show colored pixels. However, these pixels may be noises because they are found in all color zones. Mg added samples emitted no luminescence. Therefore, Mg would not play significant role in luminescence characteristics.

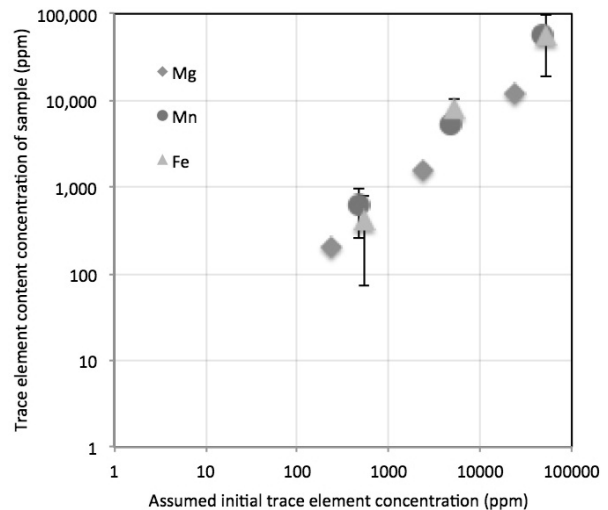


Fig. 1. The amount of elements measured by LA-ICP-MS is proportional to the amount of added elements

	R	Y	G	B	gap	Total
Mn (470ppm)	24592	328099	0	0	0	352691
Mn (4700ppm)	347579	0	0	0	0	347579
Mn(47000ppm)	0	26	0	0	0	26
Mg (240ppm)	58	14	0	11	6	89
Mg (2400ppm)	2	0	0	0	0	2
Mg (24000ppm)	3	17	0	0	0	20
Fe (530ppm)	3942	1269	402	68	635	6316
Fe (5300ppm)	26	18	0	87	7	138
Fe (53000ppm)	45	33	5	0	12	95
Pure calcite	40	0	0	0	0	40

Table 1. The results of TLCI investigation. Number of pixels in each color zone is counted. R stands for red, Y for yellow, G for green, B for blue, and gap for other color.

### REFERENCES:

- [1] A. Inagaki et al., J. Geol Soc. Japan 116 (2010) XIX-XX
- [2] M. Ogata, Sci. Rep. Kanazawa Univ. 58 (2014) 1-12

## CO5-5 Fission Track Ages of Sedimentary Rocks from Accretionary Belt in the Kii Peninsula

H. Ohira and A. Takasu

Department of Geoscience, Shimane University

**INTRODUCTION:** Fission track dating was applied for sedimentary rocks of Kii peninsula, Wakayama prefecture. The aim of this study is to estimate depositional periods and thermal histories of sedimentary rocks in relation with burial-uplift processes during accretion process. In recent study, the Cretaceous Shimanto Belt in this area is newly divided into several accretionary complexes showing zonal structure, Ryujin, Miyama, Yukawa and Hanazono complexes, from the south to north [1]. FT age variations across the Shimanto belt in the Kii region and relationship between FT ages and thermal and burial/uplift history has been precisely discussed mainly for areas of the north side including a part of Hanazono complex [2].

**EXPERIMENTS:** Samples collected from each units of the Shimanto belt were crashed and sieved and heavy minerals were concentrated by common method. Zircon and apatite were abundant in almost samples but less amounts in the Miyama complex. Zircons were mounted in PFA Teflon, and then polished to reveal entire internal surface. Samples were etched in a NaOH-KOH eutectic melt at 225°C [3] for 20-32 hours and were irradiated at pneumatic tube of graphite facility (Tc-pn) of Kyoto University Reactor (KUR). FT densities were measured using optical microscope at 1000× magnification with a dry objective 100×. FT ages were calculated by trackkey program [4].

**RESULTS:** Fission track grain ages show wide variations in each sample but the youngest modes in histograms show a systematical tendency from south to north, probably corresponding to depositional period and thermal histories during burial-uplift process of each geological unit. Ranges and modes in histograms for each complexes are as follows; Ryujin (53-92Ma; 60Ma), Miyama (57-197Ma; 68Ma), Yukawa (94-300Ma; 126Ma), and Hanazono (55-93; 68Ma). FT ages become old from southernmost Ryujin complex toward the northern Yukawa complex, but the Hanazono complex in northernmost district show young age again. The gap of age between the Yukawa and Hanazono complex and rejuvenation of FT age in the Hanazono complex is compatible

with that the “Yanase Fault” is important thrust system which dividing complexes of this area and the Hanazono complex was exposed to relatively higher temperature due to deep burial. Almost FT grain ages from the Yukawa complex show entirely older than the estimated depositional period, indicating that sample was not affected by heating up to enough temperature to reset FT ages. On the contrary, the youngest age component in the Ryujin complex (59Ma) is significantly younger than the limit of depositional period (68-78Ma). This result probably indicates that most of FT grain ages of Ryujin complex were reset by thermal affect during burial process to a deeper level, or the depositional age of the Ryujin complex is actually younger than previous interpretation. Detail track length measurement will be required for the solution of above discussion.

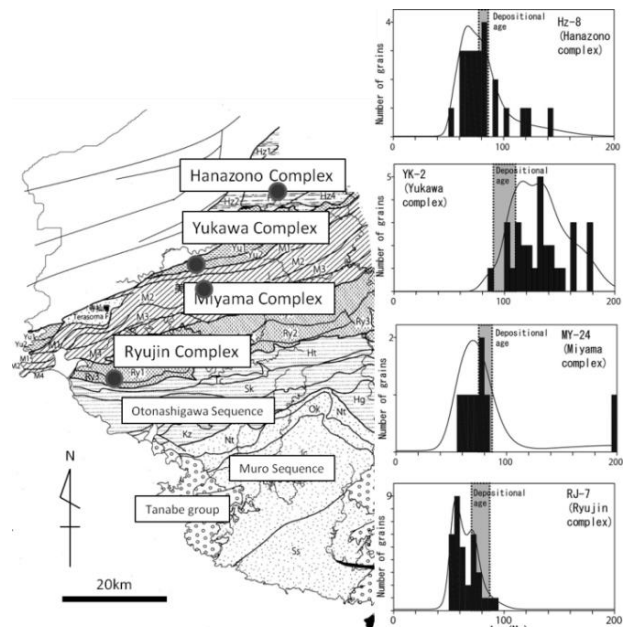


Fig.1 FT age histogram and geological map with each complex boundary [5].

- [1] Suzuki H. and Nakaya S., 2012, The Assoc. Geological Collaboration in Japan, Monograph 59, 273-282 (in Japanese with English abstract).
- [2] Hasebe N. and Tagami T., 2001, Tectonophysics 331, 247-267.
- [3] Gleadow A.J.W. *et al.*, 1976, Earth and Planetary Science Letter, 33, 273-276.
- [4] Dunkle, I., 2002, Computer & Geosciences, 28, 3-12.
- [5] Suzuki H., 2012, The Assoc. Geological Collaboration in Japan, Monograph 59, 101-110 (in Japanese with English abstract)

## CO5-6 Trace Amounts of Halogens (Cl, Br and I) in Manganese Nodule Reference Materials

M. Ebihara and S. Sekimoto<sup>1</sup>

Graduate School of Science, Tokyo Metropolitan University

<sup>1</sup>Research Reactor Institute, Kyoto University

**INTRODUCTION:** Accurate and reliable data of halogen abundance have been rarely reported for terrestrial samples, such as manganese nodule materials. Since halogens differ in volatility from element to element, their content and relative abundance are highly informative when discussing the petrogenesis of such samples. Recently, we have improved the radiochemical neutron activation analysis (RNAA) procedure for trace amounts of halogens (Cl, Br and I) [1]. In this study, our RNAA was applied to two manganese nodule materials that are available in U.S. Geological Survey (USGS) and then, our RNAA values were compared with the literature values.

**EXPERIMENTS:** Trace amounts of Cl, Br and I in the two manganese nodules (Nod-P-1 and Nod-A-1) were determined by RNAA. The RNAA procedure is described elsewhere [1-2]. Those samples were repeatedly analyzed more than two times.

**RESULTS:** The two manganese nodules (Nod-P-1 and Nod-A-1) analyzed using RNAA in this study were also analyzed using inductively coupled plasma double focusing sector field mass spectrometry (ICP-SFMS) [3] for bromine and iodine. Our RNAA values and the ICP-SFMS values are shown in Table 1. Before analysis by ICP-SFMS, the nodule materials were subjected to the acid digestion procedure, in which the nodule materials are heated with the mixture of concentrated nitric, hydrochloric and hydrofluoric acids by using microwave. The digestion solution was diluted appropriately and then introduced into the ICP-SFMS instrument.

**Table 1:** Cl, Br and I contents in USGS manganese nodule materials analyzed by RNAA in this study<sup>a</sup> and from the Literature

sample		Cl(mg kg <sup>-1</sup> )	Br(mg kg <sup>-1</sup> )	I(mg kg <sup>-1</sup> )
Nod-P-1	RNAA (n = 4)	1380 ± 140	5.93 ± 0.76	157 ± 17
	ICP-SFMS <sup>15</sup>	- <sup>b</sup>	30.3 ± 2.2	31.4 ± 0.3
Nod-A-1	RNAA (n = 2)	4410 ± 160	14.8 ± 0.5	367 ± 9
	ICP-SFMS <sup>15</sup>	- <sup>b</sup>	40.9 ± 0.7	47.7 ± 3.2

<sup>a</sup>Mean values followed by standard deviations (1σ) (n=3, 4). Mean values followed by an uncertainty which is simply the value calculated from two individual uncertainty values. (n=2) <sup>b</sup>Not reported.

Our RNAA data for Nod-P-1 and Nod-A-1 are not consistent with the literature data obtained by ICP-SFMS for both bromine and iodine. As for iodine the ICP-SFMS values are lower than the RNAA values. Such an inconsistency between RNAA values and ICP-SFMS values also may be derived from the loss of iodine in the acid digestion procedure with heating by the microwave. To prevent the loss of iodine, the digestion solution should not be heated in principle, or heating of the digestion solution must be achieved with extreme care. Regarding bromine, on the other hand, the ICP-SFMS values are higher than the RNAA values by a factor of about three to five. Such an inconsistency between RNAA values and ICP-SFMS values may be due to the ability of this ICP-SFMS instrument, especially to background [4]. Bromine is determined by ICP-SFMS and/or ICPMS using the isotope <sup>79</sup>Br and <sup>81</sup>Br. The mass of those two bromine isotopes is next and very close to the biatomic (<sup>40</sup>Ar<sup>40</sup>Ar)<sup>+</sup> molecule of mass 80. Since argon is so abundant in the plasma of the ICP-SFMS and/or ICPMS, the combination of two <sup>40</sup>Ar ions causes a large peak at mass 80 whose peak tail could interfere with either stable isotope of bromine. Additionally, there are several potential interferences on <sup>79</sup>Br and <sup>81</sup>Br; (<sup>40</sup>Ar<sup>39</sup>K)<sup>+</sup>, (<sup>63</sup>Cu<sup>16</sup>O)<sup>+</sup> and (<sup>40</sup>Ar<sup>38</sup>Ar<sup>1</sup>H)<sup>+</sup> interference with <sup>79</sup>Br and (<sup>40</sup>Ar<sup>41</sup>K)<sup>+</sup>, (<sup>65</sup>Cu<sup>16</sup>O)<sup>+</sup> interference with <sup>81</sup>Br signals, respectively [4]. To quantify <sup>79</sup>Br successfully without interference of (<sup>40</sup>Ar<sup>39</sup>K)<sup>+</sup> and (<sup>63</sup>Cu<sup>16</sup>O)<sup>+</sup> nor of (<sup>40</sup>Ar<sup>38</sup>Ar<sup>1</sup>H)<sup>+</sup>, the ICP-SFMS instrument should be operated in resolution (m/δm) of >10000 or >5000, respectively. (A required resolution for successful quantification of <sup>79</sup>Br is explained in the Supporting Information.) In case of the literature values for bromine, however, the ICP-SFMS instrument was operated in medium resolution mode (m/δm=4500) for <sup>79</sup>Br, and interference of (<sup>40</sup>Ar<sup>39</sup>K)<sup>+</sup> and (<sup>63</sup>Cu<sup>16</sup>O)<sup>+</sup> cannot be removed from <sup>79</sup>Br signal. A possible explanation of higher bromine values in ICP-SFMS than in RNAA could be an overestimation due to the interference at mass 79 in the ICP-SFMS instrument. Since the ICP-SFMS operation in high resolution mode (HRM) is generally the operation in resolution (m/δm) of 9000-10000, it is fundamentally impossible to quantify <sup>79</sup>Br successfully without interference of (<sup>40</sup>Ar<sup>39</sup>K)<sup>+</sup> and (<sup>63</sup>Cu<sup>16</sup>O)<sup>+</sup> even using the HRM. This suggests that bromine-separation as a pretreatment of samples is essential for bromine-determination using ICP-SFMS and/or ICPMS.

### REFERENCES:

- [1] S. Sekimoto and M. Ebihara, *Anal. Chem.*, **85** (2013) 63366341.
- [2] S. Sekimoto and M. Ebihara, in preparation.
- [3] M.D. Axelsson *et al.*, *Analyst*, **127** (2002) 76-82.
- [4] J. Hammerli *et al.*, *Chem. Geol.*, **337-338** (2013) 75-87.

## CO5-7 Application of Neutron Activation Analysis to Micro Gram Scale of Solid Samples

S. Sekimoto, N. Shirai<sup>1</sup>, M. Ebihara<sup>1</sup>

Research Reactor Institute, Kyoto University

<sup>1</sup> Graduate School of Science, Tokyo Metropolitan University

**INTRODUCTION:** Since instrumental neutron activation analysis (INAA) is a non-destructive and multi-elemental analysis method, it is suitable for precious samples and, especially, for such specimens as those highly desired to be neither physically decomposed nor chemically dissolved. Meteorites are the best example for such samples. Chondritic meteorites (chondrites) and iron meteorites contain relatively high contents of Co and Ir compared with those in the earth crust. As Co and Ir have high sensitivity in NAA, they can be good markers for the identification of such extraterrestrial materials. In NAA of chondrites, a few tens mg of specimen is commonly used. For such a case, a few hundred  $\mu\text{g kg}^{-1}$  of Ir and a few hundred  $\text{mg kg}^{-1}$  of Co can be reliably determined. When an extremely small size (e.g., micro gram) of samples such as micrometeorites recovered on the Earth surface and tiny particles returned from extraterrestrial asteroids are to be analyzed by INAA, the conventional INAA procedure used for a few tens mg is not suitable. For such tiny samples, neutron irradiation with high neutron flux and long irradiation time (namely, high neutron dose) is required. For the irradiation with high neutron dose, polyethylene bags for holding samples are not usable because they are prone to radiation damage. Polyethylene bags are also not suitable for holding tiny grain samples. It is, therefore, very important to design an appropriate sample holder for irradiating small grain samples. As we use a relative method for quantification, in this report, the preparation of reference samples and the evaluation for their suitability are described in detail.

**EXPERIMENTS:** Two reference samples with different elemental compositions were used; the Allende meteorite powder (1.66 mg) prepared by the Smithsonian Institution (USMN 3529; split 22 and position 6) and the basaltic rock reference sample JB-1 prepared by Geological Survey of Japan (1.12 mg). Each sample was sealed into a synthesized quartz tube (1 mm inner  $\phi$  and 2.7 mm outer  $\phi$  x 35 mm length), which was then wrapped with Al foil for the safety. The neutron irradiation was performed for 45 hours at the hydro-irradiation port of Kyoto University Reactor (KUR) in Kyoto University Research Reactor Institute (KURRI) under 1MW operation.

**RESULTS:** For quantification in INAA, two reference samples (the Allende meteorite and the JB-1 basalt) having different elemental contents were used. We have conducted similar INAA experiments where tiny grain samples collected by the spacecraft were analyzed by

using Allende and JB-1 as reference samples. Hereafter, these experimental runs named run-2 [1] and run-3 [2] are discussed in comparison with the present study, which is named run-1. It is meaningful to compare the activity of radioactive nuclides used in INAA for two different reference samples. We discuss the gamma rays counting rate per unit mass for each target element, hereafter gamma-ray intensity, among three runs. The gamma rays counting rate is gamma ray counts per second and correspond to gamma ray energies designated for individual nuclides ( $^{24}\text{Na}$ ,  $^{46}\text{Sc}$ ,  $^{59}\text{Fe}$ ,  $^{140}\text{La}$ ,  $^{153}\text{Sm}$ ,  $^{58}\text{Co}$ ,  $^{60}\text{Co}$ ,  $^{65}\text{Zn}$  and  $^{51}\text{Cr}$ ). Those nine nuclides were determined both for Allende and JB-1. Relative gamma-ray intensities of  $^{24}\text{Na}$ ,  $^{46}\text{Sc}$  and  $^{59}\text{Fe}$  in both reference samples are highly consistent for the three runs. Such a consistency can also be seen for Fe reagents. Kong and Ebihara [3] evaluated the consistency in elemental contents in the mg size of JB-1 and confirmed that JB-1 is well homogenized for its use in mg. We confirm that Allende can also be used as a reference sample for mg scale of sample at least for Na, Sc and Fe. On the other hand, Allende and JB-1 show a small inconsistency, most of which may be due to poor counting statistics for either sample. For example, Allende tends to have relatively low contents of rare earth elements (La and Sm), whereas JB-1 has a low content of Ni and Zn. Depending upon elemental contents, either Allende or JB-1 may be used for a reference sample.

There appears an apparent inconsistency in Cr data between the two reference samples, with JB-1 having systematically higher gamma-ray intensity. This is undoubtedly due to an erroneous reference value ( $425 \text{ mg kg}^{-1}$ ) of Cr for JB-1. If a proposed value ( $475 \text{ mg kg}^{-1}$ ) [3] is instead used, an excellent consistency can be seen as shown in Fig. 1 for  $^{51}\text{Cr}$ .

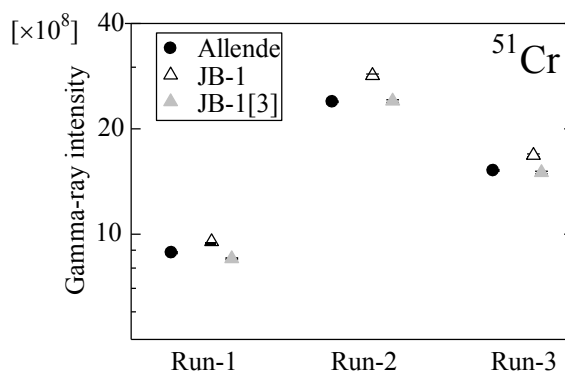


Fig. 1. Gamma-ray intensities of  $^{51}\text{Cr}$  in reference monitors for run-1, run-2 and run-3.

### REFERENCES:

- [1] M. Ebihara *et al.*, Meteorit. Planet. Sci., **50** (2015) 243-254.
- [2] M. Ebihara *et al.*, Science, **333** (2011) 1119-1121.
- [3] P. Kong and M. Ebihara, Geochem. J., **31** (1997) 339-344.

## CO5-8 Probability distribution of SEL occurred on on-board computer (OBC) mounted on small-scale satellite

H. Masui, T. Tomioka, K. Taniwak, M. Cho and K. Takamiya<sup>1</sup>

Kyushu Institute of Technology

<sup>1</sup>Research Reactor Institute, Kyoto University

**INTRODUCTION:** Recently universities and venture businesses actively develop small-scale satellites. For the small-scale satellites, many COTS (Commercial-off-the-shelf) components are used. The COTS components are not enough durable for space radiation environment. In particular, a microprocessor embedded to OBC suffers a problem of Single Event Latch-up (SEL). Horyu-2 was the small-scale satellite developed by Kyushu Institute of Technology (KIT) and actually suffered many on orbit anomalies due to SEL[1-2]. Therefore, the radiation test is important for small-scale satellite using the COTS to characterize the radiation effect and to find most durable COTS. However, a radiation test using an accelerator is not readily available. Since 2012, KIT has been conducting radiation test using <sup>252</sup>Cf for small-scale satellite. In this report, recent radiation tests, using <sup>252</sup>Cf, has been reported. This ground experiment data was analyzed and compared with the on-orbit data acquired from Horyu-2 in order to investigate the nature of anomaly.

**EXPERIMENTS:** Figure 1 shows the schematic of test configuration. A microprocessor, as device under test (DUT), was set in a vacuum chamber. The pressure during the test was approximately 30 Pa. The model number of microprocessor was HD64F36057FZJV and its plastic cover was removed. The same model microprocessor was mounted on Horyu-2. The radiation source of <sup>252</sup>Cf was mounted on XYZ stage. By changing a distance from the test sample to <sup>252</sup>Cf, radiation flux was calculated and controlled. DAQ and PC1 measured a voltage and current of the microprocessor. PC2 monitored the operation of microprocessor with RS232 communication. Just after the SEL occurred each time, a reset command was sent to the microprocessor. If the microprocessor was not recovered due to SEL, power was turned off.

**RESULTS:** 100 times SELs were observed and the time between SELs was measured for each flux condition. Figure 2 shows the probability distribution of a SEL occurrence with respect to time[3] at three different distances. As shown in Fig. 2, the time between SLEs is increased with increasing of the flux and the probability follows the Poisson distribution. Table 1 shows a SEL occurrence time and the cross-section for ground experimental. On-orbit data from 2012 to 2015 is also shown. A simple average SEL occurrence time was  $1.2 \times 10^7$  sec (= 139 days) from the orbit data. The cross-section derived

from the ground test is  $2.8 \times 10^5$  to  $1.4 \times 10^6$  times the cross-section derived from the on-orbit data.

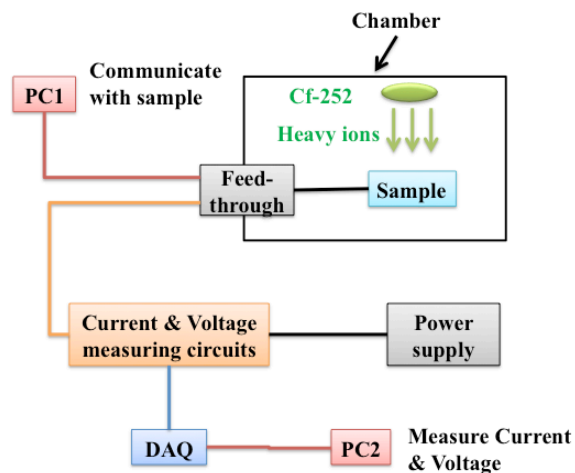


Fig. 1 Test configuration

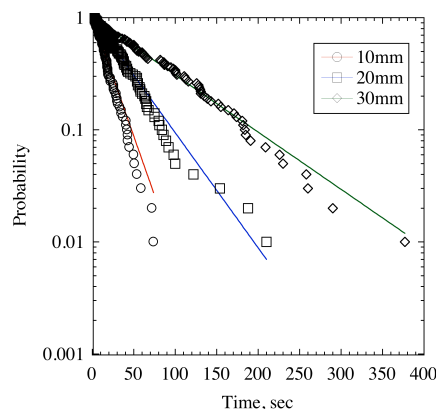


Fig. 2 Probability of SEL occurrence for various fluxes

Table 1 Comparison between <sup>252</sup>Cf test and on-orbit anomaly

	<sup>252</sup> Cf test			Orbit
Flux, 1/cm <sup>2</sup> /s	37	13	6.4	64
Simple average time, s	19.3	42.2	86.3	$3.4 \times 10^6$
Cross section of SEL, x 10 <sup>-3</sup> cm <sup>2</sup>	1.3	1.8	1.8	$1.3 \times 10^{-6}$

### REFERENCES:

- [1] M. Cho et al., The Japan Society for Aeronautical and Space Sciences, 12(0), 17-24, 2013.
- [2] Y. Seri et al., SSC13-X-8, Small Satellite Conference, August, 2013.
- [3] T. Tomioka et al., Acta Astronautica, submitted for publication.

採択課題番号 26053

カリフォルニウム線源を使用した衛星搭載用

通常採択

オンボードコンピュータに発生するシングルイベントの模擬試験および試験方法の確立

(九工大・先端) 増井博一、富岡孝裕、谷脇康洋、趙孟佑 (京大・原子炉) 高宮幸一

## CO5-9 Instrumental Photon Activation Analysis of Geological and Cosmochemical Samples

N. Shirai, S. Sekimoto<sup>1</sup>, M. Ebihara

Department of Chemistry, Tokyo Metropolitan University  
<sup>1</sup>Research Reactor Institute, Kyoto University

**INTRODUCTION:** Bulk chemical compositions for terrestrial and cosmochemical materials are significantly important to elucidate the formation, evolution processes and magmatism of planetary bodies. Compared to geological samples, cosmochemical samples pose several severe requirements to their analytical methods for chemical compositions. High sensitivity and accuracy for as many as elements as possible are required for analytical methods applied to such samples because of the limitation of sample amounts usable for analysis. Non-destructive analysis for many elements is equally favorable. Nuclear analytical methods represented by prompt gamma-ray analysis (PGA), instrumental neutron activation analysis (INAA) and instrumental photon activation analysis (IPAA) meet almost all these requirements. Among these nuclear analytical methods, INAA has been commonly used as an analytical tool in cosmochemistry for a long time, while PGA and IPAA have not been very often applied to cosmochemical samples.

In IPAA, ( $\gamma, n$ ) reaction is used for the determination of elemental abundances which is an opposite reaction used in INAA. Thus, IPAA could determine elemental abundances which cannot or hardly be determined by INAA. Usually samples are irradiated by using 30 MeV electrons in IPAA. However, corrections of interferences caused by secondary nuclear reactions such ( $\gamma, p$ ) and ( $\gamma, pn$ ) are necessary. Although the sensitivity obtained by activation with 20 MeV electrons are suppressed compared with the activation with 30 MeV electrons, activation with 20 MeV electron reduces the degree of such interference reactions. In this study, we performed IPAA by using a linear electron accelerator at Kyoto University Research Reactor Institute (KURRI) and compared the results obtained by the activation with 20 MeV with those with 30 MeV.

**EXPERIMENTS:** Three GSI standards materials namely JA-2 (andesite), JB-3 (basalt) and JR-1 (rhyolite) and one cosmochemical sample (Allende meteorite) were analyzed by IPAA. Chemical reagent sample, Fe<sub>2</sub>O<sub>3</sub> powder and Cr, Mn and Ni metals were also irradiated to correct the interference reactions. Samples and chemical reagents were taken into a sample container (9 mm $\phi$ ) made of highly Al foil. Five to ten samples were stacked, among which thin foil disk (9 mm $\phi$ ) of Au as a monitor of the intensity of photon are placed. Samples in a block were put in a quartz tube. We used a linear electron ac-

celerator at the Research Reactor Institute, Kyoto University. Electrons were accelerated by the linear accelerator to about 30 and 20 MeV. After irradiation (about 30 hours), samples were taken into new Al foil and measured at the Laboratory of Radioisotopes, Tokyo Metropolitan University. For comparative method, JB-1 was used as reference standard.

**RESULTS:** Table 1 shows the interfering reactions and their contributions to nuclides produced by corresponding reactions for activation with 20 MeV and 30 MeV electrons. As shown in Table 1, significant contributions from interfering reactions were found in activation with 30 MeV electrons. Thus, determinations of Cr, Co and Mn abundances need the correction of corresponding interferences. As expected, contributions from interfering reactions with 20 MeV electrons were lower than those in activation with 30 MeV electrons.

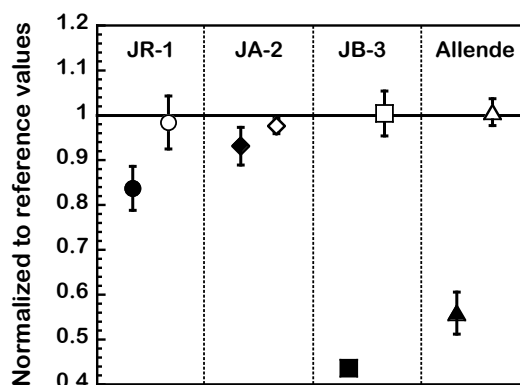


Figure 1. Our Mn values obtained by using 20 and 30 MeV electrons are compared with the corresponding reference values. Solid and open symbols represent that data are determined by using 30 and 20 MeV electrons, respectively.

A total of 17 elements (Ca, Sc, Ti, Cr, Mn, Fe, Co, Ni, Zn, As, Rb, Y, Zr, Nb, Cs, Ba and Ce) were determined in geological reference materials and the Allende meteorite. Our Cr and Mn values obtained from activation with 30 MeV electrons were different from literature values. Our Mn values obtained by using 20 and 30 MeV electrons are compared with reference values in Figure 1. For four samples, Mn values obtained by using 20 MeV electrons are consistent with reference values, while those by using 30 MeV electron are lower than literature values. Differences of Mn values in JB-3 and Allende between 30 and 20 MeV electrons are more remarkable than those in JR-1 and JA-2. Fe/Mn ratios of JR-1, JA-2, JB-3 and Allende are 8.1, 52, 60 and 162, respectively. In consideration of Fe/Mn ratios, overcorrections of the interfering reactions were responsible for these differences. For other elements, there were no differences between the two sets of our values obtained from the activations with 20 and 30 MeV electrons, which were consistent with literature values.

Table 1. Interfering reaction and correction rate for interference.

Reaction used for determination	Interfering reaction	Correction rate	
		30 MeV	20 MeV
<sup>52</sup> Cr( $\gamma, n$ ) <sup>51</sup> Cr	<sup>56</sup> Fe( $\gamma, \alpha n$ ) <sup>51</sup> Cr	0.036 mgCr/gFe	-
<sup>59</sup> Co( $\gamma, n$ ) <sup>58</sup> Co	<sup>60</sup> Ni( $\gamma, pn$ ) <sup>58</sup> Co	3.7 mgCo/gNi	0.88 mgCo/gNi
<sup>55</sup> Mn( $\gamma, n$ ) <sup>54</sup> Mn	<sup>56</sup> Fe( $\gamma, pn$ ) <sup>54</sup> Mn	6.2 mgMn/gFe	0.1 mgMn/gFe

採択課題番号 26067 放射化分析による宇宙・地球化学的試料の元素組成の定量 通常採択  
 (首都大学東京理工) 白井直樹、海老原充 (京大・原子炉) 関本俊

A. Hashiguchi, M. Yoneda, Y. Fujikawa<sup>1</sup>

Graduate School of Engineering, Kyoto University

<sup>1</sup>Research Reactor Institute, Kyoto University

**INTRODUCTION:** Perfluoro compounds (PFCs), characterized by high chemical and thermal stability, have been widely used in the world as water and oil repellent, car wax and fire extinguisher, etc. Among various PFCs, perfluorooctane sulfonate (PFOS), a linear perfluoroalkyl sulfonate with eight carbon-chain length, has been noted for its high bioaccumulation potential to wildlife and persistence in the environment. Among the various environmental problems associated with this recalcitrant substance, we were most interested in development of a practical technology that could be used to polish-up the wastewater containing PFOS.

Existing practical treatment methods for removal of PFOS from sewage effluent or wastewater are membrane filtration (especially reverse osmosis), or adsorption using activated carbon. Use of these methods has a figure of merit as they are already installed in many treatment plants, and the operation and management protocols for various micro-pollutants are fairly well established. On the other hand, PFOS is not decomposed by these methods, only concentrated in the reject or adsorbents. A technique that can decompose PFOS in the concentrate is needed.

Photo-assisted methods have been known to be effective for decomposition of pollutants in air and water. The treatment is done either via direct photoexcitation of the pollutant or mediated processes involving highly reactive radicals generated by photolysis. UV light is commonly used for the technology, but for particularly recalcitrant pollutants such as PCBs and chloro-fluoro aliphatic carbons,  $\gamma$  ray irradiation has been proved to be most effective. The OH radical, solvated electron, and radical or cation of isopropyl alcohol (added as a source of organic radicals), produced in the medium by  $\gamma$  ray, degraded the pollutants through reductive dehalogenation processes.

In our study, we irradiated the PFOS in various media with  $\gamma$  ray to investigate the possibility of decomposition of PFOS via direct photolysis or radical reactions.

**EXPERIMENTS:** A 414 TBq (as of February, 2008) <sup>60</sup>Co in  $\gamma$  ray irradiation facility in KURRI was used as a  $\gamma$  ray source. All the reagents used were Japan Industrial Standard reagent grade unless stated otherwise. Known amount of PFOS powder purchased from Wako Chemical Industry was dissolved in methanol (HPLC grade), and was used to spike alkaline isopro-

pyl alcohol (IPA) and alkaline potassium persulfate solutions. Both solutions were purged with nitrogen gas before the irradiation. The use of persulfate was tested because the substance is a known radical initiator that produces sulfate radical through  $S_2O_8^{2-} \rightarrow 2SO_4^{\cdot -}$  reaction. As a control, ethanol (a radical scavenger) spiked with PFOS was also irradiated. The IPA and persulfate solution was subjected to solid phase extraction by Oasis HLB (strongly hydrophilic and lyophobic, Waters) resin prior to determination of PFOS. Direct photolysis of solid PFOS by gamma-ray was investigated by irradiation of a 20 $\mu$ L drop of PFOS (concentration: 1g/L-methanol), dried on a microscope slide, and covered with a cover glass.

Irradiation dose was estimated by ceric sulfate dosimeter utilizing the reduction of  $Ce^{4+}$  to  $Ce^{3+}$  by the radiation, or the calculation considering the distance and angle from the <sup>60</sup>Co radiation source. Concentrations of PFOS in sub-samples collected before and after the irradiation were determined by UPLC-MS/MS (Waters).

**RESULTS:** Fig.1 shows the decrease in the numbers of PFOS molecules after gamma-ray irradiation of the dried residue of PFOS solution. The decrease of PFOS molecules was roughly proportional to the adsorbed dose. Interestingly, the rate of decrease was strongly dependent

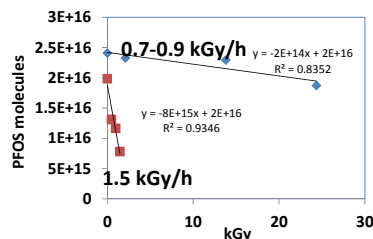


Fig. 1 Decomposition of dried PFOS residue with time (kGy)

on the dose rate, and was faster at the higher dose rate. Since the generation of radicals in the dried residue is negligible, the decomposition of PFOS is attributed to photoexcitation of PFOS followed by its decomposition. It has been known that upon irradiation with UV, perfluorooctanoic acid (PFOA), one of the PFCs known for its refractoriness, was decomposed, and the mechanism of decomposition was ascribed to direct photolysis rather than to radical reaction [1]. On the other hand, the decomposition of PFOS by UV has not been found so far. The present result indicates that high energy photon (1.16 and 1.33 MeV  $\gamma$  ray from <sup>60</sup>Co in this case) was probably needed to induce the direct photolysis of PFOS.

The decomposition of PFOS in ethanol was 30% (initially  $2.3 \times 10^{15}$  molecules) after 42 kGy (dose rate 2.7 kGy/h) of irradiation. After 38 kGy (dose rate 0.67 kGy/h) of irradiation, only 6 % of PFOS was decomposed in alkaline persulfate, while in IPA, 85% of PFOS was decomposed, due probably to the radical reactions.

**REFERENCES:**

[1] R. R. Giri *et al.*, Water Sci. & Technol., 63 (2011) 276-282.

A. Shimada<sup>1</sup>, I. Otsuka<sup>1</sup>, N. Fujii<sup>2</sup> and T. Saito<sup>2</sup>

<sup>1</sup>*Sustainable Environmental Studies, Graduate School of Life and Environment Sciences, University of Tsukuba*

<sup>2</sup>*Research Reactor Institute, Kyoto University*

**INTRODUCTION:** A historical riddle about chiral homogeneity, the origin of L-dominant amino acids in biological world, has intrigued scientists for many years, though there has been no general consensus as yet to it. Life could not be born without homochirality, that is to say, no homochirality – no life. However, we cannot imagine at all when and how the homochirality was established on early earth. Amino acids are stereochemically too labile to retain their homochiral state in natural environment because racemization pressure is overwhelmingly strong, especially in aqueous solution. An elaborate mechanism is necessary to put biological world into homochirally-stable state. The homochirality of contemporary biological world is fully guaranteed by enzyme enantioselectivity. Since the enzyme enantioselectivity has remained unclear, a deeper understanding of its mechanism is required to unravel all the riddle of the origin of homochirality. We have so far researched a mechanism of tryptophanase (TPase) enantioselectivity, with the aim of answering this difficult problem. TPase degrades L-tryptophan (L-Trp) by  $\beta$ -elimination reaction, and also synthesizes L-Trp from L-serine (L-Ser) and indole by  $\beta$ -replacement reaction by use of its absolute enantioselectivity. On the other hand, it is perfectly inert to D-tryptophan (D-Trp) and D-serine (D-Ser) at all. Additionally these D-amino acids inhibit TPase in L-Trp degradation and L-Trp synthesis from L-Ser. The present report describes to focus simply on D-Ser acting on TPase as a competitive inhibitor.

**EXPERIMENTAL:** Generally speaking, D-amino acid works as inactive or inhibitor against enzyme. D-Ser completely has no reaction to TPase. When TPase synthesizes L-Trp from L-Ser and indole, D-Ser inhibits the synthetic reaction. Since kinetic analysis was effective to probe the interaction between D-Ser and TPase, we analyzed D-Ser behavior against TPase in L-Trp synthesis in terms of it. For kinetics, reaction was conducted at 50 °C for 4 hr in Dry Thermo Unit DTU-1B with 0, 0.1, 0.2, 0.3, 0.6, or 1 M of D-Ser added in reaction mixtures that were prepared by combining the required L-Ser (10-100 mM) with fixed apotryptophanase (apoTPase, 0.46  $\mu$ M), indole (5.4 mM) and pyridoxal 5'-phosphate (PLP) concentrations (0.4 mM) in 500  $\mu$ L of 0.1 M potassium phosphate buffer (PB), adjusted to a pH of 8.3. After 4hr, the reaction mixture was cool on

ice to stop reaction. 200  $\mu$ L of the reaction mixture was filtered through Amicon Ultra Centrifugal Filters cutting more than MW 3000, immediately injected on a Crownpack CR (+) Resolution HPLC resolution column equilibrated with the degassed eluent through a Degaser, and eluted at a flow rate of 0.9 mL/min at room temperature with an HPLC pump. L-Trp synthesis from L-Ser was determined measuring with a CD-1595 detector. Ellipticity  $[\theta]$  was monitored at  $\lambda = 230$  nm with the CD detector, represented in units of mdeg. Ellipticity of the eluent was set up to zero at a wavelength of  $\lambda = 230$  nm, so the peaks of L-Trp appeared on the positive side.

**RESULTS AND DISCUSSION:** For kinetic analysis, TPase activity on L-Trp synthesis was assayed in triplicate at the same substrate concentration, averaged. Lineweaver-Burk plots were drawn based on the least squares method. The reciprocal of rate constant (ordinate) versus the reciprocal of substrate concentration (abscissa) was plotted for each concentration of D-Ser, depicting a typical competitive inhibition plot. Kinetic constants were calculated from these double-reciprocal plots, and also an inhibition constant  $K_I$  of D-Ser was determined from their slopes.  $K_m$  was 44 mM,  $V_m$   $2.2 \times 10^{-4}$  mM/s,  $k_{cat}$  0.48/s and  $K_I$  419 mM. D-Ser is a competitive inhibitor against TPase in L-Trp synthesis reaction from L-Ser and indole. Competitive inhibitor usually shares a highly structural resemblance with its substrate. D-Ser stereostructure fits into the active site structure of TPase, promptly binding there. Although D-Ser can bind with the active site, D-Ser is not involved in L-Trp synthetic reaction. Perhaps D-Ser cannot form aldimine-bond with PLP at the first step of L-Trp synthesis. However, our previous studies have reported that TPase becomes active on D-Ser in the presence of triammonium phosphate (TAP) to make the enantioselectivity flexible. TAP is the most important among ammonium phosphates because it gives TPase the highest activity on D-Ser. The presence of TAP promotes a small conformational change to TPase to fit D-Ser partly into the catalytic site of the active site and help D-Ser to form the external aldimine bond with PLP. This subtle steric interaction, whose detail is still being investigated, are very necessary to transform D-Ser from inhibitor into active substrate. Future research will determine a metabolic pathway of L-Trp synthesis from D-Ser, and also demonstrate the formation of an aldimine bond between amino group of D-Ser and PLP at the first step of this reaction in the presence of TAP.



## CO6-2 Study of Localization Estimation of Abasic Sites in DNA Irradiated with Ionizing Radiation

K. Akamatsu, N. Shikazono and T. Saito<sup>1</sup>

Irradiated Cell Analysis Research Group, Quantum Beam Science Research Center, Japan Atomic Energy Agency (JAEA)

<sup>1</sup>Research Reactor Institute, Kyoto University

### INTRODUCTION:

DNA lesions induced by ionizing radiation and chemicals can cause mutation and carcinogenesis. In particular, “clustered damage” site, that is a DNA region with multiple lesions within one or two helical turns, is believed to hardly be repaired. This damage is considered to be induced, e.g., around high-LET ionizing radiation tracks. However, detail of the damage is not known. We have already developed a method for estimating degree of localization of abasic sites (APs) in DNA using Förster resonance energy transfer (FRET). The FRET efficiency ( $E$ ) was calculated using the donor fluorescence intensities before/after enzymatic digestion of the labeled AP-DNA [1]. First, we have applied the method to  $^4\text{He}^{2+}$  (2.0 MeV/u, LET:  $\sim 70$  keV/ $\mu\text{m}$ )-  $^{12}\text{C}^{5+}$  (0.37 MeV/u, LET:  $\sim 760$  keV/ $\mu\text{m}$ )- and  $^{60}\text{Co}$   $\gamma$ -irradiated DNA in the solid state. The results showed that  $^{12}\text{C}^{5+}$  beam likely produced close APs within a track. The apparent distance calculated from the  $E$  value was approximately 17 base pairs [2]. This finding indicates that *direct radiation effect* of  $^{12}\text{C}^{5+}$  beam near the Bragg peak produces clustered DNA damage. We have recently applied the method to DNA in a cell-mimetic radical scavenging condition [3,4]. Here, we show new results using  $^4\text{He}^{2+}$  beam and  $^{60}\text{Co}$   $\gamma$ -rays.

### EXPERIMENTS:

#### ●Sample preparation and He beam irradiation

The plasmid DNA digested by Sma I was used (linear form). The DNA was dissolved to be 0.1 g/L in 0.2 M Tris-HCl buffer (pH 7.5) which is a cell-mimetic condition in relation to radical scavenging capacity. One hundred microliters of the DNA solution was transferred to an irradiation folder [2], and was irradiated with the  $^4\text{He}^{2+}$  beam (12.5 MeV/u, LET:  $\sim 19$  keV/ $\mu\text{m}$ ; TIARA, JAEA), and  $^{60}\text{Co}$   $\gamma$ -rays (LET:  $\sim 0.2$  keV/ $\mu\text{m}$ ; Kyoto University Research Reactor Institute: KURRI) were also used as a standard radiation source.

#### ●Preparation of fluorophore-labeled irradiated DNA and the FRET observation

The irradiated DNA (10  $\mu\text{L}$  in water) and 10  $\mu\text{L}$  of 100 mM Tris-HCl (pH7.5) were mixed in a microtube. Two microliters of a mixture containing AF350 (donor fluorescent probe) and AF488 (acceptor one) with a given molar ratio was added to the DNA solution and was incubated for 24 h at 35°C. The fluorophore-labeled DNA was purified by precipitation by ethanol. Twenty

microliters of water was added to the residue. The fluorescence intensities were measured both at 449 nm (ex. 347 nm for AF350) and at 520 nm (ex. 460 nm for AF488). After the measurement, the enzyme cocktail containing DNase I and phosphodiesterase I was added to the solution, followed by being incubated for 3 h at 37°C.  $E$  values were calculated from the donor intensity before/after the digestion.

### RESULTS AND DISCUSSION:

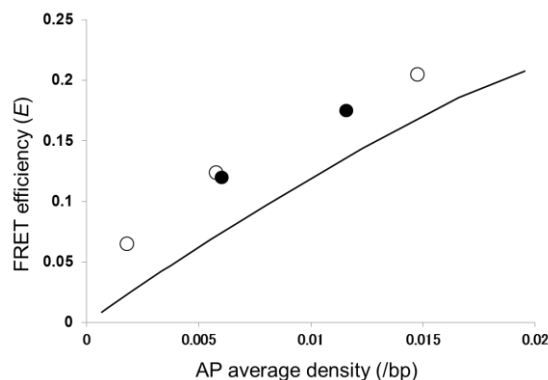


Fig. 1. Relationship between AP average density and FRET efficiency for He ion beam (●) and  $^{60}\text{Co}$   $\gamma$ -rays (○). The solid line indicates a theoretical curve for randomly-distributed APs in DNA.

As shown in Fig.1, there was no difference in FRET efficiency ( $E$ ) between the two radiation sources. But interestingly, all data points were above the curve for random distribution. This finding suggests that AP distribution for the  $\gamma$ -rays as well as that for the He beam is not completely random. This tendency is similar to the result using dry DNA as sample for irradiation [2]. A radiation “spur” on or nearby DNA might sometimes produces clustered damage. In any case, knowledge of AP distribution for  $^{60}\text{Co}$   $\gamma$ -rays as a reference is quite important to study DNA damage by ionizing radiation. More data points and discussions will be needed to elucidate the problem.

### REFERENCES:

- [1] K. Akamatsu, N. Shikazono, Anal. Biochem. **433** (2013) 171-180.
- [2] K. Akamatsu, N. Shikazono, and T. Saito, Radiat. Res. **183** (2015) 105-113.
- [3] K. Akamatsu, N. Shikazono, and T. Saito, KURRI Progress Report 2012 (2012) 256.
- [4] K. Akamatsu, N. Shikazono, and T. Saito, KURRI Progress Report 2012 (2013) 263.

Suzuki T.<sup>1</sup>, Horie K.<sup>1</sup>, Ogawa S.<sup>1</sup>, Wakamatsu E.<sup>1</sup>,  
Abe R.<sup>1</sup>, Sakurai Y.<sup>2</sup>, and Ono K.<sup>2</sup>

<sup>1</sup>Research Institute of Biomedical Sciences,  
Tokyo University of Science

<sup>2</sup>Research Reactor Institute, Kyoto University

**INTRODUCTION:** Boron neutron capture therapy (BNCT) is an attractive therapy for local tumor control in the treatment of brain tumor, melanoma, and so on [1,2]. However, some important issues are remained: the tumor-specific accumulation of highly concentrated boron, the real-time quantification of boron concentration in local tumor tissues, and the prevention of re-growth and metastasis of residual tumor cells after BNCT.

Recently, it was reported that some cancer immune therapies could achieved significant regression of tumor in clinical trials. To achieve successful tumor regression, in this study, we try to establish the combination treatments with BNCT and immunotherapy [3,4].

### Results and Discussions:

#### The effect of BNCT on immune system

Using mouse model, we examined the effect of BNCT on the antigen specific immunological response. C57BL/6 mice, which were subcutaneously administrated with 250 mg/kg BPA, and then treated with thermal neutron irradiation (1 MW, 50min in the heavy water facility of KUR). To assess the immune response, mice were immunized with antigen on footpad, and the immunological response of T cells was assessed (Fig.1A). Although transient lymphopenia was observed after neutron irradiation, the number of immune cells was restored at 11 days after treatment. Assessing IFN- $\gamma$  production, the antigen specific immune response was comparable in neutron irradiated mice, compared with control mice (Fig. 1B), suggesting that antigen-specific immune response could be induced even after neutron irradiation.

#### Anti-tumor immune response after BNCT

It was previously reported that local X ray radiotherapy lead to the augmentation of anti-tumor immune response via the induction of inflammation and immunological cell death in tumor site [5]. Hence, we examine anti-tumor immune response in hosts which received BNCT or X ray radiotherapy. Mice were challenged B16 melanoma cells on leg, and, BNCT or local X ray irradiation (12Gy) therapy were performed around 10 days after tumor challenge. Fourteen days after radiation therapy, immune response against tumor derived antigen was assessed (Fig.2 A). As a result, similar to previous reports, anti-tumor immune response was augmented by radiotherapy with X ray (data not shown).

Notably, unlike X ray irradiation, BNCT did not enhance anti-tumor immune response. Although additional immunization with peptide vaccination and CTLA4 blockade after BNCT lead to the induction of immune response, this combination therapy could not achieve tumor regression (Fig.2B and 2C). Our further interest is why BNCT could not enhance anti-tumor immune response. To understand the anti-tumor immune response during radiation therapy determines the effective combination with radiation therapy and immune therapy.

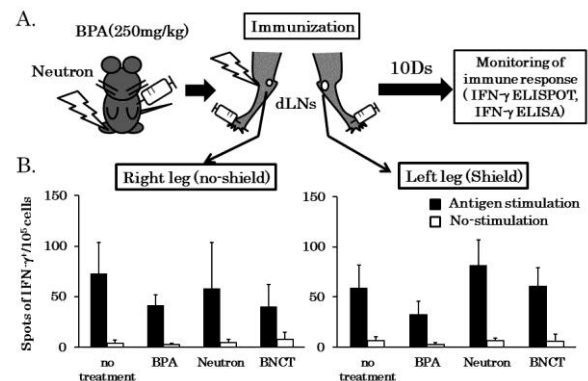


Fig 1. Antigen-specific immune response could be induced after neutron-beam irradiation. A: schema of experiment. B: Immunological responses (IFN- $\gamma$  production of T cells) in draining lymph node (dLNs).

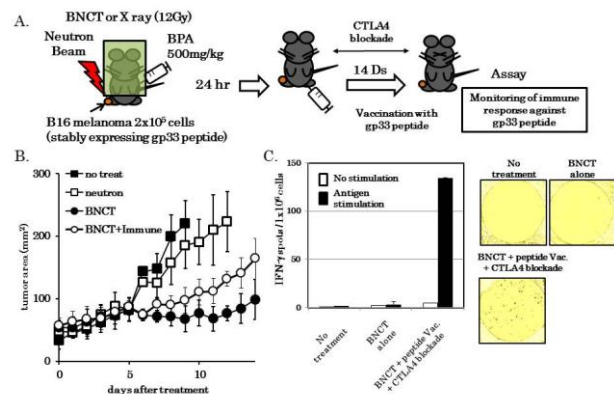


Fig 2. Anti-tumor immune response after BNCT or radiotherapy with X ray, but not BNCT, augmented immune response against tumor derived antigens. A: Schema of treatment for tumor bearing mice. B: Tumor growth. C: Number of IFN- $\gamma$  producing cells against tumor derived antigens

### REFERENCES:

- [1] M. Suzuki, *et al.* Int. J. Radiat. Oncol. Biol. Phys. 58(3): 892-896, 2004.
- [2] M. Suzuki, *et al.* Int. J. Radiat. Oncol. Biol. Phys. 60(3): 920-927, 2004.
- [3] Lifu Dengu *et al.*, J. C. I., 124 (2), 687, 2014.
- [4] M. A. Curran *et al.*, PNAS, 107(9), 4275, 2010.
- [5] Lionel A. *et al.*, Nature Med., 13(9), 1050, 2007

採択課題番号 26049 BNCT の免疫に与える影響と免疫療法による全身治療との併用の可能性 通常採択  
東理大・生命研) 安部 良、鈴木利宙、小川修平、若松 英、堀江和峰 (京大・原子炉) 櫻井良憲、  
小野公二

## CO6-4 *In situ* Visualization of Boron in Plants Using Neutron Capture Radiography

M. Kobayashi and T. Kinouchi<sup>1</sup>

Graduate School of Agriculture, Kyoto University

<sup>1</sup>Research Reactor Institute, Kyoto University

### INTRODUCTION:

Boron (B) is an essential micronutrient for vascular plants, and its deficiency is one of the major constraints on crop production worldwide [1]. Boron deficiency causes various physiological disorders including an inhibition of the development of young leaves, necrosis of tissues inside tubers or tap roots, or failure in seed set.

The understanding of physiological function of B in plants has progressed greatly during the last few decades. Boron as boric acid occurs in cell wall, and forms 1:2 borate-diol diester with specific regions of pectin [2]. The diester bonds serve as the inter-chain bridges of pectin, thereby stabilizes the cell wall structure. On the other hand, the transport and distribution of B in plant remains elusive, since no radioactive isotope with an appropriate half-life is available for this element. Revealing a differential distribution of B within tissues, if any, may give us clues to the demands for B of different cell types, hence may contribute significantly to a better understanding of the physiological role of B. Thus, in this study we have been trying to apply boron neutron capture radiography to the *in situ* visualization of B in plant roots.

### EXPERIMENTS:

Radish (*Raphanus sativus* L. *sativus*) seeds were germinated on vermiculite in a growth chamber with a light/dark regime of 18/6 h, 22°C, and 60% relative humidity. Seedlings with uniform size were transferred to solution culture, which was maintained in the same growth chamber. The nutrient solution contained B at 0.5ppm. At 10 days after transfer to solution culture, the tap roots were detached from the seedlings and fixed with glutaraldehyde. Fixed samples were embedded in OCT compound (Tissue-Tek), frozen in liquid nitrogen, and sectioned at 8- $\mu$ m thickness with freezing microtome. The ultrathin sections were transferred onto CR-39 nuclear track detector. The bright-field image of the section was taken at this point, to record the structure of tissue examined. The CR-39 plate was then irradiated with neutron for 15 min using Te-Pn facility at Kyoto University Research Reactor Institute. The irradiated CR-39 plate was etched in NaOH solution, and the resulting pits were observed under microscope.

### RESULTS AND DISCUSSION:

When the image of pits generated by neutron irradiation was merged with the section image taken prior to the irradiation, the pits were distributed unevenly over the section. Higher density of pits was found in the central

part and a circular region just inside the cortex, which are the regions rich in vascular bundles. Boron as borate diester is specifically bound to the rhamnogalacturonan II (RG-II) regions of pectin in cell wall, and the RG-II has been shown to occur in all cells of the roots at the same density [3]. Thus the distribution of B within roots seems distinct from that of its acceptor molecule.

Besides borate diesters bound to RG-II regions of pectin, B in plants can occur as free boric acid as well, when the plants are amply fed with B [4]. The free boric acid in shoots corresponds to B taken up as luxury absorption beyond the amount equivalent to that of the acceptor. Radish seedlings used in this study were grown in the presence of enough amount of B, and hence they were likely to contain both RG-II-bound and free boric acid. At present, we are not sure to which fraction of B the signals in radiography are ascribed. However, the observed pattern of pit distribution seems inconsistent with those expected for bound B: since the acceptor RG-II occurs ubiquitously and evenly within the root, the bound B is also expected to occur uniformly. Taken together, we think that the signal detected in this study probably came from soluble, free boric acid in root tissues.

Radish deficient in B sometimes accumulates a blue pigment in the roots, which is called "Ao-aza" (blue spot) symptom. Interestingly, the regions where the blue pigment (presumably anthocyanin) accumulates overlap with those showing signals in this study. It is suggested that cells in the regions may require higher supply of B than the others. In the vascular bundles occurs cambium, which contains the cells actively propagating. Higher supply of B may be necessary to support rapid cell proliferation in these tissues.

As the subject of future investigation, it is necessary to make clear which fraction of B (cell wall-bound or free boric acid) has been detected in this radiography. Growing plants under various B supply to prepare samples with different content of free boric acid, then examining the pit frequency would give useful information on this aspect. In addition, increasing the sensitivity and resolution is also necessary. Optimizing the condition of neutron irradiation or alkaline etching would be useful to solve these problems.

### REFERENCES:

- [1] V.M. Shorrocks, *Plant Soil*, **193** (1997) 121–148.
- [2] M. Kobayashi *et al.*, *Plant Physiol.*, **110** (1996) 1017–1020.
- [3] T. Matoh *et al.*, *Plant Cell Physiol.*, **39** (1998) 483–491.
- [4] T. Matoh *et al.*, *Soil Sci. Plant Nutr.*, **47** (2001) 779–784.

## CO6-5 Measurement of Transmittance Spectra of a Cryo-Sectioned Tissue of Brain Tumor C6 Model in the Sub-Terahertz Region-II

N. Miyoshi and T. Takahashi<sup>1</sup>

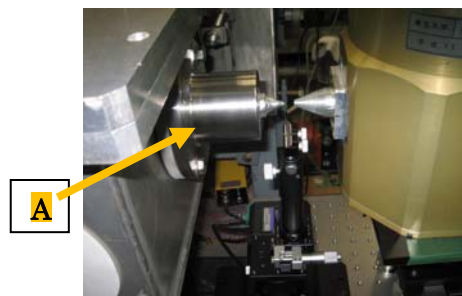
Department of Tumor Pathology, Faculty of Medicine,  
University of Fukui

<sup>1</sup> Research Reactor Institute, Kyoto University

**INTRODUCTION:** The LINAC (linear particle accelerator) technology in the millimeter and terahertz waves had been unique and had been used as a coherent synchrotron light in the research reactor institute of Kyoto university (KURRI) to observe the transmittance spectra of a sectioned tissue of raw brain tumor C6 model as a collaborate study. The absorption spectra in the sub-terahertz region had been not so clear for the raw tumor tissue although Ashworth-PC. *et al.* [1] had reported for the excised human breast cancer by a terahertz pulsed spectroscopy observed at 320 GHz, which was estimated a longer relaxation time component of the induced electricity for water molecules [2-3] in the raw tumor tissue for three years at the linear analysis.

We also estimated what kind of water molecules become dominant in the viable and necrotic cancer regions by the different measurement method as an aim of 2D mapping study.

**EXPERIMENTS:** (1) Instrument of Near-field in tera-hertz region: The photograph of the instrument was shown in **Figure 1**. Mark-A: Pre-probe Wiston cone; 50-10mm diameter, Length=60mm; the irradiate diameter=0.775mm; The concentrate light probe (diameter)=3mm. The instrument was developed by Dr. T. Takahashi in KURRI [Figure-1] for the 2D mapping analysis.



(2) Sample preparation: A cryo-sectioned (thickness=100  $\mu\text{m}$ ) tissue was prepared from the raw C6 glial tumor model using a Cryo-section Maker (Leica) and was sealed sandwich-type with saran-wrap film (thickness=10  $\mu\text{m}$ ), under freezing condition (-20 C) before the measurements.

**RESULTS:** Large amount of spectroscopic data (more than 1,000) for the 2D mapping data have been analyzed to now, but the analysis was not finished to be reported as the imaging of each water components.

### REFERENCES:

- [1] Phillip C. Ashworth, *et al.*, *Optics Express*, **17(14)**: 12444-12454 (2009).
- [2] Toshiko Fukasawa, *et al.*, *Phys. Rev. Let.*, **95**: 197802 (2005).
- [3] Hiroyuki Yada, *et al.*, *Chem. Phys. Let.*, **464**: 166-170 (2008).

## CO6-6 Design and Synthesis of New Drugs for Boron Neutron Capture Therapy and Boron Magnetic Resonance Imaging

S. Aoki<sup>1</sup>, Y. Nishiura<sup>1</sup>, T. Tanaka<sup>1</sup>, Y. Hisamatsu<sup>1</sup>, Y. Sawamoto<sup>1</sup>, Rikita Araki<sup>2</sup>, Takaomi Saido<sup>3</sup>, T. Suzuki<sup>4</sup>, K. Horie<sup>4</sup>, Ryo Abe<sup>4</sup>, S. Masunaga<sup>5</sup>, K. Natsuko<sup>5</sup>, Y. Sakurai<sup>5</sup>, and K. Ono<sup>5</sup>

<sup>1</sup>Faculty of Pharmaceutical Sciences, Tokyo University of Science

<sup>2</sup>Bruker Biospin K. K.

<sup>3</sup>RIKEN Brain Science Institute

<sup>4</sup>Research Institute of Biomedical Sciences, Tokyo University of Science

<sup>5</sup>Research Reactor Institute, Kyoto University

**INTRODUCTION:** Boron neutron capture therapy (BNCT) is one of powerful therapies for local tumor control in the treatment of brain tumor, melanoma, and so on [1]. However, some important issues are remained for the achievement of successful tumor regression: the tumor-specific accumulation of highly concentrated boron, the real-time quantification of boron concentration in local tumor tissues, and the prevention of re-growth and metastasis of residual tumor cells after BNCT. In this study, we have designed and synthesized new boron compounds appended with macrocyclic tetramines such as cyclen (1,4,7,10-tetraaminocyclododecane) for BNCT and B-MRI [2]. It was expected that boron clusters such as icosahedral carboranes would be transferred to living cells due to the dicationic properties of cyclen part at neutral pH.

Icosahedral carboranes are boron clusters composed with 10 boron atoms and 2 carbon atoms which exhibit a remarkable thermal and chemical stability. In this manuscript, we reported first example of full deboronation reaction of *o*-carborane catalyzed by copper(II) ion. Initially, we examined the deboronation reaction of *ortho*-carborane-cyclen in aqueous solution in the presence of various d-block metals such as Cu<sup>2+</sup>, Zn<sup>2+</sup>, Fe<sup>2+</sup>, Ni<sup>2+</sup> and Co<sup>2+</sup>.

### EXPERIMENTS and RESULTS:

#### Synthesis of boron compound based on

Boron is one of ultratrace elements in living systems. Previously, we have designed and synthesized boron-pendant cyclic tetraamine **1** for the in-cell <sup>11</sup>B NMR (nuclear magnetic resonance) or MRI (magnetic resonance imaging) for the detection of metal in living systems and eventually for the use in BNCT. It was reported that the C-B bond is hydrolyzed upon complexation with d-block metals to give one molecule of boric acid (B(OH)<sub>3</sub>) as well as zinc complex of *N*-benzylcyclen **2**

[3].

These results prompted us to design and synthesize its analog (**3**) having an icosahedral carborane (*o*-carborane) unit that consist 10 borons and 2 carbons as a potent carrier of boron cluster to the cancer cells. It was found that this molecule is transferred into cancer cells more effectively than **1**. Moreover, we have discovered that the *o*-carborane unit of **3** decomposes in the presence of d-block metals in aqueous solution at neutral pH and release more than 4 molecules of B(OH)<sub>3</sub> [4]. Besides, *o*-carborane analog **4** having methanol unit instead of cyclen also undergoes the full decomposition to release 10 B(OH)<sub>3</sub>. This change was successfully detected on <sup>11</sup>B NMR and MRI. Because the chemical and physical properties of <sup>10</sup>B and <sup>11</sup>B are almost identical, these probes should be useful not only for BNCT, but also for the determination of the distribution of boron-containing drugs in the bodies and of the biorelevant d-block metals.

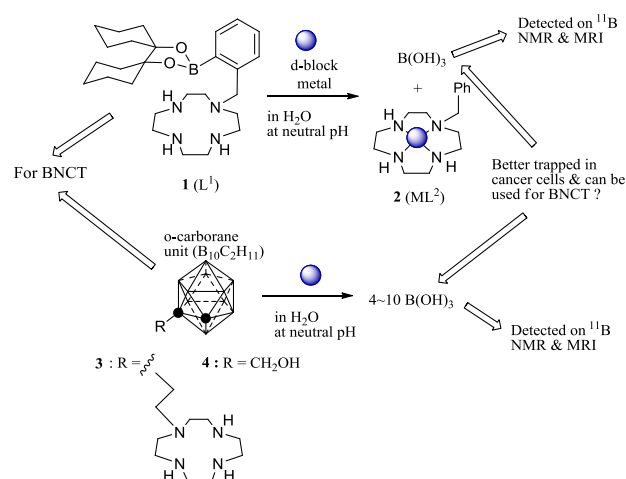


Fig 1. Design and decomposition reaction of boronylated compounds

### REFERENCES:

- [1] a) R. F. Barth *et al.*, *Clin. Cancer Res.*, **11** (2005) 3987-4002. b) R. F. Barth *et al.* *Rad. Oncol.* **7** (2012) 146-166.
- [2] a) G. W. Kalbalka, *et al.* *J. Neuro-Oncol.* **33** (1997) 153-161. b) P. Bendel, *NMR in Biomed.* **18** (2005) 74-82.
- [3] M. Kitamura *et al.*, *Inorg. Chem.* **50** (2011) 11568-11580.
- [4] Y. Nishiura *et al.*, Manuscript in preparation.

採択課題番号 26077

がん組織に集積する含ホウ素化合物の設計・合成と腫瘍への集積のホウ素 MRI に向けた基礎検討

通常採択

(東理大・薬学部) 青木 伸、西浦由紀子、田中智博、久松洋介、澤本泰宏

(ブルカーバイオスピン) 荒木力太 (理研) 西道 隆臣 (東理大・生命研) 鈴木利宙、堀江和峰、安部良 (京大・原子炉) 増永慎一郎、近藤夏子、櫻井良憲、小野公二

T. Nagasaki, R. Kawasaki, S. Iizuka, H. Yukawa, Y. Tsujimoto, M. Kirihata<sup>1</sup>, K. Tomita<sup>2</sup>, K. Katagiri<sup>3</sup>, K. Ono<sup>4</sup>, S. Masunaga<sup>4</sup>, and Y. Sakurai<sup>4</sup>

Graduate School of Engineering, Osaka City University,

<sup>1</sup> BNCT Research Center, Osaka Prefecture University,

<sup>2</sup> School of Science, Tokai University

<sup>3</sup> Institute of Engineering, Hiroshima University

<sup>4</sup> Research Reactor Institute, Kyoto University

**INTRODUCTION:** Boron Neutron Capture Therapy (BNCT) is a highly selective cancer therapy that can target single tumor cell without causing excessive radiation damage around normal cells. The success of BNCT depends on the delivery that <sup>10</sup>B compounds accumulate effectively inside the tumor cells. Clinically, boronophenylalanine (BPA) and borocaptate sodium (BSH) are currently used for BNCT as boron delivery agents but these agents have some disadvantages on accumulation or selectivity toward tumor tissue. In addition, the efficacy of boron neutron capture reaction is suppressed due to low neutron fluence. In this study, in order to improve the efficiency of neutron capture reaction, we used boron containing rare earth oxides nanoparticle (SmBO<sub>3</sub>, GdBO<sub>3</sub>, YBO<sub>3</sub>). When their diameter is suitable sizes, these nanoparticles could be significantly accumulated in tumor tissue with EPR effect. Moreover, the particle doped with europium can possess the fluorescence. This fluorescent nanoparticles are expected as novel boron delivery drugs that can diagnose and treat cancer simultaneously and efficiently.

**EXPERIMENTS:** The cell colorectal cancer line colon26 were used in this study. Boron containing rare earth oxides nanoparticles were synthesized by homogeneous precipitation method. Cationic nanoparticle are coated with anionic chondroitin sulfate (XBO<sub>3</sub>/ch, X: Sm, Gd, Y). Boron concentration was estimated by ICP-AES. Cytotoxicity of nanoparticle was estimated by WST assay.

**RESULTS AND DISCUSSION:** The TEM images showed that the particle has spherical shape with relatively homogenous distribution and its diameter is about 100 nm (Fig. 1). The result indicates that its size is suitable for EPR effect. Moreover, we evaluated its pharma-

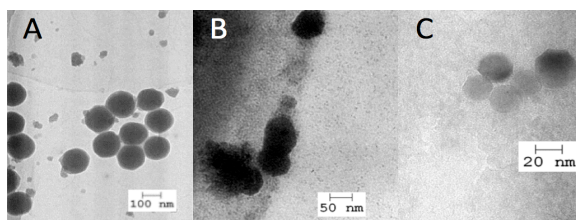


**Fig. 1** TEM images of boron-containing rare earth oxide nanoparticles; (A) SmBO<sub>3</sub>; (B) GdBO<sub>3</sub>; (C) YBO<sub>3</sub>.

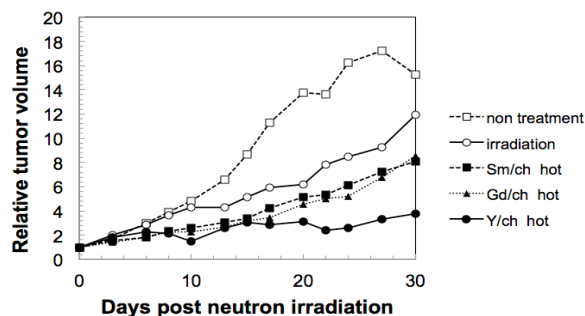


**Fig. 2** Comparison of the antitumor efficacy with rare earth oxides/chondroitin sulfate complex.

cokinetics by using BALB/c mice bearing colon26 murine carcinoma. The highest boron concentration of YBO<sub>3</sub> nanoparticle in tumor tissue was observed at 6 hours after administration by i.p. Then, BNCT was performed on tumor-bearing mice. Two hundred  $\mu$ l of nanoparticle solution (concentration of <sup>10</sup>B: 132 ppm with SmBO<sub>3</sub> and GdBO<sub>3</sub>, 88 ppm with YBO<sub>3</sub>) were injected by i.p. before 6 hr of neutron irradiation at Kyoto University Research Reactor (1 MW, 90 min,  $4.1 \times 10^{12}$  neutron/cm<sup>2</sup>). By irradiation, YBO<sub>3</sub> nanoparticle showed strongest antitumor effect among used rare earth oxides nanoparticles (Fig 2).

As the nanoparticle of the rare earth oxide could contain huge boron atoms per particle, it can deliver efficiently a lot of boron toward tumor tissue with EPR effect. Especially, As yttrium had no shield effect toward neutron, YBO<sub>3</sub> showed highest BNCT effect. Therefore, this YBO<sub>3</sub> nanoparticle is promising toward next generation BNCT.

#### REFERENCE:

[1] K. Fujita *et al.*, *J. Ceram. Soc. Jpn.*, **98**, 991 (1990).

## CO7-2 *In vivo* Evaluation of Gd-DTPA-incorporated Calcium Phosphate Nanoparticles as Neutron Capture Therapy Agent

N. Dewi<sup>1</sup>, P. Mi<sup>2,3</sup>, H. Yanagie<sup>1,4,5</sup>, Y. Sakurai<sup>4</sup>, H. Cabral<sup>2</sup>, N. Nishiyama<sup>3</sup>, K. Kataoka<sup>2,6</sup>, Y. Sakurai<sup>7</sup>, H. Tanaka<sup>7</sup>, M. Suzuki<sup>7</sup>, S. Masunaga<sup>7</sup>, K. Ono<sup>7</sup>, H. Takahashi<sup>1,4</sup>

<sup>1</sup>Dept of Nuclear Engineering & Management, Univ of Tokyo, <sup>2</sup>Bioengineering Dept, Univ of Tokyo, <sup>3</sup>Polymer chemistry division, Chemical Resource Laboratory, Tokyo Institute of Technology, <sup>4</sup>Cooperative Unit of Medicine & Engineering, Univ of Tokyo Hospital, <sup>5</sup>Dept of Innovative Cancer Therapeutics, Meiji Pharmaceutical University, <sup>6</sup>Materials Engineering Dept, The University of Tokyo, <sup>7</sup>Research Reactor Institute, Kyoto University

**INTRODUCTION:** Gadolinium-157 has been getting attention as alternative for neutron capture therapy (NCT) agent because of its high thermal neutron cross section (255 000 barns), which the highest among all stable elements. However, compared to short range secondary particles produced after neutron capture by <sup>10</sup>B isotope currently used for clinical trial of NCT, gadolinium neutron capture reaction (Gd-NCR) results in release of gamma rays, which reduce the localization effect of the treatment, which on the other side is increasing the possible additional effect if Gd-157 is accumulated to a bulk tumor cluster.

In this work, we performed *in vivo* evaluation of tumor growth suppression on multiple-injections Gd-DTPA/CaP nanoparticles mice as continued work from previous evaluation on single-injected group [1].

**EXPERIMENTS:** *In vivo* evaluation was performed on colon-26 tumor-bearing mice irradiated for 60 minutes at nuclear reactor facility of Kyoto University Research Reactor Institute with average neutron fluence of  $1.8 \times 10^{12}$  n/cm<sup>2</sup>. Experimental procedure for multiple-injected groups is illustrated in Fig. 1. Antitumor effect was evaluated on the basis of the change in tumor growth and survival rate of the mice.

**RESULTS:** Higher gadolinium accumulation in tumor site was successfully achieved for multiple injections of Gd-DTPA/CaP nanoparticles, up to more than three times compared to single injection (data not shown). There was no acute toxicity in the treated mice, indicating the promising possibility of Gd-DTPA/CaP as Gd-NCT agent. However, we could not observe better tumor growth suppression after GdNCT treatment, which indicates the possibility of neutron depression on

mice group with higher concentration of gadolinium. Nevertheless, further investigation is necessary to confirm the reason of moderate tumor growth suppression in multiple-injected mice group.

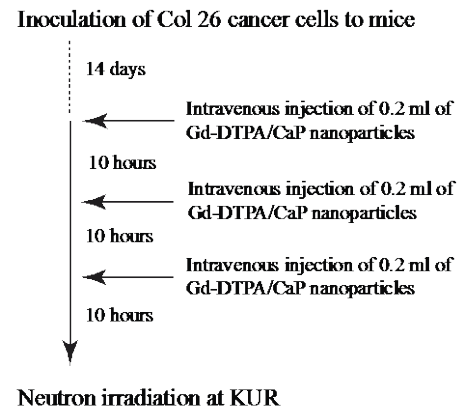


**Figure 1. Experimental procedure for multiple-injected tumor-bearing mice.**

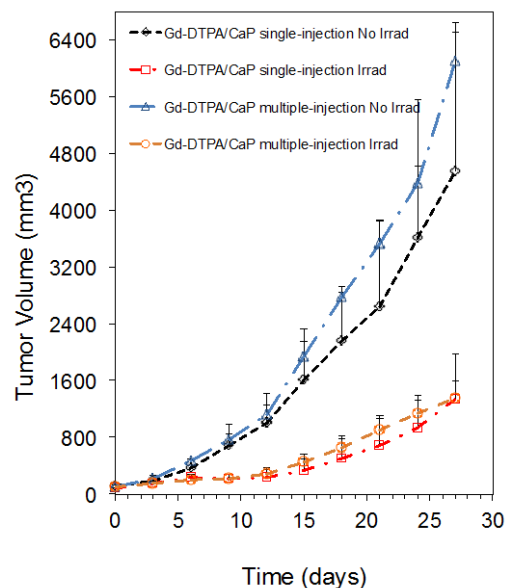


**Figure 2. Tumor growth suppression comparison between single-injected and multiple-injected Gd-DTPA/CaP.**

### REFERENCES:

- [1] Dewi N et al., KURRI Progress Report (2013) CO7-21.
- [2] Dewi N et al., Biomed & Pharmacother (2013) 67:451-7.
- [3] Mi P, et al.: J Cont. Release (2014) 174:63-7.

採択課題番号 26014 中性子捕捉療法法の一般外科領域癌への展開に向けた基礎的研究 通常採択

(東大・原子力国際専攻) 高橋浩之、柳衛宏宣、Novriana Dewi (東大・獣医) 柳川将志、飯塚智也 (東大・心臓外科) 櫻井由里子、毛利きくえ (京大・原子炉) 小野公二、増永慎一郎、鈴木実、櫻井良憲

Y. Sakurai, T. Takata, N. Fujimoto, H. Tanaka, N. Kondo, Y. Nakagawa, M. Suzuki

Research Reactor Institute, Kyoto University

**INTRODUCTION:** After the restart of the operation of Kyoto University Reactor (KUR) in May 2010, 235 clinical studies of boron neutron capture therapy (BNCT) have already been carried out as of May 2015 [1]. Also, the BNCT clinical trial using Cyclotron-based BNCT Epi-thermal Neutron Source (C-BENS) started in November 2012 [2]. In the while, the research and development into several types of accelerator-based irradiation systems are underway by several research groups in the world at present time. With this situation in mind, it is important that the physical and biological estimations for dose quantity and quality are performed consistently among several irradiation fields, and that the equivalency of BNCT is guaranteed, even across BNCT systems. The individuality of irradiation fields can stand out for the beam-quality characteristic of the incident fast neutrons, such as the mixing ratio and neutron energy spectrum. The aim of this research is the development of the phantom made of specialized materials for the estimation of the beam quality. In 2014, a feasibility study on the estimation of relative biological effectiveness (RBE) for fast neutrons, based on the simulation and experimental data obtained for the proto-type “beam-quality estimation phantom”.

**METHODS:** As a beam-quality estimation phantom, a phantom of 10% LiOH solution with 95%-enriched Li-6 was prepared [3]. The simulated thermal and fast neutron fluxes were converted into absorbed dose rates in normal tissue [4]. The composition for normal tissue was assumed to be H:11.1, C:12.7, N:2.0, O:74.2 in weight percent [5], and the density was assumed to be 1.0 g/cm<sup>3</sup>. The operation power of KUR was 1 MW.

**RESULTS:** Figures 1 and 2 show the depth distributions of the total dose rate and its breakdown in the pure water phantom and the 10%<sup>6</sup>LiOH phantom, respectively. In the pure water phantom as shown in Fig. 1, the contribution of gamma rays is dominant and it becomes larger at depth, over the interior of the phantom. In the 10%<sup>6</sup>LiOH phantom as shown in Fig. 2, the thermal neutron dose rate decreases to below almost one-thirtieth of the fast neutron dose rate. In addition, the gamma-ray dose rate decreases to the same order as the fast neutron dose rate.

**CONCLUSION:** The condition for a larger contribution of fast neutron dose is realized in the 10%<sup>6</sup>LiOH phantom. It can be expected that the accuracy for RBE estimations in biological experiments would improve using the 10%<sup>6</sup>LiOH phantom as the contribution of fast neu-

tron dose is increased to almost 50% greater than a pure water phantom for which the fast neutron dose contribution is at most 10%.

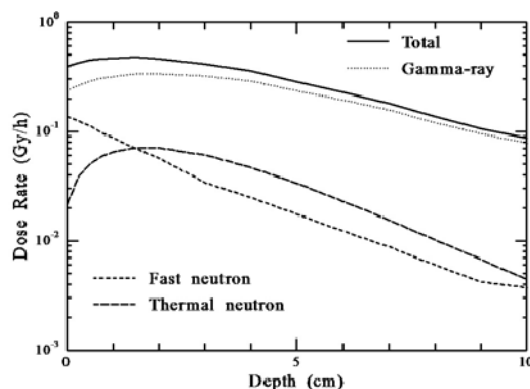


Fig. 1. Depth distributions of total dose rate and its breakdown in the pure water phantom.

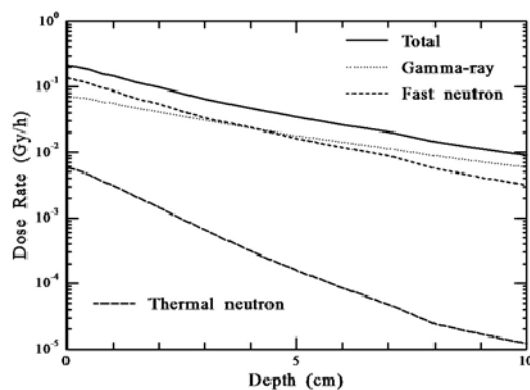


Fig. 2. Depth distributions of total dose rate and its breakdown in the 10%<sup>6</sup>LiOH phantom.

#### REFERENCES:

- [1] Y. Sakurai *et al.*, Nucl. Instr. Meth. A **453** (2000) 569-596.
- [2] H. Tanaka *et al.*, Nucl. Instr. Meth. B **267** (2009) 1970-1977.
- [3] Y. Sakurai *et al.*, Proc. 14th Int. Congr. Neutron Capture Therapy (Comision Nacional de Energia Atomica) (2010) 254-256.
- [4] R.S. Caswell *et al.*, Radiat. Res. **83** (1980) 217-254.
- [5] W.S. Synder *et al.*, Report of the Task Group on Reference Man (Pergamon Press, Oxford, 1975).



## CO7-4 A Fundamental Experiment for the Measure Against the Activation of the Irradiation-room Concrete at BNCT Facility

Y. Sakurai, T. Takata, K. Kimura<sup>1</sup>, H. Tanaka, K. Takamiya

Research Reactor Institute, Kyoto University  
<sup>1</sup>Fujita Corporation

**INTRODUCTION:** At present time, the research and development into several types of accelerator-based neutron sources for boron neutron capture therapy (BNCT) are underway by several research groups in the world, with Cyclotron-based BNCT Epi-thermal Neutron Source (C-BENS) at the head of the list [1]. In near future, BNCT using the accelerator-based neutron sources may be carried out at several places in the world. Unlike the facilities for radiation therapy and charged-particle therapy, the neutron yield is larger at BNCT facility. Then, the activation of concrete, which is a main structure of the irradiation room, is larger. The use of low-activation concrete is prefer in the viewpoints of the decrease of exposure under the work in the irradiation room, the decommissioning of the irradiation room, etc.. This research is intended to perform the characteristic estimation for low-activation concrete and confirm its usability at BNCT facility. In 2014, a fundamental experiment for the measure against the activation of concrete using an Am-Be neutron source was performed, because the operation of Kyoto University Reactor (KUR) was limited.

**METHODS:** A characteristic estimation was performed for the measure against the activation using a neutron shield for a commercially available normal concrete. A resin containing B<sub>4</sub>C, which is under development, was used as a neutron shield. This shield weakens neutron intensity to reach the concrete, by that high-energy neutrons are moderated by hydrogen in the resin and thermal neutrons are absorbed by boron in B<sub>4</sub>C. As nine resin sheets of 10-cm side, 10-cm long and 2-mm thickness were stacked on the concrete surface, the shielding performance against the Am-Be neutron source was estimated by foil activation method. Indium foil was used as an activation foil. The shielding characteristic for fast neutrons was estimated by the activity change for In-113(n,n')In-113m reaction, and the generating characteristic for the secondary thermal neutrons was estimated by the activity change for In-115(n,  $\gamma$ )In-116m reaction.

**RESULTS:** Figure 1 shows the activity changes dependent on the thickness for the resin without B<sub>4</sub>C. Figure 2 shows the activity changes dependent on the thickness for the resin with B<sub>4</sub>C. In these figures, the activity changes for In-113(n,n')In-113m and In-115(n,  $\gamma$ )In-116m are drawn. From the comparison for the former activity, it was found that the shielding effect for fast neutrons was a little smaller for the resin with B<sub>4</sub>C, as its

hydrogen density was smaller. From the comparison for the latter activity, it was found that the generation of the secondary thermal neutrons was decreased to almost one fifth for the resin with B<sub>4</sub>C. In the while, the activity, namely the thermal neutron intensity, was increased according to the thickness. This is due to the influence for the secondary thermal neutrons generated in the concrete.

**CONCLUSION:** From this experiment, it was realized again that the measure for the low activation of concrete itself, namely the development of low-activation concrete was important, even if the measure against the activation was performed using the neutron shield. The estimations for the important characteristics of low-activation concrete are planned, such as short-life activation, long-life activation, the shielding effect for neutrons and gamma rays, the generation of the secondary gamma rays, etc., when the KUR operation is restarted.

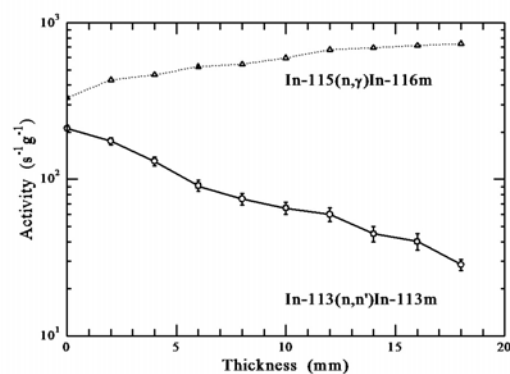


Fig. 1. Activity changes dependent on the thickness for the resin without B<sub>4</sub>C.

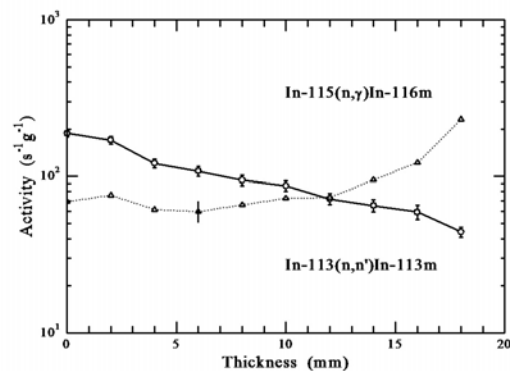


Fig. 2. Activity changes dependent on the thickness for the resin with B<sub>4</sub>C.

### REFERENCES:

- [1] H. Tanaka *et al.*, Nucl. Instr. Meth. B **267** (2009) 1970-1977.

M. Tsukimoto<sup>1</sup>, N. Mori<sup>1</sup>, K. Nishino<sup>1</sup>, T. Suzuki<sup>1</sup>, K. Horie<sup>1</sup>, K. Tanamachi<sup>1</sup>, D. Kitahara<sup>1</sup>, N. Kondo<sup>2</sup>, S. Masunaga<sup>2</sup>, Y. Sakurai<sup>2</sup>, R. Abe<sup>1</sup>

<sup>1</sup> Tokyo University of Sciences

<sup>2</sup> Research Reactor Institute, Kyoto University

**INTRODUCTION:** Radiation exposure causes DNA damage, and DNA repair systems are essential to rescue damaged cells. Release of extracellular nucleotides, such as ATP, from cells plays a role in signaling via P2 receptors. We have reported that autocrine/paracrine signaling through P2X7-dependent ATP release and activation of P2Y6 and P2Y12 receptors serves to amplify the cellular response to DNA damage caused by  $\gamma$ -irradiation [1-3].

BNCT is one of the new radiation therapy that mainly use  $\alpha$ -ray derive from  $^{10}\text{B}(n,\alpha)^7\text{Li}$  reaction.  $^{10}\text{B}$  is delivered to the cell as  $^{10}\text{B}$ -bromophenylalanine (BPA). Since it is known that melanoma tend to incorporate phenylalanine,  $^{10}\text{B}$ -BPA is well incorporated into melanoma.  $\gamma$ -ray is low-LET radiation, and BNCT is high-LET radiation.  $\gamma$ -Irradiation causes DNA damage by indirect action effect, which is mediated by reactive oxygen species. However, BNCT causes DNA damage by direct action. It is known that direct action effect is stronger than indirect action effect. Further, BNCT can irradiate cells from inside of the cell.

Recently, we have showed involvement of P2 receptors in DNA damage repair after  $\gamma$ -ray irradiation in A549 cells [2]. However, it has not yet been clear the involvement of P2 receptors in BNCT-induced DNA damage response. If the activation of P2X7, P2Y6, or P2Y12 receptor are involved in BNCT-induced DNA damage response, the antagonists of these P2 receptors enhance cytotoxicity of cancer cells by BNCT. Here, we investigated the radiosensitizing effect of P2 receptor antagonist on BNCT-induced DNA damage response and cytotoxicity.

**EXPERIMENTS:** Mouse melanoma B16 cells were incubated with 1 mM  $^{10}\text{B}$ -BPA and P2Y12 receptor antagonist clopidogrel. B16 cells were irradiated with  $\gamma$ -rays and thermal neutron beams from a nuclear reactor (Kyoto University Research Reactor Institute; 1 MW) at room temperature for a suitable time. After irradiation, the cells were incubated in humidified atmosphere of 5%  $\text{CO}_2$  in air at 37 °C.

The irradiated cells were fixed in 4% paraformaldehyde in PBS for 10 min at room temperature and permeabilized in 0.1% Triton X-100 for 5 min on ice. After incu-

bation in blocking buffer (10% FBS in PBS) for 1 h, the fixed cells were incubated with primary antibody against  $\gamma\text{H2AX}$  for 24 h at 4 °C and with 2<sup>nd</sup> antibody conjugated with FITC for 1 h. Counterstaining with Hoechst 33258 was used to verify the location and integrity of nuclei. Fluorescence images were obtained with a laser scanning confocal microscopy.

On the other hand, cell viability of irradiated cells were measured by colony formation assay.  $1.0 \times 10^3$  cells were seeded in a 100 mm dish. After incubation for 1 week, the cells were stained with 0.5% crystal violet. Colonies containing more than 50 cells were counted.

**RESULTS:** First, we tested the effect of BNCT on cell survival rate by the colony formation assay. Survival fraction of BNCT group decreased compared with group of  $\gamma$ -irradiated cells. In addition, the cytotoxic effect of BNCT was enhanced by pre-treatment with clopidogrel (Fig.1A). Next, we tested DNA damage response after BNCT by analyzing  $\gamma\text{H2AX}$  focus formation. Formation of  $\gamma\text{H2AX}$  foci that remain for 48hr was increased by BNCT. The BNCT-induced increase of  $\gamma\text{H2AX}$  foci was suppressed by pretreatment with clopidogrel (Fig. 1B).

From these results, it was suggested that P2Y12 receptor participated in DNA damage repair caused by BNCT.

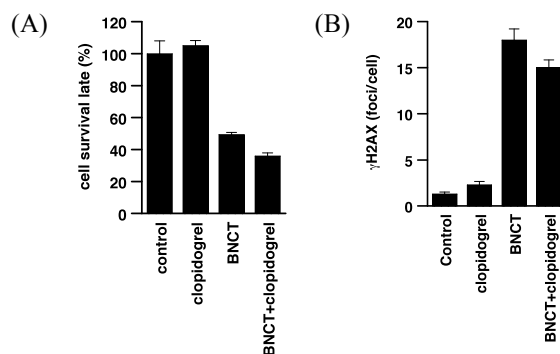


Fig.1 The effect of clopidogrel on BNCT-induced DNA damage response

### REFERENCES:

- [1] Tsukimoto M. et al., Radiat. Res. (2010) 173(3): 298-309.
- [2] Nishimaki N et al., DNA Repair (Amst). (2012) 11 (8): 657-65.
- [3] Ide S. et al., J Toxicol Sci. (2014) 39(1):15-23.

## CO7-6 Feasibility Study for Establishing QA Method for Hospital- and Reactor-based BNCT

S. Nakamura<sup>1,2</sup>, A. Urushiyama<sup>2</sup>, T. Nishio<sup>3</sup>, C. Kurokawa<sup>4</sup>, A. Wakita<sup>1</sup>, M. Ito<sup>1</sup>, M. Munechika<sup>5</sup>, H. Okamoto<sup>1</sup>, Y. Sakurai<sup>6</sup>, H. Tanaka<sup>6</sup>, N. Fujimoto<sup>6</sup> and J. Itami<sup>1</sup>

<sup>1</sup>Department of Radiation Oncology, National Cancer Center

<sup>2</sup>Rikkyo University

<sup>3</sup>Graduate School of Biomedical & Health Sciences, Hiroshima University

<sup>4</sup>Department of Radiology, Juntendo University

<sup>5</sup>Department of Human Sciences, Tokyo Metropolitan University

<sup>6</sup>Research Reactor Institute, Kyoto University

**INTRODUCTION:** In general, boron neutron capture therapy (BNCT) is currently performed using a nuclear reactor [1], [2]. Recent researches [3], [4], [5] have made possible to acquire an adequate amount of neutrons by accelerator and hospital-based accelerator-BNCT has come into reality. Therefore, National Cancer Center, Tokyo, Japan, is planning to install an accelerator-based BNCT system. Hospital-based accelerator-BNCT system has a lot of advantages. For example, there is no need to move a patient to the reactor. However, the hospital-based system also has disadvantages. In the hospital-based BNCT system, with compared with the reactor-based BNCT system, the measurement for a beam of BNCT is asked for the simplified method because the hospital-based system is restricted by an area of the institute. The purpose of this study is to establish the QA method for hospital-based BNCT.

**EXPERIMENTS:** In order to measure easily the neutron beam, new film was developed. The new film consisted of thermos luminescence phosphor. After exposure of the radiation, the output of the film with heated was read by CCD. Signal intensity was measured as the amount of light. The relationship of the film between the signal and doses were acquired with 6 MV photon beam of a medical linac in Juntendo University, Tokyo, Japan. The relationship between the signal and neutron fluence was analyzed in this study because the signal was evaluated as the dose. The experiment of neutron irradiation was performed in Kyoto University Research Reactor (KURR). In order to evaluate the film, the thermal neutron fluence was measured with the film and a gold foil, and these results were compared. However, the beam of the KURR contained both neutrons and gamma-rays. Therefore, the dose from gamma-rays was measured with the thermoluminescence dosimeter (TLD) since the film also had sensitivity to photons. The contribution from the gamma-rays to the film was considered by the result of the TLD. In order to evaluate a relationship between the

TPR<sub>20,10</sub> of a medical linac and the energy dependence of the film to gamma-rays, Monte Carlo simulation (BEAMnrc ver. 4.2.4. [6]) was used, and comparison of PDDs between measurement and simulation with the BEAMnrc were performed. Therefore, contribution of the gamma-rays was subtracted from the output of the film.

**RESULTS:** The comparison of PDDs between measurement and simulation was performed with a medical linac of 4, 6, 10, and 15 MV photon beam in National Cancer Center (NCC), Tokyo, Japan. The difference of those beams between the measurement and the simulation was within 0.59%. The relationship between TPR<sub>20,10</sub> and the calculated energy dependence which was normalized in the value of 6MV photon beam in NCC. With using those relationship and BEAMnrc, energy dependence of the film in the medical linac in Juntendo University and that in KURR was 1.002±0.003, and 0.986±0.002, respectively. Outputs of the TLD after irradiation in KURR were multiplied by a value of the ratio of energy dependence in KURR to that in Juntendo University, and the multiplied values were subtracted from the dose with the film. The relationship between the thermal neutron fluence and the dose with the film was shown in Fig. 1. The thermal neutron fluence was proportional to the dose with the film.

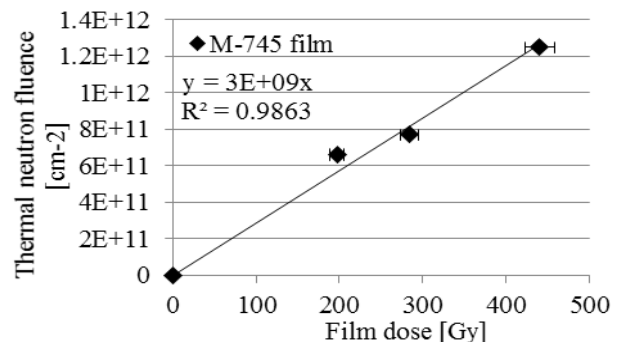


Fig. 1. The relationship between the dose with the film and thermal neutron fluence.

### REFERENCES:

- [1] K. Nakai *et al.*, Appl. Radiat. Isotopes., **69**(12): 1790-1792; (2011)
- [2] S. Masunaga *et al.*, Br. J. Radiol., **85**(1011): 249-258; (2012)
- [3] S. Kamada *et al.*, Appl. Radiat. Isotopes., **88**: 195-197; (2014)
- [4] H. Kumada *et al.*, Appl. Radiat. Isotopes., **88**: 211-215; (2014)
- [5] H. Tanaka *et al.*, Appl. Radiat. Isotopes., **69**: 1642-1645; (2014)
- [6] DWO Rogers *et al.*, Med. Phys., **22**: 503-524; (1995)

## CO9-1 Stability of Caprolactam Resin against $\gamma$ -Ray Irradiation in $\text{HNO}_3$

T. Nishida<sup>1</sup>, M. Nogami<sup>1</sup>, and N. Sato<sup>2</sup>

<sup>1</sup>Graduate School of Science and Engineering Research, Kinki University

<sup>2</sup>Research Reactor Institute, Kyoto University

**INTRODUCTION:** We have previously reported that the property of structure change in a cyclic monoamide resin consisting of poly-*N*-vinyl- $\epsilon$ -caprolactam (VEC) with a 7-membered ring by  $\gamma$ -ray irradiation in  $\text{HNO}_3$  is different from that in polyvinylpyrrolidone (PVPP), another cyclic monoamide resin with a 5-membered ring[1]. Namely, while relatively stable plural neighboring C=O groups (structure (a) in Fig. 1) were introduced for PVPP[2], such neighboring C=O groups were not observed for VEC. In this study, to clarify the more detailed degradation property of VEC, other irradiated samples were prepared and analyzed. Water-soluble *N*-methyl- $\epsilon$ -caprolactam (MEC) was also irradiated in  $\text{HNO}_3$  to evaluate the stability of VEC quantitatively.

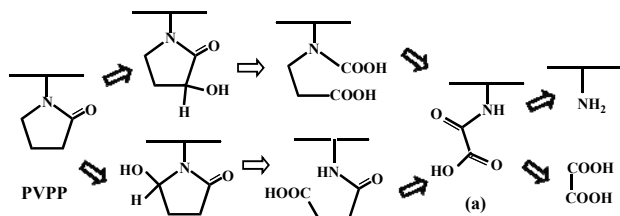


Fig. 1. Expected major route of change in chemical structure of PVPP by  $\gamma$ -ray irradiation in  $\text{HNO}_3$ [2].

**EXPERIMENTS:**  $\gamma$ -Ray irradiation to VEC was carried out similarly to the earlier study (max. 1.5 MGy)[1]. For the sample of MEC, a solution containing 1 mol/dm<sup>3</sup> (= M) MEC and 6 M  $\text{HNO}_3$  was prepared. The sample solution was put in a Pyrex tube and irradiated by the <sup>60</sup>Co source at max. 8.8 kGy/h up to 2.1 MGy at room temperature under ambient atmosphere. Irradiated samples were analyzed by <sup>1</sup>H and <sup>13</sup>C NMR. DMSO-d<sub>6</sub> containing a known weight of TMS which is a standard material was used as the NMR solvent. The residual ratio of MEC was calculated by the area ratio of each signal with that of TMS.

**RESULTS:** A crystal was observed from the supernatant obtained from the irradiated VEC. The crystal was identified as succinic acid by <sup>13</sup>C NMR analysis. The structure change in VEC is expected from the result as shown in Fig. 2, which suggests that the major route of change in chemical structure of VEC is basically identical to that of PVPP and that the resulting dicarboxylic acids differ corresponding to the number of carbon in the cyclic monoamides. The scheme is consistent with the above-mentioned fact that plural neighboring C=O groups were not observed for VEC. These facts also imply that a

5-membered ring would be necessary to obtain plural neighboring C=O groups under the present irradiation condition.

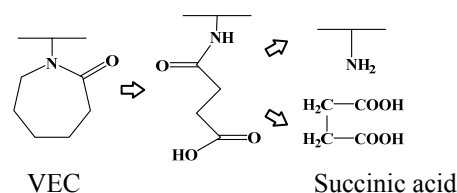


Fig. 2. Expected major route of change in chemical structure of VEC by  $\gamma$ -ray irradiation in  $\text{HNO}_3$

In a <sup>1</sup>H NMR spectrum, neat MEC showed four signals; (A)3.4, (B)2.9, (C)2.4, (D)1.6 ppm, respectively. The calculated residual ratios are shown in Fig. 3 together with the relationship between the position of hydrogen in the structure of MEC and that of the signal. The residual ratios calculated from (A), (B) and (D) show a nearly identical trend, where the residual ratios decrease linearly with an increase in dose, and ca. 50 % and 75 % are decomposed at 1 and 2 MGy, respectively. On the other hand, the residual ratio calculated from (C) is found higher than the three other systems, which would be because the signal (C) overlaps with that of degraded compounds. The dependence of residual ratio of *N*-butylpyrrolidone (NBP), one of the water-soluble 5-membered rings, under the irradiation in 6 M  $\text{HNO}_3$  on dose is difference from that of MEC. Namely, the decrease in the residual ratio of NBP decreased steeply and then gently[3]. As the result, comparing the stability of MEC with that of NBP, the residual ratio of MEC is higher than that of NBP at less than ca. 0.6 MGy, and vice versa at more than 0.6 MGy.

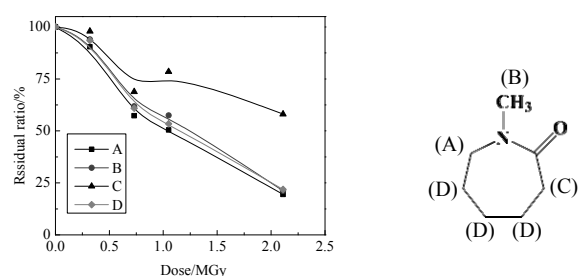


Fig. 3. Dependence of residual ratio of MEC on dose.

### REFERENCES:

- [1] T. Nishida *et al.*, KURRI Progress Report 2013 (2014) 295.
- [2] M. Nogami *et al.*, J. Radioanal. Nucl. Chem., **296** (2013) 423-427.
- [3] M. Nogami, *et al.*, Sci. China Chem., **55** (2012) 1739-1745.

採択課題番号 26013 アクチニルイオン配位性アミド化合物の耐ガンマ線性に関する研究 通常採択 (近大・理工) 西田哲大、野上雅伸 (京大・原子炉) 佐藤信浩

Y. Yasuda, Y. Kasamatsu, Y. Shigekawa, T. Ohtsuki<sup>1</sup>, K. Takamiya<sup>1</sup>, A. Shinohara

Graduate School of Science, Osaka University

<sup>1</sup>Research Reactor Institute, Kyoto University

**INTRODUCTION:** The first excited state of  $^{229}\text{Th}$  lies in extremely low energy level. The excitation energy was reported to be  $7.8 \pm 0.5$  eV [1]. This energy corresponds to vacuum ultraviolet light, and it is expected that the decay rate of  $^{229m}\text{Th}$  varies drastically depending on their chemical forms [2]. Furthermore, chemical conditions can affect the decay mode of  $^{229m}\text{Th}$  (internal conversion and/or gamma ray transition). It is also expected that  $^{229m}\text{Th}$  can be applied to a nuclear clock which has about two orders higher precision than the most precise optical clock [3]. Hence, many studies have been performed to observe the decay of  $^{229m}\text{Th}$ , especially on photon detection. However, there are not clear results directly observing the decay. It is important to observe the photons emitted from the  $^{229m}\text{Th}$  on various chemical conditions to understand the decay property of the state.

This report describes the results of photon detection for the several samples containing  $^{229m}\text{Th}$  with different chemical forms: hydroxide and fluoride.

**EXPERIMENTS:** Thorium-229m was separated from the mother nuclide  $^{233}\text{U}$  by using anion-exchange method. About 200 mg of  $^{233}\text{U}$ , containing less than 1 ppm of  $^{232}\text{U}$ , was adsorbed on the anion-exchange resin (Dowex 1×8, 200-400 mesh, 2.5 mL). Five-milliliters of 9 M HCl solution was poured into the column several times to remove  $^{229m}\text{Th}$  and the daughter nuclides. After  $^{229m}\text{Th}$  was grown in the column for a certain time: about 2 or 13 h, 5 mL of 9 M HCl solution was passed through the column to elute  $^{229m}\text{Th}$ . To prepare the hydroxide samples, 20  $\mu\text{L}$  aliquot of samarium standard solution was added and then aqueous  $\text{NH}_3$  was added to the eluent until the solution became basic. When the fluoride samples were prepared, 30  $\mu\text{L}$  aliquot of samarium standard solution and 2 mL of HF solution were added to the eluent and the solution was stirred for 2 min. Thorium-229m was coprecipitated with samarium as hydroxide or fluoride form. Each precipitate was collected on a polypropylene filter and heated to dryness.

Setup for photon detection is schematically illustrated in Fig. 1. To measure vacuum ultraviolet ray from  $^{229m}\text{Th}$  samples, we used a photomultiplier tube (PMT) for photon counting, Hamamatsu R6837, which detects 4-10 eV photons with higher than 10 percent quantum efficiency. Signals from PMT were amplified with the pre-AMP and PM-AMP. Noise was cut with the discriminator, and the signal data were accumulated in the multichannel analyzer.

**RESULTS:** In the case of the hydroxide and fluoride samples of  $^{229m}\text{Th}$  grown for about 2 h, the count rates of photons were almost the same with those of the background. In contrast, for the  $^{229m}\text{Th}$  samples grown for about 13 h, the photon emissions decaying for time were detected and the half-lives were about 1 h for hydroxide and 3 h for fluoride. For example, the result for the  $^{229m}\text{ThF}_4$  sample grown for about 13 h is shown in Fig. 2. These decaying photon emissions, however, did not seem to be the simple decay curve. In addition, if the half-lives of  $^{229m}\text{Th}$  were several hours, the photon emissions are expected to be observed for the samples grown for 2 h. Therefore, these photons might derive from the Cherenkov radiation induced by the decay of daughter nuclides such as Bi or Pb. To clarify the origin of these photons, we plan to purify  $^{229m}\text{Th}$  before measurement.

#### REFERENCES:

- [1] B. R. Beck *et al.*, LLNL-PROC-415170 (2009).
- [2] E. V. Tkalya *et al.*, Phys. Rev. C **61**, 064308 (2000).
- [3] E. Peik *et al.*, Europhys. Lett. **61**, 181 (2003).

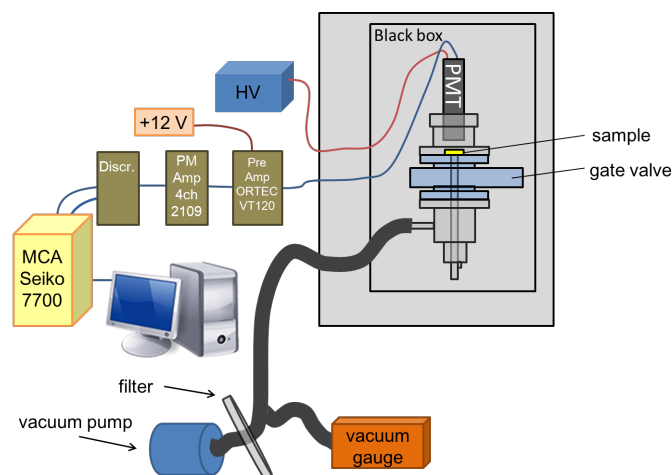


Fig. 1. Schematics of the experimental setup for photon detection.

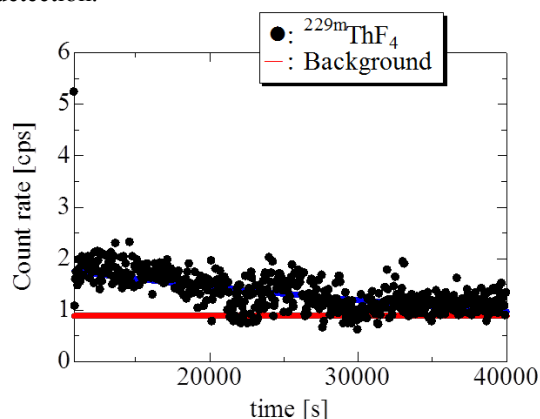


Fig. 2. Count rate of photons for the  $^{229m}\text{ThF}_4$  sample grown for about 13 h.

M. Yoneda,<sup>1</sup> S. Fukutani<sup>2</sup>, M. Ikegami<sup>2</sup>, Y. Shimada<sup>1</sup>, Y. Matsui<sup>1</sup>

<sup>1</sup>Graduate School of Engineering, Kyoto University

<sup>2</sup>Research Reactor Institute, Kyoto University

**INTRODUCTION:** After the accident of Fukushima Daiichi nuclear power plant, decontamination work has been carried out. Soil containing radioactive materials such as Cs is present in the decontamination waste. It is necessary to understand the behavior of radioactive substances in case of the incineration of waste. Therefore, in this study, the dissolution test was carried out using heat-treated soils containing Cs and Sr. Moreover, most of these kind of experiments are carried out using much higher concentration of stable isotope compared to the actual pollution concentration. Therefore, the difference of the results between in case of using high concentration stable isotope and in case of using actual level concentration of radioisotope is investigated.

**EXPERIMENTS:** The soil of the A1 layer of coniferous trees forest of Iwate University Takizawa practice forest was used for the experiment. 10 g of the soil of the A1 layer was taken and made into samples with addition of 5  $\mu\text{g}$  of stable Cs (mainly Cs-133) and Sr (mainly Sr-88) or 1250Bq of Cs -134 and Sr -85. 10 ml of distilled water was added to each soil sample, and each sample was dried for 20 hours in 45 degree Celsius temperature. Then, each sample was heated at 100, 200, 300, 400, 500, and 600 degrees Celsius using muffle furnace for one hour, and then they were let cool off naturally. After the addition of distilled water to each heat treated sample at solid-liquid ratio 1:10, they were shaken for six hours and centrifuged for ten minutes. Finally, supernatant liquid of them were filtered using 0.45  $\mu\text{m}$  filter and the filtrates were measured by Pure Ge semiconductor detector or ICP-MS.

**RESULTS:** The results are shown in Fig. 1 and Fig. 2. Fig. 1 showed that the elution rate of Cs decreased with increasing heat treatment temperature, and that there was almost no difference between in case of using high concentration stable isotope and in case of using actual level concentration of radioisotope is investigated. It is highly possible that less Cs in the decontamination waste containing soil is eluted in the environment because of the fixation of Cs in soil by the heat treatment. Fig. 2 showed that the elution rate of Sr increased with increasing the heat treatment temperature. Because of high concentration of background stable Sr, the elusion rates for stable Sr and radioactive Sr cannot be compared. However, their tendencies with the temperature of heat treatment are almost same.

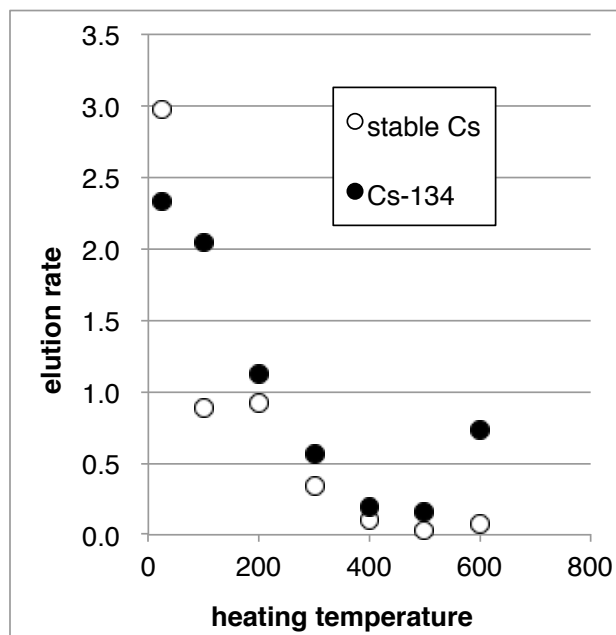


Fig. 1 Relation of elution rate of Cs and heating temperature.

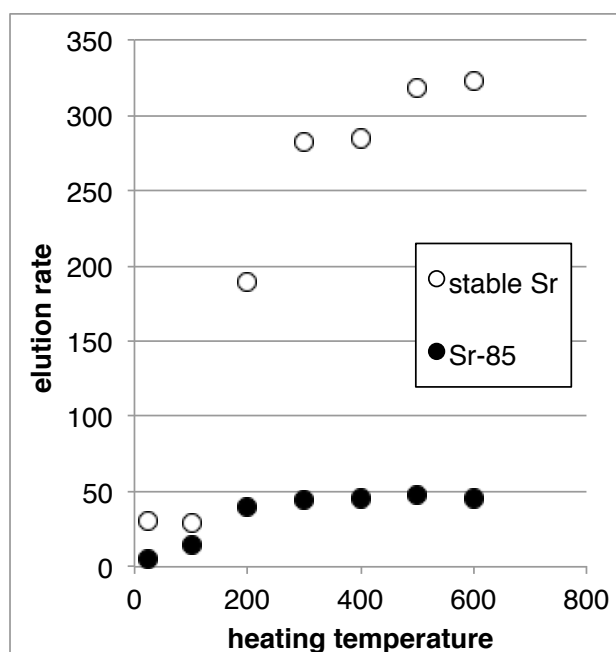


Fig. 2 Relation of elution rate of Sr and heating temperature.

N. Sei and T. Takahashi<sup>1</sup>

*Research Institute for Measurement and Analytical Instrumentation, National Institute of Advanced Industrial Science and Technology*

<sup>1</sup>*Research Reactor Institute, Kyoto University*

**INTRODUCTION:** A relativistic electron beam with a short pulse width is suitable for generating intense terahertz (THz) light. We have proposed to develop a monochromatic THz light source based on a superimposing coherent diffraction radiation (CDR). We observed a sign of the superimposing CDR to the electron-beam trajectory with an L-band electron linac at the Kyoto University Research Reactor Institute (KURRI-LINAC) [1]. However, the forward CDR interfered with coherent transition radiation (CTR) generated at a Ti window. It is difficult to evaluate the spectrum of the superimposing CDR quantitatively. The CDR is also emitted behind the electron-beam trajectory. The power of the backward CDR in the THz region is as strong as that of the forward CDR. Then, we have conducted experiments about superimposing backward CDR.

**EXPERIMENTS:** When a relativistic electron-beam emits radiation by a periodic structure, the resonance wavelength in laboratory system is influenced by Lorentz transformation. The resonance wavelength  $\lambda$  is given by

$$\lambda = \frac{l}{n} \left( \frac{1}{\beta} - \cos\theta \right), \quad (1)$$

where  $l$ ,  $\beta$ , and  $n$  are the period of the diffraction elements, the velocity of the electron divided by the speed of light, and the order of higher harmonics, respectively. The symbol  $\theta$  is the angle between the electron-beam trajectory and the direction of the CDR. It becomes  $\pi$  in the case of the backward CDR. Thus, the wavelength of fundamental harmonic of the backward CDR is the same as the double of the period of diffraction elements.

Figure 1 shows the schematic layout of the experimental setup of the backward CDR at KURRI-LINAC. Because an aluminum foil mirror was set to transport the backward CDR to the experimental room, it did not interfere with a CTR beam emitted from the Ti window. A thin aluminum plate, which was located behind the diffraction elements, prevented backward CTR generated by the vacuum chamber interfering with the backward CDR. An aluminum collimator with a diameter of 17.5 mm was located in front of the aluminum foil mirror. The distance between the aluminum foil mirror and the entrance of the diffraction elements was 120 mm, and the inner diameter of the diffraction elements was 30 mm.

Figure 2 shows spectra of the CDR when the period of the diffraction elements was 19 mm. It is noted that the

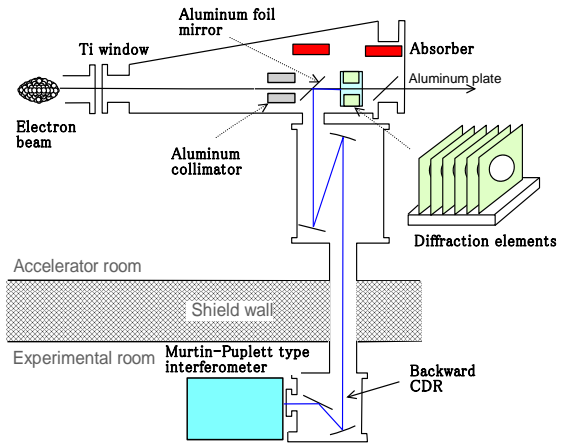


Fig. 1 Schematic layout of the CDR experiment.

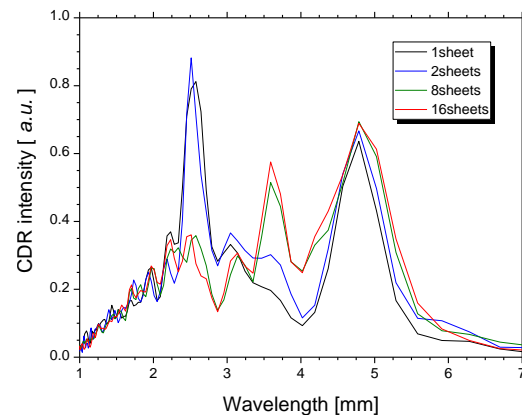


Fig. 2 Spectra of the CDR generated by the diffraction elements.

CDR intensity at wavelength around 3.8 mm, which was double of the period, increased as the number of the diffraction elements increased. However, the intensity did not increase for the number of the diffraction elements exponentially, so that the ratio that the CDR was superimposing was low. Because the bunch length of the electron beam was approximately 10 ps, the interaction length of the superimposing CDR was not longer than the resonance wavelength, and the ratio would become small as the number was larger.

**RESULTS:** We observed backward CDR generated by diffraction elements with a period of 19mm. Although an enhancement of the CDR intensity was observed at the fundamental resonance wavelength, the ratio that the CDR was superimposing was low. We will plan to use diffraction elements which had a shorter period.

**Reference:**

[1] N. Sei and T. Takahashi, KURRI Progress Report 2013 (2014) 222.

N. Higashio, H. Matsumoto, T. Takahashi<sup>1</sup>, N. Abe<sup>1</sup>

Japan Aerospace Exploration Agency

<sup>1</sup>Research Reactor Institute, Kyoto University

**INTRODUCTION:** It is well known that satellites and astronauts are always endangered in space due to plasma, radiation particles, neutral particles, ultraviolet rays/X rays and meteoroids/debris. Since we have to support JAXA's projects to keep them safe from the space environment, our group has been researching the radiation environment of space for more than 20 years. Now we are developing a sensor for the ERG (Energization and Radiation in Geospace) satellite. The purpose of the ERG satellite is to investigate the mechanism of radiation belts. It is well known that the energetic electron flux varies during geomagnetic disturbance and especially the relativistic electrons in the outer radiation belt change. However, the data of the electron (10eV - 20MeV) in radiation belt is not enough. The ERG satellite consists of four instrument parts, Plasma/Particle (PPE), geomagnetic field (MGF), Plasma wave (PWE) and electric field (PWE). Before using KURRI-LINAC (Kyoto University), we couldn't calibrate our sensor over 2 MeV electrons.

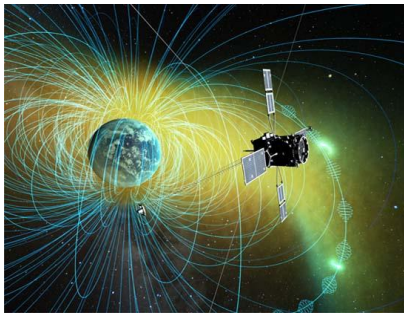


Fig. 1. ERG satellite

**EXPERIMENTS:** Our sensor that name is XEP-e (Extremely High-Energy Plasma/Particle Sensor for Electron) is one of the PPE. The XEP-e observes 400keV~20MeV electrons and has five solid-state silicon detectors (SSDs) and a high-Z scintillator (GSO). The XEP-e is Fig.2. The first SSD discriminate between electron and other particles. And The 2~5 SSDs and a high-Z scintillator detect its energy. Fig. 3.

We use KURRI-LINAC (Kyoto University) to calibrate its energy (2MeV~20MeV electron). We also use our accelerator in Tsukuba space center under 2MeV electron.

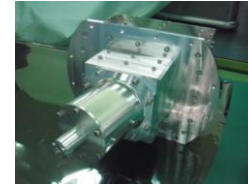


Fig. 2. XEP-e

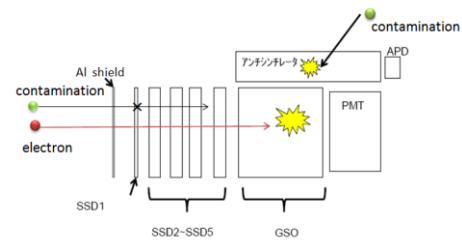


Fig. 3. Principle of the XEP-e

We need very low count rate beam (100~1000cps), so we tried to make this beam by using the XEP-e (EM) last year. And this year we calibrate the XEP-e (Flight Model). As shown in Fig. 4, the data that is got in KURRI-LINAC and simulation data (GEANT4) were very similar between 5MeV and 14MeV. It shows KURRI-LINAC can make very low count rate beam.

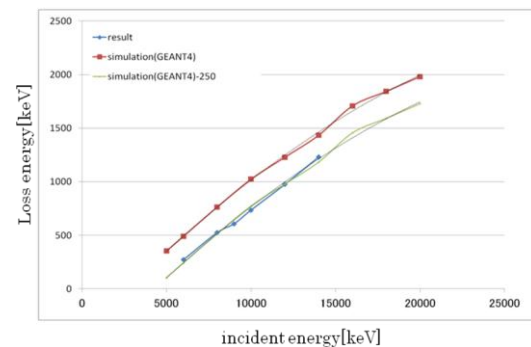


Fig. 4. Incident energy vs Loss energy of the XEP-e (energy range: 5MeV~14MeV)

### RESULTS:

There haven't been facilities that can make very low count rate beam over 2MeV in Japan. But now KURRI-LINAC (Kyoto University) can only make low count rate and monochrome beam between 5MeV and 14MeV.



T. Miura<sup>1</sup>, R. Okumura<sup>2</sup>, Y. Iinuma<sup>2</sup>, S. Sekimoto<sup>2</sup>, K. Takamiya<sup>2</sup>

<sup>1</sup>National Metrology Institute of Japan, AIST

<sup>2</sup>Research Reactor Institute, Kyoto University

**INTRODUCTION:** National Metrology Institute of Japan is responsible for developing certified reference materials (CRMs) and for establishing the traceability of SI (The International System of Units) on chemical metrology in Japan. To establish SI traceability, the primary method of measurements should be applied to the characterization of the CRMs. Recently, neutron activation analysis (NAA) using comparator standard is recognized as a potential primary ratio method [1]. Despite the potential of NAA as primary ratio method, the evaluation of the measurement uncertainty is required in any analysis. In general, there are three main components of uncertainty in NAA, that is, sample preparation uncertainty, neutron flux homogeneity, and gamma ray measurement uncertainty. Usually, flux monitor is used to correct the neutron flux in-homogeneity. However, although the flux monitor can correct the neutron flux variation using the count rate of the known amount of the monitor nuclide, it does not reflect the neutron flux of the actual sample. The most practical method to eliminate neutron flux in-homogeneity and to improve gamma ray measurement uncertainty is an internal standard method [2]. In this paper, we presented that notable capability of internal standardization in NAA for determination of Br in acrylonitrile butadiene styrene copolymer (ABS) resin as a candidate CRM.

**EXPERIMENTS:** The ABS resin candidate CRM was produced by a mixing machine. The calibration solution of Br was prepared from NMIJ primary standard solutions. The Au solution for the internal standard for Br was prepared from a high purity metal. The calibration solutions contained Br and Au as internal standard.

One hundred mg of the ABS resin samples was used for Br analysis. The Au solution was added to the samples before neutron irradiation. The neutron irradiations were performed by KUR (Kyoto University Research Reactor) TCPn (thermal neutron flux:  $8.0 \times 10^{10} \text{ cm}^{-2}\text{s}^{-1}$ ) for 6 h. The  $\gamma$  ray measurement system consisted of a Canberra GC4070-7500 Ge detector and a Laboratory Equipment Corporation MCA600

**RESULTS:** It was found that the  $^{198}\text{Au}$  sensitivity (cps/ $\mu\text{g}$ ) varied according to the sample position in the irradiation capsule. The relative standard deviation of the  $^{198}\text{Au}$  sensitivity (cps/ $\mu\text{g}$ ) was 3.8 %. The uncertainty related to the neutron flux homogeneity significantly contributes to the overall uncertainty, if an internal standard is not applied. The amount of Br in the ABS resin sample was determined by calibration curve method using internal standardization. The linearity of calibration curve was improved by internal standard. The relative standard uncertainty related to the calibration curve linearity was improved to 0.36 % to 0.87 %. The analytical results of Br in BCR-681 certified reference material of polyethylene resin by proposed method were in excellent agreement with the certified value only using internal standard.

The analytical results of Br in ABS resin sample by proposed method was  $575 \text{ mg/kg} \pm 8.0 \text{ mg/kg}$  ( $n=8$ ). The relative expanded uncertainty ( $k=2$ ) was 1.4 %.

**REFERENCES:**

- [1] R.Greenberg, P. Bode, E. De Nardi Fernandes, *Spectrochim. Acta B*, 66 (2011) 193-241.
- [2] T. Miura, K.Chiba, T. Kuroiwa, T. Narukawa, A.Hioki, H. Matsue, *Talanta*, 82 (2010) 1143-1148.

T. Hirayama, N. Yamashita<sup>1</sup>, S. Akimoto<sup>1</sup>, M. Fujimori<sup>1</sup>,  
T. Matsuoka<sup>1</sup>, M. Hino<sup>2</sup> and T. Oda<sup>2</sup>

Dept. of Mechanical Engineering, Doshisha University  
<sup>1</sup>Dept. of Mechanical Engineering, Doshisha University  
<sup>2</sup>Research Reactor Institute, Kyoto University

**INTRODUCTION:** Tribology is one of academic disciplines covering friction, wear and lubrication in engineering for a lot of industrial applications such as bearings, gears, engine pistons in car and so on. Formation of adsorbed additive layer on metal substrates has attracted attention as an effective way to reduce friction. There are a lot of studies investigating the relationship between the kind of additives and their tribological properties, but the formation process of the adsorbed layer is still unknown. On these backgrounds, this study investigated the formation and desorption process of adsorbed additive layer onto metal surface by means of attenuated total reflection infrared spectroscopy (ATR-IR) and neutron reflectometry (NR) with time slice mode.

**EXPERIMENTS:** Thin copper film was deposited onto silicon wafer as target substrate for the study. Poly-alpha-olefin and palmitic acid were selected as base oil and oiliness additive, respectively. The time dependences of IR absorbance profiles and neutron reflectivity profiles are shown in Figs. 1 and 2. We can see that the IR peaks from COO bonds gradually grown up after the injection of base oil with oiliness additive. On the other hand, the neutron reflectivity profiles did not change regardless of time. These results indicated that the physisorption of oiliness additive molecules was quickly completed and the chemisorption was gradually proceeded. To investigate the effect of rolling friction, we designed the sample holders with rolling friction mechanism for ATR-IR and NR. The obtained results are shown in Figs. 3 and 4. The IR profiles showed the desorption of additive layer, but the NR profiles did not change even after the rolling friction.

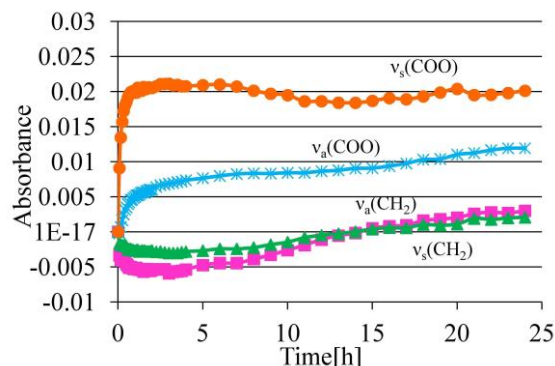


Fig. 1. Time dependence of IR absorbance peaks

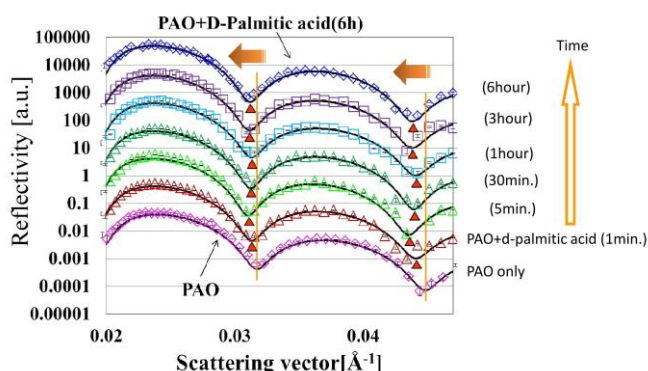


Fig. 2. Time dependence of neutron reflectivity profiles obtained by SOFIA at BL16 in J-PARC MLF

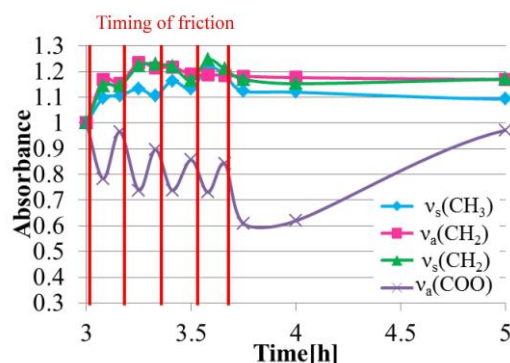


Fig. 3. Time dependence of IR absorbance peaks after rolling friction

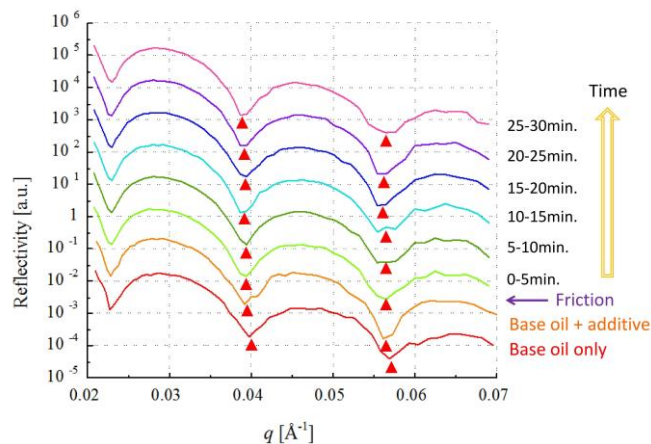


Fig. 4. Time dependence of NR profiles after rolling friction

**CONCLUSIONS:** The additive molecules made the condensed layer around the top surface by physisorption, and they gradually reacted by chemisorption. The rolling friction process peeled the adsorbed additive molecules off from the surface temporarily, but the layer was quickly repaired. ATR-IR and NR were quite effective to see the adsorption and desorption processes with separating 'physisorption' and 'chemisorption'.

## CO12-3 Characteristic Measurement of Neutron Detector for Fukushima Debris

M. Kureta<sup>1</sup>, M. Komeda<sup>1</sup>, K. Takamiya<sup>2</sup>

<sup>1</sup>Japan Atomic Energy Agency

<sup>2</sup>Research Reactor Institute, Kyoto University

### INTRODUCTION:

New hybrid detector called B-10+ detector has been developed by GE Reuter-Stokes. The detector is what combines B-10 lined proportional counter with He-3 counter. A big feature of B-10+ detector is reducing costs while the performance doesn't decrease much. We have developed NDA system against the Fukushima debris, and then we are considering applying the B-10+ detector instead of He-3 detector that has been most popular for general NDA systems. The original experiment plan at KUR was twice experiments at the B-4 port, and once experiment with high gamma ray and neutron flux at the area under the core. We could carry out the first experiment in 2014. In the experiment using the B-4 port, we obtained fundamental data of B-10 detector such as the pulse shape and plateau.

### EXPERIMENTS:

The B-10+ detector is 100cm in length. And the gas pressure including He-3 is approximately 1 atm. Three types of amplifiers were used. A current amplifier and charge amplifier are developed by our group, and another is a charge amplifier from PDT Inc. He-3 detector (4 atm) was also used in order to compare detection efficiency with B-10+ detector. The high voltage power supply was ORTEC 556H, DC supply was KIKUSUI PDM-3, and counter was ORTEC 872.

### RESULTS:

As shown Fig.1, the current amplifier and charge amplifier caused pile-up, which was also observed on an oscilloscope. Therefore we measured neutron flux through an absorber, the plateau region was observed clearly. Due to the limited machine time, data of the attenuated flux was not obtained by using a current amplifier, and data after the plateau region was not done. Some measurements by He-3 were carried out. As an easy reference, measurement result by He-3 detector indicates that B-10+ detector has 40% detection efficiency of He-3 detector. Fig.2 shows a pulse from a charge amplifier on an oscilloscope. The width was approximately 1  $\mu$ s that was the same degree as using He-3 at another measurement. Fig.3 shows an output spectra for a B-10+ detector. A sharp peak of He-3 was not observed. The reason is considered that the effect of the He-3 gas is not stronger than the lined B-10 since the amount of He-3 gas is reduced. We will investigate characteristics of B-10+ detector in high gamma ray field as future work. After that, we will try experiments applying B-10+ detectors to NDA system.

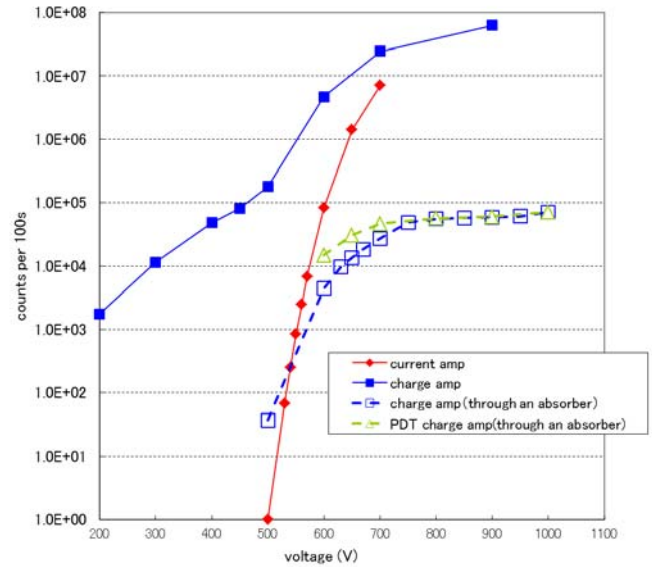


Fig.1 Plateau measurements of B-10+ detector with three kinds of amplifiers



Fig.2 A pulse from B-10+ detector using a charge amplifier

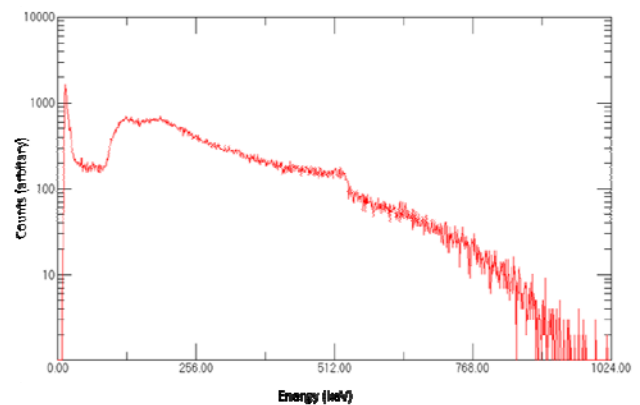


Fig.3 B-10+ detector spectrum using a charge amplifier

K. Toh, K. Soyama, T. Nakamura, M. Hino<sup>1</sup>, and T. Oda<sup>2</sup>

*J-PARC Center, Japan Atomic Energy Agency*

<sup>1</sup>*Research Reactor Institute, Kyoto University*

<sup>2</sup>*Graduate School of Science, Kyoto University*

**INTRODUCTION:** Multiwire-type two-dimensional neutron detectors using helium-3 gas are widely used in neutron scattering experiment facilities because of their high detection efficiency, low gamma-ray sensitivity, and excellent long-term stability. We have developed an advanced multiwire-type two-dimensional neutron detector system without compromising the otherwise excellent performance of the conventional detector [1, 2]. A short response time and better spatial resolution can be obtained in this system by using an individual line readout method. Additionally, optical devices have been developed and incorporated in the system for long-distance signal transmission and insulation between the detector heads and the signal processing circuits. In this present study, we performed neutron irradiation experiments at KUR.

**EXPERIMENTS:** The multiwire element, which is developed for individual line readout, has 128 anode wires, 128 cathode wires for the y-axis, 128 cathode strips for the x-axis, and a wire/strip pitch of 1 mm. The amplifier-shaper-discriminator boards have a total of 256 channels to process each cathode signal line. Field-programmable gate array based digital signal processing and digital signal encoding are used to calculate signal position with a sampling frequency of 106 MHz. Dedicated optical signal transmission devices are designed to use multimode optical fibers at a wavelength of 850 nm. List-mode data with the x- and y-positions and the time of flight are recorded using a data acquisition system (MPA-3, Fast Comtec). Neutron irradiation is performed using a neutron beam line CN3 at the KUR.

**RESULTS:** Fig. 1 shows a typical response when a  $1.0 \times 1.0 \text{ mm}^2$  neutron beam is irradiated on the detector, and the response at the peak position onto the x-axis is shown in Fig. 2. As seen in Fig. 2, there are some background signals. It is considered that these signals arise from neutron scattered by the beam line, the collimator, the window and the fill gas. Fig. 3 shows the reactor power dependence to the measured counts of the developed detector system. The developed detector showed a linear response up to the full power, 5 MW, of KUR reactor and the counting rate at 5 MW was approximately  $2.1 \times 10^5 \text{ cps}$ .

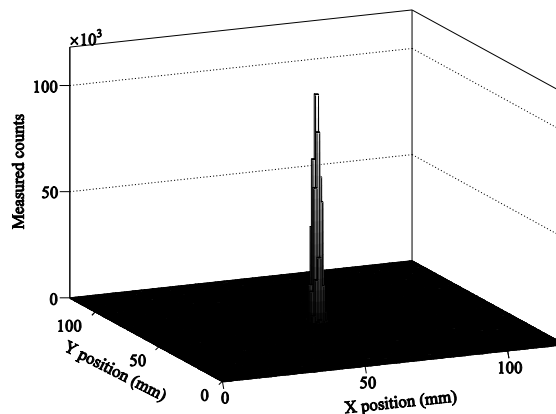


Fig. 1 Image of collimated neutron beam with size of  $1 \times 1 \text{ mm}^2$ .

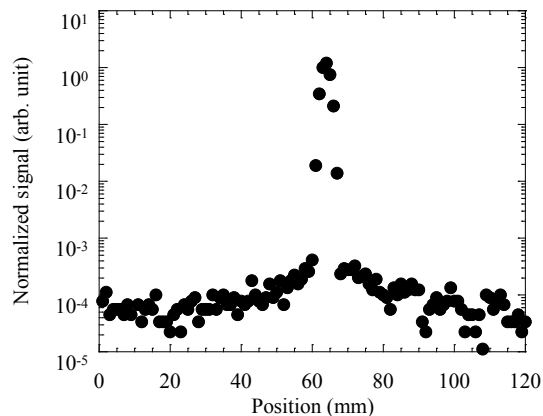


Fig. 2 one dimensional response at peak position.

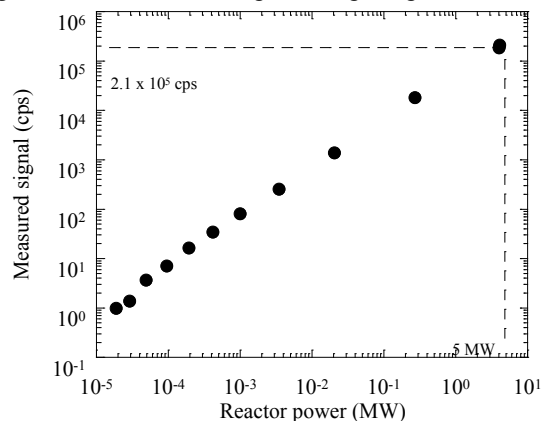


Fig. 3 Measured counts of developed system under neutron irradiation as a function of KUR reactor power.

### REFERENCES:

- [1] K. Toh *et al.*, Nucl. Instr. and Meth., **726** (2013) 169-174.  
 [2] K. Toh *et al.*, J. Phys.: Conf. Ser. **528** (2014) 012045.

F. Kitatani<sup>1</sup>, H. Tsuchiya<sup>1</sup>, M. Koizumi, J. Takamine<sup>1</sup>, J. Hori<sup>2</sup>, M. Sano<sup>2</sup>, K. Takahashi<sup>2</sup>, K. Nakajima<sup>2</sup>, and H. Unesaki<sup>2</sup>

<sup>1</sup> Research Group for Nuclear Sensing, JAEA

<sup>2</sup> Research Reactor Institute, Kyoto University

**INTRODUCTION:** Neutron Resonance Densitometry (NRD) [1, 2] is an assay technique of nuclear materials in particle-formed debris that contains various nuclides, such as of structural materials and the others. It is a combination of two techniques: Neutron Resonance Transmission Analysis (NRTA) [3], and Neutron Resonance Capture Analysis (NRCA) [4] or Prompt Gamma-ray Analysis (PGA). Containing nuclides in a sample are identified by NRCA/PGA. The information of NRCA/PGA is used in NRTA analysis to quantify nuclear material isotopes. A neutron time of flight (TOF) method is used in NRD measurements. A facility consisting of a neutron source, neutron flight paths, and detectors, is required. One of the distinctive features is utilization of a short flight path; this increases the neutron beam strength, and reduces construction cost in a practical applications. On the other hand, that reduces resolving power in TOF measurements, and increases neutron background. In order to investigate the effect of neutron flight length, we carried out NRTA experiments with a short neutron flight path constructed at the Kyoto University Research Reactor Institute - Linear Accelerator (KURRI-LINAC).

**EXPERIMENTS:** Experiments were carried out with a 7.5-m flight path. The experimental room and the neutron source were separated by 2-m-thick concrete wall. A 2-m-long neutron transport tube was installed in the experimental room as shown in Fig. 1. The center of it was an Al vacuum chamber, the cavity of which was 200 mm in diameter; both sides were shielded by 2-mm-thick Al plates. The chamber was surrounded by 5-mm-thick B<sub>4</sub>C-doped silicone rubber (B<sub>4</sub>C 40%). The outside of the rubber was high density polyethylene plates (460 x 460 mm). The neutron beam was collimated to be 50 mm in diameter in front of the transport tube. A <sup>6</sup>Li scintillation detector (Saint-Gobain GS20; 100 x 100 x 10 mm) was used to measure transmission neutrons. The incident neutron flux was monitored by a BF<sub>3</sub> neutron detector placed near the exit of the concrete wall.

Sample and filter plates (100 x 100 mm) were placed in front of the transport tube: In (0.2 mm), Ag (0.25 mm), W (0.5 mm), and Pb (10 mm). The neutron pulse width was controlled by the pulse width of the LINAC electron beams, which were 500 ns, 2 μs and 4 μs.

**RESULTS:** Figure 2 shows TOF neutron transmission spectra. The ordinates are the normalized neutron counts,

and the abscissa time interval after neutron pulse generations. The dips in the spectra around 192 and 102 ns are resonances of <sup>183</sup>W at 7.64 eV and 27.0 eV, respectively. Since the origin of the spectra is relevant to the beginning of electron pulse injection, the ends of the dips come later as the electron pulse width increases. The dip at 27.0 eV is not clearly seen with 4-μs electron pulse width.

**SUMMARY:** In measurements of NRD, the quantity of the nuclear materials is determined from NRTA spectra in the neutron energy range of less than 30 eV [1, 2]. At KURRI-LINAC, we have examined NRTA with a 7-m flight path. The resonance dips of <sup>183</sup>W at 27 eV was successfully observed with an electron pulse width less than 2 μs. This indicates the applicability of short-flight-path TOF system to nuclear material quantification. The importance of the pulse width of neutron beam should be noted. Both simulation studies and experiments are expected for realistic design of a TOF facility of nuclear material quantification.



Fig. 1. A neutron transport tube. A neutron detector was placed on the table.

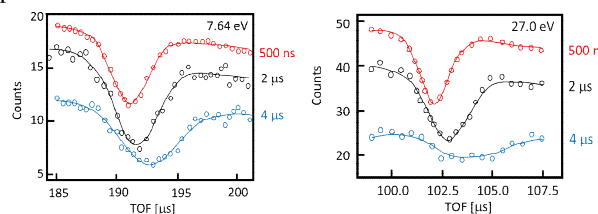


Fig. 2. TOF neutron transmission spectra. The base lines are adjusted, and the curves are added for the sake of readers.

#### REFERENCES:

- [1] H. Harada *et al.*, Nuclear Data Sheets **118**, p502 (2014).
- [2] F.Kitatani *et al.*, J. Nucl. Sci. Tech. **51**, p1107 (2014)
- [3] P. Schillebeeckx *et al.*, Nuclear Data Sheets **113**, p3054 (2012).
- [4] P. Schillebeeckx *et al.*, JINST **7**, C03009 (2012).

# CO12-6 Test of a Microcell Multi-Wire Proportional Chamber for a Muon-Electron Conversion Search Experiment, DeeMe

H. Natori, N. Abe<sup>1</sup>, M. Aoki<sup>2</sup>, Y. Igarashi, S. Ito<sup>2</sup>, S. Mi-hara, D. Nagao<sup>2</sup>, T. D. Nguyen<sup>2</sup>, T. M. Nguyen<sup>2</sup>, H. Nishiguchi, Y. Seiya<sup>3</sup>, K. Shimizu<sup>3</sup>, T. Takahashi<sup>1</sup>, Y. Takezaki<sup>3</sup>, N. Teshima<sup>3</sup>, K. Yamamoto<sup>3</sup>

High Energy Accelerator Research Organization (KEK)

<sup>1</sup> Research Reactor Institute, Kyoto University

<sup>2</sup> Department of Physics, Osaka University

<sup>3</sup> Department of Physics, Osaka City University

**INTRODUCTION:** DeeMe [1] pursue mu-e conversion in nuclear field, which will be a clear evidence of the new physics if it is found, because Standard Model of elementary particle physics predicts it beyond an experimental reach. Detector is required to measure electron momentum precisely after a huge pulse of prompt timing charged particles, whose width and instantaneous hit rate is expected to be approximately 200ns and 70GHz/mm<sup>2</sup>. Such a large input will make usual wire chamber detectors inactive due to space charge effect. We developed a new technique to make a chamber to be tolerant to a large input pulse.

**EXPERIMENTS:** Experimental setup is shown schematically in Fig. 1. Electron beam collimated to 16mm x 19mm penetrates Multi-Wire Proportional Chamber (MWPC) and beam counters. Beam rate is tuned changing current of electron gun heater.

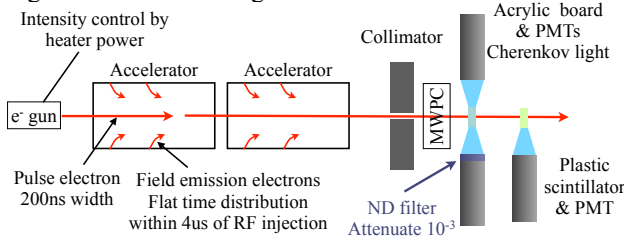


Fig. 1 Schematics of experimental setup

A huge pulse of prompt timing is emulated by tuned pulse from electron beam gun. Delayed electron signals are emulated by field emission electrons.

Electrical field contour inside the chamber calculated is shown in left of Fig. 2. Anode wires with 1450V and potential wires with 0V are put alternately. During a huge pulse are coming, potential wires are applied with 1450V as shown in right of Fig.2. With this setting, slope of electric field near anode wire become gentle that avalanche multiplication is suppressed. Temporary muting the chamber during a burst pulse is expected to help to suppress the space charge effect. Rectangular pulsed high voltage is applied to potential wire to recover quickly

after the blinded period. Because of the very high and rapid voltage up and down motion, readout electronics suffers from large current input derived from the HV switching. We also developed a readout system which tolerates to high current input.

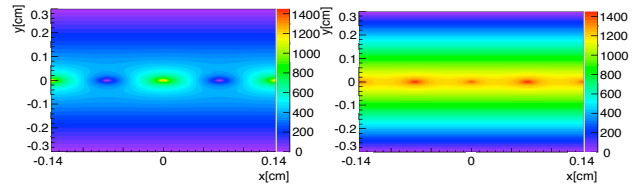


Fig. 2 Calculated electrical field contour. Anode-wire 1450V, Potential-wire 0V(left figure), 1450V(right figure)

**RESULTS:** Fig. 3 shows an output result of the chamber. Electrons from beam gun tuned to be 70GHz/mm<sup>2</sup> in instantaneous hit rate are not amplified in the chamber with applying pulsed high voltage to potential wire. This enabled single electron detection coming after the burst pulse. Noise derived from the HV switching is always the same, so we can eliminate the noise by subtracting averaged waveform of plural numbers of events. We succeeded to obtain a clear electron signal after the burst pulse avoiding the space charge effect by a burst pulse of charged particles.

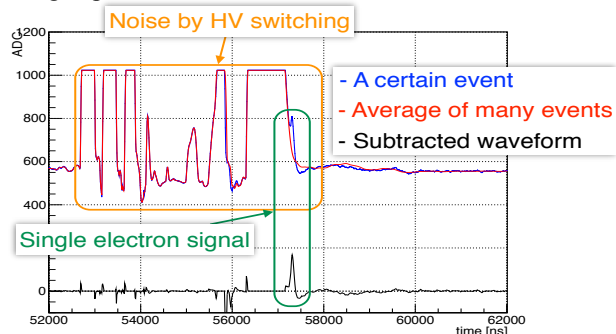


Fig. 3 Waveform of the chamber with electron beam gun pulse and HV swithing

**REFERENCES:**

[1] H. Natori, on behalf of the DeeMe Collaboration, Nucl. Phys. B Proc. Suppl. Vol. 248-250 (2014)

採択課題番号26046 ミューオン電子転換過程探索実験DeeMe用極小セル型チェンバーの 通常採択ビーム試験

(KEK) 名取寛顕、五十嵐洋一、西口創、三原智 (京大・原子炉) 阿部尚也、高橋俊晴 (阪大・理) 青木正治、伊藤慎太郎、N. D. Thong、N. M. Truong、長尾大樹 (大阪市大・理) 清水宏祐、清矢良浩、竹崎優斗、手島菜月、山本和弘

M. Takagaki<sup>1,2</sup>, G. Shimazaki<sup>1</sup>, S. Masunaga<sup>3</sup>

<sup>1</sup>College of Nursing, Aino University

<sup>2</sup>Graduate School of Human and Environmental Studies,  
Department of Anthropology, Kyoto University

<sup>3</sup>Graduate School of Science, Research Reactor Institute,  
Kyoto University

Aside the pros and cons of the use of nuclear power as an energy source, it seems to be useful in understanding the nuclear reactors to describe them as an ethnography based on the narrative data of nuclear researchers. By describing the reactor as a scientific ethnography, it is expected to be highlighted the problem of nuclear reactors and low-level radiation environment from a new angle. Then, it is expected to provide further knowledge for living in the contact zone between the field we live in safely (normal) and low-level radiation field (pathological), and going into patho and/or coexisting with patho.

This is a very unique study that an ethnographer who is a radiation physicist, a physician and also an anthropologist participates in wide-range observation of nuclear research. The researchers have been forced to include *Fukushima* as an enlarged research field, and it is regarded as a chance to write up the excellent scientific ethnography by doing this rather. On 2014-2015, we have mainly investigated previous research, and preliminary investigation has been carried out with biologists and physicists involved in nuclear science at the Kyoto University. Their narrative indicated here was traumatic narrative of *Fukushima* that suddenly appeared in their research field of nuclear science. Sometime it was a narrative of the confusion of the researchers themselves, although almost of the nuclear scientists have investigated sincerely with the nuclear reactor research as an energy source of the human being. The radioactivity that has been discarded and released has been completely isolated in a managed environment from the living space. Conversely, by this act, understanding of nuclear reactors and low-level radiation environment, and also constructing networks among various sub-specialists structurally become difficult. The reason why researcher's confusion about Fukushima accident is so strong, I think because our wisdom as the central pillar of our ego might be extremely imbalanced state. As being symbolically shown in *Fukushima*, because wisdom of nuclear science has extremely hypertrophied

self-righteously, once it fall into a little collapse, lack of resilience of human wisdom for stabilization and repair becomes embody.

By analyzing the narrative concerning the reactor of nuclear researchers, to describe the ethnography of nuclear reactor and nuclear waste that is also a study object of researchers themselves seems to lead to development of a new approach to the methodology of cultural anthropology. Such ethnography seems to be very useful for human society by targeting to nuclear reactor as thing. Many nuclear physicists have focused on the following statement of Prof. Wolfgang Weiss;

*“The most serious damage caused by Fukushima accident is that people lost trust for science and scientists. This certainly will influence long-term human history, and we cannot recover such situation so easily. We scientists are responsible to such situation.”*

Latour has pointed out that the dynamic and contingent elements intervene in the process of establishing the level of intellectual authority and knowledge that circulates within the scientific community. Case of Fukushima accident shows this extremely and plainly. It is expected to also lead to scientific achievements, such as actor network theory by scientific anthropological comparison analysis of the various disciplines of nuclear reactor researchers as different cultures. And also, ethnographic research might be very helpful tool for well public understanding of reactor and/or low dose radiation field, and then might regain confidence of scientists.

The understanding and knowledge of the researchers of KUR for their acceptance of this ambitious study is greatly appreciated. A new division for Ethnographic Study for Nuclear Science is expected to be established in KUR. This research is supported by Grant-in-Aid for Scientific Research for 2014-2016, No.26580152, JSPS. We are now promoting our fieldwork and are planning to publish ethnography of nuclear reactor on 2017.

#### REFERENCES:

- [1]K. Azuma, et al., Sekaishiso-sha. (2014)
- [2]B.Latour, Routledge.(2013)
- [3]W.Allison, Wada Allison Pub. (2009)
- [4]AESJ, Fukushima Accident Report. Shinppy-sha. (2014)

## CO12-8 Effective Measures on Safety, Security, Hygiene and Disaster Prevention in Laboratories

T. Iimoto<sup>1</sup>, R. Hayashi<sup>1</sup>, T. Saito<sup>1</sup>, A. Yasmi<sup>1</sup>, S. Higaki<sup>1</sup>, A. Sugiyama<sup>1</sup>, N. Kutsuna<sup>1</sup>, A. Kobashi<sup>1</sup>, K. Tanoi<sup>1</sup>, T. Suzuki<sup>1</sup>, K. Kamiko<sup>1</sup>, T. Takahashi<sup>2</sup>, S. Takahashi<sup>2</sup>

<sup>1</sup>The University of Tokyo

<sup>2</sup>Research Reactor Institute, Kyoto University

### INTRODUCTION:

Important research aspects can be found in the following keywords such as safety, security, hygiene and disaster prevention. Nuclear research reactor is one of representative facilities together with these keywords under their operation. It is effective to investigate the latest status on practical measures on these keywords in various facilities including nuclear research reactors, to compare each other among facilities, and to discuss more effective or optimized ones for our positive safety management. Through this process, it is also effective to investigate the latest international and/or national regulations and the movement of revision of them. This total discussion contents and its fruit are directly useful for all relating laboratories.

### RESEARCH APPROACH:

General research approach is as follows.

- Measures of safety management during operation or standstill status of the real facilities would be investigated. This information would be used for our research discussion on the positive and more optimized safety management.
- It would not be a single year research, but maybe two to three years research for one theme.
- Information source of facilities would not be only KUR, KUACA or the other facilities in Kyoto University, but also the Kinki university research nuclear reactor or the facility of National Institute of Fusion Science, etc. This research is an active joint-research with these relating facilities and positive researchers on safety management.
- One of the distinctive features of this research is to involve office staffs as cooperators as well as researchers and technical staffs. In The University of Tokyo, most of the members in Division for Environment, Health and Safety are office staffs who knows real situation of safety management in laboratories very well.

Discussion target in BY of 2014 was determined as "safety control in use of small amount nuclear materials" through our internal member discussion. We investigated the related regulations and their application as well as the fact-finding in use of small amount of uranium and thorium in Japanese laboratories.

### USE & MANAGE OF SMALL AMOUNT of U & Th:

When using small amount of uranium or thorium up to 300g (DU, NU) and/or 900g (Th), most of safety control procedures requested as radioactive materials are exempted by related regulations. Weighing control of nuclear elements is only requested by regulation. This causes easy usage of uranium and thorium in laboratories. For example, it is convenient that uranium acetate or uranium nitrate could be used for biology research to observe chromosomes clearly. Natural occurring radioactive materials (NORM) such as minerals and seawater samples including uranium and thorium would also be troublesome sources which could be enriched through some research processes, and then would change into high concentration radioactive materials as a result legally. This is a representative technologically enhanced NORM (TENORM). TENORM is one of headache materials in laboratory. Even the amount is quite small, the nuance of terms of "nuclear" "uranium" and "thorium" will give a big impact on society when some accidents or troubles happen. We can use these materials easily and conveniently, however these are strictly controlled by the international regulations on their transfer. The latest guideline on NORM and TENORM safety management by the Japanese regulatory body was published in 2009 to support the safety management. These situations must be identified and understood by all stakeholders. Framework of related education for safety managers and users should be adequately established and applied. All stakeholders should understand their risk level and features of nuclear materials as radioactive materials. This could lead reasonable and optimized safety management in laboratories.

### NEXT RESEARCH TARGETS;

Education framework, curriculum and textbooks for safety managers and users as well as relating officers to fill up the nuclear material controlling sheet for the use of small amount of uranium and thorium should be discussed. This discussion should be based on the additional investigation and analysis of the way to use, control and storage the materials in laboratories.

### REFERENCES:

- [1] T. IIMOTO, Environ. & Safety, 4(3),1-8 (2013)
- [2] T. IIMOTO et.al., Safety Engineering,48(4),215-221 (2009)
- [3] T.IIMOTO et.al., Isotope News, 566,64-67, (2001)
- [4] MEXT, Guideline for Safety Management of NORM and Consumer Products (2009)

採択課題番号 26054

実験施設における安全衛生・セキュリティ・防災等の効果的な対応と対策に関する研究

通常採択

(東大)飯本武志、林瑠美子、齊藤拓巳、安見厚志、桧垣正吾、杉山 暁、朽名夏磨、小橋浅哉、田野井慶太郎、鈴木崇彦、神子公男、布川 淳、小原佑介、前寺郁彦(京大・原子炉)高橋知之、高橋千太郎



Y. Arimoto<sup>1</sup>, P. Geltenbort<sup>2</sup>, S. Imajo<sup>3</sup>, Y. Iwashita<sup>4</sup>,  
M. Hino<sup>5</sup>, R. Katayama<sup>6</sup>, M. Kitaguchi<sup>7</sup>, K. Mishima<sup>1</sup>, R.  
Sakakibara<sup>7</sup>, Y. Seki<sup>8</sup>, H. M. Shimizu<sup>7</sup> and T. Yoshioka<sup>9</sup>

<sup>1</sup>KEK, <sup>2</sup>ILL, <sup>3</sup>Dep. of Phys. Kyoto Univ., <sup>4</sup>ICR Kyoto Univ.,  
<sup>5</sup>KURRI, <sup>6</sup>Dep. of Phys. Univ. of Tokyo, <sup>7</sup>Dep. of Phys.  
Nagoya Univ., <sup>8</sup>Sch. of Eng. Univ. of Tokyo, <sup>9</sup>Dep. of Phys.  
Kyushu Univ.

**INTRODUCTION:** A large amount of CP violation (CPV) is necessary to solve matter and anti-matter asymmetry problem in the universe. However, the amount of CPV standard model predicts is too insufficient to explain it. The fact indicates that the new physics beyond standard model (BSM) exists and supplies the lack of CPV. The neutron intrinsic electric dipole moment (nEDM) is sensitive to CPV that BSM provides. Therefore, we can effectively search BSM with precise nEDM measurement.

The nEDM can be obtained from the ultracold neutron (UCN) spin precession in a storage container under homogeneous electric and magnetic fields. In the experiment, the loss of UCNs and their polarization occur due to interaction between UCNs and wall material, which make statistical precision worse. It is therefore important to develop new wall material with low loss probabilities. On the other hand, in the case that UCNs are transported from a pulsed UCN source, by decelerating fast UCNs and/or by accelerating slow UCNs properly, these UCNs can be focused on a storage container at the same time, which achieves drastic improvement of statistical precision [1]. However, if diffuse scattering induced by rough wall arises, the degree of improvement decreases. It is hence also important to develop a wall material with as smooth surfaces as neutron mirrors have.

**Ni-Mo FABRICATION WITH VACUUM EVAPORATED MACHINE:** Nickel-Molibdenum alloy (NiMo) of 15 weight percent and 9.1 g/cm<sup>3</sup> is known as one of the promising low loss materials. We fabricated test samples made of NiMo with KURRI vacuum evaporated apparatus and aimed for 100 nm thickness on SUS304 and Si-wafer substrates.

**RESULT AND CONSIDERATION:** We succeeded in NiMo film deposition itself. However, two undesirable features appeared as follows:

- (1) The densities of test samples were only 6.3 to 6.6 g/cm<sup>3</sup> by measuring XRR, which is far less than expected value, 9.1 g/cm<sup>3</sup>. Hence, our deposited NiMo film cannot be used as a wall material for nEDM.
- (2) In this fabrication, a bumping phenomenon could not be suppressed. Consequently, these surfaces were so rough that it could not be used as neutron mirrors.

The facts of (1) and (2) help us to understand what phenomenon occurred while NiMo ingot evaporating. These are as follows:

- (a) There is a possibility that NiMo ingot material included gasses and it caused bumping phenomenon of (2). If it true, gasses could also affect the density decrease of (1).
- (b) The deposited NiMo films preserve the nature of Ni-Mo alloy; Otherwise, the density of test samples should close to the one expected for Ni, 8.9 g/cm<sup>3</sup>, because the Ni vapor pressure is 10<sup>5</sup> times higher than Mo at 2000 K.
- (c) In spite of (b), the vapor pressure of NiMo alloy was quite low. Probably, NiMo vapor was not efficiently transported at substrates from evaporation source position, which could cause the density decrease of (1).
- (d) There is a possibility that the crystal structure of the deposited NiMo films varied from that of NiMo ingot. If it true, it could affect the density decrease of (1).

(a), (b), (c) and (d) give us quite an important information for next desirable fabrication test with vacuum evaporation deposition. First, we should use degassed NiMo ingot to solve the problem of (a). Second, to compensate the shortage of NiMo vapor pressure ((b) and (c)), a next vacuum evaporated deposition should be conducted by attracting ionized NiMo vapor to substrates with a bias voltage. Third, to avoid structure change of (d), Ni and Mo are evaporated simultaneously so that the composition of deposited NiMo film becomes 15 weight percent and 9.1 g/cm<sup>3</sup>.

**SUMMARY:** The material with low loss probabilities and smooth surfaces is desired for nEDM experiment. NiMo of 15 weight percent and 9.1 g/cm<sup>3</sup> is known as one of the promising low loss materials. We therefore fabricated test samples using NiMo ingot with KURRI vacuum evaporated apparatus. Although we succeeded in NiMo film deposition itself, the densities of test samples were only 6.3 to 6.6 g/cm<sup>3</sup>, and these surfaces were too rough to use neutron mirrors. To solve these problems, it is desirable that next fabrication with vacuum evaporation deposition should be performed using two evaporation source of degassed Ni and Mo ingot, and by attracting ionized NiMo vapor to substrates with a bias voltage.

#### REFERENCES:

- [1] Y. Arimoto *et al.*, Phys. Rev. A86 (2012) 023843.

**II. PUBLICATION LIST**  
**(APRIL 2014 – MARCH 2015)**

## 1. Slow Neutron Physics and Neutron Scattering

### Papers

Distinct Features of the Histone Core Structure in Nucleosomes Containing the Histone H2A.B Variant  
M. Sugiyama, Y. Arimura, K. Shirayama, R. Fujita, Y. Oba, N. Sato, R. Inoue, T. Oda, M. Sato, R. K. Heenan and H. Kurumizaka

Biophysical Journal, **106** (2014) 2206-2213.

A Novel Magnet Design Using Coated Conductor for Spiral Sector FFAG Accelerators

K. Goda, N. Amemiya, T. Nakamura, Y. Mori, T. Ogitsu, T. Kurusu and M. Yoshimoto  
IEEE TRANSACTIONS ON APPLIED SUPERCONDUCTIVITY, **24** (2014) 4402605.

Conformational Characterization of a Protein Complex Involving Intrinsically Disordered Protein by Small-angle Neutron Scattering Using the Inverse Contrast Matching Method: a Case Study of Interaction Between  $\alpha$ -synuclein and PbaB Tetramer as a Model Chaperone

M. Sugiyama, H. Yagi, T. Yamaguchi, K. Kumoi, M. Hirai, Y. Oba, N. Sato, L. Porcar, A. Martel and K. Kato  
J. Appl. Crystallogr., **47** (2014) 430-435.

Development of Highly-mechanically Polished Metal-substrate for Neutron Supermirrors

S. Takeda, J. Guo, S. Morita, H. Ono, T. Oda, J. Kato, H. Sato, M. Hino, Y. Yamagata and M. Furusaka  
J. Phys. Conf. Ser., **528** (2014) 12011-6.

Production of Ultra cold Neutrons by a Doppler Shifter with Pulsed Neutrons at J-PARC

K. Mishima, S. Imajo, M. Hino, T. Ino, Y. Iwashita, R. Katayama, M. Kitaguchi, T. Oda, H. M. Shimizu, M. Utsuro, S. Yamashita and T. Yoshioka  
J. Phys. Conf. Ser., **528** (2014) 12030-8.

Temperature Dependence of the Nanostructure in a PbSe–ZnSe Composite thin Film

Y. Oba, S. Abe, M. Ohnuma, N. Sato and M. Sugiyama  
J. Phys. D: Appl. Phys., **47** (2014) 6.

New Fabrication Method for an Ellipsoidal Neutron Focusing Mirror with a Metal Substrate

J. Guo, S. Takeda, S. Morita, M. Hino, T. Oda, J. Kato, Y. Yamagata and M. Furusaka  
Opt. Express., **22** (2014) 24666-24677.

Observation of the Spatial Distribution of Gravitationally Bound Quantum States of Ultracold Neutrons and Its Derivation Using the Wigner Function

G. Ichikawa, S. Komamiya, Y. Kamiya, Y. Minami, M. Tani, P. Geltenbort, K. Yamamura, M. Nagano, T. Sanuki, S. Kawasaki and M. Hino  
Phys. Rev. Lett., **112** (2014) 71101.

Distribution of Glass Transition Temperature in Multilayered Poly (Methyl Methacrylate) Thin Film Supported on a Si Substrate as Studied by Neutron Reflectivity

R. Inoue, M. Nakamura, K. Matsui, T. Kanaya, K. Nishida and M. Hino  
Phys. Rev. E, **88** (2014) 32601.

Numerical Simulation of BL06 Neutron Beamline for "VIN ROSE" at J-PARC/MLF

T. Oda, M. Hino, M. Kitaguchi, Y. Kawabata, N. L. Yamada and H. Seto  
Progress in Nuclear Science and Technology, **4** (2014) 214-217.

Structure of Silver Bromide Doped Chalco Genide Glasses

Y. Onodera, T. Usuki, T. Nasu and S. Kohara

Solid State Ionics, **262** (2014) 469-471.

## Books

Hemoglobin (Crystallography in Japan (II)) (in Japanese)

Y. Morimoto

Crystallographic Society of Japan, (2014).

## Reviews

Structural Study of Amorphous and Nano-crystalline Materials by Neutron Scattering (in Japanese)

T. Fukunaga

HAMON, **24** (2014) 94-99.

## 2. Nuclear Physics and Nuclear Data

### Papers

The Influence of p53 Status in Glioblastoma on the Effects of Boron Neutron Capture Therapy

K. Seki, Y. Kinashi and S. Takahashi

Anticancer Res., **35** (2015) 169-174.

A Nuclear Data Project on Neutron Capture Cross Sections of Long-Lived Fission Products and Minor Actinides

M. Igashira, T. Katabuchi, H. Harada, S. Nakamura, A. Kimura, N. Iwamoto, J. Hori and Y. Kiyonagi

Nucl. Data Sheets, **118** (2014) 72-77.

Cross Section Measurement of  $^{237}\text{Np}(n, g)$  at J-PARC/MLF/ANNRI

K. Hirose, K. Furutaka, K. Y. Hara, H. Harada, J. Hori, M. Igashira, T. Kamiyama, T. Katabuchi, A. Kimura, T. Kin, F. Kitatani, Y. Kiyonagi, M. Koizumi, M. Mizumoto, S. Nakamura, M. Oshima and Y. Toh

Nucl. Data Sheets, **119** (2014) 48-51.

Capture Cross-section Measurement of  $^{241}\text{Am}(n, g)$  at J-PARC/MLF/ANNRI

H. Harada, M. Ohta, A. Kimura, K. Furutaka, K. Hirose, K. Y. Hara, T. Kin, F. Kitatani, M. Koizumi, S. Nakamura, M. Oshima, Y. Toh, M. Igashira, T. Katabuchi, M. Mizumoto, K. Kino, Y. Kiyonagi, T. Fujii, S. Fukutani, J. Hori and K. Takamiya

Nucl. Data Sheets, **119** (2014) 61-64.

Measurements of Capture Gamma Rays from the Neutron Resonances of  $^{74}\text{Se}$  and  $^{77}\text{Se}$  at J-PARC/MLF/ANNRI

J. Hori, H. Yashima, S. Nakamura, K. Furutaka, K. Y. Hara, H. Harada, K. Hirose, A. Kimura, F. Kitatani, M. Koizumi, M. Oshima, Y. Toh, M. Igashira, T. Katabuchi, M. Mizumoto, T. Kamiyama, K. Kino and Y. Kiyonagi

Nucl. Data Sheets, **119** (2014) 128-131.

Measurement of Capture Gamma Rays from  $^{99}\text{Tc}$  Neutron Resonances at the J-PARC/ANNRI

K. Kino, F. Hiraga, T. Kamiyama, Y. Kiyonagi, H. Harada, K. Y. Hara, K. Hirose, A. Kimura, F. Kitatani, S. Nakamura, M. Igashira, T. Katabuchi, M. Mizumoto and J. Hori

Nucl. Data Sheets, **119** (2014) 140-142.

Cross Section Measurements of the Radioactive  $^{107}\text{Pd}$  and Stable  $^{105}, ^{108}\text{Pd}$  Nuclei at J-PARC/MLF/ANNRI

S. Nakamura, A. Kimura, F. Kitatani, M. Ohta, K. Furutaka, S. Goko, K. Y. Hara, H. Harada, K. Hirose, T. Kin, M. Koizumi, M. Oshima, Y. Toh, K. Kino, F. Hiraga, T. Kamiyama, Y. Kiyonagi, T. Katabuchi, M. Mizumoto, M. Igashira, J. Hori, T. Fujii, S. Fukutani and K. Takamiya

Nucl. Data Sheets, **119** (2014) 143-146.

Measurements of Neutron Capture Cross Sections of  $^{112}\text{Sn}$  and  $^{118}\text{Sn}$  with J-PARC/MLF/ANNRI

A. Kimura, K. Hirose, S. Nakamura, H. Harada, K. Y. Hara, J. Hori, M. Igashira, T. Kamiyama, T. Katabuchi, K. Kino, F. Kitatani, Y. Kiyanagi, M. Koizumi, M. Mizumoto and Y. Toh  
Nucl. Data Sheets, **119** (2014) 150-153.

Measurements of Cross Sections for Neutron-induced Reactions on Chromium and Yttrium Targets at 197 MeV  
S. Sekimoto

Nucl. Data Sheets, **119** (2014) 197-200.

A New Signal Processing Technique for Neutron Capture Cross Section Measurement Based on Pulse Width Analysis

T. Katabuchi, T. Matsushashi, K. Terada, M. Mizumoto, K. Hirose, A. Kimura, K. Furutaka, K. Y. Hara, H. Harada, J. Hori, M. Igashira, T. Kamiyama, F. Kitatani, K. Kino, Y. Kiyanagi, M. Koizumi, S. Nakamura, M. Oshima and Y. Toh

Nucl. Data Sheets, **119** (2014) 398-400.

Measurements of High-Energy Excited States and  $\gamma$ -Rays of Fission Products with a  $4\pi$  Clover Detector

Y. Shima, Y. Kojima, H. Hayashi, A. Taniguchi and M. Shibata

Nucl. Data Sheets, **120** (2014) 30-32.

Half-Life Measurements of Excited Levels in Fission Products around Mass Number 150

Y. Kojima, Y. Shima, H. Hayashi, A. Taniguchi and M. Shibata

Nucl. Data Sheets, **120** (2014) 52-55.

Energy Resolution of Pulsed Neutron Beam Provided by the ANNRI Beamline at the J-PARC/MLF

K. Kino, M. Furusaka, F. Hiraga, T. Kamiyama, Y. Kiyanagi, K. Furutaka, S. Goko, K. Y. Hara, H. Harada, M. Harada, K. Hirose, M. Ooi, M. Ohta, M. Oshima, Y. Toh, M. Igashira, T. Katabuchi, M. Mizumoto and J. Hori

Nucl. Instrum. Methods, **A 736** (2014) 66-74.

Pulse-width Analysis for Neutron Capture Cross-section Measurement Using an NaI(Tl) Detector

T. Katabuchi, T. Matsushashi, K. Terada, T. Arai, K. Furutaka, K. Y. Hara, H. Harada, K. Hirose, J. Hori, M. Igashira, T. Kamiyama, A. Kimura, K. Kino, F. Kitatani, Y. Kiyanagi, M. Koizumi, M. Mizumoto, S. Nakamura, M. Oshima and Y. Toh

Nucl. Instrum. Methods. Phys. Res. A, **764** (2014) 369-377.

Radiation Shielding Experiments for Composites Based on Pb-shot and Boride

J. Hori, H. Yashima, K. Miyamoto, S. Okuda, M. Ishihara, S. Kito and M. Atarashi

Progress in Nuclear Science and Technology, **4** (2014) 635-638.

Measurements of the Neutron Activation Cross Sections for Bi and Co at 386 MeV

H. Yashima, S. Sekimoto, K. Ninomiya, Y. Kasamatsu, T. Shima, N. Takahashi, A. Shinohara, H. Matsumura, D. Satoh, Y. Iwamoto, M. Hagiwara, K. Nishiizumi, M.W. Caffee and S. Shibata

Radiat. Prot. Dosimetry, **161 No. 1-4** (2014) 139-143.

New Application for Boron Neutron Capture Therapy

M. Suzuki

Radioisotopes, **64** (2015) 59-66.

## Proceedings

Measurement of Neutron Capture Cross Section of  $^{232}\text{Th}$  in the Low Energy Region

J. Hori, T. Sano, Y. Takahashi, H. Unesaki and K. Nakajima

PHYSOR2014, Kyoto, Japan (Sept. 28- Oct. 3, 2014) 1.

Survey on Effect of Crystal Texture of Beryllium on Total Cross-Section to Improve Neutronic Evaluation in JMTR  
N. Takemoto, T. Imaizumi, N. Kimura, K. Tsuchiya, J. Hori, T. Sano and K. Nakajima  
PHYSOR2014, Kyoto, Japan (Sept. 28- Oct. 3, 2014) 1.

Development of a New Type of Manganese Bath for Determination of Neutron Emission Rate of a Neutron Source  
T. Matsumoto, H. Harano, A. Masuda and J. Hori  
2014 IEEE Nuclear Science Symposium, Seattle, USA (Nov. 8-15, 2014) 1-5.

Development of a Neutron Transport System for Neutron Resonance Densitometry  
F. Kitatani, M. Koizumi, H. Tsuchiya, J. Takamine, M. Kureta, H. Harada, M. Seya, J. Hori and T. Sano  
Proc. of the 49th KURRI Scientific Meeting, KURRI (Jan. 28-29, 2015) 41.

## Reviews

Kyoto University Research Reactor Institute Electron Linear Accelerator Neutron Source (in Japanese)  
J. Hori, T. Sano and Y. Takahashi  
Isotope News, **717** (2014) 38-40.

## 3. Reactor Physics and Reactor Engineering

### Papers

A New Concept of Monte Carlo Kinetics Parameter Calculation Using Complex-valued Perturbation  
T. Yamamoto and H. Sakamoto  
Ann. Nucl. Energy., **71** (2014) 480-488.

Optimised Mounting Conditions for Poly (Ether Sulfone) in Radiation Detection  
H. Nakamura, Y. Shirakawa, N. Sato, T. Yamada, H. Kitamura and S. Takahashi  
Int. J. Rad. Appl. Instrum. A, **91** (2014) 131.

Measurements of Turbulence in a Liquid-metal Two-phase Flow by Using Miniture Electro-magnetic Probe  
G. Ariyoshi, Y. Asai, D. Ito, Y. saito and K. Mishima  
Japanese Journal of Multiphase Flow, **27-5** (2014) 615-622. (in Japanese)

Heat Transfer Study for ADS Solid Target - Surface Wettability and its Effect on a Boiling Heat Transfer-  
D. Ito, K. Hase and Y. Saito  
Nuclear Backend and Transmutation Technology for Waste Disposal: Beyond the Fukushima Accident,  
**ISBN 978-4-431-55110-2** (2014) 95-105.

Experimental Study of Flow Structure and Turbulent Characteristics in Lead-bismuth Two-phase Flow  
G. Ariyoshi, D. Ito and Y. Saito  
Nuclear Backend and Transmutation Technology for Waste Disposal: Beyond the Fukushima Accident,  
**ISBN 978-4-431-55110-2** (2014) 107-115.

Heterogeneity Effect on Neutron Shielding in Borated Concrete and Monte Carlo-Based Cross Section  
Homogenization Method for Particle Dispersed Media  
T. Yamamoto  
Progress in Nuclear Science and Technology, **4** (2014) 404-407.

Undoped Poly (Phenyl Sulfone) for Radiation Detection  
H. Nakamura, Y. Shirakawa, N. Sato, H. Kitamura and S. Takahashi  
Radiat. Meas., **73** (2015) 14.

Implications for Quinone Cofactor Biogenesis in Amine-oxidizing Enzymes

A. Kita, M. Mure and K. Miki

SPring-8/SACLA Research Report, **SectionA, Vol.3, No. 1** (2015) 1-5.

## Proceedings

Implementation of Two-group Interfacial Area Transport in a One-dimensional Computational Environment

J.P. Schlegel, T. Hibiki, M. Ishii, X. Shen and S. Appathurai

Proceeding of International Topical Meeting on Advances in Thermal Hydraulics 2014 (ATH'14)

Reno, Nevada, USA, Paper No.: 042 (Jun. 15-19, 2014) 555-567.

Experimental Benchmarks on the Thorium-Loaded Accelerator-Driven System at the Kyoto University Critical Assembly

C. H. Pyeon

Technical Mtg. (TM) of “Collaborative Work on Accelerator Driven Subcritical Systems (ADS) and Use of Low-Enriched Uranium (LEU) in ADS” (invited), IAEA, Hefei, China (Sept. 8-12, 2014).

Preparation of Minor Actinides Irradiation in Accelerator-Driven System with 100 MeV Protons at Kyoto University Critical Assembly

T. Yagi, C. H. Pyeon, Y. Takahashi and K. Nakajima

Proc. Actinide and Fission Product Partitioning and Transmutation, Thirteenth Information and Exchange Mtg (13IEMPT), OECD/NEA, Seoul, Korea (Sept. 23-26, 2014).

Investigation on Subcriticality Measurement Using Inherent Neutron Source in Nuclear Fuel

T. Shiozawa, T. Endo, A. Yamamoto, C.H. Pyeon and T. Yagi

PHYSOR2014, Kyoto, Japan (Sept. 28- Oct. 3, 2014).

Concept of Capture Credit Based on Neutron Induced Gamma Ray Spectroscopy

Y. Nauchi, H. Ohta, H. Unesaki, T. Sano and T. Yagi

PHYSOR2014, Kyoto, Japan (Sept. 28- Oct. 3, 2014) 1.

Neutronic Characteristics of Solid Pb-Bi Target in Accelerator-Driven System at Kyoto University Critical Assembly

C. H. Pyeon, H. Nakano, M. Yamanaka, T. Yagi and T. Misawa

PHYSOR2014, Kyoto, Japan (Sept. 28- Oct. 3, 2014).

Monte Carlo Perturbation Analysis on Isothermal Temperature Reactivity Coefficient of Light-Water Moderated and Reflected Critical Assembly

B. K. Jeon, H. J. Shim and C. H. Pyeon

PHYSOR2014, Kyoto, Japan (Sept. 28- Oct. 3, 2014).

Measurement of Subcriticality Using Delayed Neutron Source Combined with Pulsed Neutron Accelerator

T. Misawa, T. Yagi, and C. H. Pyeon

PHYSOR2014, Kyoto, Japan (Sept. 28- Oct. 3, 2014).

Measurement of Large Negative Reactivity of an Accelerator-Driven System in the Kyoto University Critical Assembly

A. Sakon, K. Hashimoto, M. A. Maarof, M. Kawasaki, W. Sugiyama, C. H. Pyeon, T. Sano, T. Yagi and T. Ohsawa

PHYSOR2014, Kyoto, Japan (Sept. 28- Oct. 3, 2014).

Accuracy of Thorium-Loaded Accelerator-Driven System at Kyoto University Critical Assembly

M. Yamanaka, C. H. Pyeon, T. Yagi and T. Misawa

PHYSOR2014, Kyoto, Japan (Sept. 28- Oct. 3, 2014).

Analysis of Integral Experiment for Thorium Fuel Cycle at Kyoto University Critical Assembly

Y. Takahashi, T. Sano, J. Hori, H. Unesaki and K. Nakajima

PHYSOR2014, Kyoto, Japan (Sept. 28- Oct. 3, 2014).

Void Transit Time Calculations by Neutron Noise of Propagation Perturbation Using Complex-valued Weight Monte Carlo

T. Yamamoto

PHYSOR2014, Kyoto, Japan (Sept. 28- Oct.3, 2014).

Power Spectral Analysis for a Subcritical Reactor System Driven by a Pulsed Spallation Neutron Source

A. Sakon, S. Hohara, W. Sugiyama, K. Hashimoto, C. H. Pyeon, T. Sano and T. Yagi

PHYSOR2014, Kyoto, Japan (Sept. 28- Oct.3, 2014) 1.

Statistical Error Estimation Using Bootstrap Method for the Feynman- $\alpha$  method

T. Endo, T. Shiozawa, A. Yamamoto, C.H. Pyeon and T. Yagi

ANS 2014 Winter Meeting, Anaheim, CA, USA (Nov. 9-13, 2014) 1204-1207.

Study on Boiling Heat Transfer for ADS Solid Target - Surface Wettability & Micro-Bubble Emission Boiling -  
D. Ito, M. Kato and Y. Saito

9<sup>th</sup> Korea-Japan Symposium on Nuclear Thermal Hydraulics and Safety (NTHAS-9),

Buyeo, Korea (Nov. 16-19, 2014) 49.

Local Measurements of 3-D Bubble Velocity Vector, Bubble Diameter and Interfacial Area Concentration in a Vertical Large Diameter Square Duct

X. Shen, T. Hibiki, H. Sun and H. Nakamura

Proceeding of the 9<sup>th</sup> Japan-Korea Symposium on Nuclear Thermal Hydraulics and Safety (NTHAS-9),

Buyeo, Korea (Nov. 16-19, 2014) N9P0011.

## Books

Frontiers and Progress in Multiphase Flow I (in Japanese)

(Chapter 2 Flow Characteristics and Void Fraction Prediction in Large Diameter Pipes)

X. Shen, JP Schlegel, P. Joshua, S. Chen, S. Rassame, MJ. GriffithsMatthew, T. Hikiki and M. Ishii

Springer, (2014).

## Others

Increment of Capacity of Casks for LWR Spent Fuel Transport (3) Demonstration of Quantification of Neutron Leakage from a Fuel Assembly

Y. Nauchi, T. Kameyama, H. Unesaki, T. Misawa, T. Sano and T. Yagi

CRIEPI Research Report, **L11004** (2012).

## 4. Material Science and Radiation Effects

### Papers

The Spin State of Iron in Fe<sup>3+</sup>-bearing Mg-perovskite and Its Crystal Chemistry at High Pressure

I. Mashino, E. Ohtani, N. Hirao, T. Mitsui, R. Masuda, M. Seto, T. Sakai, S. Takahashi and S. Nakano

Am. Mineral., **99** (2014) 1555-1561.

Frequency Domain Monte Carlo Simulation Method for Cross Power Spectral Density Driven by Periodically Pulsed Spallation Neutron Source Using Complex-valued Weight Monte Carlo

T. Yamamoto

Ann. Nucl. Energy., **63** (2014) 711-720.



A Neutron Dynamic Therapy with a Boron Tracedrug UTX-51 Using a Compact Neutron Generator  
H. Hori, R. Tada, Y. Uto, E. Nakata, T. Morii and K. Masuda  
*Anticancer Res.*, **34** (2014) 4557-4560.

Positron Annihilation Study for Enhanced Nitrogen-vacancy Center Formation in Diamond by Electron Irradiation at 77K

Z. Tang, T. Chiba, Y. Nagai, K. Inoue, T. Toyama and M. Hasegawa  
*Appl. Phys. Lett.*, **104** (2014) 72101.

Synchrotron Radiation-Based Mössbauer Spectra of  $^{174}\text{Yb}$  Measured with Internal Conversion Electrons  
R. Masuda, Y. Kobayashi, S. Kitao, M. Kurokuzu, M. Saito, Y. Yoda, T. Mitsui, F. Iga and M. Seto  
*Appl. Phys. Lett.*, **104** (2014) 82411.

Dose-rate Effect was Observed in T98G Glioma Cells Following BNCT

Y. Kinashi, K. Okumura, Y. Kubota, E. Kitajima, R. Okayasu, K. Ono and S. Takahashi  
*Appl. Radiat. Isot.*, **88** (2014) 81-85.

Facile One-Pot Synthesis of [1, 2, 3]Triazolopyridines from 2-Acylpyridines by Copper(II)-Catalyzed Oxidative N-N Bond Formation

T. Hirayama, S. Ueda, T. Okada, N. Tsurue, K. Okuda and H. Nagasawa  
*Chem. Eur. J.*, **20** (2014) 4156.

Extranuclear Dynamics of  $^{111}\text{Ag}(\rightarrow^{111}\text{Cd})$  Doped in AgI Nanoparticles

W. Sato, R. Mizuuchi, N. Irioka, S. Komatsuda, S. Kawata, A. Taoka and Y. Ohkubo  
*Chem. Phys. Lett.*, **609** (2014) 104-107.

Predominance of Covalency in Water-Vapor-Responsive MMX-Type Chain Complexes Revealed by  $^{129}\text{I}$  Mössbauer Spectroscopy

H. Iguchi, S. Kitao, M. Seto, S. Takaishi and M. Yamashita  
*Dalton Trans.*, **43** (2014) 8767-8773.

Slow Dynamics of Supercooled Liquid Revealed by Rayleigh Scattering of Mössbauer Radiation Method in Time Domain

M. Saito, A. Battistoni, S. Kitao, Y. Kobayashi, M. Kurokuzu, Y. Yoda and M. Seto  
*Hyperfine Interact.*, **226** (2014) 629-636.

Development of  $^{125}\text{Te}$  Synchrotron-Radiation-Based Mössbauer Spectroscopy

M. Kurokuzu, S. Kitao, Y. Kobayashi, M. Saito, R. Masuda, T. Mitsui, Y. Yoda and M. Seto  
*Hyperfine Interact.*, **226** (2014) 687-691.

Boron Neutron Capture Therapy for Advanced Salivary Gland Carcinoma in Head and Neck

T. Aihara, N. Morita, N. Kamitani, H. Kumada, K. Ono, J. Hiratsuka and T. Harada  
*Int. J. Clin. Oncol.*, **19** (2014) 437-444.

Effects of Mg Substitution on Crystal Structure and Hydrogenation Properties of  $\text{Pr}_{1-x}\text{Mg}_x\text{Ni}_3$

K. Iwase, N. Terashita, K. Mori, S. Tashiro, H. Yokota and T. Suzuki  
*Int. J. Hydrogen Energy*, **39** (2014) 12773-12777.

Formation Energy of Oxygen Vacancies in ZnO Determined by Investigating Thermal Behavior of Al and In Impurities

S. Komatsuda, W. Sato and Y. Ohkubo  
*J. Appl. Phys.*, **116** (2014) 183502.

Relaxation Transition in Glass-forming Polybutadiene as Revealed by Nuclear Resonance X-ray Scattering

T. Kanaya, R. Inoue, M. Saito, M. Seto and Y. Yoda

J. Chem. Phys., **140** (2014) 144906.

Spatial Correlation between Chemical and Topological Defects in Vitreous Silica: Uvresonance Raman Study

M. Saito, F. D'Amico, F. Bencivenga, R. Cucini, A. Gessini, E. Principi and C. Masciovecchio

J. Chem. Phys., **140** (2014) 244505.

Selective Hg(II) Adsorption from Aqueous Solutions of Hg(II) and Pb(II) by Hydrolyzed Acrylamide-grafted PET Films

N. Rahman, N. Sato, M. Sugiyama, Y. Hidaka, H. Okabe and K. Hara

J. Environ. Sci. Health. A, **49** (2014) 798-806.

Early Stage Irradiation Effects in F82H Model Alloys

S.S. Huang, X.Q. Pan, K. Sato, Q. Xu and T. Yoshiie

J. Nucl. Mater., **449** (2014) 248-251.

A replica Technique for Extracting Precipitates from Neutron-irradiated or Thermal-aged Vanadium Alloys for TEM Analysis

K. Fukumoto and M. Iwasaki

J. Nucl. Mater., **449** (2014) 315-319.

Studies on ADS as a neutron source at the Kyoto University Research Reactor Institute

T. Yoshiie, K. Fukumoto, Y. Ishi, D. Ito, Y. Kuriyama, T. Misawa, Y. Mori, T. Nagasaka, K. Nakajima, Y. Oki,

C.H. Pyeon, Y. Saito, K. Sato, X.Z. Shen, S. Shibata, T. Uesugi and Q. Xu

J. Nucl. Mater., **450** (2014) 16-19.

Positron Annihilation Spectroscopy of Ferritic/Martensitic Steels F82H and T91 Irradiated with Protons and Neutrons at PSI

K. Sato, S. Kawamoto, K. Ikemura, V. Krsjak, C. Vieh, R. Brun, Q. Xu, T. Yoshiie and Y. Dai

J. Nucl. Mater., **450** (2014) 59-63.

Positron Annihilation and TEM Studies in Ion Irradiated Fe and Fe-Cr Model Alloys of Ferritic/Martensitic Steel

Q. Xu, Y. Sugiura, X.Q. Oan, K. Sato, T. Yoshiie, H. Tsuchida and A. Itoh

J. Nucl. Mater., **455** (2014) 122-125.

Structural Origin of Ionic Conductivity for  $\text{Li}_7\text{P}_3\text{S}_{11}$  Metastable Crystal by Neutron and X-ray Diffraction

Y. Onodera, K. Mori, T. Otomo, H. Arai, Y. Uchimoto, Z. Ogumi and T. Fukunaga

J. Phys. Conf. Ser., **502** (2014) 12021.

Formation of Cu Precipitates in A High-Energy-Particle-Irradiated and Thermally Aged Fe-0.6Cu Alloy

K. Sato, Q. Xu, X.Z. Cao, P. Zhang, B.Y. Wang and H. Tsuchida

J. Phys. Conf. Ser., **505** (2014) 12011.

Positron Beam Facility at Kyoto University Research Reactor

Q. Xu, K. Sato, T. Yoshiie, T. Sano, H. Kawabe, Y. Nagai, K. Nagumo, K. Inoue, T. Toyama, N. Oshima,

A. Kinomura and Y. Shirai

J. Phys. Conf. Ser., **505** (2014) 12030.

Thermal Stability of Locally-Associated Al and In Impurities in Zinc Oxide

S. Komatsuda, W. Sato and Y. Ohkubo

J. Radioanal. Nucl. Chem., (2014) 1249-1252.

- Hierarchical Structure–property Relationships in Graft-type Fluorinated Polymer Electrolyte Membranes Using Small- and Ultrasmall-angle X-ray Scattering Analysis  
T. D. Tap, S. Sawada, S. Hasegawa, K. Yoshimura, Y. Oba, M. Ohnuma, Y. Katsumura and Y. Maekawa  
*Macromolecules*, **47** (2014) 2373-2383.
- Comparison between In-Situ and Post-Irradiation Cyclic Deformation Structures in Ni by 150 MeV Proton Irradiation  
T. Yoshiie, K. Sato, Q. Xu, Y. Ishi, T. Uesugi, Y. Kuriyama and Y. Mori  
*Mater. Trans.*, **55** (2014) 434-437.
- Surface Observation of LaNi<sub>5</sub> under Deuterium Atmosphere Using Small-Angle Neutron Scattering  
K. Mori, K. Iwase, Y. Oba, T. Fukunaga and M. Sugiyama  
*Mater. Trans.*, **55** (2014) 1643-1646.
- High-pressure Radiative Conductivity of Dense Silicate Glasses with Potential Implications for Dark-magmas  
M. Murakami, A. F. Goncharov, N. Hirao, R. Masuda, T. Mitsui, S-M. Thomas and C. R. Bina  
*Nat. Commun.*, **5** (2014) 5428.
- Positron Annihilation Study of Vacancy-Type Defects in Fast-Neutron-Irradiated MgO/nAl<sub>2</sub>O<sub>3</sub>  
A.Z.M.S. Rahman, Z.X. Li, X.Z. Cao, B.Y. Wang, L. Wei, Q. Xu and K. Atobe  
*Nucl. Instr. & Meth. Phys. Res. B*, **335** (2014) 70-73.
- Neutron-enhanced Annealing of Ion-implantation Induced Damage in Silicon Heated by Nuclear Reactions  
A. Kinomura, T. Yoshiie, A. Chayahara, Y. Mokuno, N. Tsubouchi, Y. Horino, Q. Xu, K. Sato, K. Yasuda and R. Ishigami  
*Nucl. Instrum. Methods. Phys. Res. B*, **334** (2014) 48-51.
- Material Activation Benchmark Experiments at the NuMI Hadron Absorber Hall in Fermilab  
H. Matsumura, N. Matsuda, Y. Kasugai, A. Toyoda, H. Yashima, S. Sekimoto, H. Iwase, K. Oishi, Y. Sakamoto, H. Nakashima, A. Leveling, D. Boehnlein, G. Lauten, N. Mokhov and K. Vaziri  
*Nuclear Data Sheets*, **120** (2014) 219-221.
- Hydrogen Trapping under the Effect of W-C Mixed Layers  
N. Liu, J. Huang, K. Sato, Q. Xu, L. Q. Shi and X. Y. Wang  
*Nucl. Fusion*, **54** (2014) 33013.
- Determination of Dynamical Parameters in Liquids by Homodyne Transient Grating Spectroscopy at Large Angles  
R. Cucini, A. Battistoni, A. Gessini, F. Bencivenga, E. Principi, M. Saito, F. D'Amico, R. Sergo and C. Masciovecchio  
*Optics Letters*, **39** (2014) 5110-5113.
- Detection of Boron-Containing Amino Acids and Peptides Using Fluorescent Boron-Sensor  
Y. Hattori, M. Ishimura, Y. Ohta, H. Takenaka and M. Kirihata  
*Peptide Science 2014*, (2014) 295.
- Studies of Interaction between He and Elements with Mass Number 140 in Fe by Time-Differential Perturbed-Angular-Correlation Measurements  
Y. Ohkubo, A. Taniguchi, Q. Xu, M. Tanigaki and K. Sato  
*Philos. Mag. Lett.*, **94** (2014) 470-477.
- Neutron-irradiation-induced Near-infrared Emission in Alpha-Al<sub>2</sub>O<sub>3</sub>  
A. Z. M. S. Rahman, X. Cao, L. Wei, B. Wang, H. Ji, T. Yang, Q. Xu and K. Atobe  
*Philos. Mag. Lett.*, **94** (2014) 211-216.

Detection of Spinel  $\text{ZnIn}_2\text{O}_4$  Formed as Nanostructures in ZnO

W. Sato, S. Komatsuda, Y. Yamada and Y. Ohkubo

Phys. Rev. B, **90** (2014) 235204.

The Effect of hot DMSO Treatment on the  $\gamma$ -ray-induced Grafting of Acrylamide onto PET Films

N. Rahman, N. Sato, M. Sugiyama, Y. Hidaka, H. Okabe and K. Hara

Polym. J., **46** (2014) 412-421.

Research activities on JASMIN: Japanese and American Study of Muon Interaction and Neutron Detection

H. Nakashima, N.V. Mokhov, Y. Kasugai, N. Matsuda, Y. Iwamoto, Y. Sakamoto, D. Boehnlein, A. Leveling, K. Vaziri, R. Coleman, D. Jensen, E. Ramberg, A. Soha, T. Sanami, H. Matsumura, M. Hagiwara, A. Toyoda, H. Iwase, H. Hirayama, T. Nakamura, S. Sekimoto, H. Yashima, T. Kajimoto, N. Shigyo, K. Ishibashi, N. Nakao, N. Kinoshita, K. Oishi, H.S. Lee and K. Niita

Progress in Nuclear Science and Technology, **4** (2014) 191-196.

Novel Monolayer Shields of a Neutron Powder Diffractometer SPICA at BL09 of J-PARC

M. Kawai, M. Yonemura, S. Torii, T. Muroya, K. Mori, T. Fukunaga, K. Okuno, K. Takeda, K. Niita and T. Kamiyama

Progress in Nuclear Science and Technology, **4** (2014) 156-159.

Measurement and Analysis of Neutron and Photon dose Rate in Concrete Shield of 120-GeV Proton Accelerator Facility

K. Oishi, K. Kosako, Y. Kasugai, N. Matsuda, H. Yashima, S. Sekimoto, H. Matsumura, A. Toyoda, H. Iwase, N. Mokhov, A. Leveling, D. Boehnlein, K. Vaziri, H. Nakashima and Y. Sakamoto

Progress in Nuclear Science and Technology, **4** (2014) 197-200.

Activation Detector Measurements at the Hadron Absorber of the NuMI Neutrino Beamline at Fermilab

N. Matsuda, Y. Kasugai, H. Matsumura, H. Iwase, A. Toyoda, H. Yashima, S. Sekimoto, K. Oishi, Y. Sakamoto, H. Nakashima, T. Nakamura D. Boehnlein, G. Lauten, A. Leveling, N. Mokhov and K. Vaziri

Progress in Nuclear Science and Technology, **4** (2014) 337-340.

Radionuclides in the Cooling Water Systems for the NuMI Beamline and the Antiproton Production Target Station at Fermilab

H. Matsumura, S. Sekimoto, H. Yashima, A. Toyoda, Y. Kasugai, N. Matsuda, K. Oishi, K. Bessho, Y. Sakamoto, H. Nakashima, D. Boehnlein, G. Lauten, A. Leveling, N. Mokhov and K. Vaziri

Progress in Nuclear Science and Technology, **4** (2014) 372-375.

Comparison of Activity among Fluorescent Lamps and Light Emitting Diodes Lamps Exposed to Secondary Particles in Accelerator Rooms

A. Toyoda, H. Matsumura, K. Masumoto, S. Sekimoto, H. Yashima, N. Matsuda, Y. Kasugai, Y. Sakamoto, H. Nakashima, G. Lauten, A. Leveling, N. Mokhov, K. Vaziri, K. Oishi, M. Kuroyanagi, F. Nobuhara and K. Takahashi

Progress in Nuclear Science and Technology, **4** (2014) 384-387.

Reflectivity Enhancement in Titanium by Ultrafast XUV Irradiation

F. Bencivenga, E. Principi, E. Giangristostomi, R. Cucini, A. Battistoni, F. D. Amico, A. D. Cicco, S. D. Fonzo, A. Filipponi, A. Gessini, R. Gunnella, M. Marsi, L. Properzi, M. Saito and C. Masciovecchio

Sci. Rep., **4** (2014) 4952.

Neutron Diffraction Studies on Structural Effect for Ni-doping in  $\text{LiCo}_{1-x}\text{Ni}_x\text{O}_2$

D. S. Adipranoto, T. Ishigaki, A. Hoshikawa, K. Iwase, M. Yonemura, K. Mori, T. Kamiyama, Y. Morii and M. Hayash

Solid State Ionics, **262** (2014) 92-97.

Visualization of Conduction Pathways in a Lanthanum Lithium Titanate Superionic Conductor Synthesized by Rapid Cooling

K. Mori, S. Tomihira, K. Iwase and T. Fukunaga  
Solid. State. Ionics., **268** (2014) 76-81.

Advanced Biological Treatment of Groundwater with Elevated Concentration of Arsenic and Ammonium

Y. Fujikawa, P. D Hung, K. Furukawa and A. Hashiguchi  
The 20th Symposium on Soil and Groundwater Contamination and Remediation, **20** (2014) 136-140.

Elution Characteristics of Radioactive Materials in Heat-treated Soil (in Japanese)

M. Ikegami, Y. Takase, S. Fukutani, M. Yoneda, Y. Shimada and Y. Matsui  
The 20<sup>th</sup> Symposium on Soil and Groundwater Contamination and Remediation, **20** (2014) 545-547.

Measurement of Air dose Rates Over a Wide Area Around the Fukushima Dai-ichi Nuclear Power Plant Through a Series of Car-borne Surveys

M. Andoh, Y. Nakahara, S. Tsuda, T. Yoshida, N. Matsuda, F. Takahashi, S. Mikami, N. Kinouchi, T. Sato, M. Tanigaki, K. Takamiya, N. Sato, R. Okumura, Y. Uchihori and K. Saito  
J. Environ. Radioact., **139** (2015) 266-280.

<sup>235</sup>U/<sup>238</sup>U Isotopic Ratio in Plant Samples from Fukushima Prefecture

Y. Shibahara, T. Kubota, T. Fujii, S. Fukutani, T. Ohta, K. Takamiya, R. Okumura, S. Mizuno and H. Yamana  
J. Radioanal. Nucl. Chem., **303** (2015) 1421-1424.

<sup>57</sup>Fe Polarization-Dependent Synchrotron Mössbauer Spectroscopy Using a Diamond Phase Plate and an Iron Borate Nuclear Bragg Monochromator

T. Mitsui, Y. Imai, R. Masuda, M. Seto and K. Mibu  
J. Synchrotron Rad., **22** (2015) 427-435.

A Model Survey Meter Using Undoped Poly (Ether Sulfone)

H. Nakamura, Y. Shirakawa, M. Kanayama, N. Sato, H. Kitamura and S. Takahashi  
Nucl. Instrum. Methods. Phys. Res. A, **780** (2015) 127.

## Proceedings

Behavior of Cesium and Strontium in Waste Incineration

H. Aoki, K. Oshita, S. Fukutani, K. Shiota, T. Fujimori and M. Takaoka  
8th i-CIPEC, Hang Zhou, China (2014).

Observation of Multiferroicity in GaFeO<sub>3</sub> by Mössbauer Spectroscopy

S. Nakamura, Y. Kobayashi, S. Kitao, M. Seto and A. Fuwa  
Int. Conf. on Strongly Correlated Systems 2014 (J. Phys. Conf. Ser. 592), Grenoble, France (2014) 12122.

Comparison of Solvent Power of N-PD and 2-PD toward Stereoregular Isotactic PAN

M. Minagawa, M. Shimuzu, T. Katoh, N. Sato and T. Matsuyama  
The Fiber Society 2014 Spring Annual Meeting and Technical Conference, Liberec, Czech  
(May. 21-23, 2014) 107-108.

## Reviews

Structures and Ion Conduction Pathways of Amorphous Lithium Ion Conductors (in Japanese )

K. Mori, T. Fukunaga and Y. Onodera  
HAMON, **24** (2014) 267-272.

Metal Nano Particles Fabrication under High Energy Irradiation Fields (in Japanese)

F. Hori

Materials Science & Technology, **84** (2014) 50.

Numerical Investigation Suggested for Brilliancy of Jewels as Detection of Scattered Light; (1) Estimation of Cut Diamonds Considering Light Source and Observer (in Japanese )

A. Kawaguchi

Yamanashi-Kenma-Houshoku-Shinbun, **672** (2015) 6.

## 5. Geochemistry and Environmental Science

### Papers

Measurement of Large Negative Reactivity of an Accelerator-Driven System in the Kyoto University Critical Assembly

A. Sakon, K. Hashimoto, M. A. B. Maarof, M. Kawasaki, W. Sugiyama, C.H. Pyeon, T. Sano, T. Yagi and T. Ohsawa  
J. Nucl. Sci. Technol., **51** (2014) 116-126.

A Study on Redox Sensitive Elements in the Sediments at Dredged Trenches in Tokyo Bay by Instrumental Neutron Activation Analysis

T. Yamagata, K. Shozugawa, R. Okumura, K. Takamiya and M. Matsuo

J. Radioanal. Nucl. Chem., **303** (2015) 1179-1183.

Bacterial Diversity in Biological Filtration System for the Simultaneous Removal of Arsenic, Iron and Manganese from Groundwater

R. T. Chhetri, I. Suzuki, T. Fujita, M. Takeda, J. Koizumi, Y. Fujikawa, A. Minami, T. Hamasaki and M. Sugahara

J. Water. Environ. Technol., **12** (2014) 135-149.

Proposal of Simplified Strong Ground Motion Prediction Method for Synthetic Procedure Using Fault Model Reflecting Nonlinear Site Effect

T. Ikeda, K. Konagai, K. Kamae, K. Irikura, T. Kiyota and K. Meguro

Japan Society of Civil Engineers, **Vol.70, No. 4** (2014) 252-262.

Elution Characteristics of Cs and Sr in Heat-treated Soil (in Japanese)

M. Ikegami, Y. Takase, T. Kometani, M. Yoneda, Y. Shimada, Y. Matsui and S. Fukutani

Journal of Japan Society of Civil Engineers, Ser. G (Environmental Research), **70(7)** (2014) 203-208.

Change of Leaching Characteristics of Cs and Sr from Soil by Wet and Dry Cycles (in Japanese)

T. Kometani, M. Yoneda, Y. Shimada, Y. Matsui, S. Fukutani and M. Ikegami

The 20<sup>th</sup> Symposium on Soil and Groundwater Contamination and Remediation, **20** (2014) 652-656.

Stratigraphy of the Tetori Group and the Jinzu Group (new name) in Gifu and Toyama Prefectures, Central Japan (in Japanese)

M. Matsukawa, M. Fukui, Y. Ogawa, T. Tano, K. Koarai, H. Ohira and K. Hayashi

The Journal of the Geological Society of Japan, **120** (2014) 147-164.

Rapid Survey of Four Asp Isomers in Disease-Related Proteins by LC-MS Combined with Commercial Enzyme

H. Maeda, T. Takata, N. Fujii, H. Sakaue, S. Nirasawa, S. Takahashi, H. Sasaki and N. Fujii

Anal. Chem., **87** (2015) 561-568.

Tetrakis (p-carboranylthio- tetrafluorophenyl) Chlorin (TPFC): Application for Photodynamic Therapy and Boron Neutron Capture Therapy

R. Hiramatsu, S. Kawabata, H. Tanaka, Y. Sakurai, M. Suzuki, K. Ono, S. Miyatake, T. Kuroiwa, E. Hao, M. Graca and H. Vicente

J. Pharm. Sci., **104** (2015) 962-970.

## Proceedings

Slab-derived Noble Gases and Halogens with a Sedimentary Pore-fluid Signature

H. Sumino, M. Kobayashi, A. Shimizu, L. Jepson, D. Chavrit, C. Toyama, J. Kimura, Y. Muramatsu, R. Burgess and C.J. Ballentine

Geofluid-3: Nature and Dynamics of Fluids in Subduction Zones, Tokyo, Japan (2014) 3.

Elucidation of the Uptake Route of Radionuclides in Deciduous and Coniferous Trees Using Radio Cesium and Radio Potassium in Annual Tree Rings

T. Ohta, Y. Mahara, H. Ogawa, A. Kumata, R. Fujinaga, A. Nishi and T. Igarashi

Proc. 15th workshop on Environmental Radioactivity, Tsukuba, Japan (2014) 228-232.

Noble Gases in the Chelyabinsk Meteorite

M.K. Haba, H. Sumino, K. Nagao, H. Mikouchi, M. Komatsu and M.E. Zolensky

The 45th Lunar and Planetary Science Conference, Texas, USA (2014) 1732.

The Origin of H<sub>2</sub>O-rich Fluids in Mantle Wedge Peridotites Revealed by Halogens and Noble Gases

M. Kobayashi, H. Sumino, K. Nagao, S. Ishimaru, S. Arai, M. Yoshikawa, T. Kawamoto, Y. Kumagai  
And T. Kobayashi

Geofluid-3: Nature and Dynamics of Fluids in Subduction Zones, Tokyo, Japan (Apr. 28- May2, 2014) 21.

Difference in Removal Rate of Arsenite and Arsenate from Groundwater in Biological Filtration Systems- Results of on-site Voltammetric Analysis and XAFS Analysis

Y. Fujikawa, P. Lewtas, S. Tani, K. Takada, Ph.D. Hung, T. Homma and H. Ozaki

ICAEC2014, Bangkok (Nov. 24-26, 2014) 147.

## Reviews

Analysis of Environmental Samples Using Synchrotron Radiation: Speciation of Elements by XAFS (in Japanese)

Y. Fujikawa

Journal of Environmental Conservation Engineering, **43(4)** (2014) 220-225.

## 6. Life Science and Medical Science

### Papers

The Structure of a Deoxygenated 400 kDa Haemoglobin Reveals Ternary- and Quaternary-structural Changes of Giant Haemoglobins

N. Numoto, T. Nakagawa, R. Ohara, T. Hasegawa, A. Kita, T. Yoshida, T. Maruyama, K. Imai, Y. Fukumori and K. Miki

Acta Cryst., **D 70** (2014) 1823-1831.

Pilot Clinical Study of Boron Neutron Capture Therapy for Recurrent Hepatic Cancer Involving the Intra-arterial Injection of a (10) BSH-containing WOW Emulsion

H. Yanagie, S. Higashi, K. Seguchi, I. Ikushima, M. Fujihara, Y. Nonaka, K. Oyama, S. Maruyama, R. Hatae, M. Suzuki, S. Masunaga, T. Kinashi, Y. Sakurai, H. Tanaka, N. Kondo, M. Narabayashi, T. Kajiyama, A. Maruhashi, K. Ono, J. Nakajima, M. Ono, H. Takahashi and M. Eriguchi

Appl. Radiat. Isot., **88** (2014) 32-37.

Design and Synthesis of 8-Hydroxyquinoline -based Radioprotective Agents

S. Ariyasu, A. Sawa, A. Morita, K. Hanaya, M. Hoshi, I. Takahashi, B. Wang and S. Aoki

Bioorg. Med. Chem., **22** (2014) 3891.

Impact of DNA Repair Pathways on the Cytotoxicity of Piperlongumine in Chicken DT40 Cell-lines  
S. Okamoto, T. Narita, H. Sasanuma, S. Takeda, S. Masunaga, T. Bessho and K. Tano  
*Genes Cancer*, **5** (2014) 285-292.

Safety and Effectiveness of Stereotactic Body Radiotherapy for a Clinically Diagnosed Primary Stage I Lung Cancer Without Pathological Confirmation  
K. Sakanaka, Y. Matsuo, Y. Nagata, S. Maki, K. Shibuya, Y. Norihisa, M. Narabayashi, N. Ueki, T. Mizowaki and M. Hiraoka  
*Int. J. Clin. Oncol.*, **19**(5) (2014) 814-821.

In vitro Amyloidogenic Peptides of Galectin-7: Possible Mechanism of Amyloidogenesis of Primary Localized Cutaneous Amyloidosis  
K. Ono, E. Fujimoto, N. Fujimoto, M. Akiyama, T. Satoh, H. Maeda, N. Fujii and S. Tajima  
*J. Biol. Chem.*, **289** (2014) 29195-29207.

Inflammation as well as Angiogenesis may Participate in the Pathophysiology of Brain Radiation Necrosis  
E. Yoritsune, M. Furuse, H. Kuwabara, T. Miyata, N. Nonoguchi, S. Kawabata, H. Hana Hayasaki, T. Kuroiwa, K. Ono, Y. Shibayama and S. Miyatake  
*J. Radiat. Res.*, **55** (2014) 803-11.

Emerging Issues in RadioGenic Cataracts and Cardio Vascular Disease  
N. Hamada, Y. Fujimichi, T. Iwasaki, N. Fujii, M. Furuhashi, E. Kubo, T. Minamino, T. Nomura and H. Sato  
*J. Radiat. Res.*, **55** (2014) 831-846.

X-ray Structure Determination and Deuteration of Nattokinase  
Y. Yanagisawa, T. Chatake, S. Naito, T. Ohsugi, C. Yatagai, H. Sumi, A. Kawaguchi, K. Chiba-Kamosida, M. Ogawa, T. Adachi and Y. Morimoto  
*J. Synchrotron Rad.*, (2014) 875-879.

Comparison of Effect of Gamma Ray Irradiation on Wild-type and N-terminal Mutants of  $\alpha$ A-crystallin  
S. Ramkumar, N. Fujii, N. Fujii, B. Thankappan, H. Sakaue, K. Ingu, K. Natarajaseenivasan and K. Anbarasu  
*Mol Vis.*, **20** (2014) 1002-1016.

The BRCA2 Gene is a Potential Molecular Target during 5-fluorouracil Therapy in Human Oral Cancer Cells  
Y. Nakagawa, A. Kajihara, A. Takahashi, N. Kondo, E. Mori, T. Kirita and T. Ohnishi  
*Oncol. Rep.*, **31** (2014) 2001-2006.

Crystal Structure of Phosphopantothenate Synthetase from *Thermococcus kodakarensis*  
A. Kishimoto, A. Kita, T. Ishibashi, H. Tomita, Y. Yokooji, T. Imanaka, H. Atomi and K. Miki  
*PROTEINS: Structure, Function and Bioinformatics*, **82** (2014) 1924-1936.

Effects of Carotenoids on Damage of Biological Lipids Induced by Gamma Irradiation  
T. Saito and N. Fujii  
*Radiat. Phys. Chem.*, **98** (2014) 57-63.

Significance of Fractionated Administration of Thalidomide Combined with  $\gamma$ -ray Irradiation in Terms of Local Tumor Response and Lung Metastasis  
S. Masunaga, Y. Sanada, T. Moriwaki, K. Tano, Y. Sakurai, H. Tanaka, M. Suzuki, N. Kondo, M. Narabayashi, T. Watanabe, Y. Nakagawa, A. Maruhashi and K. Ono  
*World. J. Oncol.*, **5** (2014) 155-165.



New Quaternary Arsenide Oxides with Square Planar Coordination of Gold(I) – Structure,<sup>197</sup>Au Mössbauer Spectroscopic, XANES and XPS Characterization of Nd<sub>10</sub> Au<sub>3</sub> As<sub>8</sub> O<sub>10</sub> and Sm<sub>10</sub> Au<sub>3</sub> As<sub>8</sub> O<sub>10</sub>  
T. Bartsch, O. Niehaus, D. Johrendt, Y. Kobayashi, M. Seto, P. M. Abdala, M. Bartsch, H. Zacharias, R. Hoffmann, B. Gerke, U. Rodewald and R. Pöhlitzgen  
Dalton Trans., **44** (2015) 5854-5866.

Corrosion of Copper in Water and Colloid Formation under Intense Radiation Field  
K. Bessho, Y. Oki, N. Akimune, H. Matsumura, K. Masumoto, S. Sekimoto, N. Osada, N. Kinoshita, H. Monjushiro and S. Shibata  
J. Radioanal. Nucl. Chem., **303** (2015) 1117-1121.

Copper Isotope Effect in Serum of Cancer Patients. A Pilot Study  
P. Telouk, A. Puisieux, T. Fujii, V. Balter, V. Bondanese, A. P. Morel, G. Clapisson, A. Lamboux and F. AlbaredoLBARÈDE  
Matallomics, **7** (2015) 299-308.

## Proceedings

Crystal Structure of Archaeal Phosphopantothenate Synthetase  
A. Kita, A. Kishimoto, T. Ishibashi, H. Yomita, Y. Yokooji, T. Imanaka, H. Atomi and K. Miki  
The 23<sup>rd</sup> Congress and General Assembly of the International Union of Crystallography, Montreal (Aug. 5-12, 2014)  
C455.

Partial Oxygen-dissociation of Crystalline Giant Hemoglobin  
N. Numoto, T. Nakagawa, A. Kita, N. Ito, Y. Fukumori and K. Miki  
The 23<sup>rd</sup> Congress and General Assembly of the International Union of Crystallography, Montreal (Aug. 5-12, 2014)  
C474.

Weak Interaction of an Inhibitor in the 20S Proteasome  
T. Murakami, H. Yamaguchi, U. Bahrudin, A. Kita, U. Hisatome, Y. Saeki, K. Tanaka, M. Unno and Y. Morimoto  
The 23<sup>rd</sup> Congress and General Assembly of the International Union of Crystallography, Montreal (Aug. 5-12, 2014)  
C487.

Rapid Analysis of D-amino acids in Proteins Using LC-MS  
N. Fujii  
Origins 2014, Nara, Japan (July 6-11, 2014) 14.

Protein Aggregation and Racemization of Amino Acids  
N. Fujii, N. Fujii, T. Takata, H. Maeda and H. Sakaue  
Japan-Hungary Joint Seminar "Mechanism and Regulation of Aberrant Protein Aggregation", Osaka, Japan  
(Nov. 18-20, 2014).

The Hunt for D-aspartyl Endopeptidase in Various Living Things: Vertebrates, Aquatic Animals and Plants  
T. Kinouchi and N. Fujii  
The 2<sup>nd</sup> International Conference of D-Amino Acid Research IDAR2014, Tochigi, Japan (Sept. 2-5, 2014) 16.

Oxidation and Racemization of Rat Lens Crystallins by gamma Irradiation  
I. Kim, T. Saito and N. Fujii  
The 2<sup>nd</sup> International Conference of D-Amino Acid Research IDAR2014, Tochigi, Japan (Sept. 2-5, 2014) 29.

Isomerizations of Aspartyl Residues in Lens Crystallins from Age-related Cataracts  
T. Takata, H. Sakaue and N. Fujii  
The 2<sup>nd</sup> International Conference of D-Amino Acid Research IDAR2014, Tochigi, Japan (Sept. 2-5, 2014) 69.

Inversion of Aspartyl Residue Disturbs Assembly of Crystallin in Human Cataract Lens

H. Sakaue, T. Takata, N. Fujii, H. Sasaki and N. Fujii

The 2<sup>nd</sup> International Conference of D-Amino Acid Research IDAR2014, Tochigi, Japan (Sept. 2-5, 2014) 77.

A Novel Rapid Comprehensive Analysis of D-amino Acids in Cataract Lens Proteins Using LC-MS

N. Fujii

The 2<sup>nd</sup> International Conference of D-Amino Acid Research IDAR2014, Tochigi, Japan (Sept. 2-5, 2014) 28.

Analysis of Aspartyl Isomers in Skin Protein by LC-MS/MS

Y. Suzuki, N. Fujii and H. Sakaue

The 2<sup>nd</sup> International Conference of D-Amino Acid Research IDAR2014, Tochigi, Japan (Sept. 2-5, 2014) 78.

## Books

Protein Modifications by Aging, Gamma-ray and UV Irradiation, and their Rapid Survey. Chap 16, Biomolecules Under Extreme Environments, CSJ Current Review17 (in Japanese)

N. Fujii

Kagakudojin, (2014).

Cancer Treatments Targeting Adaptive Responses to Oxidative Stress  
Medicine of Oxidative Stress

H. Nagasawa

SHINDAN TO CHIRYO SHA (2014).

Isomerizations of Aspartyl Residues in Lens Crystallins from Age-related Cataracts

N. Fujii, T. Takata, N. Fujii and H. Sasaki

Asia ARVO, Yokohama, Japan (Feb. 16-19, 2015).

New Enzyme-Targeting Radiosensitization Treatment KORTUC, its Basis and Clinical Application of KORTUC (Kochi Oxidol-Radiation Therapy for Unresectable Carcinomas) (in Japanese)

S. Masunaga

Shinohara Publisher Inc, (2015).

New Developments in Tryptophan Research

A. Shimada and I. Otsuka

Nova Science Publishers, (2015).

## Reviews

Current Status of Radiation Biology (in Japanese)

S. Masunaga

Jastro Newsletter, **112** (2014) 38.

Intrinsic and Extrinsic Factors Influencing the Radio-sensitivity (in Japanese)

S. Masunaga

Jastro Newsletter, **112** (2014) 42-44.

D-amino Acid as a Biomarker for the Photo-aging Mechanism (in Japanese)

N. Fujii

Journal of Clinical and Experimental Medicine (IGAKU NO AYUMI), **248** (2014) 602-607.

New Analysis of Aspartyl Isomers in Cataractous Lens Proteins (in Japanese)

N. Fujii and N. Fujii

The Journal of the Japanese Society for Cataract Research, **26** (2014) 33-36.

Abnormal Aggregation of Proteins Induced by Biologically Uncommon D-aspartyl Residues and Age-related Diseases (in Japanese)

N. Fujii

Vitamins, **88** (2014) 419-424.

From the Viewpoint of Tumor Biology (Biology for Tumor Therapy) (in Japanese)

S. Masunaga

Radioisotopes, **64** (2015) 69-79.

## Others

A Method for the Detection of Iron(II) Ion by a Novel Selective Fluorescence Probe (in Japanese)

H. Nagasawa and T. Hirayama

Japanese Patent Application No. 2014-007140.

A New Diagnostic Agent for Hypoxia Related Ocular Diseases (in Japanese)

S. Fukuda, T. Oshika, K. Okuda and H. Nagasawa

Japanese Patent Application No. 2014-200397.

## 7. Neutron Capture Therapy

### Papers

Overview of the Re-initiation of BNCT Clinical Studies at the University of Tsukuba

T. Aihara, H. Kumada, T. Wada, H. Ishikawa, N. Fukumitsu, K. Oonishi, K. Tanaka, M. Mizumoto, H. Numajiri, K. Nakai, T. Yamamoto, T. Sakoda, A. Hara, A. Matsumura, M. Suzuki and H. Sakurai

16<sup>th</sup> Neutron Capture Therapy, (2014) 86-87.

A Simple Strategy to Decrease the Incidence of Fatal Carotid Blowout Syndrome after BNCT for Head and Neck Cancers (in Japanese)

T. Aihara, N. Morita, N. Kamitani, H. Kumada, K. Oonishi, M. Suzuki, J. Hiratsuka and H. Sakurai

16<sup>th</sup> Neutron Capture Therapy, (2014) 171-172.

Synthesis and in Vitro Evaluation of Thiododeborated  $\alpha$ ,  $\alpha$ -cycloalkylamino Acids for the Treatment of Malignant Brain Tumors by Boron Neutron Capture Therapy.

Y. Hattori, S. Kusaka, M. Mukumoto, M. Ishimura, Y. Ohta, H. Takenaka, K. Uehara, T. Asano, M. Suzuki, S. Masunaga, K. Ono, S. Tanimori and M. Kirihata

Amino Acids, **46** (2014) 2715-2720.

Higher Order Mode Analyses of Power Spectral Density and Feynman-alpha Method in Accelerator Driven System with Periodically Pulsed Spallation Neutron Source

T. Yamamoto

Ann. Nucl. Energy., **66** (2014) 63-73.

An NDT Study of a Boron Tracedrug UTX-51 for Glycated BSA as an AGE Model

R. Tada, Y. Uto, S. Masunaga, Y. Kinashi, K. Ono and H. Hori

Anticancer Res, **34** (2014) 4503-4507.

- Effect of Terrigenic He Components on Tritium-helium Dating: A Case Study of Shallow Groundwater in the Saijo Basin  
Y. Mahara, T. Ohta, N. Morikawa, T. Nakano, M. Tokumatsu, S. Fukutani and T. Igarashi  
*Appl. Geochem.*, **50** (2014) 142-149.
- Pilot Clinical Study of Boron Neutron Capture Therapy for Recurreced Hepatic Cancer using Intra-Arterial Injection of 10BSH Entrapped WOW Emulsion  
H. Yanagie, S. Higashi, K. Seguchi, I. Ikushima, M. Fujihara, K. Oyama, Y. Nonaka, S. Maruyama, R. Hatae, M. Suzuki, S. Masunaga, T. Kinashi, Y. Sakurai, H. Tanaka, N. Kondo, T. Kajiyama, A. Maruhashi, K. Ono, J. Nakajima, M. Ono, H. Takahashi and M. Eriguchi  
*Appl. Radiat. Isot.*, **88** (2014) 32.
- BNCT for Advanced or Recurrent Head and Neck Cancer  
T. Aihara, N. Morita, N. Kamitani, H. Kumada, K. Ono, J. Hiratsuka and T. Harada  
*Appl. Radiat. Isot.*, **88** (2014) 12-15.
- Dose Estimation for Internal Organs during Boron Neutron Capture Therapy for Body-trunk Tumors  
Y. Sakurai, H. Tanaka, M. Suzuki, S. Masunaga, Y. Kinashi, N. Kondo, K. Ono and A. Maruhashi  
*Appl. Radiat. Isot.*, **88** (2014) 43-45.
- Boron Neutron Capture Therapy as New Treatment for Clear Cell Sarcoma: Trial on Different Animal Model  
T. Andoh, T. Fujimoto, T. Sudo, M. Suzuki, Y. Sakurai, T. Sakuma, H. Moritake, T. Sugimoto, T. Takeuchi, H. Sonobe, A. L. Epstein, Y. Fukumori, K. Ono and H. Ichikawa  
*Appl. Radiat. Isot.*, **88** (2014) 59-63.
- Gadolinium-loaded Chitosan Nanoparticles for Neutron-capture Therapy: Influence of Micrometric Properties of the Nanoparticles on Tumor-killing Effect  
H. Ichikawa, T. Uneme, T. Andoh, Y. Arita, T. Fujimoto, M. Suzuki, Y. Sakurai, H. Shinto, T. Fukasawa, F. Fujii and Y. Fukumori  
*Appl. Radiat. Isot.*, **88** (2014) 109-113.
- Study on Detecting Spatial Distribution of Neutrons and Gamma Rays Using a Multi-imaging Plate System  
K. Tanaka, Y. Sakurai, S. Endo and J. Takada  
*Appl. Radiat. Isot.*, **88** (2014) 143-146.
- Evaluation of Thermal Neutron Field Using a Cyclotron-based Neutron Source for Alpha Autography  
H. Tanaka, Y. Sakurai, M. Suzuki, S. Masunaga, T. Mitsumoto, Y. Kinashi, N. Kondo, M. Narabayashi, Y. Nakagawa, T. Watanabe, N. Fujimoto, A. Maruhashi and K. Ono  
*Appl. Radiat. Isot.*, **88** (2014) 153-156.
- Spermidinium Closo-dodecaborate-encapsulating Liposomes as Efficient Boron Delivery Vehicles for Neutron Capture Therapy  
S. Tachikawa, T. Miyoshi, H. Koganei, M. E. El-Zaria, C. Viñas, M. Suzuki, K. Ono and H. Nakamura  
*Chem. Commun.*, **50** (2014) 12325.
- Optimization of Biguanide Derivatives as Selective Antitumor Agents Blocking Adaptive Stress Responses in the Tumor Microenvironment  
K. Narise, K. Okuda, Y. Enomoto, T. Hirayama and H. Nagasawa  
*Drug Des. Devel. Ther.*, **8** (2014) 701.
- Effect of Bevacizumab Combined with Boron Neutron Capture Therapy on Local Tumor Response and Lung Metastasis  
S. Masunaga, Y. Sakurai, K. Tano, H. Tanaka, M. Suzuki, N. Kondo, M. Narabayashi, T. Watanabe, Y. Nakagawa, A. Maruhashi and K. Ono  
*Exp. Ther. Med.*, **8** (2014) 291-301.

Evaluation of Boron Content Liposome Modified Protein-transduction Domains for Boron Neutron Capture Therapy  
M. Shirakawa, K. Nakai, F. Yoshida, A. Zaboronok, T. Yamamoto and A. Matsumura  
Int. J. Emerg. Technol. Adv. Eng., **4** (2014) 074-9.

Tetrakis (p-Carboranylthio-Tetrafluorophenyl) Chlorin (TPFC): Application for Photodynamic Therapy and Boron Neutron Capture Therapy  
R. Hiramatsu, S. Kawabata, H. Tanaka, Y. Sakurai, M. Suzuki, K. Ono, SI. Miyatake, T. Kuroiwa, E. Hao and MG. Vicente  
J Pharm Sci., **104(3)** (2014) 962-70.

Boron Carbide Particle as a Boron Compound for Boron Neutron Capture Therapy  
T. Iwagami, Y. Ishikawa, N. Koshizaki, N. Yamamoto, H. Tanaka, S. Masunaga, Y. Sakurai, I. Kato, S. Iwai, M. Suzuki and Y. Yura  
J. Nucl. Med. Radiat. Ther., **5** (2014) .

Mockup Experiments on the Thorium-Loaded Accelerator-Driven System in the Kyoto University Critical Assembly  
C. H. Pyeon, T. Yagi, K. Sukawa, Y. Yamaguchi and T. Misawa  
Nucl. Sci. Eng., **177** (2014) 156-168.

A Case of Radiation-induced Osteosarcoma Treated Effectively by Boron Neutron Capture Therapy  
G. Futamura, S. Kawabata, H. Siba, T. Kuroiwa, M. Suzuki, N. Kondo, K. Ono, Y. Sakurai, M. Tanaka, T. Todo and S. Miyatake  
Radiat. Oncol., **9** (2014) .

The Roles of Platelet-Derived Growth Factors and their Receptors in Brain Radiation Necrosis  
T. Miyata, T. Toho, N. Nonoguchi, M. Furuse, H. Kuwabara, E. Yoritsune , S. Kawabata, T. Kuroiwa and SI. Miyatake  
Radiat. Oncol., **11** (2014) .

Detection of  $\gamma$ H2AX Foci in Mouse Normal Brain and Brain Tumor after Boron Neutron Capture Therapy  
N. Kondo, H. Michiue, Y. Sakurai, H. Tanaka, Y. Nakagawa, T. Watanabe, M. Narabayashi, Y. Kinashi, M. Suzuki, S. Masunaga and K. Ono  
Rep. Prac. Oncol. Radiother., **in press** (2014) .

Atmospheric Direct Uptake of Radiocaesium into Trees from the Fukushima Nuclear Accident and its Fate  
Y. Mahara, T. Ohta, H. Ogawa and A. Kumata  
Scientific Report, **4** (2014).

Study of Neutron Irradiation on F82H Alloys by Mössbauer Spectroscopy  
S.S. Huang, S. Kitao, Y. Kobayashi, T. Yoshiie, Q. Xu, K. Sato and M. Seto  
J. Nucl. Mater., **456** (2015) 266.

Preliminary Study of MAGAT Polymer Gel Dosimetry for Boron-neutron Capture Therapy  
S. Hayashi, Y. Sakurai, R. Uchida, M. Suzuki, S. Usui and T. Tominaga  
J. Phys. Conf. Ser., **573** (2015).

Mössbauer Spectroscopy of the Magnetic-Field-Induced Ferroelectric Phase of CuFeO<sub>2</sub>  
S. Nakamura, Y. Kobayashi, S. Kitao, M. Seto, A. Fuwa and N. Terada  
J. Phys. Soc. Jpn., **84** (2015) 24719.

Cherenkov Counting of  $^{90}\text{Sr}$  and  $^{90}\text{Y}$  in Bark and Leaf Samples Collected Around Fukushima Daiichi Nuclear Power Plant

T. Kubota, Y. Shibahara, S. Fukutani, T. Fujii, T. Ohta, M. Kowatari, S. Mizuno, K. Takamiya and H. Yamana  
J. Radioanal. Nucl. Chem., **303** (2015) 39-46.

Theoretical and Experimental Study of the Vibrational Frequencies of  $\text{UO}_2^{2+}$  and  $\text{NpO}_2^{2+}$  in Highly Concentrated Chloride Solutions

T. Fujii, A. Uehara, Y. Kitatsuji and H. Yamana  
J. Radioanal. Nucl. Chem., **303** (2015) 1015-1020.

Local Structures at In Impurity Sites in ZnO Probed by the TDPAC Technique

W. Sato, S. Komatsuda, Y. Yamada and Y. Ohkubo  
J. Radioanal. Nucl. Chem., **303** (2015) 1201-1204.

Neutron Activation Analysis of Iron Meteorites

N. Shirai, Y. Hidaka, A. Yamaguchi, S. Sekimoto, M. Ebihara and H. Kojima  
J. Radioanal. Nucl. Chem., **303** (2015) 1375-1380.

$^{235}\text{U}$   $^{238}\text{U}$  Isotopic Ratio in Plant Samples from Fukushima Prefecture

Y. Shibahara, T. Kubota, T. Fujii, S. Fukutani, T. Ohta, K. Takamiya, R. Okumura, S. Mizuno and H. Yamana  
J. Radioanal. Nucl. Chem., **303** (2015) 1421-1424.

Chemical and Mineralogical Compositions of Two Grains Recovered from Asteroid Itokawa

M. Ebihara, N. Shirai and S. Sekimoto  
Meteorit. Planet. Sci., **50** (2015) 243-254.

Development of KURAMA-II and its Operation in Fukushima

M. Tanigaki, R. Okumura, K. Takamiya, N. Sato, H. Yoshino, H. Yoshinaga, Y. Kobayashi, A. Uehara and H. Yamana  
Nucl. Instrum. Meth. Phys. Res., **781** (2015) 57-64.

Optical Characteristics of Pure Poly (vinyltoluene) for Scintillation Applications

H. Nakamura, Y. Shirakawa, N. Sato, H. Kitamura, O. Shinji, K. Saito and S. Takahashi  
Nucl. Instrum. Methods. Phys. Res. A, **770** (2015) 131.

## Proceedings

Boron-containing Rare Earth Oxides Nanoparticles for Boron Neutron Capture Therapy

T. Nagasaki, R. Kawasaki, S. Masunaga, Y. Sakurai and K. Tomita  
2014 MRS Spring Meeting & Exhibit, San Francisco, CA, USA (2014).

Fatal Carotid Blowout Syndrome after BNCT for Head and Neck Cancers

T. Aihara, N. Morita, N. Kamitani, H. Kumada, K. Ohnishi, H. Ishikawa, N. Fukumitsu, M. Suzuki, T. Harada Y. Sakurai and J. Hiratsuka  
The 11<sup>th</sup> Congress on Neutron Capture Therapy, Osaka, Japan (2014) 63.

Development of a Real-time Thermal Neutron Monitor and its Clinical Application

T. Aihara, N. Morita, N. Kamitani, H. Kumada, K. Ohnishi, H. Ishikawa, N. Fukumitsu, M. Suzuki, T. Harada Y. Sakurai and J. Hiratsuka  
The 11<sup>th</sup> Congress on Neutron Capture Therapy, Osaka, Japan (2014) 85.

#### Fatal Carotid Blowout Syndrome after BNCT for Head and Neck Cancers

T. Aihara, N. Morita, N. Kamitani, H. Kumada, K. Ohnishi, M. Suzuki, J. Hiratsuka, H. Sakurai and T. Harada  
The 76<sup>th</sup> Annual Meeting of the Society of Practical Otolaryngology, Morioka, Japan (2014) 143.

#### Cyclotron-based Epithermal Neutron Source (C-BENS) for Boron Neutron Capture Therapy

H. Tanaka, Y. Sakurai, M. Suzuki, S. Masunaga, T. Mitsumoto, A. Maruhashi and K. Ono  
Asian Forum for Accelerators and Detectors 2015, Hsinchu, (2015).

#### The Past, Present, and Future of the Reactor-based Neutron Source at Kyoto University Reactor

Y. Sakurai, H. Tanaka, T. Takata, N. Fujimoto, M. Suzuki, S. Masunaga, Y. Kinashi, N. Kondo, M. Narabayashi, Y. Nakagawa, T. Watanabe, K. Ono and A. Maruhashi  
The 2<sup>nd</sup> KURRI International Workshop on BNCT - Basic Science and Technology for BNCT -, Kyoto, Japan (Dec. 9-10, 2014).

#### The Dependency of CBE Factors on the Concentration of Administered Neutron Capture Agents in BNCT

S. Masunaga, Y. Sakurai, H. Tanaka, K. Tano, M. Suzuki, N. Kondo, M. Narabayashi, T. Watanabe, Y. Nakagawa, A. Maruhashi and K. Ono  
The 2<sup>nd</sup> KURRI International Workshop on BNCT - Basic Science and Technology for BNCT - Kyoto, Japan (Dec. 9-10, 2014).

#### Melanoma-Targeting Boron Delivery System Using Kojic Acid-Carborane Conjugate

T. Nagasaki, R. Kawasaki, Y. Hattori, Y. Sakurai, H. Tanaka, S. Masunaga, K. Ono and M. Kirihata  
The 2<sup>nd</sup> KURRI International Workshop on BNCT - Basic Science and Technology for BNCT -, Kyoto, Japan (Dec. 9-10, 2014).

#### Development of Real Time Neutron Monitors for BNCT

H. Tanaka, Y. Sakurai, M. Suzuki, S. Masunaga, Y. Kinashi, K. Taki, T. Fujii, N. Fujimoto, T. Takata, T. Watanabe, Y. Nakagawa, M. Narabayashi, N. Kondo, A. Maruhashi and K. Ono  
The 2<sup>nd</sup> KURRI International Workshop on BNCT - Basic Science and Technology for BNCT -, Kyoto, Japan (Dec. 9-10, 2014).

#### Clinical Experiences of Boron Neutron Capture Therapy to Recurrent Rectal Cancers

H. Yanagie, K. Oyama, R. Hatae, S. Maruyama, Y. Ohno, S. Kurokawa, Y. Nonaka, H. Sugiyama, Y. Furuya, K. Taniike, M. Suzuki, S. Masunaga, T. Kinashi, Y. Sakurai, N. Kondo, M. Narabayashi, H. Tanaka, A. Maruhashi, K. Ono, J. Nakajima, M. Ono, H. Takahashi and M. Eriguchi  
Book of Abstracts for 16<sup>th</sup> International Congress on Neutron Capture Therapy, Helsinki (Jun. 14-19, 2014) 56-57.

#### Boron Neutron Capture Therapy as New Treatment for Clear Cell Sarcoma: Trial on a Lung Metastasis Model of Clear Cell Sarcoma

T. Andoh, T. Fujimoto, M. Suzuki, T. Sudo, Y. Sakurai, H. Tanaka, I. Fujita, N. Fukase, H. Moritake, T. Sugimoto, T. Sakuma, H. Sasai, T. Akisue, M. Kirihata, Y. Fukumori, K. Ono and H. Ichikawa  
Book of Abstracts for 16<sup>th</sup> International Congress on Neutron Capture Therapy, Helsinki (Jun. 14-19, 2014) 79-80.

#### Examination of the Usefulness as the New Boron Compound of ACBC-BSH

G. Futamura, S. Kawabata, S. Miyatake, T. Kuroiwa, Y. Hattori, M. Kirihata, H. Tanaka, Y. Sakurai, S. Masunaga and K. Ono  
Book of Abstracts for 16<sup>th</sup> International Congress on Neutron Capture Therapy, Helsinki (Jun. 14-19, 2014) 81-82.

#### Potential of Boron Neutron Capture Therapy for Malignant Peripheral Nerve Sheath Tumor

T. Fujimoto, T. Andoh, Y. Tokunaga, T. Sudo, I. Fujita, N. Fukase, T. Takeuchi, H. Sonobe, M. Inoue, T. Hirose, T. Sakuma, S. Yamamoto, S. Atagi, Y. Sakurai, H. Ichikawa, K. Ono and M. Suzuki  
Book of Abstracts for 16<sup>th</sup> International Congress on Neutron Capture Therapy, Helsinki (Jun. 14-19, 2014) 90-91.

Feasible Evaluation of WOW Emulsion as Intra-arterial Boron Delivery Carrier for Neutron Capture Therapy to Hepatocellular Carcinoma

H. Yanagie, T. Kajiyama, M. Fujiwara, R. Mizumachi, Y. Murata, Y. Sakurai, K. Mouri, A. Shinohara, T. Matsukawa, Y. Oomori, Y. Morishita, N. Dewi, M. Yanagawa, S. Higashi, I. Ikushima, K. Seguchi, K. Yokoyama, T. Iizuka, Y. Nonaka, H. Sugiyama, Y. Furuya, Y. Sakurai, H. Tanaka, M. Suzuki, S. Masunaga, K. Oyama, T. Nakagawa, R. Nishimura, K. Ono, M. Ono, J. Nakajima, M. Eriguchi and H. Takahashi

Book of Abstracts for 16<sup>th</sup> International Congress on Neutron Capture Therapy, Helsinki (Jun. 14-19, 2014) 98-99.

Study on the Improvement of Depth dose Distribution Using Multiple-field Irradiation in Boron Neutron Capture Therapy

N. Fujimoto, H. Tanaka, Y. Sakurai, N. Kondo, M. Narabayashi, Y. Nakagawa, T. Watanabe, Y. Kinashi, S. Masunaga, A. Maruhashi, K. Ono and M. Suzuki

Book of Abstracts for 16<sup>th</sup> International Congress on Neutron Capture Therapy, Helsinki (Jun. 14-19, 2014) 101-102.

A study of Effective dose for Tumor in BNCT

Y. Sakurai, H. Tanaka, N. Fujimoto, N. Kondo, M. Narabayashi, Y. Nakagawa, T. Watanabe, Y. Kinashi, M. Suzuki, S. Masunaga, A. Maruhashi and K. Ono

Book of Abstracts for 16<sup>th</sup> International Congress on Neutron Capture Therapy, Helsinki (Jun. 14-19, 2014) 104-105.

Experimental Trial of Measuring Spatial Distribution of Neutrons and Gamma Rays in BNCT Using Multi Imaging Plate System

K. Tanaka, Y. Sakurai, S. Endo, H. Tanaka and J. Takada

Book of Abstracts for 16<sup>th</sup> International Congress on Neutron Capture Therapy, Helsinki (Jun. 14-19, 2014) 109-110.

Alanine Dosimeter Response Characteristics for Charged Particles in BNCT

T. Kawamura, R. Uchida, H. Tsuchida, H. Tanaka and Y. Sakurai

Book of Abstracts for 16<sup>th</sup> International Congress on Neutron Capture Therapy, Helsinki (Jun. 14-19, 2014) 115-116.

Study on the Accelerator-based Neutron Source Using Be(p,n) Reaction with Proton Energy of Lower than 30 MeV

H. Tanaka, Y. Sakurai, M. Suzuki, S. Masunaga, N. Fujimoto, Y. Kinashi, N. Kondo, T. Takata, T. Watanabe, M. Narabayashi, A. Maruhashi and K. Ono

Book of Abstracts for 16<sup>th</sup> International Congress on Neutron Capture Therapy, Helsinki (Jun. 14-19, 2014) 126-127.

The Improvement of the Energy Resolution in Epi-thermal Region of Bonner Sphere Using Boric Acid Solution Moderator

H. Ueda, H. Tanaka and Y. Sakurai

Book of Abstracts for 16<sup>th</sup> International Congress on Neutron Capture Therapy, Helsinki (Jun. 14-19, 2014) 148-149.

Clinical Results of Boron Neutron Capture Therapy for the Patients with Malignant Meningioma

S. Kawabata, S. Miyatake, G. Futamura, R. Hiramatsu, Y. Matsushita, M. Furuse, Y. Tamura, T. Kuroiwa, H. Tanaka, Y. Sakurai, S. Masunaga, M. Suzuki and K. Ono

Book of Abstracts for 16<sup>th</sup> International Congress on Neutron Capture Therapy, Helsinki (Jun. 14-19, 2014) 169-170.



- Three in One: a Multifunctional Antitumor Sensitizer for Photodynamic, Boron Neutron Capture and Proton Therapies  
N. Miyoshi, S. K.Kundu, H. Tanaka, Y. Sakurai, M. Suzuki, A.V. Zaitsev, V.A. Ol'shevskaya, G.N. Rychkov, K. Ono, V.N.Kalinin and A. A.Shtil  
Book of Abstracts for 16<sup>th</sup> International Congress on Neutron Capture Therapy, Helsinki (Jun. 14-19, 2014) 173-174.
- Significance of Combined Treatment with Bevacizumab in Boron Neutron Capture Therapy in Terms of Local Tumor Response and Lung Metastasis  
S. Masunaga, Y. Sakurai, K. Tano, H. Tanaka, M. Suzuki, N. Kondo, M. Narabayashi, T. Watanabe, Y. Nakagawa, A. Maruhashi and K. Ono  
Book of Abstracts for 16<sup>th</sup> International Congress on Neutron Capture Therapy, Helsinki (Jun. 14-19, 2014) 177-178.
- Detection of Plasmid Strand Breaks in Boron Neutron Capture Reaction  
E. Okamoto, K. Nakai, F. Yoshida, M. Miyakawa, Y. Yamamoto, H. Tanaka, Y. Sakurai, S. Masunaga, T. Yamamoto and A. Matsumura  
Book of Abstracts for 16<sup>th</sup> International Congress on Neutron Capture Therapy, Helsinki (Jun. 14-19, 2014) 179.
- Localized dose Delivering by Ion Beam Irradiation for Experimental Trial of Establishing Brain Necrosis Model  
T. Takata, N. Kondo, Y. Sakurai, H. Tanaka, T. Hasegawa, K. Kume and M. Suzuki  
Book of Abstracts for 16<sup>th</sup> International Congress on Neutron Capture Therapy, Helsinki (Jun. 14-19, 2014) 184.
- Experimental Trial of Establishing Brain Necrosis Mouse Model Using Proton Beam  
N. Kondo, Y. Sakurai, T. Takata, H. Tanaka, N. Takai, K. Kume, T. Watanabe, T. Toho, S. Miyatake, M. Suzuki, S. Masunaga and K. Ono  
Book of Abstracts for 16<sup>th</sup> International Congress on Neutron Capture Therapy, Helsinki (Jun. 14-19, 2014) 183-184.
- Novel Multi-linked Mercaptoundecahydrododecaborate (BSH) Fused Cellpenetrating Peptide Accelerated Boron Neutron Capture Therapy (BNCT)  
H. Michiue, Y. Sakurai, N. Kondo, M. Kitamatsu, F. Bin, K. Nakajima, Y. Hirota, S. Kawabata, T. Nishiki, I. Ohmori, K. Tomizawa, S. Miyatake, K. Ono and H. Matsui  
Book of Abstracts for 16<sup>th</sup> International Congress on Neutron Capture Therapy, Helsinki (Jun. 14-19, 2014) 187-188.
- Kojic Acid Modified O-carborane/Hydroxypropyl- $\beta$ -cyclo-dextrin Complex as Novel BNCT Drug for Melanoma  
T. Nagasaki, R. Kawasaki, Y. Sakurai, S. Masunaga, K. Ono and M. Kirihata  
Book of Abstracts for 16<sup>th</sup> International Congress on Neutron Capture Therapy, Helsinki (Jun. 14-19, 2014) 222-223.
- Stimuli-responsive Drug Delivery System: Photoresponsive Gene Delivery System for Gene Therapy and Boron Delivery System for Neutron Capture Therapy  
T. Nagasaki  
7<sup>th</sup> KIFEE International Symposium on Environment, Energy and Materials, Kyoto, Japan (Mar. 1-3, 2014).
- Clinical Results of Boron Neutron Capture Therapy for Cutaneous Malignant Melanoma (in Japanese)  
J. Hiratsuka, N. Kamitani, S. Sasaoka, Y. Sakurai and M. Suzuki  
The 11<sup>th</sup> Congress on Neutron Capture Therapy, Osaka, Japan (Mar. 1-3, 2014) 69.
- A Remodelling Study of the Reactor-based Irradiation Facility for Boron Neutron Capture Therapy at Kyoto University Research Reactor Institute  
Y. Sakurai, T. Takata, H. Tanaka, N. Fujimoto, N. Kondo, Y. Nakagawa, T. Watanabe, M. Narabayashi, Y. Kinashi, M. Suzuki, S. Masunaga, K. Ono and A. Maruhashi  
Book of Abstracts for 14<sup>th</sup> Asia-Oceania Congress of Medical Physics & 12<sup>th</sup> South East Asia Congress of Medical Physics (AOCMP/SEACOMP 2014), Ho Chi Minh City (Oct. 23-25, 2014) 126.

Significance of Administering Bevacizumab Combined with Boron Neutron Capture Therapy in Terms of Local Tumor Control and Lung Metastatic Potential

S. Masunaga, Y. Sakurai, K. Tano, H. Tanaka, M. Suzuki, N. Kondo, M. Narabayashi, T. Watanabe, Y. Nakagawa, A. Maruhashi and K. Ono

The 56<sup>th</sup> Annual Meeting of the American Society for Therapeutic Radiology and Oncology, San Francisco, USA (Sept. 14-17, 2014) 796.

Development of a Real-time Dosimeter for Boron Neutron Capture Therapy

H. Tanaka, Y. Sakurai, M. Suzuki, S. Masunaga, T. Takata, N. Fujimoto, K. Taki, A. Maruhashi and K. Ono

Book of Abstracts for the 7<sup>th</sup> Korea-Japan Joint Meeting on Medical Physics, Busan (Sept. 25-27, 2014) 141.

Clinical Application of Scintillator with Optical Fiber Detector as a Real-time Thermal Neutron Monitor during Boron Neutron Capture Therapy

M. Ishikawa, K. Ono, A. Matsumura, T. Yamamoto, J. Hiratsuka, S. Miyatake, I. Kato, Y. Sakurai and H. Kumada

Book of Abstracts for the 7<sup>th</sup> Korea-Japan Joint Meeting on Medical Physics, Busan (Sept. 25-27, 2014) 129.

Advances in BNCT at Kyoto University Research Reactor Institute -from reactor-based BNCT to Accelerator-based BNCT

Y. Sakurai

Book of Abstracts for the 7<sup>th</sup> Korea-Japan Joint Meeting on Medical Physics, Busan (Sept. 25-27, 2014) 26.

Preliminary Study of MAGAT Polymer Gel Dosimetry for Boron-neutron Capture Therapy

S. Hayashi, Y. Sakurai, R. Uchida, M. Suzuki, S. Usui and T. Tominaga

Book of Abstracts for 8<sup>th</sup> International Conference on 3D Radiation Dosimetry (IC3D Dose), Ystad (Sept. 4-7, 2014) 14.

## Reviews

The First Case in the World of BNCT for a Patient with Head and Neck Cancer (in Japanese)

I. Kato and S. Kawabata

PET Journal, **25** (2014) 10-11.

Boron Neutron Capture Therapy (BNCT)

I. Ota and T. Kitahara

The Society of Practical Otolaryngology, **107** (2014) 937-946.

BNCT for Refractory Cancer

M. Suzuki

Electrical Review, **5** (2015) 10-11.

## 8. Neutron Radiography and Radiation Application

### Papers

Neutron Radiography and Numerical Simulation of Mixing Behavior in a Reactor for Supercritical Hydrothermal Synthesis

K. Sugioka, K. Ozawa, S. Takami, T. Tsukada, T. Adschiri, K. Sugimoto, N. Takenaka and Y. Saito

AIChE J., **60** (2014) 1168.

A New Class of High-contrast Fe(II) Selective Fluorescent Probes Based on Spirocyclized Scaffolds for Visualization of Intracellular Labile Iron Delivered by Transferrin

M. Niwa, T. Hirayama, K. Okuda and H. Nagasawa

Org. Biomol. Chem., **12** (2014) 6590-6597.

Estimation of Frost Formation by using Neutron Radiography : Estimation of Frost Deposition and Mass Transfer Coefficient on Cold Flat Plate (in Japanese)

R. Matsumoto, T. Yoshimura, H. Umekawa, T. Ami, D. Ito and Y. Saito

Transactions of the Japan Societt of Refrigerating and Air Conditioning Engineers, **Feb-31** (2014) 207.

## Proceedings

Quantitative Estimation of Frost Formation on Plate-fin Tube Heat Exchanger by Neutron Radiography

R. Matsumoto, T. Yoshimura, H. Umekawa, T. Ami, D. Ito and Y. Saito

15th International Heat Transfer Conference, Kyoto, Japan (2014) 15.

Visualization of Water Accumulation Process in Polymer Electrolyte Fuel Cell using Neutron Radiography

H. Murakawa, K. Sugimoto, N. Kitamura, M. Sawada, H. Asano, N. Takenaka and Y. Saito

Proc. the 10th World Conference on Neutron Radiography, Grindelwald, Switzerland (Oct. 5-10, 2014) 175.

Visualization and Measurement of Adsorption/Desorption Process of Ethanol in Activated Carbon Adsorber

H. Asano, K. Murata, N. Takenaka and Y. Saito

Proc. the 10th World Conference on Neutron Radiography, Grindelwald, Switzerland (Oct. 5-10, 2014) 184.

Study on the Effect of Micro Porous Layer on Water Transport Phenomena in PEFC by Using Neutron Radiography

H. Murakawa, K. Sugimoto, N. Kitamura, H. Asano, N. Takenaka and Y. Saito

Proc. the 15th International Heat Transfer Conference (IHTC-15), Kyoto, Japan (Mar. 1-3, 2014) 15.

## 9. TRU and Nuclear Chemistry

### Papers

Density Functional Theory Estimation of Isotope Fractionation of Fe, Ni, Cu and Zn Among Species Relevant to Geochemical and Biological Environments

T. Fujii, F. Moynier, J. B. Toft and F. Albare`de

Geochim. Cosmochim. Acta, **140** (2014) 553-576.

Redox Equilibrium of the  $UO_2^{2+}/UO_2^+$  Couple in  $Li_2MoO_4$ - $Na_2MoO_4$  Eutectic Melt at 550°C

T. Nagai, A. Uehara, T. Fujii, N. Sato, H. Kofuji, M. Myochin and H. Yamana

J. Nucl. Mater., **454** (2014) 159-163.

Coprecipitation Behaviors of Zr, Hf, and Th with Sm Hydroxide for Chemical Study of Element 104, Rf

Y. Kasamatsu, K. Toyomura, N. Shiohara, T. Yokokita, Y. Komori, A. Kino, T. Yoshimura, N. Takahashi, H. Haba, Y. Kudou, H. Kikunaga, T. Mitsugashira, T. Ohtsuki, K. Takamiya and A. Shinohara

J. Nucl. Radiochem. Sci., **14** (2014) 7-11.

Analysis of Cesium Isotope Compositions in Environmental Samples by Thermal Ionization Mass Spectrometry- 1. A Preliminary Study for Source Analysis of Radioactive Contamination in Fukushima Prefecture

Y. Shibahara, T. Kubota, T. Fujii, S. Fukutani, T. Ohta, K. Takamiya, R. Okumura, S. Mizuno and H. Yamana

J. Nucl. Sci. Technol., **51** (2014) 575-579.

Complex Light Source Composed from Subterahertz-wave Coherent Synchrotron Radiation and an Infrared Free-electron Laser at the Laboratory for Electron Beam Research and Application

N. Sei, H. Ogawa, K. Hayakawa, T. Tanaka, Y. Hayakawa, K. Nakao, T. Sakai, K. Nogami and M. Inagaki

J. Opt. Soc. Am. B, **31** (2014) 2510.

Raman Spectroscopic Study on  $\text{NpO}_2^+$ - $\text{Ca}^{2+}$  Interaction in Highly Concentrated Calcium Chloride

T. Fujii, A. Uehara, Y. Kitatsuji and H. Yamana

J. Radioanal. Nucl. Chem., **301** (2014) 293-296.

Solvent Extraction of Mo(V) and Mo(VI) from Hydrochloric Acid into Aliquat 336 Chloroform Solution

T. Yokokita, Y. Kasamatsu, K. Ooe, T. Yoshimura, N. Takahashi, Y. Komori and A. Shinohara

J. Radioanal. Nucl. Chem., **301** (2014) 751.

Undoped Polycarbonate for Detection of Environmental Radiation

H. Nakamura, Y. Shirakawa, H. Kitamura, N. Sato and S. Takahashi

Japanese Journal of Health Physics, **49** (2014) 98.

Blended Poly (Ether Sulfone) and Poly (Ethylene Naphthalate) as a Scintillation Material

H. Nakamura, Y. Shirakawa, N. Sato, H. Kitamura and S. Takahashi

Nucl. Instrum. Methods. Phys. Res. A, **759** (2014) 1.

Solvent Extraction Using Carrier-free Radiotracers of Mo and W from HCl and HCl/LiCl Solutions into Aliquat 336

T. Yokokita, K. Ooe, Y. Kasamatsu, T. Yoshimura, N. Takahashi, N. Shiohara, K. Takamiya, Y. Komori, Y. Kikutani, A. Kino and A. Shinohara

J. Radioanal. Nucl. Chem., **303** (2015) 1091.

Comparison of the Decay Constants of  $^{51}\text{Cr}$  with Metal, Oxide, and Chromate Chemical States

H. Kikunaga, K. Takamiya, K. Hirose and T. Ohtsuki

J. Radioanal. Nucl. Chem., **303** (2015) 1581-1583.

## Others

Structural analysis on Cations in Molten Sub-halide Systems: Fluoride Addition on UV-vis Spectra of

Neodymium cation in Molten Chlorides

H. Matsuura, A. Nezu and H. Akatsuka

Bulletin of Research Laboratory for Nuclear Reactors, **38** (2014) 12.

## 10. Health Physics and Waste Management

### Papers

Unraveling Low-level Gamma Radiation-responsive Changes in Expression of Early and Late Genes in Leaves of Rice Seedlings at Litate Village, Fukushima

G. Hayashi, J. Shibata, T. Imanaka, K. Cho, A. Kubo, S. Kikuchi, K. Satoh, S. Kimura, S. Ozawa, S. Fukutani,

S. Endo, K. Ichikawa, G.K. Agrawal, S. Shioda, M. Fukumoto and R. Rakwal

J. Hered., **105** (2014) 723-738.

Estimation of  $\beta$ -ray dose in Air and Soil from Fukushima Daiichi Power Plant Accident

S. Endo, K. Tanaka, T. Kajimoto, N.T. Thanh, J.M. Otaki and T. Imanaka

J. Radiation Research, **55** (2014) 476-483.

Isotopic Compositions of Transuranic Nuclides Released by the Fukushima Dai-ichi Nuclear Power Plant Accident: with Emphasis on Cm Isotopes

M. Yamamoto, A. Sakaguchi, S. Ochiai and T. Imanaka

J. Radioanal. Nucl. Chem., **300** (2014) 1045-1052.

Development of On-site Heavy Metal Analysis Method and Technology for Selective Removal of Radioactive Cesium in the Extracts of Designated Wastes (in Japanese)

Y. Fujikawa, H. Ozaki, P. Wei, H. Tsuno, A. Fujinaga, S. Taniguchi, R. Takanami, L. Paul and S. Sakurai  
Proceedings of the 15th Workshop of Environmental Radioactivity, **15** (2014) 277-286.

Measurement of the Displacement Cross-section of Copper Irradiated with 125 MeV Protons at 12 K

Y. Iwamoto, T. Yoshiie, M. Yoshida, T. Nakamoto, M. Sakamoto, Y. Kuriyama, T. Uesugi, Y. Ishi, Q. Xu, H. Yashima, F. Takahashi, Y. Mori and T. Ogitsu  
J. Nucl. Mater., **458** (2015) 369-375.

Estimation of the Contribution of Short-lived Radioiodines to the Thyroid dose for the Public in Case of Inhalation Intake Following the Fukushima Accident

S.M. Shinkarev, K.V. Kotenko, E.O. Granovskaya, V.N. Yatsenko, T. Imanaka and M. Hoshi  
Radiat. Prot. Dosimetry., **164** (2015) 51-56.

Localization Estimation of Ionizing Radiation-induced Abasic Sites in DNA in the Solid State Using Fluorescence Resonance Energy Transfer

K. Akamatsu, N. Shikazono and T. Saito  
Radiat. Res., **183** (2015) 105-113.

## Reviews

Decontamination Technology of Designated Wastes as Specified in Act on Special Measures Concerning the Handling of Radioactive Pollution &#8211; Procedures of the on-site Test (in Japanese)

Y. Fujikawa, H. Ozaki, H. Tsuno, A. Fujinaga, S. Taniguchi, R. Takanami, K. Fujiwara, S. Sakurai and L. Paul  
Environmental & Sanitary Engineering Research, **28(3)** (2014) 127-134.

## 11. Accelerator Physics

### Papers

Precise Determination of Bromine in PP Resin Pellet by Instrumental Neutron Activation Analysis Using Internal Standardization

T. Miura, R. Okumura, Y. Iinuma, S. Sekimoto, K. Takamiya, M. Ohata and A. Hioki  
J. Radioanal. Nucl. Chem., **303** (2015) 1417-1420.

Target Depth Dependence of Damage Rate in Metals by 150 MeV Proton Irradiation

T. Yoshiie, Y. Ishi, Y. Kuriyama, Y. Mori, K. Sato, T. Uesugi and Q. Xu  
Nucl. Instrum. Meth. B., **342** (2015) 166-169.

### Proceedings

Transport of Terahertz-wave Coherent Synchrotron Radiation with a Free-electron Laser Beamline at LEBRA

N. Sei, H. Ogawa, K. Hayakawa, T. Tanaka, Y. Hayakawa, K. Nakao, T. Sakai, K. Nogami and M. Inagaki  
35th International Free Electron Laser Conference, Basel, Switzerland (Aug. 25-29, 2014) 541.

## 12. Others

### Papers

Au Electrodeposition at the Liquid-Liquid Interface: Mechanistic Aspects

A. Uehara, T. Hashimoto and R. A. W. Robert  
Electrochim. Acta, **118** (2014) 26-32.

ASEAN Energy Security: An Indicator-based Assessment

K. Kanchana and H. Unesaki

Energy Procedia, **56** (2014) 163-171.

Risk Assessment of the Intake of Foods and Soil with the Radionuclides and the Air Radiation Dose after the Fukushima Nuclear Disaster

A. Fujinaga, M. Yoneda and M. Ikegami

J. Eng. Gas. Turbine. Power, **136(8)** (2014) 1-7.

Performance Evaluation of High-pressure MWPC with Individual Line Readout under Cf-252 Neutron Irradiation

K. Toh, T. Nakamura, K. Sakasai, K. Soyama and H. Yamagishi

J. Phys.: Conf. Ser., **528** (2014) 12045.

High Linear-energy-transfer Radiation can Overcome Radioresistance of Glioma stem-like Cells to Low Linear-energy-transfer Radiation

Y. Hirota, SI. Masunaga, N. Kondo, S. Kawabata, H. Hirakawa, H. Yajima, A. Fujimori, K. Ono, T. Kuroiwa and SI. Miyatake

J. Radiat. Res., **55** (2014) 75-83.

Effect of Ultraviolet and Radiation on Surface Wettability (in Japanese)

D. Ito, D. Nishi and Y. Saito

Japanese Journal of Multiphase Flow, **27-5** (2014) 555-561.

Hydrogen Trapping under the Effect of W-C Mixed Layers

N. Liu, J. Huang, K. Sato, Q. Xu, L. Q. Shi and Y. X Wang

Nucl. Fusion, **54** (2014) 33013.

Verification of Terahertz-wave Spectrophotometry by Compton Backscattering of Coherent Synchrotron Radiation

N. Sei and T. Takahashi

Phys. Lett. A, **378** (2014) 303-307.

Wide Dynamic Range Neutron Flux Monitor having Fast Time Response for the Large Helical Device

M. Isobe, K. Ogawa, H. Miyake, H. Hayashi, T. Kobuchi, Y. Nakano, K. Watanabe, A. Uritani, T. Misawa,

T. Nishitani, M. Tomitaka, T. Kumagai, Y. Mashiyama, D. Ito, S. Kono, M. Yamauchi and Y. Takeiri

Rev. Sci. Instrum., **85** (2014) 11.

Effect of Particle Size on Risk Assessment of Direct Soil Ingestion and Metals Adhered to Children's Hands at Playgrounds

M. Ikegami, M. Yoneda, T. Tsuji, O. Bannai and S. Morisawa

Risk Analysis, **34(9)** (2014) 1677-1687.

$\alpha$ B- and  $\beta$ A3-crystallins Containing D-Aspartic Acids Exist in a Monomeric State

H. Sakaue, T. Takata, N. Fujii, H. Sasaki and N. Fujii

Biochim. Biophys. Acta., **1854** (2015) 1-9.

## Proceedings

Bee and Wasp Stings: Analysis and Education in University

R. Kuroda, K. Yamamoto, T. Umekage, T. Iimoto and Y. Okubo

1st Asian Conf. on Safety and Education in Laboratory, The University of Tokyo, JAPAN (2014).

Framework of Radiological Safety for Natural Radioactive Materials (NORM/TENORM) and Related Education  
T. Iimoto, R. Hayashi, R. Kuroda and K. Yamamoto  
1<sup>st</sup> Asian Conf. on Safety and Education in Laboratory, The University of Tokyo, JAPAN (2014) .

Publishing Tool for Information of Environment, Health and Safety in Uto쿄  
H. Takizawa, Y. Okubo, T. Iimoto, R. Hayashi, R. Kuroda, K. Yamamoto and R. Dobashi  
1<sup>st</sup> Asian Conference on Safety and Education in Laboratory, The University of Tokyo, JAPAN (2014) .

Basic Research on Radiation Tests Suitable For Nano-Satellites  
T. Tomioka, H. Masui, M. Cho and K. Takamiya  
65<sup>th</sup> Int. Astronautical Congress, Toronto, Canada (2014).

## Books

Synergy in Supramolecular Chemistry  
S. Aoki, M. Zulkefeli, Y. Hisamatsu and M. Kitamura  
CRC, (2015).

Fundamentals of General, Organic, and Biological Chemistry (7th Edition) (in Japanese)  
J. M. MuMurry, D. S. Ballantine, C. A. Hoeger and V. E. Peterson  
Maruzen (2015).

## Reviews

Development of a GPS-based Autonomous Radiation Monitoring System, KURAMA (in Japanese)  
M. Tanigaki  
Chemical Engineering, **VOL.59 No.3** (2014).

DNA Structures  
T. Chatake  
Crystallography in Japan (II), (2014) 218-219.

Development of a GPS-based Autonomous Radiation Monitoring System, KURAMA/KURAMA-II (in Japanese)  
M. Tanigaki  
Collections of the Removal Techniques of Radioactive Materials, (2015).

---

KURRI Progress Report 2014

Issued in July 2015

by the Research Reactor Institute, Kyoto University  
Kumatori-cho, Sennan-gun, Osaka 590-0494 Japan

Tel. +81-72-451-2300

Fax. +81-72-451-2600

In case that corrections are made, an errata will be provided  
in the following webpage:

<http://www.rr.i.kyoto-u.ac.jp/PUB/report/PR/ProgRep2014/ProgRep2014.html>

Publication Team

ETO, Hiroko  
IKEGAMI, Maiko  
INOUE, Rintaro (Subchief)  
KAWAGUCHI, Akio  
MORI, Kazuhiro (Chief)  
NAKAMURA, Hidehito  
NAKATSUKA, Hiroto  
NAKAYAMA, Chiyoko  
OKUMURA, Ryo  
SAITO, Takeshi  
SAKURAI, Yoshinori (Subchief)  
TAKAHASHI, Toshiharu  
XU, Qiu  
YAMAMOTO, Toshihiro  
YOKOTA, Kaori

---